Luiz Alberto Lisboa da Silva Cardoso

Dynamic Inductive Wireless Power Transfer for Lightweight Electric Vehicles

March 2023

Universidade do Minho

Luiz Alberto Lisboa da Silva Cardoso

Dynamic Inductive Wireless Power Transfer for Lightweight Electric Vehicles

Submitted to the Department of Industrial Electronics, in Partial Fulfillment of the Requirements for the Degree of Doctor of Philosophy in Engineering Design and Advanced Manufacturing, in the framework of the Leaders for Technical Industries MIT Portugal Program.

Thesis advisors:

Prof. João Luiz Afonso

Prof. Andrés Augusto Nogueiras Meléndez

March 2023

AUTHOR RIGHTS AND TERMS OF USE BY THIRD PARTIES

This is an academic work that can be used by third parties, if license rules are respected, as well as good and internationally accepted practices, concerning the author's rights and connected rights. These referred license rules are summarized below. If any use of the work is required, in conditions not in agreement if the so indicated license rules, permission should be obtained from the author, via the RepositóriUM of the University of Minho.

Applicable License Terms

Creative Commons Attribution-ShareAlike 4.0 International (CC BY-SA 4.0)

https://creativecommons.org/licenses/by-sa/4.0/

Dynamic Inductive Wireless Power Transfer for Lightweight Electric Vehicles
Luiz Alberto Lisboa da Silva Cardoso – University of Minho

ii

Acknowledgements

Dynamic Inductive Wireless Power Transfer for Lightweight Electric Vehicles
Luiz Alberto Lisboa da Silva Cardoso – University of Minho

iii

Above all, my tender thanks to my parents, Alberto and Edna, always living in my heart, for their love, for their words and their dedicated support. They showed me that love and responsibility are what ultimately makes the world sustainable.

Along this journey, which took much of my time and dedication, I also suffered some major losses, which disrupted my life and my work, and were only surpassed with the support and love from my friends and family. Even then, for every moment I lived, I am thankful, for I could finally learn that the less we have, the better we understand our needs. This change in perspective was a giant leap for me, and helped me consolidate the philosophical basis of my own work, which, hopefully, can be one more small step towards a sustainable future, for all of our kids.

Dynamic Inductive Wireless Power Transfer for Lightweight Electric Vehicles
Luiz Alberto Lisboa da Silva Cardoso – University of Minho

iv

Statement of Integrity

I hereby declare having conducted this academic work with integrity, and I confirm that I have not used plagiarism or any form of undue use of information or falsification of results along the process leading to its elaboration. I further declare that I have also fully observed the Code of Ethical Conduct of the University of Minho.

Dynamic Inductive Wireless Power Transfer for Lightweight Electric Vehicles
Luiz Alberto Lisboa da Silva Cardoso – University of Minho

v

Abstract

The modal shift to electric mobility is perceived worldwide as a great technological advance to reduce the emission of greenhouse gases and air pollution, especially in urban areas. In conjunction with the large-scale adoption of renewable energy sources, the electrification of vehicles is envisaged as an ultimate solution to a zero carbon footprint in transports. However, the per capita consumption levels of raw materials and energy in today's industrialized societies are historically very high, and may constitute a possible menace to the equilibrium of life on Earth, and to the long term economic sustainability of mankind. Even then, the current trends in the electrification of the urban fleet do not yet indicate an effective handling of this more general problem, or even the consciousness for a necessary change in this consumption pattern.

This research was originated based on the perception that, concerning transports and transportation infrastructure, in addition to the electrification technology, it is also highly desirable to reduce the energy expenditure and the allocation of raw materials, for a more sustainable and egalitarian economy. Motivated by this inspiration, we propose, prospect, and demonstrate the technical viability of a new transport mode variant, the human-inductively-powered lightweight electric vehicle (HIPLEV), which is the combination of the relatively new technology of dynamic inductive wireless transfer with the well-established, and environmentally friendly, human-powered pedal vehicles. The new resulting hybrid soft transport mode is not expected to replace standard, purely electric vehicles, in all applications, but, if consistently supported by new urban architectural guidelines, it might help the cities to achieve a more sustainable transportation profile, and improve our quality of life.

Keywords: Electric mobility, human-powered vehicles, lightweight electric vehicles, economic sustainability, smart cities, dynamic inductive wireless power transfer.

Dynamic Inductive Wireless Power Transfer for Lightweight Electric Vehicles
Luiz Alberto Lisboa da Silva Cardoso – University of Minho

vi

Resumo

A progressiva introdução da mobilidade elétrica é percebida, a nível mundial, como um grande avanço tecnológico que permitirá redução na emissão de gases de efeito estufa e na poluição do ar, especialmente nos entornos urbanos. Juntamente com a adoção em larga-escala de fontes de geração de energia renováveis, a eletrificação de veículos é antevista como uma solução definitiva para a anulação da pegada de carbono dos transportes. Entretanto, os níveis de consumo per capita de energia e matérias-primas nas atuais sociedades industrializadas são historicamente muito altos, e também se constituem de uma possível ameaça ao equilíbrio da vida na Terra, e à sustentabilidade econômica da humanidade, a longo prazo. Apesar disso, a tendência atualmente percebida da eletrificação veicular ainda não reflete uma adequada consideração deste problema mais geral, nem mesmo indica a existência de uma conscientização para a necessidade de mudança nesse elevado padrão de consumo.

Para além da eletrificação dos transportes, é então também altamente desejável reduzir-se os gastos energéticos e o consumo de matérias-primas na implementação e operação da infraestrutura de transportes, para uma economia sustentável, e que contemple mais equitativamente toda a sociedade. Alinhado com esse objetivo, este trabalho propõe, prospecta e demonstra a viabilidade técnica de um nova variante de transporte, o veículo à tração humana eletricamente assistido por transferência indutiva de potência (HIPLEV), uma combinação da relativamente nova tecnologia de transferência de potência elétrica sem fios a veículos, por indução magnética, aos veículos de tracção humana – uma solução considerada de baixo nível tecnológico, mas bastante accessível e ambientalmente correta. Este novo meio híbrido de transporte resultante não será expectavelmente empregável em todas as aplicações, mas, se consistentemente apoiado pela adoção de novas diretrizes arquitetônicas urbanas, poderá contribuir para que as cidades atinjam um superior patamar de sustentabilidade nos transportes, e nos propiciem melhor qualidade de vida.

Keywords: Mobilidade elétrica, veículos de propulsão humana, veículos elétricos leves, sustentabilidade, cidades inteligentes, transferência de energia sem fios.

Dynamic Inductive Wireless Power Transfer for Lightweight Electric Vehicles
Luiz Alberto Lisboa da Silva Cardoso – University of Minho

vii

Resumen

La movilidad eléctrica se percibe a nivel mundial como un gran avance tecnológico para reducirse la emisión de gases de efecto invernadero y la contaminación atmosférica, especialmente en las zonas urbanas. En conjunto con la adopción a gran escala de fuentes de energía renovables, la electrificación de vehículos se prevé como una solución para alcanzar una huella de carbono más próxima a cero en la operación de los medios de transporte. Sin embargo, los niveles de consumo per cápita de materias primas y energía, en las sociedades industrializadas hoy, están históricamente muy altos, y también pueden constituir una posible amenaza al equilibrio de la vida en la Tierra, y a la sostenibilidad económica de la humanidad a largo plazo. Aun así, las tendencias actuales en la electrificación de la flota urbana todavía no indican un manejo efectivo de este problema más general, ni siquiera la conciencia de ser necesario un cambio en este patrón de consumo.

Esta investigación se originó en la percepción de que, en materia de transportes e infraestructura de transporte, además de la adopción de la tecnología de electrificación, también es altamente deseable reducir el gasto energético y la asignación de materias primas, para una economía más sostenible e igualitaria. Motivados por esta inspiración, proponemos, prospectamos y demostramos la viabilidad técnica de una nueva variante de medio de transporte, el vehículo de propulsión humana eléctricamente asistido por transferencia inductiva de energía (HIPLEV), que es la combinación de la relativamente nueva tecnología de transferencia inalámbrica de potencia con los vehículos de tracción humana, hoy considerados de baja tecnología, pero respetuosos con el medio ambiente. No se espera que ese nuevo modo de transporte híbrido resultante reemplace a los vehículos eléctricos más pesados, en todas las aplicaciones, pero, si es apoyado por nuevas directivas arquitectónicas urbanas, podría ayudar a las ciudades a lograr un perfil de transporte más sostenible y mejorar nuestra calidad de vida.

Keywords: Movilidad eléctrica, vehículos de tracción humana, vehículos eléctricos ligeros, sostenibilidad, ciudades inteligentes, transferencia de energía inalámbrica.

Dynamic Inductive Wireless Power Transfer for Lightweight Electric Vehicles
Luiz Alberto Lisboa da Silva Cardoso – University of Minho

viii

Contents

Dynamic Inductive Wireless Power Transfer for Lightweight Electric Vehicles
Luiz Alberto Lisboa da Silva Cardoso – University of Minho

ix

Dynamic Inductive Wireless Power Transfer for Lightweight Electric Vehicles
Luiz Alberto Lisboa da Silva Cardoso – University of Minho

x

Dynamic Inductive Wireless Power Transfer for Lightweight Electric Vehicles
Luiz Alberto Lisboa da Silva Cardoso – University of Minho

xi

Dynamic Inductive Wireless Power Transfer for Lightweight Electric Vehicles
Luiz Alberto Lisboa da Silva Cardoso – University of Minho

xii

Dynamic Inductive Wireless Power Transfer for Lightweight Electric Vehicles
Luiz Alberto Lisboa da Silva Cardoso – University of Minho

xiii

Acronyms and Abbreviations

AC	Alternating current
ASL	Auxiliary Scanning LIDAR
BDC	Brushed DC electric motor
BLDC	Brushless DC electric motor
BMS	Battery management system
CIF	Price of good, including cost, insurance, and freight
COTS	Commercial off-the-shelf (system or component available commercially)
CSAIL	(MIT) Computer Science and Artificial Intelligence Laboratory
DC	Direct current
DIWPT	Dynamic inductive wireless power transfer
EAPC	Electrically Assisted Power Cycle, the same as EPAC
EMF	Electromagnetic field
EOM	Electro-optical monitor
EPAC	Electric Pedal-Assisted Cycle (according to EN 15194), the same as EAPC
ETRTO	European Tire and Rim Technical Organization
EU	European Union
EV	Electric vehicle(s)
FEM	Finite Element Method
FIR	Finite impulse response
GEPE	Group of Energy and Power Electronics of Centro Algoritmi, University of Minho
GNSS	Global navigation satellite system
GPS	The Global Positioning System
HF	High frequency band (3 MHz to 30 MHz)
HIPLEV	Human-inductively-powered lightweight electric vehicle(s)

Dynamic Inductive Wireless Power Transfer for Lightweight Electric Vehicles
Luiz Alberto Lisboa da Silva Cardoso – University of Minho

xiv

HPV   Human powered vehicle

ICNIRP   International Commission on Non-Ionizing Radiation Protection

ICS   Inductive Coupling System

IEC   International Electrotechnical Commission

IGBT   Insulated Gate Bipolar Transistors

i-Lane(s)   Inductively electrified lane(s) (for DIWPT vehicular applications)

IMU   Inertial Measurement Unit

IRPA   International Radiation Protection Association

ISO   International Organization for Standardization

IWPT   Inductive wireless power transfer

KAIST   Korea Advanced Institute of Science and Technology

LEV   Lightweight electric vehicle(s)

LF   Low frequency band (30 kHz to 300 kHz)

LIDAR   Light Detection and Ranging

LIMUM   LIDAR and IMU controller module

MDF   Medium density fiberboard

MIT   Massachusetts Institute of Technology

MOSFET   Metal Oxide Semiconductor Field Effect Transistor

OLED   Organic light-emitting diode

OLEV   On-Line Electric Vehicle, from KAIST.

ORNL   Oak Ridge National Laboratory, USA

PATH   Program for Advanced Transit and Highways

PCD   Proximity Coupling Device (an RFID reader)

PEDELEC   Pedal electric cycle.

PICC   Proximity Integrated Circuit Card (an RFID tag)

PMM   Power measurement module

PP   Parallel-parallel (impedance compensation)

Dynamic Inductive Wireless Power Transfer for Lightweight Electric Vehicles
Luiz Alberto Lisboa da Silva Cardoso – University of Minho

xv

PS	Parallel-serial (impedance compensation)
PWM	Pulse width modulation
RFID	Radio Frequency Identification
rms	Root Mean Square
RPEV	Roadway Powered Electric Vehicle
RTK	Real-Time Kinematic
RX	Receiver, reception
SAE	SAE International, formerly known as the Society of Automotive Engineers
SDL	Secondary Data Logger
SHF	Super high frequency band (3 GHz to 30 GHz)
SLAM	Simultaneous localization and mapping
SP	Serial-parallel (impedance compensation)
SS	Serial-serial (impedance compensation)
TX	Transmitter, transmission
UHF	Ultrahigh frequency band (300 MHz to 3 GHz)
ULisboa	University of Lisbon
UMinho	University of Minho
UPorto	University of Porto
USA	United States of America
UVigo	University of Vigo
Wi-Fi	Wireless fidelity - digital wireless communication channel using some of the IEEE 802.11 variant standards.
WPT	Wireless power transfer
ZCS	Zero Current Switching
ZVS	Zero Voltage Switching

Dynamic Inductive Wireless Power Transfer for Lightweight Electric Vehicles
Luiz Alberto Lisboa da Silva Cardoso – University of Minho

xvi

List of Figures

Dynamic Inductive Wireless Power Transfer for Lightweight Electric Vehicles
Luiz Alberto Lisboa da Silva Cardoso – University of Minho

xvii

Dynamic Inductive Wireless Power Transfer for Lightweight Electric Vehicles
Luiz Alberto Lisboa da Silva Cardoso – University of Minho

xviii

Dynamic Inductive Wireless Power Transfer for Lightweight Electric Vehicles
Luiz Alberto Lisboa da Silva Cardoso – University of Minho

xix

Dynamic Inductive Wireless Power Transfer for Lightweight Electric Vehicles
Luiz Alberto Lisboa da Silva Cardoso – University of Minho

xx

Dynamic Inductive Wireless Power Transfer for Lightweight Electric Vehicles
Luiz Alberto Lisboa da Silva Cardoso – University of Minho

xxi

Dynamic Inductive Wireless Power Transfer for Lightweight Electric Vehicles
Luiz Alberto Lisboa da Silva Cardoso – University of Minho

xxii

Dynamic Inductive Wireless Power Transfer for Lightweight Electric Vehicles
Luiz Alberto Lisboa da Silva Cardoso – University of Minho

xxiii

Dynamic Inductive Wireless Power Transfer for Lightweight Electric Vehicles
Luiz Alberto Lisboa da Silva Cardoso – University of Minho

xxiv

Dynamic Inductive Wireless Power Transfer for Lightweight Electric Vehicles
Luiz Alberto Lisboa da Silva Cardoso – University of Minho

XXV

Dynamic Inductive Wireless Power Transfer for Lightweight Electric Vehicles
Luiz Alberto Lisboa da Silva Cardoso – University of Minho

xxvi

Dynamic Inductive Wireless Power Transfer for Lightweight Electric Vehicles
Luiz Alberto Lisboa da Silva Cardoso – University of Minho

xxvii

List of Tables

Dynamic Inductive Wireless Power Transfer for Lightweight Electric Vehicles
Luiz Alberto Lisboa da Silva Cardoso – University of Minho

xxviii

Dynamic Inductive Wireless Power Transfer for Lightweight Electric Vehicles
Luiz Alberto Lisboa da Silva Cardoso – University of Minho

xxix

Symbology

The following symbols express, or are preferably used in association with, the following constants, variables, or concepts, except where otherwise explicitly defined in the text:

Symbols starting with a letter from the Roman alphabet:

A	Ampère (unit of current in the International System of Units).
B	Magnetic vector field, magnetic field density (T).
b_1	External diameter of the $10G1.5mm^2$ cable used in the primary coil windings.
b_2	External diameter of the cable of which the secondary coil winding is made of.
B_G	Time-independent magnetic (vector) field in region $G \subset \mathbb{R}^3$.
C	Capacitance.
c	Ground clearance of the HIPLEV's secondary coil to ground, with the HIPLEV standing in a perfectly upright position.
D	Width of a primary coil.
d	Width of a secondary coil.
$\widetilde{D}$	Heuristic quasi-optimum approximation for the width of the oblong rectangular primary coil that induces maximum voltage on the HIPLEV's secondary coil.
$\bar{d}$	Average width of the secondary coil turns.
D_e	Width of the central lane stripe where the secondary coil within which the secondary coil can be displaced with the maximum nominal transfer power P_E still assured.
d_L	Calibrated reading beam length from the left LIDAR to the (left) corridor wall.
d_R	Calibrated reading beam length from the right LIDAR to the (right) corridor wall.
dB T	Decibel-Tesla - magnetic field unit in decibels (dB), referenced to 1 Tesla.
E	Electric vector field (V/m) or electric potential (V).
F	Faraday (unit of capacitance in the International System of Units).
f	Frequency.

Dynamic Inductive Wireless Power Transfer for Lightweight Electric Vehicles
Luiz Alberto Lisboa da Silva Cardoso – University of Minho

xxx

f_{even}	Even split frequency of a resonant system.
f_{odd}	Odd split frequency of a resonant system.
g	Standard acceleration of gravity on the Earths' surface, 9.81 m/s^2
h	Distance between the parallel support planes for primary and secondary coils.
H	Henry (unit of inductance in the International System of Units).
H	Magnetic field strength (A/m).
h_f	Height of the lane surface above the landing zone surface for the primary coil windings, in the HIPLEV prototype.
I	Electric current.
j	Complex number $\sqrt{-1}$.
J_{B_G}	Jacobian of the vector field B_G.
k	Magnetic coupling coefficient.
L	Inductance.
ℓ	Length of a rectangular coil or a rectangular coil turn.
$\check{\ell}_1$	Estimated length of the oblong coil with rounded extremities that has the same inductance of a rectangular coil with length ℓ_1 and its same width.
ℓ_G	Distance between two consecutive primary coils in the HIPLEV i-lane.
ℓ_P	Length of the oblong primary coil with rounded extremities of the HIPLEV prototype.
M	Mutual inductance.
N	Depending on the context, either an integer number representing the number of turns of some coil or the normal (Gaussian) probability distribution.
P	Power.
$\hat{P}_1$	Estimated power losses on the primary coil.
$\hat{P}_2$	Estimated power losses on the secondary coil.
$\hat{P}_R$	Estimated power losses on the rectifier circuit and DC capacitor filter.
p_d	Pitch distance between two consecutive secondary coil turns in the HIPLEV.
P_E	Maximum regulated power transfer over of a IWPT link.
P_H	Nominal maximum power of a powertrain.

Dynamic Inductive Wireless Power Transfer for Lightweight Electric Vehicles
Luiz Alberto Lisboa da Silva Cardoso – University of Minho

xxxi

P_r Radiated power.

Q Quality factor (of a reactive component).

R Electrical resistance.

$R_{2,AC}$ Estimated AC resistance of the secondary coil in a IWPT configuration.

R_r Radiation resistance.

$\dot{S}$ Phasor representing (total) power.

$\dot{U}$ Phasor U, for any upper-dotted symbol U.

v Velocity (vector).

V Volt (unity of voltage in the International System of Units).

V Voltage.

V_D Voltage drop across a diode polarized with a forward bias voltage.

V_L Nominal DC output voltage of design to the powertrain.

w_B Maximum reference width for a bicycle.

w_C Width of the reference corridor for measuring the lateral displacements of the EOM.

w_e Maximum allowed width of a secondary coil to be installed on the HIPLEV.

w_F Width of a filamentary rectangular oblong primary coil that maximizes the flatness of the induced voltage on a filamentary rectangular secondary coil at the center-alignment point, as the secondary coil is laterally displaced over the primary coil.

w_L Depending on the context, either the minimum recommended paved lane width for the HIPLEV or the distance between opposite external faces of the housing of the electro-optical monitor.

w_P Width of a filamentary rectangular oblong primary coil that maximizes the induced voltage on a filamentary rectangular secondary coil, in center-alignment conditions between primary and secondary coils.

w_T Minimum total lane width recommended for the HIPLEV.

Z Impedance.

Dynamic Inductive Wireless Power Transfer for Lightweight Electric Vehicles
Luiz Alberto Lisboa da Silva Cardoso – University of Minho

xxxii

Symbols starting with a letter from other alphabets:

γ_h	Optimum h/d ratio for maximum linearity of the induced voltage on a filamentary rectangular secondary coil due to a single, infinitely long, filamentary primary conductor.
δ	Electromagnetic skin depth (due to skin effect).
Δt	Time delay.
η	Electrical efficiency.
η_{batt}	Efficiency of the onboard energy storage device, either a battery or a supercapacitor bank, or an association of them.
η_{DC}	An efficiency measure from a DC input voltage to a DC output voltage.
λ_0	Wavelength in free space of electromagnetic wave with frequency f_0.
Λ_1	Estimated incremental distributed inductance along the longitude of the primary coil designed for the HIPLEV (expressed in Henry per meter).
μ	Magnetic permeability.
μ_0	Magnetic permeability of free space.
ξ	Normalized induced voltage on the secondary coil by an oblong primary coil.
ρ_{Cu}	Electric resistivity of copper at 20 C.
φ_{max}	Maximum inclination angle for the HIPLEV.
ω	Angular frequency.
Ω	Ohm (unit of resistance in the International System of Units).
л	Lightweightness coefficient, mass ratio of a vehicle to its payload (the 13th letter of the Cyrillic alphabet, pronounced /elʲ/).
מ	Function representing the inductance of a rectangular coil (the 13th letter of the Hebrew alphabet, pronounced /mem/).
ש	Ratio of secondary to primary phasor currents in a magnetic link (the 21st letter of the Hebrew alphabet, pronounced /ʃɪn/).

Warning: (i) Symbols not listed in this section may find different meanings in different contexts, and their definition will be provided locally at the point of occurrence in the text. (ii) Local symbol definitions have precedence over the symbol definitions provided in this section.

Dynamic Inductive Wireless Power Transfer for Lightweight Electric Vehicles
Luiz Alberto Lisboa da Silva Cardoso – University of Minho

xxxiii

Preface and Dedication

The sparkle over the human-inductively-powered lightweight electric vehicle (HIPLEV) concept was originated from my personal experience as a biker and the observation of the enthusiastic acceptation of the bicycle as a preferred transport by my young children, years ago, when we were living in Rio de Janeiro. In our neighborhood there was an urban lake with slightly more than 7 km of perimeter, around which a bike lane provided our daily connection to the school, the club, shopping and, in the weekends, to our favorite restaurant and other amusing rides. This simple vehicle is fun to use, environmentally friendly, affordable, and more than enough to satisfy a significant part of our urban displacement requirements, if we live in a city with favorable topography, reasonably good weather and adequate cycling infrastructure.

The consolidation of the main ideas for this thesis only came though during the Eurobike 2014, in Friedrichshafen, when I finally realized the enormous potential of the lightweight electrically assisted vehicles. In this short trip, already living in Europe, I was accompanied by my then 10-year-old son, who, after enjoying a demo riding and enthusiastically approving one of the e-bikes at the show, commented how cool would it be if he could just ride "forever", without having to stop for recharging, or anything. One more of his frequent serendipitous but profound reflections...

I quickly evaluated that my son's demand would be completely satisfied if energy could be continuously transferred to the bicycle while it was being ridden. Reviewing the bibliography, it did not take much to come across KAIST achievements with the On-Line Electric Bus, which had recently been successfully prototyped and tested, and to discover all the rising interest in dynamic inductive wireless power transfer. Well, if dynamic induction could work for a bus, it could possibly work for a bike as well. Also, since the basic operation mode for e-bikes and other lightweight pedal vehicles relies on pure human powered traction, I realized that these vehicles could optionally completely dismiss the use of a standard battery, being capable of providing new distinctive sustainable commuting services when wirelessly powered. The research work just followed to prove its viability.

Not being sure about whether the HIPLEV concept will someday be considered for large-scale adoption, this small contribution effort to a sustainable world is then dedicated to all of our kids, who with their serendipity and natural-born wisdom can change the world for much better — as long as they keep faithful to their own inspiration, and remember that some work, often, lots of work, must follow, for ideas do not usually became reality by themselves...

Dynamic Inductive Wireless Power Transfer for Lightweight Electric Vehicles
Luiz Alberto Lisboa da Silva Cardoso – University of Minho

xxxiv

"I would prize every invention of science made for the benefit of all. There is a difference between one invention and another. I should not care fur poisonous gases capable of killing masses of men at a time. I also have no consideration for machinery which is meant either to enrich a few at the expense of the many, or without reason, to displace the labour of the people. The machine should not be allowed to cripple the limbs of man."

Mohandas Karamchand Gandhi (Mahatma Gandhi)

(https://www.mkgandhi.org/)

Dynamic Inductive Wireless Power Transfer for Lightweight Electric Vehicles
Luiz Alberto Lisboa da Silva Cardoso – University of Minho

XXXV

Chapter 1

Introduction

The modal shift to electric mobility is worldwide perceived as a key technological advance to reduce the emission of greenhouse gases and the air pollution, especially in urban areas. In conjunction with the large-scale adoption of renewable energy sources, the electrification of vehicles is envisaged as an ultimate strategy to achieve zero direct greenhouse gas emissions in most transportation applications. However, indirect emissions, those generated in the production and distribution of the vehicles products [1], should also be considered. The levels of per capita raw materials and energy consumption observed in today's industrialized societies are historically very high, and also represent a risk factor for the equilibrium of the environment [2]. Concerning electric mobility, the trends in the electrification of the urban fleet by the replacement of internal combustion engine vehicles, by electric vehicles with even more powerful engines, do not indicate a change in this consumption pattern.

For a desirable sustainable economy and social equality, it then seems also important to reduce the total energy expenditure, the consumption of raw materials in transports, and the associated carbon footprint of the manufacturing of vehicles and vehicular infrastructure. Based on this perception, this work proposes and prospects the viability of combining the newly developed technology of dynamic inductive wireless power transfer with the well-established, relatively old, but environmentally friendly, human-powered vehicles. The design approach is strongly interdisciplinary, requiring a joint analysis of human powered vehicles and different other technologies for its idealization, implementation, and evaluation. The final result is the conceptual development and prototyping of a new transport mode variant, the human-inductively-powered lightweight electric vehicle (HIPLEV), which is shown to be technologically viable, and a promising sustainable response for urban transportation, particularly in commuting applications.

Figure 1 depicts the context of the thesis research as a germinating plant, which, in its leaves, shows the main results achieved by the work, namely:

- The theoretical analysis of Inductive Wireless Power Transfer (IWPT) and Dynamic IWPT (DIWPT) systems, bringing new interpretations and tools to the analysis of the basic IWPT

Dynamic Inductive Wireless Power Transfer for Lightweight Electric Vehicles
Luiz Alberto Lisboa da Silva Cardoso – University of Minho

1

compensation topologies, and new theorems that help the magnetic field design of the cross-section of oblong inductively electrified lanes (i-lanes).

- The HIPLEV concept itself, a new urban transport mode variant, based on lightweight electrically assisted human-powered vehicles.

- A successful laboratory implementation of the first known HIPLEV prototype, which was built by the adaptation of a popular Electric Pedal-Assisted Cycle (EPAC) type bike.

- A new measurement technique and prototype tool system, to help evaluate the behavior and performance of DIWPT systems, when the vehicle misalignment from the center of lane is varied under dynamic conditions.
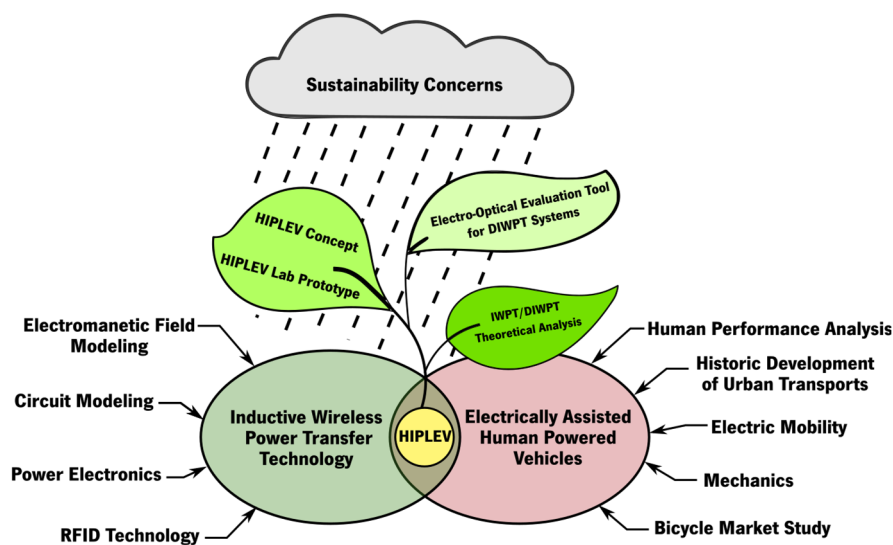
Figure 1: Contextual elements of the thesis research and the results achieved.

The research was supported by five institutions in three countries. In an initial stage, along 2014 and up to early 2015, it was conducted at the University of Minho (UMinho), University of Porto (UPorto) and the University of Lisboa (UL/IST), in Portugal, covering base studies and initial considerations. This study phase eventually led to the top-down definition of the thesis research theme in the middle of 2015. After a few prototype implementations at the University of Minho, to refine the goals of the work, a research stay was started at the University of Vigo (UVigo), Spain, which lasted until the end of 2017. There, for about two and a half years, prototypes of i - lanes for lightweight electric vehicles (LEV) and the adaption of an e-bike with an inductive energy harvest system were accomplished and evaluated. In 2018, the research was hosted by the Computer Science and Artificial Intelligence Laboratory (CSAIL) of the Massachusetts Institute of Technology (MIT), United States, where the conceptualization and development of an electro-optical equipment for aiding the dynamic evaluation of i-lanes and vehicles was accomplished.

Dynamic Inductive Wireless Power Transfer for Lightweight Electric Vehicles
Luiz Alberto Lisboa da Silva Cardoso – University of Minho

2

Theoretical analysis and reflections on all results obtained during the experimental phase of the work were matured into the proposition of the HIPLEV, with all work translated into this final thesis report, with the conclusion that the proposed concept is valid, technologically viable and constitutes a promising non-exclusive adequate sustainable response for urban transportation, particularly in commuting applications.

Although different areas of knowledge were conjugated in this research, its focal subject is the magnetic field design for dynamic inductive wireless power transfer for electric mobility. Circuit theory, power electronics and mechanical analysis were regarded as support tools and minimally developed, whereas essential. Thus, in the experimental work, maximum effort was made on the reuse of existing electronics modules, with the necessary adaptations, when required, leaving circuit optimization for a follow-up development work. An exception to this was the development of the electro-optical tool for DIWPT evaluation, that, unparalleled in its approach, required specific software and electronics design to be fully implemented.

In the following sections of this introductory chapter, the objectives of the thesis research are asserted, and its contributions summarized, in association with the publications so far released. The contents of the other chapters are also commented, to facilitate an organized reading of the thesis, allowing readers to directly jump into the sections of their major interest.

1.1   Objectives, Approach and Contributions

The main objective of this doctoral thesis is to explore aspects of the application of the technology of dynamic inductive wireless power transfer to electrically assisted cycles, such as e-bikes, e-trikes, and other lightweight human powered vehicles. This association, unaddressed in the literature by the time of our first publication, led us to propose the creation of a new variation of the cycling transport, one that draws less resources for its implantation and less electric energy for its operation, than alternative heavier urban traffic, either electric or fuel-based. This was accomplished by:

- The comprehensive study of the IWPT technology, with the identification of the design paradigms that would best fit the requirements of DIWPT for lightweight, lower power, electric transports.

- The review of the evolution of the technology and performance limits of pedal-powered cycles, specifically, bikes and velomobiles.

Dynamic Inductive Wireless Power Transfer for Lightweight Electric Vehicles
Luiz Alberto Lisboa da Silva Cardoso – University of Minho

3

- The study of recent data of the bike and e-bike markets, aiming a future perspective for the popularity and availability of e-bikes among the population, to support their use as a leverage for a possible introduction of the HIPLEV, and a justification for the necessary investment in the electrification of bike lanes.

- The adaptation of an e-bike with an especially designed harvesting system that is able to draw energy from such a compatible (and also especially designed) inductive lane (i-lane), providing the experimental evidence of the feasibility of the concept.

- The initial stationary evaluation and of the above design.

- The development of a new specialized tool that can facilitate the detailed dynamic performance analysis of DIWPT systems such as the HIPLEV. In order to limit the total effort and resources allocated to the thesis research, this actual, detailed data collection was left for future work though, as it will require a more realistic test range, with a longer i-lane segment, outdoors, involving road construction works.

1.2   Publications

The publications in international journals, book chapters and international conferences, which have resulted from the research activity associated to this work, are listed below, each followed by a short commentary linking the publication with some contribution of this work. The first five of these publications contain the key ideas related to the thesis research, while the other three consist in collateral results, as a consequence of the involvement in the study of accessory technologies to the DIWPT design. The theorems developed and some implementation details, however, remain yet undisclosed, and shall be published only after reviewed and approved by the thesis committee.

[3]   L. A. L. Cardoso, M. C. Martinez, A. A. N. Melendez, and J. L. Afonso, "Dynamic inductive power transfer lane design for e-bikes," in *2016 IEEE 19th International Conference on Intelligent Transportation Systems (ITSC)*, 2016, pp. 2307–2312.

In this first publication, the design of an inductive lane for e-bikes and the possibility of the reuse of this combination of technologies in other lightweight EV was reported, together with the electrification and adaption of a standard bike to harvest energy from that lane, by using inductive wireless power transfer. Key point in that design was the installation of a secondary coil around the rear wheel of the bike, in such a way that it neither interferes with the pedaling nor with the bike maneuvering, while making turns or going up and down smooth ramps. Special emphasis

Dynamic Inductive Wireless Power Transfer for Lightweight Electric Vehicles
Luiz Alberto Lisboa da Silva Cardoso – University of Minho

4

was given on reporting experimental results, proving that it is viable to achieve 250 W of net power transfer between the i-lane and the powertrain of an e-bike over a 27 cm-wide center strip of the lane, more the 20 cm width that is minimally required for an average cyclist to keep balance while riding a bike on a straight line at speeds above 11.3 km/h [4]. Further, the power transfer can be increased up to 400 W, along all the width a 20 cm-wide central strip, within which the rider remains most of the time, when pedaling.

The extra power transferred above the minimum required 250 W permits extra energy to be stored on board of the vehicle, in either a standard battery or a short-term storage supercapacitor, which will keep the vehicle electrically assisted at 250 W, even when traversing the gaps in between multiple such electrified path modules, where no energy from the lane is available. This power level of 250 W was chosen by design because it is the nominal maximum power level of assistance to the powertrain recommended for an EPAC class e-bike in the European Union [5]. By having 400 W available in the center strip, transient power demands in excess of 50% of the base 250 W value, which can be easily observed in real systems (resulting in an instantaneous power demand in excess of 375 W), can also be more easily accommodated. The designed lane was not optimized for efficiency or misalignment tolerance, but rather, all effort was directed to making the prototype as simple as possible, avoiding the use of either expensive software magnetic core materials or true litz wire, in both primary and secondary, to facilitate an implementation that could simply validate the concept.

Under these conditions, an electrical efficiency of 64% was initially achieved at the center of the lane and reported in the paper. This efficiency was latter improved to above 65%, by fixing the workbench setup, and it is believed to be possibly further improved to a figure closer to 70%, just by a circuit optimization design phase. But even at this relatively low efficiency level, the HIPLEV overall energy consumption can be much less than that of standard road electric vehicles, for the same payload, in urban and commuting transportation tasks. Also, the system affordability of the HIPLEV is expected to be brought into a cost range compatible with that of e-bikes and bike lanes.

Last, a new technique was proposed for synchronizing the energization of the primary coils in the presence of a vehicle, using near-field RFID. After some modeling improvements and further testing, this technique was detailed in a second paper, in the following year.

[6]   L. A. L. Cardoso, J. L. Afonso, M. C. Martinez, and A. A. N. Meléndez, "RFID-Triggered Power Activation for Smart Dynamic Inductive Wireless Power Transfer," in *IECON - The Annual*

Dynamic Inductive Wireless Power Transfer for Lightweight Electric Vehicles
Luiz Alberto Lisboa da Silva Cardoso – University of Minho

5

Conference of the IEEE Industrial Electronics Society (IES), October 29 - November 1, 2017, 2017.

While in the first paper the emphasis was on the power transfer design, in this second paper a more detailed description is given on the technique invented to switch the power of the primary coils on and off. This was accomplished by placing an RFID reader at the extremity of each primary coil, which is the entry point for a one-way traffic. This RFID reader was then used to detect and identify an RFID tag placed on the secondary coil, installed on the e-bike. A microcontroller, having the continuously updated information coming from the RFID reader, detects the presence of the vehicle at the beginning of the coil run, verifies that the tag identifier is in association with an authorization to drive power from the lane, and, within about 30 ms, triggers the primary coil power on. The power excitation of the primary coil is later turned off irrespectively of the RFID reading status, after the vehicle has passed over the coil, when the power demand is detected to have been reduced below a pre-determined level, or when a time-out parameter is reached.

Because the magnetic field from the power coils can interfere with the RFID readings, and even be destructive to the RFID circuitry, some modifications were made to the RFID circuitry itself, and special attention was given on the collocation of the coils: On the lane side, the primary power coil and RFID reader coil were positioned in magnetic orthogonality to each other, the same technique being used on board of the vehicle to position the RFID tag coil with respect to secondary coil, which can also generate a strong magnetic field. The decoupling of the RFID reader coil from the secondary power coil, and of the RFID tag coil from the primary power coil, could be achieved by frequency separation only (the power transfer occurs around 50 kHz, and the RFID works at 13.56 MHz), due to the relatively greater distance between the coils in these pairs. The level of separation achieved for the power and RFID systems was enough to prevent the power coils from damaging the RFID sensor and tag, but not enough to prevent occasional interference in the RFID data transfer. However, in the scheme used, this was not an issue, because the RFID was used only to trigger WPT initiation, with all valid RFID readings performed when the primary coil being crossed is still off, and the RFID tag is far enough from other neighbor primary coils that could possibly be energized. At the time of detection, the secondary is then not yet energized as well, thus, also unable to induce noise on the RFID reader. Due to speed limitations of the RFID reading code implemented, the maximum transit speed of a vehicle that would still guarantee virtually 100% vehicle detection was estimated to be in the range of 30 km/h to 35 km/h. While this is not a high speed, relatively to standard road traffic, it is entirely compatible with the maximum speed at which an EPAC is specified to receive electrical assistance, which is 25 km/h.

Dynamic Inductive Wireless Power Transfer for Lightweight Electric Vehicles
Luiz Alberto Lisboa da Silva Cardoso – University of Minho

6

[7]   L. A. Lisboa Cardoso, D. Fourie, J. J. Leonard, A. A. Nogueiras Meléndez, and J. L. Afonso, "Electro-Optical System for Evaluation of Dynamic Inductive Wireless Power Transfer to Electric Vehicles," in *Green Energy and Networking*, 2019, pp. 154–174.

The characterization of power transfer as a function of the in-lane lateral alignment of a vehicle is crucial to guarantee that the DWIPT to the EV occurs at a designed nominal power levels and time pattern. In [3], the lateral misalignment effects were measured with the e-bike stationary. This provided a good system characterization, since the quasi-stationary approach for DIWPT holds at the speed and dimensions of terrestrial EVs, at the induction frequency range used. However, it was perceived as highly convenient to be able to evaluate the DIWPT under real maneuverability conditions of an EV, which, depending on the circuit implementation, might potentially interfere in the dynamical performance. In this way, thinking of new future circuit implementations, the design and development of a special opto-electric instrumentation system was undertaken. This system was successfully completed, and the results reported in this third publication.

The designed system simultaneously collects the EV's dynamic misalignment, angular attitude, and power data, while it is running over DIWPT lanes. The system is based on LIDAR, inertial and power sensors, installed on board of the vehicle, which are synchronously read, and their data time-tagged and transmitted to a ground-fixed analysis station, by means of a customized UHF relay link. The hardware and software developed can handle the collection of 6 kilo-samples per second of simultaneous position and attitude of the e-bike, synchronized with electrical data showing the received power and the electric status of the powertrain. Although the system was inspired by the case of instrumenting the developed HIPLEV prototype, its characteristics would fit a wider class of vehicles, not being limited, for instance, to the lower speed of bikes. The system was successfully tested indoors, using a non-electric bike, and became an independent and more general contribution of the thesis work to the development of DIWPT systems. As the next step a full outdoor DIWPT lane for electric bikes would have to be built to allow the dynamic evaluation of system developed in [3] and [6], but it was not possible to include this development effort in the thesis framework, due to time and resources limitations, and this was left as a recommendation for a future work.

[8]   L. A. L. Cardoso, A. A. N. Meléndez, L. A. S. B. Martins, and J. L. Afonso, "Human-Inductively Powered Lightweight Electric Vehicles: Sustainable Transportation for the Smart City," in Proc. 4th International Conference on Energy and Environment: bringing together Engineering and Economics, 2019, pp. 185–190.

In this paper, the concept of the Human-Inductively Powered Lightweight Electric Vehicle (HIPLEV) and its perspective applications are introduced, which, ultimately, is the application for the results achieved in [3] and [6], the design of an inductively powered e-bike and its i-lane. The HIPLEV is proposed in the quest for energy conservation and more sustainable personal transportation. It opens unprecedented application possibilities for hybrid human-powered lightweight electric vehicles, such as e-bikes, electric rickshaws and similar lower mass, lower power vehicles. Their combined use with dynamic inductive wireless power transfer lanes is predicted to deliver sustainable urban and commuting transportation services, constituting an alternative to heavier personal cars and even to public transports, in many application contexts.

[9]   J. A. Afonso, H. G. Duarte, L. A. L. Cardoso, V. Monteiro, and J. L. Afonso, "Wireless Communication and Management System for E-Bike Dynamic Inductive Power Transfer Lanes," Electronics, vol. 9, no. 9, p. 1485, 2020.

This article resulted from the investigation and prototype implementation of a simple Wi-Fi - based management system for inductive lanes specifically proposed for e-bikes in [3] and [6], and extends the basic authorization schema initially proposed for energizing the primary coils of the lanes. While in the first implementation of the system the authorization was granted via enquires to a fixed, pre-loaded, local list of valid vehicle identifiers, in [9] this list can be dynamically updated via message exchanging with a central server that keeps a database of vehicles. This opens the path for future implementation of higher application layers that, for instance, will be able to monitor, authorize the safe handling of a large number of vehicles. It would also permit toll collection on large scale lane systems for HIPLEV's – although the author would rather prefer the system to evolve, in the future, into a toll-free, city-provided infrastructure for transport, as a foment for social equality, much in alignment with the cycling philosophy.

[10] V. Monteiro, J. A. Afonso, T. J. C. Sousa, L. L. Cardoso, J. G. Pinto, and J. L. Afonso, "Vehicle Electrification: Technologies, Challenges, and a Global Perspective for Smart Grids," in *Innovation in Energy Systems*, T. S. Ustun, Ed. Rijeka: IntechOpen, 2019.

In this book chapter, a general survey of vehicle electrification technologies is provided, where the author's main contribution was the writing of section 4, "Vehicle electrification: a comprehensive perspective of wireless charging systems."

[11]   L. A. L. Cardoso, V. Monteiro, J. G. Pinto, M. Nogueira, A. Abreu, J. A. Afonso, J. L. Afonso, "Design of an intrinsically safe series-series compensation WPT system for automotive LiDAR", MDPI Electronics, vol. 9, no.1, p. 86, Jan. 2020, ISSN: 2079-9292, DOI: 10.3390/electronics9010086.

In this article, a practical design methodology for SS-compensated IWPT topologies exhibiting frequency splitting, where the magnetic coupling coefficient is constant (as described in section 2.5.2), is proposed. In this solution, the overloading of the primary circuit is avoided, in case of incidental unloading of the secondary, what makes the system intrinsically safe. Instead of using the principal resonance frequency f_0, the operation point is set closer to the higher resonance split frequency f_{even}, with the equivalent load resistance R_L seen by the secondary set to a value above that required for maximum power output at that frequency. The solution was successfully used to build a prototype of a wireless power supply for a LIDAR unit, revealing a good balance between efficiency, safety, and flexibility of employment. Also, as part of the development, a robust method for experimentally evaluating the power transferred over the IWPT air-gap was derived, based on the direct synchronous measurement of primary and secondary currents, and their FFT decomposition into harmonic components.

[12]   J. L. Afonso, L. L. Cardoso, D. Pedrosa, T. Sousa, L. Machado, M. Tanta, V. Monteiro, "A Review on Power Electronics Technologies for Electric Mobility", MDPI *Energies*, vol. 13, no. 23, p. 6343, Dec. 2020, DOI: 10.3390/en13236343.

In this article, a general survey of the power electronics for application in electric vehicles is provided, where the author's main contribution was given in section 2.2, "Inductive Wireless Battery Charging", presenting the basic theory, the current achievements, and the trends in the application of both stationary and dynamic inductive wireless power transfer.

1.3   Organization of the Thesis

In this first chapter, a brief presentation of the motivation for the research, a summary of the methodological approach used, the contributions and publications achieved along the research are provided in the former sections.

Chapter 2 brings the essential technical background for the design of inductive wireless power transfer (IWPT), which is being progressively more used in recent years, and it is expected to be consolidated as one of the standard interfaces for stationary vehicular charging. Effort was

Dynamic Inductive Wireless Power Transfer for Lightweight Electric Vehicles
Luiz Alberto Lisboa da Silva Cardoso – University of Minho

9

made to explain basic circuit concepts in order to facilitate the reader whose background is mostly related to transportation systems. In addition to theory, some simulations and experiments are punctually provided to illustrate the main concepts. Although the subject is already extensively covered by recent literature, new graphical tools are introduced for visualization of IWPT parameters, which shall help in design procedures.

In Chapter 3, the theory, some of the most relevant concepts and prior designs and developments in the application of IWPT to moving objects, known as dynamic inductive wireless power transfer (DIWPT), are introduced. Design strategies and parameters are discussed, together with the presentation of some of the most interesting concepts and prototype implementations of DIWPT observed in the literature. In section 3.6.3, some theorems concerning DIWPT based on oblong primary coils are derived, that are crucial to the design and experimental development achievements reported in Chapter 5.

Chapter 4 brings into focus the Lightweight Electric Vehicles (LEV), highlighting their possible role as a complementary resource in the urban sustainable development. This is succeeded by one of the main thesis statements, which is the usefulness of the association of hybrid electric-human-powered lightweight vehicles with the imminently available DIWPT technology. General design requirements and considerations are given, in preparation for the design and characterization of the prototypes implemented in Chapter 5.

Chapter 5 describes the power transfer design for the HIPLEV, and its initial stationary evaluation, which can be considered the most critical aspect for proving the feasibility of the HIPLEV concept, and the main contribution of this thesis research. This previously unseen design method developed can be applied to other DIWPT applications as well, where the electrical y mechanic characteristics of the EV to be powered are imposed to the problem. Chapter 5 also describes a new near-field wireless power control variant scheme, based on the reuse of RFID hardware and software protocols, which can be used by the HIPLEV. Chapter 5 extensively uses previous art and new theoretical analysis reviewed and developed in Chapters 2 and 3, to satisfy the HIPLEV requirements, identified in Chapter 4. The experimental results achieved reveal the technical viability of the HIPLEV concept. The vehicle adapted in this first HIPLEV prototype is the most emblematic and par excellence representative of the LEV, the standard upright two-wheel e-bike, which is also one of the most difficult of them to adapt, due its unique mechanic features. The conclusion is, if the concept can work with upright bikes, it can work even better with other more refined cycle types, such as recumbent faired velomobiles. Some other important questions,

Dynamic Inductive Wireless Power Transfer for Lightweight Electric Vehicles
Luiz Alberto Lisboa da Silva Cardoso – University of Minho

10

such as the full EMF exposure compliance and the economic evaluation of HIPLEV, however, are not in the focus of this work and were left for future research.

Chapter 6 describes a general electro-optical instrumentation technique, conceived for dynamically testing a wide class of DIWPT configurations, including the HIPLEV. After the main results of the thesis were conquered, as reported in Chapter 5, a prototype instrument, based on the idea, was also developed, and submitted to initial stationary power tests and dynamic positioning tests, using a non-electric bicycle as the testing platform. Favorable experimental results were also obtained, indicating that the proposed technique permits the dynamic characterization and evaluation of DIWPT performance, concerning the simultaneous measurement of electrical parameters and dynamic misalignment tolerance, which is recognized as one of most critical aspects in DIWPT applications for land transports.

In this manner, except by the common application point of view, results in Chapter 6 are entirely independent from the main results in previous chapters. It was included in this thesis not only due to its originality and pertinence to the development of DIWPT configurations, but also because it is a promising low-cost precision tool to conduct future dynamics tests of HIPLEV systems, which are deemed as necessary. A graphic description of the interdependence of the Chapters is shown in Figure 2, and might help the reader navigate through the thesis.

At the beginning of each of these chapters, a short synopsis is provided, to help contextualize the reader and, as much as possible, to facilitate the independent reading of different chapters. In Chapter 7, a summary of the main contributions achieved is provided, together with the conclusions driven from the work accomplished. Finally, some suggestions for future investigative work are also presented.

More than 90% of the other following pages of this thesis were written to review and develop the mathematical insight and algorithms used to solve the DIWPT requirements and other engineering problems associated to the implementation and rigorous testing of HIPLEVs. However, it is in Chapter 4 where the facts and thoughts that inspired the mathematical development of this thesis are briefly recollected.

According to the reader's own experience and background, either more or on the electrical engineering field or more on transport systems, the preferable order for reading the thesis chapters might be different, with Chapter 4 alternatively coming before Chapter 2 and Chapter 3.

Dynamic Inductive Wireless Power Transfer for Lightweight Electric Vehicles
Luiz Alberto Lisboa da Silva Cardoso – University of Minho

11

**Chapter 1
(Introduction)**

**Chapter 2
(IWPT)**

**Chapter 4
(The HIPLEV Concept)**

**Chapter 3
(DIWPT)**

**Chapter 5
(DIWPT Design,
Lab HIPLEV Protototype
Power Transfer Tests)**

**Chapter 6
(Electro-Optical Monitor)**

**Chapter 7
(Conclusion)**

Thesis Research Scope
Future Research Work

EMF Protection Design Refinement

Pilot Outdoors Lane for HIPLEV

Dynamic Tests of the HIPLEV

Economic Impact Evaluation

Urban Architecture Review

Figure 2: Organization and interdependence of the thesis chapters.

Dynamic Inductive Wireless Power Transfer for Lightweight Electric Vehicles
Luiz Alberto Lisboa da Silva Cardoso – University of Minho

12

Chapter 2

Inductive Wireless Power Transfer

In this chapter a review of the concept, some historic milestones, and the most important theoretical aspects of this technology are presented. Some state-of-the-art applications and achievements are also illustrated, in preparation for the discussions of the next chapter. Portions of the text and some of the figures in this introductory chapter were extracted or adapted from the author's contributions to [10], [11] and [12].

Throughout the literature, the Inductive Wireless Power Transfer (IWPT) is either simply referred as Inductive Power Transfer (IPT) or Wireless Power Transfer (WPT) as well. This phenomenon, that results from the interaction between two or more non-galvanically coupled electric circuits, by means of their magnetic field, was early observed by Michel Faraday in 1831, while experimenting with an "induction ring", which was actually a toroidal transformer of iron core [13]. The same phenomenon was later exploited by Nikolas Tesla, by using air core resonant coils at higher frequencies, to achieve very high voltages in his lightening demonstrations. While the development of electric transformers using ferromagnetic cores became one the foundations for the distribution of alternated current at 50 and 60 Hz, the use of air core configurations for power applications, for many decades, remained restricted, due to the difficult of building efficient and powerful electrical oscillators at higher frequencies.

With the development of solid-state power electronics, it became progressively more practical to implement efficient circuitry to drive primary coils at higher frequencies and power levels. The subject regained increasingly attention in the 1990s [14], and a great publicity along 2007, with the publication of the experimental achievements of Kurs, Karalis, and others [15] [16] at the Massachusetts Institute of Technology, in which a bulb attached to a receiver secondary coil was wirelessly lightened with 60 W at 40% electric efficiency, 2 m away from the transmitter primary coil. The distance in between coils was 4 times larger than the 50 cm diameter of the coils, was small enough to prevent a large power loss in electromagnetic radiation at the 9.9 MHz frequency employed, although incompatible with current EMF safety recommendations [17]. In these last ten years, IWPT became a technology of wide interest in the engineering community, frequently as a means of wirelessly recharging batteries of mobile appliances.

Dynamic Inductive Wireless Power Transfer for Lightweight Electric Vehicles
Luiz Alberto Lisboa da Silva Cardoso – University of Minho

13

2.1 Magnetic Induction

Cored inductive power transfer is a popular technology that has been extensively used since the electric transformers have been invented [18], and it is based on the magnetic induction effect earlier observed and explored by Michael Faraday in 1831 [19] [20]: When two coils are wound around a body of magnetic material (the "core"), their electrical behaviors are mutually interdependent. This happens in such a way that energy can be exchanged between the coils and, ultimately, between the circuits they are connected to, by means of a commonly shared magnetic field. This is not itself an invention, but rather, a natural phenomenon that is easier to observe when the core material has a high magnetic permeability, but that also occurs even if the core is constituted by air or, simply, by vacuum.

After Faraday's work, James C. Maxwell developed a theory [21] that, further than consolidating all the mathematical relations between electrical and magnetic fields, predicted the existence of electromagnetic waves, that could potentially make an electric circuit radiate energy to the free space, irrespectively of the existence of another circuit to sense that energy.

In a sequence of experiments from 1886 to 1889 [22], while seeking evidence for the electromagnetic waves predicted by Maxwell, Heinrich R. Hertz first came across IWPT, by realizing that it was possible to produce a spark in between the terminals of a Riess coil, when switching electric current in another of these coils, positioned close to the first one, in a parallel plane [23]. This short-range phenomenon, which can be purely credited to magnetic induction, constituted a variant of the "cored" induction, discovered by Faraday in 1831, in his ring transformer experiment. In the latter cases, where there is no solid material to serve as a path for the magnetic field all the way between the two coils, the pair of coils form an "air-gapped" magnetic coupling, and the phenomenon is often referred to as "wireless" power transfer (WPT) or, more precisely, inductive wireless power transfer (IWPT).

Soon it was realized that, in IWPT, the transmission of energy was not 100% efficient, the losses being later explained by (i) the energy dissipated in the electrical resistance of the conductors of both coils; (ii) the energy dissipated in the core material (if not air-gapped), that can be due to either induced parasitic (eddy) currents or magnetic reluctance; and (iii) the energy that is radiated to free-space by the coils. All these losses vary with the working frequency. Noticeably, the frequency dependency of conductive losses in (i) is due to skin and proximity effects [24], that results from the interaction of the conductor with the magnetic fields respectively generated by the current passing on that same conductor and other nearby conductors, making the current

Dynamic Inductive Wireless Power Transfer for Lightweight Electric Vehicles
Luiz Alberto Lisboa da Silva Cardoso – University of Minho

14

distribution uneven along the conductive elements in the cross-section, and thus, increasing the apparent resistance of the coil windings.

2.2   Near Field versus Far Field Electromagnetic Interaction

One of the critical requirements for inductive power transfer by magnetic resonance is that the coils operate in a low enough frequency, so that the energy they lose to the environment by electromagnetic radiation is negligible. This condition is called near field operation and it is the intended operational mode for IWPT systems. In order to be achieved, the dimensions of the coils must be significantly less than the wavelength associated to the frequency of the current feeding the coils. When the dominant part of the energy is otherwise transferred by radiation, the electromagnetic interaction between two antennas is named of far field interactions, which is used in standard radio-communication systems, but is not the intended operation for IWPT systems.

Although some WPT configurations can be devised to operate in the radiative near-field (Fresnel) transition region, resulting in improved efficiencies over the standard far-field WPT configuration [25], the achievable efficiency level in near-field IWPT is commonly higher than either far-field configurations. In addition, in all far-field configurations, part of the energy is also radiated to unwanted directions and targets, potentially causing interference in other systems.

Because of these conditions, in most high-power WPT designs the near-field WPT operation is preferred, whenever the relative distance of the between the transmitter and receiver antennas can be relatively small, compared to the size of the largest of these antennas. To ensure that any particular WPT configuration operates in near-field operation, it is necessary to keep the energy radiated by the antennas to negligible levels.

The power radiated by an antenna can be calculated by first estimating its radiation resistance R_r. The power radiated by the antenna, P_r, is then expressed by:

$$P_r = R_r\, I_{rms}^2 \tag{2.1}$$

where I_{rms} is the rms current feeding the antenna at frequency f_0, corresponding to the wavelength λ_0.

The radiation resistance of loop antennas of a total length much smaller than the wavelength in free space associated to the current feeding that loop can be approximated by the radiation resistance R_r of a circular loop antenna with the same loop area, A_0 [26], which is given in [27]:

Dynamic Inductive Wireless Power Transfer for Lightweight Electric Vehicles
Luiz Alberto Lisboa da Silva Cardoso – University of Minho

15

$$R_r \;=\; 320\,\pi^4 \left(\frac{N\,A_0}{\lambda_0^2}\right)^2 \Omega\,, \tag{2.2}$$

where N is the number of turns of the antenna and λ_0 is the wavelength of the current traversing the antenna, which can be assumed to be constant in amplitude along the antenna in these relatively small antennas, and therefore equal to the current feeding the loop.

For instance, if the primary induction coil is considered to be perfectly rectangular, with length and width respectively a and b, its radiation resistance and the radiated power P_r of the primary loop can be approximated respectively by (2.3), directly derived from (2.2):

$$R_r \;=\; 320\,\pi^4 \left(\frac{N\,a\,b}{\lambda_0^2}\right)^2 \Omega \tag{2.3}$$

As an example, if a single-loop (single turn) primary coil is 0.5 m wide and 4 m long, and operates at the frequency of 100 kHz, the associated wavelength is 2997.9m, its radiation resistance is approximately 1.5436×10^{-9} Ω and, at loop current of 100 A rms, it will radiate only 15.4 µW. The same coil operating at the lower frequency of 85 kHz would radiate 8.1 µW, and, at 50 kHz, only 1 µW, as summarized in Table 1, and this power value that would further decrease with the fourth power of the frequency. If a secondary coil is being induced by a primary coil, the former will also be subjected to radiation losses, which are similarly calculated.

Table 1: Power radiated by a 0.5 m wide x 4 m long coil at different frequencies and current levels.

Current (A rms)	Radiated Power (µW)		
	at 50 kHz	at 85 kHz	at 100 kHz
50	0.2	2.0	3.9
75	0.5	4.5	8.7
100	1.0	8.1	15.4

The radiated power is an important parameter to control in IWPT design, not only for the system efficiency, but principally, for safety and electromagnetic compatibility issues, as the system is not expected to cause electromagnetic interference in other systems using the same band of the spectrum. Power levels in the order a few µW, as those found in Table 1, however, would rarely interfere with other circuitry away from the radiating primary coil because, at this low frequencies, the circuitry subject to receiving this power as an interference signal would have to be of large dimensions, in the other of the wavelength, to exhibit a significative antenna gain, and be capable of capturing a significant amount of the radiated power.

Dynamic Inductive Wireless Power Transfer for Lightweight Electric Vehicles
Luiz Alberto Lisboa da Silva Cardoso – University of Minho

16

The radiated power can thus be limited by a priori limiting the maximum current, frequency, and dimensions of the primary coils in an IWPT design, or it can be otherwise checked and reduced along the optimization phase of the design. If many primary coils distributed in a region of the space are coherently excited at the same frequency, the power incident on a given receiver may add-up by constructive interference, and this may constitute a further concern for the IWPT design.

2.3 Principles of Inductive Wireless Power Transfer

In both "cored" or "wireless" versions, when submitted to sinusoidal oscillations of sufficiently low frequency f_0 (i.e., producing a negligible radiated power), the magnetic coupling can be modeled in terms of phasors, by ideal linear circuit components, as shown in Figure 3.

(a) (b)
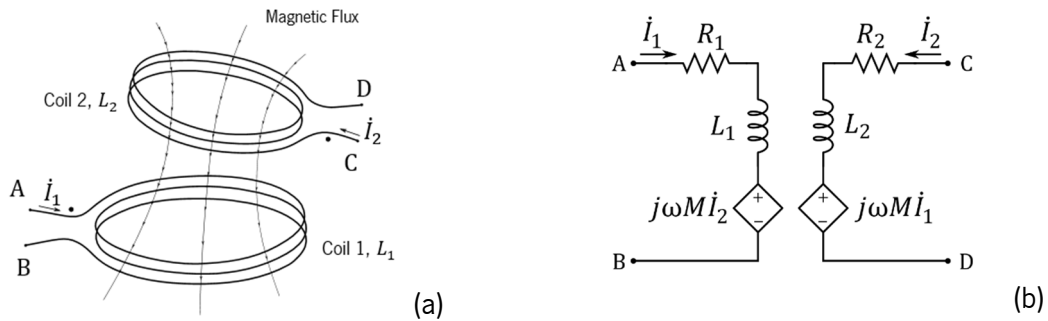
Figure 3. Two non-radiating magnetically coupled coils (a) and their simplified circuit model (b).

In this model, $\omega = 2\pi f_0$, and M is the mutual inductance between the coils. R_1 and R_2 depend on both skin and proximity effects and, for any fixed frequency operation f_0, they should be recalculated, so that the model can still conserve its linearity. In this manner, in sinusoidal regimen, with no radiation assumed for the magnetic coupling, the power transferred from Coil 1 to Coil 2 is given by the phasor $\dot{S}_{1,2}$:

$$\dot{S}_{1,2} \;=\; \dot{V}_{M_1} \dot{I}_1^* \;=\; j\,\omega\,M\,\dot{I}_1^*\,\dot{I}_2 \,, \tag{2.4}$$

where for $i \in \{1, 2\}$, $\dot{V}_{M_i}$ and $\dot{I}_i$ are the phasors representing respectively the voltage across the dependent voltage source and the current flowing on side i of the magnetic coupling.

The real power $P_{1,2}$ transferred from Coil 1 to Coil 2 is then given by:

$$P_{1,2} \;=\; \mathrm{Re}\big(\dot{S}_{1,2}\big) = \omega\,M\,\mathrm{Re}\big(\dot{I}_1\big)\,\mathrm{Im}\big(-\dot{I}_2\big) - \omega\,M\,\mathrm{Re}\big(\dot{I}_2\big)\,\mathrm{Im}\big(-\dot{I}_1\big) \tag{2.5}$$

Assuming, without loss of generality, that the zero-phase reference is that phase of current $\dot{I}_1$, this expression further simplifies to:

Dynamic Inductive Wireless Power Transfer for Lightweight Electric Vehicles
Luiz Alberto Lisboa da Silva Cardoso – University of Minho

17

$$P_{1,2} = \omega M \operatorname{Re}(\dot{I}_1) \operatorname{Im}(-\dot{I}_2), \qquad (2.6)$$

Expression (2.5) can be perceived geometrically as:

$$P_{1,2} = \omega M \, I_{rms_1} \, I_{rms_2} \, \sin(\varphi_1 - \varphi_2), \qquad (2.7)$$

where $\varphi_1 - \varphi_2$ is the angle difference between the phase of current in Coil 1 (the primary coil) to the phase of current in Coil 2 (the secondary coil), which will be referred as the compensation angle. Noticeable, if $\sin(\varphi_1 - \varphi_2) < 0$, $P_{1,2}$ is negative, and the power is actually transferred backwards, that is, from Coil 2 to Coil 1, what constitute the basis for implementation of bidirectional IWPT configurations.

For fixed RMS values I_{rms_1} and I_{rms_2}, f_0 and M, it can be seen that the transferred power will be positive and maximized when $\varphi_1 - \varphi_2 = \pi/2$, that is, when $\dot{I}_2$, the current entering the reference node on Coil 2 has a phase delay of $\pi/2$, with respect to the phase of $\dot{I}_1$, the current entering the reference node on Coil 1. This condition is met when:

$$-\dot{I}_2 = \alpha \, j \, \dot{I}_1 = \beta \left(j \, \omega \, M \, \dot{I}_1 \right), \quad \alpha, \beta > 0, \qquad (2.8)$$

and it is equivalent to requiring the current $-\dot{I}_2$ leaving the reference node of Coil 2 to be in phase with the voltage $E_2 = j\omega M \dot{I}_1$ induced on the secondary, a condition that is met when the total equivalent impedance driven by E_2 is purely resistive. Once fixing the magnetic coupling inductive parameters (L_1, L_2, M) and f_0, this can be achieved by introducing a compensation network in the secondary circuit. From (2.7), it can also be seen that, at the resonance condition given by (2.8), in order to obtain larger values for $P_{1,2}$, either f_0, M, I_{rms_1} or I_{rms_2} have to be increased.

When the operating frequency, the resonant frequency of the primary (transmitting) and secondary (receiving) coils circuits are the same, the currents on the coils are greatly increased, and the power levels achieved can be very high, at high efficiency levels, a condition called magnetic resonance coupling, early observed by Nikola Tesla along his work with AC currents [28].

One last remark is that $P_{1,2}$, in (2.7), is the power transferred though the magnetic link between the two coils, not the power delivered to the resistive load attached to the secondary (Coil 2). Part of $P_{1,2}$ is expected to be dissipated on the resistive components of both the secondary coil itself and the compensation network used to adjust the phase of $\dot{I}_2$. Although this approximation can be done, as the WPT efficiency becomes sufficiently high.

Dynamic Inductive Wireless Power Transfer for Lightweight Electric Vehicles
Luiz Alberto Lisboa da Silva Cardoso – University of Minho

18

2.4 Self and Mutual Inductance Calculations

Essential to the prediction of power transference between energized coils, and thus, to the design of IWPT configurations, are:

- The calculation of the maximum current that a conductor can handle, at a given frequency; or conversely, what conductive cross-section a conductor must have in order to handle, at that frequency, some required current.

- The calculation of mutual inductances between two coils; or equivalently, the determination of their geometry to implement the some required mutual inductance value.

- The calculation of self-inductances of coils, to determine how to electrically excite their terminals in order to obtain the required design current.

These problems can be solved by numeric simulation using finite element modeling (FEM); if required, in a number of iterations, to determine some feasible or optimum solution. This method can be complemented or, sometimes, replaced by simplified algebraic calculations, using formulae previously developed, often compromising precision and computational effort.

To support other applications in general physics, such as radio communications, analytical studies and formulae of inductance of conductive geometries were early developed [29] [30], which hold, to a good approximation, valid and useful even today. In the design of the HIPLEV, oblong coils are used, and the calculation of the inductance of rectangular coils is especially useful.

2.4.1 The Inductance of a Rectangular Coil

One of the popular shapes of coils used in IWPT is the rectangular form, which is used in the design of the inductive lane for the HIPLEV (as detailed in Chapter 5), to approximate the inductance of oblong coils, where the extremities are not necessary perfectly rectangular. The formula for calculation of the inductance ℶ of a rectangular coil of round wire of relative magnetic permeability μ_r is presented in [31], and reproduced here for the study of some of its properties, which is used (in Section 5.9) in the design of the primary coil for the HIPLEV prototype.

$$\beth(a, b, r, \mu_r) =$$

$$= \frac{\mu_0}{\pi}\left(a \log\left[\frac{2ab}{r(a+d)}\right] + b \log\left[\frac{2ab}{r(b+d)}\right] + 2d - (a+b)\left(2 - \frac{\mu_r}{4}\right)\right), \tag{2.9}$$

where a and b are the lengths of its sides, r the radius of the wire, and $d = \sqrt{a^2 + b^2}$.

Dynamic Inductive Wireless Power Transfer for Lightweight Electric Vehicles
Luiz Alberto Lisboa da Silva Cardoso – University of Minho

19

If curves of ɮ versus the length a of the coil are plot for different values of b, when both a and b are much larger than r, it is verified that for every different b, ɮ can be approximated by an affine function of a, provided that a is large enough. This approximation is apparently very good for $a \geq 2b$, as show in Figure 4. This can be interpreted as the inductance of a rectangular coil being sum of a fixed "inductance of the extremities", which mostly depends on the width and the radius of the wire, and the inductance of the central portion of the coil, i.e., the inductance of the two parallel conductors along the length of the coil, from which the extremities were excluded.
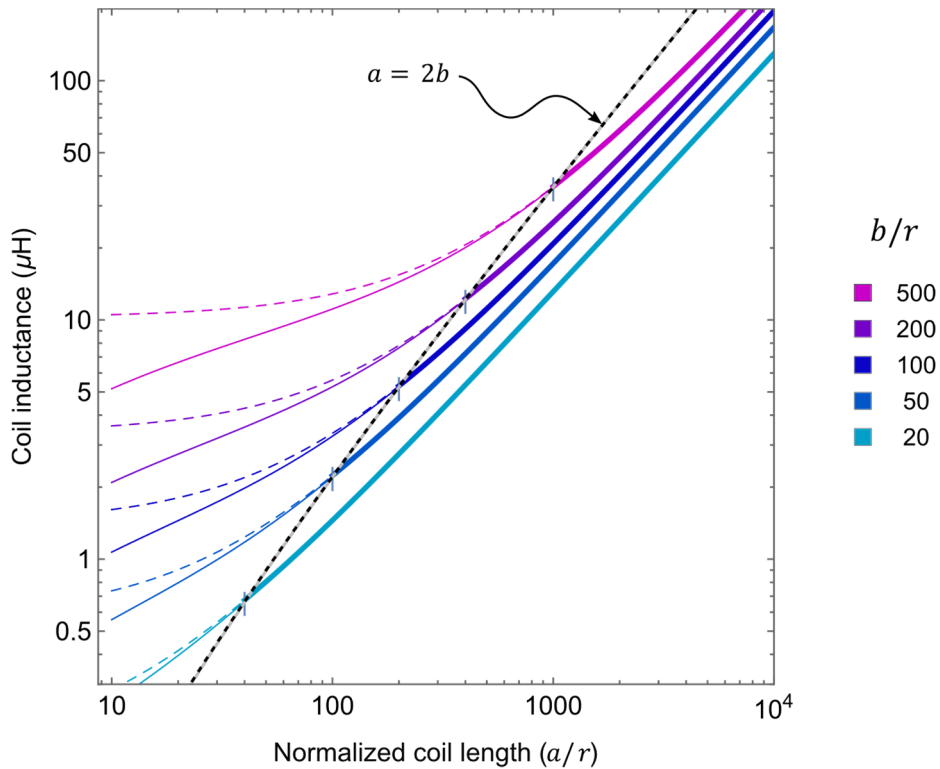
Figure 4: Inductance of rectangular coil compared with adjusted affine function of its length.

In the graph of Figure 4, the inductance curves were traced for the case where the radius of the conductor $r = 10$ mm. Both the length and the width are normalized to this radius. The continuous curves correspond to the actual inductance curves, while the dashed curves of the same color are the corresponding affine approximations. The black dashed line define the region $(a > 2b)$ where the approximation can be considered good. As an additional verification, the maximum errors under the affine approximation are also plot Figure 5, confirming that, for $a \geq 2b$, the error is less 1.5% for $b = 20r$, and less than 1.1% for $b = 50r$. For all b/r ratios, the error decreases rapidly if the ration a/b is further increased:

Dynamic Inductive Wireless Power Transfer for Lightweight Electric Vehicles
Luiz Alberto Lisboa da Silva Cardoso – University of Minho

20
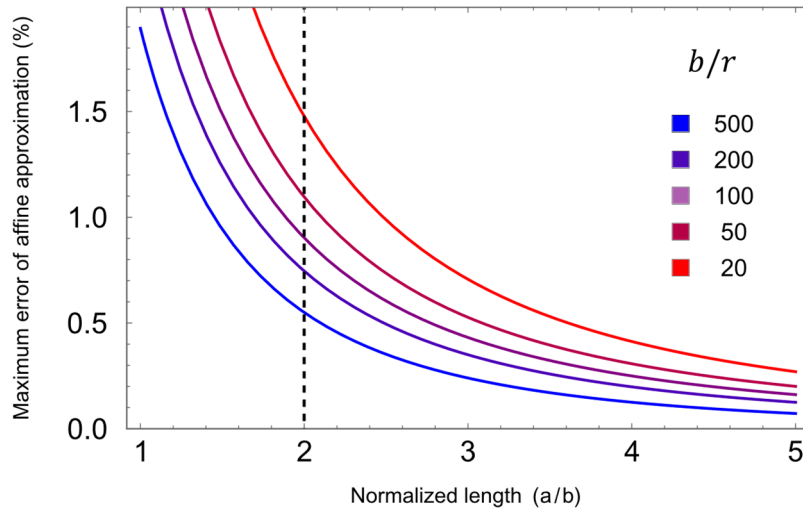
Figure 5: Inductance of rectangular coil compared with adjusted affine function of its length.

Then it is also possible to express ꓤ as:

$$\text{ꓤ}(a, b, r, \mu_r) \cong \text{ꓤ}(a_0, b, r, \mu_r) + (a - a_0)\Lambda(b, r, \mu_r) \qquad (2.10)$$

for any $a_0 \geq 2b$. Noticeably, for the case that both b and r are fixed and $\mu_r = 1$, the term $\Lambda(b, r, \mu_r)$ is a constant, meaning that, in an rectangular coil, there is an increment of inductance proportional to increment in length, above the minimum length a_0. The term $\text{ꓤ}(a_0, b, r, \mu_r)$, which is the inductance of a rectangular coil with same cross-section and length a_0, can be interpreted as the "inductance of the extremities" of the coil with the overall length a_0.

Due to vanishing mutual inductance between the center segment of the coil and its extremities, as the length is increased, a similar approximation is also expectedly possible for other types of oblong coils, irrespectively of the detail of geometry of its extremities. Intuitively, this approximation should hold as long as the windings at the extremities of the coil are actually confined to the extremities of the coil, and have an inductance comparable to that of the extremities of a rectangular coil of same size.

2.5 The Serial-Serial Compensated IWPT

The principle of IWPT by magnetic resonance coupling is exemplified and analyzed on basis of the so called serial compensated magnetic coupling circuit, which was the simplest and first engineered compensation network. This is achieved when the resistive load R_L is connected to Coil 2 through a circuit network that transforms the load impedance R_L into a new impedance Z_2

Dynamic Inductive Wireless Power Transfer for Lightweight Electric Vehicles
Luiz Alberto Lisboa da Silva Cardoso – University of Minho

21

that perfectly "compensates" (in the sense that it cancels the complex component of) the impedance of branch of the model formed by R_2 and L_2, as shown in Figure 6(a).

(a)   (b)
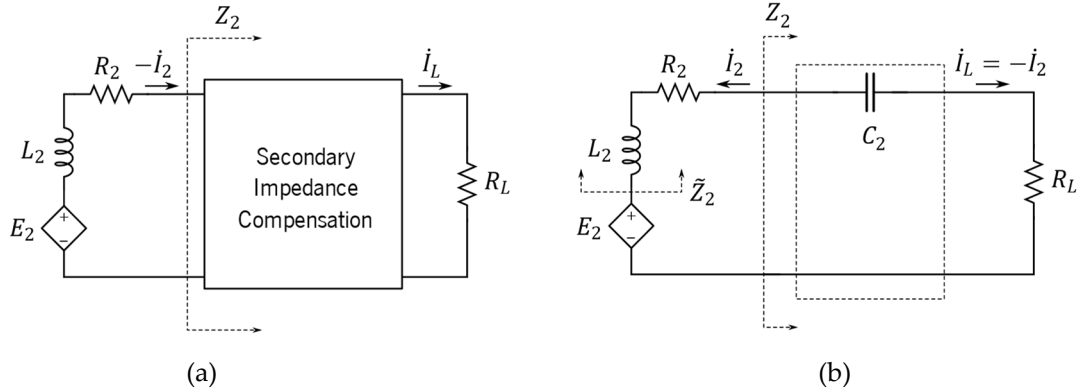
Figure 6: Impedance compensation network in the secondary (a), implemented by a series capacitor (b).

It is constituted of a single capacitor in series with the load, as shown in Figure 6(b), a configuration already used by Nikola Tesla in the late 19th Century [28]. In this configuration, the reactive component of the equivalent impedance $\tilde{Z}_2$, as seen by E_2:

$$\tilde{Z}_2 \; = \; j\omega L_2 \; + \; R_2 + \; Z_2 \; = \; R_2 + \; R_L \; + \; j\left(\omega L_2 - \frac{1}{\omega C_2}\right), \tag{2.11}$$

is canceled, assuring that $\sin(\varphi_1 - \varphi_2)$ in (2.7) is maximized to 1. At $\omega = 2\pi f_0$, this happens when $L_2 C_2 = 1/(2\pi f_o)^2$, or equivalently, when C_2 assumes the value:

$$[C_2]_{S-Res} \; = \; \frac{1}{(2\pi f_o)^2 \, L_2} \tag{2.12}$$

If the mutual inductance M is low enough compared with L_1 and L_2, the back-induced voltage $E_1 \; = \; j\omega M \dot{I}_2$ will be sufficiently small not to significantly influence the current $\dot{I}_1$. Under this approximation, the current $I_{rms_2} = \left| \dot{I}_2 \right|$ will also be maximized (resonance condition on the secondary) by $C_2 = [C_2]_{S-Res}$, as can be derived from (2.13):

$$\dot{I}_2 \; = \; \frac{E_2}{\tilde{Z}_2} \; = \; \frac{-j\,\omega\,M}{j\left(\omega\,L_2 - \frac{1}{\omega\,C_2}\right) \; + \; (R_2 + R_L)}\,\dot{I}_1 \tag{2.13}$$

By defining $\boldsymbol{\upsilon}$ as the ratio between $\dot{I}_2$ and $\dot{I}_1$, it follows that:

$$\boldsymbol{\upsilon} \; = \frac{\dot{I}_2}{\dot{I}_1} \; = \; \frac{-j\,\omega\,M}{r + jx}, \qquad r = R_2 + R_L, \qquad x = \omega\,L_2 - \frac{1}{\omega\,C_2}, \tag{2.14}$$

$$\boldsymbol{\upsilon} - \left(-\frac{j\,\omega\,M}{2r}\right) = -\frac{j\,\omega\,M}{2r}\,\frac{r - j\,x}{r + j\,x} = -\frac{j\,\omega\,M}{2r}\,\frac{1 - \frac{j\,x}{r}}{1 + \frac{j\,x}{r}} \tag{2.15}$$

Dynamic Inductive Wireless Power Transfer for Lightweight Electric Vehicles
Luiz Alberto Lisboa da Silva Cardoso – University of Minho

22

Because of this mathematical structure, the ratio $\dot{I}_2/\dot{I}_1$ as function of the load R_L and the compensation capacitor C_2 can be plot as in Figure 7, built in analogy to the Smith chart [32][33], where $\dot{I}_1$ is assumed, without loss of generality, to have zero phase.
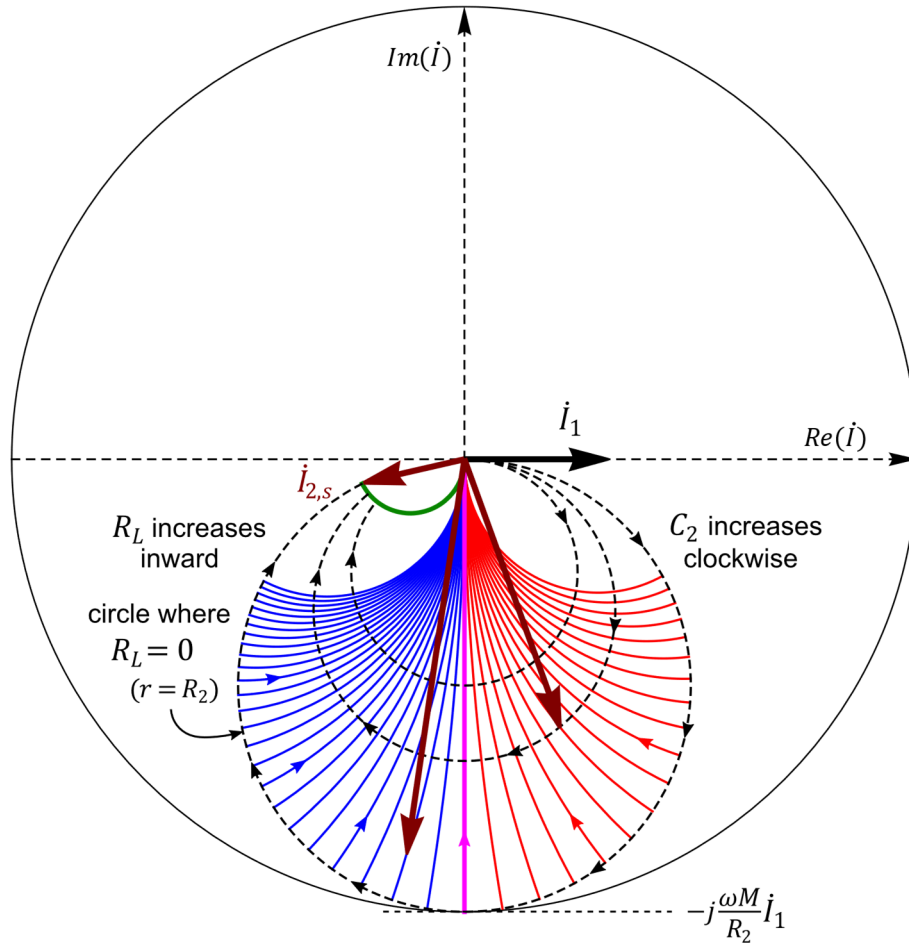
Figure 7: Variation of $\dot{I}_2$ as function of the load R_L and the secondary compensation capacitor C_2, if $\dot{I}_1$ is fixed and used as the zero-phase reference.

The dashed circles are the loci for constant load R_L, the most external one corresponding to $R_L = 0$. The red and blue curves are also arcs of circles, the loci for different constant C_2, the red curves corresponding to $C_2 < [C_2]_{S-Res}$, and the blue ones to $C_2 > [C_2]_{S-Res}$.

The limit condition where $C_2 \longrightarrow \infty$, corresponding to the non-resonant, purely inductive coupling of R_L to L_2, is given by the by the small green arc on the third quadrant of the chart in Figure 7. In particular, with L_2 short-circuited, the current $\dot{I}_{2,s}$ is obtained. This $\dot{I}_{2,s}$ tends to be in the opposite direction to the current $\dot{I}_1$, as to cancel the magnetic flux induced by $\dot{I}_1$ on Coil 2, not been perfectly so due to the parasite Coil 2 resistance, R_2. The magnitude of $\dot{I}_{2,s}$ is limited by the total current $N_1 \dot{I}_1$, where N_1 is the number of turns of Coil 1. It can be much less than $N_1 \dot{I}_1$, as it will decrease with decreasing magnetic coupling between the two coils, what happens when the distance between the coils is increased, for instance.

Dynamic Inductive Wireless Power Transfer for Lightweight Electric Vehicles
Luiz Alberto Lisboa da Silva Cardoso – University of Minho

23

By the use of the compensation capacitor C_2 in the circuit, the current limitation $|\dot{I}_2| \leq |\dot{I}_{2,s}|$ can be overcome, and more power can be transferred from Coil 1 to Coil 2.

When $C_2 = [C_2]_{S-Res}$, the expression of current $\dot{I}_2$ in terms of $\dot{I}_1$ simplifies to:

$$\dot{I}_2 = \frac{-j\,\omega\,M\,\dot{I}_1}{R_2 + R_L}, \tag{2.16}$$

and $\dot{I}_2$ assumes negative values on the imaginary axis, with its locus on the magenta line segment in Figure 7. At this resonant condition, the back-induced voltage, $E_1 = j\omega M \dot{I}_2$, is a real multiple of $\dot{I}_1$. If Coil 1 is externally excited by a power source of constant voltage V_0 (RMS) and a similar serial compensation network is used in the primary side, as shown in Figure 8, the primary circuit behaves as loaded by a purely resistive load, and I_{rms_1} is maximized.
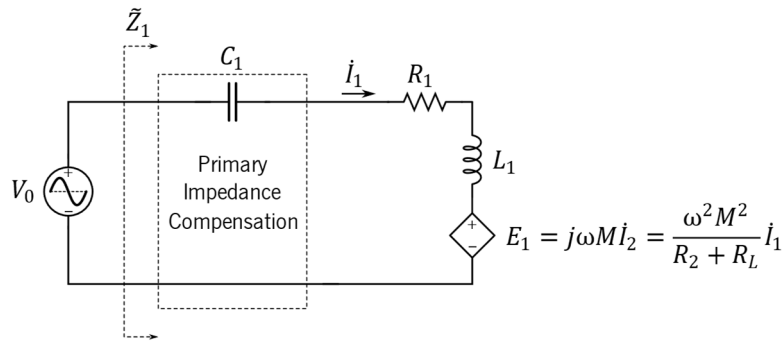
Figure 8: Introduction of an impedance compensation network (serial) in the primary circuit.

This is established by considering the equivalent impedance $\tilde{Z}_1$ seen by the voltage source V_0, that, with C_1 in series, becomes:

$$\tilde{Z}_1 = \frac{1}{j\,\omega\,C_1} + j\,\omega\,L_2 + R_1 + \frac{\omega^2 M^2}{R_2 + R_L}, \tag{2.17}$$

Having the capacitor C_1 as the free variable, $|\tilde{Z}_1|$ is minimized, and I_{rms_1} is maximized (resonant condition on the primary circuit), when C_1 is equal to $[C_1]_{S-Res}$:

$$[C_1]_{S-Res} = \frac{1}{(2\pi f_o)^2 L_1} \tag{2.18}$$

This maximizes the power dissipated on E_1, which is in fact transferred to the secondary and, proportionally, delivered by E_2 to the load, via R_2. Again, this approximation for the condition of maximum power transfer is only acceptable If the mutual inductance M is low enough compared with L_1 and L_2 (low coupling coefficient k). In general, relative maxima in the power transfer functions will be found in operation frequencies that, depending on the load conditions, may be different than the resonance frequency f_0. That is, the overall maximum for $P_{1,2}$, in (2.7), will be

Dynamic Inductive Wireless Power Transfer for Lightweight Electric Vehicles
Luiz Alberto Lisboa da Silva Cardoso – University of Minho

24

potentially achieved with the factor $\sin(\varphi_1 - \varphi_2) < 1$ instead. This often happens in association with the occurrence of more than one relative maxima in $P_{1,2}$, and it is known as the frequency splitting phenomenon, discussed in Section 2.5.2.

The serial compensation, when used in both the primary and secondary circuits, originates what is called the Serial-Serial compensation topology, or abbreviately, SS-compensation, one the most widely used configurations for IWPT.

Another general observation is that, at the resonance frequency f_0, a system of linear complex equation is defined on the phasors $\dot{I}_1$ and $\dot{I}_2$:

$$\dot{V}_0 \;=\; R_1\,\dot{I}_1 + j\,\omega\,M\,\dot{I}_2 \tag{2.19}$$

$$j\,\omega\,M\,\dot{I}_1 \;=\; -(R_L + R_2)\,\dot{I}_2 \tag{2.20}$$

Solving the system, expressions for $\dot{I}_1$ and $\dot{I}_2$ are obtained and respectively given in equations (2.27) and (2.37), from where it can be noticed that the current on the secondary, $\dot{I}_2$, is delayed $\pi/2$ relatively to the current on the primary circuit for $\dot{I}_1$, thus satisfying (2.8).

$$\dot{I}_1 \;=\; j\,\frac{(R_L + R_2)}{\omega\,M}\,\dot{I}_2 \tag{2.21}$$

$$\dot{I}_2 \;=\; -j\,\frac{\omega\,M\,\dot{V}_0}{R_1\,(R_2 + R_L) + \omega^2 M^2} \tag{2.22}$$

Equation (2.22) can be rewritten as equation (2.23):

$$-I_2 \;=\; \frac{j\,\dot{V}_0\left[\dfrac{\omega\,M}{R_1}\right]}{R_L + \left[R_2 + \dfrac{\omega^2\,M^2}{R_1}\right]} \tag{2.23}$$

Hence, at resonance condition, the relationship between the load R_L and the current $I_L = -I_2$ on load R_L can be promptly recognized as the load equation of a Thévenin equivalent circuit, where the equivalent source voltage phasor, $\dot{V}_{th}$, and the equivalent series impedance R_{th} are given by equations (2.24) and (2.25):

$$\dot{V}_{th} \;=\; j\,\dot{V}_0\left[\frac{\omega\,M}{R_1}\right] \tag{2.24}$$

Dynamic Inductive Wireless Power Transfer for Lightweight Electric Vehicles
Luiz Alberto Lisboa da Silva Cardoso – University of Minho

25

$$R_{th} \;=\; R_2 \;+\; \frac{\omega^2 \, M^2}{R_1} \tag{2.25}$$

The maximum power will be developed over the load R_L when it is equal to R_{th}:

$$R_{max\,power} \;=\; R_{th} \;=\; R_2 \;+\; \frac{\omega^2 \, M^2}{R_1} \;=\; R_2\,(1 + k^2 Q_1 Q_2), \tag{2.26}$$

where the Q_i are the quality factors (or "Q-factors") of the coils L_i, defined by:

$$Q_i \;=\; \frac{\omega_0 \, L_i}{R_i}\,, \qquad i \in \{1,2\} \tag{2.27}$$

The maximum power that can be transferred over the magnetic link to R_L is then:

$$P_{max} \;=\; \frac{\left(V_{rms_0}\right)^2 \omega^2 M^2}{4 R_1^2 \left(R_2 + \dfrac{\omega^2 M^2}{R_1}\right)} \;=\; \frac{\left(V_{rms_0}\right)^2}{4 R_1} \; \frac{1}{1 \;+\; \dfrac{1}{k^2 Q_1 Q_2}}\,, \tag{2.28}$$

The Thèvenin equivalent given by (2.24) and (2.25) only models the relation of the load R_L with the IWPT system, and it is not good for directly evaluating the total power lost in the system itself, that is, lost on the windings of Coil 1 and Coil 2, which, at maximum power transfer condition, can be much higher than the power delivered to R_L. So, regarding the efficiency, the maximum power output condition is usually not a good design option.

2.5.1 Efficiency and Power Output in a SS-Compensated IWPT

For a good IWPT system, where are looking for systems requiring minimum building efforts (cost, materials, size) that can transfer a specified maximum nominal power, with an acceptably high efficiency. Even with both primary and secondary circuits at resonance conditions, the energy transmission efficiency of a magnetic coupling will be less than 100%, due to the non-zero equivalent electrical resistance of the coils.

The electrical efficiency, η, of a SS-Compensated IWPT at the resonance frequency f_0, with $\omega \;=\; 2\pi f_0$, can be calculated by the ratio between the power delivered by the primary source $\dot{V}_0$ and the power consumed at the load R_L:

$$\eta \;=\; \frac{\dot{I}_2 \, \dot{I}_2^* \, R_L}{\dot{V}_0 \, \dot{I}_1^*} \;=\; \frac{j\,\omega\,M\,\dot{I}_2\,R_L}{\dot{V}_0\,(R_2 + R_L)} \;=\;$$

Dynamic Inductive Wireless Power Transfer for Lightweight Electric Vehicles
Luiz Alberto Lisboa da Silva Cardoso – University of Minho

26

$$= \frac{\omega^2 M^2 \, R_L}{(R_2 + R_L)\,(R_1\,(R_2 + R_L) + \omega^2 M^2)} \; =$$

$$= \frac{1}{\left(1 + \frac{R_2}{R_L}\right)\left(1 + \frac{R_1(R_2 + R_L)}{\omega^2 M^2}\right)} \; , \tag{2.29}$$

or, expressing η in terms of the quality factors Q_i (2.27):

$$\eta \; = \; \frac{1}{\left(1 + \frac{R_2}{R_L}\right)\left(1 + \dfrac{1 + \frac{R_L}{R_2}}{k^2 Q_1 Q_2}\right)} \tag{2.30}$$

Considering all other circuit elements given, then η can be regarded as a real continuous and differentiable function of the load R_L, defined for all $R_L > 0$. The conditions for $R_L = R_{\eta_{max}}$ to be a point of relative maximum of η are (2.31) and (2.33):

$$\left.\frac{\partial \eta}{\partial R_L}\right|_{R_{\eta_{max}}} = \; 0, \quad R_{\eta_{max}} > 0 \tag{2.31}$$

$$\left.\frac{\partial^2 \eta}{\partial R_L^2}\right|_{R_{\eta_{max}}} < \; 0, \quad R_{\eta_{max}} > 0 \tag{2.32}$$

This calculation has been accomplished [34], [35], resulting in only one point of relative maximum in the interval $R_L > 0$, which then is the point of maximum in η. This point is given by:

$$R_L \; = \; R_{\eta_{max}} \; = \; R_2 \sqrt{1 + k^2 \, Q_1 \, Q_2} \; , \tag{2.33}$$

so, the maximum achievable efficiency η_{max} at the resonant frequency f_0 can be calculated by substituting (2.33) in (2.30):

$$\eta_{max} \; = \; \frac{k^2 \, Q_1 \, Q_2}{\left(1 + \sqrt{1 + k^2 \, Q_1 \, Q_2}\,\right)^2} \; , \tag{2.34}$$

From (2.26) and (2.33), it can be further noticed that $R_{\eta_{max}}$ is incidentally equal to geometric mean of R_2 and $R_{max\,power}$:

$$R_{\eta_{max}} \; = \; \sqrt{R_2 \; R_{max\,power}} \tag{2.35}$$

Dynamic Inductive Wireless Power Transfer for Lightweight Electric Vehicles
Luiz Alberto Lisboa da Silva Cardoso – University of Minho

27

By replacing R_L by $R_{max\,power}$, as given by equation (2.26), into equation (2.30), it is possible to calculate the efficiency at the maximum power condition $\eta_{\max\,power}$, which is visibly less than $1/2$, as expected:

$$\eta_{max\,power} = \cfrac{1}{2\left(1 + \cfrac{1}{1 + k^2 Q_1 Q_2}\right)\left(1 + \cfrac{1}{k^2 Q_1 Q_2}\right)} < \frac{1}{2} \tag{2.36}$$

For values of $Q_F = k\sqrt{Q_1 Q_2}$ much greater than 1, $\eta_{\max\,power}$ approaches the limiting 50%, while η_{max} can be approximated by:

$$\eta_{max} \cong \tilde{\eta}_{max} = 1 - \frac{2}{k\sqrt{Q_1 Q_2}} = 1 - \frac{2}{Q_F}, \tag{2.37}$$

where $Q_F = k\sqrt{Q_1 Q_2}$ is defined as the magnetic coupling quality factor.

Thus, when both primary and secondary are tuned to excitation frequency f_o (magnetic resonance condition), the behavior of η_{max} as function of Q_F is a sigmoidal curve, as shown in Figure 9:
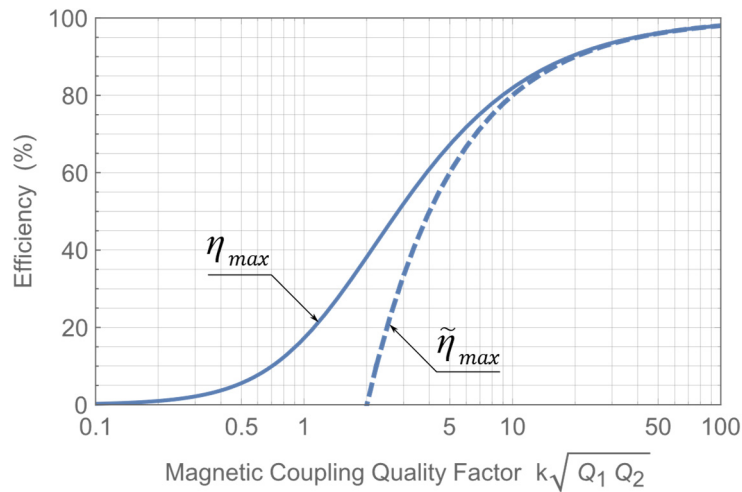
Figure 9: Maximum achievable efficiency in a SS-compensated IWPT, at the fundamental resonant frequency f_o, as a function of the quality factor of the magnetic coupling.

This characteristic curve reveals, for instance, that in order for a magnetic coupling to electric efficiencies over 85% it is necessary that $Q_F > 12.3$, and for efficiencies over 95%, $Q_F > 39$. As the desired efficiency comes closer to 100% it is more difficult to implement the system, because the required quality factors of both primary and secondary increase exponentially. In this case a large magnetic coupling coefficient, k, as close as possible to 1, is highly recommendable, if the application permits.

Dynamic Inductive Wireless Power Transfer for Lightweight Electric Vehicles
Luiz Alberto Lisboa da Silva Cardoso – University of Minho

28

From Figure 9 and expressions (2.27) and (2.37), it also possible to see that the simpler expression $\widetilde{\eta}_{max}$ (2.37) is a good approximation for η_{max} (within 2% error) when the magnetic coupling quality factor Q_F is larger than 10.7.

Typical behavior patterns of the efficiency as a function of the normalized R_L to R_2 ratio, for the magnetic resonance condition in circuits where $R_1 = R_2$, are shown in Figure 9, where the color of the plotted curves, ranging from red (lower curve) to blue, correspond respectively to Q_F values ranging from ascending value 1 to 100, in the set $\{1, 2, 5, 10, 20, 50, 100\}$. If the value of the load resistor, R_L, does not exactly match its optimum value, the electrical efficiency that will be actually obtained from the magnetic coupling is less than η_{max} for each curve, which is only achieved when condition (2.33) is met, that is, when $R_L/R_2 = k\sqrt{Q_1 Q_2}$.
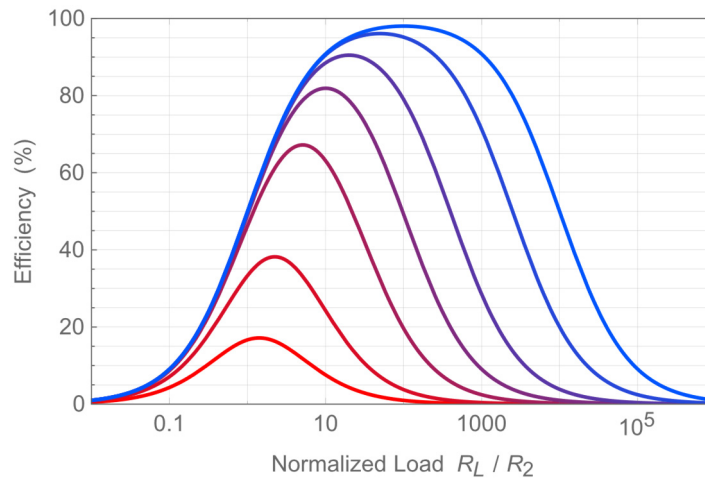
Figure 10: Curves of efficiency of the magnetic coupling in a SS-compensated IWPT, as a function of the normalized load R_L/R_2, parametrized by different quality factors, $k\sqrt{Q_1 Q_2}$.

In an IWPT design at a fixed frequency f_o, given a desired load R_L, the ratio R_L/R_2 can be adjusted to its optimum target value $k\sqrt{Q_1 Q_2}$ with either of two main strategies. The first one is by changing the geometry and constitution of the coils, consequently, their parameters in the model. To achieve this, for instance, the number of turns and the size of Coil 2, as well as the constitution of its wiring, can be varied. But this may affect the voltage induced in the secondary too, so in this procedure it would also be possibly necessary to change Coil 1 configuration accordingly.

A second possible strategy is, instead of changing the magnetic coupling, keep its configuration, and modify the apparent load R_L that is seen by Coil 2, by means of the introduction of another impedance converter in between the secondary circuit and R_L, as shown in Figure 11.

Dynamic Inductive Wireless Power Transfer for Lightweight Electric Vehicles
Luiz Alberto Lisboa da Silva Cardoso – University of Minho

29

This converter should ideally act as a lossless voltage transformer, matching the load to the phase-compensated secondary circuit.
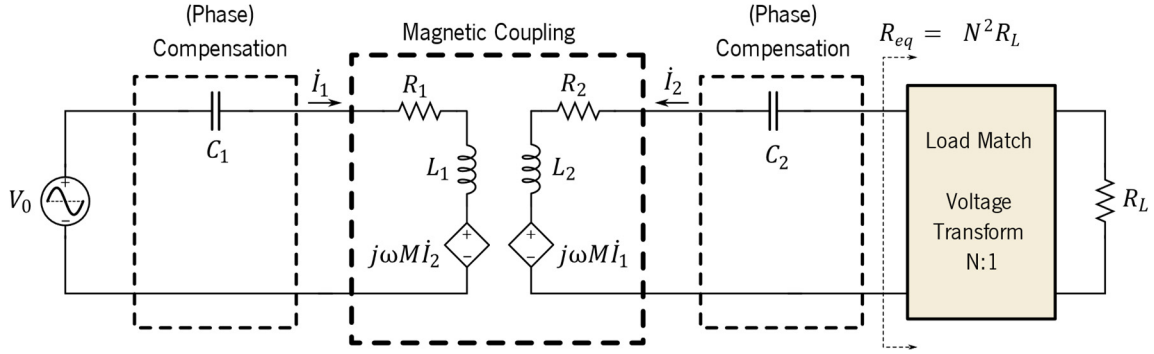
Figure 11: Load-matching in a SS-compensated IWPT.

If $N:1$ is the voltage transformation ratio of the load-matching section, the equivalent resistance seen by the secondary at the input terminals of the voltage transformer will be:

$$R_{eq} \;=\; N^2 R_L \tag{2.38}$$

The necessary N for achieving the maximum efficiency η_{max} in the IWPT will be such that:

$$N^2 R_L \;=\; R_{\eta_{max}} \;=\; R_2 \sqrt{1 + k^2\, Q_1\, Q_2} \;\cong\; R_2\, Q_F \tag{2.39}$$

$$\Rightarrow \quad N \;=\; \sqrt{\frac{R_2}{R_L} \sqrt{1 + k^2\, Q_1\, Q_2}} \;\cong\; \sqrt{\frac{R_2}{R_L}\, Q_F} \tag{2.40}$$

Since the circuit model works with AC current and voltage levels, the voltage transformation at the secondary can be simply implemented by a cored $N:1$ electric transformer, one with low losses at the operating frequency f_o, which is presumed to be the only allowed operation frequency, directly linked to the impedance compensation property.

Eventually, an SS-compensated IWPT configuration can be forced to operate in a frequency that is different from the primary and secondary resonant frequency f_0. Figure 12 shows the computed efficiency surface in this general situation, in which circuit parameters were fixed for a resonance set at f_0, but the IWPT circuit can be operated away from f_0 as well. This example was run with $k = 0.3$, $R_1 = R_2 = 0.1\Omega$, $C_1 = C_2 = 1\mu F$ and $f_0 = 100$ kHz. The red dotted curve is the output of the maximum efficiency function, extrapolated for frequencies other than the resonance frequency f_0 for which this function is originally defined. The blue dotted curve is the locus of the maximum efficiency points, if the compensation capacitors were continuously readjusted for each new frequency f. It can be noticed that the curve of the extrapolated maximum

Dynamic Inductive Wireless Power Transfer for Lightweight Electric Vehicles
Luiz Alberto Lisboa da Silva Cardoso – University of Minho

30

efficiency (red dots) only touches the efficiency surface at the plane defined by $Log_{10}(f/f_0) = 0$ (that is, at $f = f_0$), giving false and too optimistic estimates for the efficiency at frequencies other than f_0. However, for frequencies f higher than f_0, the estimation given by extrapolating the maximum efficiency function is apparently lower than the real efficiency (blue dots) that could be achieved if capacitors were readjusted for resonance at each corresponding frequency f. It is also possible to observe that the value of R_L at the maximum efficiency only coincides with that given by (2.33) at $f = f_0$.
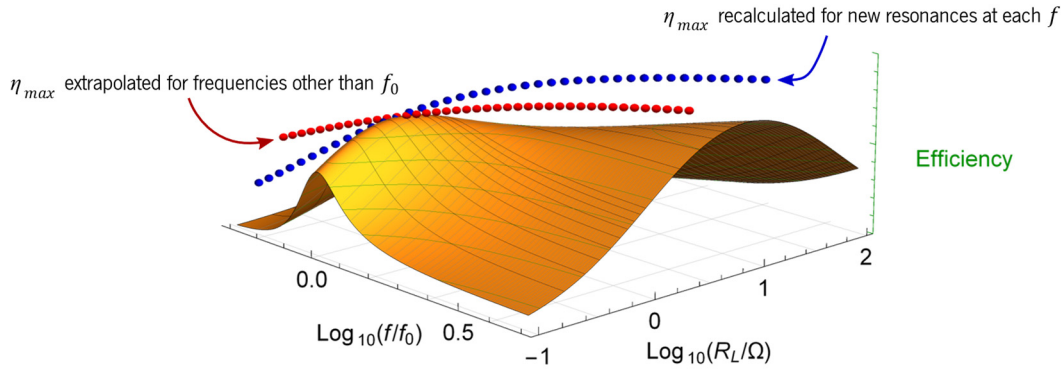
Figure 12: Typical efficiency behavior in a SS-compensated WPT coupling.

This example also shows that even not being possible to exceed the maximum efficiency η_{max} while operating at the associated resonant frequency f_0, it may be possible to find, for the same IWPT configuration, another operation point that exhibits an efficiency which is greater than this η_{max} at f_0. At this new operation point, however, the resulting output power is potentially different from that at f_0, as addressed in section 2.5.2.

If the load R_L requires DC current instead of AC, R_L will be usually connected to the secondary compensation circuit through a rectifier and a DC filter. In this case, a DC-DC converter can be used to match the load to $R_{\eta_{max}}$, for optimum efficiency. However, as a rectifier is a nonlinear element, the characteristic output response curve will be not linear as well, and a new optimum R_L for the efficiency, $R_{\eta_{max}}^{DC}$, will arise and should be considered instead. In [36], it is shown that not only $R_{\eta_{max}}^{DC}$ can be larger than $R_{\eta_{max}}$, but also that the rectifier load causes a change in the secondary impedance, thus requiring some adjustment in the compensation network, to keep an optimum efficiency.

After design conditions for the target efficiency η_{max} are established, the output power at the at the operation point $(f_0, R_{\eta_{max}})$ can be calculated by:

Dynamic Inductive Wireless Power Transfer for Lightweight Electric Vehicles
Luiz Alberto Lisboa da Silva Cardoso – University of Minho

31

$$P_{\eta_{max}} = \eta_{max} \; P_{\eta_{max}}^{in} \tag{2.41}$$

Observing (2.17), at the resonance condition, $P_{\eta_{max}}^{in}$ can be computed as:

$$P_{\eta_{max}}^{in} = \frac{(V_{0rms})^2}{R_1 + \dfrac{\omega^2 M^2}{R_2 + R_L}} = \frac{(V_{0rms})^2}{R_1} \frac{k^2 Q_1 Q_2}{1 + \sqrt{1 + k^2 Q_1 Q_2}}, \tag{2.42}$$

and then $P_{\eta_{max}}$ becomes:

$$P_{\eta_{max}} = \frac{(V_{0rms})^2}{R_1} \frac{1}{A} \left(1 - \frac{2}{A + 1}\right), \tag{2.43}$$

where:

$$A = \sqrt{1 + k^2 Q_1 Q_2} \tag{2.44}$$

When the magnetic coupling quality factor Q_F is high enough, it is possible to approximate A by Q_F (2.37), and then (2.41) can be further simplified to:

$$P_{\eta_{max}} \cong \frac{1}{Q_F} \left(1 - \frac{2}{Q_F + 1}\right) \frac{(V_{0rms})^2}{R_1} \cong \frac{1}{Q_F} \frac{(V_{0rms})^2}{R_1} \tag{2.45}$$

In a typical design approach, once established an adequate equivalent load for the secondary, the target efficiency of the magnetic coupling and the overall IWPT efficiency can be met, except for the introduction of some loss factor exhibited by the voltage transformer (Figure 11). The desired output power level (2.45) can then be set by adjusting the amplitude of the voltage source V_0. If this cannot be directly accomplished because the power source V_0 is a fixed specified value, another voltage transformation could be used in the primary circuit.

If the required IWPT power is close to but less than the available output power $P_{\eta_{max}}$ at the operation point where η_{max}, alternatively, the primary circuit can be detuned from the resonance condition, thus reducing the primary current and lowering the transferred power to the target value. This can be done by either slightly changing the compensation circuits or the operation frequency. But this will also cause some change the system efficiency, due to the displacement of the operation point away from the previously calculated resonance condition [11]. In some circumstances, the efficiency may even improve with respect to η_{max} at f_0, revealing that the resonant frequency chosen at first might have not been optimal for the circuit. To minimize iterated

Dynamic Inductive Wireless Power Transfer for Lightweight Electric Vehicles
Luiz Alberto Lisboa da Silva Cardoso – University of Minho

32

checks on the design, efficiency and power output can be jointly considered, as discussed in Section 2.5.2.

The task of building a magnetic coupling with a reasonably high efficiency then translates into the problem of building resonant pairs coil-capacitor with high quality factors Q_i, as high as necessary to compensate for the low magnetic coupling coefficient k between these coils. Further than that, when choosing circuit parameters and an operation point, the designer should be able to balance the efficiency with the required output power under the application constraints.

Worthwhile mentioning, the overall system efficiency of an IWPT system shall be further reduced by the intrinsic efficiencies of power converters on the primary side as well as rectifiers and other eventual converters on the secondary, used in series association with the magnetic coupling. For instance, in a given IWPT configuration, if the primary converter, the magnetic coupling and the secondary rectifier/converter have each an efficiency of 95%, the total net efficiency will be $0.95^3 = 85.7\%$.

2.5.2 Resonant Frequency Splitting in SS-Compensation

It is long known that, in a double tuned coupled circuit, when the mutual inductive coupling coefficient is increased above a critical value, two resonance peaks in frequency may appear instead of one [24]. This phenomenon, early observed in the design of communication circuits, was called resonant frequency splitting, or simply, frequency splitting, and it is also referred to as frequency bifurcation [37]. In IWPT applications, this translates into the possibility that the circuits have peak power responses in two distinct frequencies, neither of them the predicted resonant frequency f_0 for the primary or secondary RLC branches individually.

The simplified mathematical formulation shown in section 2.5, that leads to the development in section 2.5.1, hides the frequency splitting effect, which may only become experimentally evident when either the magnetic coupling coefficient k is not small enough, or the load resistor R_L is not high enough, to justify the approximations used in the optimal choice of $[C_1]_{S-Res}$ (2.18) and $[C_2]_{S-Res}$ (2.12). A more detailed analysis reveals a subtle behavior in the SS topology.

The implicit initial consideration that conceals frequency splitting is the heuristics adopted for partial optimization of $P_{1,2}$, in (2.7), by individually and sequentially maximizing its factors: Firstly, $\sin(\varphi_1 - \varphi_2)$ is maximized, by making it equals to 1 and forcing the phase of $\dot{I}_2$ to be $\pi/2$ delayed with respect to the phase of $\dot{I}_1$. Then, restricted to this condition, I_{rms_2}, s maximized,

Dynamic Inductive Wireless Power Transfer for Lightweight Electric Vehicles
Luiz Alberto Lisboa da Silva Cardoso – University of Minho

33

and finally, restricted to these two previous conditions, I_{rms_1} is maximized. By doing this, the circuit parameters chosen for the compensation network may not lead to the true maximum in the power transfer, not even to a relative maximum in the frequency × load domain. Since the subsequent load matching for the best efficiency is based on the circuit parameters induced by this heuristic, the computed load of maximum efficiency (2.33) is also potentially not what it should be in the missed point of maximum power transfer. These approximations, as mentioned, are only good when the back induced voltage in the primary circuit by the secondary current $\dot{I}_2$ is negligible.

In general, due to dependency of current $\dot{I}_1$ on $\dot{I}_2$ as well, the maximum in the product of currents I_{rms_2} and I_{rms_2} will not be achieved exactly at $C_2 = [C_2]_{S-Res}$, although this is the condition to obtain the phase difference $\varphi_1 - \varphi_2 = \pi/2$, that maximizes the $\sin(\varphi_1 - \varphi_2)$ factor in the expression for the inductively transferred power (2.7). So, to obtain an exact solution for any frequency f, with $\omega = 2\pi f$, under the linear model of Figure 11, the complex linear system that should be considered instead is given by (2.48) and (2.49):

$$\dot{V}_0 = R_1 \dot{I}_1 + j\dot{I}_1\left(\omega L_1 - \frac{1}{\omega C_1}\right) + j\,\omega\,M\,\dot{I}_2 \tag{2.46}$$

$$j\,\omega\,M\,\dot{I}_1 + \left(R_L + R_2 + j\left(\omega L_2 - \frac{1}{\omega C_2}\right)\right)\dot{I}_2 = 0 \tag{2.47}$$

If C_1 and C_2 are set to values that produce resonance at f_o, with $\omega_0 = 2\pi f_0$, respectively with L_1 and L_2, then solving the above system for the phasor currents $\dot{I}_1$ and $\dot{I}_2$ leads to an exact expression for P_{out}, the power output over R_{eq}:

$$P_{out} = \frac{k^2\,R_{eq}\,C_1\,C_2\left(V_{0_{rms}}\right)^2\lambda^6\,\omega_0^2}{(R_1 C_1 + (R_2 + R_{eq})C_2)^2\lambda^2(\lambda^2 - 1)^2\omega_0^2 + (2\lambda^2 - 1 - (1 - k^2)\lambda^4 + R_1(R_2 + R_{eq})C_1 C_2\lambda^2\omega_0^2)^2}, \tag{2.48}$$

where $\lambda = f/f_o$ is the normalized frequency of operation, f_o is the resonance frequency of the isolated primary and secondary branches, as in (2.18) and (2.12), and $\omega_0 = 2\pi f_o$. An equivalent expression for P_{out} was provided in [38]. At frequency f_o, that is, when $\lambda = 1$, (2.48) becomes equivalent to the simpler form:

$$P_{out} = \frac{k^2 Q_1 Q_2 R_2 R_{eq}\left(V_{0_{rms}}\right)^2}{R_1\left(R_2(1 + k^2 Q_1 Q_2) + R_{eq}\right)^2}, \tag{2.49}$$

where quality factors Q_1 and Q_2 are defined as in (2.27).

Dynamic Inductive Wireless Power Transfer for Lightweight Electric Vehicles
Luiz Alberto Lisboa da Silva Cardoso – University of Minho

34

While it is not immediate to extract some insight from direct algebraic manipulation of the general expression (2.48), by plotting curves of $P_{out} \times (\lambda, k)$, it is apparent that, depending on the combination of values of the magnetic coupling coefficient k and the load R_L, the IWPT may present one or two maxima in λ. Figure 13 exemplifies this behavior when the model is run with parameters $R_1 = R_2 = 0.1\Omega$, $C_1 = C_2 = 1\,\mu F$, and $f_o = 100\,kHz$, and, without loss of generality $R_L = R_{eq}$, case where the necessary voltage transform to match de load R_L to the IWPT output is the identity. It then can be seen that, for a low enough R_L, as k increases from a value close to zero towards 1, at some point, the single existing peak in the power curve starts to flatten out, and then two peaks are observed in the transferred power. As k continues to increase, these two new resonance frequencies get further apart from each other and from the original resonant frequency f_o, thus causing what is called the frequency splitting phenomenon.

For a given load R_L, there is a certain $k_{max} < 1$ that maximizes the transferred power. When R_L is low enough to enable frequency splitting, this k_{max} is less than a critical value of k, k_s, above which the splitting is actually observed. When R_L is high enough, as in Figure 13a, on the contrary, there is no frequency splitting, no matter how large the coefficient k can be.
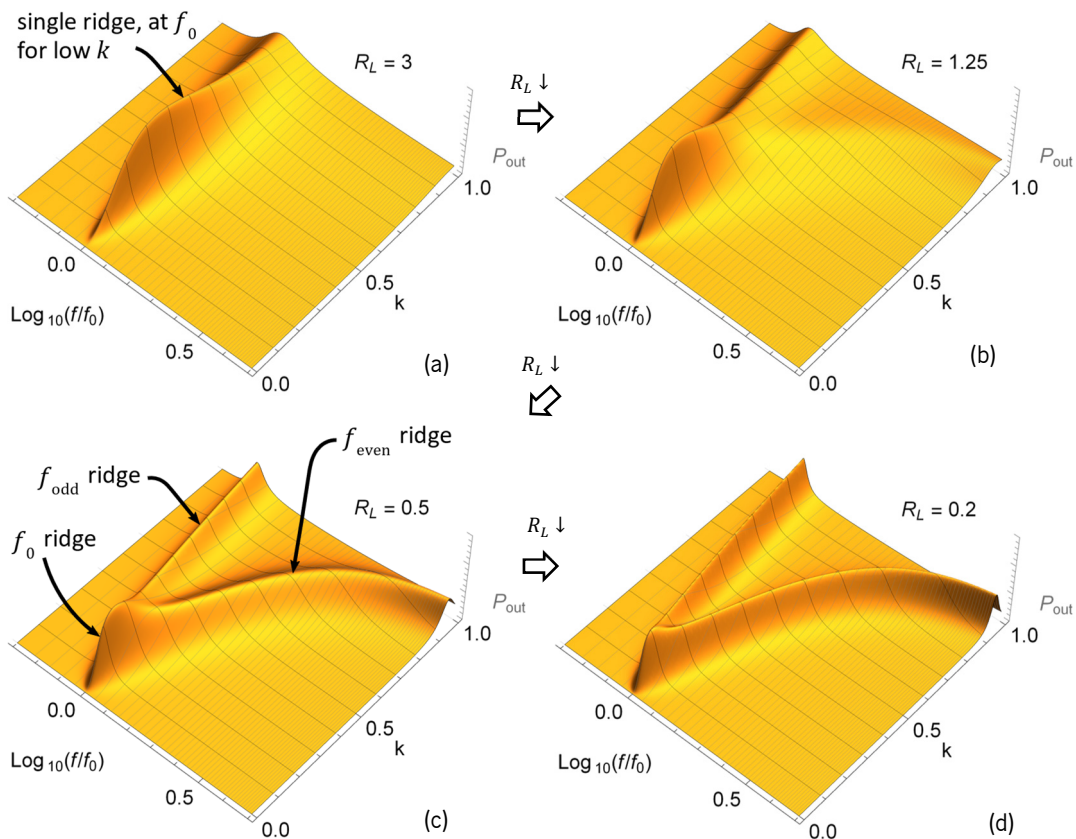
Figure 13: Evolution of the power output in a SS-compensated IWPT, as a function of the normalized frequency, f/f_0, and k, as the equivalent load R_L is decreased.

Dynamic Inductive Wireless Power Transfer for Lightweight Electric Vehicles
Luiz Alberto Lisboa da Silva Cardoso – University of Minho

35

As R_L is lowered, following the sequence from Figure 13b to Figure 13d, it can be noticed that the single initial resonance frequency f_0 is actually split into two other frequencies, if k is large enough. These frequencies are often referred in the literature as f_{odd}, which is lower than f_0, and f_{even}, higher.

Some approximated formulations can be found in the literature, associated with the addition of further simplifying hypotheses. For instance, in the case that primary and secondary circuits are equal, with $C_1 = C_2$, $L_1 = L_2$, R_1 can be neglected when compared to $|\omega_0 L_1|$ and R_L is much larger than R_2, expression (2.48) is reduced to:

$$P_{out} \cong \frac{(V_{0_{rms}})^2 k^2 \Lambda^3}{R_L(Q_S^2 + (1 - 4Q_S^2)\Lambda - 2(1 - 3Q_S^2 + k^2 Q_S^2)\Lambda^2 - (4(1 - k^2)Q_S^2 - 1)\Lambda^3 + (1 - k^2)^2 Q_S^2 \Lambda^4)}, \qquad (2.50)$$

where $\Lambda = (f/f_o)^2$ and Q_S is the loaded quality factor of the secondary, given by:

$$Q_S = \frac{\omega\,L}{(R_2 + R_L)} \cong \frac{\omega\,L}{R_L} \qquad (2.51)$$

Under this simplified model, an analytical solution for f_{odd} and f_{even} has been found [38]:

$$\{f_{odd}, f_{even}\} = \left\{ f_0 \sqrt{\frac{(2 - 1/Q_s^2) \pm \sqrt{(2 - 1/Q_s^2)^2 - 4(1 - k^2)}}{2(1 - k^2)}} \right\}, \qquad (2.52)$$

whenever $k > k_s$, where:

$$k_s = \frac{1}{Q_s} \sqrt{1 - \frac{1}{4Q_s^2}} \qquad (2.53)$$

For large values of Q_S and magnetic coupling coefficients k that sufficiently exceeds the critical value k_s, the new odd and even resonance frequencies can be approximated by:

$$f_{odd} = \frac{1}{\sqrt{1 + k}}\,f_o\,, \qquad (2.54)$$

$$f_{even} = \frac{1}{\sqrt{1 - k}}\,f_o \qquad (2.55)$$

At $k = k_s$ (at the frequency splitting point), the overall resonance frequency f_s can be also estimated by [38]:

$$f_s = \frac{f_0}{\sqrt{1 - \frac{1}{2Q_s^2}}} \qquad (2.56)$$

Dynamic Inductive Wireless Power Transfer for Lightweight Electric Vehicles
Luiz Alberto Lisboa da Silva Cardoso – University of Minho

36

For large values of Q_s, it can be noticed that f_s is close to, but slightly greater than f_0. If k is greater than k_s, as given by (2.53), then magnetic resonance will be found at two other frequencies that can be significantly different from f_0. This behavior and simplified formulation, as given by (2.54) and (2.55), has been characterized by many other authors since Terman [24], and used and radio circuit design, but it also has to be considered in IWPT design, either to avoid the frequency splitting operation [39] [40], or just to tune circuits to the adequate operating frequency [11]. General expressions for f_{even} and f_{odd}, in conditions where the primary and secondary branch resonance frequencies of an SS-compensated circuit, respectively f_1 and f_2, may be different from each other is given in [41], and will coincide for the case where $f_1 = f_2 (= f_0)$. This calculation corresponds to geometrical construction visualized in Figure 14.

$$f_{odd} = \sqrt{\frac{f_1^2 + f_2^2 - \Delta}{2(1 - k^2)}} \; , \tag{2.57}$$

$$f_{even} = \sqrt{\frac{f_1^2 + f_2^2 + \Delta}{2(1 - k^2)}} \; , \tag{2.58}$$

where: $\qquad \Delta = \sqrt{(f_1^2 + f_2^2)^2 - 4(1 - k^2) f_1^2 f_2^2} \tag{2.59}$
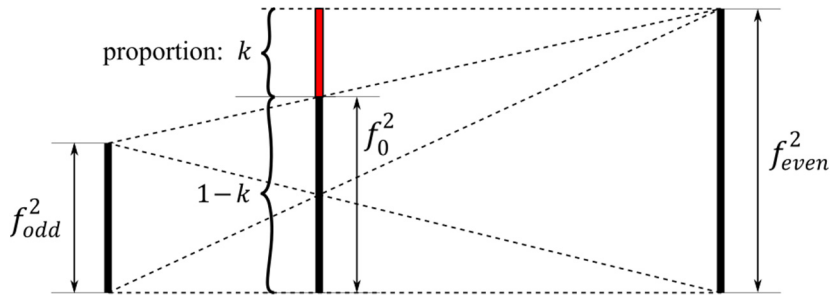
Figure 14: Geometric interpretation of the relationship of the split-frequencies f_{even} and f_{odd}, f_0 and k.

The frequency splitting phenomenon in systems with varying k, can be better visualized and understood by plotting sequences of power surfaces defined on the space of operation points (f, R_L). For this purpose plots of $P_{out} \times (f, R_L)$ for different k values are drawn in Figure 15, using the same circuit parameters as those used to run the example in Figure 13. The general effect observed in the power output, when k is varied from zero to one, is the actual splitting in the power ridge, for higher loads (lower values of R_L), as shown in the sequence from Figure 15a to Figure 15d. It can be also noticed that the main peak in the transferred power at f_0 is displaced toward larger values of the load R_L as k is increased. The red arrows indicate the displacement

Dynamic Inductive Wireless Power Transfer for Lightweight Electric Vehicles
Luiz Alberto Lisboa da Silva Cardoso – University of Minho

37

tendency of the resonance frequencies in the $f \times R_L$ plane, as k is increased and the black arrows mark the resonance frequencies, f_{odd}, f_0 and f_{even}.
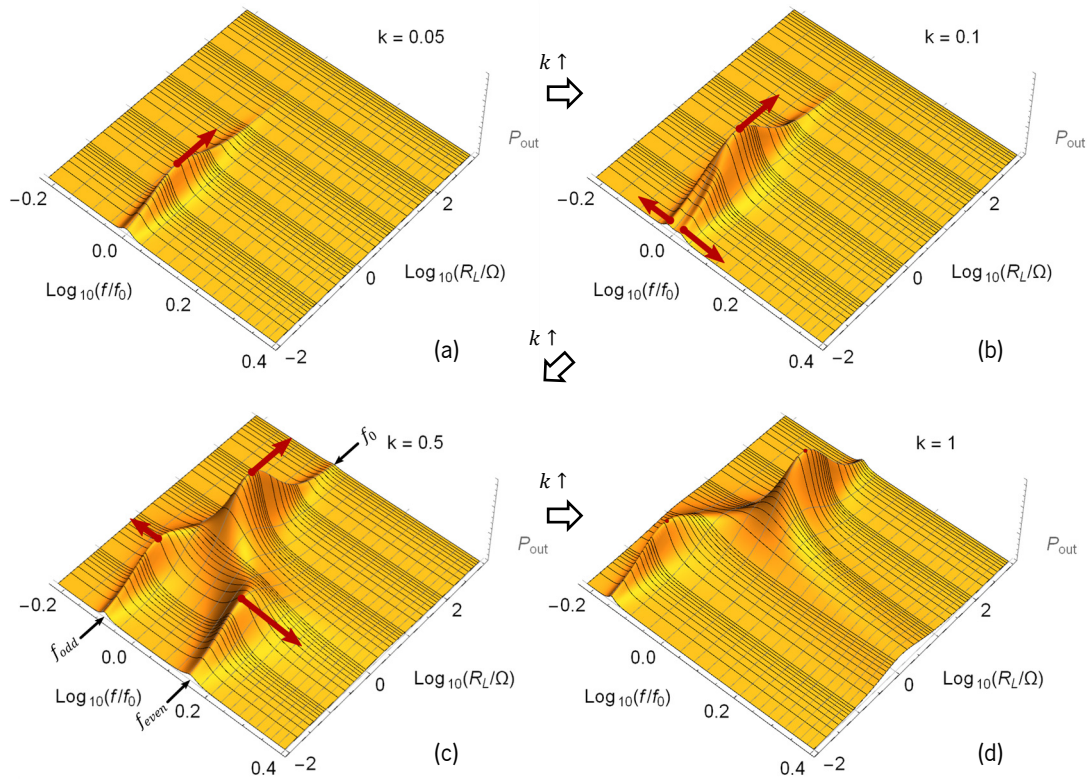
Figure 15: Frequency splitting behavior in a SS-compensated IWPT circuit, as k is increased.

Since the magnetic coupling factor is associated with the materials and the geometry of the coils involved in an IWPT configuration, applications where k varies are usually associated with some dynamic behavior in the geometry of the coils or their cores, such as a change in relative position. The SS-compensation circuit favors the design of IWPT using a single fixed operating frequency in these conditions of a varying k, as long as the circuit parameters are previously adjusted to match the operation frequency f_o.

The graphics in Figure 13 and Figure 15, however, say nothing about efficiency. Similarly as the output power (2.48), based on (2.46) and (2.47), exact algebraic expressions for the input power and for the efficiency of the SS compensation can be computationally derived, with the aid of software tools for algebraic manipulation. These expressions have a large number of terms and are not practical to analyze analytically. Their results, however, can be visualized graphically.

In applications where the parameter k is fixed, the analysis can be accomplished by plotting superposed efficiency contour maps over the surface defined by the output power of an SS-compensated IWPT, as a function of the operation point (f, R_L). This approach is illustrated in the example of Figure 16, where the following parameters were used $k = 0.5$, $f_0 = 100$ kHz,

Dynamic Inductive Wireless Power Transfer for Lightweight Electric Vehicles
Luiz Alberto Lisboa da Silva Cardoso – University of Minho

38

$C_1 = C_2 = 1\ \mu F$, $L_1 = L_2 = 2.53\ \mu H$ and $R_1 = R_2 = 30\ m\Omega$. If the analysis is more of qualitative nature, the input voltage is irrelevant, as long as P_{out} is plotted in normalized scale.
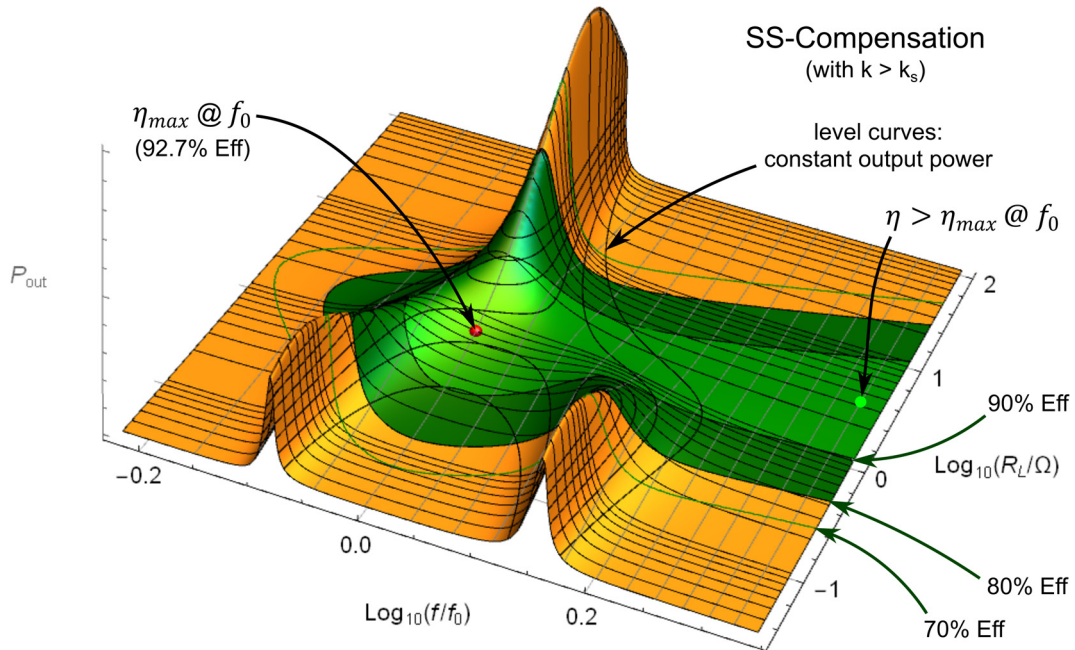
Figure 16: Bounded efficiency regions (green) drawn over the power output surface of a SS-compensated IWPT coupling, having the frequency of operation and the equivalent output load as free parameters.

In Figure 16, the thin green contour curve indicates the loci of the points where the efficiency equals to 70%, while the green shaded regions indicate efficiencies in between 80% and 90% (dark green) and over 90% (light green). Both the frequency, normalized by the ratio f/f_0, and the equivalent R_L are plotted in logarithm scale, to facilitate the analysis over a wider dynamic range of these parameters. The red dot is placed at the point with coordinates implied by (i) the primary and secondary isolated branch resonance, f_0, (ii) the optimum load $R_{\eta_{max}}$ for best efficiency at f_0, as given by (2.39), and (iii) the output power $P_{\eta_{max}}$, as given by (2.45). In this particular example, η_{max} is approximately 92.7%. The power can be increased beyond $P_{\eta_{max}}$ if the operation point is shifted towards one the power peak ridges, associated with the resonating frequencies f_0, f_{even} and f_{odd}, thus leading to an increase in the power transferred to the load. But this will tend to decrease the resulting efficiency. For the ideal SS-compensation IWPT model, using parameters with no frequency dependency, there may be, on the other hand, an operation point at a higher frequency than f_0, where an efficiency higher than η_{max} is found, although the output power is be potentially much less than $P_{\eta_{max}}$ (e.g., the point marked with the green dot on Figure 16).

While giving a good intuitive understanding of the joint behavior of output power and efficiency, the three-dimensional plotting scheme is not as practical, for design purposes, as its

Dynamic Inductive Wireless Power Transfer for Lightweight Electric Vehicles
Luiz Alberto Lisboa da Silva Cardoso – University of Minho

39

simpler two-dimensional counterpart. This is shown for the new example of Figure 17, where a 40 W power output is desired with an efficiency equal to or better than 90%.
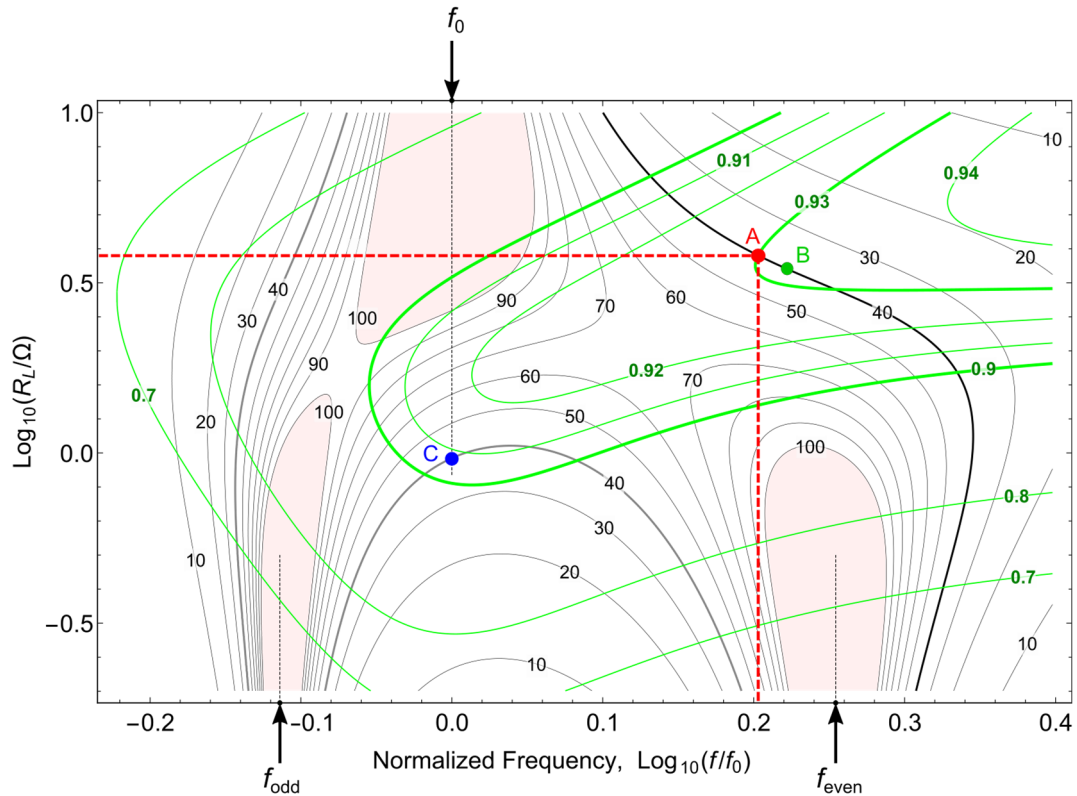
Figure 17: Typical constant output power (black) and constant efficiency (green) contours of a SS-compensated WPT coupling, having the frequency of operation and equivalent output load as free parameters.

Since the power output is now relevant for the solution, instead of the qualitative approach for power visualization used when plotting Figure 16, the actual value of the input voltage, V_{0rms}, should be also considered. Because the method of analysis uses exact expressions for power and efficiency, even asymmetries in the primary and secondary circuit can be easily handled. The SS-compensation in Figure 17, for instance, was run with the following circuit parameters: V_{0rms} =10.8 V rms, $k = 0.69$, $f_0 = 52$ kHz, $L_1 = 6.79$ µH, $L_1 = 7.74$ µH, $C_1 = 1.38$ µF, $C_2 = 1.21$ µF, and $R_1 = R_2 = 70$ mΩ. The horizontal axis is the logarithm of normalized frequency, ranging from 0.6 (corresponding to $f = 31.2$ kHz) to 2.5 (corresponding to $f = 130$ kHz), and the vertical axis, the equivalent output resistive load, ranging from 0.2 Ω to 10 Ω, also in logarithm scale.

Level curves are plot for both power and efficiency, with value tags on it: The black curves are the loci of constant output power in multiples of 10 W, until 100 W, while the green curves are the loci of constant efficiency, for values from 70% to 80%, in increments of 10%, and higher than 90%, in increments of 1%. For the target design power output, 40 W, it is possible to pick any

Dynamic Inductive Wireless Power Transfer for Lightweight Electric Vehicles
Luiz Alberto Lisboa da Silva Cardoso – University of Minho

40

operation point on one of the three black contour curves (constant output power) marked "40". As an example, at point "A", marked in red in Figure 17, corresponding to an excitation frequency of approximately 83.0 kHz and an equivalent output load of 3.8 Ω, the resulting efficiency will be 93%, because "A" is also on a constant efficiency contour curve labeled "0.93". It is also possible to predict that at point of operation "B", marked in green, close to point "A" and over the same black contour of 40 W, the efficiency will be slightly higher than 93%, but still less than 94%. If, however, the frequency operation is kept at the resonance frequency of primary and secondary branches, $f_0 = 52$ kHz, for a 40 W output, the operation point "C" would have to be selected, and the efficiency would decrease to slightly less than 91%, worse than that at "A" or "B". Not within plotting range of Figure 17, another solution at f_0 could possibly exist for a much higher resistive load than that at point "C", but at a much lower efficiency.

From Figure 17 it can also be verified that for higher power output levels, operation should be close to the resonant frequency f_0, for higher load resistances, or to the split frequencies f_{odd} and f_{even}, for lower load resistances. The pink-colored regions, approximately centered on these frequencies, indicate the locus for the points of operation, in the range of frequencies and loads plotted, where output power in excess of 100 W can be achieved, at the expense of a reduction in the efficiency.

For applications with varying magnetic coupling factor, k, the analysis can be alternatively accomplished by mapping efficiency contour plots over power surfaces built on the $\{(f, k)\}$ domain, such as those in drawn in Figure 13. At any k, however, operating at maximum power output reduces the best possible efficiency that can be attainable by the adequate load matching. While the maximum possible efficiency at f_0 is η_{max}, as calculated by (2.34), the efficiency at this same frequency on an arbitrary load may be much less, depending on how apart from $R_{\eta_{max}}$ (2.33) the load R_L is.

2.5.3 Relation between the Secondary Coil Current and the DC Load

In many IWPT applications, the AC induced voltage on the secondary is required to supply power to a DC load. In a series-compensated secondary, often a rectifier circuit constituted of a diode bridge is connected to output of the compensated secondary, and the remaining AC voltage passing through this rectifier is filtered out by a capacitor, modifying the configuration of the secondary circuit in Figure 6b to that shown in Figure 18.

Dynamic Inductive Wireless Power Transfer for Lightweight Electric Vehicles
Luiz Alberto Lisboa da Silva Cardoso – University of Minho

41
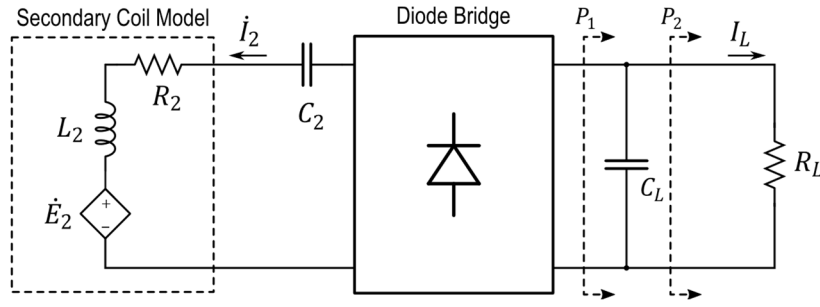
Figure 18: DC load attached to a series-compensated secondary through a full-wave rectifier and a filter capacitor.

Under perfect compensation of the secondary coil inductance, for large enough loads (low enough R_L) and amplitudes of $\dot{E}_2$ much larger than the voltage drop across de diode bridge, $2V_D$, the current I_2 can be approximated by a purely sinusoidal wave, represented by the phasor $\dot{I}_2$. In this condition, due to the conservation of energy, the input power P_1 to the lossless filter capacitor C_L, which is given by the constant voltage V_{DC} multiplied by the average value of a sinusoid with amplitude equal to $\sqrt{2}\,I_{2,rms}$, must be equal to power P_2 delivered to load R_L, given by $V_{DC}\,I_L$. This leads to the approximation in (2.60):

$$V_{DC}\,\frac{2}{\pi}\sqrt{2}\,I_{2,rms} \cong V_{DC}\,I_L, \tag{2.60}$$

which simplifies to:

$$I_{2,rms} \cong \frac{\pi}{2\sqrt{2}}I_L \tag{2.61}$$

2.5.4 Relation between the Induced Voltage and the DC Load Voltage

Under the same simplifying considerations made in 2.5.3, the input voltage to the bridge rectifier in Figure 18 can be approximated by a square wave with amplitude $V_{DC} + 2V_D$, with 50 % duty cycle, which has a first order harmonic component that approximately corresponds, due to band pass characteristics of the L_2C_2 resonator branch, to the induced voltage signal, $\dot{E}_2$:

$$\frac{4}{\pi}(V_{DC} + 2V_D) \cong \sqrt{2}\big(E_{2,rms} - I_{2,rms}\,R_2 \big) \tag{2.62}$$

$$\Longrightarrow E_{2,rms} \cong \frac{2\sqrt{2}}{\pi}(V_{DC} + 2V_D) + I_{2,rms}\,R_2 \tag{2.63}$$

Results in (2.61) and (2.63) facilitate enormously the estimation of both the required current on the secondary coil and the required induced voltage in an IWPT configuration, when using a serial-compensated secondary.

Dynamic Inductive Wireless Power Transfer for Lightweight Electric Vehicles
Luiz Alberto Lisboa da Silva Cardoso – University of Minho

42

2.5.5 Secondary Coil Current as a Function of Induced Voltage

Based on the results in Sections 2.5.3 and 2.5.4, an approximated value for the secondary coil current can be expressed as a function of the (open circuit) induced voltage in the same secondary coil, if tank serial resistance R_2, the power P_{DC} dissipated on the load R_L, and the forward voltage drop V_D on the diodes are also known.

The power dissipated on the load, P_{DC}, can be expressed as the product of the approximation of I_L and the approximation of the voltage on the load, V_{DC}. Using (2.61) to express I_L and (2.63) to express V_{DC}, it results in:

$$\left(I_{2,rms} \frac{2\sqrt{2}}{\pi} \right) \left(\frac{\pi}{2\sqrt{2}} \left(E_{2,rms} - I_{2,rms}\, R_2 \right) - 2V_D \right) \cong P_{DC} \,, \tag{2.64}$$

which can be re-written as:

$$I_{2,rm}^2\, R_2 - I_{2,rms} \left(E_{2,rms} - V_D \frac{4\sqrt{2}}{\pi} \right) + P_{DC} \cong 0 \tag{2.65}$$

Recognizing (2.65) as a second degree quadratic equation in $I_{2,rms}$, the two possible solutions satisfying this equation are:

$$I_{2,rms,1} \cong \frac{E_{2,rms} - V_D \frac{4\sqrt{2}}{\pi} - \sqrt{\Delta}}{2R_2} \tag{2.66}$$

and

$$I_{2,rms,2} \cong \frac{E_{2,rms} - V_D \frac{4\sqrt{2}}{\pi} + \sqrt{\Delta}}{2R_2} \tag{2.67}$$

where:

$$\Delta = \left(E_{2,rms} - V_D \frac{4\sqrt{2}}{\pi} \right)^2 - 4\, R_2 P_{DC} \tag{2.68}$$

In practical applications $E_{2,rms}$ is much larger than $2V_D$, and the equivalent AC resistance R_{AC} of the rectifier connected to the load R_L is also much larger than R_2. Then, if Δ is divided by $R_2 + R_{AC}$, it follows that:

$$\frac{\Delta}{R_2 + R_{AC}} \cong \frac{\left(E_{2,rms} \right)^2}{R_2 + R_{AC}} - 4 \frac{R_2}{R_2 + R_{AC}} P_{DC} \tag{2.69}$$

Dynamic Inductive Wireless Power Transfer for Lightweight Electric Vehicles
Luiz Alberto Lisboa da Silva Cardoso – University of Minho

43

The term $E_{2,rms}^2/(R_2 + R_{AC})$ in the right side of (2.69) is recognized as the total power supplied by the induced voltage, which, in practical IWPT applications, should be on the same order of P_{DC}, because the power loss on R_2 should be much less than the power on R_L. Under these considerations, it can be seen not only that $\Delta > 0$, but also that Δ is dominated by the value of $E_{2,rms}^2$. So, in gross approximation, $\sqrt{\Delta}$ is smaller, but has the same magnitude of $E_{2,rms} - 4\sqrt{2}\,V_D/\pi$.

If (2.67) would be a valid solution for the problem,

$$I_{2,rms,2} \cong \frac{E_{2,rms} - V_D \dfrac{4\sqrt{2}}{\pi}}{R_2} \cong \frac{E_{2,rms}}{R_2} \tag{2.70}$$

However, this would imply in R_{AC} being negligible in face of R_2, what violates the hypothesis that, in the IWPT configuration, the opposite should happen, i.e., R_2 is much less than R_{AC}. Therefore, the solution (2.67) should be discarded, and the expression (2.66) should instead be used for approximating the value of $I_{2,rms}$.

Another less intuitive but mathematically simpler manner of realizing this is to consider that $E_{2,rms}$ is usually greater than twice the voltage drop on R_2 plus $2\sqrt{2}/\pi$ times the voltage drop on the diode bridge ($2V_D$):

$$E_{2,rms} > 2R_2 I_{2,rms} + V_D \frac{4\sqrt{2}}{\pi} \tag{2.71}$$

This guarantees that only the solution $I_{2,rms,1}$, with the term $-\sqrt{\Delta}$, should be considered:

$$\pm\sqrt{\Delta} = 2R_2 I_{2,rms} + V_D \frac{4\sqrt{2}}{\pi} - E_{2,rms} < 0 \tag{2.72}$$

Hence $I_{2,rms}$ can be approximated by:

$$I_{2,rms} \cong \frac{E_{2,rms} - V_D \dfrac{4\sqrt{2}}{\pi} - \sqrt{\left(E_{2,rms} - V_D \dfrac{4\sqrt{2}}{\pi}\right)^2 - 4R_2 P_{DC}}}{2R_2} \tag{2.73}$$

This expression is especially useful for estimating $I_{2,rms}$ when the DC load is constituted by a DC-DC converter regulating voltage to a constant resistance, because, in this situation, the power P_L supplied to the resistor is fixed, and the power input to the DC-DC, depending on the implementation of the DC-DC converter, is also approximately fixed and equal to P_L/η.

Dynamic Inductive Wireless Power Transfer for Lightweight Electric Vehicles
Luiz Alberto Lisboa da Silva Cardoso – University of Minho

44

In the case of constant power load constituted of a buck converter feeding a fixed resistance, it is typically required that, for the regulation to occur, the input voltage must be greater than the established output voltage V_L by a minimum voltage drop ΔV_{DC}. Then for the approximation (2.73) it should be further required that:

$$V_{DC} \cong \frac{\pi}{2\sqrt{2}} \left(E_{2,rms} - I_{2,rms}\, R_2 \right) - 2V_D \geq \Delta V_{DC} + V_L \tag{2.74}$$

which equivalent to require that:

$$E_{2,rms} \geq E_{2,min} = \frac{2\sqrt{2}}{\pi}(V_L + \Delta V_{DC} + 2V_D) + \frac{\pi}{2\sqrt{2}} \frac{P_L/\eta}{(\Delta V_{DC} + V_L)} R_2 \,, \tag{2.75}$$

where η is the efficiency of the DC-DC converter.

The maximum required secondary rms current, subjected to the condition that the DC-DC buck converter can still regulate voltage V_L on the load, is verified at $E_{2,rms} = E_{2,min}$ and can be obtained by replacing $E_{2,rms}$, given by (2.75) in (2.73):

$$I_{2,max} \cong \frac{\pi}{2\sqrt{2}} \frac{P_L/\eta}{(\Delta V_{DC} + V_L)} \,, \tag{2.76}$$

Figure 19 shows a typical curve of the current established on the secondary coil as a function of the induced voltage (on the same coil), for a constant DC power load implemented by a DC-DC converter feeding a fixed resistor. In this example, the circuit parameters were set at $V_L = 37.5$, $\Delta V_{DC} = 2$ V, $V_D = 0.7$ V, $R_2 = 150$ mΩ, $P_L = 400$ W, and $\eta = 0.942$.
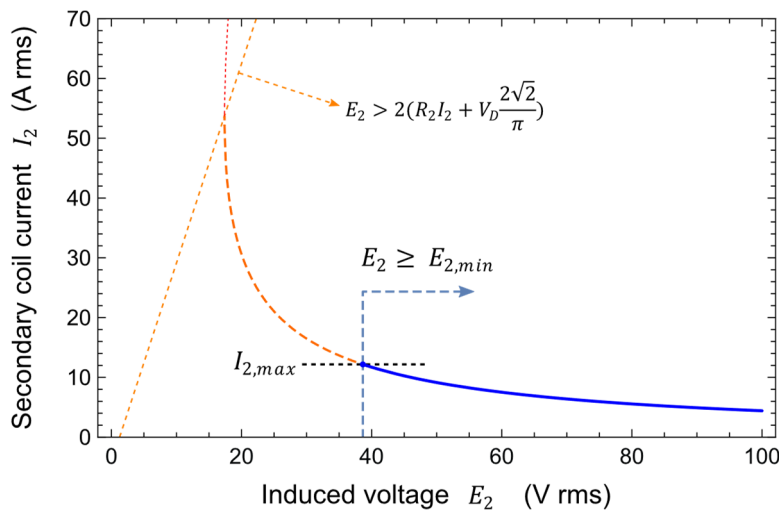
Figure 19: Typical secondary coil current as a function of the induced voltage for a constant DC power.

The blue segment of the curve is the valid solution region, where the induced voltage is high enough for the DC-DC converter to deliver the required power P_L at a fixed regulated voltage V_L.

Dynamic Inductive Wireless Power Transfer for Lightweight Electric Vehicles
Luiz Alberto Lisboa da Silva Cardoso – University of Minho

45

The orange dashed part of the curve could be used it the DC-DC converter is of buck-buster type, being capable of accepting input voltages that are smaller than the required regulated output voltage V_L, however the approximation (2.73) becomes worse for higher currents.

2.6   The Serial-Parallel-Compensation Topology

Frequency splitting is not unique to SS-compensated circuits. This phenomenon can occur, and be exploited, in other circuit topologies as well, due to the presence of multiple poles in the circuit transfer function and the joint dependence of their location on the coupling coefficient and the load. Another similar compensation topology exhibiting frequency splitting, that is also of simple construct and often used in IWPT applications is the Serial-Parallel (SP) compensation [42], where on the secondary side there is a capacitor in parallel with the load, as shown in Figure 20.
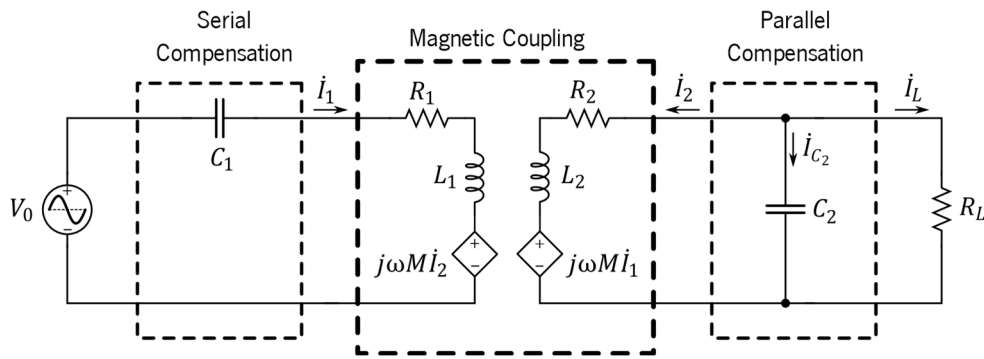
Figure 20: SP-Compensated IWPT circuit.

Using the system of linear equations given by (2.77) and (2.78), it is possible to calculate analytically all the response functions of the SP-compensated IWPT.

$$\dot{V}_0 \;=\; R_1\,\dot{I}_1 + j\,\dot{I}_1\left(\omega\,L_1 - \frac{1}{\omega\,C_1}\right) + j\,\omega\,M\,\dot{I}_2 \tag{2.77}$$

$$j\omega M\,\dot{I}_1 + \dot{I}_2\left(R_2 + j\,\omega\,L_2 + \frac{R_L}{1 + j\,\omega\,C_2 R_L}\right) = 0 \tag{2.78}$$

If C_1 and C_2 are set to the natural resonance frequency of respectively the primary and secondary circuits when these are decoupled, the power output response of the SP-compensated circuit, for instance, can be analytically calculated as:

$$P_{out} = \frac{k^2 R_L C_1 C_2 \left(V_{0\,rms}\right)^2 \lambda^4 \omega_0^2}{\lambda^2\,X^2 + \omega_0^2\,Y^2}, \tag{2.79}$$

where:

Dynamic Inductive Wireless Power Transfer for Lightweight Electric Vehicles
Luiz Alberto Lisboa da Silva Cardoso – University of Minho

46

$$X = 1 - \lambda^2 + k^2\lambda^2 + \omega_0^2(R_1 C_1 R_2 C_2 + (1 - \lambda^2)(R_1 C_1 + R_2 C_2)R_L C_2) \, , \qquad (2.80)$$

$$Y = (R_2 + R_L)C_2 - \lambda^2(R_1 C_1 + R_2 C_2 + R_L C_2(2 - \lambda^2 + k^2\lambda^2 + R_1 C_1 R_2 C_2 \omega_0^2)))^2 \qquad (2.81)$$

and, likewise to the SS-compensated circuit,

$$\omega_0^2 \;=\; \frac{1}{L_1 C_1} \;=\; \frac{1}{L_2 C_2} \qquad\qquad (2.82)$$

Running the model for the SP-compensated circuit with the same parameters as those used to generate Figure 13, results in the plots of Figure 21, where the power output surface, as a function of the normalized frequency $\lambda = f/f_o$ (in logarithm scale), and the magnetic coupling coefficient, k, is shown for different load conditions.
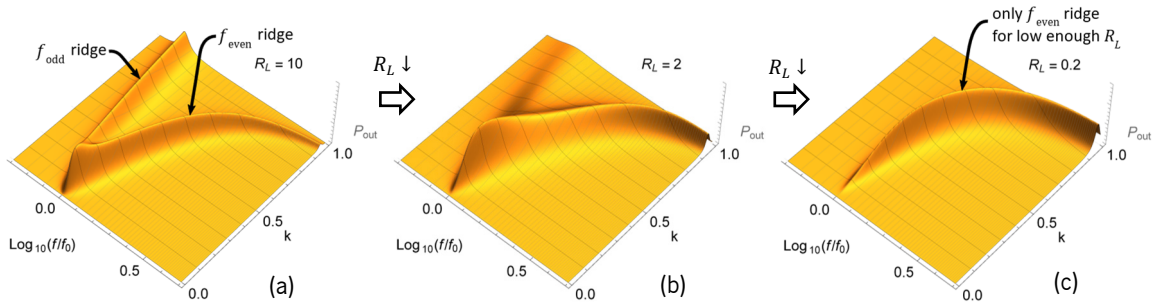
Figure 21. Evolution of the power output in a SP-compensated IWPT, as a function of the normalized frequency, f/f_0, and k, as the load R_L is decreased.

It can be noticed that the power output characteristic of the SP-compensated circuit loaded with a high R_L, as shown in Figure 21a, resembles that of a SS-compensated circuit loaded with low R_L, as shown in Figure 13d, in both cases with maxima at frequencies f_{odd} and f_{even}. As the SP-compensated circuit load R_L is decreased, oppositely to what happens in the SS-compensated case when R_L is increased, the f_{odd} ridge disappears and the response at f_{even} is reinforced, with an observable displacement towards f_0, as shown in Figure 21c.

Expressions for the input power and, thus, for the true efficiency of the SP compensation, η_{SP}, can be computationally derived with the aid of software tools for algebraic manipulation. The results are again better visualized by plotting superposed contour maps of the output power and the efficiency. Using the same circuit parameters as those used to draw the SS-compensated example of Figure 16 results in the SP-compensated typical plot of Figure 22.

Dynamic Inductive Wireless Power Transfer for Lightweight Electric Vehicles
Luiz Alberto Lisboa da Silva Cardoso – University of Minho

47
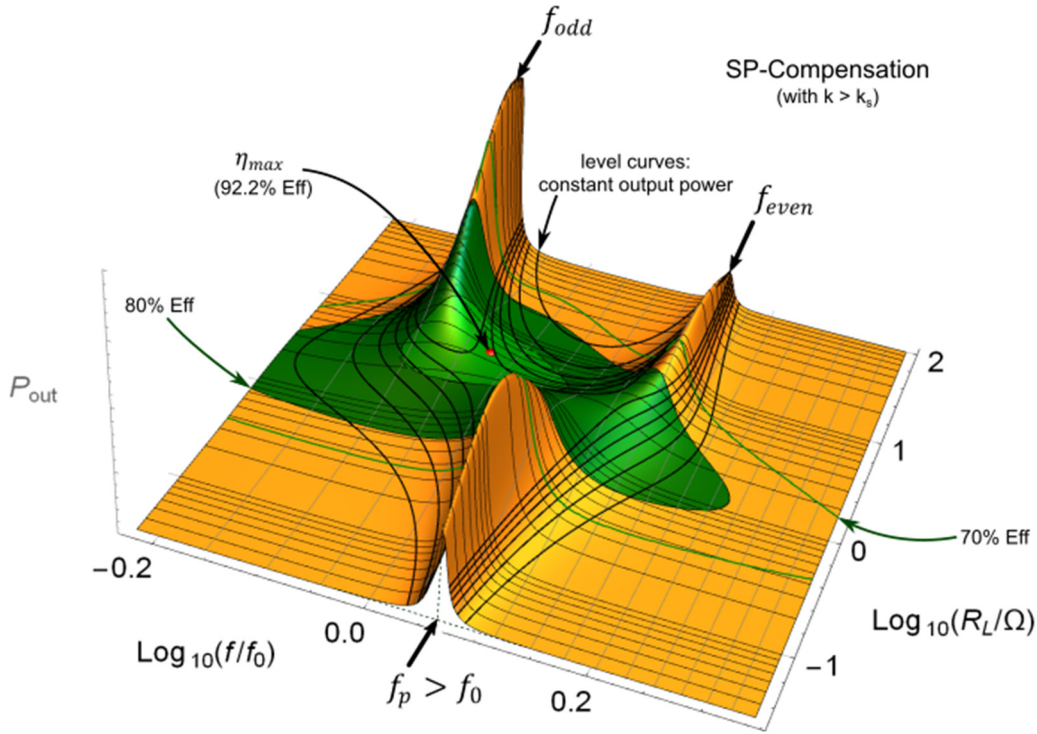
Figure 22: Bounded efficiency regions (green) drawn over the power output surface of a SP-compensated IWPT coupling, having the frequency of operation and the equivalent output load as free parameters.

The SP-compensation output response is similar to that of the SS-compensation, however as k is increased, differently from the SS-compensation case, the frequency splitting is observed at the high values of the equivalent secondary load R_L, not on the low values. Likewise, in SP-compensation, a single power peak is observed at lower enough values of R_L, whereas a single power peak was observed at high enough values, in the case of SS-compensation. The new resonant frequencies at high enough R_L values, f_{odd} and f_{even}, are given by the same equations (2.54) and (2.55), as in the SS-compensated case, departing from f_0 as k is increased. In the SP case, however, in the low values of R_L a new resonant frequency f_p occurs, with $f_p > f_0$, in place of the constant resonance frequency f_0. This frequency f_p, departing from $f_p = f_0$ for $k = 0$, also increases with the increase in k, being calculated by considering the required primary capacitance for resonance of the unloaded secondary ($R_L = 0$), as can be derived from the expression in Table I of [41] (SP topology), here also reproduced in Table 2:

$$C_1 = \frac{1}{\omega_p^2 \left(L_1 - \dfrac{M^2}{L_2}\right)} \tag{2.83}$$

$$\Rightarrow L_1 C_1 = \frac{1}{\omega_p^2 \left(1 - \dfrac{M^2}{L_1 L_2}\right)} = \frac{1}{\omega_p^2 (1 - k^2)} \tag{2.84}$$

Dynamic Inductive Wireless Power Transfer for Lightweight Electric Vehicles
Luiz Alberto Lisboa da Silva Cardoso – University of Minho

48

But, by hypothesis (2.82), $L_1 C_1 = L_2 C_2 = 1/\omega_p^2$, so:

$$f_p = \frac{1}{\sqrt{1-k^2}} \, f_o \qquad (2.85)$$

Instead of using a three-dimensional plot, the analysis and design of a SP-compensated IWPT circuit, as in the case of SS, can also be facilitated by the use of joint power and efficiency contour maps. An example, using the same circuit parameters as those used to generate the chart in Figure 17, is given in Figure 23, where the same plotting scales and color convention for the contour curves and peak power surfaces were also used.
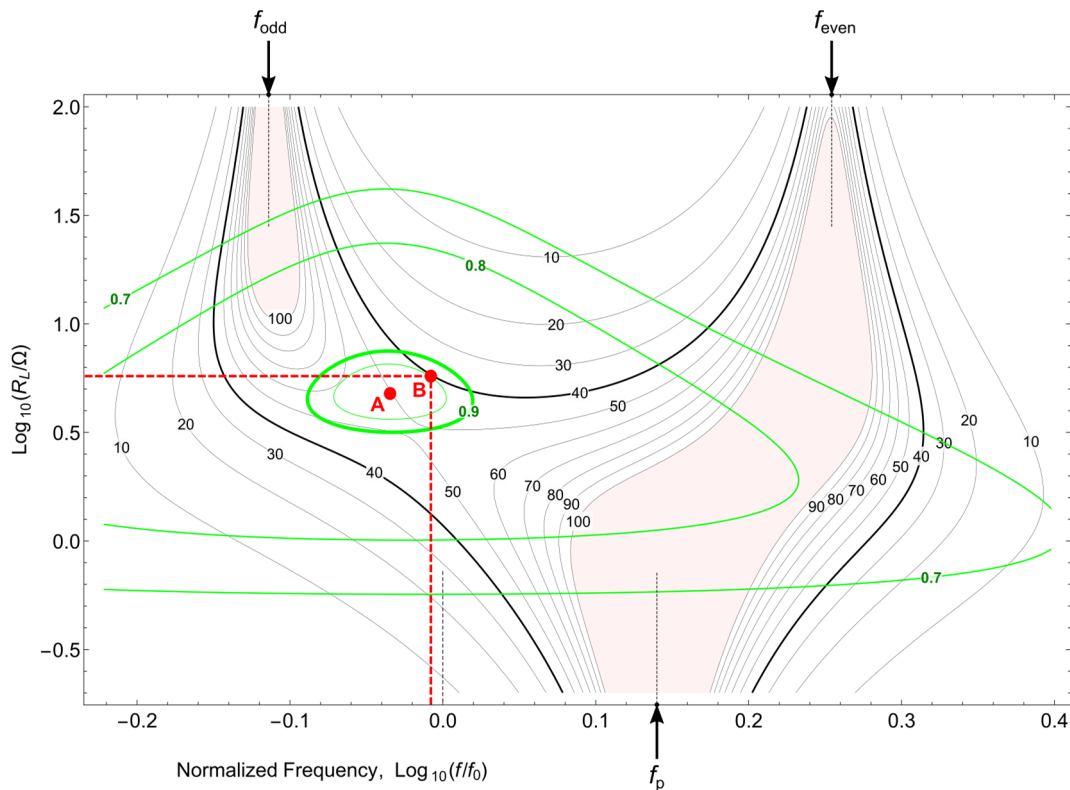
Figure 23: Typical constant output power (black) and constant efficiency (green) contours of a SS-compensated WPT coupling, having the frequency of operation and equivalent output load as free parameters.

Point "A", marked with a red dot in the middle of the central lighter green spot (efficiency ≥ 90%), is the operation point where the overall maximum achievable efficiency η_{max} is obtained, which, in this example, incidentally happens to be approximately 92.2%. Point "A" lies between the power ridges associated to f_p and f_{odd}, at a frequency lower than f_0, that tends to f_0 as k is decreased to zero.

The power output at point "A", $P_{\eta_{max}}$, can visibly be exceeded, if the operation point "climbs" one of the power ridges (best observed in Figure 22), associated to the resonance frequencies f_{odd}, f_p and f_{even}. But, just as in the SS-compensation case, this would come at

Dynamic Inductive Wireless Power Transfer for Lightweight Electric Vehicles
Luiz Alberto Lisboa da Silva Cardoso – University of Minho

49

the expense of a decrease in efficiency, as the operation point would be departing from the red dot. For fixed k, a good strategy design to satisfy a required power output level, with an efficiency bounded to a minimum given value, is to select the operation point on one of the power contour curves satisfying that required power, as close as possible to the point of η_{max}. More precisely, the point where the contour curve for the required power is tangent to contour curve of highest possible efficiency should be selected as the operation point. In the example of Figure 23, if the required output power is 40 W, for instance, the thick black curves indicate the locus for this power, and point "B" should be the preferable choice for the operation point.

Considering (2.54), (2.55) and (2.85), it can be noticed that product of f_{odd} and f_{even} is equal to the product of f_0 and f_p:

$$f_o\ f_p\ =\ f_{odd}\ f_{even}\,, \tag{2.86}$$

an expression that leads to a simple geometric interpretation, shown in Figure 24, that helps in the design of SP-compensated circuits (and PP-compensated too, as explained in section 2.7).
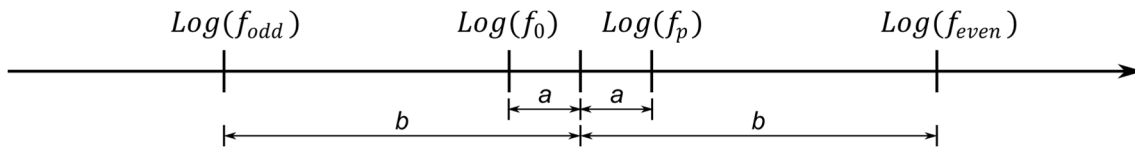
Figure 24: Geometric interpretation of the relative positioning of the resonant frequencies in SS and SP-compensated IWPT circuits on a logarithm scale.

Because in the SP-compensation all resonant frequencies in the frequency splitting zone ($k\ >\ k_s$) are dependent on k, an IWPT implementation where k is expected to vary along the power transfer process may be more complex to design than it is in the SS case, usually requiring some sort of frequency tracking mechanism, even if the load is constant.

These characteristics may lead to the choice of an SP-compensated IWPT over an SS-compensated topology, or vice versa, depending on whether the impedance of the load being respectively higher or lower, and ultimately, on the actual point of operation $(f,\ R_L)$ satisfying the constraints of each particular IWPT application.

2.7   Comparison of the Basic-IWPT Compensation Topologies

The SS and SP topologies, together with their counterpart topologies in which the primary circuit is current-fed, respectively the parallel-serial (PS) and parallel-parallel (PP) compensated topologies, are referred to as the basic IWPT compensation topologies. The SS, SP, PP and PS

Dynamic Inductive Wireless Power Transfer for Lightweight Electric Vehicles
Luiz Alberto Lisboa da Silva Cardoso – University of Minho

50

basic topologies are summarized in Figure 25, where, for simplicity, the equivalent winding loss resistors R_1 and R_2 have been omitted from the models.
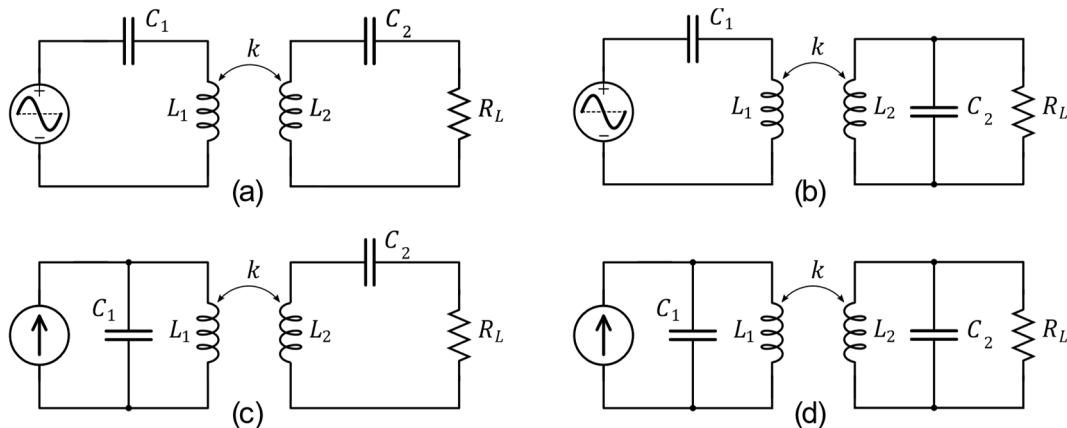
Figure 25. Summary of basic compensation topologies used in IWPT: (a) SS, (b) SP, (c) PS and (d) PP.

Similar to the SS and SP-compensated topologies, presented in sections 2.5 to 2.7, Parallel-Series (PS) and Parallel-Parallel (PP) compensation circuits are defined by alternatively using a capacitor in parallel in the primary as a compensation device, a configuration that requires, instead, excitation from an alternate current source.

The PS and the PP-compensated topologies have distinct power requirements in terms of the power source that feds to the primary circuit, but they have similar power responses and efficiency patterns respectively to the SS and SP-compensated ones. This happens under the assumption that the topologies with a capacitor in parallel with primary coil are fed by a current source, whereas those with a capacitor in series with the primary coil, by a voltage source. The equivalence, under the point of view of the secondary load R_L, follows by the Thévenin's theorem.

Concerning the currents and voltage levels demanded from the input power source, the equivalence is not applicable, in the sense that, to transmit the same power, the power source of a PS-compensated configuration will generally work better with larger input currents than one that is SS-compensated, while the necessary voltage to drive an SS-compensated IWPT will tend to be higher than that used to drive a PS-compensated configuration. Similar happening when comparing the PP to the SP-compensated networks.

One of the firsts in depth general comparisons of these four basic compensation topologies, aiming their use in wireless power transfer applications, was brought by Wang, Covic and Stielau [43]. Similarly to the simplification adopted in Figure 25, Wang et al. also assumed in their analysis the resistors R_1 and R_2 of the linear magnetic coupling model to be zero. However, instead of setting the individual isolated resonant frequencies of both primary and secondary circuits to the

Dynamic Inductive Wireless Power Transfer for Lightweight Electric Vehicles
Luiz Alberto Lisboa da Silva Cardoso – University of Minho

51

same frequency, f_0, and analyzing the transfer characteristic of the resulting WPT for variable coupling coefficient and operating frequency, as done in the previous sections in this chapter, Wang et al. kept the overall resonant frequency at the value of the secondary resonance frequency, f_0. This step in the design paradigm is accomplished by tunning the primary circuit in each of the topologies to a different frequency, by adjusting the value of C_1 according to Table 2.

Table 2: Secondary impedance reflected on primary circuit, Z_r, and optimal primary capacitor, C_1, for maximum power transfer in SS, SP, PS and PP compensation topologies.

Topology	Reflected Impedance Z_r (of the secondary onto the primary circuit)	C_1
SS	$\dfrac{\omega_0^2 M^2}{R_L}$	$\dfrac{1}{\omega_0^2 L_1}$
PS		$\dfrac{L_1}{\left(\dfrac{\omega_0^2 M^2}{R_L}\right)^2 + \omega_0^2 L_1^2}$
SP	$\dfrac{M^2 R_L}{L_2^2} - j\dfrac{\omega_0 M^2}{L_2}$	$\dfrac{1}{\omega_0^2\left(L_1 - \dfrac{M^2}{L_2}\right)}$
PP		$\dfrac{L_1 - M^2/L_2}{\left(\dfrac{M^2 R_L}{L_2^2}\right)^2 + \omega_0^2\left(L_1 - \dfrac{M^2}{L_2}\right)}$

However, except in the case of SS-compensation, this design approach and analysis may be not the most convenient one, when the IWPT configuration is going to be used in DIWPT applications, where variable magnetic coupling coefficients, k, are likely to be encountered. For the other topologies, SP, PS and PP, this would require the capacitor C_1 or ω_0 to be continuously adjusted, as k and M vary, to keep an optimum power transfer, which is not usually practical, especially if more than one secondary is simultaneously harvesting energy from the primary.

If this inconvenience is disregarded, the analysis provided by Wang et al. is very interesting, for they have established that all these basic IWPT topologies [43], as displayed in Figure 25, are prone to exhibit frequency splitting, also called as the frequency bifurcation phenomenon. The condition for frequency splitting to occur have been expressed as a function of the loaded quality factors of the primary, Q_P, and secondary, Q_S, as calculated in Table 3.

Dynamic Inductive Wireless Power Transfer for Lightweight Electric Vehicles
Luiz Alberto Lisboa da Silva Cardoso – University of Minho

52

Table 3: Loaded quality factors for SS, SP, PS and PP IWPT topologies.

Topology	Q_P	Q_S
SS, PS	$\dfrac{L_1 R_L}{\omega_0 M^2}$	$\dfrac{\omega_0 L_2}{R_L}$
PS, PP	$\dfrac{\omega_0 L_1 L_2^2}{M^2 R_L}$	$\dfrac{R_L}{\omega_0 L_2}$

In approximate terms, it has been determined that bifurcation will not occur when $Q_P > Q_S$. More precisely, bifurcation will not occur only when the condition given by Table 4 is verified.

Table 4: Loaded quality factors for SS, SP, PS and PP IWPT topologies.

Topology	Condition for no Frequency Bifurcation
SS	$Q_P > Q_S \left(\dfrac{4 Q_S^2}{4 Q_S^2 - 1} \right)$
SP, PP	$Q_P > Q_S + \dfrac{1}{Q_S}$
PS	$Q_P > Q_S.$

In some applications authors try to avoid frequency splitting [39] [40], what simplifies the calculation of circuit parameters for IWPT. Instead, with the graphical analysis exemplified in sections 2.5 and 2.6 it is possible to compute any desired operation point, exploiting the output response abnormalities caused by frequency splitting. The procedure is however computationally intensive, and some numeric computing tool should be employed.

The SS and SP-compensated topologies are possibly the most popular so far observed in academic studies and most real-world implementations. Excited by an alternated voltage source in the primary side, they are simpler to implement, easier to analyze than the more complex topologies, and still can successfully handle a large number of applications. For wireless vehicular charging power ranges from a few kilowatts to a few tens of kilowatts, a number of laboratory implementations report the use the SS and SP-compensation schemata [44], with some authors having identified efficiency advantages of the SS over the SP-compensated circuits for this type application [45]. This advantage can be relativized by the fact that the parallel compensation may be the preferable topology to be used if high currents and power levels are to be achieved, and either the input or output voltage is restricted not to be exceedingly high. This will often be the case in circumstances where the mutual inductance between the coils is low. In principle, the

Dynamic Inductive Wireless Power Transfer for Lightweight Electric Vehicles
Luiz Alberto Lisboa da Silva Cardoso – University of Minho

53

efficiency will depend on the passive components of the compensation circuits having less losses, and this is more related to the quality factor of the components themselves and the choice of the more favorable operation point, which may be different for each topology, similarly to what happens with the power output (compare results in Figure 13 and Figure 21). This conclusion is supported by a case study [46] where the SP efficiency is reported to be better than that of the SS-compensation when lower magnetic coupling coefficients, resulting from asymmetry in the coils, are observed, and worse otherwise.

Under the perspective of a DIWPT application, it is more useful to compare the compensation topologies according to the variability of the magnetic coupling coefficient, k.

2.7.1 Comparison of IWPT Circuits under Constant k

For the SS-compensated coupling, the transferred power will be very high at the resonant frequency f_o, for adequately large values of R_L, or at any of the split frequencies f_{odd} and f_{even}, for low values of R_L. However, for high efficiency in the power transfer, the operation point should be set away from the maxima in transferred power. Other than that, structural improvements to the efficiency come when the magnetic coupling quality factor, $k\sqrt{Q_1 Q_2}$ is increased. That is, when higher frequencies are used and the circuit components exhibit low losses at these higher frequencies, or, when the magnetic coupling coefficient k is made as high as possible, if it happens to be a free design parameter. The parameter k can be increased, for instance, when coils of comparable size are approached to each other, or when magnetic shaping is implemented, by means of the use of soft magnetic core materials, such as high quality (low losses) ferrites.

Formulation found in the literature can help the design in the simpler cases [35], as exemplified in this work for the SS and SP-compensation circuits with coils of high quality factors that are not heavily loaded. But, in general, numerical simulation is the prevalent tool for both IWPT evaluation and design. Its use becomes especially necessary if other more complex compensation circuit topologies are investigated, and the appearance of multiple resonance frequencies is expected, or if non-linear elements, such as a rectifier as an output stage, are introduced in the circuit, leading to more difficult and impractical exact algebraic analysis.

By the use of superposed contour maps of constant output power and efficiency, as exemplified in sections 2.5 (Figure 17) and 2.6 (Figure 23), it is possible to either analyze an existing IWPT configuration, refine its circuit parameters, or optimize the choice of the point of operation, accordingly to some simultaneously given efficiency and power output requirements.

Dynamic Inductive Wireless Power Transfer for Lightweight Electric Vehicles
Luiz Alberto Lisboa da Silva Cardoso – University of Minho

54

These contour maps can be used analyze and design other circuit compensation topologies as well and the requirements for power and efficiency can also be expressed in terms of maximum and minimum boundaries, instead of single target values.

For the same fixed circuit parameters used in the examples of Figure 16 and Figure 22, the power output and efficiency patterns are compared in Figure 26. Under the assumption of lossless ideal power sources, similar graphics can be drawn when comparing power and efficiency in the PS and PP configurations.
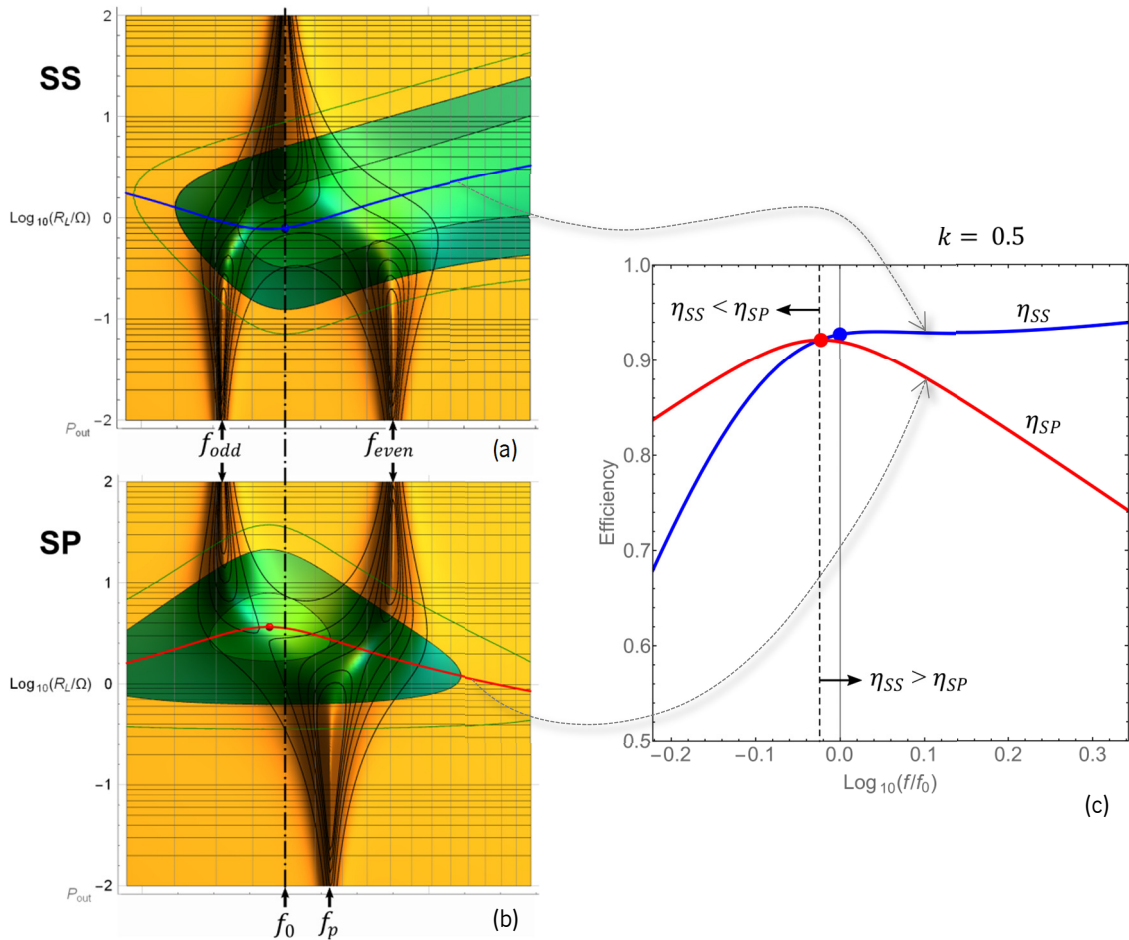
Figure 26: Comparison of power output (black contours) and efficiency patterns (green shades and contour) between IWPT topologies with series-loaded (a) and parallel-loaded (b) secondary; and efficiency values (c).

The blue curve, in Figure 26a, and red curve, in Figure 26b, indicate the loci of the maximum achievable efficiency at different operation frequencies, respectively for the SS and SP cases. In the SS-compensation (Figure 26a), the blue dot on the blue curve indicates the operation point at the resonance frequency f_0 where the best efficiency is found, while in the Figure 26b the red dot on the red curve indicates the point of operation with overall maximum SP-efficiency.

At f_0, there is a slight advantage, in terms of efficiency, for the SS-compensation. At higher than f_0 frequencies, higher efficiencies than that observed at the red dot will be found, provided

Dynamic Inductive Wireless Power Transfer for Lightweight Electric Vehicles
Luiz Alberto Lisboa da Silva Cardoso – University of Minho

55

the equivalent load R_L is conveniently adjusted. At frequencies that are lower enough than f_0, the efficiency of the SP-compensation will be higher than that of SS-compensation. It should be emphasized, however, that this apparent improvement of the SS-compensation over the SP-compensation only holds when the both SS and SP-compensation circuits are implemented using the same design resonance frequency f_0 for the primary and secondary branches, when individually considered (i.e., calculated as if the magnetic coupling was zero). But this is a restriction that need not to be adopted when designing SS and SP configuration in a competitive basis. In fact, it is possible to pick a resonant frequency f_0^{SP} for the individual branches of a SP-compensated IWPT, with f_0^{SP} higher than the base resonant frequency of the SS-compensated topology, f_0^{SS}, in such a way that the point of maximum efficiency in the SP configuration is found exactly at f_0^{SS} , and choose f_0^{SS} as the operating frequency in both circuits. This would diminish the difference in the SS and SP efficiencies at that operation point.

For fixed-k operation, the choice of the operation point presumes a compromise between efficiency and output power. The higher the efficiency, the better, subjected to the satisfaction of the minimum power requirements of the application.

2.7.2 Comparison of IWPT Circuits under Variable k

When k is allowed to vary, the frequencies f_{odd}, f_{even} and, for the SP and PP topologies, the f_p as well, will also vary, being displaced further away from f_0 as k is increased. In these conditions, the SS or the PS-compensated IWPT are the preferable choice, for it will more easily allow to sustain a predetermined output power level at the fixed resonant frequency f_0 exhibited in these compensation circuits. In the same circumstances, the PP and SP-compensation topologies with fixed circuit parameters would require more elaborated frequency track schemes to sustain the output power, resulting in a more complex implementation, even if the load is kept constant (k cannot be assumed constant in DIWPT configurations). For this reason, the SS and PS-compensated topologies are deemed as more adequate for applications where the magnetic coupling coefficient varies dynamically.

The relative efficiency performance of SS and PS topologies can be visualized in Figure 27 for the whole valid range of k, by concatenating plots similar to that in Figure 26c. Similar plots could be derived to compare PS and PP topologies.

Dynamic Inductive Wireless Power Transfer for Lightweight Electric Vehicles
Luiz Alberto Lisboa da Silva Cardoso – University of Minho

56
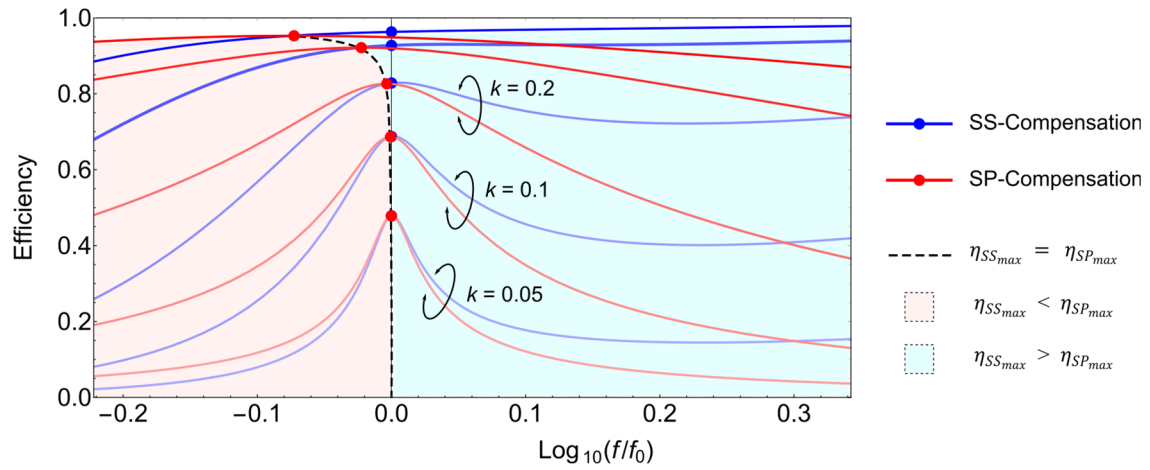
Figure 27: Family of SS and SP efficiency curves as the magnetic coupling coefficient k is varied.

Analyzing the curves of Figure 27, it is possible to verify that, between two WPT circuits tuned to the same resonant frequency f_0, the one with the serial compensation in the secondary and the other with parallel compensation, the serial compensated will have slightly better efficiency that the parallel compensated when both are operated in frequency in the vicinity of f_0. However, this difference is negligible when $k \leq 0.2$. The black dashed line in Figure 27 is the locus of the points where these two efficiencies are equal.

In many practical applications in where k dynamically varies, the value range for this parameter is in the interval $[0, k_{max}]$, often with k_{max} significantly less than the unity. So, the choice of for a SS/PS or PP/SP compensated WPT topology will not be critical, under the point of view of the efficiency achieved, and this design option can rely on other practical requirements. The choice, ultimately, may depend on the voltage and current levels required by the load, for the same power level. The variable k is a common assumption, for instance, in most dynamic inductive wireless power transfer (DIWPT) applications, as described in Chapter 3.

2.8   Other Circuit Compensation Topologies

Other topologies using arbitrarily more complex passive matching circuits can also be used to connect the load and the power source through a magnetic coupling. Authors have been investigating such topic and extensive reviews on compensation topologies and their uses in IWPT are available [47] [48]. The general approach to evaluate any compensation topology is to recognize it as a passive two-port network.

For instance, all the basic IWPT compensation topologies, as shown in Figure 25, can be thought of as two-port network that is constituted of cascaded two-port networks, in which the

Dynamic Inductive Wireless Power Transfer for Lightweight Electric Vehicles
Luiz Alberto Lisboa da Silva Cardoso – University of Minho

57

central one is the linear transformer model, usually expressed as an impedance matrix, as in (2.87), where $Z_{11} = j\omega L_1$, $Z_{12} = Z_{21} = j\omega M$ and $Z_{22} = j\omega L_2$.

$$\begin{bmatrix} \dot{V}_1 \\ \dot{V}_2 \end{bmatrix} = \begin{bmatrix} Z_{11} & Z_{12} \\ Z_{21} & Z_{22} \end{bmatrix} \begin{bmatrix} \dot{I}_1 \\ \dot{I}_2 \end{bmatrix} \tag{2.87}$$

The corresponding circuit model interpretation is shown in Figure 28, which is the usual manner to represent a magnetic coupling, as previously shown in Figure 3b.
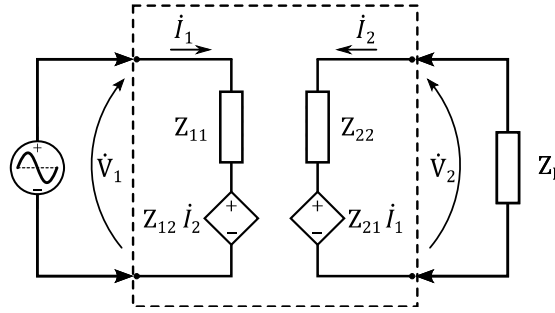
Figure 28: Impedance model for a passive two-port network.

However, the two-port network can be alternatively expressed by an ABCD linear model, in which the voltage and current phasors of the two ports are related by (2.110):

$$\begin{bmatrix} \dot{V}_2 \\ \dot{I}'_2 \end{bmatrix} = \begin{bmatrix} A & B \\ C & D \end{bmatrix} \begin{bmatrix} \dot{V}_1 \\ \dot{I}_1 \end{bmatrix} \tag{2.88}$$

where $\dot{I}'_2 = -\dot{I}_2$ (in the ABCD model, the positive conventional direction of the secondary current is the opposite of that in the impedance model, to facilitate the computation of cascaded two-port networks).

So, expressing $\dot{I}'_2$, in terms of $\dot{I}_2$:

$$\begin{bmatrix} \dot{V}_2 \\ -\dot{I}_2 \end{bmatrix} = \begin{bmatrix} A & B \\ C & D \end{bmatrix} \begin{bmatrix} \dot{V}_1 \\ \dot{I}_1 \end{bmatrix} \tag{2.89}$$

These coefficients A, B, C and D can be expressed in terms of the impedance parameters of the two-port network:

$$\begin{bmatrix} A & B \\ C & D \end{bmatrix} = \begin{bmatrix} \dfrac{Z_{22}}{Z_{12}} & Z_{21} - \dfrac{Z_{11}Z_{22}}{Z_{12}} \\ -\dfrac{1}{Z_{12}} & \dfrac{Z_{11}}{Z_{12}} \end{bmatrix} \tag{2.90}$$

The ABCD-model was used in to demonstrate that the expression for maximum efficiency η_{max} of any two-port network, coupled to the source and the load by respectively input and output

Dynamic Inductive Wireless Power Transfer for Lightweight Electric Vehicles
Luiz Alberto Lisboa da Silva Cardoso – University of Minho

58

matching networks [49], where the authors still considered the primary voltage source with an intrinsic associated output impedance. Here, for simplification, the output impedance of the source is considered null. Then, in these conditions, the maximum efficiency of the two-port network is given by:

$$\eta_{max} = \frac{\chi}{\left(1 + \sqrt{1 + \chi}\right)^2},$$ (2.91)

where:

$$\chi = \frac{|Z_{12}|^2}{Re(Z_{11})Re(Z_{22}) - Re(Z_{12}^2)}$$ (2.92)

Exemplifying the use of this more general approach, it can be derived that for the SS-compensated topology:

$$\chi = \frac{\omega^2 M^2}{R_1 R_2 + \omega^2 M^2}$$ (2.93)

Recalling that $M^2 = k^2 L_1 L_2$ and that the quality factors Q_i are defined as in (2.27), then χ can be written:

$$\chi = \frac{k^2 \omega L_1 \omega L_2}{R_1 R_2 + k^2 \omega L_1 \omega L_2} = \frac{k^2 Q_1 Q_2}{1 + k^2 Q_1 Q_2},$$ (2.94)

and replacing χ in (2.91) the expression for η_{max} becomes:

$$\eta_{max} = \frac{k^2 Q_1 Q_2}{\left(1 + \sqrt{1 + k^2 Q_1 Q_2}\right)^2},$$ (2.95)

exactly as directly derived before for the SS-Compensated IWPT topology, in (2.34).

One advantage in the ABCD modeling for assessing η_{max} is recognizing that the magnetic coupling, formed just by the coupled coils and no compensation circuit, is a two-port itself and the maximum achievable total efficiency of the IWPT circuit formed by cascading lossless primary and secondary compensation circuits is the same as the base magnetic coupling. That means that the expression of the maximum achievable efficiency η_{max} (2.34) and (2.95), derived for the SS-compensated case, holds for the SP, PS and PP cases well, as it will hold for other arbitrary compensation topologies, as long as the compensation circuit components added to the primary and secondary circuits are lossless, and all losses of the compensated coupling can be accounted

Dynamic Inductive Wireless Power Transfer for Lightweight Electric Vehicles
Luiz Alberto Lisboa da Silva Cardoso – University of Minho

59

to the equivalent serial resistors R_1 and R_2 of the coil windings. Naturally, for each compensation topology, this η_{max} will be achieved for potentially different optimum loading conditions.

In practice, the electronic components in the compensation circuits do have parasitic resistances, which will add extra losses in the power transfer. So, it can be expectable that more complex compensation circuits may tend to be less efficient than a simpler one, with less components. This as well may not be true in all cases, because the losses depend not only on the number of components and their parasitic resistances, but also on the current pattern flowing in each of them. As a general rule, unless some specific circuit behavior is sought, more complex compensation circuits should be avoided, and only modeling and circuit simulation can precisely anticipate the actual efficiency of an IWPT configuration.

2.9   Power Electronics for WPT

As exposed in Section 1, power electronics is one of the tools, not the focus of this work. However, it is necessary to briefly consider some of the basic concepts and most popular circuit types available to drive the primary coil, because the WPT behavior can be affected by its characteristics, and vice-versa. In the same manner, the designer should be aware of the options for harvesting energy at the output terminals of the secondary compensation circuit, since in all cases of interest in the electric mobility application, the target load requires a DC voltage, instead of the AC voltage at the WPT operation frequency. Although the electric motor inside an EV may actually require either DC or AC current, from the systemic point of view, the motor is always used in connection with a specific power electronics module, called motor controller, which will always receive DC power, originally coming from the EV's main battery. The motor controller then converts the DC power according to the intended mechanical response from the motor being controlled, and generates the corresponding DC or AC power signals to drive it.

Figure 29 shows the representation of at typical IWPT system architecture, where the active power electronics are self-contained functional blocks inserted in the primary, to transform the available power source into high frequency AC at the required power level, and in the secondary, to rectify and filter the induced voltage on secondary, as well as to provide the DC impedance match that may be eventually also required, as referred in Section 2.5.1.

Dynamic Inductive Wireless Power Transfer for Lightweight Electric Vehicles
Luiz Alberto Lisboa da Silva Cardoso – University of Minho

60
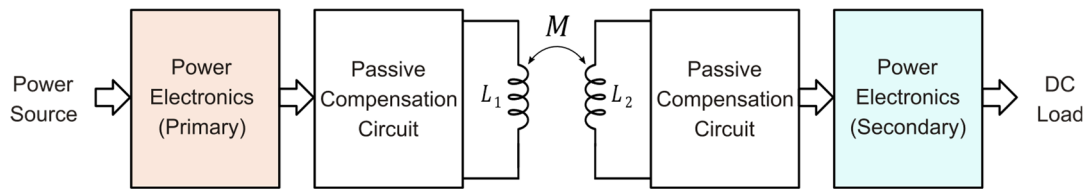
Figure 29: Typical insertion of active power electronics blocks in a IWPT system.

Most power electronics functionality required for IWPT applications can be built by the proper association of three elementary power blocks: The AC-DC converter, which is called rectifier, the DC-AC converter, which is commonly called as "inverter" and the DC-DC converter. These blocks may either have fixed behavior, or similarly to what happens with a motor controller, can be optionally monitored and controlled by intelligent electronics (processors), that will implement more complex characteristics of the converter. In the scope of this work, in order to implement the prototype and validate the HIPLEV concept, simpler, fixed behavior converters will suffice. The converters circuit blocks are represented by their symbols in Figure 30.

(a) AC-DC converter (rectifier)   (b) DC-AC converter (inverter)   (c) DC-DC converter
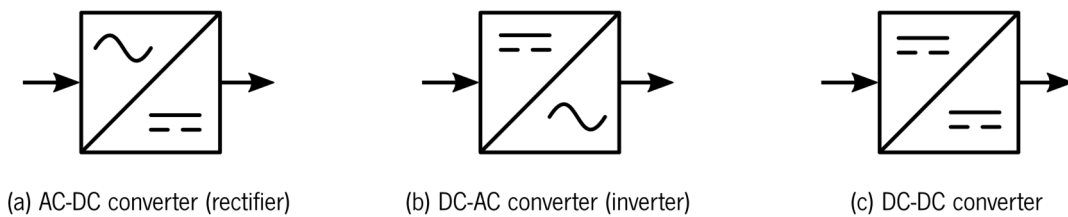
Figure 30: Symbology for the elementary power electronic converters used in this work.

The power source indicated as an input in the IWPT system architecture can be either AC or DC. When it is AC, it will usually be supplied by the power grid, at the frequencies of 50 Hz or 60 Hz worldwide, which are inadequately low for direct driving of the magnetic coupling. The power electronics connected to the primary coil then first rectifies the grid power to an adequate value V_{DC}, which is then inverted, i.e., transformed into a square wave power signal at the IWPT design operating frequency f_q. Often, as seen in sections 2.5 and 2.6, f_q will be close to the intrinsic resonant frequency of both primary and secondary compensation circuits, in such a way that the compensated magnetic coupling will function as a band-pass filter for f_q, and, for the purpose of computing voltages and currents across the magnetic coupling, only the fundamental sinusoidal component of the power signal will give a good approximation for the primary and secondary currents, as well as the nominal power output values.

In this section, the most basic topologies of inverters used to energize the primary coils and generate the AC magnetic field that allows the IWPT to occur are presented and discussed. Using only two power transistors, the simplest of these circuits presented is the Mazzilli-Baxandall auto-

Dynamic Inductive Wireless Power Transfer for Lightweight Electric Vehicles
Luiz Alberto Lisboa da Silva Cardoso – University of Minho

61

resonant inverter. Because of that, and in alignment with the design directives for the HIPLEV (section 5.1) this is the topology of choice for the implementation of an i-lane for our first HIPLEV prototype. Despite being sometimes regarded as an unstable cheap circuit, most commonly used in inductive heating, the Mazzilli-Baxandall driver has proved in the simulation and in the lab to be a robust and, although exhibiting a mathematically sophisticated model, completely predictable, being adequate for industrial use in different applications [50], if carefully designed and used within its operational envelope. The analysis developed, numeric example and simulations further presented in 2.9.4 are then not incidental, but intentionally use the same voltage and power levels required in the prototype, which uses the exact same circuit drawn in Figure 46, with nominal parameters as in Table 5, among which some were finely tuned to achieve the required circuit performance.

2.9.1 Resonant Inverters using Full H-Bridge

One of the simplest power circuits that is also popularly used in IWPT designs is shown in Figure 31. It uses a full h-bridge inverter to generate the high frequency power component that is fed to the compensation network of the primary coil. The h-bridge is formed by two "arms", each consisting of the series association of two active switches, which can be bipolar transistors, Insulated Gate Bipolar Transistors (IGBT), Metal Oxide Semiconductor Field Effect Transistor (MOSFET), or any other electronic switching device. In each arm, at any given time, only one switch is supposed to be in the conductive state. The timing and levels of the control lines for theses switches also guarantee that, during normal operation, different arms of the h-bridge are in complementary state, in such a way that, in Figure 31, point A and B are alternately connected to the positive and negative poles of V_{DC}, but always with opposite polarity. This continuous ON and OFF commuting generates a square wave with frequency f_q and amplitude V_{DC} in between terminals A and B. $C_{D,1}$ and $C_{D,2}$ are the decoupling capacitors for the two half-bridges. They are inserted in parallel for decoupling of the two half-bridges from parasitic inductances, which, except from L_P, are not shown in the schematics.
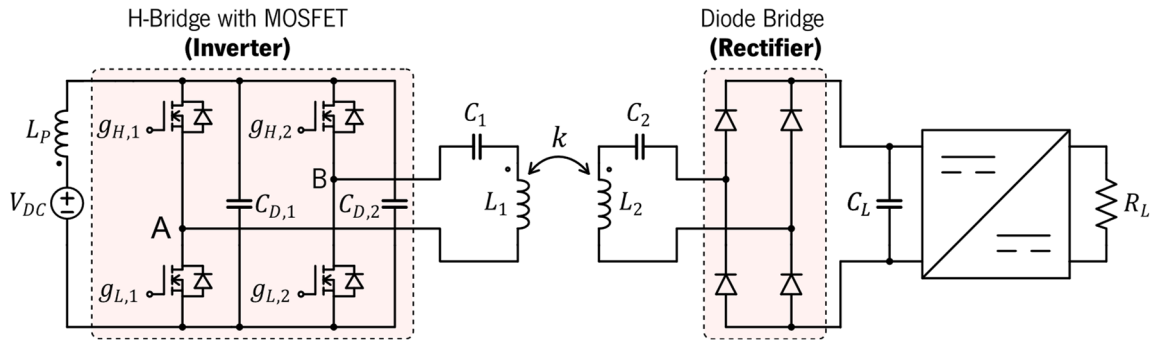
Figure 31: H-bridge driving primary coil of a SS-compensated magnetic coupling, with a diode bridge as a rectifier and a DC-DC converter for load matching in the secondary.

Specifically, in the example of Figure 31, MOSFETs are used, and the control signals are the gate signals $g_{H,1}$, $g_{L,1}$, $g_{H,2}$ and $g_{L,2}$. These signals have to be generated by the adequate voltage level translation of the respective digital signals $\tilde{g}_{H,1}$, $\tilde{g}_{L,1}$, $\tilde{g}_{H,2}$ and $\tilde{g}_{L,2}$, derived from a common inverter controller, as shown in Figure 32.
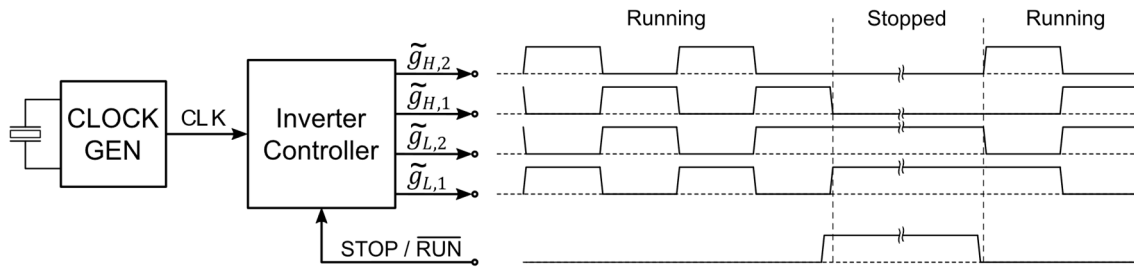
Figure 32: Logical control signals for the gate drivers of the H-bridge inverter.

Common to all DIWPT applications, the primary coil has to be energized only at proper times, when a secondary pick-up coil is ready to harvest energy. So, the oscillation of the primary circuit must be turned on and off accordingly. A standard way to implement this is illustrated in the timing chart of Figure 32, by the use of a control signal named $\mathrm{STOP}/\overline{\mathrm{RUN}}$. When this signal is logically low ($\overline{\mathrm{RUN}}$), the gate signals oscillate in synchronism, to promote the switching of the MOSFETs. When it is brought to a logically high level (STOP), the cycles are terminated, with the lower transistors being shortened to the negative terminal of V_{DC}, which is usually the zero voltage reference, and the higher transistors shortened to the positive terminal of V_{DC}.

Inverter controller logic, as well as the clock generator ("CLOCK GEN") can be normally implemented in micro-controller, by software, which further allows the fine adjustment of the fundamental frequency of the IWPT, according to the designed operation frequency.

The compensation network, with primary and secondary circuits tuned to the resonant frequency f_0, which is close to f_q, behaves as band pass filter, so that, for the effect of the WPT

Dynamic Inductive Wireless Power Transfer for Lightweight Electric Vehicles
Luiz Alberto Lisboa da Silva Cardoso – University of Minho

63

calculations, the equivalent sinusoidal input voltage V_{AB} to the primary compensation circuit can be approximated by the first harmonic component of the square wave in between A and B. For square waves with 50% duty-cycle, the amplitude of the equivalent sinusoidal input voltage between points A and B would be $4/\pi$ times the amplitude of the squared wave.

Variants of the circuit in Figure 31 can be implemented, usually aiming an improvement in efficiency. For instance, active rectification may be used in the secondary, as shown in the schematics of Figure 33, where the gates of the MOSFET at the secondary are driven to reinforce the direct conductivity of their clamp diodes. In this way, the direct voltage across the diodes of the rectifier bridges is reduced, and the losses on the secondary can be minimized. The gates drivers should sense the voltage across points C and D to determine which gates, whether $r_{H,1}$ and $r_{L,2}$ (if $V_C < V_D$), or $r_{H,2}$ and $r_{L,1}$ (if $V_C > V_D$) should be active at any given time. The capacitor C_L across the H-bridge works as a DC filter for the voltage being input to the DC-DC converter.
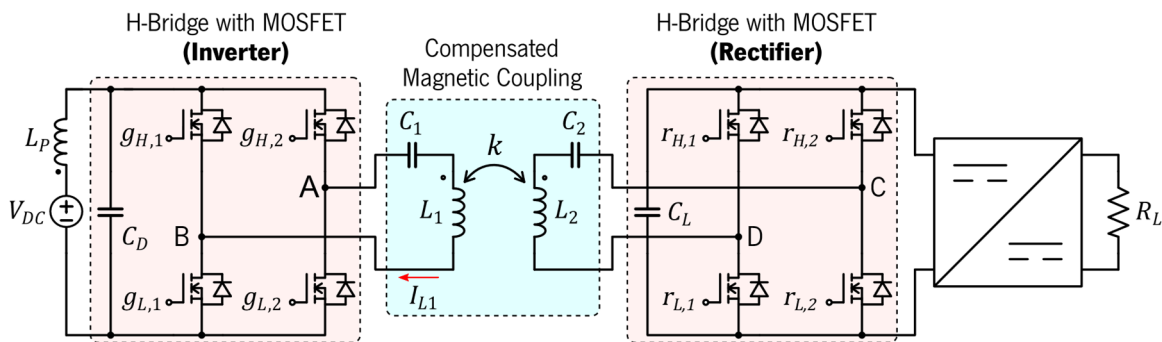
Figure 33: H-bridge driving primary coil of a SS-compensated magnetic coupling, with another H-bridge functioning as a rectifier at the secondary and a DC-DC converter for load matching.

The MOSFETs act as switches during the normal operation. When gate signal is above the threshold limit $V_{GS(th)}$, the transistor is switched ON and the resistance of the MOSFET channel drops from a quasi-open circuit to a very low value $R_{DS(ON)}$, and current can flow through the channel. If power is connected through an external load in series with either of these terminals, the drain to source voltage, V_{DS} can decrease to a minimum, which is the product of $R_{DS(ON)}$ by the current established by external constraints.

So, after any switching transition, MOSFETs under directly polarization, will either be in the OFF state and have $I_{DS} = 0$, or in the ON state, when the power dissipated by the transistor will be very low, because $R_{DS(ON)}$ is usually also very low, if compared with other elements in the circuit. However, the power dissipation is the average of the product of the voltage across the drain to source and the drain current, which, during the transitions of state, may happen to be both

Dynamic Inductive Wireless Power Transfer for Lightweight Electric Vehicles
Luiz Alberto Lisboa da Silva Cardoso – University of Minho

64

simultaneously high. This condition will lead to a high instantaneous power dissipation, that, in association with high switching frequencies, can increase average power dissipated to an inconveniently high figure, and spoil the system efficiency.

To reduce these switch losses on the MOSFETs, the transition of the gate signals should ideally occur when either $I_{DS} = 0$, which is called the Zero Current Switching (ZCS), or $V_{DS} = 0$, which is called the Zero Voltage Switching (ZVS). Under either of these conditions, the inverter can safely drive the circuit, the H-bridge inverter is said to works as a resonant converter.

2.9.1.1 Operation Frequency of the H-Bridge Inverter

When driving a resonant load with an H-bridge, the choice of the frequency of operation f_q should not be completely arbitrary. Tuning the operation frequency of the inverter to match the natural resonance frequency f_0 of the magnetic coupling (and attached load) is a critical issue for the efficiency of the system. A slightly higher efficiency of the magnetic coupling itself (blue-shaded area in Figure 33) may be found in a frequency other than f_0, as seen in 2.5 (for the series-compensated secondary) and 2.6 (for the parallel-compensated secondary). But there is a stronger reason to do this.

In a circuit exhibiting resonance, the current will naturally tend to oscillate after an stimulus is injected, such as voltage step across its terminals. The sequence of events in the vicinity of the inversion of the polarity of the h-bridge output voltage can be seen in Figure 34, obtained by numeric simulations with the LT Spice software [51], for the case where $f_q < f_0$. Focusing on the half-bridge which midpoint is A, it can be realized that, when the transistor Q_{High} is cut-off, the voltage on A swings immediately from V_{DC} to zero. At this time, since the current I_{L1} is negative (it is entering the bridge at point A), this current flow is automatically redirected to the protection diode of Q_{High}, causing the voltage drop $V_{DS}(Q_{High})$ to be $-V_F$, where V_F is the forward voltage on that diode. After the dead-time t_d, just before Q_{Low} is finally switched ON, to complete the switching of the half-bridge, the drain-to-source voltage Q_{Low} will be high, at $V_{DC} + V_F$, causing a high displacement current in the transistor, that will cause a peak in $I_{DS}(Q_{Low})$ to momentarily occur, until the new voltage $V_{DS}(Q_{Low})$ stabilizes at $-I_{L1}.r_{DS(ON)} > 0$. So, the ZVS condition is not met. In addition to the resulting power losses, depending on the transistor parameters, there a the possibility that this current surge can be destructive to MOSFET Q_{Low} [52].

Dynamic Inductive Wireless Power Transfer for Lightweight Electric Vehicles
Luiz Alberto Lisboa da Silva Cardoso – University of Minho

65
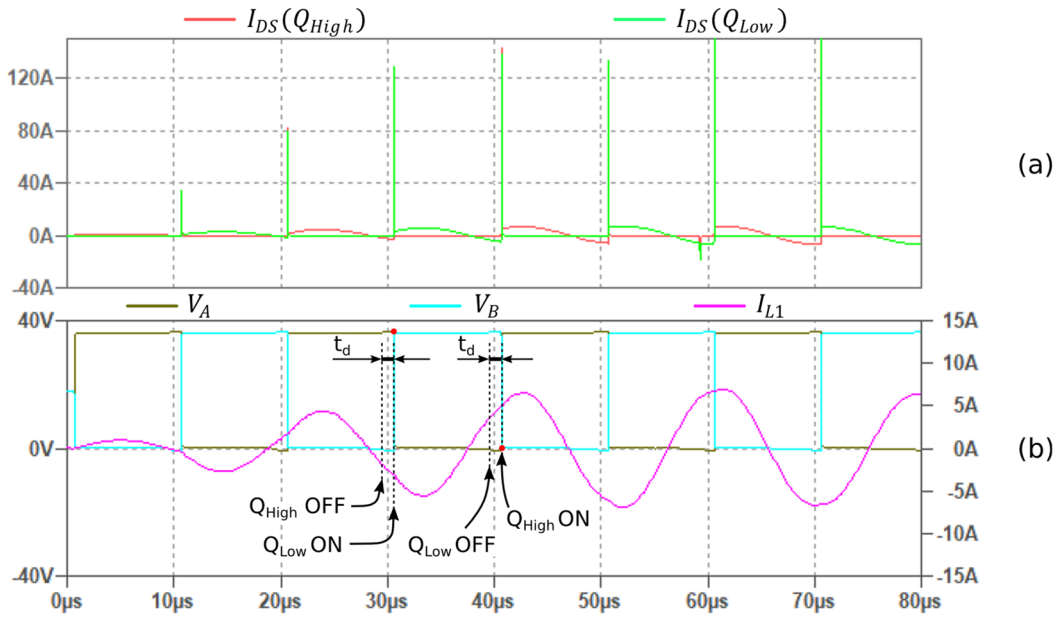
Figure 34: Simulated waveforms of an H-bridge driving a resonant serial LC load at a **lower** frequency than the natural resonant frequency of the load: (a) Drain to source currents on the MOSFETs driving midpoint A; (b) output voltages on midpoints A and B, and current supplied to the load at A.

The same current surges will be similarly present when the half-bridge output is switched from zero (almost zero, since $r_{DS(ON)}$ is not zero) to V_{DS}, in which case the current I_{L1} will be positive (leaving the bridge at point A), and the voltage drop $V_{DS}(Q_{High})$ will also be also high when Q_{High} is switched ON. And they will equally happen on the other half-bridge of the H-bridge, and, in a real circuit, could have been minimized with the use of snubber resistive-capacitive circuit branches across the MOSFETs. But the point, in this example, is just to show the issues with this inadequate switching strategy for the H-bridge inverter.

When $f_q > f_0$, on the contrary, these current surges do not happen, as it can be seen in Figure 35, also obtained by numeric simulation with LT Spice software. Again, focusing on the half-bridge which midpoint is A, it can be realized that this time the current I_{L1} will be positive (leaving the bridge at point A), when the transistor Q_{High} is cut-off. The current flow will be instead automatically redirected to the protection diode of Q_{Low}, causing the voltage drop $V_{DS}(Q_{Low})$ to be $-V_F$. So, when Q_{Low} is switched on, the voltage drop across its terminals will be already low, thus avoiding current surges on $I_{DS}(Q_{Low})$. Similar happening when Q_{High} is switched ON.

Dynamic Inductive Wireless Power Transfer for Lightweight Electric Vehicles
Luiz Alberto Lisboa da Silva Cardoso – University of Minho

66
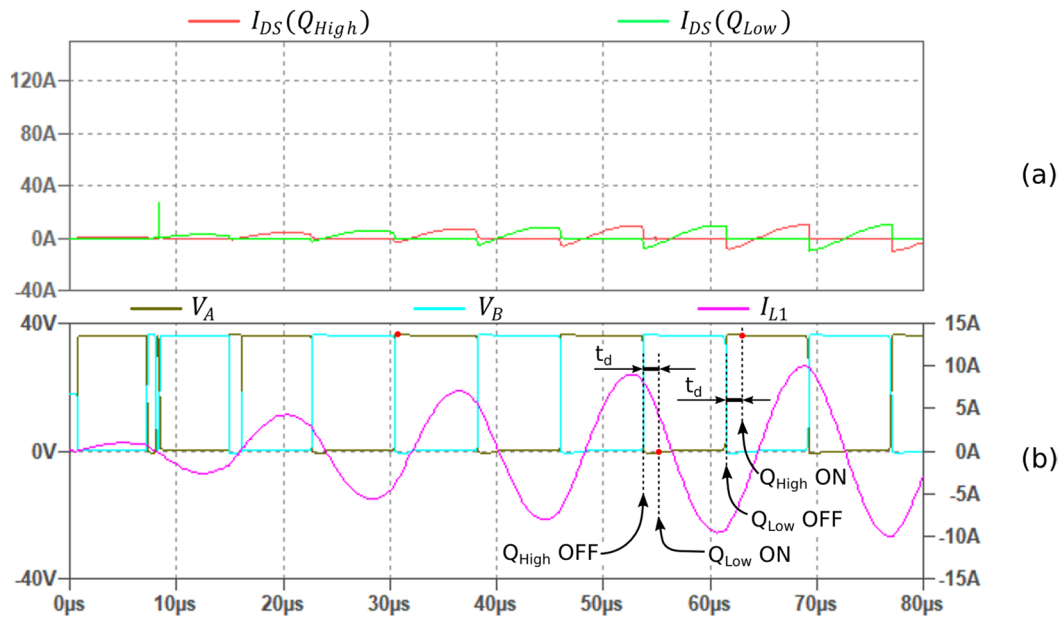
Figure 35: Simulated waveforms of an H-bridge driving a resonant serial LC load at a **higher** frequency than the natural resonant frequency of the load: (a) Drain to source currents on the MOSFETs driving midpoint A; (b) output voltages on midpoints A and B, and current supplied to the load at A.

It is then a customary practice to drive the resonant tank at $f_q > f_0$, with f_q as close as safely possible to f_0. This avoids switching a MOSFET ON when there is already voltage with a magnitude equal to $V_{DC} + V_F$ across its drain and source terminals, where V_F is the directed voltage drop on a conducting protection diode. In this manner, the ZVS condition is assured and there will be no extra losses to current displacement to charge de MOSFET, a process that also produces inconvenient surges on the power supply, constitute a source of electromagnetic interference EMI, and additionally, can ultimately damage the transistors themselves.

In general, the resulting waveform of the current supplied by the H-bridge to the load is not a perfect sinusoidal function as Figure 34 and Figure 35 may suggest, but rather, a similar-shaped signal that can be approximated by segments of sinusoidal waveforms, within which, the resonant circuit responds freely. In the case of the SS-compensated circuit of Figure 33, the condition of resonant driving, which also depends on the mutual inductance, can then be evaluated by inspecting the current waveform on the primary coil, L_1 [53] [54], as indicated in Figure 36.

Dynamic Inductive Wireless Power Transfer for Lightweight Electric Vehicles
Luiz Alberto Lisboa da Silva Cardoso – University of Minho

67
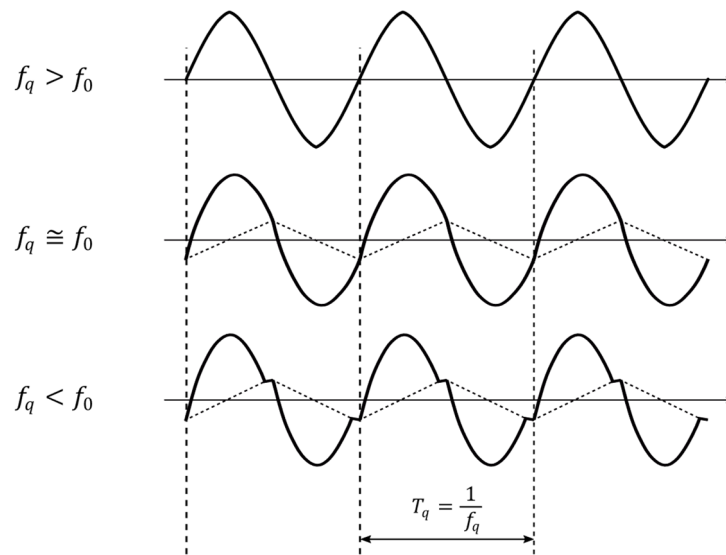
Figure 36: Typical waveforms of the primary coil current on a H-bridge driven resonant IWPT.

When operating very close to the resonance condition, the prompt identification of the relative value of the operation frequency with respect to the natural resonance frequency may be largely difficulted, if the instrument measuring the primary current does not have a bandwidth that is much greater than then base frequency f_q, or if it presents too much phase distortion over its frequency band.

In the next section, a prototype built in order to verify and understand practical issues in the design and implementation using H-bridge resonant converters is described. This work, although not incorporated in the final HIPLEV prototype, was considered an important step to consolidate the option for an auto-resonant power circuit in its implementation.

2.9.1.2 Experimentation with a Resonant Converter using a COTS H-Bridge

In order to have more practical experience with power electronics and their issues when used as a component system in a IWPT system, two prototypes using H-bridge inverters were built and tested. In a first implementation, some COTS sub-systems were used as components: An H-bridge originally designed for brushed DC (BDC) motor control, a power source, a DC-DC converter, and a digital frequency generator, to which were added an especially designed gate signals conditioning module, to adjust a duty cycle of slightly less than 100%, as required by the module. A capacitor bank and a COTS inductor were connected in series with the H-bridge output, to serve as the serial resonant tank. The system was tested in an open secondary configuration, just to acquire more insight into the H-bridge inverter itself.

Dynamic Inductive Wireless Power Transfer for Lightweight Electric Vehicles
Luiz Alberto Lisboa da Silva Cardoso – University of Minho

68

In this first implementation, the COTS H-bridge used was originally intended to drive DC brushed motors, with an alleged nominal maximum current of 100 A. It requires a PWM input signal to control motor speed with a maximum nominal modulating frequency of 60 kHz, and two signals to select the control the switching of individual branches of the H-bridge, and establish the direction of the motor, forward or reverse. This module was provided with only basic interface documentation, in which no implementation internals were specified, so it was treated as a system component. It was recognized that, by supplying gate enabling signals in a continuous alternance, as if continuedly commanding changes in the motor rotation direction, and a PWM frequency with an active duty cycle is correspondence with the gate signals, it is possible to use the same hardware as the H-bridge driver of a resonant load.

The gate control signals are constituted by two periodic pulse trains at drive frequency, at 180° out of phase from each other. The operation frequency was set at the maximum acceptable by the H-bridge module specification, $f_q = 60$ kHz. To illustrate the principle of operation, a duty cycle of 85% was chosen and implemented with a simple circuit using TTL digital discrete logic circuits, as shown in Figure 37.
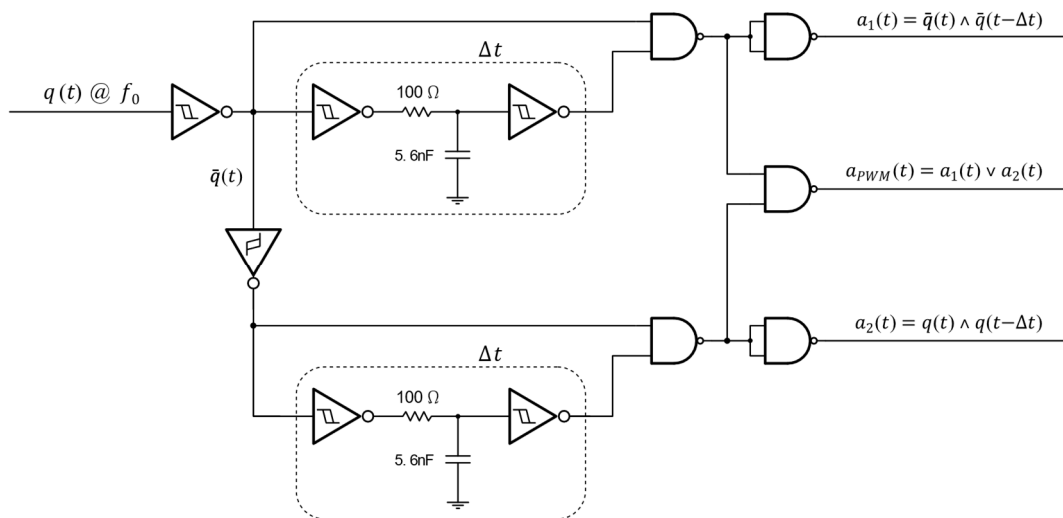
Figure 37: Diagram the simple controller circuit designed to generate the control signal for the COTS H-bridge.

The circuit introduces a delay Δt in a base 50% duty cycle square signal $q(t)$ and its complement, $\bar{q}(t)$, to generate the gate control signals a_1 and a_2, as well as the required PWM control signal a_{PWM}, with the same active duty cycle as that of the gate control signals. The required delay Δt for a given duty cycle λ can be calculated by:

$$\Delta t = \frac{1}{f_q}\left(1 - \frac{\lambda}{2}\right),$$

(2.96)

Dynamic Inductive Wireless Power Transfer for Lightweight Electric Vehicles
Luiz Alberto Lisboa da Silva Cardoso – University of Minho

69

Therefore, for the desired duty cycle of 85%, at $f_q = 60$ kHz, a $\Delta t = 1.25$ µs was implemented. Alternatively, these control signals could have been generated by a microcontroller, making the duty cycle of the PWM re-programmable to any desired value, and thus reducing the current on the primary coil to a fraction of its maximum possible value, while keeping the drive frequency constant. The circuit implemented provided the three waveforms necessary to drive the H-bridge module, as shown in Figure 38.
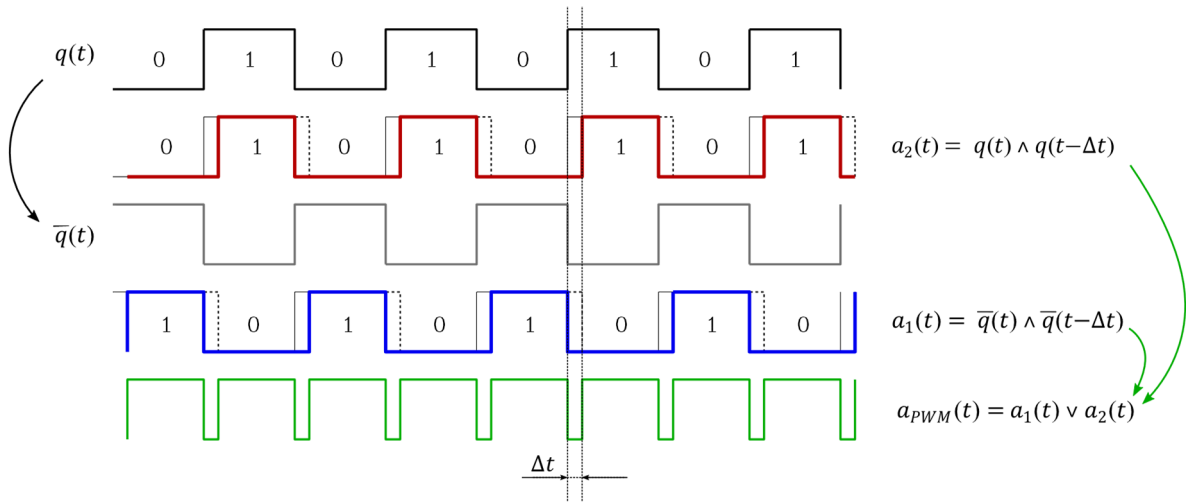
Figure 38: Waveforms of the H-bridge control signals.

In the prototype, a COTS digital frequency generator, programmable in both frequency and duty cycle, was used to supply the reference signal $q(t)$, at 60 kHz, with a 50% duty cycle. For a safety startup, these two parameters are set before the modules are integrated, and remain stored in the non-volatile memory of the frequency generator.

The prototype, shown in Figure 39, is then completed by a 36 V DC power source (main power supply to the H-bridge), a low power DC-DC converter to derive the 5 V from the power source, which is used to power the frequency generator and the gate control circuit, and a simple line filter, inserted in between the DC power source and the H-bridge. The line filter is included to protect the power source from the residual oscillations in the DC power produced by the switching of the transistors in the H-bridge.

Dynamic Inductive Wireless Power Transfer for Lightweight Electric Vehicles
Luiz Alberto Lisboa da Silva Cardoso – University of Minho

70
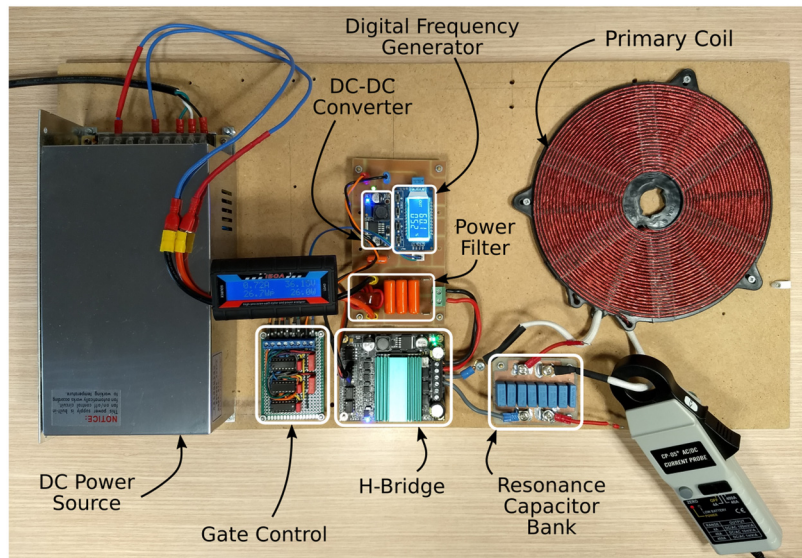
Figure 39: Prototype of H-bridge resonant inverter built and tested.

The output terminals of the H-bridge, indicated by A and B in Figure 33, which are usually connected to terminals of a DC motor, in the original application of this module, are then connected to the terminals of the primary side of the compensated magnetic coupling, constituted by series connection of a resonance capacitor bank (73.3 nF) and a commercial flat spiral primary coil (102 μH), which have a natural resonance f_0 at approximately 58 kHz. The measured waveforms of the resulting primary current and the control signals, after setting the drive frequency f_q at approximately 60.3 kHz, are shown in Figure 40.
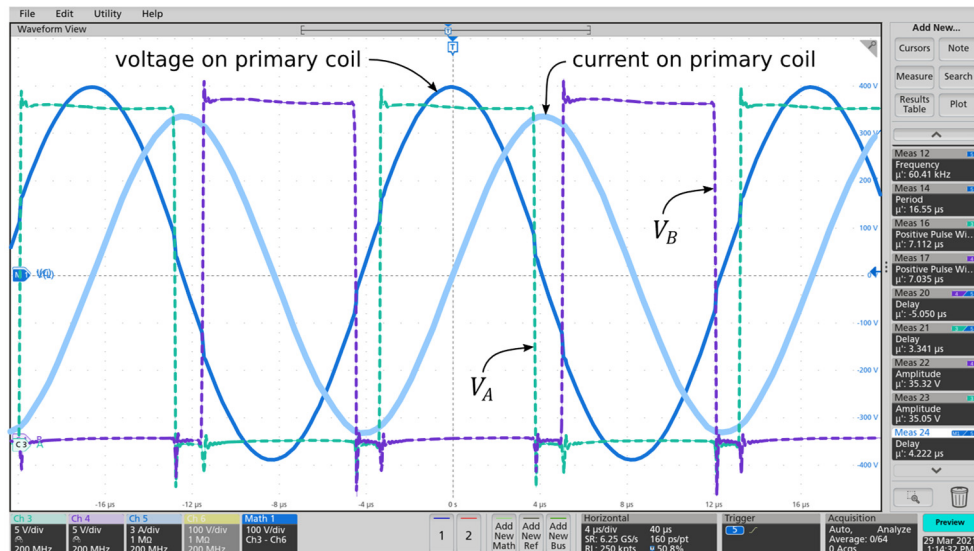
Figure 40: Observed waveforms of outputs of the H-bridges, V_A (channel Ch3) and V_B (channel Ch4), and the resulting current I_{L1} (channel Ch5) and voltage V_{L1} (channel Math 1) over the primary coil.

As expected, it can be seen in the graph, a hard-copy taken from the oscilloscope screen (Tektronix MSO46) that current waveform (light blue curve) shows no apparent distortion, indicating that operation is set near resonance. It can be deduced, however, that there is some

Dynamic Inductive Wireless Power Transfer for Lightweight Electric Vehicles
Luiz Alberto Lisboa da Silva Cardoso – University of Minho

71

distortion, because the voltage across L_1 is not a perfect sinusoid, reflecting the voltage switching of the H-bridge. It can also be noted that the current derivative is in phase with the voltage output on point A, as in the case of Figure 35, giving a visual indication that the driving frequency imposed by the H-bridge is actually greater than f_0.

No effort was made to build a secondary side to complete an IWPT configuration. Rather, this prototype was used in the study off the proximity effect, described in 2.10.2.

Among the basic WPT compensation topologies, as described in section 2.7, it can be noticed that in SP and PP-compensated circuits, the reflected impedance Z_r of the secondary onto the primary circuit has a purely complex term associated to M^2, independently of the load characteristic. This does not happen in the case of SS and PS-compensated circuits, when the load R_L is purely resistive. So, in DIWPT applications, where some variation in the mutual inductance M is expected, it should be more difficult to keep a H-bridge inverter in good resonant condition by adjusting a fixed frequency of operation, when driving WPT circuits using these compensation topologies. Because of this, when using resonant converters in DIWPT, the SS and PS topologies should be preferentially used. But even then, the use of a fixed frequency driving frequency might bring some difficulties, as exposed in section 2.9.2.

2.9.2 Issues of Simple Resonant Converters in WPT

Resonant inverters of fixed frequency are intrinsically very stable. However, the obtention of a good resonant-drive condition, where both the power wireless power link and the inverter efficiencies are high, is subjected not only to robust design and careful adjustment of this operation frequency: The temperature and aging stability of circuit parameters of the inverter, the compensation networks, the magnetic coupling, and the load itself, are also critical for this condition to be maintained. So, for long term operation, in some applications it may not be enough to have the initial nominal value of these parameters within strict design limits.

In the case of stationary IWPT systems, when efficiency is often the top priority of the design, it is usual to establish some feedback from the secondary to the primary, and use this information to produce an error signal that becomes an input to control the operation of the inverter, and track the resonant condition under slight mispositioning of the coils. This procedure automatically adjusts the frequency of operation to compensate for minor variations of the magnetic coupling coefficient around a design target but, ultimately, it also handles the variation of other circuit parameters in the IWPT configuration.

Dynamic Inductive Wireless Power Transfer for Lightweight Electric Vehicles
Luiz Alberto Lisboa da Silva Cardoso – University of Minho

72

The information signal derived from the secondary, for instance, can be explicitly passed to the primary as digitally codified message, through a wireless communication link established in between the primary and secondary, as proposed in SAE Recommended Practice, SAE J2847-6 [55]. This technique involves algorithmic control, a relatively complex addition to the pure inductive coupling model, but implementations using it are already reported [56].

Alternatively, this feedback can result from electric signals that can be sensed in the primary itself, such as the secondary reflected impedance and the active power being injected in the primary coil. The inverter frequency can then be adjusted for optimal efficiency while the amplitude and duty cycle can be further adjusted and used in conjugation with the frequency to achieve some specific power or voltage level on the load.

This simpler adaptive approach may be particularly useful in DIWPT systems as well, where three sources of intrinsic potential variability are found:

(i)   The variation of the magnetic coupling parameters, due to the relative movement of primary and secondary coils.

(ii)   The variation of the power instantaneously demanded by the secondary of a vehicle and its battery management system, which may depend on the traffic conditions and the grading of the lane where some particular primary coil is installed.

(iii)   The dispersion of parameters existing in the combinations of multiple interactions of the many primary coil modules often used in an inductive lane, and the many vehicles that are eligible to harvest energy from them, can cause variability of design parameters from one to another lane-vehicle interaction, as shown in Figure 46.
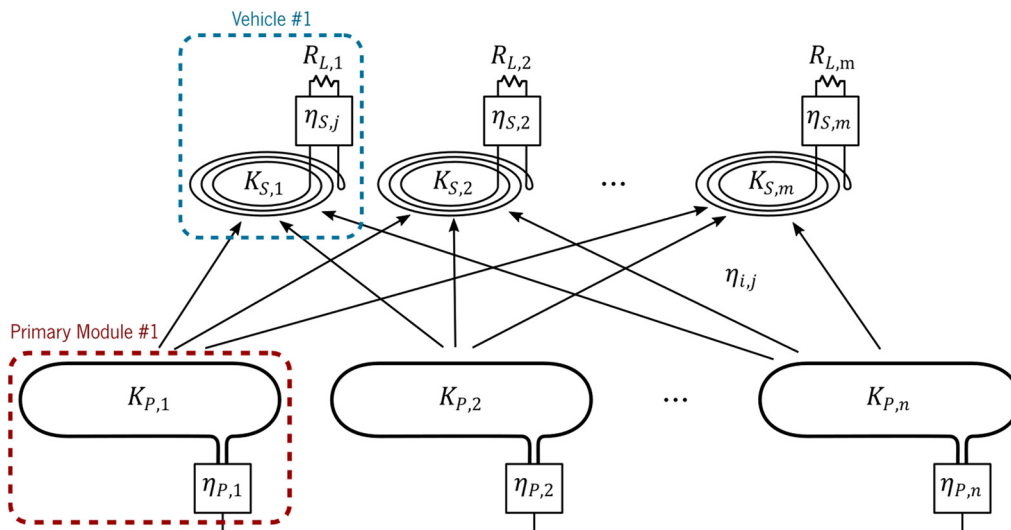
Figure 41: DIWPT interactions between any of the n primary coils in a lane and m vehicles.

Dynamic Inductive Wireless Power Transfer for Lightweight Electric Vehicles
Luiz Alberto Lisboa da Silva Cardoso – University of Minho

73

Yet referring to Figure 46, this means that while the design inductance value for all primary coils $K_{P,i}$, with $1 \leq i \leq n$, is L_1, but the actual value for each of these coils may be $L_{P,i}$, modeled for instance as samples of independent aleatory variables distributed as $N\left(L_1, \sigma_{L,1}^2\right)$, similar happening with other circuit parameters in any primary module or vehicle.

(iv)   The variability caused by aging and temperature variations, which may be particularly relevant, due to the fact that primary modules are deployed outdoors in large numbers, often underneath the surface of lane, and they will age, being especially prone to parameter drifting, due to ambient conditions, without being easily replaced or individually readjusted by some maintenance procedure.

Because of all this, individual fixed adjustment of each inverter driving a primary may become a too expensive and poorly effective strategy to circumvent parameter dispersion, when dealing with vehicular DIWPT applications. The power electronics design should account for all these sources of variability, and the auto-resonant inverter is deemed as an adequate approach because it avoids keeping readjusting or re-tuning individual primary modules.

The need to transfer power to from multiple different primary power modules to multiple different secondary sets (on board of multiple vehicles) creates the need to accommodate more parameter dispersion. The expected average efficiency of an inverter in the system will be lower than that that could be achieved by careful fixed adjustment of a single coil pair in a stationary IWPT. The same happens with the average power transfer itself.

The efficiency so far studied in sections 2.5 through 2.8 respect to the magnetic coupling and attached compensation networks, and do not include the losses in the primary power source and rectification stages of the IWPT chain. In those studies, the power signal to be fed to the primary compensation network is considered to be generated by an ideal voltage or current alternating sources, whereas it is actually implemented by the inverter at the primary side.

For the analysis of the efficiency a single interaction of a primary coil in the lane and a vehicle, from the many pair that can be incidentally formed during the operation of the lane, the block diagram in Figure 29 can then be rearranged into that shown in Figure 42.

Dynamic Inductive Wireless Power Transfer for Lightweight Electric Vehicles
Luiz Alberto Lisboa da Silva Cardoso – University of Minho

74
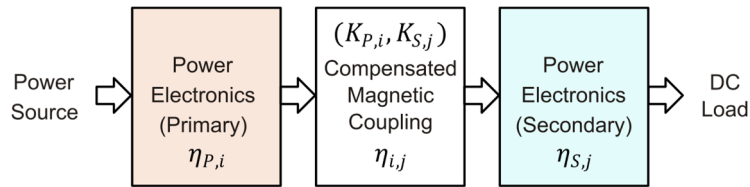
Figure 42: The IWPT as serial chain of power electronics blocks.

The total efficiency η_T of the system during the interaction of primary module i and vehicle j is then obtained by the product of the efficiencies in the IWPT chain:

$$\eta_{T(i,j)} = \eta_{P,i}\,\eta_{i,j}\,\eta_{S,j} \qquad (2.97)$$

To exemplify how difficult it can be, to achieve higher overall efficiency levels (above 90%), let us considerer that typical efficiencies of commercially produced power electronics and magnetic coupling elements can be aleatorily distributed in the range of $\eta = $ 85% to 95%, with an expected average of 90%. The overall efficiency will then be in the range of η^3, that is, from about 61% to 90%, with an expected average of only 73%.

The efficiency of the power electronics in the secondary, usually a rectifier circuit followed by a level translation DC-DC converter is not structurally affected by the change of the operating frequency, although the power losses in individual components may vary and, to some extent, can potentially impact it. On the other hand, the efficiency $\eta_{S,j}$ is often more dependent on the power level itself. This is easier to see in the case of a simple rectifier diode bridge, where the voltage drop across the diodes is approximately constant around nominal current, and does not change significantly from one component sample to another of the same type. In these conditions, the efficiency of the rectifier bridge will not vary much with the frequency varying around a given design operation point f_0, but rather, it will decrease as the fraction of the power dissipated on the bridge is increased, which happens as the DC output voltage is also increased. In this case, the variability of $\eta_{S,j}$ then ultimately depends on the load conditions.

So, especially in a DWIPT design, the problem of keeping the efficiency and nominal transferred power above given minimum design values falls principally on the variability in η_T, and ultimately on the variability of $\eta_{P,i}$ and $\eta_{i,j}$, over a large number of possible combinations of the multiple instances of primary modules and vehicles.

Dynamic Inductive Wireless Power Transfer for Lightweight Electric Vehicles
Luiz Alberto Lisboa da Silva Cardoso – University of Minho

75

2.9.3 Auto-Resonant Inverters

Instead of using a fixed drive frequency, in some applications it is convenient to use inverter circuit topologies exhibiting auto-oscillation. In these inverters, the amplitude of oscillation is often automatically regulated, independently of the load, with either a ZVS or ZCS condition being also established. In this manner, the $\eta_{P,i}$ in (2.97) are minimized, potentially yielding better overall efficiencies $\eta_{T(i,j)}$, for the different pairs (i,j) of primary power module and secondary power harvesting circuit (in the case of DIWPT, in a vehicle).

The oscillation in these topologies is usually produced by a resonant "tank", which is stimulated by injection of energy in amplified feedback, sensed from its natural response waveform. This stimulus can be linear (proportional to the sensed feedback) or nonlinear. For efficiency reasons, nonlinear feedback by current or voltage switching is often more advantageous, and preferred in power circuits. In the case of IWPT, the resonant tank can be considered to include, or to be influenced by, the overall assembly constituted by the magnetic coupling, all the connected compensation circuits, the rectifier in the secondary and a DC resistive load itself.

2.9.3.1 The Baxandall Auto-Resonant Inverter

One of the first popular designs of a sinusoidal waveform auto-resonant inverter using solid state technology (initially, BJTs) as active switches was introduced by Peter J. Baxandall in 1959 [57]. It uses an out of phase feedback to inject control current in the base of each of the two only transistors in the circuit, Q_1 and Q_2. This feedback is directly obtained from a secondary winding L_B magnetically coupled to the primary coil L_1, the inductive component of main resonant tank of the inverter, formed by parallel association of L_1 and C_1, as shown in Figure 43a. Although topologically similar to the design introduced a few years before, by Bright and Royer [58], this latter used the saturation properties of the magnetic core and generated a signal that is approximately a square wave, while in Baxandall's there is a resonant tank forcing a sinusoidal output, which is more adequate for using in WPT applications.

Dynamic Inductive Wireless Power Transfer for Lightweight Electric Vehicles
Luiz Alberto Lisboa da Silva Cardoso – University of Minho

76
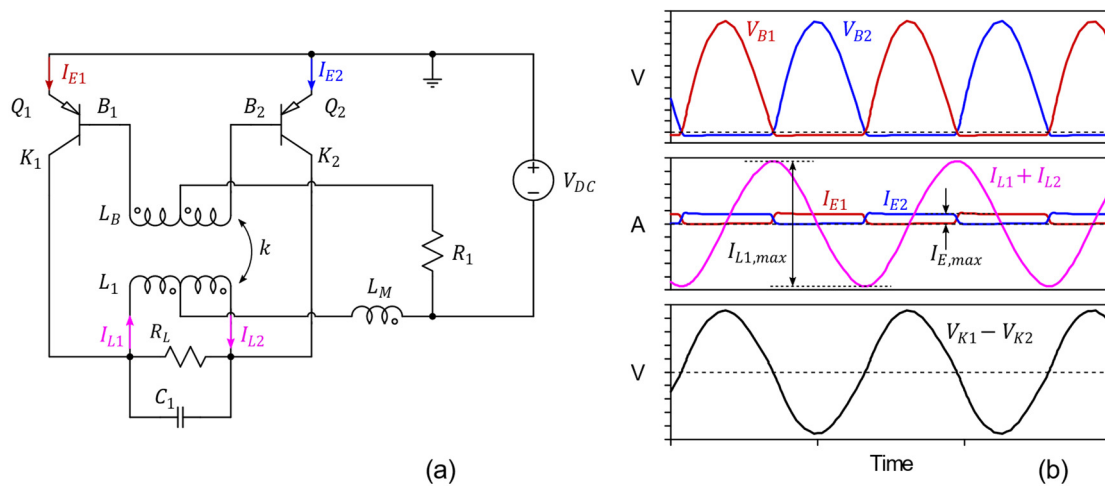
Figure 43: Baxandall resonant inverter circuit topology (a) and main electric waveforms.

Still in the schematics of Figure 43a, the voltage power source V_{DC} is connected to the center tap of L_1 through an inductor L_M of a much larger value than L_1, what makes the ensemble approximately equivalent to a current source injecting current in this center tap. This current finds its path back to the ground reference (which, in this design, is assigned to the positive pole of the power source) through either the Q_1 or Q_2, but not both at the same time, because the terminals of L_B inject differential currents in the bases B_1 or B_2 of the transistors with opposite polarities. Since the bases of the transistors are fed with a 180° out of phase signal sample of the current flowing respectively through the collector of each transistor, the system oscillates permanently, with the resonant tank being alternately loaded to maximum current levels in both directions.

The waveforms of the main signals in the circuit are established as shown in Figure 43b. The diode formed by at the base-emitter N-P junction of each transistor conducts and saturates the transistors alternately voltages. Each of the voltages V_{B1} and V_{B1} are negative with a magnitude of collector–emitter saturation voltage, $V_{CE(sat)}$ when the transistor is in the "open" state and current can flow from the emitter to the collector. V_{B1} and V_{B1} will alternately go to the maximum amplitude value picked at L_B. The current injected at the center tap of L_1 will then alternately pass through Q_1 or Q_2. The waveforms of the emitter currents I_{E1} and I_{E2} will be approximately square waves of opposite phase, as represented by the red and blue curves on the second graph. Due to the resonant tank, however, the sum of the currents flowing through the two halves of L_1 will be a sinusoidal wave form, drawn in magenta, in the same scale of the emitter currents I_{E1} and I_{E2} on the same graph.

Dynamic Inductive Wireless Power Transfer for Lightweight Electric Vehicles
Luiz Alberto Lisboa da Silva Cardoso – University of Minho

77

Very important, the transistors in this auto-resonant configuration are switched at (or very close to) zero voltage, thus reducing the switching losses, what would improve the efficiencies $\eta_{P,i}$, if used in a DIWPT system, as illustrated in Figure 42.

Although this circuit was proposed using PNP bipolar junction transistors (BJT), other active elements can be used as controlled switches. Due to its improved switching characteristics, modernly MOSFETs are commonly used instead of BJTs.

A non-auto-resonant variant of the Baxandall inverter, where the switches are driven close to the resonant frequency by an external gate control circuit, is shown in Figure 44, was analyzed by Edry and Ben-Yaakov in 1993, as they proposed its use in a DC-DC converter [59]. For boost operation, the external gate control keeps the operating frequency, f_s, greater or equal to the natural resonance frequency of the circuit, f_0, and the resulting waveforms of V_{DS1} and V_{DS2} are similar to that observed for V_{B1} and V_{B2}, in the case of Baxandall's auto-resonant inverter. The total current flowing in L_1 also has a sinusoidal waveform, with a magnitude that can be much higher the that of the current flowing though the switches (the transistors), as in the former case.
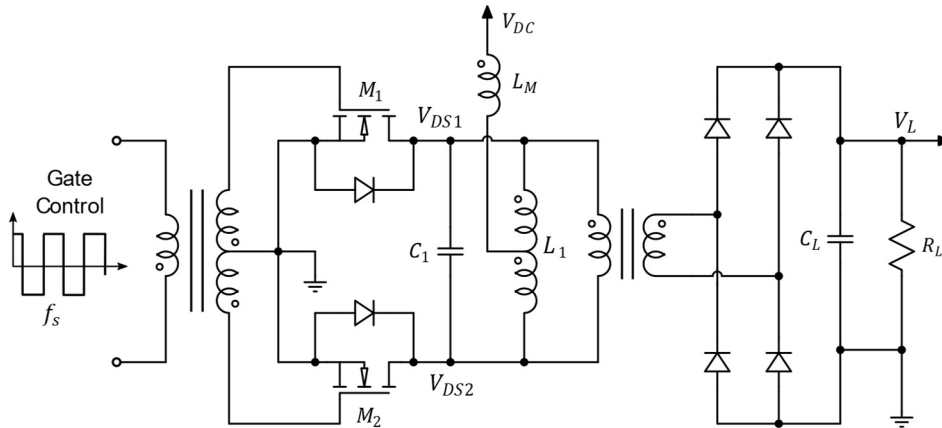
Figure 44: Edry's and Ben-Yaakov's variant of Baxandall's inverter in a DC-DC converter application.

By considering that L_M is much higher than L_1, and that the current is injected in the center tap is approximately constant, Edry and Ben-Yaakov demonstrated [59] that the amplitude $V_{D,max}$ of $V_{DS1} - V_{DS2}$ can be estimated by:

$$V_{D,max} = \pi V_{DC} \frac{f_0}{f_s} \tag{2.98}$$

In the particular case where f_s is set equal to f_0, such as the original Baxandall auto-resonant configuration:

Dynamic Inductive Wireless Power Transfer for Lightweight Electric Vehicles
Luiz Alberto Lisboa da Silva Cardoso – University of Minho

78

$$V_{D,max} = V_{L1,rms}\sqrt{2} = \pi V_{DC} \qquad (2.99)$$

The Baxandall circuit and their variants exhibit an useful property that could be explored in WPT configurations: the current obtained on L_1 can be much higher than the currents traversing the transistors. This means that the terminals of L_1 could be used to drive a magnetic antenna for WPT or, if another secondary is directly coupled to L_1 this coil of the resonant tank, could itself be used as a magnetic antenna.

2.9.4 The Mazzilli-Baxandall Auto-Resonant Inverter

Auto-resonant inverters such as Baxandall's automatically achieve two important conditions for power transfer and efficiency in IWPT applications:

(i)   The resulting oscillating frequency is that of natural resonance of the circuit being driven. That includes the reflected impedance in the primary circuit of the compensation circuit and load attached to the secondary coil.

(ii)   They work close to zero voltage switching (ZVS) conditions, with the auto-established operation frequency resulting in minimum switching losses.

One of the simplest inverter auto-resonant circuits, is a ZVS resonant inverter which is attributed to Mazzilli [60] [61], the so called Royer-Mazzilli inverter or, simply the ZVS Mazzilli driver, shown in Figure 45. It is a converter that currently finds popular use in induction heating and other consumer applications, due to its low complexity and cost. Its name refers to the original design by Bright and Royer, however it is probably best described as variant of the auto-resonant circuit of Baxandall. The main contribution in the Bright and Royer original circuit design [58] is perhaps the manner the feedback signal is taken from a secondary winding that is magnetically coupled to the coil of the resonant tank, which is actually not used in this new version of the circuit. Rather, the feedback signal for controlling switch (transistor) in the Royer-Mazzilli inverter is directly derived from the main voltage over the other switch, which is expected to have opposite phase to the first branch being switched. Because of that, in this work this circuit is referred to as the Mazzilli-Baxandall inverter, or simply, the Mazzilli inverter.

In the schematics, the two MOSFETs, represented without the body diodes, for simplicity, are set in the push-pull configuration just as in the Edry and Ben-Yaakov converter [59]. The polarization of the MOSFET gates, however, sets the switches in the operation point for ON state.

Dynamic Inductive Wireless Power Transfer for Lightweight Electric Vehicles
Luiz Alberto Lisboa da Silva Cardoso – University of Minho

79
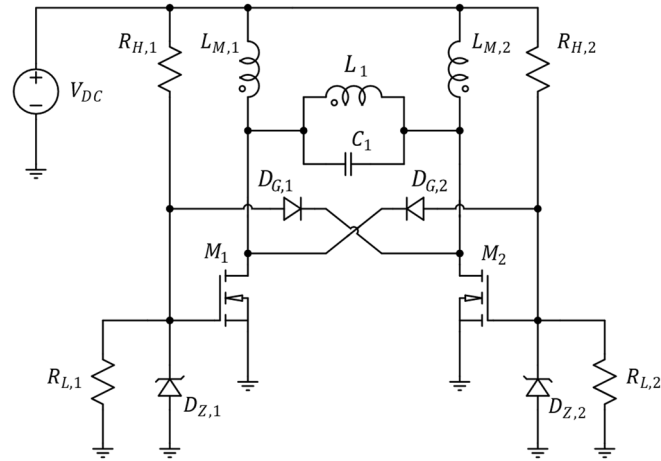
Figure 45: Mazzilli-Baxandall auto-resonant inverter.

The inverter works similarly to the Baxandall circuit. Still referring to Figure 45, the gate of each transistor M_i is polarized by resistors $R_{H,i}$ and $R_{L,i}$ at the breakdown voltage of the Zener diode $D_{Z,i}$, chosen above the gate threshold voltage $V_{GS(th)}$ and less than the maximum acceptable gate-to-source voltage, $V_{GS,max}$. So, when transistor M_i is cut-off, M_i will be saturated, with V_{DSi} becoming low, and vice-versa. Gate diodes $D_{G,i}$, permit a fast gate discharge of M_i when the drain voltage of M_j (which at this point is cut off) falls below $V_{GS(th)}$ plus the direct voltage drop across $D_{G,i}$, and transistor M_i is also cut off, allowing the voltage V_{DSi} start to increase. V_{DSi} will eventually surpass $V_{GS(th)}$ minus the direct voltage drop across $D_{G,j}$, and that will cut-off transistor M_j, assuring that V_{DSj} will stay low for the next half cycle, while the voltage over the drain V_{DSi} of the first transistor rises and is cycled by the resonant tank, reaching a maximum value of πV_{DC} and then falling back towards zero again, which will lead to a continuous repetition of the same sequence of events with transistors i and j reversed. These half cycles sustain each other, causing the oscillation to be perpetuated. A similar split-capacitor resonant converter variant of the Mazzilli inverter load dependent zero voltage switching control was proposed and analyzed, which can alternatively be further controlled in either buck or boost mode [62].

2.9.4.1 Application of the Mazzilli-Baxandall Inverter in IWPT Systems

In the Mazzilli inverter, the coil L_1 of the resonant rank does not need to have a center tap, as it is in Baxandall's original circuit, because separate current sources, formed by direct connection of the switches to the power source through a large inductance, force currents also separately over each of the two switches, which are connected to the tank. This facilitates the design of IWPT systems based on this circuit design, where the coil of the resonant tank, L_1 can be the primary coil itself as shown in Figure 46.

Dynamic Inductive Wireless Power Transfer for Lightweight Electric Vehicles
Luiz Alberto Lisboa da Silva Cardoso – University of Minho

80
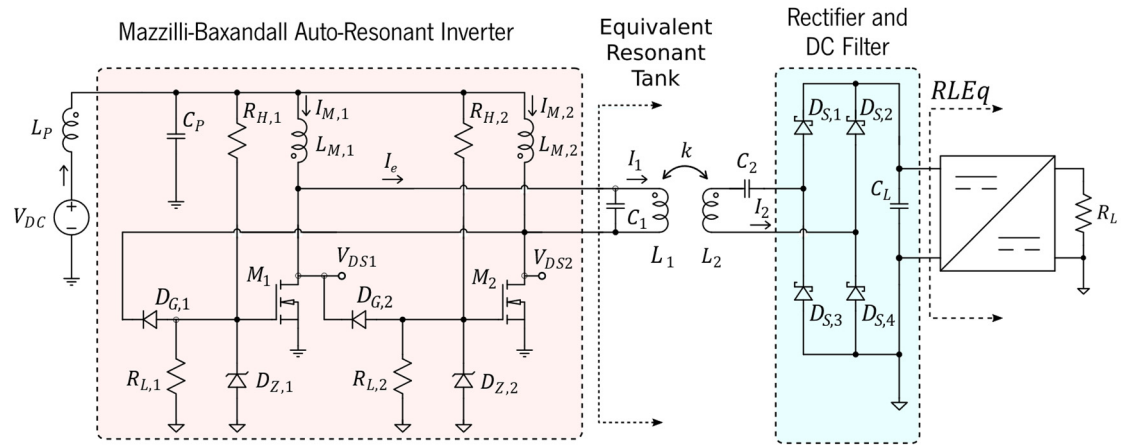
Figure 46: Mazzilli auto-resonant inverter driving the primary coil of a PS-compensated magnetic coupling, with a diode bridge as a rectifier, at the secondary.

The inverter itself is the dashed, pink-shaded area, depicted separated from its resonant tank. The model implicitly includes and considers the effects of the reflected impedance of the secondary side of the IWPT. This circuit was simulated with parameters shown in Table 5, aiming the excitation of a primary coil with a current of 65.4 A rms at approximately 51 kHz.

Table 5: Component parameters used in simulation of the Mazzilli-Baxandall driven IWPT.

Component Symbol	Value/Description
V_{DC}	48 V (with series internal resistance of 0.1 Ω)
L_p	10 µH
C_p	400 µF
$R_{H,1}, R_{H,2}$	470 Ω
$R_{L,1}, R_{L,2}$	10 kΩ
$D_{Z,1}, D_{Z,2}$	12 V, 1 A max current
$D_{G,1}, D_{G,2}$	FR103
$L_{M,1}, L_{M,2}$	150 µH (with series resistance of 50 mΩ)
M_1, M_2	IRFP260N
L_1	5.17 µH (with series resistance of 17 mΩ)
C_1	1.97 µH (with series resistance of 20 mΩ)
k	0.1137
L_2	106.9 µH (with series resistance of 20 mΩ)
C_2	96 nF
$D_{S,1} \dots D_{S,4}$	Schottky rectifier diodes, $V_{rmax} = 100$ V
C_L	470 µF
$RLEq$	3.6 Ω

The circuit in Figure 46, and most of the parameter values in Table 5 correspond exactly to those in the actual circuit used in Chapter 5 for the conceptual testing of the HIPLEV prototype.

Dynamic Inductive Wireless Power Transfer for Lightweight Electric Vehicles
Luiz Alberto Lisboa da Silva Cardoso – University of Minho

81

The major exception is that, later, by introducing concrete values of R_L and the parameters of the particular DC-DC converter used, new values for $RLEq$ are prone to arise. Also, in this model some components were considered as ideal, with no losses (e.g., C_2), or their power losses were likely underestimated (such as L_1 and L_1). Numeric simulations were then conducted using the SPICE [63] based software simulator LTSpice [64], to verify the waveforms, predict the main IWPT electrical performance parameters and understand some limitations of the circuit.

The main waveforms resulting from numeric simulation are shown in Figure 47, where it can be noticed that the current generated in the primary coil with an amplitude $I_{1,max}$ of 92.3 A. This current is, as desired, much larger than the peak current alternately observed to be flowing in each of the transistors, $I_{DS,max} = 15.7$ A, a ratio of almost six times. This avoids the use of transistors with higher current capacity. The main voltages and currents, as well as the resulting operating frequency are shown in Table 6.
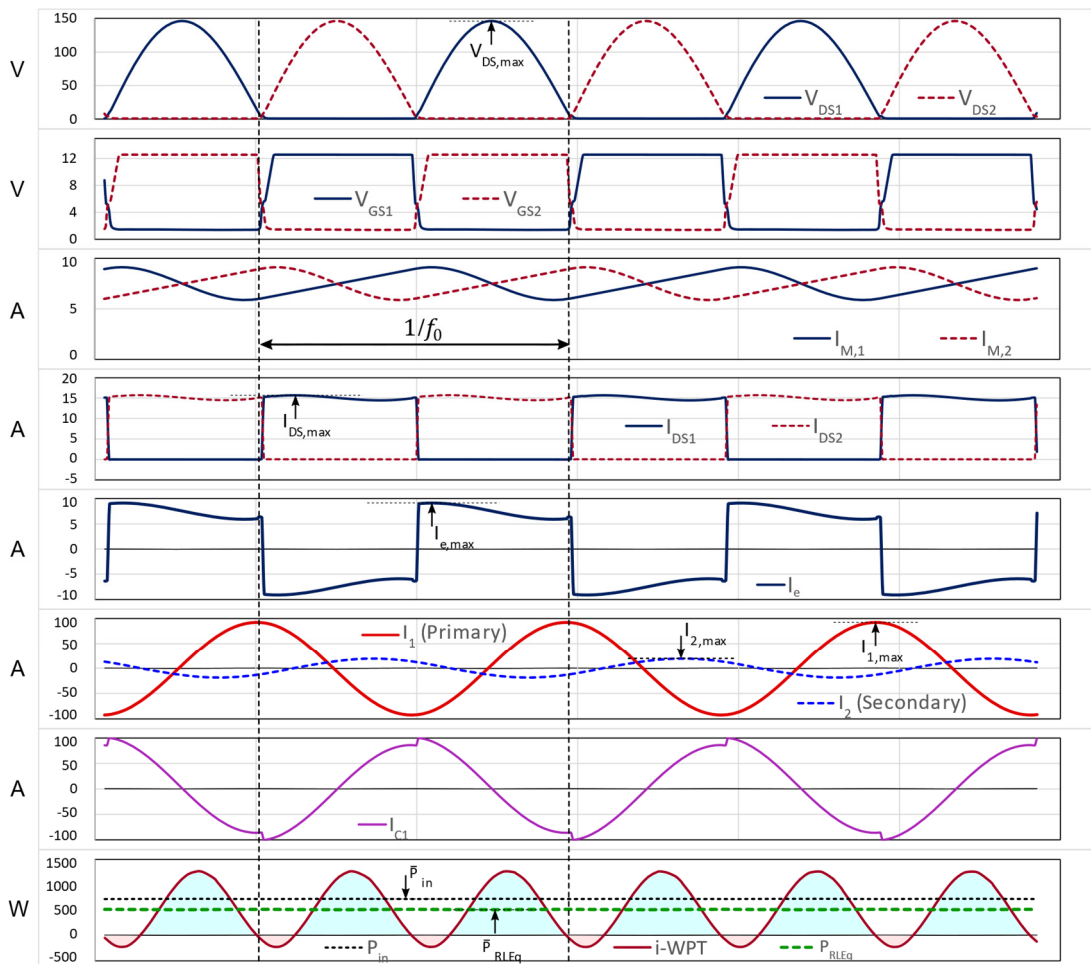
Figure 47: Main waveforms of the WPT driven by an auto-resonant Royer-Mazzilli inverter, as obtained by numeric simulation with LTSpice, using the circuit parameters in Table 5.

Dynamic Inductive Wireless Power Transfer for Lightweight Electric Vehicles
Luiz Alberto Lisboa da Silva Cardoso – University of Minho

82

It is remarkable that, with a peak drain current of only $I_{DS,max} = 15.7$ A, a sinusoidal primary current with a peak value of $I_{1,max} = 92.3$ A can be obtained. This large primary current allows an inductive power transfer to the load in excess of 500 W, even with such a low power supply and small magnetic coupling factor $k = 0.1137$. The small inductance value of the primary coil (5.17 μH), on the other hand, keeps the voltage on its terminals to a relatively low value of 103.3 V rms at the current level achieved.

Table 6: Main circuit voltages and currents resulting from numeric simulation of the Royer-Mazzilli driven IWPT.

Component Symbol	Value/Description
$V_{DS,max}$	146.1 V
$V_{DS1} - V_{DS2}$	103.3 V rms
f_0	51.9 kHz
$I_{DS,max}$	15.7 A
$I_{e,max}$	9.13 A
$I_{1,max}$	92.3 A
I_1	65.3 A rms
$I_{2,max}$	18.8 A
I_2	13.3 A rms
$\bar{P}_{in}$	722 W
$\bar{P}_{RLEq}$	515.5 W
$\eta_{in,RLEq}$	71.4%

The estimated efficiency $\eta_{in,RLEq} = 71.4\%$ is measured from the DC power source to $RLEq$, which is the input of the DC-DC converter used to match the DC load R_L. This efficiency figure for $\eta_{in,RLEq}$ is very much dependent on the actual values of the small series resistances in the model of L_1 and C_1, which were not measured, but arbitrarily set in this simulation.

The total efficiency of the system shall then be calculated by:

$$\eta_M = \eta_{in,RLEq} \ \eta_{DC-DC} \qquad\qquad (2.100)$$

where η_{DC-DC} is the efficiency of the DC-DC converter.

As shown in Figure 48, the circuit responds with the rising rate of the power delivered to the equivalent load $RLEq$ on the order of 100 kW/s, a figure of merit that is, in a first instance, dominated by the use of the capacitor C_L, necessary to filter the DC output from the rectifier.

Dynamic Inductive Wireless Power Transfer for Lightweight Electric Vehicles
Luiz Alberto Lisboa da Silva Cardoso – University of Minho

83
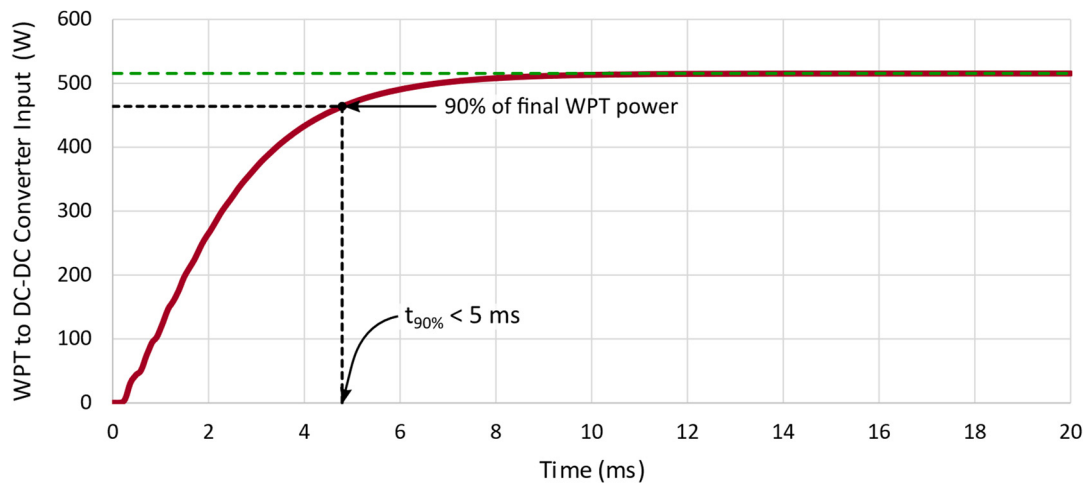
Figure 48: Time response of WPT increase, from primary coil activation to final stable value.

This response curve obtained from simulation indicates that 90% of the final power level delivered to the load will be achieved in about 5 ms, with the final power level obtained in around 12 ms. For most stationary IWPT applications, this performance is satisfactory, for 12 ms is less the duration of one cycle of the power grid voltage.

To analyze this parameter in automotive DIWPT and determine whether it is satisfactorily low in some concrete application, it is necessary to consider factors such as the speed of the vehicles harvesting energy and the length of the DIWPT interaction zone along the vehicle's path over the primary coil. To illustrate this, let us consider an hypothetical case where a vehicle is running at 100 km/h, in 5 ms it will displace about 14 cm over the primary coil and in 12 ms it will displace about 33 cm. If both the primary and secondary coil are as short as 50 cm long and they useful interaction length is 60 cm, 5 ms is about $14/60 \cong 23\%$ of the interaction time. So, considering that full power is established on the load 5 ms after the vehicle has entered the harvest zone, in 23% of the opportunity windows for energy harvest the energy transfer will be impaired by 55% (one minus half of 90%), on average, if the primary coil is enabled synchronously to the entrance of the vehicle in that harvest zone. However, if the vehicle is slower or longer primary coils are used, the loss of the opportunity window for power harvesting may be not as relevant.

2.9.4.2 Characteristic Output Curve of the Mazzilli-Baxandall Inverter IWPT

The output waveforms of the Mazzilli-Baxandall inverter are simple. However, when it drives a primary coil which is coupled to a compensated secondary coil connected to a load circuit, as in a typical IWPT configuration, such as that in Figure 46, the interactions are complex, and involve elements with non-linear models, such as the rectifier and the DC-DC converter, in the secondary, and the MOSFETs in switched operation, on the primary side.

Dynamic Inductive Wireless Power Transfer for Lightweight Electric Vehicles
Luiz Alberto Lisboa da Silva Cardoso – University of Minho

84

Figure 49 shows typical output characteristic curves of the DC-filtered output of the rectifier, which is connected to the input of the DC-DC converter: These curves are obtained by circuit simulation, when the magnetic coupling coefficient linking primary and secondary coils, $k = 0.106$, the primary coil $L_1 = 5.12$ µH, $C_1 = 1.914$ µF, $C_P = 470$ µF, $V_{DC} = 49$ V and the other circuit parameters are as described in Table 5. In the plot, the black dashed curve is obtained when capacitor $C_2 = C_{res} = 92.1$ nF, tunning the secondary to the same resonance frequency of the inverter (when the secondary is not highly loaded).
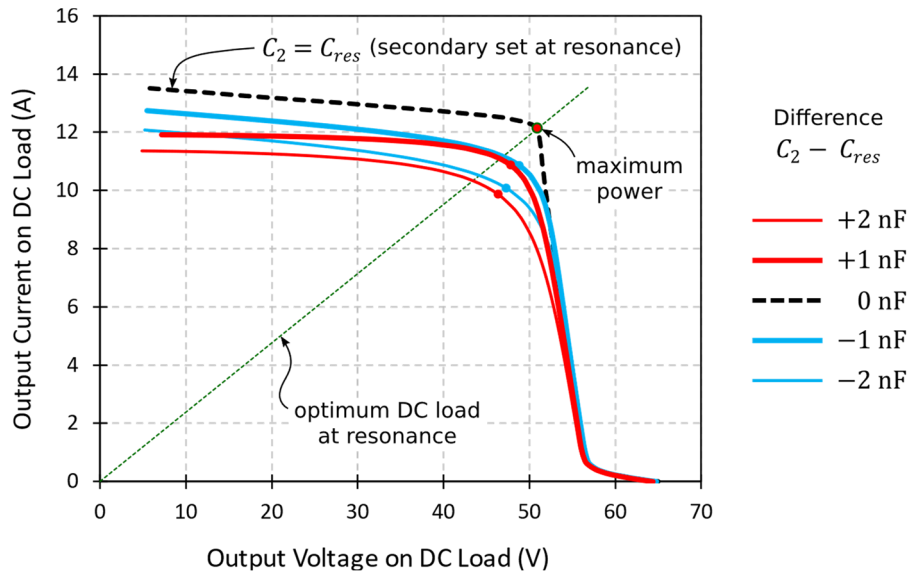
Figure 49: Characteristic output curve of Mazzilli-Baxandall-inverter-driven IWPT.

Still in the plot of Figure 49, the red curves are obtained when the secondary is overcompensated, that is, when C_2 capacitors have values that are higher than that at resonance. Similarly, the blue curves are obtained when the secondary is undercompensated, that is, when C_2 capacitors with values lower than the resonant value are used. The overall effect of offsetting the value of C_2 away from the resonance point, in both cases, is to diminish the maximum power that can be transferred to the load.

This can be better observed if the power output on the DC load is plotted against the DC voltage on its terminals, as shown in Figure 50.
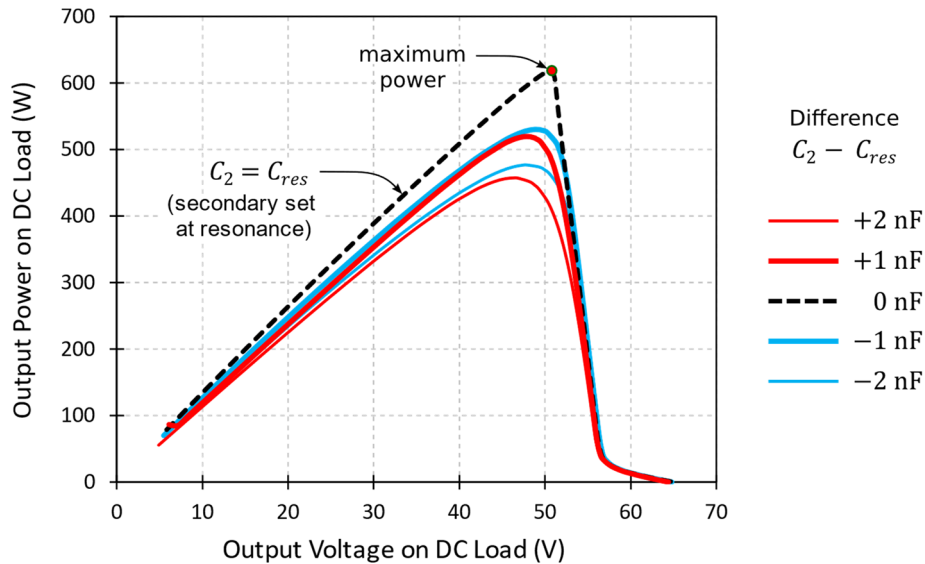
Figure 50: Power transferred to DC load by a Mazzilli-Baxandall-inverter-driven IWPT.

Remarkably, the adjustment of the value of the secondary capacitor C_2 is critical, if operation close to the point of maximum power transfer is required. In this numerical example, for instance, a reduction in the maximum power of about 14% is observed at a deviation of only $\pm 1.1\%$ in the capacitance of C_2 away from the capacitance value that is required for resonance, C_{res}.

So, while every effort should be made to match C_2 to the ideal compensation capacitance C_{res}, in a robust design (with respect to C_2 and the inductance of the secondary coil) the power to be transferred at the operation point should not be set very close to the maximum transferrable power, where the sensitivity to the match of C_2 to C_{res} is higher. This can be done, for example, by clipping the output voltage to a fixed output value on given output load. In a vehicular DIWPT application, this voltage will be usually set to that required by the powertrain.

2.9.4.3 Effect of Parasitic Capacitances on the Secondary Coil on the Output

When the coil of a serial compensated WPT circuit, either primary or secondary, has many turns, which are not enough spaced from each other, the physical implementation of the coil may often be more precisely modeled by considering the existence of a parasitic capacitance in parallel with the terminals of that coil. That is, the resulting WPT circuit model has to consider this capacitance as well, with the response characteristics potentially deviating from that of pure SS-compensated model. By using parallel compensation on the primary side, the Mazzilli-Baxandall auto-resonant inverter already has a capacitor C_1 in parallel to the primary coil, so it is easy to adjust the value of C_1 to compensate this effect. But this circuit may be especially sensitive to parasitic capacitances on the secondary coil, which is serial-compensated. The resulting model to

Dynamic Inductive Wireless Power Transfer for Lightweight Electric Vehicles
Luiz Alberto Lisboa da Silva Cardoso – University of Minho

86

consider is then represented in the schematic diagram of Figure 51, where the parasitic capacitance $C_{2,p}$ is highlighted.
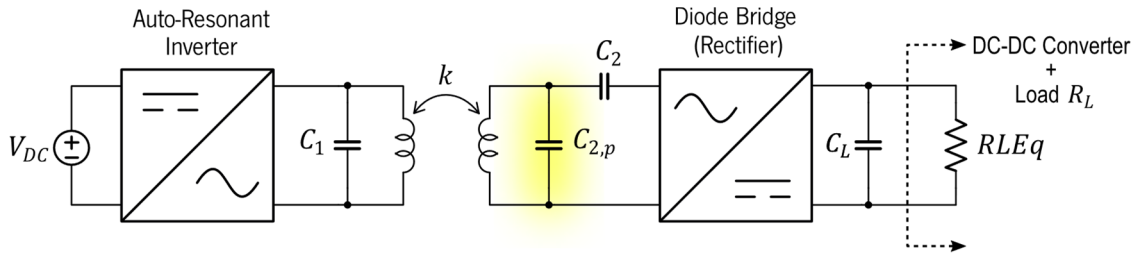
Figure 51: Mazzilli-Baxandall driven PS-compensated WPT architecture, with the inclusion of the parasitic capacitance $C_{2,p}$ in the model of the secondary compensation circuit.

Figure 52a shows a family of output characteristic curves for the Mazzilli-Baxandall circuit in Figure 46, where it is added a parasitic parallel capacitance $C_{2,p}$ across the terminals of the secondary coil, L_2. These curves were traced using the LTSpice [64] simulator, again using the parameters in Table 5, and capacitances $C_{2,p}$ increasing from zero (thicker curve) to a maximum of $16\,nF$ (thinner curve), in the discreet set $\{0, 0.5\text{ nF}, 1\text{ nF}, 2\text{ nF}, 4\text{ nF}, 8\text{ nF}, 16\text{ nF}\}$. These values, for the adopted resonance capacitor $C_2 = 96$ nF, correspond respectively to the fractions $\{0, 0.5\%, 1.0\%, 2.0\%, 4.0\%, 7.7\%, 14.3\%\}$ of the total secondary capacitance, $C_{2,p} + C_{2,p}$. In the same manner, the effect of this parasitic capacitance on the load output regulation is shown in Figure 52b, revealing that for any $C_{2,p}$.there is a current threshold that, if exceeded, will result in a large increase in the observed ripple on the output equivalent DC load $RLEq$.
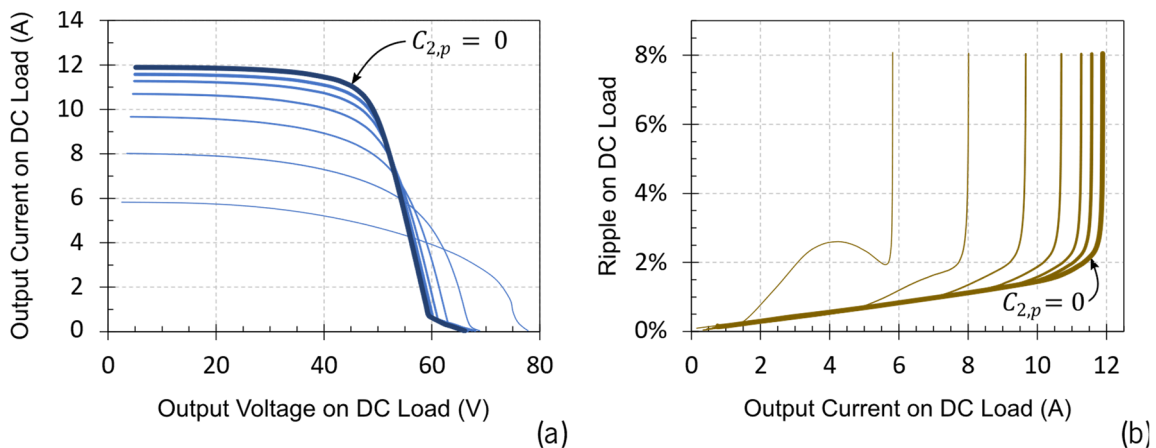
Figure 52: Behavior of (a) output characteristic curve and (b) ripple in the Royer-Mazzilli driven PS-compensated WPT, as the parasitic capacitance $C_{2,p}$ is increased, by numeric simulation with LTSpice.

The observed effect is that this parasitic capacitance on the secondary coil can clearly impair the maximum output current for high load values (associated to low load resistances and low output voltages), decreasing the maximum transferable power with these higher loads. However, it can slightly increase the available current and power for lighter loads (of higher resistance).

Dynamic Inductive Wireless Power Transfer for Lightweight Electric Vehicles
Luiz Alberto Lisboa da Silva Cardoso – University of Minho

87

Another highly undesirable characteristic is that, as shown in in Figure 52b, the presence of $C_{2,p}$ also abruptly spoils the load regulation earlier, as the load current is increased.

Concerning the power transferred to the load, the effect of this parasitic capacitance can be observed on the curves, also obtained by simulation, drawn in Figure 53a and Figure 53b.
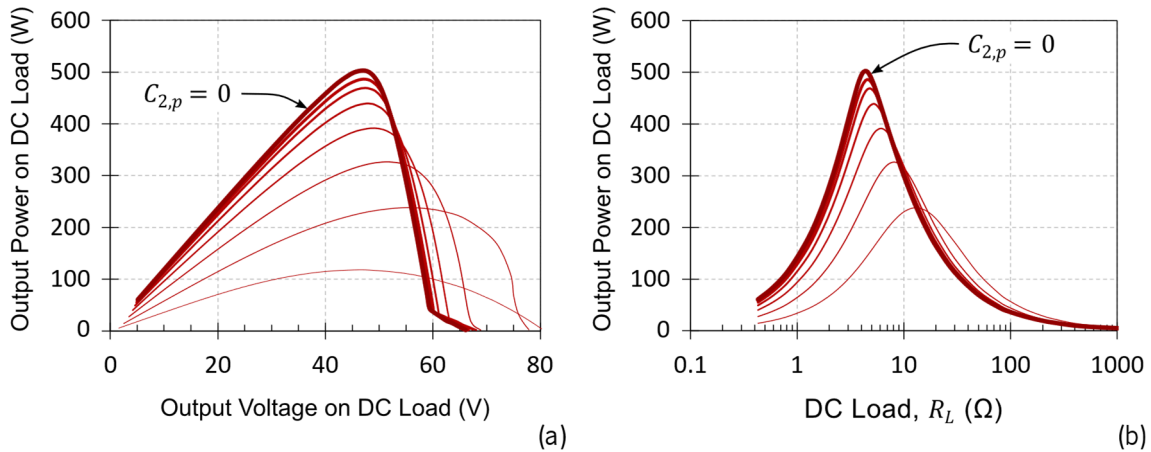
Figure 53: Simulated behavior of the DC power output in the Royer-Mazzilli driven PS-compensated WPT, when the parasitic capacitance $C_{2,p}$ is increased, as a function of (a) the output voltage and (b) the equivalent DC load.

The parasitic capacitance is a difficult to model collateral design parameter that, in general, should be made as small as possible. As indicated by Figure 52a, it can be indirectly evaluated from the output characteristic V x I of the Mazzilli-Baxandall WPT, and, once modeled and considered in the design, predictable results for the power transfer characteristic of this architecture can be expected.

In the frequency range currently used in automotive IWPT applications, from 10 kHz to 100 kHz, $C_{2,p}$ commonly has a very small value though, if compared to the secondary resonance capacitor. In this case, it may be even possible to consider the intentional addition a physical small value (less than 1% of C_2) capacitor in parallel to the secondary coil. The justification for this new capacitor is that, at the expense of a slight reduction on the maximum load current and transferable power, by dominating the value of $C_{2,p}$, it will make the circuit response more predictable and, principally, more independent of the dispersion of the parasitic capacitance, which can vary from one implementation instance of L_2 to another of the same nominal inductance value.

2.9.4.4 Effect of Parasitic Capacitances of the Secondary Coil on the Primary Circuit

The dependency of the primary current on the value of $C_{2,p}$, for a resonant series capacitor C_2 with a fixed value capacitance (96 nF) slightly above the value that would make the secondary resonant at the oscillation frequency, is shown in Figure 54a and, zoomed in the primary current

Dynamic Inductive Wireless Power Transfer for Lightweight Electric Vehicles
Luiz Alberto Lisboa da Silva Cardoso – University of Minho

88

axis, in Figure 54b. In both of these figures, the thicker curve is associated with the ideal $C_{2,p} = 0$, and thinner curves to progressively higher parasitic capacitances. The points of maximum power transfer to the load are indicated by red dots.
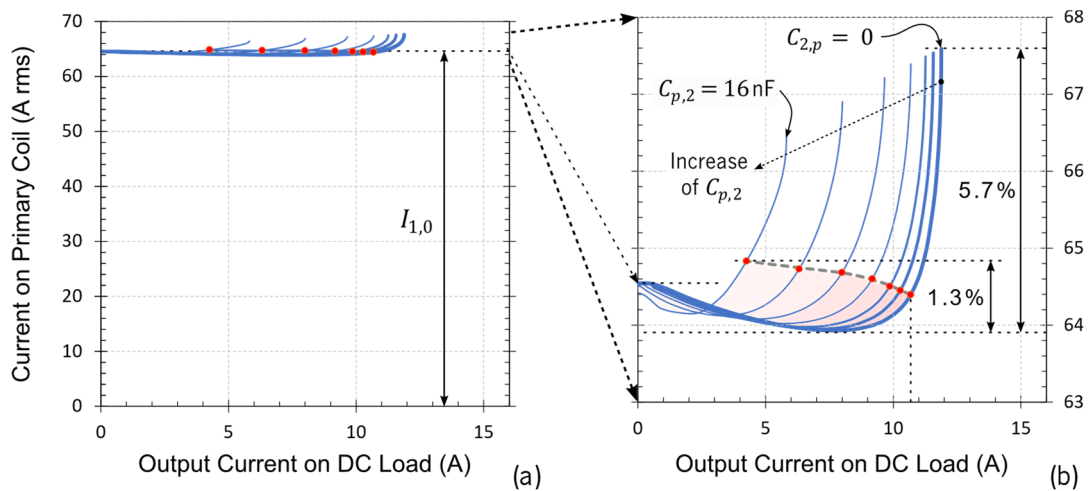
Figure 54: Variation of the primary coil current in response to the DC output current (a), and the same zoomed to show the target operation zone (b).

As expected, due to the low magnetic coupling coefficient, k, the resulting primary current is essentially constant, independent of the output current on the DC load, except when the output current on the DC load significantly surpasses the value the output current of the point of maximum power transfer. The increase of the primary current implies the increase of primary winding and inverter losses, so it should be avoided. To accomplish this, the operation point of the circuit must preferably lie in the pink shaded zone indicated in the zoomed in plot of Figure 54b, where the darker the shade the lower parasitic capacitance is present, and the better it is in terms of the maximum transferable power that can be achieved with at the same primary current level. Additionally, exceeding the output current at the point of maximum power transfer by a significant amount and causing the primary current to increase abruptly, may endanger the physical integrity of the electronic components on the primary circuit (including the primary coil itself).

The behavior of the relative phase between secondary and primary currents, on the other hand, is also impacted by the secondary parasitic capacitance, as shown in Figure 55.

Dynamic Inductive Wireless Power Transfer for Lightweight Electric Vehicles
Luiz Alberto Lisboa da Silva Cardoso – University of Minho

89
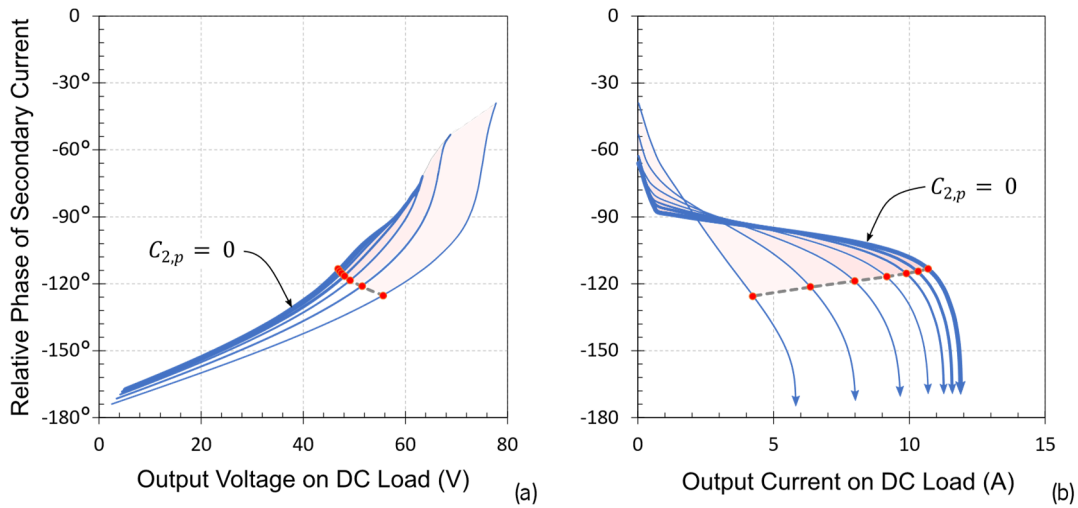
Figure 55: Relative phase of the secondary current with respect to primary current, as the Dc load is increased: (a) as a function of the DC output voltage and (b) as a function of the DC output current.

It can be notice that by working with lighter loads (higher output voltages and lower output currents) than that observed at the point of maximum power transfer (red dots in both Figure 55a and Figure 55b) brings the additional advantage of conveying the relative phase of secondary and primary currents closer to $-\pi/2$ (90° of arc), what tends to be beneficial for the efficiency of the magnetic coupling.

2.9.4.5 Circuit Auto Resonant Behavior Due to Frequency Splitting

Referring to the uncoupled circuit in Figure 45, and considering symmetrical branches with $L_{M,1} = L_{M,1} = L_M$, as normally adopted in the design of Mazzilli-Baxandall auto-resonant inverters, the natural oscillation frequency of the primary tank (and thus, the oscillation frequency), f_0, can be calculated by:

$$ f_0 \;=\; \frac{1}{2\pi\sqrt{(L_1 // L_M)C_1}} \;=\; \frac{1}{2\pi\sqrt{\dfrac{L_1 L_M}{L_1 + L_M}C_1}} \,, \tag{2.101} $$

This is so because, in terms of AC signal, in each half cycle of the oscillation, the primary coil L_1 is connected in parallel with just one of the $L_{M,i}$, $i \in \{1, 2\}$. That is, in each half-cycle, L_1 has one of its terminals connected to $L_{M,i}$ and kept floating (the associated transistor M_i is open), while the opposite terminal of L_1 is shortened to ground, through the other MOSFET M_j, $i \neq j$. Since the other terminal of $L_{M,i}$ is connected to V_{DC}, that is, it is also AC-grounded, L_1 and $L_{M,i}$ can be considered in parallel, under the AC perspective. Similar occurs in the next half-cycle, when L_1 can be considered in parallel with $L_{M,j}$, for AC signals.

Dynamic Inductive Wireless Power Transfer for Lightweight Electric Vehicles
Luiz Alberto Lisboa da Silva Cardoso – University of Minho

90

Looking at (2.101), it can be seen that, in a first approximation, when $L_{M,1}$ and $L_{M,2}$ are much higher that L_1, the magnitude of the oscillation frequency can then be determined by the resonant primary tank $\{L_1, C_1\}$.

According to the results in section 2.5, which equally apply to either SS or current driven PS-compensated IWPT topologies, under small enough loading, the maximum circuit response will be found asymptotically found at the same resonant frequency f_0 of the uncoupled inverter (2.101). The auto-resonant excitation is then reinforced at this frequency, also causing the Mazzilli-Baxandall inverter to oscillate at f_0. However, when the load is increased, the maximum response will progressively migrate from f_0 to one of the split-frequencies f_{odd} or f_{even}. If the equivalent DC resistance of load $RLEq$ (Figure 46) is less than a critical value, the point of maximum response can abruptly shift from one to the other of these split-frequencies. This circuit response causes the oscillation frequency of the auto-resonant inverter to vary accordingly, as shown in the family of curves obtained by simulation with LTSpice, in Figure 56.
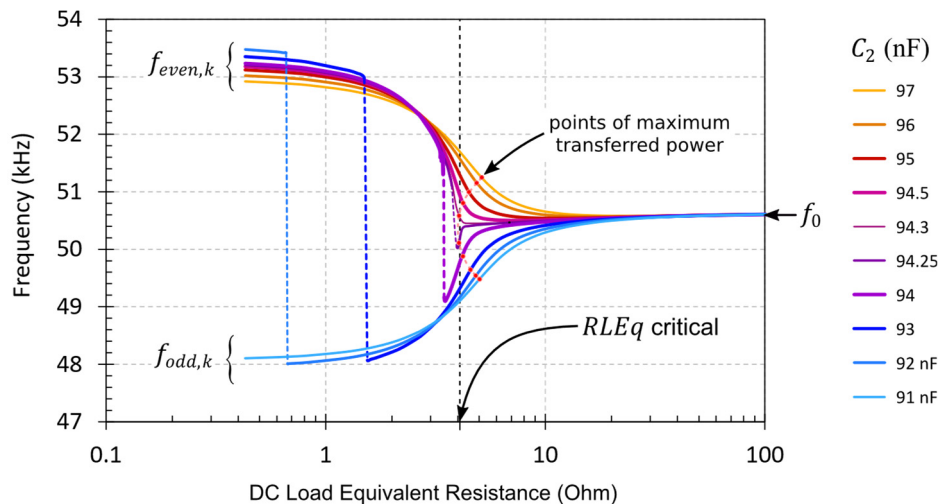
Figure 56: Oscillation frequency resulting from coupling of a series compensated secondary circuit to the primary coil of the resonant tank a Mazzilli-Baxandall auto-resonant inverter, obtained by numeric simulation.

Each of these curves were obtained for a different compensation capacitance, plus a parasitic secondary capacitance of 1 nF, with all other circuit parameters as in Table 5. The main effect of a small parasitic parallel capacitance in the secondary coil is a small shift in the resonant frequency, or conversely, in the required serial compensation capacitance for the same given resonant frequency. For the parameters used in the simulation, it can be seen that if the secondary is overcompensated with $C_{2,k}$, the oscillation frequency will remain approximately constant at f_0, then, as the load is increased, start to glide towards $f_{even,k}$. If the secondary in undercompensated

Dynamic Inductive Wireless Power Transfer for Lightweight Electric Vehicles
Luiz Alberto Lisboa da Silva Cardoso – University of Minho

91

though, as the load is increased, the oscillation frequency will initially shift towards $f_{odd,k}$, then eventually abruptly jumping to the ridge leading to $f_{even,k}$.

The curves of primary current follows a similar pattern to those of the oscillating frequency, with higher currents being eventually achieved as the load is increased, as shown in Figure 57.
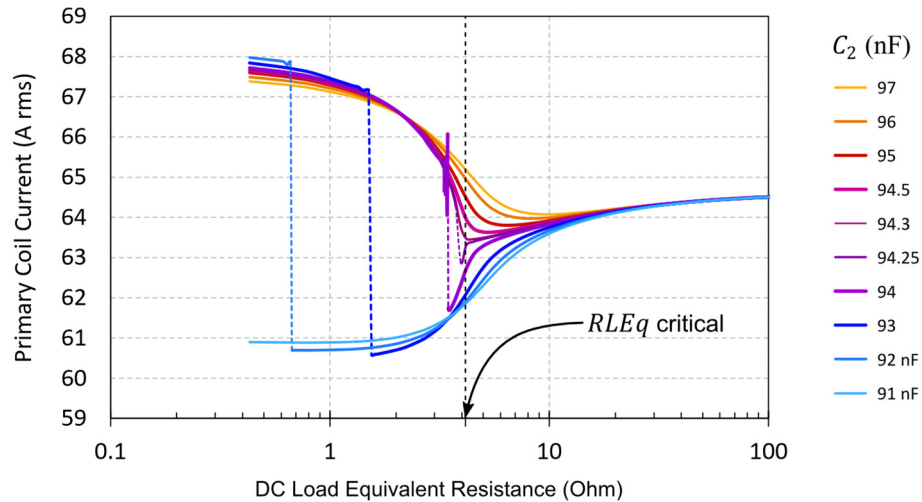
Figure 57: Primary current resulting from coupling of a series compensated secondary circuit to the primary coil of the resonant tank a Mazzilli-Baxandall auto-resonant inverter, obtained by numeric simulation.

In both plots, it can be noticed that, starting from a very lightly loaded secondary (load with high resistance), as the load is increased the frequency and the primary current initially decay slightly then, if the resistance of load falls beyond a critical value of $RLEq$, there is a split behavior. If the secondary is overcompensated (hot colored curves in the graphs of Figure 56 and Figure 57), the frequency of oscillation and primary current also slightly decay with the increase of the load, but then they increase as the load is further increased. If the secondary is undercompensated (cold colored curves in the graphs of Figure 56 and Figure 57), after a slight initial decrease the frequency and primary current tend to decay further and more pronouncedly, as the load is increased, until a point where they abruptly invert this tendency, causing both the frequency and primary current to jump up. For each level of undercompensation, there will be a loading point at which, if the load increases further, both the frequency and the current will increase abruptly, and continue to increase as the load is increased even more.

This anomalous behavior, observed in an IWPT configuration driven by an auto-resonant inverter, when the secondary coil is undercompensated, may produce an instability of the circuit in the vicinity of the critical loading level that causes the frequency jump. To avoid this undesired operation characteristic, it is then recommended that the resonant capacitor is carefully adjusted to avoid undercompensation. For the same reason, it is an additional cautionary measure to avoid

Dynamic Inductive Wireless Power Transfer for Lightweight Electric Vehicles
Luiz Alberto Lisboa da Silva Cardoso – University of Minho

92

loading the secondary excessively. This does not constitute any limitation for the efficacy of an IWPT system itself because it is not necessary to load the secondary beyond the point of frequency switching in order to establish maximum power transfer.

2.9.4.6 Monitoring the Electric Stress from the Primary Side

Concerning the undesirable abrupt increase of the primary current due to a heavily loaded secondary, showed in Figure 52b and Figure 54, a simple safe design rule for the Mazzilli-Baxandall driven IWPT was derived, which was exemplified in Figure 61. Without further especial arrangements, the implementation of a safe design using this technique then relies on the current self-limiting behavior of the load attached to the output of the rectifier, or on the imposition of such limitation by the secondary circuit. Since the load current is not directly monitorable from the primary side, the task of keeping the circuit in the safe zone is, in principle, out of the direct control of the primary circuit.

However, even without using an explicit message passage schema to measure the load current and make this information available to some circuit protection on the primary side, it is possible to implement a simple safeguard for keeping the system operating in the recommended zone, other than simply limiting the power input from the DC power source. This can be achieved by noticing that, in this circuit topology, as explained in the previous topic and showed in Figure 56 and Figure 57, the load also affects the frequency of operation, which can be equally monitored from the primary side, as it is in the secondary. For the properly overcompensated secondary coil (using $C_2 = 96$ nF), the simulation results in Figure 58 show, for different values of the secondary parasitic capacitance, how the frequency of oscillation and the power in transferred in the Mazzilli-Baxandall inverter driven IWPT can vary, as the load is increased from zero (open secondary) to a heavily loaded condition, following the orientation given by the arrows associated to each blue curve.

Dynamic Inductive Wireless Power Transfer for Lightweight Electric Vehicles
Luiz Alberto Lisboa da Silva Cardoso – University of Minho

93
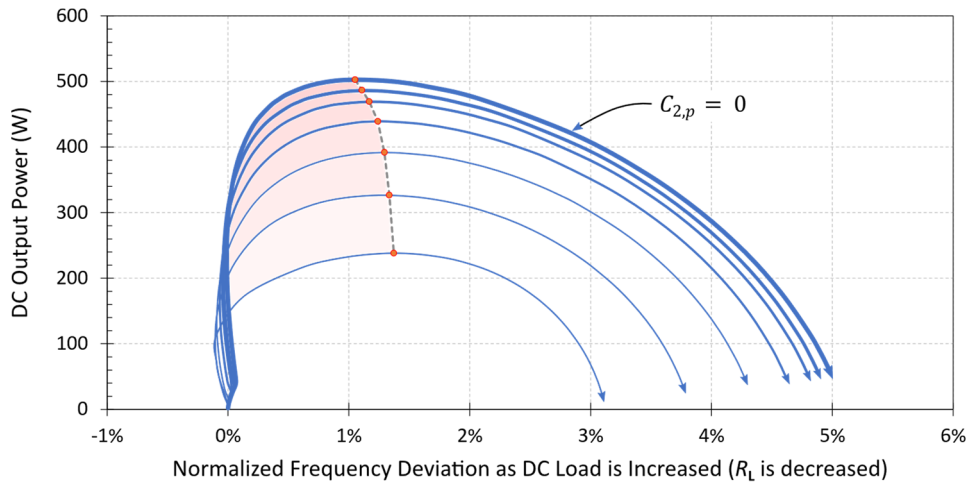
Figure 58: Normalized frequency deviation and DC output power response to an increase in the DC load, when the secondary coil is overcompensated.

Depending on the secondary parasitic capacitance, for low DC output power values the oscillation frequency can initially decrease or increase somewhat from that of the no-load condition. But eventually, and before the power transferred to the load reaches its maximum, the frequency becomes monotonically crescent with the DC load (decrescent with the load resistance).

Based on this behavior, the primary circuit can then be designed to shut down the inverter, if the oscillation frequency exceeds some predetermined value, that one associated with the maximum power transfer. For increased safety, and to account for the case in which the secondary is incidentally undercompensated, the inverter protection should also be triggered if the frequency is too much lowered from the unloaded nominal valued. For the lab prototypes developed in Chapter 5, these circuit protection schemes were not required, because the main concern was neither circuit optimization of a featured final product, but rather conceptual demonstration.

2.9.4.7 Maximum Required Secondary Coil Current

In the simulations so far used in the analysis of the Mazzilli-Baxandall IWPT configuration, an equivalent DC resistance RLE_q replaced the DC-DC converter and the load R_L, because they were not crucial for the analysis of the stability of the circuit and the estimation of the power transferred. However, independently of the actual inverter circuit topology used to drive the primary coil, an useful relation between the load current and the maximum secondary current on a series compensated coil can be established, when a DC-DC converter is inserted in between the rectifier and the load, limiting the load voltage to the nominal desired value V_L. The maximum required secondary coil current can be determined from the nominal DC current on load in two steps: First, based on the characteristics of the DC-DC converter, it is possible to determine the required input

current to the DC-DC converter itself, I_{DC-in}. Then, under the approximation that the current on the loaded secondary is purely harmonic, by conservation of energy, it is observed that the rms current on the secondary coil $I_{2,rms}$ should be proportional to I_{DC-in}, by a factor of $\pi/2\sqrt{2} \cong 1\frac{1}{9}$. That is, the maximum required $I_{2,rms}$ is about 11.1% higher than I_{DC-in}. To derivate this relation, let us then model the DC-DC converter as in Figure 59 and equations (2.102) and (2.103).
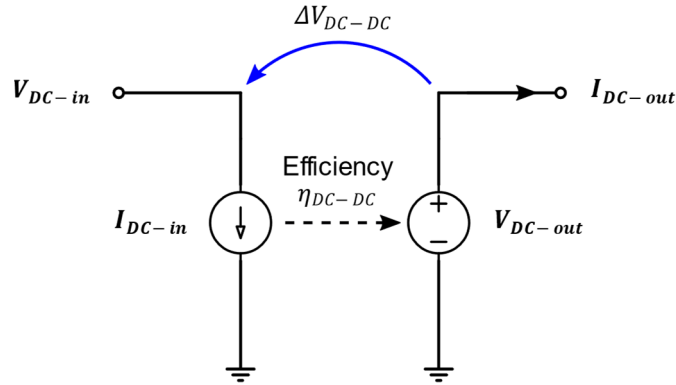
Figure 59: Simplified model for the DC-DC converter at the secondary of the Mazzilli-Baxandall-inverter-driven IWPT.

$$0 \leq V_{DC-out} \leq \min\{V_L, V_{DC-out} - \Delta V_{DC-DC}\} \tag{2.102}$$

$$I_{DC-in} = \frac{V_{DC-out}}{\eta_{DC-DC}\, V_{DC-in}}\, I_{DC-out}\, , \tag{2.103}$$

where η_{DC-DC} is the efficiency of the DC-DC converter, which can be considered approximately constant for a range of loads close to the nominal load. Inequation (2.102) merely denotes that, for a proper regulation of the output voltage V_{DC-in}, due to implementation paradigms, is normally required to be above V_{DC-out} by an approximately given constant voltage drop, ΔV_{DC-DC}.

Based on (2.61), it follows that:

$$I_{2,rms} \cong \frac{\pi}{2\sqrt{2}} I_{DC-in} \tag{2.104}$$

At the critical relative position of the secondary coil over the primary coil where the induced voltage is barely the minimum required input voltage for a proper DC load voltage regulation by the DC-DC converter, the input current to the DC-DC converter, I_{DC-in}, in (2.104), can be replaced by the expression in (2.103), giving (2.105).

$$I_{2,rms} \cong \frac{\pi}{2\sqrt{2}} \frac{V_{DC-out}}{\eta_{DC-DC}\,(V_{DC-out} + \Delta V_{DC-DC})}\, I_{DC-out}\, , \tag{2.105}$$

which is immediately recognized as (2.76).

Dynamic Inductive Wireless Power Transfer for Lightweight Electric Vehicles
Luiz Alberto Lisboa da Silva Cardoso – University of Minho

95

Including the DC-DC converter model (of Figure 59) with parameters $\eta_{DC-DC} = 94.5\%$ and $\Delta V_{DC-DC} = 2$ V in the simulation of the circuit in Figure 46, as a replacement to RLE_q, and keeping V_L set to 36.5 V, the relation between the AC secondary coil current and the DC load current in input range is then obtained as a family of curves, one for each output power level of the DC - DC converter. The results, shown in Figure 60, indicate an apparent proportionality of $I_{2,rms}$ with respect to I_{DC-in}, until the factor k is increased enough to produce a voltage V_{DC-in} that is equal to $V_L + \Delta V_{DC-DC}$, in good agreement with the predicted approximated relation in (2.105). Beyond this point, the load current becomes constant, and the secondary coil current decreases because, according to (2.73) and as exemplified in Figure 19, when the induced voltage is further increased, the same required input power can be obtained with less current supplied by the secondary coil.
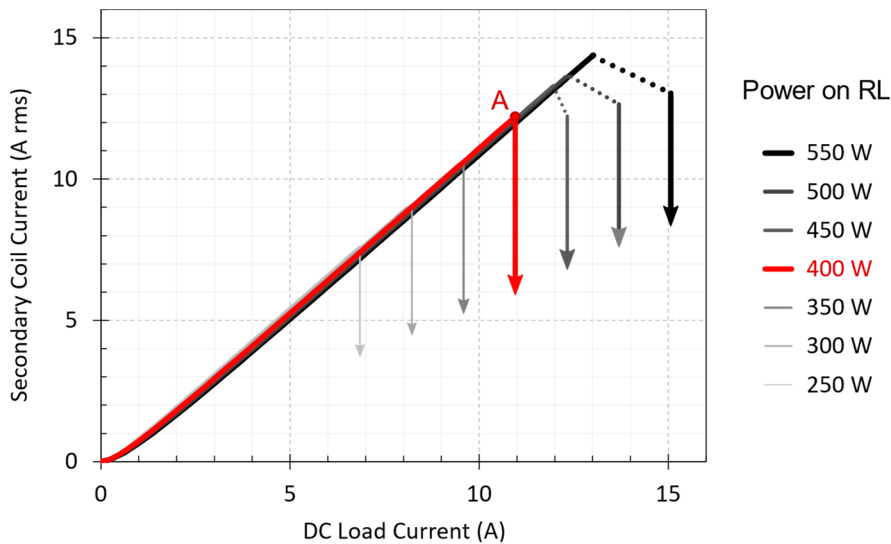
Figure 60: Numeric simulation of the relation between the secondary coil current and the DC load current on a Mazzilli-Baxandall-inverter-driven IWPT, as k is increased.

The curves are traced as the magnetic coupling factor k is elevated from zero to a maximum test value, with arrows indicating the direction of this increase, and indicate the circuit behavior in steady state. It can be observed that, when the DC-DC converter on the secondary is adjusted for a constant power demand over the load R_L, as k is increased, the rms current on the secondary and the DC current on the load will be approximately proportional to each other, until a point where k is large enough to induce a secondary voltage that is above the minimum required input for the DC-DC converter to start effectively regulating the load at voltage V_L. From this point on, the load power and the DC load current are kept constant to their nominal value as k is further increased, while the required secondary coil current starts to decrease, as a result of the presumed constant efficiency η_{DC-DC} of the DC-DC converter and the slightly increase of the efficiency of the rectifier

Dynamic Inductive Wireless Power Transfer for Lightweight Electric Vehicles
Luiz Alberto Lisboa da Silva Cardoso – University of Minho

96

stage, with larger amplitudes of the secondary coil voltage. So, (2.105) estimates the worst-case value (maximum) for the secondary coil current.

Exemplifying the use of (2.105), for this circuit simulation, at point A, on the verge of the DC-DC regulation at 400 W of output power (red curve), the DC load current approaches the nominal value of $400\,W/36.5\,V \cong 11.0\,A$. At this point, the maximum secondary current is 12.1 A rms, while its predicted value, using (2.105), is 12.2 A. For a DC-DC converter with an efficiency $\eta_{DC-DC} = 90\%$, this maximum required secondary current would be 12.9 A instead.

2.9.4.8 Design Recommendations for Mazzilli-Baxandall Driven IWPT

Two design recommendations that can be directly derived from the previous observations and discussions are:

(i)   The serial compensation capacitor should be adjusted to make the secondary loop resonate as close as possible to the frequency of the unloaded, auto-resonant Mazzilli-Baxandall inverter driven primary. However, the nominal value of this capacitor should be carefully set to avoid undercompensation in all circumstances; that is, better slightly overcompensated than undercompensated. Especially in a DIWPT vehicular application, where multiple primary coils and inverters are used, that means to handle the dispersion of the primary coil excitation frequency by compensating the secondary to the lowest expectable inverter frequency.

(ii)   The parasite parallel capacitance in the secondary should be kept low, by careful design of the secondary coil itself.

(iii)   The abrupt switching between split frequencies should be avoided, not setting the operation point too much far inside the constant DC output current region, by limiting the nominal maximum power to be less than the maximum transferable power, what can be easily done by setting an inferior limit for the resistance of the DC load.

Concerning recommendation (iii) let us, for instance, consider a Mazzilli-Baxandall IWPT configuration exhibiting the characteristic output curve of in Figure 61, where the maximum transferable power, slightly over 450 W, is delivered at point of operation M. The maximum intended power transfer level should then be less than that associated to point M, for instance, 400 W. If the minimum useful transferred power is 100 W, then the IWPT power is to lie in the range from 100 W and 400 W. In these circumstances, it can be noticed that there are two a priori

Dynamic Inductive Wireless Power Transfer for Lightweight Electric Vehicles
Luiz Alberto Lisboa da Silva Cardoso – University of Minho

97

possible operation zones where this power level is satisfied: The first, associated with higher loads, in between points A and C, and the second, associated with lower loads (with higher resistance), in between points B and D. According to the design recommendation (ii), the second of these operation zones, the green segment of the power curve (in Figure 61) should be the preferred one, because, by working there, the magnitude of primary current will be lower, the efficiency will then be expectably higher, and the load regulation will be improved, with no frequency or primary current instabilities observed. Also, an excessively loaded secondary, and the consequent elevation of the primary current, not only would cause extra losses, but it could as well damage the transistors or other circuit elements, a sufficient reason to completely avoid it.
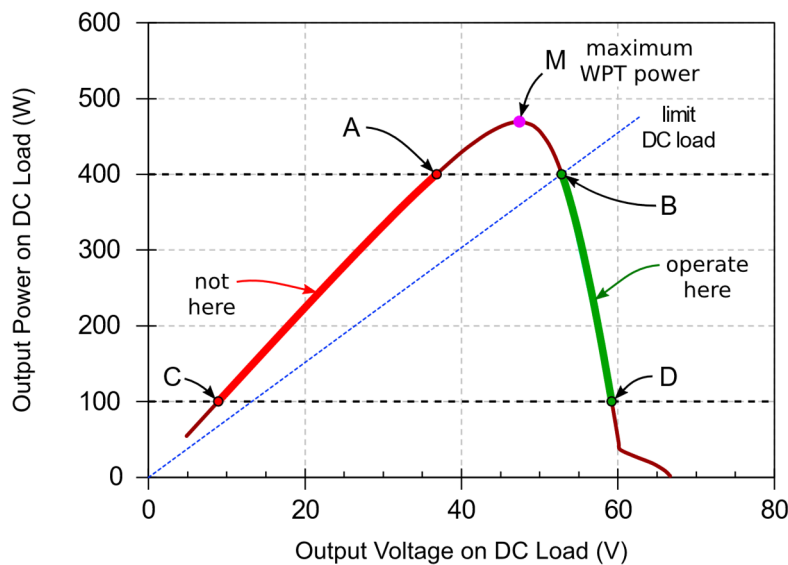
Figure 61: Comparing two points of operation of a Mazzilli inverter with the same transferred power to the DC load.

With the use of a step-down DC-DC converter as a post-regulation device to the rectifier stage, the operation on the green segment of the curve is easily and naturally obtained, if the output load (a powertrain, for instance) is adequately limited.

2.9.4.9 Efficiency of the Mazzilli-Baxandall Inverter-Based IWPT

The efficiency of the magnetic coupling used in a Mazzilli driven IWPT is given by the same expression previously derived (2.95). However, in the overall IWPT efficiency, the losses in the auto-resonant inverter itself as well as in the rectifier on the secondary should also be considered. An algebraic expression for the overall efficiency a Mazzilli-Baxandall inverter driven IWPT could be derived, but due to its complexity, it would possibly not add much insight to the design itself. Rather, the efficiency curve can be drawn based on circuit simulation. For the circuit in Figure 46, where a parasite parallel capacitance of 1 nF was added to the secondary coil, the efficiency curves for different secondary compensation capacitances is shown in Figure 62.

Dynamic Inductive Wireless Power Transfer for Lightweight Electric Vehicles
Luiz Alberto Lisboa da Silva Cardoso – University of Minho

98
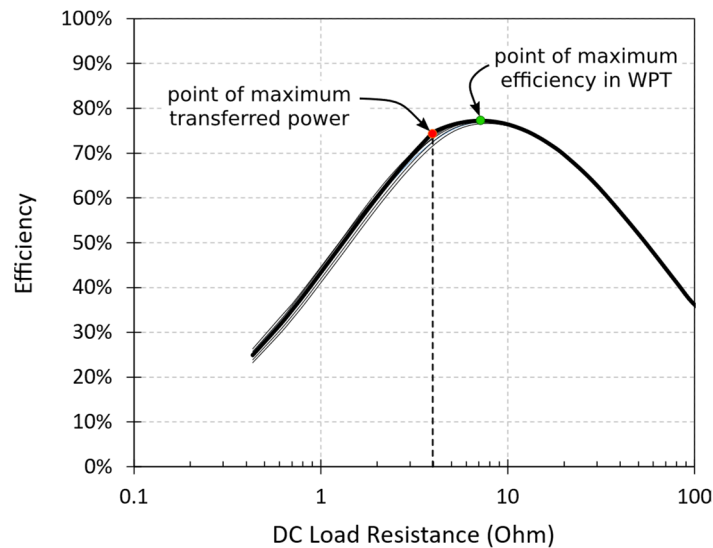
Figure 62: Efficiency as a function of the load, with almost completely superposed curves obtained from numeric simulation for different values of the secondary compensation capacitor.

It can be noticed that all the curves corresponding to different compensation level are almost coincident, as the efficiency is mostly dependent on the loss parameters of the system components, such as the ON resistivity of the MOSFETs, the voltage drop on the rectifier diodes and the quality factors of the primary and secondary tanks themselves. The point of maximum efficiency, as expected, is found at an operation point where the secondary is less loaded than when maximum power is transferred. And that is one more reason to abide by the previously stated design recommendation of limiting the nominal power to be less than that that can be maximally transferred.

2.9.4.10 Baxandall-Mazzilli Driven IWPT with a Variable Magnetic Coupling

All analyses done so far in this section, concerning the behavior of the Mazzilli-Baxandall inverter driven IWPT, considers a fixed magnetic coupling coefficient, k. This is perfect for a stationary IWPT configuration, but definitely not the case for a typical DIWPT vehicular application, where the positioning of the secondary coil is expected to vary relative to the primary coil.

Similarly, as it has been done with other parameters, the variation of k can also be considered in circuit simulations. For a given vehicular DIWPT it is reasonable to assume that a maximum nominal magnetic coupling coefficient k_0 exists, and it is usually obtained when the vehicle (secondary coil) is center-aligned on the i-lane (primary coil). But the case where $k > k_0$ must also be considered. For instance, if some irregularity on the lane makes the secondary coil become momentarily lower than its nominal height above ground.

Dynamic Inductive Wireless Power Transfer for Lightweight Electric Vehicles
Luiz Alberto Lisboa da Silva Cardoso – University of Minho

99

In Figure 46, if a variable resistive equivalent load RLE_q is considered in place of the regulated load formed by the DC-DC converter and RL, and keep the other circuit parameters given by Table 5, but, instead of using k fixed at 0.1137, varying k in increments of 0.025, a family of characteristic output curves can be obtained. This is shown in Figure 63, where the darker and thicker curve corresponds to the most favorable coil-to-coil alignment conditions (largest k).
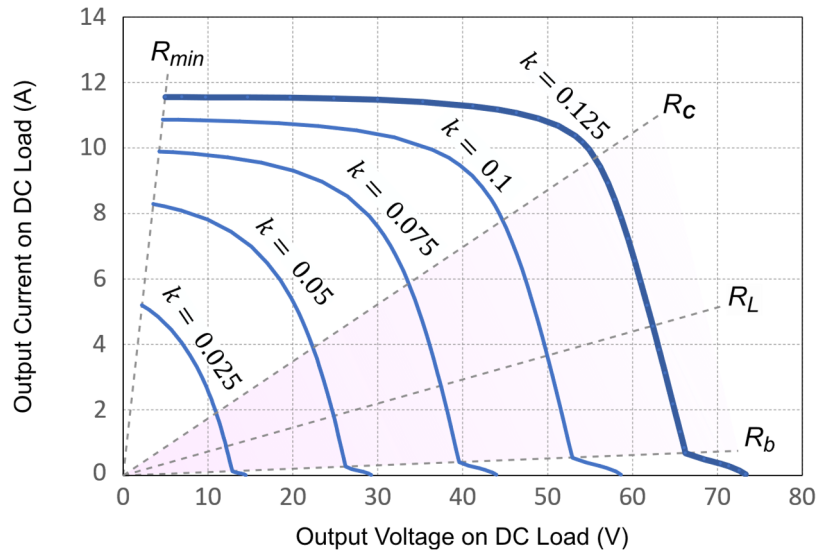
Figure 63: Characteristic output curves of a WPT configuration driven by an Royer-Mazzilli inverter, with no DC-DC converter before the load, for different coupling coefficients k, obtained by numeric simulation with LTSpice.

As expected for this low magnetic coupling coefficient range, which is typical for air-cored DIWPT configurations, for a given load condition, the output voltage on the load seen before the load matching DC-DC converter is proportional to the magnetic coupling coefficient itself, as long as R_L is kept higher than a minimum critical value, R_C. Incidentally, the value of R_C approximately coincides with the operation point where maximum efficiency is met.

So, although the circuit can work with any load $R_L \geq R_{min}$, for both avoiding frequency splitting and oscillation instability, and having approximately linearly predictable induced voltage responses, it is recommended to keep $R_L \leq R_C$. Desirably, for maximum efficiency the operation point should be defined by $R_L = R_C$, at best alignment conditions (higher possible k) in DIWPT configurations. Last, because a very high value for R_L (close to open circuit condition) produces a small peak in the output voltage of the rectifier, which may stress the DC-DC converter, it is also recommended, if the application permits, to keep $R_L \leq R_b$, resulting in the preferred operation region which is shown in pink shade in Figure 63. Otherwise, the DC-DC converter should simply be designed to handle the whole input voltage in the operation range.

Dynamic Inductive Wireless Power Transfer for Lightweight Electric Vehicles
Luiz Alberto Lisboa da Silva Cardoso – University of Minho

100

The optimum matched load zone may be clearer to observe in the graph of the corresponding family of power output curves, shown in Figure 64, where the maximum available power (the peak in the red curves) is never the actual maximum target output power, for efficiency and frequency stability safe-guard reasons.
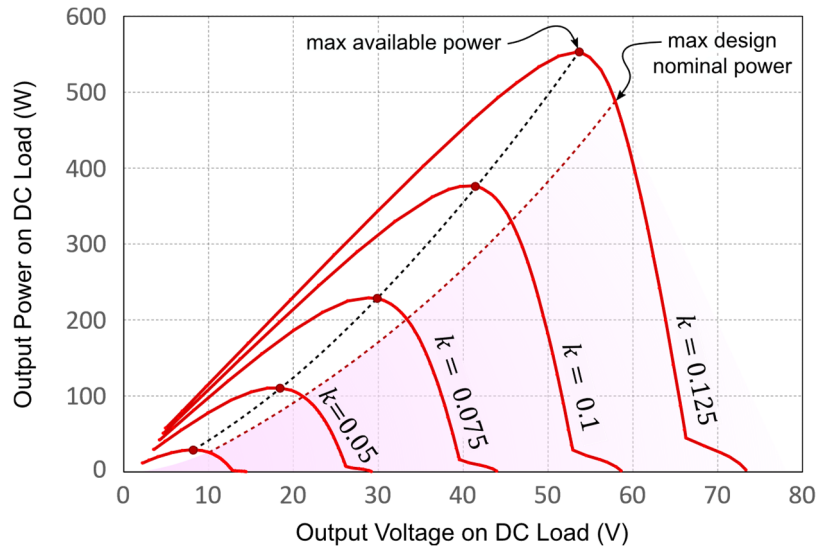
Figure 64: Power output curves of a PS compensated WPT driven by an Royer-Mazzilli inverter, as a function of the voltage output, for different coupling coefficients k, obtained by numeric simulation with LTSpice.

Another chart characterizing the same circuit behavior is obtained when the output power (from the rectifier) delivered to the input of DC-DC converter is drawn against the values of the matched DC load R_L, as shown in Figure 65. The curves give a clear indication that the maximum accepted load increases, that is, the minimum accepted load resistance decreases, as the magnetic coupling coefficient is decreased, what makes the optimally adjusted R_L for k_{max} a safe value for all k range, from zero to k_{max}.
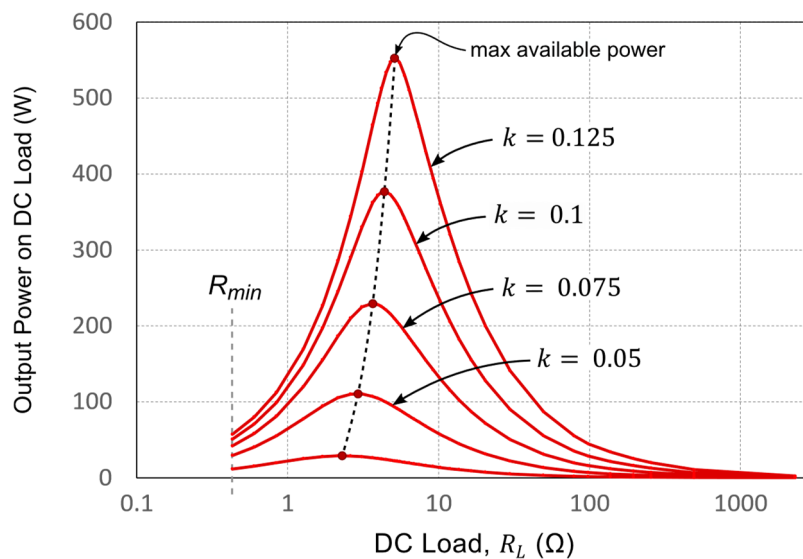
Figure 65: Power output curves of a PS compensated WPT driven by an Royer-Mazzilli inverter, as a function of the output DC load, R_L, for different coupling coefficients k, obtained by numeric simulation with LTSpice.

Dynamic Inductive Wireless Power Transfer for Lightweight Electric Vehicles
Luiz Alberto Lisboa da Silva Cardoso – University of Minho

101

The Baxandall-Mazzilli driven IWPT is fail-safe concerning an unexpected increase in the magnetic coupling coefficient, k, that, in DIWPT for electric mobile applications, could happen, for instance, if the distance between coils is accidentally decreased from its minimum nominal value. If the resonance tanks are adjusted at the maximum nominal k_{max}, which is usually found at the central-alignment condition between secondary and primary coils, this increase in k would only produce a reduction in the power level that is wirelessly transferred, with no impairment to the efficiency, as shown in the simulation results in Figure 66.
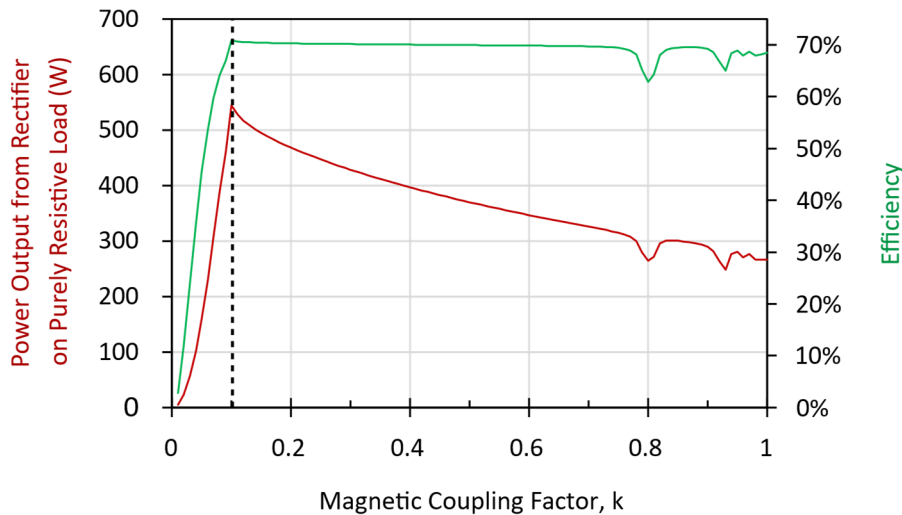
Figure 66: Power output and efficiency of a PS-compensated WPT driven by an Royer-Mazzilli inverter, as a function of k, with no DC-DC converter before the DC load, R_L, obtained by numeric simulation with LTSpice.

The addition of the DC-DC converter at the secondary, to match the load and regulate the voltage at the desired power level, for instance, 400 W, make the circuit further insensitive to unexpected increases in k, as shown in the zoomed in graph of Figure 67.
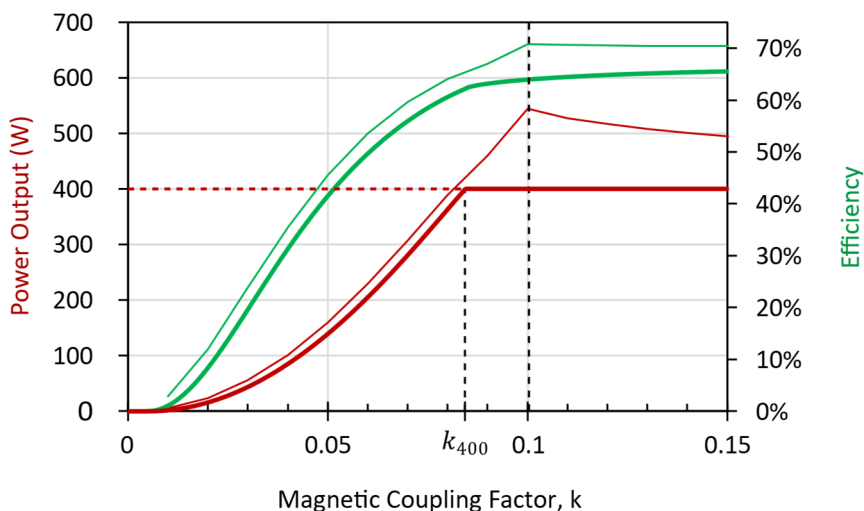
Figure 67: Power output and efficiency of a PS-compensated WPT, when driven by the Royer-Mazzilli inverter.

Dynamic Inductive Wireless Power Transfer for Lightweight Electric Vehicles
Luiz Alberto Lisboa da Silva Cardoso – University of Minho

102

When the sizes of primary and secondary coils in a DIWPT configuration are very dissimilar, which is often the case when oblong primary coils are used, the maximum possible k is intrinsically limited to a value that is much less than the unity. So, in these conditions, the circuit behavior in the vicinity of $k = 1$ is not of practical relevance anyway.

These results were obtained by numeric simulation (with LTSpice) of the PS-compensated WPT circuit, when driven by the Royer-Mazzilli inverter. The DC load R_L used, is such that it will sink 400 W when the DC-DC converter output is set to the desired nominal output voltage $V_L = 36.5V$, that is $R_L \cong 3.33\ \Omega$. The predicted maximum efficiency in the best alignment conditions is slightly over 65%.

So, in Figure 67, the thick red curve is the power at the output of the DC-DC converter, a function P_{400} of k, and the thick green curve is overall DC-to-DC efficiency function, when the output voltage is likewise clipped by the DC-DC converter. The thin curves, red and green, are the same as in Figure 66, here drawn to scale for reference only, respectively the power output and the total DC-to-DC efficiency, when the equivalent matched load to R_L, R_{LEq}, is directly connected to the output of the rectifier, with no DC-DC converter being used.

It can be seen that for $k < k_{400}$, the input voltage (from the rectifier) to the DC-DC converter is not high enough for the converter's output to sustain the nominal voltage of 36.5 V, so the power on R_L will be less than $p_i = 400$ W. Also noticeable, the thin and thick curves do not coincide for $k < k_{400}$ because the efficiency of the DC-DC converter in a real implementation is always lower than 100%.

If such Mazzilli-Baxandall driven PS-compensated IWPT is used in a DIWPT configuration д, where $k_д$ is a function of the position that describes the variable magnetic coefficient factor, then the available output power can be estimated by the composition $P_{400} \circ k_д$, that is the output power will be given by $P_{400}\big(k_д(x)\big)$, where the relative position x is usually the lateral misalignment of the secondary coil (onboard of the vehicle) from the center of the primary coil (in the lane).

In a real DC-DC converter implementation, also often a maximum output current and input voltage range are specified, potentially posing additional restrictions on the interval of k where the nominal output power can be obtained. If the magnetic coupling factor is very high, in the no-load conditions the voltage output of the rectifier can exceed the maximum voltage acceptable by the DC-DC converter. On the other extreme, if it is not high enough in order to generate an induced

Dynamic Inductive Wireless Power Transfer for Lightweight Electric Vehicles
Luiz Alberto Lisboa da Silva Cardoso – University of Minho

103

voltage that is minimally necessary to guarantee the proper operation of the DC-DC converter, depending on the specific design, the output can be zeroed, producing no output power.

The maximum output current of the DC-DC converter is capable to supply, $I_{DC\text{-}DC,max}$, should be at least equal to that required to deliver the indexed power p_i at the required output voltage V_L:

$$I_{DC\text{-}DC,max} \geq \frac{V_L^2}{p_i}$$

(2.106)

Improvements of this simple version of the Baxandall-Mazzilli Driven IWPT circuit may be the target for another specific optimization work in power electronics. In this work this circuit topology is safely used without any further improvement of added development, with the mere purpose of generating the required current to excite the primary coil and test the magnetic link design of the HIPLEV prototype, as described in Chapter 5.

2.10 Factors Affecting the Efficiency of a Magnetic Coupling

In circuit modeling of an IWPT configuration, the real coils are assumed to behave each as an ideal inductor in series with a fixed value resistor, both invariant with frequency. The value of the coil auto-inductance, which corresponds to the reactive impedance of the coil in the model, is usually a good approximation if parasitic interwinding capacitances are low enough for the frequency band exploited. The modeling of the series resistor as a frequency independent, fixed-valued component, however, can easily produce a large error in the estimation of system efficiency. This phenomenon may happen even at lower frequencies, depending on the dimensions and construction of the coils' windings, being called skin effect.

Also, the increase of the apparent resistance of a conductor with the increase of the frequency of the current is aggravated when other wires carrying AC current are placed next to the first conductor, establishing a mutual influence that will increase the resistive losses in all of the conductors in the neighborhood. This second phenomenon, which is called the proximity effect, is of the same nature of the skin effect, and it should also be taken in consideration in IWPT design.

2.10.1 Skin Effect

The electric current flowing through a circular cross-section wire is only uniform across the diameter of the wire for constant DC currents. For harmonic (sinusoidal) currents, the radial

Dynamic Inductive Wireless Power Transfer for Lightweight Electric Vehicles
Luiz Alberto Lisboa da Silva Cardoso – University of Minho

104

distribution of the current density tends to concentrate in a thin cylindrical external layer of the conductor. The width of this layer, called the skin depth δ [65], is given by equation (2.107):

$$\delta = \sqrt{\frac{\rho}{\pi f \mu}}, \tag{2.107}$$

where f is the frequency of the current, ρ the resistivity of the wire and μ its magnetic permeability.

This phenomenon, known as skin effect, is known, modeled and employed in radio design since the early radio era [24] and can be entirely modeled and calculated by developing the differential equations resulting from the application of Maxwell's Equations to the problem. One of its main consequences is that the apparent resistance of a wire becomes higher, as the frequency is raised. Specifically, for the circular cross-section case, when a phasor current $\dot{I}_0$ passes through an infinitely long conductor of radius R, the phasor current density $\dot{J}$ can be expressed by a function of the radius r, normalized by skin depth δ:

$$\dot{J}(r) = \frac{\dot{I}_0(j-1)}{2\pi\delta R} \frac{J_0\left(\frac{r}{\delta}(j-1)\right)}{J_1\left(\frac{R}{\delta}(j-1)\right)}, \tag{2.108}$$

or equivalently:

$$\dot{J}(r) = \frac{\dot{I}_0}{\pi\sqrt{2}\delta R} \frac{ber_0\left(\frac{r}{\delta}\sqrt{2}\right) + j\,bei_0\left(\frac{r}{\delta}\sqrt{2}\right)}{bei_0'\left(\frac{r_0}{\delta}\sqrt{2}\right) - j\,ber_0'\left(\frac{r_0}{\delta}\sqrt{2}\right)} = \tag{2.109}$$

$$= \frac{\dot{I}_0}{\pi\delta R(1-j)} \frac{ber_0\left(\frac{r}{\delta}\sqrt{2}\right) + j\,bei_0\left(\frac{r}{\delta}\sqrt{2}\right)}{bei_1\left(\frac{r_0}{\delta}\sqrt{2}\right) - j\,ber_1\left(\frac{r_0}{\delta}\sqrt{2}\right)}, \tag{2.110}$$

where the functions J_n are the Bessel functions of the first kind and n-th order, the functions ber_n and bei_n are the Kelvin Functions of n-th order, and ber_n' and bei_n' their derivatives [66]. The Kelvin Functions can be numerically calculated by the series (2.111) and (2.112) [65]:

$$ber_n(x) = \sum_{m=0}^{\infty} \frac{cos\left((3n+2m)\frac{\pi}{4}\right)\left(\frac{x}{2}\right)^{2m+n}}{m!\,\Gamma(n+m+1)} \tag{2.111}$$

$$bei_n(x) = \sum_{m=0}^{\infty} \frac{sin\left((3n+2m)\frac{\pi}{4}\right)\left(\frac{x}{2}\right)^{2m+n}}{m!\,\Gamma(n+m+1)} \tag{2.112}$$

Dynamic Inductive Wireless Power Transfer for Lightweight Electric Vehicles
Luiz Alberto Lisboa da Silva Cardoso – University of Minho

105

Illustrating the application of equation (2.110), Figure 68 shows the current distribution across an axial cross-section of such a cylindrical wire, as the frequency is varied from a low value (red curve) to a higher value (blue curve). The curves, instead of plotted for specific frequencies, are plotted for several normalized skin depths, δ_{skin}/R, as δ_{skin} itself is a function of the frequency (2.107).
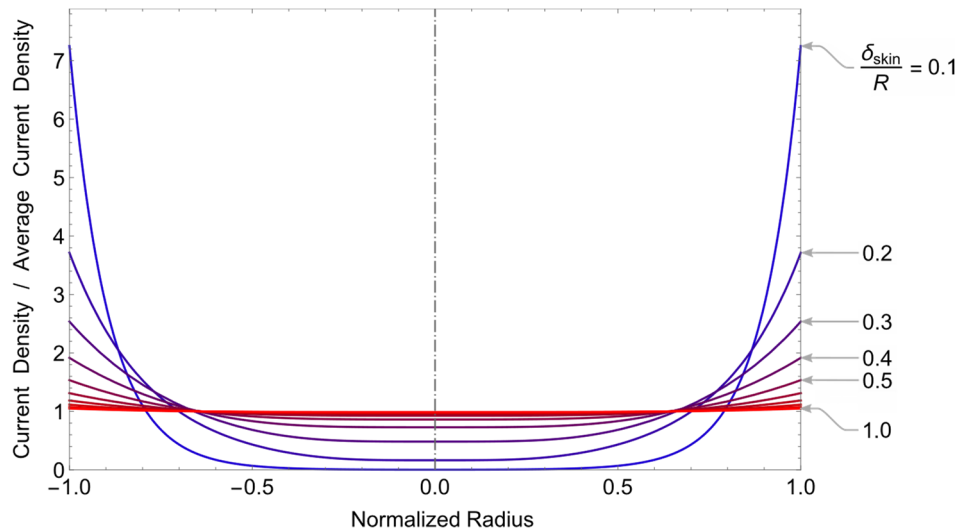
Figure 68: Distribution of current density along the diameter of a circular cross-section wire.

A similar plot is shown in Figure 69, where, this time, each curve is, instead, normalized to the current density at the external cylindrical surface of the wire, for which the radius is R, at that frequency and the associated skin depth.
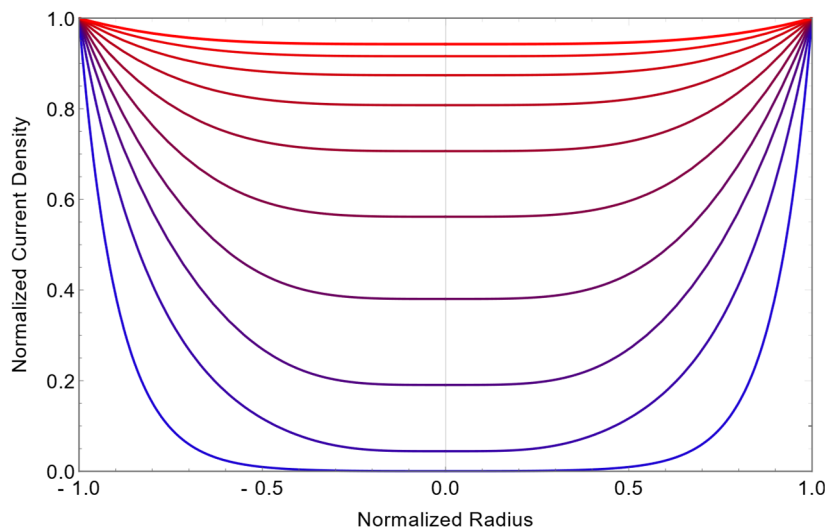
Figure 69: Relative distribution of current density along the diameter of a circular cross-section wire.

In both Figure 68 and Figure 69, the red curve is the current density for a skin depth $\delta = R$, where it is already noticeable (especially in Figure 69) a slight sagging from the horizontal straight line, the characteristic uniform density distribution of a DC current. The following curves with a

Dynamic Inductive Wireless Power Transfer for Lightweight Electric Vehicles
Luiz Alberto Lisboa da Silva Cardoso – University of Minho

106

growing bluish color tone, from the upper one to lower one, are obtained for progressively lower equally spaced ratios δ/R, in decrement steps of 0.1, the last one, touching the zero density in the center of the cylinder, corresponding to $\delta/R = 0.1$. For $\delta/R \leq 0.1$, the AC resistance of the wire can be approximated by the DC resistance of a hollow cylinder with the same external diameter of the solid wire and cylindrical walls with thickness δ.

While the magnitude of the current density decreases from the external surface of the circular conductor inward to the center, its phase cycles with period $2\pi\delta$, as illustrated in FEM simulations results shown in Figure 70, where a cooper wire with 10 mm of diameter subjected to a 50 kHz AC current of $\dot{I}_0 = 1$ A of amplitude was modeled, using COMSOL Multiphysics software.

(a) Normalized amplitude of current density   (b) Phase of current density
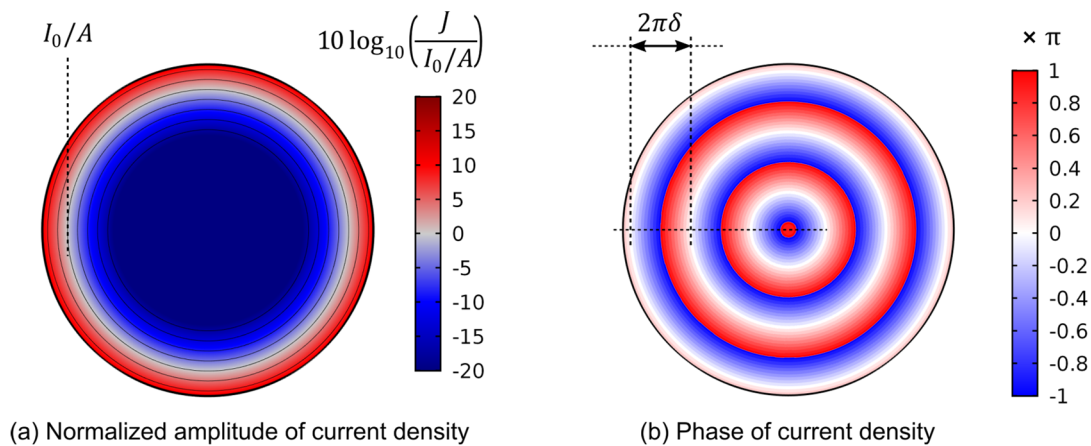
Figure 70: FEM simulation of current density along the diameter of a circular cross-section wire.

In Figure 70a, the color scale varies with the logarithmic of the amplitude of the current density $\dot{J}$, normalized to the average current density I_0/A that is forced into the wire, which has a cross-section area A. In the same Figure 70a, the thin black concentric rings, spaced by distance δ (one skin depth, approximately 0.29 mm for copper at 50 kHz), from the outmost to the innermost, mark cylindric layers with current densities at a geometric progression with ratio e^{-1}. The blue region in the center of the wire is, visibly, depleted from current, which is concentrated on the thin external red layer.

The behavior of the phase of the current density is, on the other hand, is shown in Figure 70b: The current density phase is progressively delayed, from the external surface of the wire inward, cyclically, with a period along the radius of $2\pi\delta$, until it reaches the center of the wire.

The amplitude and phase evolution from the external surface of the conductor to its center follow the pattern of a wave penetrating the material, conjugating progressive phase delay and attenuation, as the wave penetrates the conductor. In good conductors, such as metals, the

Dynamic Inductive Wireless Power Transfer for Lightweight Electric Vehicles
Luiz Alberto Lisboa da Silva Cardoso – University of Minho

107

amplitude of the current density close to the center of the wire is often negligible, and the phase information, except very close to external surface of the wire, is also irrelevant. The simulations also indicate that the current phase on the surface of the wire is slightly advanced, with respect to the phase of the overall current I_0. Because the voltage drop across a wire is commonly measured at the external surface of the wire, this result is compatible with the self-inductance perceived on the wires.

The concentration of the current on a thin external layer of the cylindrical conductor, however, increases the power dissipation for a given total current, and makes its apparent equivalent resistance vary with the frequency. The new apparent resistance of the conductor, when submitted an alternated current, at a frequency f, is called the AC resistance, often denoted by R_{AC}. The ratio of R_{AC} to the DC resistance of the conductor, R_{DC}, can then be computed by:

$$\lambda(f) = \frac{R_{AC}(f)}{R_{DC}} = \frac{P_{AC}(f)}{P_{DC}} = \frac{\int_0^R (2\pi r \|j(r)\|)^2 \frac{\rho\,\ell}{2\pi r}\,dr}{\frac{\rho\,\ell}{\pi R^2} \left\| \int_0^R 2\pi r j(r)\,dr \right\|^2},$$

(2.113)

where j is the current density along the cross-section of the cylindrical conduction, which, by symmetry depends only on r, P_{AC} is the power dissipated on the conductor at the frequency f, P_{DC} is the power dissipated on the conductor when the same total DC current is passing, ρ is the resistivity of the conductor, ℓ its length, and R its radius.

Simplifying (2.117), it turns out that $\lambda(f)$ is independent of both ρ and ℓ:

$$\lambda(f) = \frac{R_{AC}(f)}{R_{DC}} = \pi R^2 \frac{\int_0^R 2\pi r \|j(r)\|^2\,dr}{\left\| \int_0^R 2\pi r j(r)\,dr \right\|^2},$$

(2.114)

By using (2.110), $\lambda(f)$ can be evaluated by numeric integration of (2.114). Also, since R_{DC} is easily calculated based on the resistivity and dimensions of the conductor, it also possible to use (2.114), to directly compute the AC resistance $R_{AC}(f)$. Exemplifying, for the cases of two copper conductors with circular cross-sections of 1.0 mm^2 and 1.5 mm^2, considering a resistivity $\rho_{Cu} = 1.71 \times 10^{-8}$ (at 20°C) and a relative magnetic permeability μ_r=0.999991, let us first compute the DC linear resistivity of each wire, which are given in Table 7.

Table 7: Linear resistivity of copper wires at 20°C, under DC excitation.

Area of Cross-Section	Radius	Linear Resistivity
1.0 mm^2	0.564 mm	17.1 mΩ/m
1.5 mm^2	0.691 mm	11.4 mΩ/m

Dynamic Inductive Wireless Power Transfer for Lightweight Electric Vehicles
Luiz Alberto Lisboa da Silva Cardoso – University of Minho

108

Then, using (2.114), the AC resistances of these two wires can be plot as a function of the frequency of excitation, as shown in Figure 71.
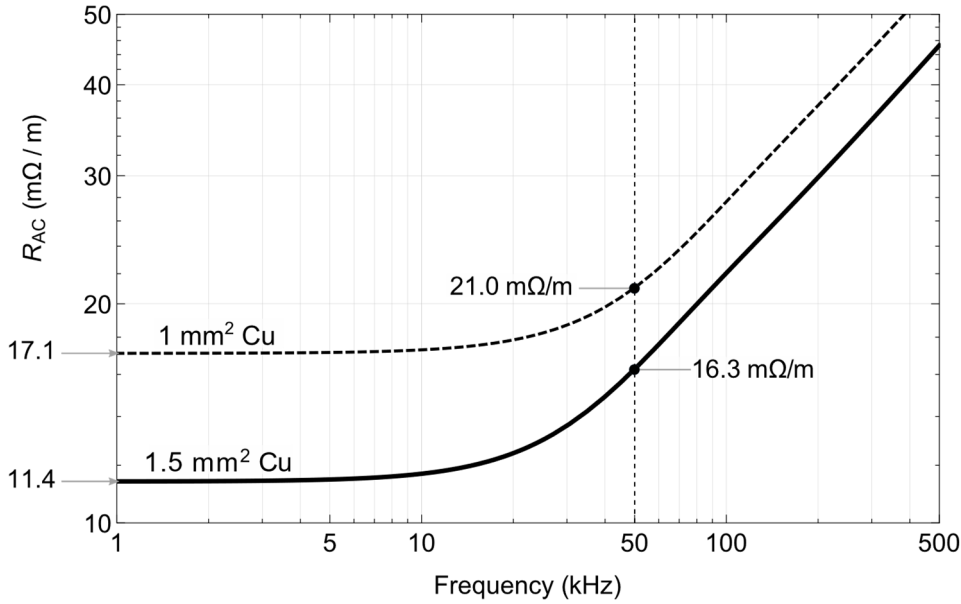
Figure 71: Linear resistivity of copper wires of circular cross-section as a function of the frequency.

From Figure 71 it is easily derived that for DC, or frequencies lower than 3 kHz, both wires with 1.0 mm^2 and 1.5 mm^2 have practically a constant linear resistivity. As the frequency is increased, the resistivities of both wires also increase, with the resistivity of the 1.5 mm wire increasing first. At 50 kHz, their resistivities are 21.0 mΩ/m and 16.3 mΩ/m, respectively 22.8% and 42.3% higher than their DC resistivities.

If the wire cross-section is not circular, the current will still concentrate on its outer layer, but an exact algebraic expression may be not as easy to compute. In either case, for a large enough frequency, such that the skin depth at the conductor that is much smaller than the dimensions of its cross section, the AC resistance to DC resistance of a winding becomes approximately proportional to the square root of the frequency [24], that is:

$$\frac{R_{AC}}{R_{DC}} \cong K \sqrt{f}, \quad K \text{ constant, when } \delta = \sqrt{\frac{\rho}{\pi f \mu}} < \cdots < R \qquad (2.115)$$

This fact makes it not possible to indefinitely obtain more efficient IWPT configurations, just by increasing the frequency. The skin effect tends to cause the quantity $k\sqrt{Q_1 Q_2}$ to be proportional to $\sqrt{f}$, not to f, as it would be expected by using simple serial resistance models for the primary and secondary coils of Figure 3b:

Dynamic Inductive Wireless Power Transfer for Lightweight Electric Vehicles
Luiz Alberto Lisboa da Silva Cardoso – University of Minho

109

$$k\sqrt{Q_1 Q_2} \;=\; k\sqrt{\frac{\omega\, L_P\; \omega\, L_S}{r_{L_P}\, r_{L_S}}} \;=\; k\, 2\pi f \sqrt{\frac{L_P\, L_S}{r_{L_P}\, r_{L_S}}} \tag{2.116}$$

Effectively, in (2.116), expressing r_{L_P} and r_{L_S} in accordance with (2.115), it follows that:

$$\lim_{f\to\infty}\frac{k\sqrt{Q_1 Q_2}}{\sqrt{f}} \;=\; \lim_{f\to\infty} k\, 2\pi\sqrt{f}\sqrt{\frac{L_P\, L_S}{R_{DC}(r_{L_P})\, K_{L_P}\sqrt{f}\; R_{DC}(r_{L_S})\, K_{L_S}\sqrt{f}}} \tag{2.117}$$

$$=\;\; k\, 2\pi\sqrt{\frac{L_P\, L_S}{K_{L_P}\, K_{L_S}\, R_{DC}(r_{L_P})\, R_{DC}(r_{L_S})}} \;=\; \tag{2.118}$$

$$k\,\lambda_H,\;\; \lambda_H \in \mathbb{R}$$

$$\Rightarrow\;\; k\sqrt{Q_1 Q_2} \;\cong\; k\,\lambda_H\sqrt{f}, \quad \text{for } f > \cdots > \frac{\rho\, R^2}{\pi\,\mu} \tag{2.119}$$

So, while the maximum achievable efficiency for "lower" frequencies can be given by

$$\eta_{max} \;=\; \frac{k^2\, Q_1\, Q_2}{\left(1 + \sqrt{1 + k^2\, Q_1\, Q_2}\,\right)^2} \;\cong\; \frac{(\lambda_L)^2\, k^2\, f^2}{\left(1 + \sqrt{1 + (\lambda_L)^2\, k^2\, f^2}\,\right)^2}, \tag{2.120}$$

at high enough frequencies f, due to the skin effect, the maximum achievable efficiency becomes:

$$\eta_{max} \;\cong\; \frac{(\lambda_H)^2\, k^2\, f}{\left(1 + \sqrt{1 + (\lambda_H)^2\, k^2\, f}\,\right)^2} \tag{2.121}$$

So, as the frequency is increased, the efficiency of the magnetic coupling will also increase, but will be limited to a final maximum possible value. However, by increasing the frequency, the power loss in other electronic components of the IWPT system will likely increase as well. This will eventually lead to a point where a marginal gain in the magnetic coupling will not compensate for the losses in the rest of the system, and the overall system efficiency will start to decrease with the increase of the frequency.

In general, simulations with the method of finite element modeling should be applied to calculate the actual current distribution in a conductor and its resulting AC equivalent resistance at the any given frequency, thus permitting the numerical evaluation of the actual efficiency.

2.10.1.1 Litz Wire

One common strategy to minimize the losses that occur due to skin effect, making it possible to sustain large values of $k\sqrt{Q_1 Q_2}$ at higher frequencies, is to use many parallel-connected, symmetrically twisted wires of smaller diameter, instead of a single larger diameter wire. That will

Dynamic Inductive Wireless Power Transfer for Lightweight Electric Vehicles
Luiz Alberto Lisboa da Silva Cardoso – University of Minho

110

enable the IWPT configuration to follow equation (2.120) and handle currents more efficiently at higher frequencies. These twisted multi-stranded conductors are called "litz wire", coined from the German word "Litzendraht" (stranded). Techniques for designing with litz wiring are well documented [67], [68] and effectively improve efficiency. However, the extensive of use of litz wires can significantly increase the cost of the windings (see Table 16).

2.10.2 Proximity Effect

When two or more conductors or cables in the same vicinity are conducting AC current, or when more than one wire are packed in parallel in a cable, an additional phenomenon, similar to the skin effect is verified: The magnetic fields generated by the currents flowing in each wire interact with the currents in the other wires, altering the current density further than what would be expected by the skin effect alone, as exemplified in section 2.10.1. This happens because the eddy currents that are induced on the conductors occur as a response to any current, indistinctively, either flowing in the same conductor or in another conductor in the vicinity.

The apparent effect is that AC currents flowing in parallel tend to disperse, no matter if they are contained in the same or in insulated conductors. For instance, if two wires of circular cross-section and the same radius are set in parallel, are carrying identical currents in the same direction, the current density flowing in each wire will be displaced to the side in opposition to the vicinity of the other conductor, as shown in Figure 72. In this example, the two wires together (right picture) exhibit each a resistance 16% greater than if they were 4.86 diameters apart (left picture), causing a power loss increase of 16% in the wires.
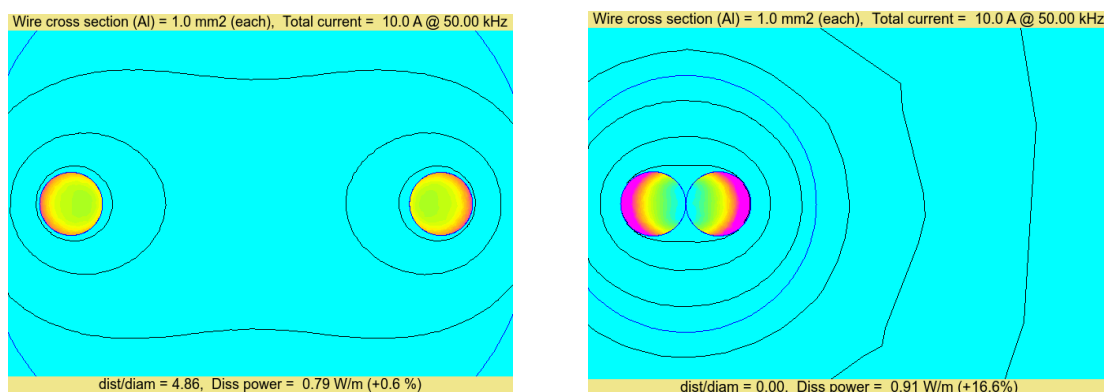
(a) Conductors far apart.   (b) Conductors close to each other.

Figure 72. FEM simulation showing the proximity effect in two circular cross-section wires.

Dynamic Inductive Wireless Power Transfer for Lightweight Electric Vehicles
Luiz Alberto Lisboa da Silva Cardoso – University of Minho

111

The technique to model this interaction is the same used for the skin effect, however, since the geometries involved can be arbitrarily complex, an exact closed expression to compute the proximity effect is usually difficult to obtain.

2.10.2.1 Consequences of the Proximity Effect in a Single Isolated Coil

The first practical consequence of the skin effect on a single isolated coil is that the geometry of the coil affects not only its inductance, but also, its equivalent series resistance in a linearized approximation model, even if the coil is constituted of a long wire with constant cross-section. The magnetic field generated by the current flowing in one segment of the coil will interact with other neighbor segments inducing potentials and eddy currents on them. This will increase power dissipation, according to the shape of the coil, even if the current phasor is kept constant.

So, the proximity effect has to be considered in any detailed analysis. The effect can more intuitively seen as if the serial resistor of the linear model were not evenly "distributed" along the conductor that constitutes the coil, but rather, concentrated where the alternating magnetic field is stronger. To exemplify this effect and gain familiarity with IWPT design issues, a dedicated prototype was specially built (section 2.9.1). The IWPT configuration was assembled using, as the primary, a flat spiral coil constituted of 27 turns of a 30x28AWG cable, formed of 30 individual conductors each of 0.32 mm in diameter, giving a total cross-section of about 2.43 mm^2, as shown in top view in Figure 73a. The coil, a COTS component normally used in induction ovens, has 6 radially distributed ferrite cores on the side that is not shown in the photo, to emulate a ferrite plane and reinforce the magnetic field. These ferrite cores increase the coil inductance from 78 μH to approximately 102 μH, allowing more power to be handled at the same current level.
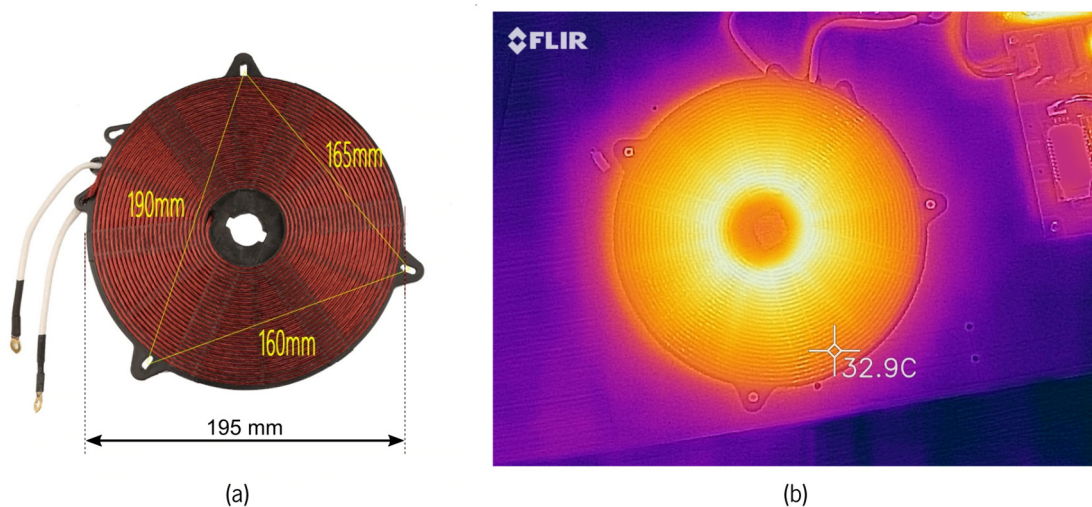
Figure 73: Proximity effect causing non uniform heating of an spiral coil.

Dynamic Inductive Wireless Power Transfer for Lightweight Electric Vehicles
Luiz Alberto Lisboa da Silva Cardoso – University of Minho

112

In Figure 73b, the same coil of Figure 73b is also photographed in top view by a FLIR One Pro thermal imaging camera, after some time the system had been energized with a current of approximately 5 A rms, at 60 kHz. The color transitions from yellow to violet indicate decreasing temperatures (yellow is hotter than orange). The temperature on the coil cable near the external turn can be read at 32.9°C. Not shown in in Figure 73b, the temperature close to the innermost turn of the coil, by similar process, was also measured, at 44.3°C. The ambient temperature during the experiment was 21.3°C.

The values of temperature rise above the ambient temperature, respectively calculated as 23°C and 11.3°C, when close to inner and outer rims of the coils, are approximately proportional to the linear power dissipation density at these points of the cable, when the assembly is in thermal equilibrium. So, the linear power dissipation density varies along the coil. Since the power dissipated is proportional to the resistance and the current traversing the coil and its cross-section are the same along all cable length, it can be concluded that the variation in the power density should be attributed to an apparent variation of the resistivity (Ω/m) of the coil along its length. In fact, the actual temperature elevation differences, as it is observed in the coloring of Figure 73b, would likely be even more pronounced if copper were not such a good heat conductor as well.

At the frequency used in the experiment (60 kHz), the skin depth in copper is approximately 0.27 mm, which is on the order of diameter of the individual conductors (0.32 mm) in the cable bundle that forms the coil winding. This guarantees that a highly pronounced skin effect is not present. However, as seen, although the net current is the same throughout the coil cable, the temperature visibly rises more on the center turns.

The results from a simplified FEM simulation of the magnetic field in the central plane of the coil is shown in Figure 74, considering, as a simplification, a single wire with the same equivalent total area of the cross-section. In this plot the black continuous curve indicates the value of the magnetic field amplitude inside the conductors, and the black dashed curves, outside. The pink shaded areas highlight the magnetic field plots within the innermost three turns and the outermost turn (27th turn), at 70 m away from the innermost (1st) turn. The red dashed curve is the envelope of the values of the magnetic field intensity at the inner limit of the conductors, and green dashed curve, similarly, is the outer limit. The blue curve with blue with blue shaded area is the envelope of the magnetic field intensity in the center of the cross-sections of each turn.

Dynamic Inductive Wireless Power Transfer for Lightweight Electric Vehicles
Luiz Alberto Lisboa da Silva Cardoso – University of Minho

113
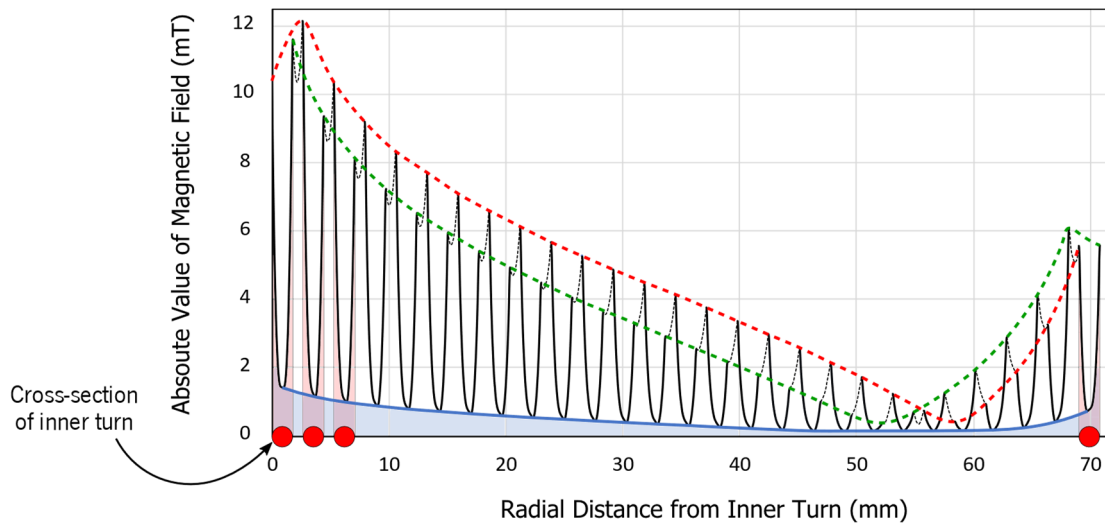
Figure 74: Magnetic field intensity along one radius at the central plane of the spiral coil.

It can be noticed that the amplitude of the magnetic field is much stronger on the periphery of the conductors than in the center, due to model simplification that enhances the skin effect, by considering a single conductor of 1.76 mm in diameter, instead of the bundle of 30 conductors of 0.32 mm diameter.

The plot in Figure 74 can be qualitatively compared with the temperature distribution suggested by the thermal image of the energized coil, resulting that, as general rule, the temperature is higher where the magnetic field intensity is also higher. This is observed at all radial distances, except close to the external turns, possibly due to the presence of the terminals of the coil, which, due to the thermic conductivity of copper, serve as a heatsink to the other turns, making the observed temperature on the last inner and outer coil decrease. Possibly because of that, the outer turn (27th) does not show a slightly higher temperature than the 23rd and 24th turns, which, according to this principle should be coldest. Other reasons for this minor deviation from the expected behavior may be that: (i) the magnetic field is even more intensified close to the center of the coil, where the extremities of the ferrite bars come closer to each other; (ii) the turns closer to the borders can dissipater better, because the temperature in their vicinity is lower than that in the middle of the coil; and (iii) the thermal camera coloring scheme is not adequate for distinguishing the small differences in temperature.

Overall, the results from the experiment are compatible with the hypothesis of the equivalent resistance per length of conductor being higher in the inner turns, where the magnetic field is stronger, as expected due to the proximity effect.

Dynamic Inductive Wireless Power Transfer for Lightweight Electric Vehicles
Luiz Alberto Lisboa da Silva Cardoso – University of Minho

114

2.10.2.2 Consequences of the Proximity Effect in Two Magnetically Coupled Coils

One of the subtle consequences of the proximity effect is that the linear model of a magnetic coupling, as represented in Figure 3, changes when the distance between the two coils is varied. The linearization can always be used as an approximation, but what happens is that the perceived value of the serial winding loss resistors R_1 and R_2 does not hold constant if the distance between the coils or, equivalently, if their mutual coupling is variated, even if the exciting frequency and currents are kept constant.

When two coils of the same time of that in Figure 73a are configured in parallel planes, aligned by their center axis, the experimentation can show that the linear model of the resulting magnetic coupling may exhibit strong variability in their parameters, according to the air-gap (distance between the coils), when both coils carry alternated current on the same fixed frequency.

The variation in the inductance can be easily understood and modeled, due to the presence of magnetic core on each of the coils. When the coils became sandwiched in between the equivalent ferrite planes of both coils, the self-inductance of each coil, as well as the mutual inductance is increased. As expected, when the distance between the coils is reduced and the ferrite planes of the coils come close together, the self and mutual magnetic fluxes, and all the associated inductance parameter are increased. This can be seen in the plots of Figure 75.
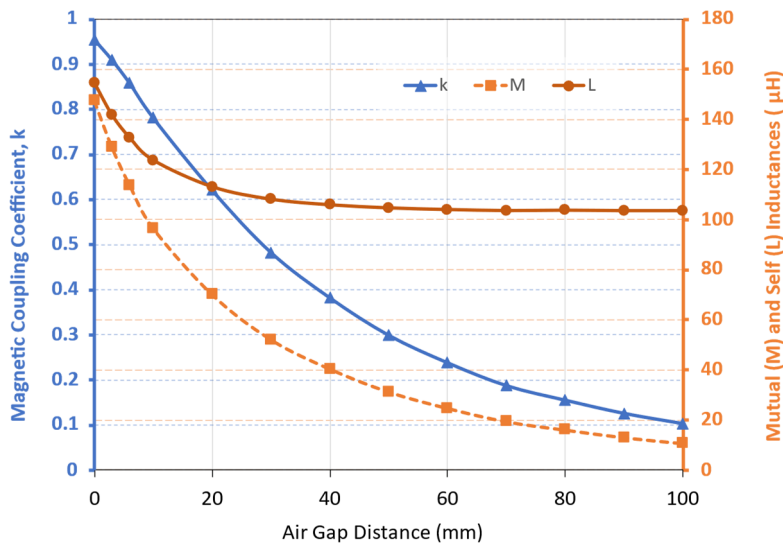
Figure 75: Experimental variation of self and mutual inductances of the magnetic coupling of two spiral coils.

In the experiment, the equal self-inductances were measured directly with Hioki's 3532-50 LCR HiTESTER. The mutual inductance was also evaluated with the same equipment, by measuring the serial connection of the coils in both the flux-additive configuration, which leads to

Dynamic Inductive Wireless Power Transfer for Lightweight Electric Vehicles
Luiz Alberto Lisboa da Silva Cardoso – University of Minho

115

the measurement of $2L + 2M$, and the flux-subtractive configuration, in which it is possible to directly measure $2L - 2M$.

The same measurements also give the serial resistance of each configuration, so it is possible plot, for each air-gap distance de values of serial resistance found for each of the equal coils in three different circumstances: (i) When there is no current in the other coil (open secondary); (ii) when in flux-additive (zero phase between coil currents), and (iii) when in flux-subtractive (currents in coils in opposite phases). The results are plot in Figure 29.
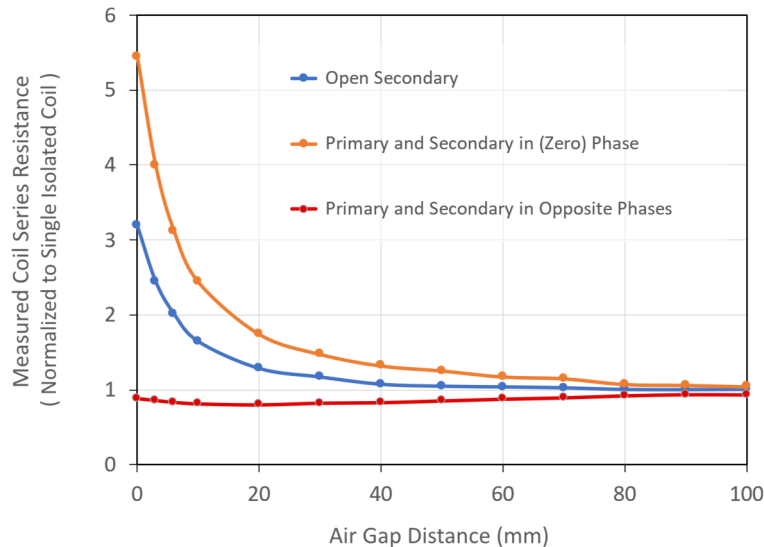
Figure 76: Experimental variation of serial resistance of spiral coils in magnetic coupling.

The curves in Figure 76 demonstrate that the series resistance in the model depend not only on the air-gap, but also on the relative phase of the current flowing in both coils. So, although it can be used as an proximation, the linear transform model (Figure 3), in real configurations, only holds for constant relative phase currents flowing in primary and secondary coils and constant air-gap. In the case of these flat spiral coils, this dependence, for many applications, is only relevant (>15% resistance difference for in phase and out of phase currents) when the magnetic coupling is larger than 0.15.

Transformers normally used in power applications have higher k values. However, they also normally have ferromagnetic cores and work with low frequencies. In these conditions, the extra losses due to the proximity effect are often dominated by core losses and low frequency resistive winding losses, and the proximity effect may go unnoticed. Since coils used in IWPT generally have high quality factors, this the anomality in the linear model will similarly not affect much the calculation of the induced voltage, as well as the transferred power. But it might affect estimations of the electrical efficiency, especially when the magnetic coupling coefficient is high.

Dynamic Inductive Wireless Power Transfer for Lightweight Electric Vehicles
Luiz Alberto Lisboa da Silva Cardoso – University of Minho

116

The proximity effect is also an important factor affecting the efficiency obtained by the use of litz wires, as well as it will influence the choice of the separation distance between neighbor turns in the design of a coil, that is, the "pitch" of the coil winding. A closed analytical form for computing this effect is not simple to derive, in a general case. In litz cabling, approximations can be used as a design tool [69].

As conclusion, it can be predicted that either in litz wire, or in WPT configurations with magnetic couplings of high k, whenever more precise estimations are required in a design, finite element model simulations will be the preferred approach to provide a reliable numerical solution.

2.11 EMF Exposure Control

Electromagnetic fields can produce hazardous effects on living biological tissues, particularly on human beings. So, the control the EMF exposure levels is a major concern in the design of all apparatus that people can be in contact with, including transportation systems [70]. Although current studies are not conclusive about all possible consequences of intense electromagnetic fields on health, the experience obtained so far has been studied since 1992 by the International Commission on Non-Ionizing Radiation Protection (ICNIRP), an institution that sporadically publishes reports and recommendations concerning maximum safe human exposure levels to EMF. ICNIRP succeed in that mission the International Non-Ionizing Radiation Committee of the International Radiation Protection Association IRPA/INIRC, created in in 1977 and who started publishing similar reports early in 1988 [71]. The first ICNIRP design guide recommending maximum acceptable exposure levels covering the entire frequency range of time-varying EMF (up to 300 GHz) was only established in 1998 [71]. An updated design recommendation document was then issued in 2010 and became largely accepted by engineering community as a design guideline and conformity check rule, establishing maximum refence levels for EMF exposure by range of frequencies and type of exposure, that can be either occupational or intended for the general public [72].

According to the ICNIRP-2010 document, occupational exposures occur under subjectively described circumstances where adults, "with appropriate advice and training, it is reasonable for workers voluntarily and knowingly to experience transient effects...," effects which "are not believed to result in long-term or pathological health effects." In the document, it is still enforced that, at these maximum exposure levels, simultaneous exposure to all parts of the body should be limited.

Dynamic Inductive Wireless Power Transfer for Lightweight Electric Vehicles
Luiz Alberto Lisboa da Silva Cardoso – University of Minho

117

In near-field applications, such as the non-radiating oscillating magnetic fields involved in the implementation of Inductive Power Transfer, using frequencies up to 10 MHz, these recommended maximum field strengths for occupational exposure can be summarized by the frequency-parametrized limits given in Table 8.

Table 8: ICNIRP-2010 RMS reference levels for occupational exposure to time-varying EMF.

Frequency range	E-field strength (kV/m)	Magnetic field strength (A/m)	Magnetic flux density (T)
1 Hz–8 Hz	20	$1.63 \times 10^5/f^2$	$0.2/f^2$
8 Hz–25 Hz	20	$2 \times 10^4/f$	$2.5 \times 10^{-2}/f$
25 Hz–300 Hz	$5 \times 10^2/f$	8×10^2	1×10^{-3}
300 Hz–3 kHz	$5 \times 10^2/f$	$2.4 \times 10^5/f$	$0.3/f$
3 kHz–10 MHz	1.7×10^{-1}	80	1×10^{-4}

The limits on EMF strength for general public exposure limits are such that they are always less than or equal to those established for occupational exposure at any given frequency, as shown in Table 9 and, based on current scientific knowledge, are supposedly capable of assuring that no short or long term compromise in observed the health individuals. These limits, mentioned in the ICNIRP guides as reference values, actually changed from the 1998 edition[71] to the 2010 edition [72], reflecting better understanding of EMF risks. For some frequency bands, the limits were increased, in some others, they were reduced.

Table 9: ICNIRP-2010 RMS reference levels for general public exposure to time-varying EMF.

Frequency range	E-field strength (kV/m)	Magnetic field strength (A/m)	Magnetic flux density (T)
1 Hz–8 Hz	5	$3.2 \times 10^4/f^2$	$4 \times 10^{-2}/f^2f$
8 Hz–25 Hz	5	$4 \times 10^3/f$	$5 \times 10^{-3}/f$
25 Hz–50 Hz	5	1.6×10^2	2×10^{-4}
50 Hz–400 Hz	$2.5 \times 10^2/f$	1.6×10^2	2×10^{-4}
400 Hz–3 kHz	$2.5 \times 10^2/f$	$6.4 \times 10^4/f$	$8 \times 10^{-2}/f$
3 kHz–10 MHz	8.3×10^{-2}	21	2.7×10^{-5}

An update to [71] was issued by ICNIRP in 2020 [17], reflecting newer recommended limits and design approach in the 100 kHz to 300 GHz band. For instance, in this latter recommendation the general public maximum exposure levels are explicitly divided in whole-body exposure and

Dynamic Inductive Wireless Power Transfer for Lightweight Electric Vehicles
Luiz Alberto Lisboa da Silva Cardoso – University of Minho

118

local exposure, for short duration or longer duration exposures ($\geq$ 6 min), as shown in Figure 77. However, these new recommendations did not affect the former recommendations for frequencies lower than 100 kHz.

General Public
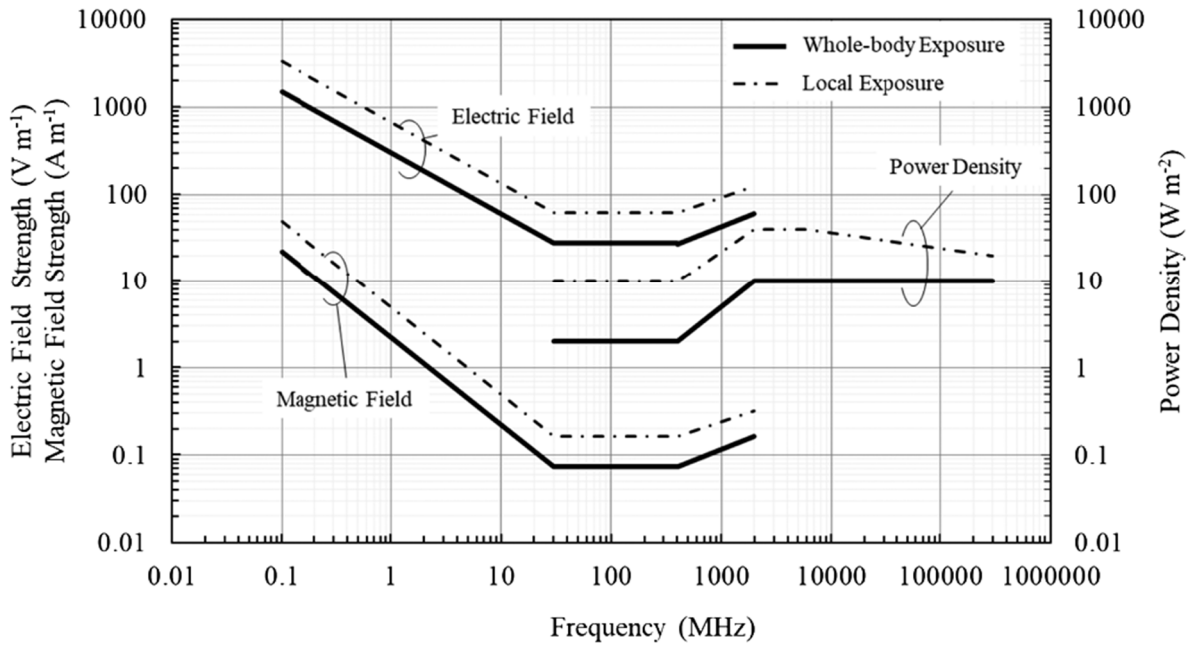
Figure 77: New EMF limit recommendations for exposures longer than 6 minutes (figure extracted from ICNIRP, "Guidelines for Limiting Exposure to Electromagnetic Fields (100 kHz to 300 GHz)," Health Phys., vol. 118, no. 5, pp. 483–524, 2020.

Concerning IWPT design for LEV, practical magnetic resonance frequencies will typically range in the 20 kHz to 100 kHz sub-band, due to current economic and technological issues. But, for this frequency band, no major change was introduced by [17]. Therefore, when considering the use of coil antennas that are very short (non-radiating) relatively to wavelength of the exciting current in the primary coil, and frequencies up to 100 kHz, the ICNIRP current recommendations can be reduced to the limits expressed in Table 10.

Table 10: Maximum ICNIRP recommended EMF maximum RMS exposure levels to non-radiating magnetic fields involved in the implementation of IPT in the 3 kHz to 100 kHz band. Values are rms.

	General public exposure ☺	Occupational exposure 😐
Maximum electrical field strength	83 V/m	170 V/m
Maximum magnetic flux density	27 µT	100 µT

Dynamic Inductive Wireless Power Transfer for Lightweight Electric Vehicles
Luiz Alberto Lisboa da Silva Cardoso – University of Minho

119

In automotive and general transport application, both passengers and pedestrians should be considered in the general public class, so the actual limits to be observed for the electric and magnetic field are respectively 83 V rms/m and 27 μT rms. So, in any design, within the spaces and zones that are prone to be accessed by humans, the field intensities should be lower than these limits.

In spite of its importance, this research focuses on conceptual design validation of power transfer and does not include EMF compliance verification.

Even then, design paradigms were adopted to ensure pedestrian a priori protection by design, by limiting the minimum distance (lane width) from the primary coils to the pedestrians, assumedly outside de inductive lanes. Concerning the rider protection, although some general preventive measures were also adopted, a general approach for EMF exposure control design, including shielding design, was left outside the scope of these work, and left as future research. This is due both to the amount of effort involved and the requirement of specialized equipment for EMF verification, not available at the time of prototype development.

2.12 Power Grid Impact

Different classes of power grid integration problems may arise, and must be a priori considered in the design of an IWPT system, examples of these problems are:

(i)   Electric noise can cause mutual interference, i.e., noise on the grid can affect system operation and, reciprocally, system operation can cause noise on grid, and disturb normal operation of other equipment in the vicinity of the system;

(ii)   System reactive impedance or unbalanced consumption per phase can disturb the overall balance of the grid, being inconvenient for grid stability and economy.

(iii)   The circuits driving the primary coils can spoil the grid power quality, if these circuits exhibit strong non-linear behavior.

(iv)   The total electric demand of long i-lane sections cannot exceed the local grid capacity at any point of integration along the section.

Grid impact should be specifically considered in the design of power inverters that will induce high frequency current in primary coils on the lane side, being important issue to address in high quality commercial DIWPT systems. This problem will be expectedly more pronounced in DIWPT

Dynamic Inductive Wireless Power Transfer for Lightweight Electric Vehicles
Luiz Alberto Lisboa da Silva Cardoso – University of Minho

120

systems deployed to support standard heavy EV than those for lightweight EV, where the required power levels per vehicle and per length of deployed lane is lower. There are standard design blocks that have been successfully applied in this situation [73], however, this design effort was intentionally left out the scope of this thesis research work.

2.13 Conclusion

In this Chapter, some of the most important aspects of the IWPT design were reviewed. IWPT circuits can be implemented with simple circuits and compensation topologies involving a minimum number of components. The different compensation circuits have different characteristics, but share some general common predictors, such as the maximum efficiency in the power transfer at the natural resonant frequency. The stationary and dynamic IWPT configurations can both be driven by resonant or auto-resonant circuits.

The Mazzilli Baxandall auto-resonant inverter is one of the simplest circuits available that can be used to drive primary coils in a DIWPT systems. Despite its simplicity, it automatically keeps constant the voltage across the terminals of the primary coil, independently of the load attached to the secondary coil. In DIWPT configurations where the magnetic coupling coefficient is expected to be very low, such as those using oblong coils, the current back-induced in the primary tends to be low as well. Since the back-induced current is orthogonal to the driver generated current, the variation caused in the primary current due to load variations is even lower. In summary, this makes the resulting primary current approximately constant as well, as the load is varied, what greatly simplifies the design.

The mathematics and the analysis of an IWPT design is well known, but it can be subtle. For any well characterized configuration, it is possible to accurately predict the resulting efficiency and power transfer levels. However, due to multi-disciplinary considerations and the large number of free variables involved, the inverted problem can be hard to solve: How to establish the dimensions, geometry, materials and excitation of a configuration and accomplish the detailed design of a magnetic link to satisfy some given WPT transfer requirement, specially, in a DIWPT application.

This process may turn surprisingly laborious, considering the small number of main components required for its implementation, and several simplifications must be adopted. This is one of the main points of this work, which is preliminarily studied in Chapter 3 and fully developed in Chapter 5. Due to effort limitations established for the thesis work, some crucial aspects of the

Dynamic Inductive Wireless Power Transfer for Lightweight Electric Vehicles
Luiz Alberto Lisboa da Silva Cardoso – University of Minho

121

design, other than purely the transfer and the control of power, are intentionally not covered. In particular, the shielding design on the vehicle's side and the experimental verification of the full compliance to recommended EMF exposure limits have their own complexity, and are left out of the scope of an initial concept validation of the HIPLEV, as introduced in Chapter 4.

Dynamic Inductive Wireless Power Transfer for Lightweight Electric Vehicles
Luiz Alberto Lisboa da Silva Cardoso – University of Minho

122

Chapter 3

Dynamic Inductive Wireless Power Transfer

In Chapter 2 the main theorical aspects of Inductive Wireless Power Transfer (IWPT) were presented, considering that the relative position of the secondary coil involved in the power transfer is fixed, relatively to the primary coil, which is the so called stationary case. In the present chapter, the design principles of Dynamic Inductive Wireless Power Transfer (DIWPT) and its ongoing development are the focus. Here, the term "dynamic" refers to the condition that power transfer is assumed to happen at nominal average power levels, on the contrary of the stationary case, while there is relative movement between a secondary coil set and a primary coil set. Firstly idealized by the end of the nineteenth century, DIWPT was then motivated by the new electric trams that started to appear at that time [74][75]. In these applications, electric energy had to be transferred from current-carrying wires, attached to ground-fixed structures, to the power train of an EV, along its self-propelled displacement, so, inductive means were envisioned to avoid the wear out in between galvanic contacts due to friction. However, as exposed in section 3.2, these early designs did not result in readily available commercial technology.

Despite of DIWPT was initially thought of for vehicles running on tracks, a major part of current research and development efforts comprises road applications, with the ultimate goal that the onboard energy storage requirements can be reduced and, simultaneously, the autonomy of EV can be extended. The technology has been so far exploited in industrial and robotics application cases [76], where it may be even possible that the need for long term energy storage on the vehicle or robot is entirely suppressed. Other applications, not related to transportation, such as implantable or wearable [77] WPT-powered devices, may also fit in the DIWPT scope.

Many DIWPT concepts and prototypes targeting electric mobility have been developed its conception in the late 19th century, to a point that the technology is about to become commercially available, at least for road use: In the current year, 2020, a pilot deployment of a DIWPT system with a total electrified road section of 1.6 km, the longest so far built, shall be commissioned to link by heavy traffic the airport of Visby, Sweden, to the center of that city [78] [79]. But there are still a lot of possibilities to be used and issues to be overcome, the future of DIWPT being still uncertain.

Dynamic Inductive Wireless Power Transfer for Lightweight Electric Vehicles
Luiz Alberto Lisboa da Silva Cardoso – University of Minho

123

Along this chapter, after a brief introduction to the conceptual elements and terminology involved in DIWPT design and implementation, a short review of some milestones in the development of this technology is provided. Next, the principal design aspects addressed in previously implemented prototypes and the choices of DWIPT system parameters are discussed. Finally, some representative state-of-the-art projects and prototypes are reported, pointing to the development trends in the area, in preparation to the presentation of new possible perspectives for DIWPT transportation applications and instrumentation, introduced in chapters 4, 5, and 6, which consist in the main contribution of this work.

3.1   Stationary versus Dynamic Inductive WPT

In Dynamic Inductive Wireless Power Transfer (DIWPT) applications, a nominal average power must be transferred in between primary and secondary coils while they are in relative movement to each other. For the analysis of both stationary and dynamic WPT applications, complete theoretical support was provided in 1861 by Maxwell's Theory of Electromagnetism and equations [80],[81], as popularized in Heaviside's vector notation in 1894 [82], which consistently and precisely model all purely electromagnetic macroscopic terrestrial phenomena so far observed [83]. Although the covariant form of Maxwell equations appears to hold experimentally, even under the physical circumstances where the special theory of relativity has to be considered, the analysis of DIWPT in terrestrial transportation applications, as a low speed, low acceleration, low energy phenomenon, does not require relativistic approach. The only possibly subtle exception to that is the implicit consideration of the existence of the magnetic field itself, which can be shown to strictly related to the electric field (and vice-versa), as consequence of the relative movement of electrically charged bodies [84]. Because of that, throughout this work, no explicit consideration of the principle of relativity is made.

The voltage induced in a receiving coil is the time derivative of the total magnetic flux crossing that coil. It will depend not only on the variation of the magnetic flux due to the time-varying activity of the entities that source the magnetic field density vector field B causing the magnetic flux, but also, on the variation of the flux caused by the displacement of that coil in space, unless the magnetic field is invariant in space, in the reference frame of the coil. Therefore, in general, the voltage induced in a moving coil, $V^D(t)$, will be potentially different from the voltage $V^0(t)$ induced on the same coil, by the same magnetic field B, if the coil were stationary (velocity $v = 0$) with respect to all the sources creating the magnetic field B, as illustrated in Figure 78.

Dynamic Inductive Wireless Power Transfer for Lightweight Electric Vehicles
Luiz Alberto Lisboa da Silva Cardoso – University of Minho

124

(a) Stationary induction case.
(b) Dynamic induction case.
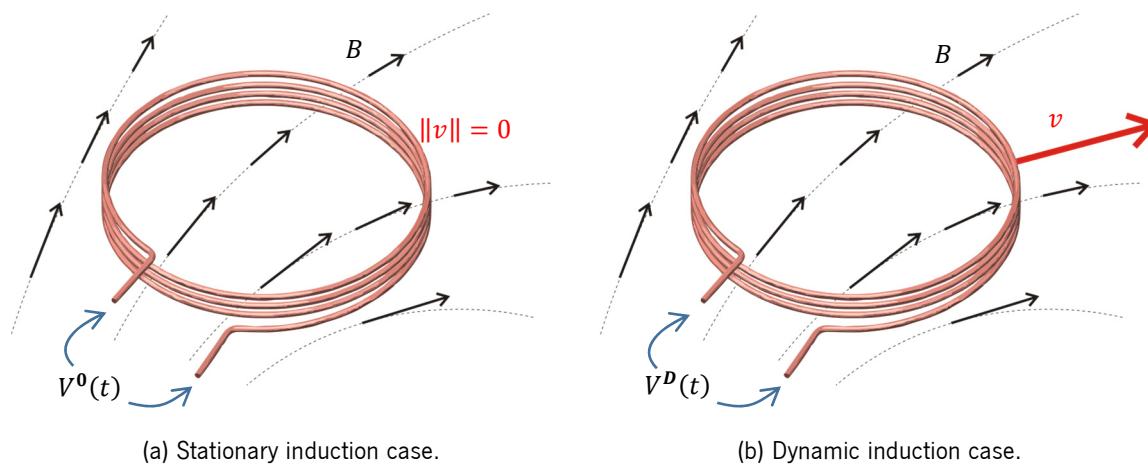
Figure 78. Voltage induced on a coil subjected to the same magnetic field in stationary and dynamic conditions.

The magnetic field will be invariant in space, in the reference frame of the coil, thus resulting in equal voltages $V^0(t)$ and $V^D(t)$, when all entities generating the vector field B keep their relative position to the coil. That is, when these sources move (and rotate) solidary to the coil in its reference frame. Intuitively, the magnetic field is expected to be approximately invariant in the coil space, causing these two induced voltages to be approximately equal, when either the sources of magnetic field are very far from the coil or, equivalently, when the dimensions of the coil are very small, with respect to the coil speed, and the coil is keeping the angular orientation relative to the (average) local magnetic field, that is, it is not rotating.

However, as it will be shown in the next section, for most electric mobility application cases, the commonly high range of induction frequencies used in inductive WPT and the relatively low speed of vehicles with respect to the wireless transfer ground structures, making it possible to approximate $V^D(t)$ by $V^0(t)$. For this reason, in most cases, a DIWPT system powering an EV can be designed or analyzed as a quasi-stationary WPT, that is, considering that the power transfer to a vehicle can be calculated and averaged as if the WPT between lane coils and the vehicle's pick-up coil would happen with the EV at rest at each point along all of its path.

3.1.1 Dynamically Induced Voltage

Let us assume that a primary coil consists of a wire loop that can be modeled as a closed continuously curve K that is continuously differentiable at all except a finite number of points - what is always a reasonable assumption for thin conductive wire loops that are composed of a finite number of "smooth" curved wire segments. If K displaced in a region G of the three-dimensional Euclidean space where there is a time-varying magnetic flux vector field B, then the integral of the time-varying electric vector field E on the closed path K is well defined and,

Dynamic Inductive Wireless Power Transfer for Lightweight Electric Vehicles
Luiz Alberto Lisboa da Silva Cardoso – University of Minho

125

according to the Maxwell-Faraday equation, the dynamically induced voltage V_K^D on the wire loop can be expressed as:

$$V_K^D(t) = \oint_K E.dK = -\frac{d\Phi_S}{dt} = -\frac{d}{dt}\int_S B.dS,$$ (3.1)

where S is any orientable surface delimited by the curve K, such that $K = \partial S$. This expression was experimentally found truth and holds independently of the sources of the magnetic field B, which can be permanent magnets, other loops with variable current along the path of the wire, either fixed or moving in G, or an arbitrary combination of them. A geometrical view of this modeling of the wire loop moving in the magnetic field is shown in Figure 79, where two different states of the wire loop, at times t and $t + \Delta t$ are represented.
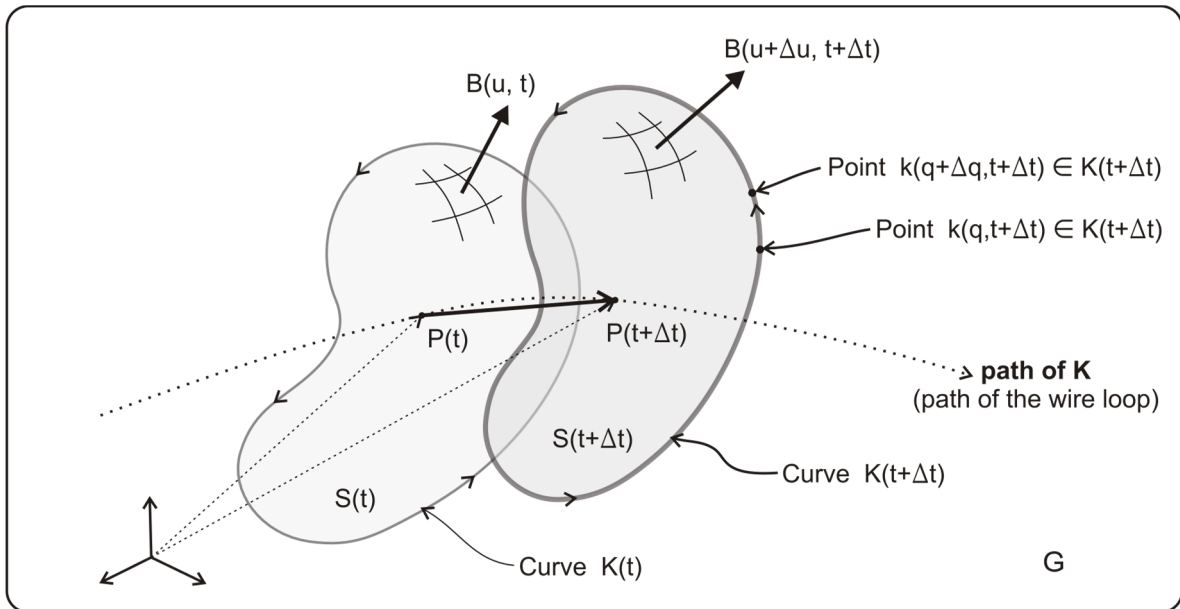
Figure 79: Modeling the displacement of a wire loop in a magnetic flux vector field.

At each time t, the wire loop, has its centroid at $P(t) \in G$, and defines the position of curve $K(t)$, for which a surface $S(t)$ is considered. The total magnetic flux, due to B, crossing the oriented surface S, given by Φ_S, is also a function of the time and the point $P(t)$ where the primary coil is located, and does not depend on the actual surface S, but rather on the contour curve K of S.

The time derivative of the flux of a vector field through a moving element of area, as expressed in (3.1), can be calculated by applying a two-dimensional variant of the Leibniz Integral Rule theorem [85], which is also presented in a more general form in [86], resulting in the expression:

Dynamic Inductive Wireless Power Transfer for Lightweight Electric Vehicles
Luiz Alberto Lisboa da Silva Cardoso – University of Minho

126

$$V_K^D(t) = -\int_S \frac{\partial B}{\partial t}.dS + \oint_K (v \times B).dK - \int_S (\nabla.B)v.dS \qquad (3.2)$$

However, according to Maxwell-Gauss equation, $\nabla.B = 0$, and then (3.2) becomes:

$$V_K^D(t) = -\int_S \frac{\partial B}{\partial t}.dS + \oint_K (v \times B).dK, \qquad (3.3)$$

which is also given in [87]. The first term of the right side of equation (3.3) can be promptly identified as the voltage V_K^0 induced on the wire loop as if B would depend only on t, that is, as if the wire loop $K(t)$ were permanently "at rest" (stationary) at position $P(t)$:

$$V_K^0(t) = -\int_S \frac{\partial B}{\partial t}.dS, \qquad (3.4)$$

so, (3.3) can be re-written as:

$$V_K^D(t) = V_K^0(t) + \oint_{K(t)} (v \times B).dK, \qquad (3.5)$$

The second term on the right, in expressions (3.3) and (3.5), which can be named $V_K^v(t)$, is a component of the induced voltage that simultaneously depends on both the velocity field v of the wire loop and on the magnetic field B at time t along the curve $K(t)$, so it can be writen:

$$V_K^D(t) = V_K^0(t) + V_K^v(t) \qquad (3.6)$$

This new component $V_K^v(t)$ is not observed when the wire loop is stationary in G, and it does not directly depend on the time-varying pattern of the magnetic field B, but rather on the instantaneous spatial distribution of B at time t, as if it were a constant field in time with the incidental value B_t.

Noticeably, the assumptions made on the curve $K(t)$ are general enough not to restrict the validity of (3.6) if the wire loop is accelerating, rotating, bending, expanding or contracting, or even changing its shape with time, as long as these changes are "smooth", and there is always a surface comprised by $K(t)$ that remains orientable. In order to enhance the intuitive perception of this movement-dependent term of the induced voltage, and how it will affect DIWPT analysis and design, a few special cases are considered in the following sections.

Dynamic Inductive Wireless Power Transfer for Lightweight Electric Vehicles
Luiz Alberto Lisboa da Silva Cardoso – University of Minho

127

3.1.1.1 Dynamically induced voltage due to DC components of the magnetic field

A time-invariant component B_{DC} of B, such that:

$$B(u, t) = B_{DC}(u) + B_{AC}(u, t), \tag{3.7}$$

will have no effect in the "stationary" term $V_K^0(t)$, for $\partial B / \partial t = \partial B_{AC} / \partial t$. But it will cause the "dynamically" induced component $V_K^v(t)$ of $V_K^D(t)$, in (3.6), to split in two potentially non-zero terms, $V_K^{v,B_{DC}}(t)$ and $V_K^{v,B_{AC}}(t)$, which will depend on the joint pattern of velocity field v and the magnetic field B itself, as derived from (3.5):

$$V_K^D(t) = V_K^0(t) + \oint_{K(t)} (v \times B_{DC}). dK + \oint_{K(t)} (v \times B_{AC}). dK, \tag{3.8}$$

or equivalently:

$$V_K^D(t) = V_K^0(t) + V_K^{v,B_{DC}}(t) + V_K^{v,B_{AC}}(t), \tag{3.9}$$

where:

$$V_K^{v,B_{DC}}(t) = \oint_{K(t)} (v \times B_{BC}). dK \tag{3.10}$$

and

$$V_K^{v,B_{AC}}(t) = \oint_{K(t)} (v \times B_{AC}). dK \tag{3.11}$$

B_{DC} can be regarded as the component of vector field B that could result, for instance, from a mix of stationary permanent magnets and primary loops of constant current placed along the path of the wire loop given by $K(t)$. B_{AC}, on the other hand, is the time-varying component, and could be the net result of moving magnets and time-varying currents in primary loops placed in the neighborhood of the moving wire loop under consideration, which, in this case, plays the role of a secondary coil.

If the vector field v is such that the cross product $v \times B_{DC}$ is constant along $K(t)$, then the term of the induced voltage on the wire loop due to B_{DC} is zero, because the integral of the oriented differential elements dK over curve K is also zero:

Dynamic Inductive Wireless Power Transfer for Lightweight Electric Vehicles
Luiz Alberto Lisboa da Silva Cardoso – University of Minho

128

$$V_K^{v,B_{DC}}(t) = \oint_{K(t)} (v \times B_{DC}).\,dK = (v \times B_{DC}).\left[\oint_{K(t)} dK\right] = 0 \qquad (3.12)$$

One particular case, in which $v \times B_{DC}$ is constant, resulting in $V_K^{v,B_{DC}}(t) = 0$, as anticipated in section 3.1, is when both v and B_{DC} are spatially invariant, corresponding to the situation of a rigid wire loop travelling on either a solidary or a hypothetically uniform magnetic field, a configuration where it is also experimentally observed no induced voltage on the wire loop. Worthwhile mention, even for a rigid body, the velocity vector field v is not necessarily constant along K, when the centroid $P(t)$ of $K(t)$ is moving with constant velocity v_K: If the wire loop defined by $K(t)$ is spinning, the velocity vector v on the points of $K(t)$ will be dispersed around the average velocity v_K of the wire loop, what will potentially cause a non-zero induced voltage, even while moving in a constant, uniform magnetic field.

3.1.1.2 Dynamically induced voltage on a spinning wire loop moving in space

Let us consider that the wire loop given by $K(t)$ is spinning with angular frequency $\omega \neq 0$ around its centroid at position $P(t)$, while it moves (translation) in G with velocity v_K. If at some initial time t_0 the centroid is at position $P_0 = P(t_0)$, then the centroid position in given by:

$$P(t) = P_0 + \int_{t_0}^{t} v_K \; dt, \qquad (3.13)$$

Recognizing $K(t)$ as the image of a joint function k of the time t and of an independent parameter $q \in \mathbb{R}$, with k continuous, and differentiable in all points where the corresponding point in $K(t)$ is also differentiable, it is possible to write that:

$$K(t) = \{k(q,t) \in \mathbb{R}^3 \mid q \in Q = [q_1, q_2] \subset \mathbb{R}\} \qquad (3.14)$$

where, at any time t, $k(q_1, t) = k(q_2, t)$, for $K(t)$ is a closed path. Then, the point $k(q,t)$ can be expressed by its relative position r with respect to P, such that:

$$k(q,t) = P(t) + r(q,t), \qquad (3.15)$$

Using (3.13), and the expression (3.15) becomes:

$$k(q,t) = P_0 + \int_{t_0}^{t} v_K \; dt + r(q,t), \qquad (3.16)$$

Dynamic Inductive Wireless Power Transfer for Lightweight Electric Vehicles
Luiz Alberto Lisboa da Silva Cardoso – University of Minho

129

from where the velocity v is given by:

$$v = \frac{dk(u,t)}{dt} = v_K + \frac{\partial r(q,t)}{\partial t} + \frac{\partial r(q,t)}{\partial q} \cdot \frac{\partial q}{\partial t} \qquad (3.17)$$

Because the parametric variable q, that generates $K(t)$, is independent of time t, $\partial q / \partial t = 0$, then (3.17) is simply:

$$v = v_K + \frac{\partial r(q,t)}{\partial t} \qquad (3.18)$$

In addition, because the loop is spinning about $P(t)$ with angular velocity vector ω, $\partial r(q,t)/\partial t$ is the radial velocity with respect to $P(t)$, which can be expressed by the cross-product of ω and $r(q,t)$:

$$\frac{\partial r(q,t)}{\partial t} = \omega \times r(q,t) \qquad (3.19)$$

Then substituting (3.19) in (3.17), the velocity field on the point $k(q,t)$ of $K(t)$:

$$v(q,t) = v_0 + \omega \times r(q,t) \qquad (3.20)$$

Because $K(t)$ and the relative position vectors $r(q,t)$ are spinning together and being measured in the same reference frame of vector fields B and v, it is possible to abstract the specific time t and the specific point of $K(t)$ associated with parameter $q \in Q$, and simply denote the velocity vector field as:

$$v = v_K + \omega \times r \qquad (3.21)$$

Finally, substituting (3.21) in (3.5), an expression for computing the dynamically induced voltage on a loop that spins around (its centroid) $P(t)$, which is moving with velocity v_K on an arbitrary time-varying vector field B is given by:

$$V_K^D(t) = V_K^0(t) + \oint_{K(t)} (v_K \times B).\,dK + \oint_{K(t)} \left((\omega \times r) \times B \right).\,dK, \qquad (3.22)$$

Now noticing that:

Dynamic Inductive Wireless Power Transfer for Lightweight Electric Vehicles
Luiz Alberto Lisboa da Silva Cardoso – University of Minho

130

$$V_K^{v_K,B}(t) = \oint_{K(t)} (v_K \times B). \, dK,$$
(3.23)

and naming:

$$V_K^{\omega,B}(t) = \oint_{K(t)} ((\omega \times r) \times B). \, dK,$$
(3.24)

it is possible to write:

$$V_K^D(t) = V_K^0(t) + V_K^{v_K,B}(t) + V_K^{\omega,B}(t)$$
(3.25)

The dynamically induced voltage on the wire loop at instant t_1, $V_K^D(t_1)$, is then the sum of three terms:

(i)   The first term, $V_K^0(t_1)$, is the induced voltage on the wire loop as if it were stationary at the position $P(t_1)$, with no angular rotation, under the effect of the time-varying magnetic field B.

(ii)   The second term, $V_K^{v_K,B}(t_1)$, is the voltage that would be induced on the wire loop if it were passing with constant velocity v_K at the point $P(t_1)$, without spinning, but with the same spatial orientation it would have at time t_1 due to the spinning movement given by ω, travelling on a time-invariant magnetic field $B(t_1)$.

(iii)   The third term, $V_K^{\omega,B}(t_1)$, corresponds to the voltage that would be induced on the same wire loop if it were spinning with angular velocity ω fixed at position $P(t_1)$, while surrounded by a time-invariant magnetic field $B(t_1)$.

This physical interpretation of (3.25) requires some abstraction, since all voltages V_K^0, $V_K^{v_K,B}$ and $V_K^{\omega,B}$ are all functions of the time themselves, but the expression provides a tool for the computation of the dynamically induced voltage $V_K^D(t)$.

It is still possible to consider (3.7) again and write that:

$$V_K^{v_K,B}(t) = V_K^{v_K,B_{DC}}(t) + V_K^{v_K,B_{AC}}(t)$$
(3.26)

and

Dynamic Inductive Wireless Power Transfer for Lightweight Electric Vehicles
Luiz Alberto Lisboa da Silva Cardoso – University of Minho

131

$$V_K^{\omega,B}(t) = V_K^{\omega,B_{DC}}(t) + V_K^{\omega,B_{AC}}(t) \tag{3.27}$$

further breaking (3.25) into:

$$V_K^D(t) = V_K^0(t) + V_K^{v_K,B_{DC}}(t) + V_K^{v_K,B_{AC}}(t) + V_K^{\omega,B_{DC}}(t) + V_K^{\omega,B_{AC}}(t) \tag{3.28}$$

The voltage component associated with the effect of the spinning movement in the time-invariant magnetic field B_{DC}, $V_K^{\omega,B_{DC}}(t)$, for instance, is the prevalent term in rotative generators, mostly used for grid and off-grid higher power level generation, while $V_K^{v_K,B_{DC}}(t)$ is the prevalent term in linear generators used in some energy harvesting devices, as in [88],[89]. The first term of the dynamically induced voltage, $V_K^0(t)$, on the other hand, is the only relevant term in stationary inductive WPT applications, in which the relative position of the secondary coil is fixed with respect to the primary coils that produces the magnetic field B.

3.1.1.3 Case of a non-spinning coil not subjected to an external DC magnetic field

In a typical DIWPT configuration for electric mobility applications, the secondary coil, as given by the curve $K(t)$, can be assumed to be a rigid body that is neither spinning nor making turns of significant magnitude along its path, and that implies an equivalent angular velocity of the secondary coil that can be neglected ($\omega \cong 0$), and thus, the term $V_K^{\omega,B}(t)$ will be approximately zero in (3.25).

In the same way, considering that no permanent magnets or primary coils carrying constant currents are normally, by design, placed along the path of an EV (and the secondary coil), it can be assumed that no external DC magnetic field component will act on $K(t)$, so $V_K^{v_K,B_{DC}}(t) = 0$.

Under the above conditions, the dynamically induced voltage on secondary coil on-board of an EV, $V_K^D(t)$, can be expressed as:

$$V_K^D(t) \cong V_K^0(t) + V_K^{v_K,B_{AC}}(t) \tag{3.29}$$

3.1.2 Dynamically Induced Voltage under Sinusoidal Sources

The dynamically induced voltage given by expression (3.22), or even that in the simplified case of non-spinning coils not subjected to DC magnetic fields, as in (3.29), may be difficult to calculate in a general case, due to the interaction of the velocity vector with the magnetic field

Dynamic Inductive Wireless Power Transfer for Lightweight Electric Vehicles
Luiz Alberto Lisboa da Silva Cardoso – University of Minho

132

vector in the integrands of these expressions. But some few extra considerations, commonly found in real-world electric mobility applications of DIWPT, can lead to the possibility of simplifying the calculation of the dynamically induced voltage. In fact, in many circumstances it will be shown that it is even possible to neglect the terms of the induction voltage due to the relative movement of the coils, allowing the approximation of $V_K^D(t)$ by $V_K^0(t)$ only, as if the moving coil were at rest in all points of its trajectory.

So, in the case of a non-spinning coil that moves at constant velocity v_K and is not subjected to a DC magnetic field component, let us further assume that the time-varying magnetic vector field B_{AC} has a periodic sinusoidal dependence on time t, with frequency f_0, being expressed as:

$$B_{AC}(p,t) = B_G(p)\,cos(2\pi f_0 t + \theta_0)\,, \qquad p \in G \tag{3.30}$$

where the vector field B_G is not time-dependent. Without loss of generality, let us also assume that the phase $\theta_0 = 0$; then, expanding (3.4):

$$V_K^0(t) = -\int_S \frac{\partial B_{AC}}{\partial t}.dS = 2\pi f_0\,sin(2\pi f_0 t)\int_S B_G.dS \tag{3.31}$$

and expanding (3.5):

$$V_K^{v_K,B_{AC}}(t) = \oint_{K(t)} (v_K \times [B_G\,cos(2\pi f_0 t)]).dK$$

$$= cos(2\pi f_0 t)\oint_{K(t)} (v_K \times B_G).dK$$

$$= \|v_K\|\,cos(2\pi f_0 t)\oint_{K(t)} (1_{v_K} \times B_G).dK, \tag{3.32}$$

where 1_{v_K} is the unity vector with the same orientation of the velocity v_K.

By applying Stoke's theorem to (3.32), it follows that:

$$V_K^{v_K,B_{AC}}(t) = cos(2\pi f_0 t)\int_S \nabla \times (v_K \times B_G).dS, \tag{3.33}$$

where the integrand $\nabla \times (v_K \times B_G)$ can be expanded as:

$$\nabla \times (v_K \times B_G) = v_K(\nabla.B_G) - B_G(\nabla.v_K) + (B_G\,.\nabla)v_K - (v_K\,.\nabla)\,B_G \tag{3.34}$$

Dynamic Inductive Wireless Power Transfer for Lightweight Electric Vehicles
Luiz Alberto Lisboa da Silva Cardoso – University of Minho

133

In (3.34), the first term in null because $\nabla . B_G$ is null according to the Maxwell-Gauss equation for magnetism, and $\nabla . v_K$ is null by hypothesis (the velocity v_K is constant in space). It can also be noticed that for vector fields x and y, $(x . \nabla)y$ is the Jacobian of y, J_y, applied to x; so:

$$(v_K . \nabla)\, B_G = J_{B_G}(v_K) = \|v_K\|\, J_{B_G}(1_{v_K}) \tag{3.35}$$

$$(B_G . \nabla)v_K = J_{v_K}(B_G) \tag{3.36}$$

Again, because v_K is constant, $J_{v_K}(B_G) = 0$, then (3.34) becomes:

$$V_K^{v_K, B_{AC}}(t) \;=\; -\|v_K\|\, cos(2\pi f_0 t) \int_S\, J_{B_G}(1_{v_K}).\, dS, \tag{3.37}$$

where J_{B_G} is the Jacobian of the magnetic field B_G acting on the coil. Expression (3.37) conveys a more intuitive notion of $V_K^{v_K, B_{AC}}$ than (3.32), meaning that this component of the induced voltage V_K^D is proportional to the integral on S of the variation of the vector B_G in direction of v_K, as well as proportional to the speed $\|v_K\|$ itself.

In terms of phase delays, looking at (3.30) and (3.31), it can be noticed that the phase of V_K^0 is delayed from that of the magnetic field generated by the primary coil, B_{AC}, by an angle of $\pi/2$, while $V_K^{v_K, B_{AC}}$ is either in phase or in counter-phase with B_{AC}, respectively depending whether the variation of the magnetic flux on S is negative or positive when K is incrementally displaced in the direction of v_K.

Figure 80a shows the complex plots of the associated phasors $\hat{B}_{AC}$, $\hat{V}_K^0$, $\hat{V}_K^{v_K, B_{AC}}$ and $\hat{V}_K^D$ at the frequency f_0, for the case in which the secondary coil is in a position of the space where the tendency for the variation of the magnetic flux on S is positive in the direction of the velocity v_K, as illustrated in Figure 80b. Conversely, if the secondary coil is moving in a position where the tendency for the variation of the magnetic flux on S is negative in the direction of the velocity v_K, as illustrated in Figure 81b, then $V_K^{v_K, B_{AC}}$ is in phase with B_{AC}, as shown in Figure 81a. In both cases, if there is a non-zero speed $\|v_K\|$, it is expected that:

$$\left|\hat{V}_K^D\right| \;\geq\; \left|\hat{V}_K^0\right| \tag{3.38}$$

Dynamic Inductive Wireless Power Transfer for Lightweight Electric Vehicles
Luiz Alberto Lisboa da Silva Cardoso – University of Minho

134

(a)   (b)
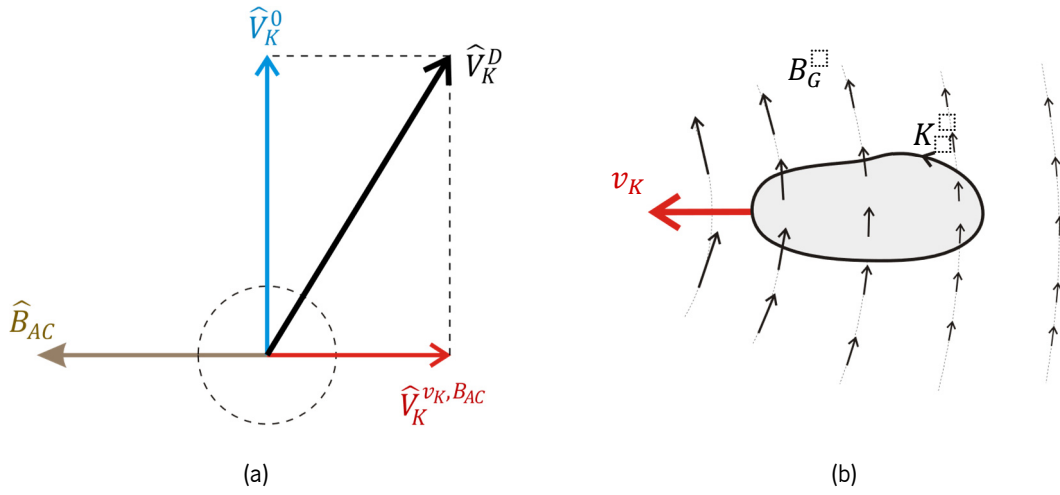
Figure 80. (a) Phasor components of the dynamically induced voltage on a secondary coil when its movement is enhancing the oriented magnetic flux on the induced coil (b).

(a)   (b)
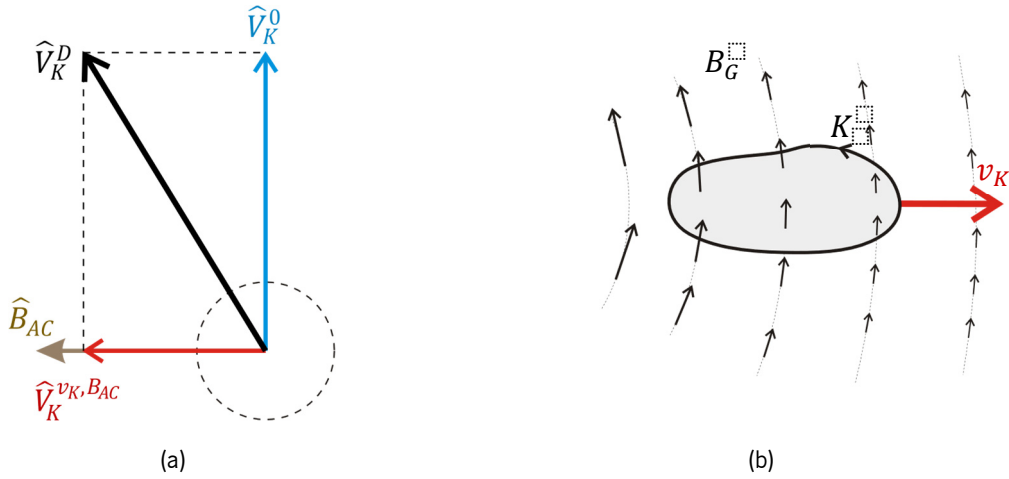
Figure 81. (a) Phasor components of the dynamically induced voltage on a secondary coil when its movement is decreasing the oriented magnetic flux on the induced coil (b).

3.1.3 Approximating DIWPT as Quasi-stationary IWPT

The magnitude ratio δ of the RMS values of $V_K^{v_K, B_{AC}}(t)$ (3.37) and $V_K^0(t)$ (3.31) can then be calculated as the modulus of δ_c:

$$\delta_c \;=\; \frac{\widehat{V}_K^{v_K, B_{AC}}}{\widehat{V}_K^0} \;=\; -j\, \frac{\|v_K\|}{2\pi f_0} \frac{\int_S \; J_{B_G}(1_{v_K}).\,dS}{\int_S \; B_G.\,dS}\,, \tag{3.39}$$

$$\delta \;=\; \frac{\left[V_K^{v_K, B_{AC}}\right]_{RMS}}{\left[V_K^0\right]_{RMS}} \;=\; |\delta_c| \;=\; \frac{\|v_K\|}{2\pi f_0} \frac{\left|\int_S \; J_{B_G}(1_{v_K}).\,dS\right|}{\left|\int_S \; B_G.\,dS\right|}\,, \tag{3.40}$$

or, according to (3.32), alternatively, as:

$$\delta = \frac{\|v_K\|}{2\pi f_0} \frac{\left| \oint_{K(t)} (1_{v_K} \times B_G).dK \right|}{\left| \int_S B_G.dS \right|},$$

(3.41)

Since the ratio of the integrals, in either (3.37) or (3.39), does not depend on $\|v_K\|$ or f_0, if the magnetic net flux of B_G though the coil is not null, it follows from (3.41) that it will be always possible to make δ smaller than any given value by also making sufficiently small the ratio $\|v_K\|/f_0$. That is, in a typical DIWPT system design, with the pick-up coil fixed on board of an EV, the higher the EV speed $\|v_K\|$ is, the higher the induction frequency f_0 has also to be in order to make it possible to approximate $V_K^D(t)$ by $V_K^0(t)$, treating the design as a quasi-stationary IWPT case. In the following paragraphs, a few more assumptions on the geometry of the problem are made to derive a criterion for checking the applicability of this approximation.

3.1.3.1 Simplified criterion for approximating DIWPT as a quasi-stationary IWPT

In order to assess whether the ratio $\|v_K\|/f_0$ is low enough as to permit the approximation of $V_K^D(t)$ by $V_K^0(t)$, or, conversely, to establish the minimum frequency f_0 for which this approximation is valid for a given maximum speed v_{max}, a relationship among $\|v_K\|$, f_0 and the geometry of the coil is initially found for an specific configuration.

So, let's first assume that the magnetic field $B_{AC}(p, t)$, acting on the secondary coil given by the curve K, is due to a single primary coil generating in the neighborhood of K, with both coils in free space, and that any point of K is at a distance $\|r\|$ from the primary coil much greater than de dimensions of the primary coil itself, as illustrated in Figure 82. Then, the time-invariant magnetic vector field B_G of (3.30) can be approximated as if it were being produced by an equivalent magnetic dipole, m, which can be expressed as [90]:

$$B_G(r) \cong B_m(r) = \frac{\mu_0}{4\pi} \left[\frac{3(m.r)r}{\|r\|^5} - \frac{m}{\|r\|^3} \right]$$

(3.42)

which can be further developed as:

$$B_G(r) \cong B_m(r) = \frac{\mu_0 \|m\|}{4\pi \|r\|^3} [3\cos\theta . 1_r - 1_m]$$

(3.43)

Dynamic Inductive Wireless Power Transfer for Lightweight Electric Vehicles
Luiz Alberto Lisboa da Silva Cardoso – University of Minho

136

where μ_0 is the uniform magnetic permeability of the free space; m is magnetic dipole vector; 1_r is the unity vector in direction of the oriented distance r to the secondary coil, show in red in Figure 82; and 1_m is the unity vector in the direction of the magnetic dipole m.

For our analysis, working in spherical coordinates (r, θ, φ), it is more convenient to re-express 1_m in terms of 1_r and 1_θ, the unity vector in direction of the polar angular displacement θ, shown in green in Figure 82:

$$1_m = \cos\theta \, . \, 1_r - \sin\theta \, . \, 1_\theta \tag{3.44}$$

Then, by substituting (3.44) in (3.43) it results that:

$$B_G(r) \cong \frac{\mu_0 \, \|m\|}{4\pi \|r\|^3} (2\cos\theta \, . \, 1_r + \sin\theta \, . \, 1_\theta) \tag{3.45}$$
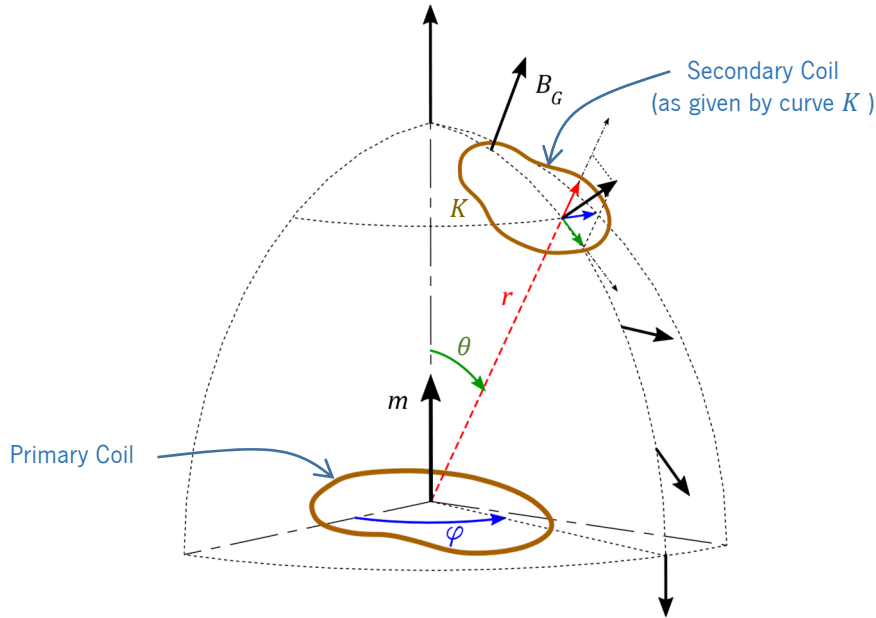
Figure 82: Special case when the primary coil can be modeled by approximation as a magnetic dipole.

Under the above conditions,

$$\oint_{K(t)} (1_{v_K} \times B_G) \, . \, dK \leq \frac{\mu_0 \, \|m\|}{\|r\|_{min}^3} \ell_K \, . \, \max_{\theta} \|(2\cos\theta \, . \, 1_r + \sin\theta \, . \, 1_\theta)\| \tag{3.46}$$

where ℓ_K is the total length of the curve, and $\|r\|_{min}$ is the minimum distance of a point in K to the position of the equivalent magnetic dipole m.

But since 1_r and 1_θ are orthogonal,

Dynamic Inductive Wireless Power Transfer for Lightweight Electric Vehicles
Luiz Alberto Lisboa da Silva Cardoso – University of Minho

137

$$\|(2\cos\theta \,.\, 1_r + \sin\theta \,.\, 1_\theta)\| \;=\; \sqrt{3\cos^2\theta + 1} \,, \tag{3.47}$$

what implies in:

$$1 \;\leq\; \|(2\cos\theta \,.\, 1_r + \sin\theta \,.\, 1_\theta)\| \;\leq\; 2 \tag{3.48}$$

Hence, (3.46) becomes:

$$\oint_{K(t)} \left(1_{v_K} \times B_G\right).\,dK \;\leq\; \frac{\mu_0\,\|m\|}{\|r\|_{min}^3} . \, 2\ell_K \tag{3.49}$$

Now, for simplicity, let us further assume that K is planar and delimits an oriented area A_K, and in search for an upper bound to the magnitude ratio δ, search for a lower bound for the integral in de denominator of (3.41).

In an well designed DIWPT configuration, in order to optimize the magnetic time-varying flux through A_K, the power transfer will occur with the secondary coil in a nominal relative position range to the primary coil such that either $1_{B_G}.\,dA$ is always positive or always negative, at all points on A_K, there existing an equivalent angle β, with $\cos(\beta) \neq 0$, such that:

$$\left|\int_A 1_{B_G}.\,dA\right| \;=\; \|A_K\|\,|\cos(\beta)| \tag{3.50}$$

The angle β can be seen as some mean value of the angle between the magnetic field B_G and the normal unit vector at each point of the area A_K and, in good DIWPT designs, it will be as close to zero or π as possible, so that the magnetic flux from primary to secondary coil is increased.

So, linking (3.45) into (3.41):

$$\left|\int_S B_G.\,dS\right| \;=\; \frac{\mu_0\,\|m\|}{4\pi} \left|\int_A \frac{(2\cos\theta \,.\, 1_r + \sin\theta \,.\, 1_\theta).\,dA}{\|r\|^3}\right| \tag{3.51}$$

So, under the constructive assumption of $1_{B_G}.\,dA$ always positive or always negative:

$$\left|\int_S B_G.\,dS\right| \;\geq\; \frac{\mu_0\,\|m\|}{\|r\|_{max}^3} \min_\theta \|(2\cos\theta \,.\, 1_r + \sin\theta \,.\, 1_\theta)\| \left|\int_A 1_{B_G}.\,dA\right| \tag{3.52}$$

Looking at (3.48) again,

Dynamic Inductive Wireless Power Transfer for Lightweight Electric Vehicles
Luiz Alberto Lisboa da Silva Cardoso – University of Minho

138

$$\left| \int_S B_G . dS \right| \geq \frac{\mu_0 \, \|m\|}{\|r\|_{max}^3} \, \|A_K\| \, \cos(\beta) \tag{3.53}$$

By combining (3.49) and (3.53) into (3.41), it results:

$$\delta \leq \frac{\|v_K\|}{\pi f_0} \frac{\ell_K \gamma^3}{\|A_K\| \, . \, |\cos(\beta)|} = \delta_L, \qquad \text{where} \quad \gamma = \frac{\|r\|_{max}}{\|r\|_{min}} \tag{3.54}$$

The relative error ε in approximating $V_K^D(t)$ by $V_K^0(t)$ is then given by:

$$\varepsilon = \frac{|\hat{V}_K^D| - |\hat{V}_K^0|}{|\hat{V}_K^0|} = \frac{|\hat{V}_K^D|}{|\hat{V}_K^0|} - 1 = \frac{\sqrt{|\hat{V}_K^0|^2 + |\hat{V}_K^{v_K,B_{AC}}|^2}}{|\hat{V}_K^0|} - 1 = \tag{3.55}$$

$$= \sqrt{1 + \delta^2} - 1 \tag{3.56}$$

In the regions where $|\hat{V}_K^{v_K,B_{AC}}|$ is to be neglected relatively $|\hat{V}_K^0|$, it is expectable that $0 < \delta < 1$, so it is possible to use the inequality:

$$\sqrt{1 + \delta^2} \leq 1 + \frac{\delta^2}{2}, \tag{3.57}$$

from where:

$$\varepsilon \leq \frac{\delta^2}{2} \leq \frac{\delta_L^2}{2} \tag{3.58}$$

Then, by forcing the limit value δ_L to be less than $\sqrt{2\varepsilon}$, for some desired some desired small enough maximum relative error ε, it will be possible to establish a condition in which the dynamically induced voltage component $V_K^{v_K,B_{AC}}$ can be neglected relatively to V_K^0, and the induced voltage, V_K^D, approximated by its purely stationary component. It is emphasized that this theoretical result was derived and holds, among other assumptions, if the primary coil geometry and distance to the secondary coil are such that the magnetic field of the primary coil can satisfactorily modeled as that of an ideal magnetic dipole, at least in the neighborhood of the secondary coil. On the other hand, by the superposition principle, (3.54) would as well hold individually for each primary coil that is sourcing the magnetic field to the secondary coil (and the associated induced voltage component), if more than one primary coil is present and close enough to influence the induced voltage on the secondary coil.

Dynamic Inductive Wireless Power Transfer for Lightweight Electric Vehicles
Luiz Alberto Lisboa da Silva Cardoso – University of Minho

139

3.1.3.2 Special Case of a Circular Secondary Coil far away from the Primary Coil

If the primary coil is circular, consisting of a N circular wire turns coinciding with a circle K of diameter D, then its total length ℓ_K and total area are given by:

$$\ell_K = N\pi D \tag{3.59}$$

$$\|A_K\| = N\pi\left(\frac{D}{2}\right)^2 \tag{3.60}$$

So (3.54), for this circular coil becomes:

$$\frac{\left[V_K^{v_K, B_{AC}}\right]_{RMS}}{[V_K^0]_{RMS}} \leq \frac{4\gamma^3\|v_K\|}{\pi f_0 D |\cos(\beta)|} \tag{3.61}$$

Exemplifying the application of (3.61), let us assume that a circular secondary coil with $D = 0.5$ m is travelling at a speed of 140 km/h, in a relative position range to a primary coil such that $\cos(\beta) \geq 0.5$, and at a sufficiently large distance, such that $\gamma \leq 1.5$. Then a sufficient condition for approximating $V_K^D(t)$ as if the secondary coil were at rest with respect to the primary coil, with an error of less than $\varepsilon_0 = 1\%$, is to require that:

$$f_0 \geq \frac{4 \times 1.5^3 \times 140 \times \dfrac{1000\,m}{3600\,s}}{\pi \times 0.5\,\text{m} \times 0.5 \times \sqrt{2 \times 1\%}},$$

$$f_0 \geq 4.7\,\text{kHz} \tag{3.62}$$

3.1.3.3 Quasi-stationary Approximation in DIWPT Design for Automotive Applications

The numbers used in the example of (3.62) are not completely incidental. The speed value of 140 km/h and the secondary coil diameter of 0.5 m can be considered within typical ranges for respectively the maximum speed and typical coil pick-up size, for an EV. However, the conservative estimation given by (3.61) assumes that the secondary coil is far away from the primary coil, relatively to the dimensions of the coils, which is a theoretical situation which is not of great interest for electric vehicles moving over an inductive lane.

In order to analyze the more useful situation whereas an EV is close to the lane, it would be necessary to look back to equations (3.29) and (3.37), and notice that:

$$V_K^D(t) \cong V_K^0(t) - \|v_K\|\cos(2\pi f_0 t)\int_S J_{B_G}(1_{v_K}).dS, \tag{3.63}$$

Dynamic Inductive Wireless Power Transfer for Lightweight Electric Vehicles
Luiz Alberto Lisboa da Silva Cardoso – University of Minho

140

Let us assume the secondary and primary coils are flat and parallel to the ground and located at distance h to each other. The differential element dS of the secondary coil will be perpendicular to the ground plane, which is also the plane on which the vehicle can move. Using the ISO 4130 three-dimensional reference system [91], which is equivalent to having the x and y components of dS zero (z is the vertical axis), that is $dS = (0, 0, dA)$. Also, since the vehicle only moves parallel to the ground plane:

$$1_{v_K} = \frac{(v_x, v_y, 0)}{\|v_K\|}, \tag{3.64}$$

where v_x is the speed of the vehicle in the direction of the road, and v_y is its speed of lateral movement with respect to the center of the road.

So, expression (3.63) becomes equivalent to:

$$V_K^D(t) \cong V_K^0(t) - cos(2\pi f_0 t) \int_S \left(\frac{\partial B_z}{\partial x} v_x + \frac{\partial B_z}{\partial y} v_y \right) dA, \tag{3.65}$$

In these conditions, expression (3.31) can also be simplified to:

$$V_K^0(t) = -\int_S \frac{\partial B_{AC}}{\partial t} . dS = 2\pi f_0 \, sin(2\pi f_0 t) \int_S B_z \, dA \tag{3.66}$$

Assuming that $v_y = 0$ and v_x is constant, and expressing the voltages in terms of phasors, the relative complex error in approximating $\hat{V}_K^D$ by $\hat{V}_K^0$, δ_c, will be given, for $\|\hat{V}_K^0\| > 0$, by:

$$\delta_c = \frac{\hat{V}_K^D}{\hat{V}_K^0} - 1 = -j \frac{v_x}{2\pi f_0} \frac{\int_S \frac{\partial B_z}{\partial x} \, dA}{\int_S B_z \, dA} \tag{3.67}$$

Both $\delta = |\delta_c|$ and ε will tend to increase as the secondary coil approaches a position in space where $\int_S B_z \, dA = 0$, that is, where the induced voltage if the vehicle were stationary, $\hat{V}_K^0$, is zero. But this is not a matter of concern, because, by design, these positions are clearly not where DIWPT operation is normally expected.

So, when the secondary coil is positioned in such a way that the primary coil is inducing non-zero voltage on it, it is possible to write:

$$\delta_c = -j \frac{v_x}{2\pi f_0} \frac{\overline{\frac{\partial B_z}{\partial x}}(S) \int_S \, dA}{\overline{B_z}(S) \int_S \, dA} = -j \frac{v_x}{2\pi f_0} \frac{\overline{\frac{\partial B_z}{\partial x}}(S)}{\overline{B_z}(S)}, \tag{3.68}$$

Dynamic Inductive Wireless Power Transfer for Lightweight Electric Vehicles
Luiz Alberto Lisboa da Silva Cardoso – University of Minho

141

where $\bar{B}_z(S)$ and $\overline{\partial B_z / \partial x}\,(S)$ are respectively the average vertical component of the magnetic field and the average derivative of the vertical component of the magnetic field with respect to x, on the area S enclosed by the secondary coil, for any given position of the vehicle.

When the area of the secondary coil is very small, it is possible to approximate (3.68) by taking the limit condition $S \longrightarrow 0$, so, where the amplitude of the magnetic field $B_z(x, y, z) > 0$:

$$\delta \cong \frac{|v_x|}{2\pi f_0} \left| \frac{1}{B_z} \frac{\partial B_z}{\partial x} \right| = \frac{|v_x|}{2\pi f_0} \left| \frac{\partial \log|B_z|}{\partial x} \right| \tag{3.69}$$

To address a popular case in automotive DIWPT applications, let us further assume that the primary coil is an oblong rectangular horizontal coil. Then, still considering that secondary coil is very small, compared to the primary coil, let us assume that it is travelling over the horizontal primary coil in center-alignment with it, at a constant height h, as shown in Figure 83.
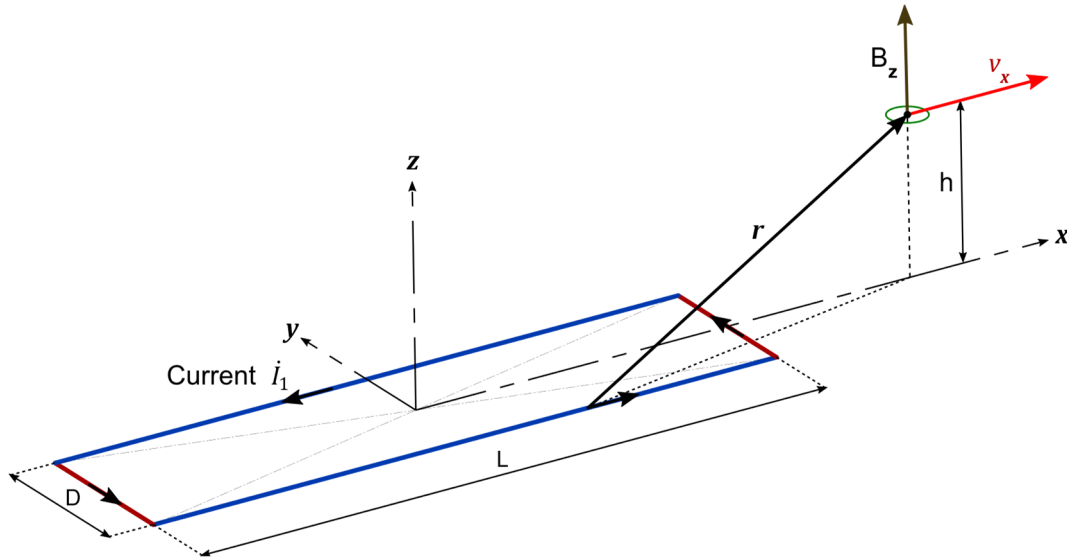
Figure 83: Rectangular primary coil in quasi-static approximation of DIWPT.

The components of B_z respectively due to the transversal (dark red in Figure 83) and axial (blue in Figure 83) segments of the primary coil can be calculated using the Biot-Savart Law by:

$$\frac{B_{z,transversal}}{(\mu \dot{\imath}_1 / 4\pi)} = \int_{-D/2}^{D/2} \left(\frac{-\left(\frac{L}{2} - x\right)}{\left(\left(\frac{L}{2} - x\right)^2 + y^2 + h^2\right)^{\frac{3}{2}}} + \frac{\left(\frac{L}{2} + x\right)}{\left(\left(\frac{L}{2} + x\right)^2 + y^2 + h^2\right)^{\frac{3}{2}}} \right) dy \tag{3.70}$$

and

$$\frac{B_{z,axial}}{(\mu \dot{\imath}_1 / 4\pi)} = \int_{-L/2}^{L/2} \frac{D}{((x - u)^2 + y^2 + h^2)^{\frac{3}{2}}} du \tag{3.71}$$

Dynamic Inductive Wireless Power Transfer for Lightweight Electric Vehicles
Luiz Alberto Lisboa da Silva Cardoso – University of Minho

142

Exemplifying with primary coil dimensions $L = 2$ m and $D = 0.5$ m, and $h = 0.2$ m, and plotting the magnetic field and its gradient along the direction x, both normalized to $\mu \dot{I}_1 / 4\pi$, it is possible to plot the graphs in Figure 84.
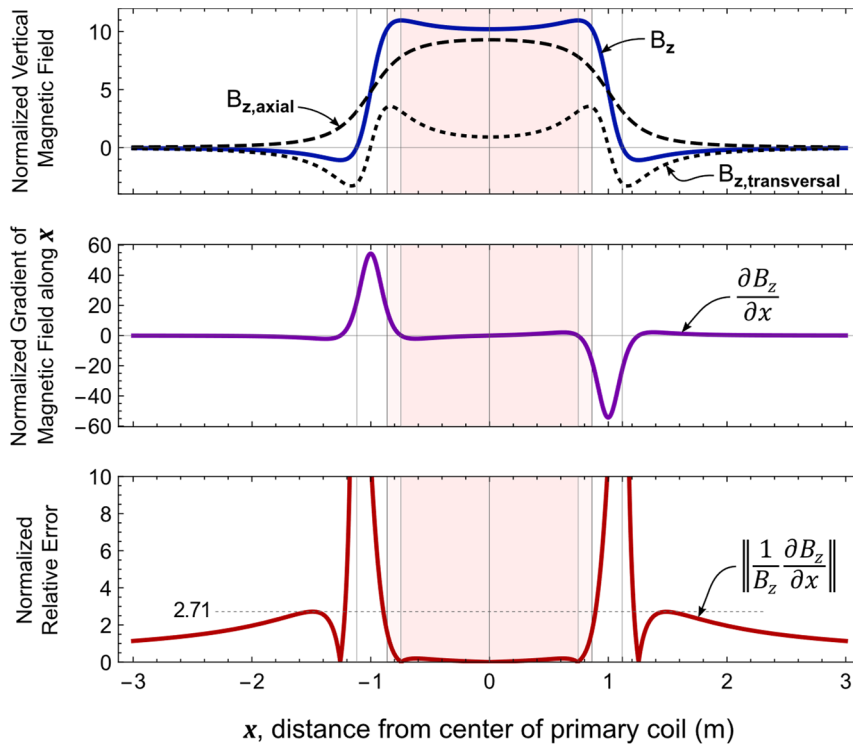
Figure 84: Error in quasi-static approximation of DIWPT using a primary rectangular coil.

Visibly, the magnitude of the normalized relative error δ is only high where the magnetic field B_z is very small (close to zero), at the transitions into and out of the main design zone for wireless power transfer. These transitions, in terms of transferred power, should be less relevant to the operation of the DIWPT, in an automotive application.

In this example, the maximum value of the normalized relative error, on the approach of primary coil is approximately 2.71, so, except near the zero crossings of B_z, the relative error observed while approximating the induced voltage as if it were resulting from a stationary experiment will be given by:

$$\delta = \frac{v_x}{2\pi f_0} 2.71 \tag{3.72}$$

Travelling at a speed $v_x = 140$ km/h, if the relative error ε is required to be less than 1%, except near the zero crossings of the magnetic field, then a sufficient condition for approximating $V_K^D(t)$ by $V_K^0(t)$, as if the secondary coil were at rest with respect to the primary coil (except very close to the zero crossing point of B_z), is that:

Dynamic Inductive Wireless Power Transfer for Lightweight Electric Vehicles
Luiz Alberto Lisboa da Silva Cardoso – University of Minho

143

$$f_0 \geq \frac{140 \times \frac{1000\,m}{3600\,s} \times 2.71}{2\pi \times \sqrt{2 \times 1\%}},$$

$$f_0 \geq 119\ \text{Hz}$$

(3.73)

Along most of the central section of the primary coil, the requirement in (3.73) is conservative, as it can be derived from the depressed central section of the curve of normalized error, in red in Figure 84. On the other hand, an elevation on the amplitude of the induced voltage V_K^D is always expected when the secondary is transitioning over the primary coil limits, where $|\partial B_z / \partial x|$ is high. This can prevent the induced voltage from reaching zero, at the zero crossings in the magnetic field, what would be expected in the stationary case.

In today's WPT and DIWPT applications, to achieve larger transferred power levels, the induction frequency f_0 is commonly found in the order of tens of kilohertz, significantly higher than both in required by either (3.62) or (3.73).

Particularly, in automotive applications, the same proposed frequency band recommended by SAE for stationary automotive recharging, which is centered at 85 kHz [92], is being used in new DIWPT transfer systems for road vehicles. So, at these commonly expected working frequencies, it can be assumed that the quasi-stationary approximation holds. The only effect unique to DIWPT, that is expected as discrepancy to this approximation, is the appearance of transient peaks in the induced voltage, when the secondary coil passes over the points of high spatial variation in the magnitude of the magnetic field generated by the primary coil.

3.2   Early DIWPT Designs

The earliest DIWPT design that was found in the literature is the French patent of a "New System for Electric Traction of Vehicles", by Maurice Hutin and Maurice Leblanc, filed on November 5, 1890, in Paris [93]. The electric vehicles were something new, and most of the efforts of the engineering community by the end of the 19th century was dedicated to the improvement of the electric power traction itself, overhead lines technology, and batteries. In addition, the necessary materials and components for adequately implementing the idea were not yet available at that time. Because of that, the design was soon completely forgotten, and so remained until 1923-24, when it was rediscovered and speculatively referenced in some French scientific magazines [94]. Forgotten again, DIWPT would be brought to public demonstration, for possibly the first time, in 1943, by the Russian scientist and engineer George Ilyich Babat, who

Dynamic Inductive Wireless Power Transfer for Lightweight Electric Vehicles
Luiz Alberto Lisboa da Silva Cardoso – University of Minho

144

designed and successfully prototyped what he called the "High-frequency Transport" [94],[95]. But the electronic tube technology Babat could use at his time only rendered him a very low electrical efficiency system, what would not yet make it possible for DWIPT to compete with other wired technologies. Because of that, DWIPT was again forgotten for a few decades more.

After the silicon solid state power electronic components became available and popular, the DWIPT concept naturally resurged with new investigations focusing public transportation [96], beginning from the 1970's on. Eventually, a dedicated research line was started at the University of Auckland, led by prof. John Talbot Boys, where the first modern DWIPT design is believed to have been accomplished [14]. In the next sections, some of these historically important designs are briefly reviewed, to help consolidate the origins and fundamental principles of DIWPT.

3.2.1 Hutin and Leblanc DWIPT Design

Hutin and Leblanc DIWPT design is embodied in the patent number 209323, granted on February 18, 1891, by the French Ministry of Commerce and Industry ("Ministère du Commerce, de l'Industrie et des Colonies"). It was conceived only about ten years after the introduction of the first electric cars was running on tracks, in 1881, according to [97], section 4.1, and [74]. It describes a system where a conductor carrying high-frequency current is laid underneath the path of a tram, parallel to the tracks, so that it can continuously transfer energy to a cylindrical pick-up coil attached to an EV running on these tracks. The pick-up coil is series-compensated by a capacitor bank and delivers electric power to the vehicle's power train, which is an AC motor. Some of the original drawings of this design, focusing the pick-up coil and cross-section of the tracks are partially reproduced and annotated in Figure 85 and Figure 86.
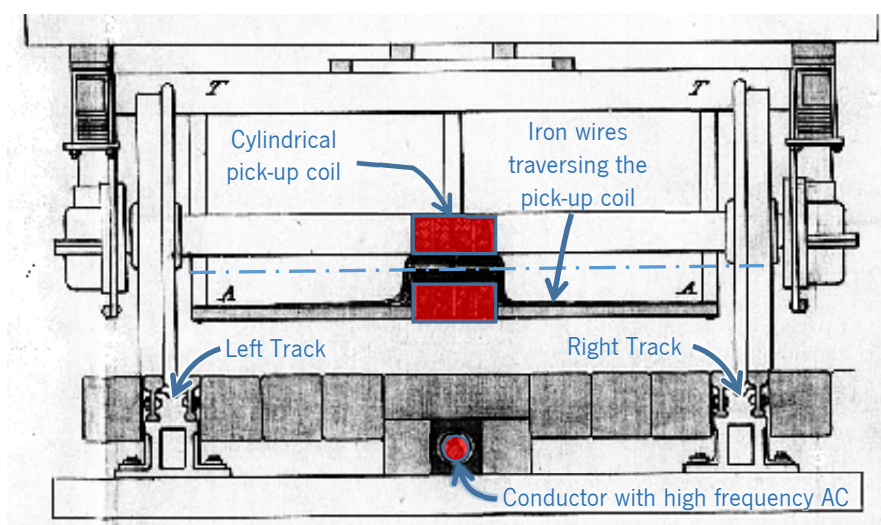
Figure 85: Hutin and Leblanc 1890 DIWPT design: Vehicle over tracks cross-section view.

Dynamic Inductive Wireless Power Transfer for Lightweight Electric Vehicles
Luiz Alberto Lisboa da Silva Cardoso – University of Minho

145

The pick-up coil is attached to a wooden plate, fixed with its axis orthogonal to the power transmitting conductor, and traversed by a bundle of iron wires, which open in a beam, forming an iron mesh over the wooden plate. This mesh concentrates the oscillating magnetic flux coming from the transmitting conductor into the pick-up coil. A simplified tridimensional drawing reconstituting the main idea of the model is provided in Figure 87.
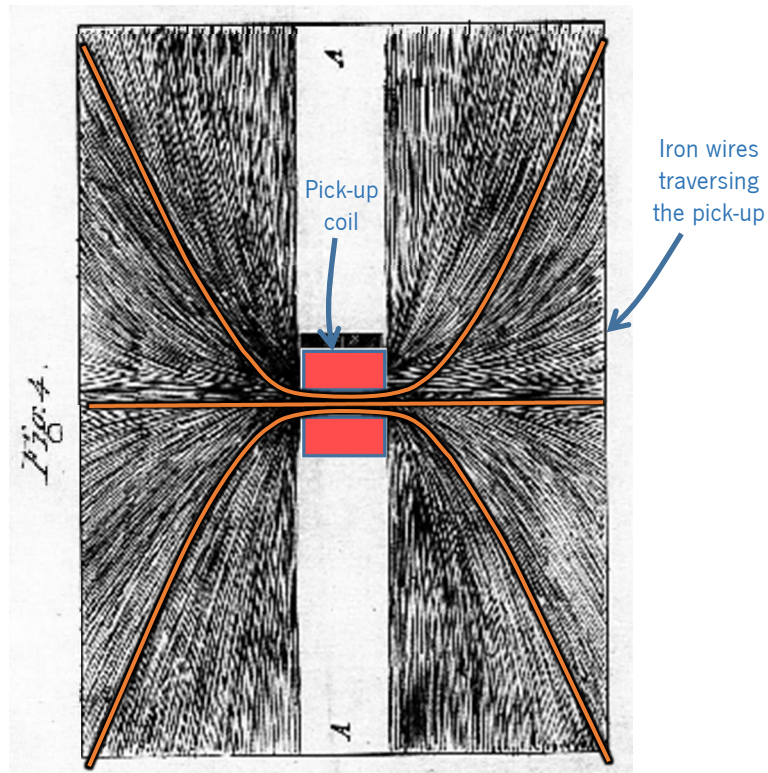
Figure 86: Hutin and Leblanc 1890 DIWPT design: Pick-up coil cross section - top view.
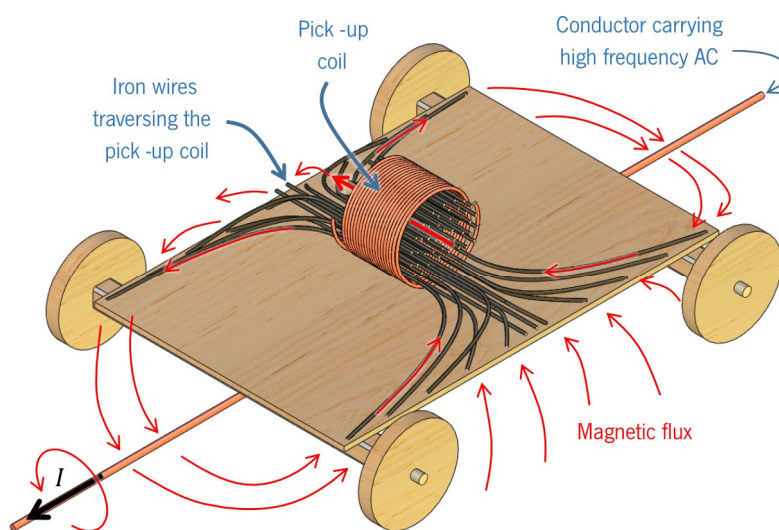
Figure 87: Hutin and Leblanc 1890 DIWPT design principle (not to scale).

Dynamic Inductive Wireless Power Transfer for Lightweight Electric Vehicles
Luiz Alberto Lisboa da Silva Cardoso – University of Minho

146

In 1894, Hutin and Leblanc also had their design patented in the United States [98], which included a new graphical illustration, reproduced in Figure 88, emphasizing the fact that the transmitting wire needed not to be on the ground, but could be aerial as well, as long as the transmitting conductor remained parallel to the vehicle route, as restrained by the tracks.
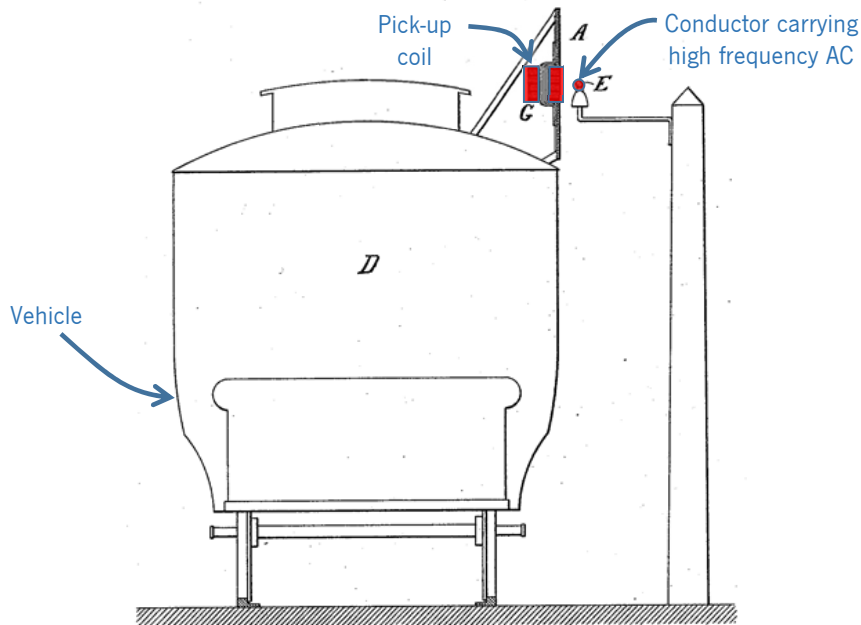
Figure 88: Alternative aerial pick-up position proposed by Hutin and Leblanc in 1894 US patent.

Hutin and Leblanc's recommended frequency of operation was "from one thousand to two thousand alternations per second", with the wooden plate support of the iron mesh "as near the surface as practicable" [98], that is, with the smallest possible air-gap distance, a value mentioned in the French original patent to be limited to 14 cm, due to railway regulations of that time. They also asserted that, due to the high magnetic permeability of the iron, 2500 times greater than that of the air, the iron mesh would redirect into the pick coil all magnetic flux lines generated by the primary transmitting conductor section beneath the mesh.

The choice of iron as the material to convey the magnetic flux into the pick-up coil at the proposed frequency of 2 kHz (certainly, for technological limitations), would likely result in an excess loss in eddy currents, even in a wired mesh. So, in order to access potential qualities for DIWPT of Hutin and Leblanc's design, a similar but improved configuration was simulated using the FEMM finite element modeling software [99]. The dimensions used in the simulated model were set approximately to the scale implicit in the patent drawings, assuming that the track gauge used was the meter gauge (1000 mm in between tracks), the one used in the first electric tram brought into public service, and popular for early trams of the time the patents were filled. The geometry of the model used in the simulations can be visualized in Figure 89.

Dynamic Inductive Wireless Power Transfer for Lightweight Electric Vehicles
Luiz Alberto Lisboa da Silva Cardoso – University of Minho

147
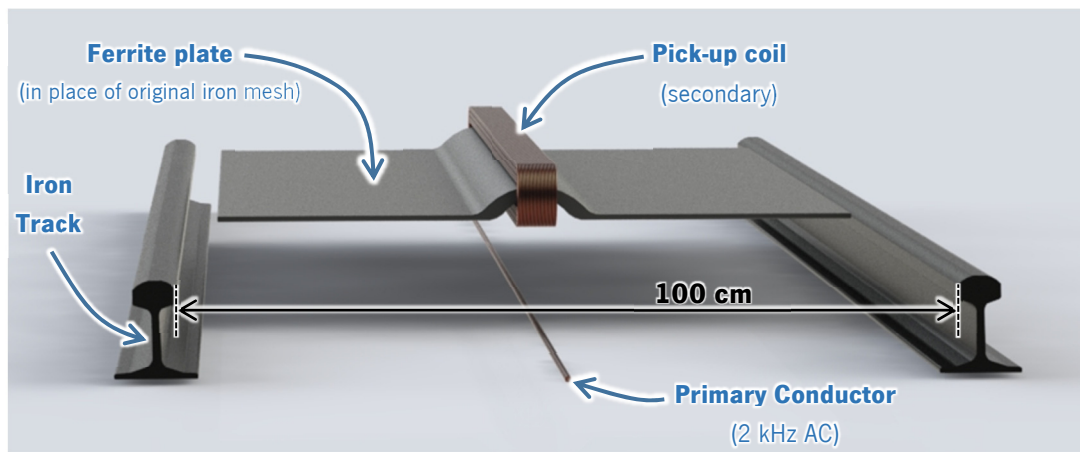
Figure 89: Geometry of a Hutin and Leblanc based DIWPT configuration used in the simulations.

While the original drawings suggest that the wooden support plate should be approximately 1000 mm wide and 1400 mm long, in the model, the ferrite plate was shortened to 900 mm wide, to avoid bringing its edges too close to the tracks. Also, litz wire, not available at the time of their invention, was used in all conductors. The main assumptions and characteristics of this improved configuration that was simulated are then listed below:

- The iron mesh was replaced by a low conductivity, high magnetic permeability modern soft magnetic ferrite (Fe-Ni-Zn-V) material, not available at the time of the invention.

- The pick-up coil was elongated to the length of the full ferrite plate used, 1400 mm, keeping a similar cross-section design as that of Hutin and Leblanc's.

- A compensated secondary nominal voltage target was set in the range of 150 V to 180 V, about the same voltage used by the DC electric motor of the first Siemens and Halske tram, in Lichterfelde, Berlin, in 1881, which was 150 V according to [100] and 180 V according to [101]. Whereas no specific arrangement or cross-section for the coil wiring was proposed in the patent, in the simulation, it was possible to achieve this voltage by using ten layers of 21 turns in the pick-up coil, in a total of 210 turns spaced at 2.67 mm, with some extra insulation layers in between layers 4 and 5, and layers 7 and 8, as shown in Figure 90.

- To reduce losses in the coil wiring, litz copper cable with 300 strands of 0.1 mm of diameter was considered in the modeling. When used at frequencies up to 100 kHz, the current capacity of such cable is approximately 9.5 A. In the simulation, 2.35 mm^2.

- The primary (transmitting) conductor, also not specified in the original patents, was modeled as litz copper wire, with 3200 strands of 0.1 mm of diameter, and a total cross-section area of 25 mm^2, thus capable of handling 100 A RMS up to 100 kHz.

Dynamic Inductive Wireless Power Transfer for Lightweight Electric Vehicles
Luiz Alberto Lisboa da Silva Cardoso – University of Minho

148

- Tracks were assumed to be made of pure iron and to have a 125 mm (5 inches) high profile, similar to those found in some meter gauge (1000 mm) railways still in operation today.

- Neglecting the thickness of the support wooden plate, the distance from the ferrite plate to ground was set at 14 cm, for being mentioned by Hutin and Leblanc as the minimum possible ground clearance according to rail regulations. Not to add further distance to the interwinding air-gap, and to favor the induction in the secondary, the transmitting cable was positioned almost exposed, tangent to the ground surface, not fully buried in the ground.

- The ground was assumed to be perfectly nonconductive, which is often not the case. No other materials or parts were included in the simulation.
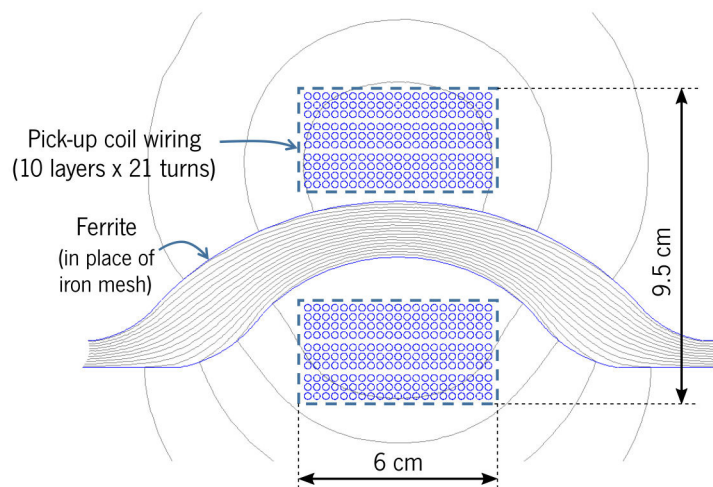
Figure 90: Detail of pick-up coil cross section used in the simulation of Hutin and Leblanc design.

This DIWPT configuration was simulated under the above mentioned assumptions and the main system parameters shown in Table 11, resulting in the induced voltages and power performance parameters indicated in Table 12.

Table 11: Main parameters of a hypothetical Hutin and Leblanc configuration used in simulation.

Parameter	Description/Value
Track gauge (distance in between tracks)	1000 mm
Ground Clearance	140 mm
Ferrite plate size (horizontal projection)	900 mm x 1400 mm
Ferrite plate border thickness	8 mm
Primary conductor position	Centered, in between tracks
Primary conductor constitution (copper)	3200 strands × 0.1 mm diameter wire (25.1 mm^2) bundled in an 8 mm diameter cable
Primary conductor nominal current	100.4 A RMS
Secondary coil conductor constitution (copper)	300 strands × 0.1 mm diameter wire (2.36 mm^2) bundled in a 2 mm diameter cable
Secondary coil winding	10 layers of 21 turns, 210 total turns

Dynamic Inductive Wireless Power Transfer for Lightweight Electric Vehicles
Luiz Alberto Lisboa da Silva Cardoso – University of Minho

149

Table 12: Performance parameters resulting from the simulation of a hypothetical Hutin and Leblanc configuration.

Results from Simulation	Description/Value
Voltage drop across primary conductor at pick-up section (1.4 m)	10.8 V RMS ∠ 12 degrees
Voltage drop across primary conductor out of pick-up section	1.45 V RMS ∠ 86 degrees / m
Secondary coil open circuit voltage	205 V RMS
Primary power debt at pick-up section	1052 W
Net power transferred (secondary @ 163 V RMS, 4.6 A RMS)	751 W
Power loss on tracks at pick-up section	200 W
Total power loss on copper at pick-up section	101 W
Power loss on copper at pick-up section (primary)	10 W
Power loss on copper at pick-up section (secondary)	91 W
Power loss on tracks out of pick-up section	2.4 W/m
Power loss on copper out of pick-up section (primary)	7 W/m
Total power loss out of pick-up section	9.4 W/m

The resulting magnetic field profiles of Figure 91 and Figure 92, where the magnetic flux density is indicated in colored layers, changing from pink (higher intensity) to blue (lower intensity). In Figure 91, the two black dashed contour curves mark the surfaces where the magnetic flux density is respectively +30dB and +20dB above the maximum ICNIRP [72] recommended exposure level for the general public at the frequency of 2 kHz, according to the conversion in Table 13. As a simplification, simulations models were developed neglecting the presence of the wheels and other metallic mechanical components of the tram, so that planar symmetry could be used as an approximation to compute the values of magnetic flux intensity at a cross-section passing through the vertical center plane of the pick-up coil.

Table 13: Correspondence of the magnetic field strength in dB, with a 0 dB reference at 40 μT.

Magnetic Flux Density (RMS)	Value in dB*
40 μT	0
126 μT	+10
400 μT	+20
1265 μT	+30
4000 μT	+40

*Using ICNIRP recommended maximum exposure level at 2 kHz as the reference level.

The absence of shielding elements in the design, associated with the high total current-turns present at the secondary coil around the ferrite plate, necessary to obtain significant power on the secondary, produces a large magnetic flux in the vicinity of the pick-up coil, which is only restrained by the iron tracks. This would create an extensive area of potentially hazardous magnetic field above the coil, as shown in Figure 91.

Dynamic Inductive Wireless Power Transfer for Lightweight Electric Vehicles
Luiz Alberto Lisboa da Silva Cardoso – University of Minho

150
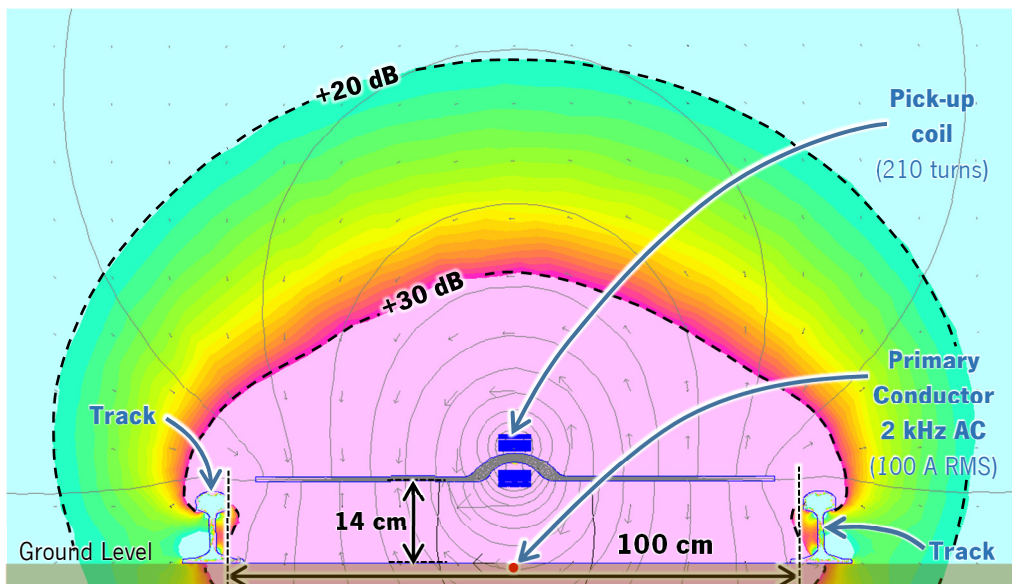
Figure 91: Magnetic field profile of a Hutin and Leblanc based configuration – pick-up section.

If the assembly would be installed on a tram car of that times, almost entirely made of wood, the magnetic field levels would potentially traverse the wooden tram floor at the coil pick-up section, exposing passengers and people standing by the tram to EMF levels that, today, are deemed as potentially dangerous to human health. Hence, the original Hutin and Leblanc's design would likely not suit current safety recommendations of EMF limit exposure. This configuration would then require magnetic shielding at the coil pick-up section, to protect passengers. In addition, at this low frequency, the shield plate that would be necessary would have to be about seven times thicker (and heavier) than that used at 85 kHz, which is the nominal value of the frequency band currently recommended by SAE for automotive WPT [92].
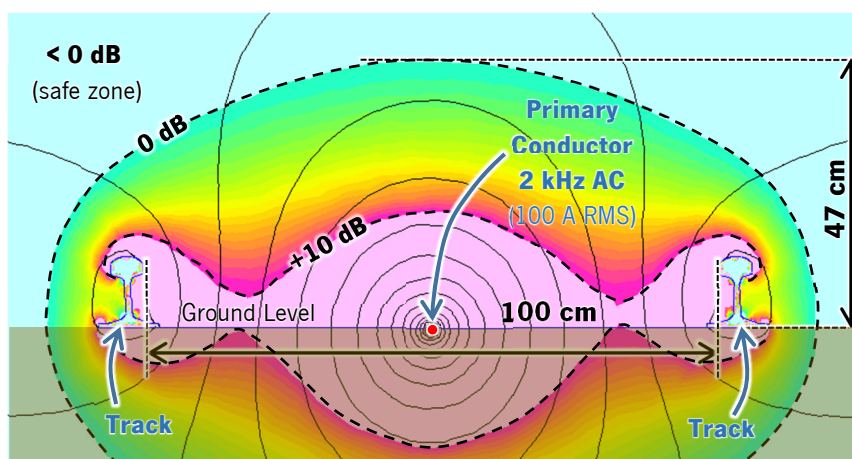
Figure 92: Magnetic field profile of a Hutin and Leblanc based configuration – out of pick-up section.

However, at the proposed current levels, the system would still be able to provide 751 W of net power per pick-up module.

Dynamic Inductive Wireless Power Transfer for Lightweight Electric Vehicles
Luiz Alberto Lisboa da Silva Cardoso – University of Minho

151

The Hutin and Leblanc DIWPT system is not known to have been actually prototyped and tested by its inventors but, based on the simulations realized, it can be concluded that, if built with modern materials and circuit components, which were not available at the time of design conception, the system would fulfil its basic DIWPT functionality, as intended by the inventors. In order to harvest enough power to move the small 1881 tram of Siemens and Halske, which had a 2.2 kW electric motor [100], it would still be necessary to install on the tram at least 3 of the pick-up modules configured as proposed in Hutin and Leblanc's patent.
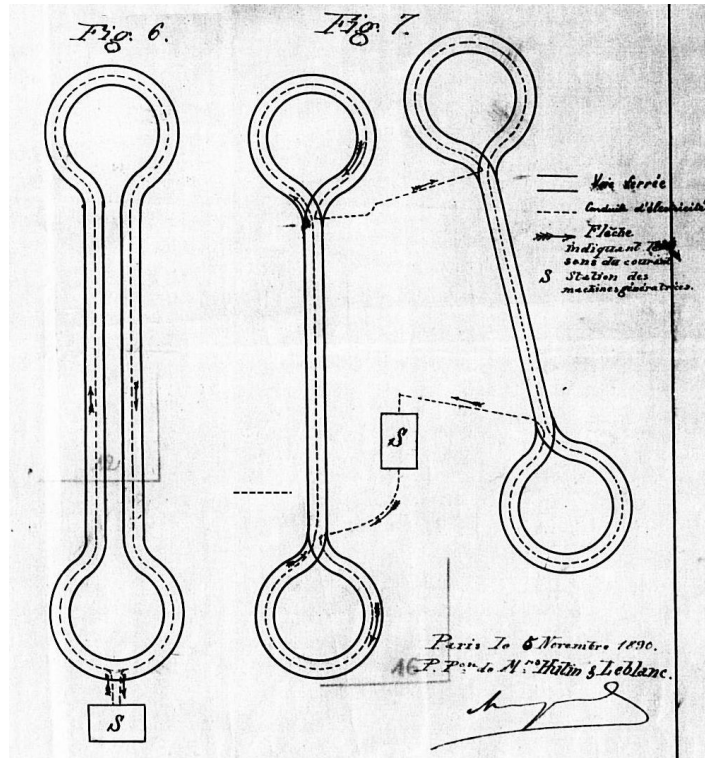
Figure 93: Hutin and Leblanc's closed inductive lanes with single primary conductor.

The overall efficiency of the system would expectably decrease as the track length would increase, due to the lack of provision for splitting the primary conductor in segments that could be switched on and off, as shown in Figure 93, reproduced from [93]. As an example, considering a tram with four pick-up modules in a closed circuit of 4900 m, corresponding to twice the 2450 m of length of the first electric tram tracks in Gross Lichterfelde [100], the system efficiency, $\eta_{(2540\ m)}$, are estimated in (3.74) and (3.75), based on the results in Table 11.

$$\eta_{(2540\ m)} = \frac{Power\ delivered\ to\ power\ train}{Power\ fed\ to\ lane} \tag{3.74}$$

$$\eta_{(2540\ m)} = \frac{4 \times 751\ W}{4 \times 1052\ W\ +\ (4900\ m - 4 \times 1.4\ m) \times 9.4\ W/m} \cong 6\% \tag{3.75}$$

Dynamic Inductive Wireless Power Transfer for Lightweight Electric Vehicles
Luiz Alberto Lisboa da Silva Cardoso – University of Minho

152

This efficiency figure of 6% refers to the DIWPT link only, not including any other losses, such as that on the AC electric motor, which, at 2 kHz, would be expectably very high, even for a laminated-core AC motor. If the system would be modified to use several shorter commutated lanes instead, arranged sequentially, for instance, of 50 m length, the new efficiency could be improved to approximately 59%, as computed in (3.76).

$$\eta_{(50\,m)} = \frac{4 \times 751\,W}{4 \times 1052\,W \,+\, (2 \times 50\,m - 4 \times 1.4\,m) \times 9.4\,W/m} \cong 59\% \qquad (3.76)$$

However, at the time of the Hutin and Leblanc's design, to switch the lane segments on and off at 100 A RMS, according to the presence of tram of each segment, relying solely on the available electromechanically devices, would not be an easy task to accomplish. The voltage V_1 required to be applied to the primary conductor loop of a full length lane of 2450 m would be approximately 7.1 kV RMS, and the lane would represent an essentially inductive load for the AC power source, as derived from (3.77).

$$V_1 = (1.45\ \text{V RMS} \angle 86\ \text{degrees}) \times (2 \times 2450 - 4 \times 1.4) \ +$$
$$+\ (10.8\ \text{V RMS} \angle 12\ \text{degrees}) \times 4\ \cong \qquad (3.77)$$
$$\cong\ 7.1\ \text{kV RMS} \angle 86\ \text{degrees}$$

Summarizing, the simulation of the DIWPT design proposed by Hutin and Leblanc indicates that the system, with minor modifications, would likely function as intended. However, it would present poor efficiency and serious potential issues concerning high exposure levels to EMF. Particularly, it would require a 2 kHz power line with several kilovolts, at approximately 100 A rms, to be laid very close to ground surface, with significant electrocution risks involved.

Despite these safety limitations and presumable low performance, Hutin and Leblanc's innovative conception was correct and, if implemented with a power train and components of modern technology, the system would work, being able to energize a vehicle with similar mechanical and electric characteristics of that of the early electric trams.

3.3　Babat's High Frequency Electric Transport System

Pursuing the same ideals of Hutin and Leblanc, George Ilyich Babat designed, prototyped and, in June of 1943, successfully demonstrated what he called the "High-frequency Transport" [94],[95]. This was the first DIWPT system known to be publicly demonstrated, and it included all the electronics for powering modular i-lanes, as well as harvesting and rectifying the electric current on board of a vehicle. It also included an urban architectural conception to integrate the

Dynamic Inductive Wireless Power Transfer for Lightweight Electric Vehicles
Luiz Alberto Lisboa da Silva Cardoso – University of Minho

153

lanes in standard roads and streets. Figure 94, extracted from Babat's English patent no. 657035 [95], and annotated with the identification of its main modules, shows the completeness of the system conceived. Two small vehicles were built for operation at Moscow Ordzhonikidze machine tool building plant [102], and the system had some international recognition at the time [94].
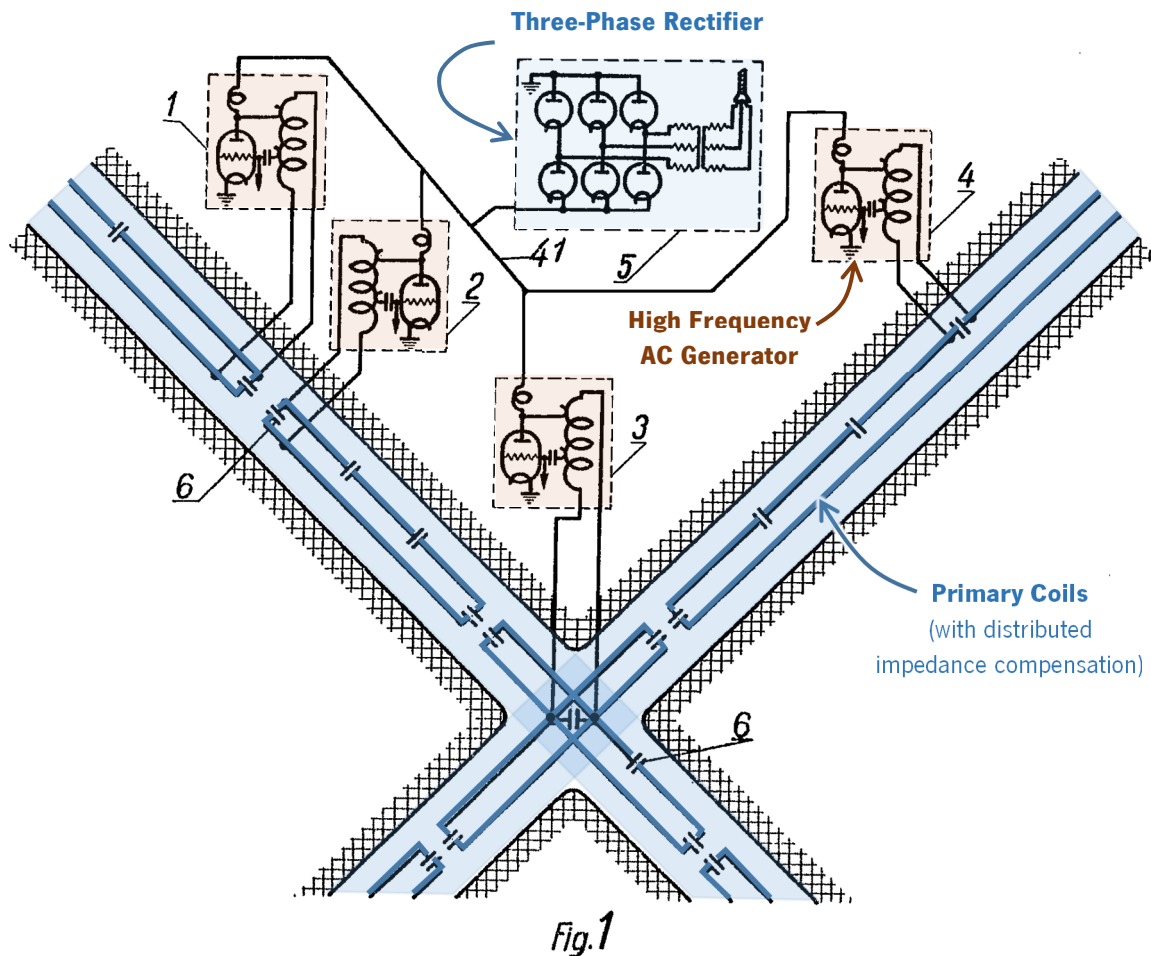
Figure 94: System architecture for lane electrification in Babat's DIWPT design.

In his design, Babat also introduced the concept of lane segmentation, with individual primary coils being activated independently, in order to increase electric efficiency. Not aware of the health issues associated with higher level of exposure to EMF fields, Babat's argument was solely to save energy, by not powering on a lane segment (primary coil) when there was no EV running over it. Figure 95, also extracted from Babat's patent, shows the high level schematics of the system, with the vehicle side in the lower part (pink shaded area) and the lane side modules in the upper part.

The system worked by keeping idle primary coils excited by a low power oscillator, part of the Power Switch Control module, which is shown in the top left corner of Figure 95. This auxiliary low power oscillator runs at the same frequency of the main AC generator of the system, all the time when no vehicle was drawing power from a given primary coil. When a vehicle would come

Dynamic Inductive Wireless Power Transfer for Lightweight Electric Vehicles
Luiz Alberto Lisboa da Silva Cardoso – University of Minho

154

by the lane and start to draw power from it, this would trigger the main AC generator, that would sustain the power transfer until the vehicle had moved out of the coil magnetic coupling zone. A relay would then switch the system back to the low-power excitation mode, waiting for the next vehicle interaction to happen.
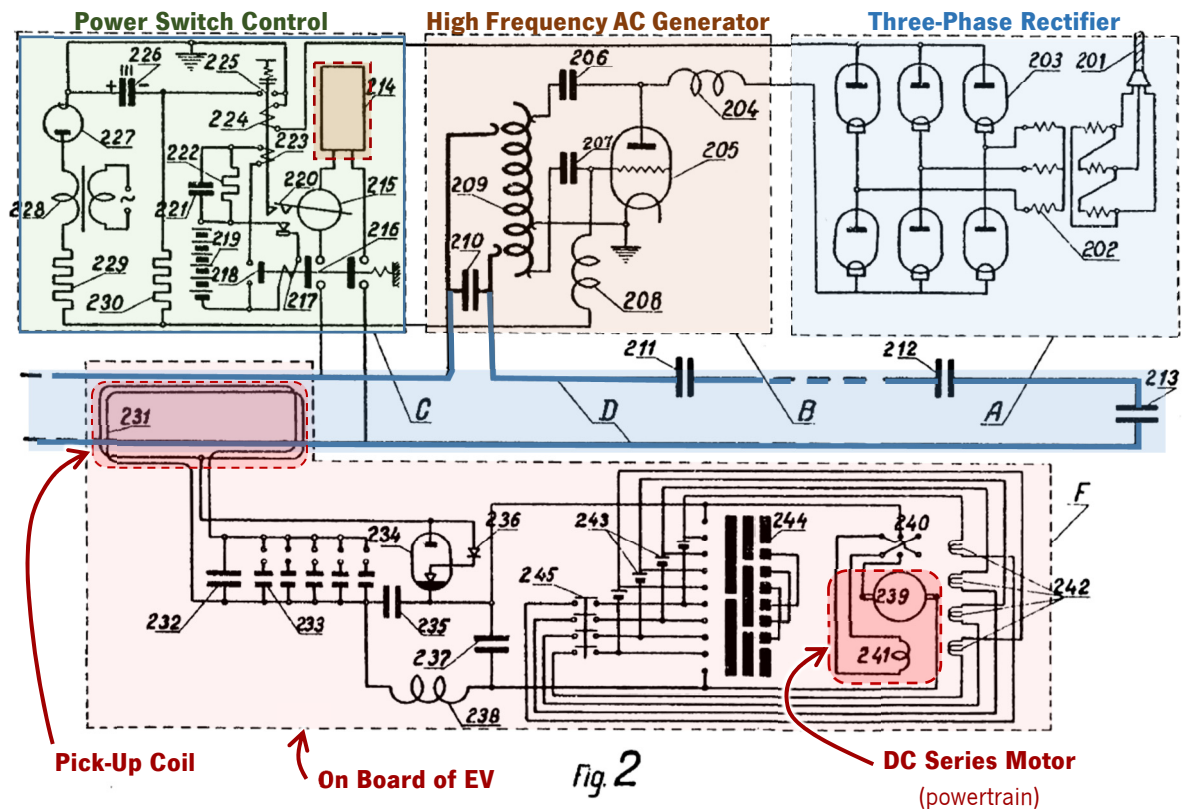
Figure 95: Lane to vehicle inductive coupling in Babat's DIWPT design.

Due to the electronic tube technology used, Babat's first system would only achieve a very low electrical efficiency, of about 4%, what did not make it competitive with other wired electrics and even non-electric transport technologies. This pioneer DIWPT design remained practically forgotten for a few decades more, until referenced by Valtchev et al. [103]. It is known that, later, Babat was able to improve the efficiency of the system, but still, with the widespread adoption of the internal combustion motors after the World War II, electric vehicles in general, and DIWPT in particular, remained of no practical use along the next decades, except for a very few specialized applications.

3.4 Modern Pioneer DIWPT Designs

All the petrol-based transport infrastructure developed during the Second World War would make the EV comparatively much less practical than vehicles with internal combustion engines. Possibly because of that, immediate research efforts towards new EV, batteries and inductive transfer diminished.

Dynamic Inductive Wireless Power Transfer for Lightweight Electric Vehicles
Luiz Alberto Lisboa da Silva Cardoso – University of Minho

155

In the scope of this work, modern designs are then considered to be those conceived after the introduction of solid state power electronics devices.

3.4.1 Bolger's DIWPT Design

In 1974, decades after Babat's experiments, a new DIWPT design was described by John Bolger, from the Lawrence Berkey Laboratory, University of California, in a US patent application, which was granted in 1975 [104]. Bolger did not specifically refer Hutin and Leblanc's or Babat's work, but his design was similar to theirs in its essence and several aspects, as shown in the annotated cross-section of Figure 96 (compare with Hutin and Leblanc's in Figure 85).
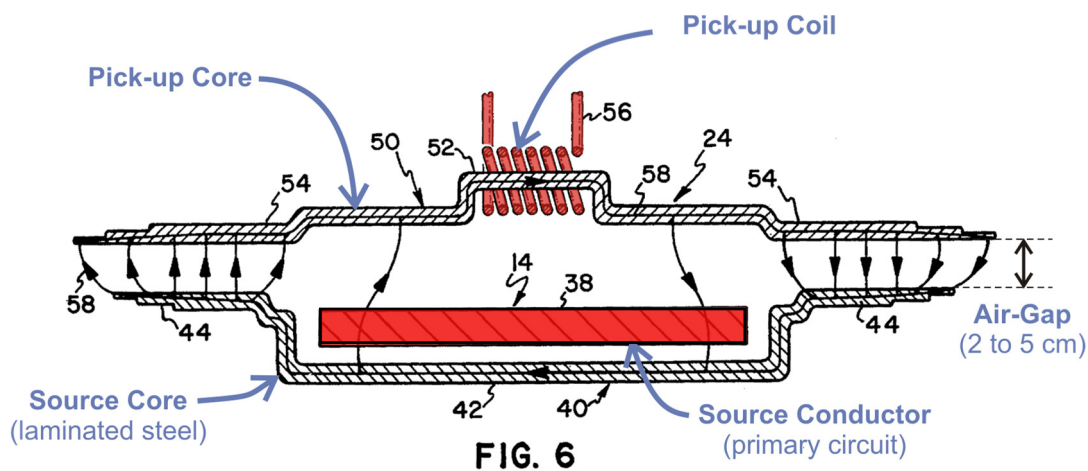
Figure 96: Cross-section of Bolger's design, annotated from Fig. 6 of US patent 3914562.

In addition to using new materials, such as laminated steel for the core sections, and improved solid state components, Bolger introduced core material on the lane side as well and defined shorter air-gap distances of 2 cm to 5 cm (3/4 to 2 inches), to help redirect and better confine the magnetic flux from the source conductor into the pick-up coil.

Instead of using ferrite materials at the pick-up and lane cores, Bolger's down-scale prototypes used laminated steel cores, which would yield improved efficiency values at the lower primary current frequency of 180 Hz. More details about the design can be found in a 1977 report by Bolger and Kirsten [105].

3.4.2 The Roadway Powered Electric Vehicle (RPEV)

Following Bolger's DIWPT, an improved design named Roadway Powered Electric Vehicle (RPEV), was conceived under the auspices of the University of California, Berkeley, and became another milestone in the development of DIWPT systems. A proof-of-concept system was constructed and tested by Systems Control Technology, Inc., Institute of Transportation Studies,

Dynamic Inductive Wireless Power Transfer for Lightweight Electric Vehicles
Luiz Alberto Lisboa da Silva Cardoso – University of Minho

156

PATH (Program for Advanced Transit and Highways) program in 1986 (Lashkari, Shladover, and Lechner 1986). Ultimately, the project goal was to establish the viability of transferring electric energy to the Inductive Coupling System (ICS) of a moving electric bus, from a coil buried beneath the road's surface, in order to overcome the range limitation posed by the need to stop to recharge batteries. This design is fully described in a California Partners for Advanced Transit and Highways' report of 1994 [96] (Systems Control Technology Inc. 1994), and consists of a

(a)   (b)
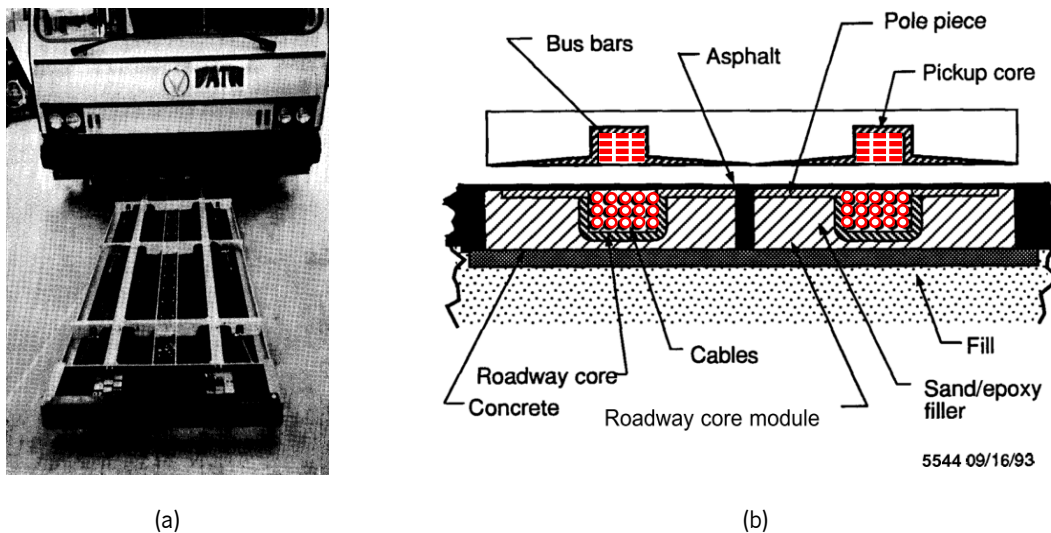
Figure 97. Road Powered Electric Vehicle inductive track and vehicle (a) and ICS cross-section (b).

In the RPEV, the Inductive Coupling System (ICS) was essentially an air-gapped transformer where the primary core and winding was embedded in the road and the secondary core and winding was on-board of the vehicle, as depicted in Figure 6. Two inductive path segments, about 61 m long each, were prototyped and laid along a 213-meters dedicated road section for the tests. An electric bus with a power train of 48 kW was adapted with the ICS. Several combinations of frequencies and primary currents were experimented, an overall DC efficiency of 60% being achieved over an air gap varying from 5 to 10 cm, passing 1200A of alternated current in the primary coil, oscillating at a frequency of 400 Hz. That could be considered a good result, considering the limited performance of solid state devices and ferromagnetic core material used at that time. In fact, the most limiting factor for scaling up the frequency met by the engineering team was not the electronics, but rather, the power losses at the core material and the noise generated by the vibration of laminated core plates in ICS. But the main technical problem found in the RPEV was the low tolerance for lateral misalignment. At 15 cm (6 inches) of lateral displacement from the center lane, the current available to recharge the battery at the required 128 V would almost fall to zero. Because of that, a lateral offset indicator was installed in the cockpit, to help the driver keeping the bus right on the energized path [96].

Dynamic Inductive Wireless Power Transfer for Lightweight Electric Vehicles
Luiz Alberto Lisboa da Silva Cardoso – University of Minho

157

The RPEV was a complete dynamic IPT concept, except that the electronics and materials technology then available was less suitable to the higher frequencies that can be used today. After the final project report of 1994, the system was also apparently forgotten, due to its complexity and cost of implementation.

3.4.3 The Development of DIWPT at University of Auckland

In the 1990's, while the Roadway Powered Electric Vehicle (RPEV) was being developed and evaluated in California, prof. John T. Boys et al, at the University of Auckland, New Zeeland, were starting other pioneer investigation on the use of then called IPT for transport applications [14]. With the focus on industrial applications, a prototype of a small car was built with an embedded pick-up coil that could move along tracks, harvesting energy from an oblong energized coil underneath it, as shown in Figure 98. The first prototype configuration achieved 5W of transferred power, at an efficiency of less than 10%, using a 10 kHz inverter. The prototype was soon improved to handle to 400 to 500 W over the IPT link at 85% efficiency, and the technology eventually was licensed, to Daifuku Company Ltd, in Japan, and later to Wampfler Ag., in Germany, a company that has been commercializing dynamic IPT-based solutions for the industry since then. The theory and principal design aspects of these fixed-track truly dynamic inductive power transfer systems were described in an early 2000 paper by Covic et al. [106].
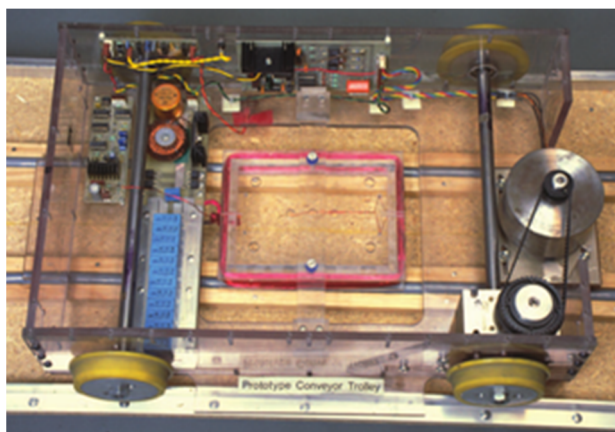
Figure 98: The prototype vehicle implemented by Boys et al., circa 1990, from [14].

This prototype was a remarkable one, for a number of factors. It was one of the first DIWPT prototypes to use higher WPT frequencies, crossing the 10 kHz barrier at significant power levels, so that it was capable of driving the powertrain of the prototype vehicle even without the use of ferromagnetic cores in the magnetic coupling, and still exhibit an electric efficiency above 80%. Second, it is an invaluable demonstration tool for the DWIPT technology, that returned to the use of tracks for mechanical constraint of the vehicle, to keep the alignment of primary and secondary

Dynamic Inductive Wireless Power Transfer for Lightweight Electric Vehicles
Luiz Alberto Lisboa da Silva Cardoso – University of Minho

158

coils, as in the original design of Hutin and Leblanc [93]. In addition, it employed simple solid-state power electronics, which can be easily procured with at a modest budged.

Because of its qualities, in the early phases of this thesis work, similar prototypes were built and evaluated, as described in Chapter 5.

3.4.4 The KAIST OLEV Bus (2008-2013)

Aware of the Roadway Powered Electric Vehicle (RPEV) concept, developed years before in California (see item 3.4.2), researchers from KAIST, the Korea Advanced Institute of Science and Technology, Daejeon, Republic of Korea, designed and implemented a series of WPT systems for standard electric buses, that run with no rails, harvesting energy from oblong coils buried underneath the road. This IWPT based transport system, under the RPEV inspiration, combined the long loop primary coils of the earlier industrial systems from University of Auckland with the stationary IPT-rechargeable buses adapted by Wampfler.

The result was a bus system where, beyond recharging at bus stops and stations, the bus can continuously harvest energy from the system, while running over primary coils. This system was named On-Line Electric Vehicle (OLEV). The first family of OLEV systems was installed in Seoul's Zoo in 2009-2010 tram-buses, as shown in Figure 99, being officially presented to the public in March 2010. The tram was run on a 2.2 km asphalted loop of roadway, of which 370 m (~17%) was electrified by IPT primary coils. The maximum power transmitted was 62 kW at 75% of electrical efficiency.

(a)   (b)

Figure 99: (a) OLEV tram in Seoul and (b) system's primary coil during the installation phase. Source: [107].

In 2013 other improved generations of the OLEV were installed in the cities of Gumi and Daejeon (ROK). These systems can deliver up to 100 kW of power to the bus, at a maximum nominal efficiency in the range of 83% (at perfect alignment condition), over an inter-coil distance

Dynamic Inductive Wireless Power Transfer for Lightweight Electric Vehicles
Luiz Alberto Lisboa da Silva Cardoso – University of Minho

159

of 20 cm. The maximum efficiency is not attained at the maximum power transfer. A maximum lateral vehicle-to-primary-coil misalignment of up to $\pm$20 cm is tolerated, but also at the expense of some loss of efficiency.

Despite these limitations, the system is reported to have favorable results since then. The electric buses when configured as OLEV require a battery that is only one fifth of the capacity of its original battery, thus saving on-board weight and battery cost. The use of this technology, however, is expanding very slowly. Possibly due to the high initial costs of the system. The electrification of those 370 m road in the first version of the system, for instance, is reported to have cost US$550,000.00, that is, approximately US$ 1.5 million per kilometer, besides the cost of the vehicle adaption [107]. Not only the electronic power circuits add cost, but the extensive use of delicate ferrite parts that are mounted along the primary coils. The system installation is now only a few years old, so there is not yet a report on the durability of these road inserted ferrite parts, which lay underneath, but relatively close to the road surface, being prone fracture and erosion, what could possibly degrade the system efficiency as the system ages.

3.4.5 Nissan 1kW Oblong Coil Lane

A simple but very representative DIWPT prototype was built Throngnumchai et al., at Nissan, Japan, in 2013 [108]. In this low power automotive DIWPT configuration, oblong air-cored primary coils were used as WPT transmitters. As a WPT receiver, a circular spiral coil using a ferrite back-plane, shielded with aluminum, was installed in a small two-seater EV. The resulting DIWPT configuration was able to transfer to the EV up to 1.176 kW, through an airgap of 100 mm.

The geometry of the coils is described in Figure 100, where the pair of coils are shown in lateral center-alignment, in top view. The coil drawn in blue is the primary oblong coil, which is excited by a nominal current of approximately 40 A rms at 90 kHz.
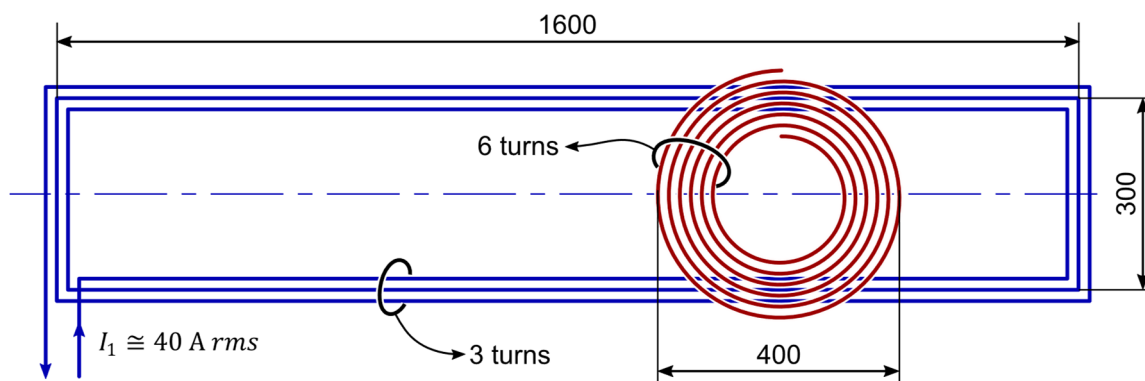
Figure 100: Geometry of primary and secondary coils in Throngnumchai's DIWPT prototype – top view, center aligned. All dimensions in millimeters.

Dynamic Inductive Wireless Power Transfer for Lightweight Electric Vehicles
Luiz Alberto Lisboa da Silva Cardoso – University of Minho

160

The nominal power is achieved with an airgap of 100 mm in between the coils. Since the primary coil lies 30 mm below ground level, the resulting estimated mechanical ground clearance of the secondary coil, when installed onboard of the vehicle, is 70 mm, as shown in Figure 101b

In best alignment conditions (centered on lane), a magnetic coupling factor of 0.09 was obtained. Although it is a low value, an efficiency of 92.8% was attained, due to the use of litz wire in all windings, and careful compensation of both primary and secondary resonant tanks. The Nissan team was able to build a 10 m long demonstration lane, by installing 5 primary coils in sequence, with an inter-coil spacing of approximately 400 mm, as shown in Figure 101a.

(a)   (b)

Figure 101: Nissan 1 kW prototype DIWPT lane under construction (a) and during tests, with the secondary coil installed on board of the New Mobility Concept Car (Renault Twizy). Extracted from [108].

The field tests were reported to be successfully carried on, with the power down-scaled to 50 W, due radio-wave power limits in Japan. This, a priori, seems an excess of carefulness, since for a 40 A rms sinusoidal excitation on the radiation resistance given by (2.3), the expected radiated power at 90 kHz is only about 1 μW per primary coil module.

This project, due to its simplicity, power transfer level, and implementation without the use of ferrite core materials embedded in the lane, can be seen as one of closest antecessors of the HIPLEV lane design. Although its predicted lateral alignment tolerance is low, and so is the estimated ground clearance of the secondary coil.

3.4.6 Oak Ridge National Laboratory In-Motion Wireless Charging

A first interesting conceptual effort towards true dynamic inductive power transfer was made by Omer Onar, John Miller, and others, in 2013-2014, at the Oak Ridge National Laboratory (ORNL), USA. Multiple standard small stationary WPT single coil modules were set in sequence very close to each other, so that a car with a pick-up coil could harvest energy in a pulsed manner,

Dynamic Inductive Wireless Power Transfer for Lightweight Electric Vehicles
Luiz Alberto Lisboa da Silva Cardoso – University of Minho

161

while travelling over the primary coils [109],[110]. In this work, it was particularly studied and demonstrated the benefit of using high capacity ultracapacitors to mitigate the power pulsations posed to the grid, another problem that may inherently arise when coupling power from a series of embedded coils. The experimental configuration is shown in Figure 102, extracted from [110].

Figure 102: The Oak Ridge National Laboratory DIWPT configurations. Photo extracted from [110].

While investigating grid conditioning problems that derive from the dynamic IPT, the ORNL team experiments endorsed that coil alignment was a major, untreated, problem to be surpassed, in order to successfully design dynamic WPT configurations for lane inductive electrification.

3.4.7 Fabric Project (2014-2018)

FABRIC is the acronym for "Feasibility analysis and development of on-road charging solutions for future electric vehicles". In this multi-national team effort, in which 24 partner institutions from 9 European countries were involved, several advances in the study of dynamic inductive wireless power transfer for electric mobility applications were obtained. Along the project, two main DIWPT-electrified prototype 100 m-long road segments, and a third one 50 m-long, were built and tested. Two of them, using replicated oblong primary coil modules, in Susa, Italy, and the other, adapting existing stationary WPT hardware from Qualcomm Halo, in Versailles, France.

In the larger Susa prototype, built by the Polytechnic of Turin on the premises of the "Centro di Guida Sicura MotorOasi Piemonte", about 50 km west of Torino, 50 9-turn 1.5 m x 50 cm rectangular air-cored primary coils were directly embedded in the pavement, resulting in a configuration similar to that used by Throngnumchai et al., in Japan (presented in section 3.4.5), as shown in Figure 103a. In the other prototype, shown in Figure 103b, 64 Qualcomm Halo stationary charging modules, which make extensive use of ferrite materials, were integrated in the

Dynamic Inductive Wireless Power Transfer for Lightweight Electric Vehicles
Luiz Alberto Lisboa da Silva Cardoso – University of Minho

162

road segment by VEDECOM and Qualcomm, in Satory, Versailles, about 30 km west of Paris, resulting in a DIWPT structure similar to the experimental configuration implemented in the Oak Ridge National Laboratory (presented in section 3.4.6).

(a)   (b)
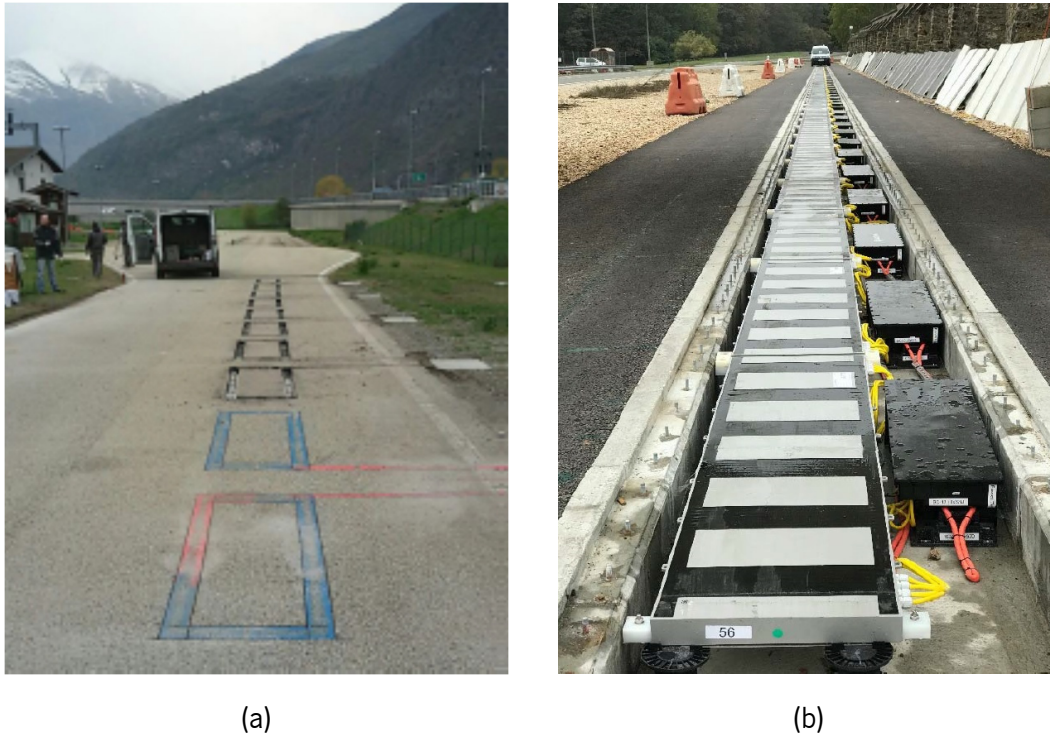
Figure 103: Main FABRIC DIWPT prototype lanes: (a) Oblong coil-based, in Susa, shown in an intermediate construction phase and (b) Qualcomm Halo modules-based, in Versailles, shown fully integrated.

In the Susa prototypes, both primary and secondary (pick-up) coils are rectangular, with the primary coils embedded in the lane being non-ferrite-cored; while the secondary coil uses both a ferrite backplane and an aluminum shield. In the Versailles prototype, all coils are of DD (double-D) type, with ferrite parts in their back, to concentrate the magnetic field, and two 10 kW pick-up pads (secondary coils) per vehicle are used, to achieve a total of 20 kW of transferred power.

The oblong primary coil type lanes (in Susa) were less complex to embed in the road pavement than the multiple ferrite-cored short IWPT modules in the Versailles lane. However, they also exhibited less power transfer capability, for similar airgaps and secondary coil ground clearance [111]. Worthwhile mentioning, while in the Susa prototypes each primary coil model has just one primary coil, each of the primary coil modules used in the Versailles prototype is built from multiple coils in quadrature, in a proprietary solution from Qualcomm Halo. The results of all main configurations achieved are described in [112] and compared in Table 14.

Dynamic Inductive Wireless Power Transfer for Lightweight Electric Vehicles
Luiz Alberto Lisboa da Silva Cardoso – University of Minho

163

Table 14: FABRIC DIWPT lane prototypes compared.

Parameter	Versailles (DD coils) Qualcomm	Susa-1: 9-turn primary coil Politecnico di Torino	Susa-2: Single turn primary coil SAET Italy
Number of Primary Coil Modules	64	46	22
Minimum WPT per Module (kW)	10	6.5	9
Operation Frequency (kHz)	85	85	85
Nominal Airgap (mm)	200	200	200
Maximum test speed (km/h)	100	50	30
Lateral Alignment Width (cm)	30	30	30
Efficiency at nominal airgap	$\leq 60.1\%$	$\geq 81\%$	$\geq 66\%$

The final FABRIC prototype lanes were the first experimental DIWPT lane segments to reach 100 m in length, while capable of simultaneously delivering 20 kW to each of two EVs running on the lane. In their best final configurations, one of the FABRIC prototypes, working with an induction frequency of 85 kHz, was able to transfer 20 kW at 60% efficiency to an EV driving up to 100 km/h, if misalignment from center lane is kept within ±15 cm (30 cm width). But the best efficiency for this same configuration was only 60.1%, at a speed of only 50 km/h. On the Susa-1 prototype an efficiency figure of at least 81% over all lateral alignment width was obtained, but the minimum sustained power was significantly less, and that was obtained at only 50 km/h.

The exact cost per kilometer achieved by the FABRIC DIWPT prototypes is not indicated, but it is presumably higher for that prototype built with ferrite-cored short primary modules (from Qualcomm). The average annual maintenance cost with the simpler DIWPT road segments developed, based on oblong primary coils, is estimated to be between 2.9 and 3.8 more than that of traditional, non-electrified roads. This information is missing or not public for the results derived by VEDECOM in the Versailles prototype, which, similarly to other verification tests of this prototype, are subject to a commercial confidentiality agreement [113].

Overall, there is no clear dominance of performance of one configuration over the others tested. Although containing great advancements over previous DIWPT design efforts, none of the FABRIC prototypes can yet be considered to be uniformly satisfactory on all performance criteria for the use with standard road electric vehicles.

Dynamic Inductive Wireless Power Transfer for Lightweight Electric Vehicles
Luiz Alberto Lisboa da Silva Cardoso – University of Minho

164

3.4.8 ElectReon (2019-2022)

One of the most recent ongoing DIWPT prototypes is that from ElectReon Wireless Ltd., Israel. The company has deployed short pilot road segments in Tel Aviv, and a total of 1.6 km DIWPT road segments along a 4.1 km route, between the airport and town center of Visby on Gotland Island, Sweden [79]. The system is reported to be capable of transferring 20 kW of power, while operating at 88-90% efficiency across an air gap of 24 to 27cm [114], which allows the primary coils to lay at 8 cm underneath the pavement level.

(a)   (b)
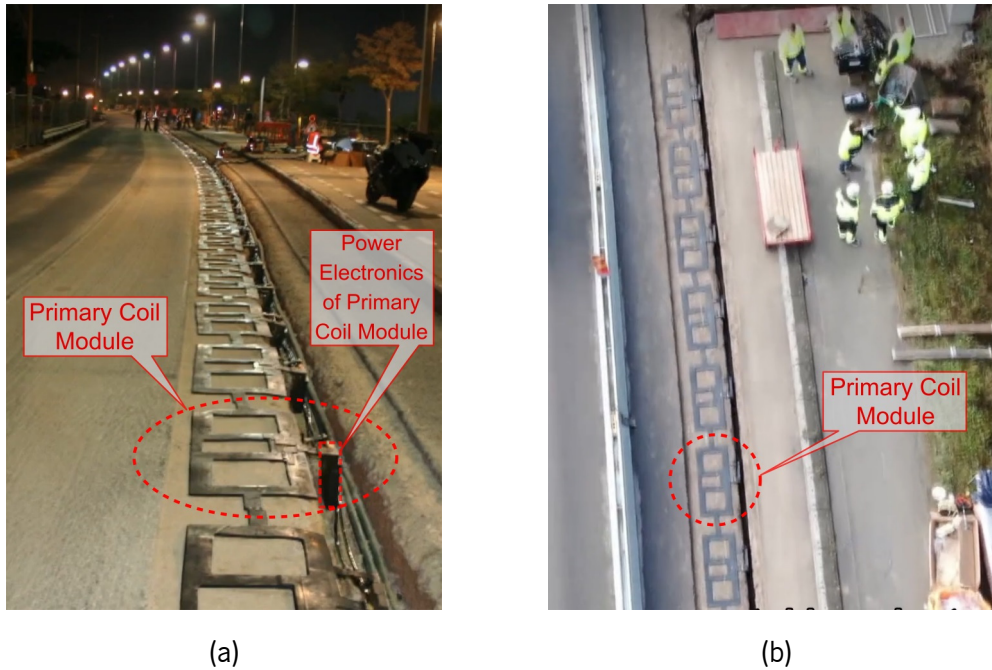
Figure 104: Electreon DIWPT deployments in: (a) Tel Aviv, Israel, annotated from [115] and (b) Gotland, Sweden, annotated from [116].

These prototypes are deemed as commercial pilot projects, and not much information on the coils, their excitation, and other functional details of the system are published, as it is known that the system is being protected by pending patent applications. However, ElectReon has made some information available on their website, including some movies, from which it is possible to have a general idea of its physical configuration and the process of deployment of this DIWPT infrastructure, as shown in Figure 104.

The primary coils are embedded in a rubber seal and apparently contain no ferrite backplanes or other magnetic shaping materials. This eases the installation process and reduces costs. The power electronics uniquely associated to each of the primary coil modules is laid next to the respective primary coil, in a vertical position, on a specially entailed groove along the road. Because of this, these components occupy a smaller footprint on the road and, at the same time, pressure from the above traffic can be alleviated, contributing not to mechanically stress the

components. The groove also serves to pass all individual power cables coming from the management units, which are located on manholes, by the side of the road.

The system installation was finished in 2021 and is currently under evaluation.

3.5   Preliminary Experimentation with DIWPT

Similarly to what has been done in the case of stationary IWPT technology, as part of the process of accumulating practical experience, after reviewing some representative DIWPT works and projects, some hands-on experience was acquired, before approaching the HIPLEV design. DIWPT downscale prototypes were initially built and qualitatively observed. In this section, some of these prototypes are briefly presented, without detailed numeric characterization, with the main conclusions derived from them.

The use of secondary coils as close as possible to oblong primary coils, and the option for making them with about the same width, is notorious in success prototype in the literature, starting with the pioneer work at the University of Auckland [14], discussed in Section 3.4.3. This is intuitively the configuration where relatively better magnetic coupling results, with also good power transfer and efficiency resulting. So, before testing the tools developed in Section 3.6.3, some free experimentation with similar configurations was considered a reasonable first step.

3.5.1 First DIWPT Prototype

In a first DIWPT prototype, a 75 cm × 13.5 cm multi-turn rectangular coil with rounded extremities, as shown in Figure 105a, was built to be used as primary coil. This coil consisted of 38 turns of AWG 22 coil copper magnet wire, exhibiting an inductance of approximately 2 mH and a DC resistance of 3.37 Ω. The AWG 22 wire has a diameter of 0.645 mm,   exhibiting   an   AC resistance just 5% higher than its DC resistance up to approximately 64.1 kHz. So, in order to minimize extraordinary losses due to skin effect, the coil was properly series-compensated and excited with approximately 350 V rms, at 53.7 kHz, making use of a COTS electronic ballast circuit used to drive 30 W fluorescent bulbs. A secondary coil of flat spiral type, with 20 cm of external diameter, was built with 20 turns of cooper wire with a 1.5 mm^2 cross-sectional area, was wound on transparent support sheet of polycarbonate. Its relative size to the primary coils, similarly to Throngnumchai's design [108], was such that the average diameter of the turns was approximately equal to the width of the primary coil, as shown in the photo Figure 105b. The position of the primary coil windings, concealed in a support frame, is indicated by red dashed lines.

Dynamic Inductive Wireless Power Transfer for Lightweight Electric Vehicles
Luiz Alberto Lisboa da Silva Cardoso – University of Minho

166

(a) (b)
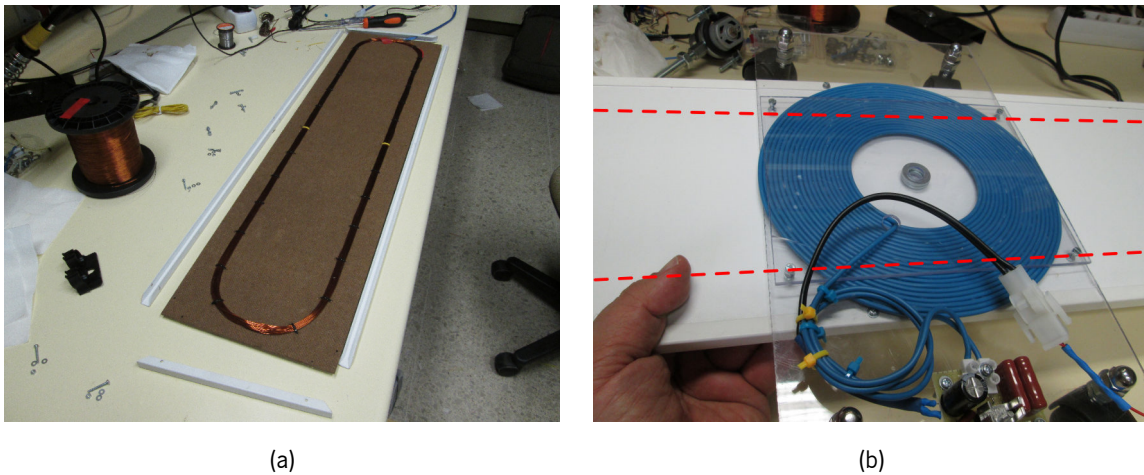
Figure 105: First DIWPT prototype: (a) a multiple-turn oblong primary coil and (b) a multiple-turn flat spiral secondary coil built with about the same average diameter as the primary coil width.

Four wheels were adapted to the polycarbonate sheet serving as the support to secondary coil, to emulate of a small vehicle that could travel over the primary coil assembly, while keeping the primary and secondary coils parallel and approximately 4 cm apart. A series compensation capacitor, a diode bridge rectifier and a filter capacitor were also installed, following the configuration in the diagram of Figure 18. This created an onboard DC-power availability, when this coil was positioned anywhere over the energized primary coil, enough to light up a 12 V 20 W bulb at full bright, as shown in Figure 106a.

(a) (b)
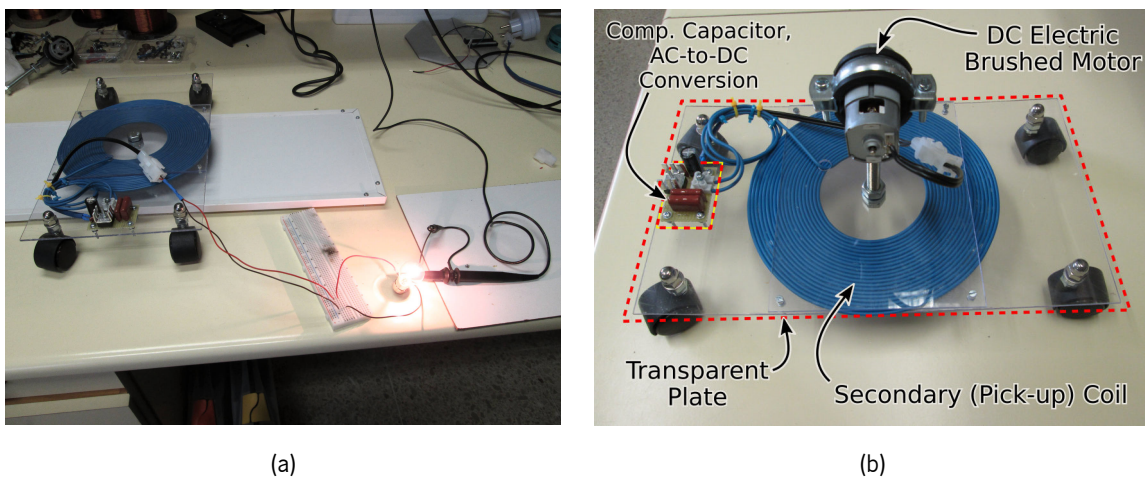
Figure 106: Wheeled secondary coil assembly emulating an electric vehicle: (a) harvesting power along the primary coil to light up a bulb, and (b) shown with its constituent parts, including a geared DC motor.

The light bulb was then disconnected, and the filtered output of the rectifier was connected to instead to a brushed DC motor, rated at 7.2 V, that was installed in a central position on the same polycarbonate sheet, about 12 cm above the secondary coil, as shown in Figure 106b.

Dynamic Inductive Wireless Power Transfer for Lightweight Electric Vehicles
Luiz Alberto Lisboa da Silva Cardoso – University of Minho

167

This simplified conceptual model of a vehicle was then successfully powered along its path over the primary coil when it was manually displaced over the primary coil. The complete configuration is shown in Figure 107a.

(a)   (b)
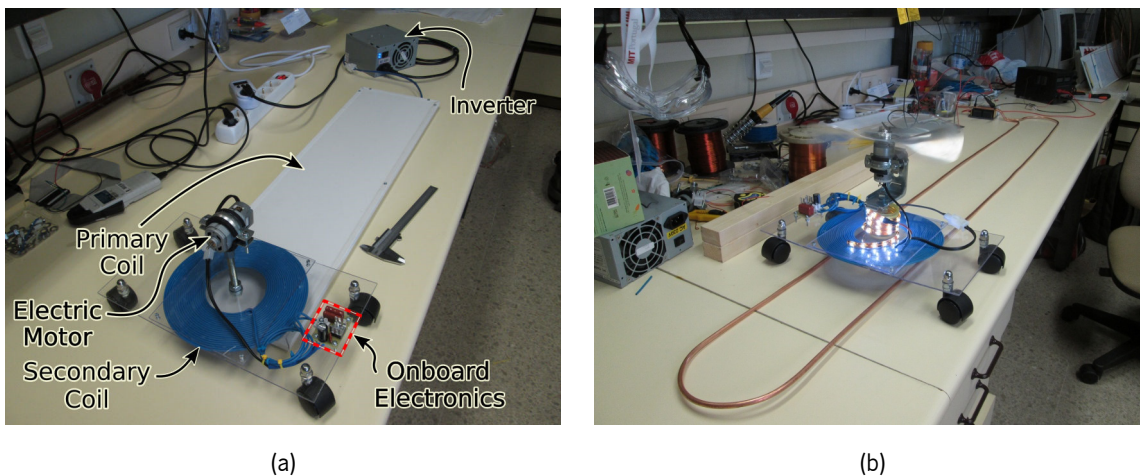
Figure 107: First initial DIWPT prototype: (a) A multiple-turn oblong primary coil and (b) a multiple-turn flat spiral secondary coil built with about the same average diameter as the primary coil width.

The electric motor was very lightly loaded because the output shaft of its gearbox was also unloaded. So, at full DC voltage, the motor speed was very high. For a visually more compelling demonstration and to keep the motor loaded, a 4-blade metallic fan was then connected to the output shaft as a mechanical load, and a LED strip was also connected to the DC output.

After several minutes observing the prototype, it was noticed that a low, very discreet spike sound could occur sporadically. All circuits were then inspected and evaluated, resulting in the discovery that that small spikes were occasionally being generated within the primary coil windings. The reason was that the magnet wire insulation was not rated to handle the high voltage that could develop on the resonating primary coil, up to 700 V -peak, with the motor turning at full power.

Even without detailed quantitative consideration of the problem, it became clear that multi-turn primary coils at the high frequencies required for IWPT are prone to develop high voltages when submitted to higher current levels. This is not only an issue for the circuit implementation, but, also, elevates the electric field intensity in the neighborhood of the primary coil, possibly making it harder for a system to comply with the ICNIRP recommendations for maximum EMF exposure levels (Section 2.11).

Based on the experimentation with this first prototype, and on these considerations about high voltages, the multi-turn design for the primary coil was abandoned, and a new 1.5 m-long, single-turn primary coil was implemented, using a 6 mm-diameter copper tube. This new coil replaced the initial primary coil in the prototype. To drive it, a COTS Mazzilli-Baxandall inverter was

Dynamic Inductive Wireless Power Transfer for Lightweight Electric Vehicles
Luiz Alberto Lisboa da Silva Cardoso – University of Minho

168

used, with the circuit parameters adjusted to excite the primary coil with about the same frequency and total current level as that used with previous primary coil assembly. The final configuration for of this first DIWPT prototype is shown in Figure 107b.

Although an emulated vehicle with no powertrain was used in this first low power prototype, one where the electric motor installed on the secondary would only spin a fan, it brought significant insight on practical aspects of DIWPT systems. In addition to the decision for the preferential use of single-turn primary coils, the criticality of maintaining a constant power availability along the predicted lateral displacement became also evident.

3.5.2 Second DIWPT Prototype

To enhance the practical knowledge in building DIWPT configuration for vehicles, one more prototype for general observation was constructed and tested. This one was a downscaled (1:16) prototype using the model of an existing commercial car the Mitsubishi Racing Lancer, from P&C Toys Co. Ltd., Guangdong, PRC. The powertrain of this model of scaled electric car requires a maximum of 20 W at 6 V DC, being normally powered by $4 \times$ AA 1.5 V batteries. The car comes with a radio control unit, operating in the 27 MHz band, which can command forward and backward movements, left and right turns. The power harvesting adaptation made on the car preserved the RF remote controls receiver and the radio control functionality, which, on board of the car, similarly to the powertrain, was also fed with the power harvested from primary coil.

The primary coil built for this configuration is very similar to that used in the first prototype, described in Section 3.5.1 (Figure 107b), about the same width, but longer. The reference circuit diagram is also that of Figure 18, however, in this case, a linear voltage regulator is used before the powertrain, to regulate the filtered output of the rectifier. To avoid spurious coupling between the energy harvesting circuit and the powertrain, an RF passive filter is installed before the radio receiver power line. The voltage regulator, for better power dissipation, is installed with a heatsink on top of the electric car, as shown in Figure 108a, while the rest of the circuit components, including a series-compensation capacitor, the rectifier bridge, and the filter capacitor, are installed inside the car, on a small PCB. The on-off switch was reconnected in such a manner that the car can be powered by wireless power harvested from with the secondary coil when it is in the OFF position, and can still normally use the energy from the batteries, when the key is ON.

The primary coil single turn winding was built with 6 mm copper tube, and framed in a 2.40 m × 20 cm white faced hardboard sheet, resulting in a coil inductance of approximately

Dynamic Inductive Wireless Power Transfer for Lightweight Electric Vehicles
Luiz Alberto Lisboa da Silva Cardoso – University of Minho

169

4.2 µH. The primary coil was excited by a Mazzilli-Baxandall inverter with 53 V rms at 56.7 kHz, resulting in primary current of approximately 35.8 A rms.

The secondary coil was inserted in the plastic chassis of the car, wound with AWG 22 magnet wire, having the largest possible dimensions still adequate for installation in the car, about 98 mm long and 130 mm wide, as shown in Figure 108b. Its width approximately coincides with the electric width of the primary coil, while the length was the largest possible, constrained to the coil fitting in between the front and rear wheels.

(a)   (b)

(c)   (d)
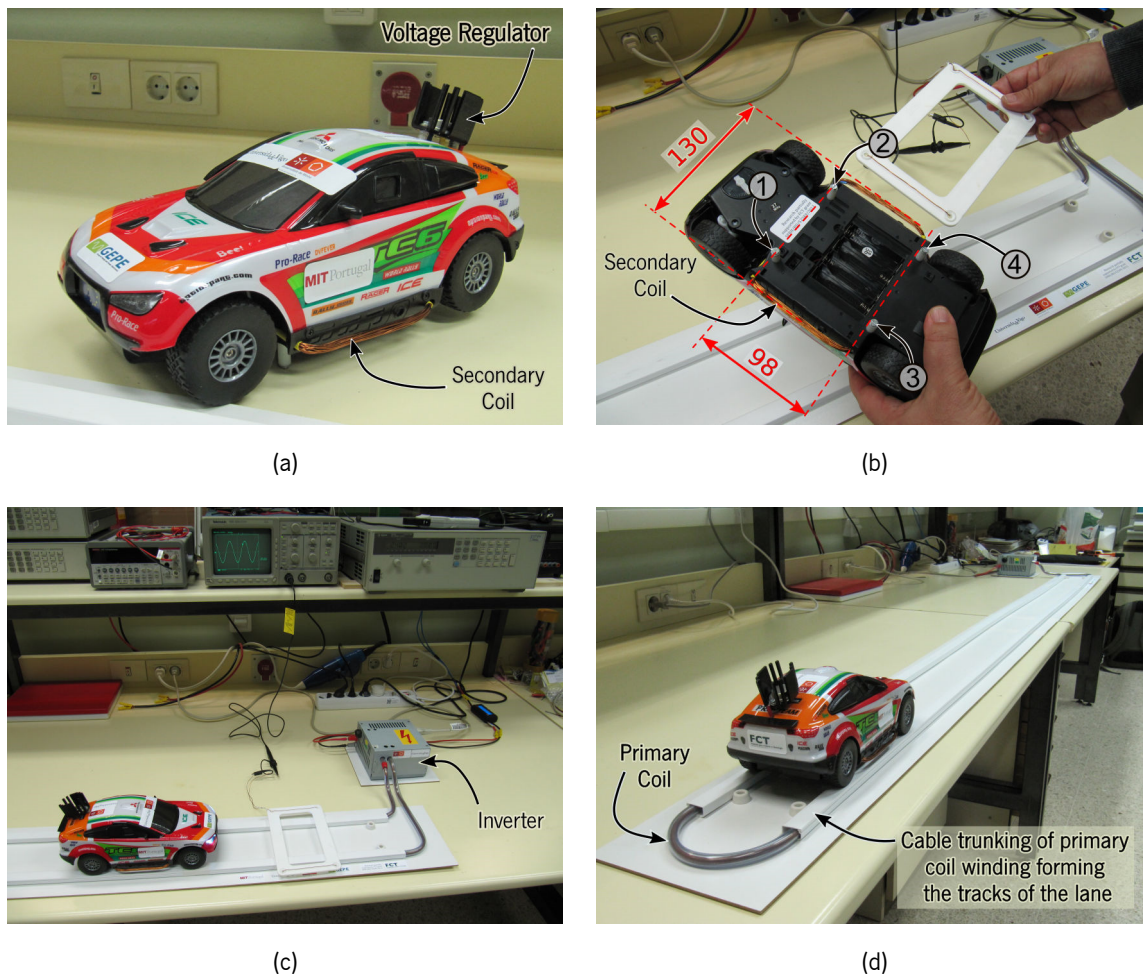
Figure 108: DIWPT prototype using a 1:16 scale electric car on a 2.40 m long × 12.5 cm wide primary coil.

The induced voltage on the secondary coil should be high enough to allow the filtered DC output of the rectifier to sustain the minimum required voltage on the linear voltage regulator (2.5 V +6.0 V), at the required maximum load current, of approximately 2.5 A. On the other hand, if the induced voltage is too high, the voltage drop across the linear voltage regulator would get too high as well, decreasing the efficiency of the system. The number of turns of the secondary coil best safely satisfying the required induced voltage range was then experimentally determined as $N = 19$.

Dynamic Inductive Wireless Power Transfer for Lightweight Electric Vehicles
Luiz Alberto Lisboa da Silva Cardoso – University of Minho

170

Adhesive PVC square cable trunking was used to hold the primary coil conductors in place, and also served as the rails for the car, as shown in Figure 108d. Four cylindrical pins were screwed to the chassis of the car, as indicated in Figure 108b, to restrain the car lateral movement and keep its wheels on the rails, not requiring a skilled pilot for the remote control, when moving car forward or backward over the primary coil.

The prototype, built with the goal of familiarization with the technique, was successfully operated, and contributed to the assimilation of the basic concepts involved in a DIWPT design, but no detailed quantitative behavior characterization was done. Also, there was no concert with ICNIRP recommendation of maximum exposure levels.

Based on multiple qualitative observations made, the following DIWPT design project directives, when using oblong coils, could for to vehicles were reinforced:

(i)   The geometry and dimensions of the vehicle dominates the determination of the shape and dimensions of the secondary coil.

(ii)   After the geometry of the secondary coil is fixed, its width closely defines the ideal width of the primary coil as well, in terms of obtaining the best power transfer level.

(iii)   With both coils parallel to the ground, the vertical distance between the primary and secondary coils should be as low as possible, for obtaining higher induced voltages.

(iv)   Except from resistive losses on the coils and other circuitry, the same power transfer level que can be obtained with more or less secondary coil turns, the difference being the output voltage at which maximum power can be transferred. In this way, the secondary coil also provides means for impedance matching the power train.

(v)   As the induced voltage is proportional to the induction frequency, this latter should be as high as possible, as long as the losses on the coil windings are not excessive, when compared to the power to be transferred. The electronics, on both primary and secondary sides, should be able to safely handle the induction frequency.

(vi)   Once fixed the induction frequency, the selection of the primary coil current and the number of turns of the secondary is joint choice, since they are directly related in the determination of the induced voltage. A too high primary coil current increases the primary winding losses, while a secondary coils of too many turns will have a

Dynamic Inductive Wireless Power Transfer for Lightweight Electric Vehicles
Luiz Alberto Lisboa da Silva Cardoso – University of Minho

171

higher total length, with possibly a smaller cross-section to fit in the same place of installation, so it will exhibit more losses, at the same giver required output current.

(vii)   In a top-down system approach, the detailing of the electronic circuits is not included in the most fundamental design level. The detailed circuit models, while important for the functionality of the system, can be abstracted from the DIWPT design itself, then individually implemented or obtained, to satisfy the required subsystem requirements.

3.6   General Aspects of the DIWPT Design

After reviewing different ideas and some of the most conspicuous prototypes described in the literature, and implementing a few small prototypes, it was possible to recognize some general parameters characterizing and influencing the behavior of a DIWPT system. From the analysis of previously conceived DIWPT systems, provided in sections 3.2 to 3.4, some generalization, and the identification of possible main issues associated with different design options for DIWPT implementations for electric mobility are herein examined.

In DIWPT, beyond seeking for good performance parameters, as in a standard, stationary IWPT design, it is a special matter of concern to obtain some extended positioning tolerance in the relative placement of the receiver (secondary coil). Because it certainly will move. Not only in the operational vicinity of one transmitter (primary coil), but along its travelling path.

Good DIWPT is achieved when the power transferred between primary and secondary coils can have an approximately steady magnitude over the required operational range of relative positioning between these coils. This effect can be obtained by:

- An approximately flat value for the mutual inductance established between primary and secondary coils, which depends on the geometry of the coils and their relative positioning;

- An adaptive electric behavior of primary and secondary circuits, capable of increasing or decreasing the current in one or both windings of the coils, as their mutual inductance varies in the opposite direction; and

- A combination of the above two techniques.

The circuit compensation technique will be able to sustain nominal power transference while the circuit limits are not exceeded, however, even then, the electric efficiency of the IWPT will be compromised when the mutual inductance is decreased. So, the dominant mechanism of a good

Dynamic Inductive Wireless Power Transfer for Lightweight Electric Vehicles
Luiz Alberto Lisboa da Silva Cardoso – University of Minho

172

DIWPT design, whenever possible, should be the stabilization of the mutual inductance in between primary and secondary coils, in the operation zones, which is a matter of geometrical design.

Positioning is usually critical for an optimum magnetic coupling factor, k, which will lead to good power transfer and electrical efficiency in a stationary IWPT application. It is then expectable that k will be averaged in the DIWPT operational region, and thus, worsened, if compared with best alignment stationary IWPT on the same coil geometry and circuit configuration. The main goal for a DIWPT design is then to simultaneously keep the required transmitter power and the average efficiency within acceptable limits, over all intended regions where dynamic relative positioning of receiver and transmitter coils are expected. Part of this effort relays on the circuit design for increased k-insensitiveness, and part, on the design of the geometry of the inductive coupling itself.

3.6.1 Magnetic-Gap

The magnetic gap is the minimum distance between magnetic or conductive components of primary and secondary coils. This distance is often also called air-gap, although it is not always filled by air only. Other mechanical conditions may impose the use of constructive materials in the bodies of the coils, or their fixture to either the vehicle or the lane, which are neither conductive nor magnetic. So, it may be possible that the mechanical free distance between the primary and secondary coils is less than the "air-gap" distance. That is, the magnetic-gap distance may be partially filled with other nonconductive and nonmagnetic materials that are not necessarily air. This is the case, for instance, when a coil has a protective plastic dome over it, or when the primary coil is underneath the ground surface, covered with stones, concrete, asphalt or other similar pavement material that exhibits poor electrical conductivity and magnetic permeability that is close to μ_0, the magnetic permeability of vacuum.

In DWIPT systems, in the same way as in stationary WPT recharging systems, the free mechanical distance between the secondary coil assembly and ground is called ground clearance. If the primary assembly is not completely buried in the ground, then the term ground clearance may alternatively refer to the free distance between the primary and secondary coil assemblies. Depending on the literature considered, the term air-gap may sometimes misleadingly refer to the ground clearance as well. These concepts are illustrated in Figure 109.

Dynamic Inductive Wireless Power Transfer for Lightweight Electric Vehicles
Luiz Alberto Lisboa da Silva Cardoso – University of Minho

173
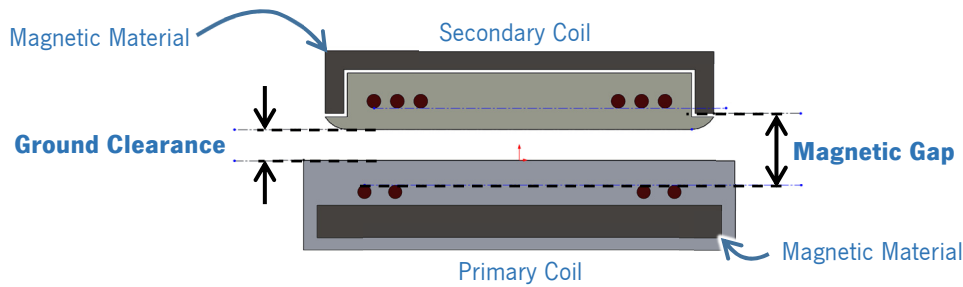
Figure 109: Magnetic gap and ground clearance.

Under the same other conditions, the larger the relative size of the magnetic gap to the major dimensions of the coils, the less will be mutual inductance and the magnetic coupling coefficient in between the two coils. As seen in Chapter 2, Figure 9, the higher the magnetic coupling coefficient, the higher the maximum efficiency level that can be potentially achieved (2.36). Also, the higher the mutual inductance, the higher the power that can be transferred between primary and secondary coils, for given exciting currents, operation frequency and compensation angle (2.7).

Because of that, all DWIPT designs tend to adopt the minimum possible magnetic gap that still satisfies the mechanical constraints of the application, such as sufficient ground clearance, to prevent the secondary assembly to touch the primary assembly (or the ground). As expected in a configuration where relative moment will exist between the coils, this satisfaction must be checked at all stationary and cinematic conditions of the vehicle. In Bolger's design [104], for instance, the pick-up coil can be lowered towards the lane, in order to optimize power transfer and efficiency, according to the road conditions. However, due to the risk of collision of the pick-up coil with the lane, this solution is mostly used in stationary recharging than in DIWPT systems.

3.6.2 Relative Sizes of Primary and Secondary Coils

For taxonomy purposes, and for organization of the analysis, in this work, when both primary and secondary coils in an inductive configuration are of similar size, the configuration will be called short-sized. When one of these coils is much longer than the other, the configuration can be called either long-primary or long-secondary, accordingly. No rigid ratio is stipulated to compare de sizes of the coils, it all depends on the approximations that can be tolerated when computing induced voltages based on the assumption of a constant magnetic field profile along the longer coil in the configuration, what will also depend on the distance of the planes containing the coils. As a practical rule, for monopole coils, one coil will be considered sufficiently longer than other, in the

Dynamic Inductive Wireless Power Transfer for Lightweight Electric Vehicles
Luiz Alberto Lisboa da Silva Cardoso – University of Minho

174

scope of this taxonomy, when it is at least two times longer, as exemplified in Figure 110, where four short secondary coils (in green) harvest power from a long primary coil (in red).
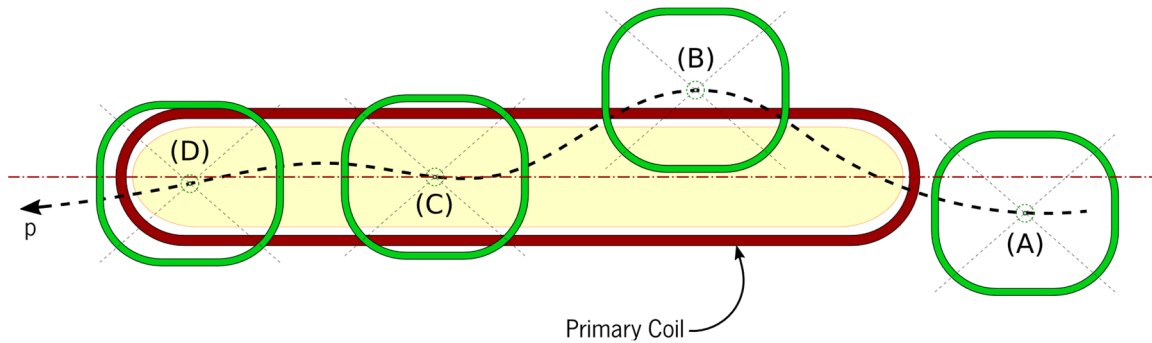
Figure 110: DIWPT over oblong primary coil.

The secondary coils at positions (A), (B), (C) and (D) can either represent four different coils or four different moments of the same secondary coil traveling along the path p. In the first case, the total power transferred by the primary coil will be the sum of powers transferred to each of the secondary coils. While in the second case, with just one secondary coil harvesting, the total power transferred to a single coil can be larger. The coil at position (A) captures only a debile magnetic flux, and is not in good condition to harvest power, it is considered off the lane. The same happens when a coil traversing the primary coil takes position (B), with a large lateral displacement away from the center longitudinal axis of the primary coil. Coils positioned over the yellowish shaded zone, such as (C) and (D), can harvest nominal power. The exact shape and size of the harvesting zone depends not only on the geometry of the coils, but also on the current excitation level of the primary coil and the harvest circuit on the secondary coils. It is one of the main tasks in DIWPT design to establish multiple adequate size harvest zones along the vehicular path, for a given nominal power transfer level.

In DIWPT systems based on long primary coils, the magnetic coupling between neighbor primary coils is intrinsically low, and the inter-primary coil distance can be very small, compared to the length of these coils, with no major concerns about mutual interference. This brings a great simplification to the design.

As a disadvantage, the magnetic coupling coefficient between each short secondary coil and a long primary is also low. When the primary coil is much longer than the secondary coil, in the best case, i.e., with these coils of the same width, in center alignment and very closely positioned on top of each other, the magnetic coupling coefficient k should still be limited to:

Dynamic Inductive Wireless Power Transfer for Lightweight Electric Vehicles
Luiz Alberto Lisboa da Silva Cardoso – University of Minho

175

$$k \leq \sqrt{\frac{\ell_2}{\ell_1}}, \tag{3.78}$$

where ℓ_1 and ℓ_2 are respectively the lengths of primary and secondary coils.

In practice, since k reduces rapidly as the separation distance between coils is increased, it can be much lower than the best-case limit (3.78). If, on the other hand, the system is implemented with short-sized coils, the magnetic coupling coefficient k can approach the unit, if primary and coils are of the exact same size and are positioned very closely on top of each other.

In other words, the use of coils of similar size increases the chances of magnetic flux concentration, under best alignment conditions. Because of that, the peak efficiency of DIWPT systems that are implemented with short-sized coils, depending on the quality factor $Q_F = k\sqrt{Q_1 Q_2}$ (2.34), tends to be higher than those implemented with long coils. The same k-advantage for short-sized coils favors the transmission of higher power levels, at the same current intensity levels.

However, short-sized coils are expected to be laid very close together, to increase the duty-cycle of power transfer, and this also raises concerns about inter-coil interference, which might bring more complexity to the system. In fact, the interaction between neighbor coils is usually carefully designed to reduce the power modulation along the vehicle's path.

Another advantage of short-sized coils is that, provided there is enough power to feed all primary coils simultaneously, the total power transferred to vehicles in a given lane segment length can be higher, for the same power handled per primary coil. This situation can be visualized in Figure 111, where four short-sized primary coils are being energized at the same time, each potentially transferring the nominal power to four different vehicles.
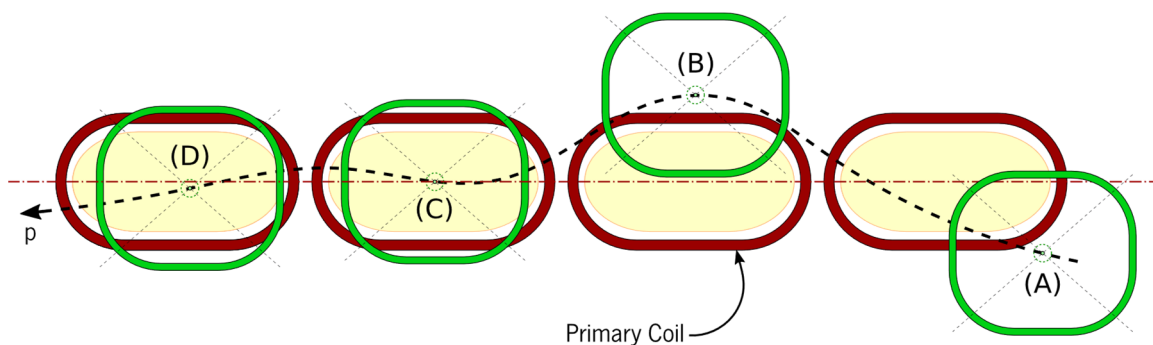
Figure 111: DIWPT over short primary coils.

Dynamic Inductive Wireless Power Transfer for Lightweight Electric Vehicles
Luiz Alberto Lisboa da Silva Cardoso – University of Minho

176

In practice, when short-sized coils are used, the primary coil itself tends to be shorter than the vehicle's length, and when two neighbor primary coils are simultaneously powered on, they are likely serving simultaneously the same secondary coil.

In the last 15 years, projects and prototypes have explored both configurations, long and short-sized coils. Due to the improved efficiency and the possibility of realization of the same power transfer levels at lower currents, there has been an observed tendency of using short-sized coils for automotive DIWPT applications (Section 3.4.8). However, this option comes with an associated higher complexity and cost, which could possibly prevent the widespread adoption of the DIWPT in large scale transport systems.

Long primary coils are also called oblong coils and, as seen in section 3.4, constitute one the most popular early design paradigms, for it minimizes the number of power electronics modules that are required along an electrified route. This reduction in complexity often comes with an associated reduction in costs, and it is a good feature for the popularization of DIWPT systems with lower cost, lower performance vehicles. Because of all these reasons, oblong primary coil systems were considered the preferential approach for the HIPLEV design, exhibiting better potential to match the economical accessibility of these simpler, more sustainable vehicles.

3.6.3 Oblong Primary Coils Lane Design

An oblong object, by definition, is one having a flat rectangular shape, or in a broad sense, an object that is longer than it is wide, with the word oblong itself coming from the Latin neuter form "oblongum", literally meaning "rather long". In English, the use of the term "oblong coil" was seen in technical reports at least as early as in the first half of the 19th Century [117][118], referring to either the mechanical or the corresponding electric parts.

Primary and secondary coils need to have similar widths, to improve power transfer. On the other hand, in DIWPT applications, secondary coils often have lengths and widths of similar magnitude, to capture maximum magnetic flux under the mechanical constraints of vehicular installation. So, when using oblong primary coils in the lane design, the length of oblong primary coil tends to be much larger than the length of the secondary coil. Because of this, the fraction of time spent by a vehicle over some primary coil (duty cycle) can be very high, if the inter-primary coil distances are made much shorter than the length of the primary coils. This simplifies the requirements for onboard energy storage, which is solely used during the transit of the vehicle in between two energized primary coils.

Dynamic Inductive Wireless Power Transfer for Lightweight Electric Vehicles
Luiz Alberto Lisboa da Silva Cardoso – University of Minho

177

In addition, oblong primary coils are specially well suited to drive dynamically i-lanes for lightweight vehicles because of their ability to provide:

Reduction in lane complexity. The number of coils and coil driver circuits (inverters and control logic) that are necessary to configure a lane of a given length is inversely proportional to length of the constituent primary coils. By reducing the number of driver circuits and coils, the complexity of the roadworks to install an inductive lane can also expectably be reduced. Although the average power to be handled by driver circuits will increase by making them drive longer coils, at the lower power levels required for lightweight vehicles, this is not an issue, for the fact that cost of circuitry is not linear with power output, being dominated by its mechanical constitution, at lower power limits.

Reduction of power modulation to vehicles. Long primary coils, when built in monopolar configuration, provide a constant cross-section magnetic pattern to energy-harvesting devices moving along it. This reinforces the quasi-stationary DIWPT behavior of the configuration, as described in 3.1.3. A uniform magnetic profile along the coil also simplifies the circuit necessary to stabilize the voltage on the powertrain (load) of the vehicle.

The main disadvantage of oblong primary coil DIWPT configurations is that, when no ferrites are used in both primary and secondary coils, to shape and concentrate the magnetic flux in between them, the magnetic coupling coefficient tends to be very low. This happens because the secondary coil is often much shorter than the primary coil, and thus, only a small fraction of the magnetic flux created at the primary coil will transverse the secondary coil, even when they are very close. As a consequence of the small magnetic coupling factor, the quality factors of the coils have to be increased, in order to keep a target efficiency value.

Also, the lower magnetic coupling will decrease the voltage induced in the secondary, making it necessary to work with high total equivalent currents on both coils to transfer energy nominal target power levels. The total equivalent current is the current on the coil winding multiplied by the number of turns. If a low number of turns is used, the DC equivalent cross-section of the coil wire has to be increased, and the required current on the driving circuit will be increased. On the other hand, if the number of turns used in the winding is increased, the required driving voltage is also increased. In both cases, more complexity (and cost) is associated with the coil components and the power electronics driving them.

Because of its simplicity, oblong primary coil designs were first addressed and used in DIWPT prototypes, as described in sections 3.4.1 to 3.4.5. Some general recommendations

Dynamic Inductive Wireless Power Transfer for Lightweight Electric Vehicles
Luiz Alberto Lisboa da Silva Cardoso – University of Minho

178

observed by authors, in all these designs, is to keep air gap as small as possible, and to use secondary coils with width that is similar to the width of the primary coil, in order to keep the magnetic coupling factor as high as possible, and weaken the power electronics requirements.

After the OLEV [119] [120] [121], the research community understood that although the oblong primary coil DIWPT concept was simple, its efficient implementation was complex, requiring the extensive use of expensive and mechanically ferrite materials embedded in the lane, and the research interest turned to multiple short primary coil designs.

In this research, the interest in brought back to oblong primary coil based DIWPT design because of the significantly lower power levels required by the traction systems of the lightweight electric vehicles (LEV).

In order to better explore and support the DIWPT design using oblong primary coils without using ferrite materials, a few theorems are derived, aiming the refinement of the general recommendations provided in previous art and research, which, in summary, consist in using primary and secondary coils of similar size, as close as possible.

<u>Lemma 1</u>: The voltage V_{ind} induced on a rectangular coil s, constituted of a single turn of filamentary wire, due to an infinitely long, straight parallel filamentary wire p, carrying a sinusoidal current I_p of constant amplitude and frequency $f_0 = 2\pi\omega_0$, when s is stationary relatively to p and located at distance h from the plane that contains p, is given by:

$$\dot{V}_{ind} = -j\,\mu\,f_0\,\dot{I}_p\,\ell\,\frac{1}{2}\ln\frac{\left(u-\frac{d}{2}\right)^2 + h^2}{\left(u+\frac{d}{2}\right)^2 + h^2}, \qquad (3.79)$$

where:

- $\dot{V}_{ind}$ is the phasor representation of the voltage V_{ind};

- μ is the magnetic permeability of the medium where the conductors are immersed;

- $\dot{I}_p$ is the phasor representing current I_p;

- ℓ is the length of the side of the rectangular coil s which is parallel to the wire p;

- d is the length of the side of the rectangular coil s which is perpendicular to p;

Dynamic Inductive Wireless Power Transfer for Lightweight Electric Vehicles
Luiz Alberto Lisboa da Silva Cardoso – University of Minho

179

- u is the oriented displacement of p relative to center plane of s which perpendicular to the plane of s and parallel to p.

- $j \in \mathbb{C}, j^2 = -1$

By being p a filamentary wire, it is assumed that regarding its effect on other conductors, the current traversing wire p can be considered concentrated on a single line, support of p, analogous happening to the filamentary wire s, which is assumed to only contain a single path where the electric field can be integrated. This assumption will approximate real problems where the distances between conductors are much greater than their diameters. Remarkably, when this assumption does not hold, (3.79) will visibly fail when p excessively approaches one of the conductors which are the parallel to p sides of the rectangular coil s. That is, expression (3.79) clearly diverges to infinity when, simultaneously, $h \rightarrow 0$ and either $u \rightarrow d/2$ or $u \rightarrow -d/2$, while it is known from experimentation that, in this case, the induced voltage V_{ind} approaches the voltage across the segment of p with length ℓ that is closest to s.

Proof of Lemma 1: For the visualization of the geometry involved in the problem, let us start by considering the cross-section of this configuration where p is inducing voltage in coil s, as shown in Figure 112, where the above linear dimensions are indicated, except ℓ, which is taken perpendicular to the cross-section.
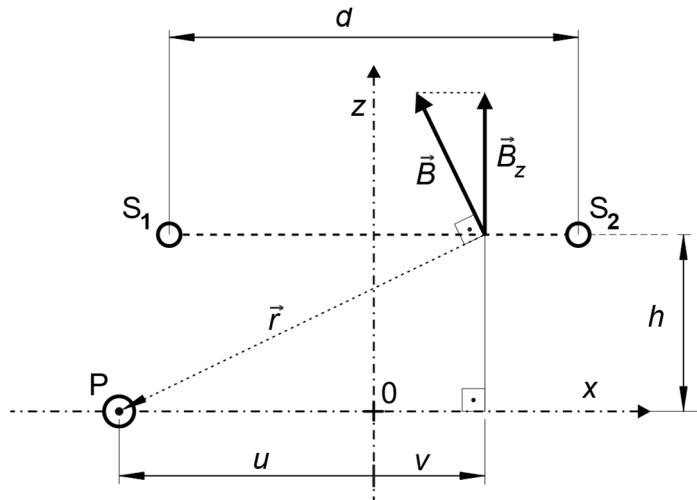
Figure 112: Reference cross-section for lemma 1.

Let S_1, S_2 and P be respectively the points where coil s and wire p intercept this cross-section. Let $\vec{B}$ be the magnetic field generated by $\dot{I}_p$ flowing on p, and $\dot{B}_z$ its complex scalar component on axis z, which is perpendicular to the plane containing s.

Dynamic Inductive Wireless Power Transfer for Lightweight Electric Vehicles
Luiz Alberto Lisboa da Silva Cardoso – University of Minho

180

In order to compute the induced voltage on s, it can used Maxwell's equation of Faraday's Law to express the induced voltage as the time derivative of the magnetic flux traversing coil s:

$$V_{ind} = \oint_s \vec{E} \cdot \vec{ds} = -\frac{d}{dt} \int_A \vec{B} \cdot \vec{dA},$$

(3.80)

where $\vec{E}$ is the electric field induced on the path corresponding to the thin wire coil s, $\vec{ds}$ is the differential element of the path of s, A is the rectangular surface enclosed by s, and $\vec{dA}$ its oriented differential area element.

Expression (3.80) can be rewritten using phasors, and considering the existing planar symmetry of $\vec{B}$ due to the infinite length of p, leading to:

$$\dot{V}_{ind} = -\frac{d}{dt} \int_{-\frac{d}{2}}^{\frac{d}{2}} \dot{B}_z \, \ell \, dv$$

(3.81)

Considering no relative movement of the coil s with respect to the wire p, the magnetic flux on s is only a function of the time, so:

$$\dot{V}_{ind} = -\int_{-\frac{d}{2}}^{\frac{d}{2}} \frac{d}{dt} \dot{B}_z \, \ell \, dv = -j\omega\ell \int_{-\frac{d}{2}}^{\frac{d}{2}} \dot{B}_z \, dv$$

(3.82)

For an infinitely long thin wire p, the magnetic field $\vec{B}$ on any point of space is perpendicular to p, thus contained in the plane parallel to the cross-section, being tangential to a circle of radius r centered at P passing on that point of space, with complex magnitude given by:

$$\dot{B} = \frac{\mu \dot{I}_p}{2\pi r}$$

(3.83)

It can be observed that:

$$\dot{B}_z = \dot{B} \cos\theta = \frac{\mu \dot{I}_p}{2\pi r} \frac{(v-u)}{r} = \frac{\mu \dot{I}_p}{2\pi} \frac{(v-u)}{h^2 + (v-u)^2}$$

(3.84)

Combining (3.82) and (3.84), and considering that $\omega = 2\pi f_0$:

Dynamic Inductive Wireless Power Transfer for Lightweight Electric Vehicles
Luiz Alberto Lisboa da Silva Cardoso – University of Minho

181

$$\dot{V}_{ind} = -j\,\mu\,f_0\,\dot{I}_p\,\ell \int\limits_{-\frac{d}{2}}^{\frac{d}{2}} \frac{(v-u)}{h^2+(v-u)^2}\,dv \qquad (3.85)$$

The integral in (3.85) can be calculate substitution, using r again:

$$r = \sqrt{h^2+(v-u)^2} \qquad (3.86)$$

$$\Rightarrow r\frac{dr}{dv} = (v-u) \qquad (3.87)$$

$$\dot{V}_{ind} = -j\,\mu\,f_0\,\dot{I}_p\,\ell \int\limits_{\sqrt{\left(u+\frac{d}{2}\right)^2+h^2}}^{\sqrt{\left(u-\frac{d}{2}\right)^2+h^2}} \frac{1}{r}\,dr\,, \qquad (3.88)$$

that can be integrated as:

$$\dot{V}_{ind} = -j\,\mu\,f_0\,\dot{I}_p\,\ell\,\frac{1}{2}\left(\ln\left(\left(u-\frac{d}{2}\right)^2+h^2\right) - \ln\left(\left(u+\frac{d}{2}\right)^2+h^2\right)\right), \qquad (3.89)$$

which is an equivalent expression to (3.79), q.e.d.

In stationary IWPT (and, by approximation, in quasi-stationary DIWPT), the problem of calculating the induced voltage is equivalent to the calculation of the mutual inductance between the rectangular coil and the infinitely long parallel wire. A trivial case of Lemma 1, whereas $h = 0$, often referred in textbooks [122], is illustrated in Figure 113.
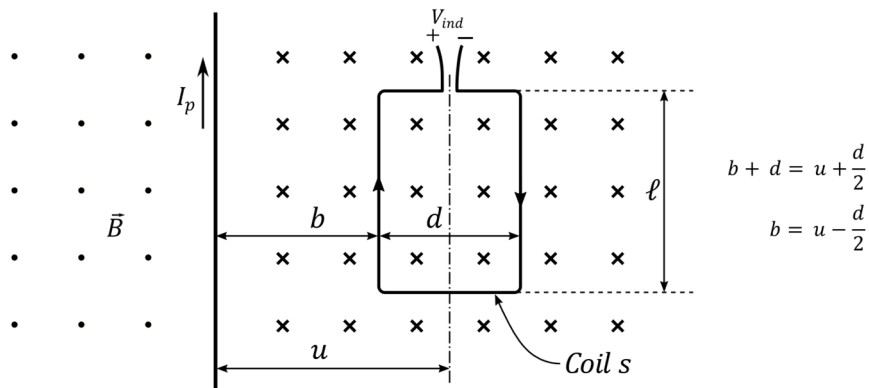
Figure 113: Trivial case of Lemma 1 with $h = 0$.

In this case, the magnetic flux traversing coil s (into the paper), Φ_s, is given by [122]:

Dynamic Inductive Wireless Power Transfer for Lightweight Electric Vehicles
Luiz Alberto Lisboa da Silva Cardoso – University of Minho

182

$$\Phi_s = \mu I_p \, \ell \, \frac{1}{2\pi} \ln \frac{b+d}{b} \, , \tag{3.90}$$

leading to the calculation of $\dot{V}_{ind}$:

$$\dot{V}_{ind} = j \, \mu \, \omega_0 \, \dot{I}_p \, \ell \, \frac{1}{2\pi} \ln \frac{b+d}{b} = -j \, \mu \, f_0 \, \dot{I}_p \, \ell \ln \frac{u - \dfrac{d}{2}}{u + \dfrac{d}{2}} \, , \tag{3.91}$$

which is consistent with (3.79) when $h = 0$.

Noticeably, the obtained expression for $\dot{V}_{ind}$ in Lemma 1 (3.79) is implicitly associated with the reference polarity of the terminals of coil s, where the right-hand rule is used for the closed curve integration of the induced electric field on s. Considering the geometry in Figure 112, the real and imaginary parts of current $\dot{I}_p$ are positive when coming out of paper, and $\dot{V}_{ind}$ expresses the differential electric potential $V_1 - V_2$, between the left (S_1) and right (S_2) terminals of s, seen from the front of the paper, when s is at open circuit condition. If the polarity convention is reverse direction, that is, measuring $V_1 - V_2$, V_{ind} would alternatively be given by the phasor $\dot{V}_{-ind}$:

$$\dot{V}_{-ind} = j \frac{\mu \, f_0 \, \dot{I}_p \, \ell}{2} \ln \frac{\left(u - \dfrac{d}{2}\right)^2 + h^2}{\left(u + \dfrac{d}{2}\right)^2 + h^2} = -j \frac{\mu \, f_0 \, \dot{I}_p \, \ell}{2} \ln \frac{\left(u + \dfrac{d}{2}\right)^2 + h^2}{\left(u - \dfrac{d}{2}\right)^2 + h^2} \tag{3.92}$$

In (3.79), it is still possible to factorize $\dot{V}_{ind}$ as:

$$\dot{V}_{ind} = -j \, \mu \, f_0 \, \dot{I}_p \, \ell \, g(u, h, d) \, , \tag{3.93}$$

where g is function of the geometry of the cross-section of the physical problem:

$$g(u, h, d) = \frac{1}{2} \ln \frac{\left(u - \dfrac{d}{2}\right)^2 + h^2}{\left(u + \dfrac{d}{2}\right)^2 + h^2} \tag{3.94}$$

The expression $\mu f_0 \dot{I}_p \ell$ depends on physical parameters which are not related to the geometry of its cross-section and assumed to be constant. So, for simplicity, it makes sense to interpret $g(u, h, d)$ as a normalized induced voltage, defined by real-valued phasor:

$$\dot{G}_{ind} = \frac{\dot{V}_{ind}}{-j \, \mu \, f_0 \, \dot{I}_p \, \ell} = g(u, h, d) \, , \tag{3.95}$$

Dynamic Inductive Wireless Power Transfer for Lightweight Electric Vehicles
Luiz Alberto Lisboa da Silva Cardoso – University of Minho

183

Having $h > 0$ and $d > 0$ as constant parameters, g can be momentarily redefined as a function of u only, and verified to be anti-symmetric, i.e., for all $u \in \mathbb{R}$:

$$g(-u) = -g(u), \tag{3.96}$$

Also, it can be noticed that g can be expressed as a multiplication of two functions, g_1 and g_2 that are each the composition of functions namely, $[\ln x]$, $[x^2]$, $[x^2 + h^2]$, $\left[x - \dfrac{d}{2}\right]$ and $\left[x + \dfrac{d}{2}\right]$, that are continuous and continuously n-differentiable in their domains, for all order $n \geq 1$:

$$g(u) = g_1(u) * g_2(u), \tag{3.97}$$

where:

$$g_1(u) = [\ln x] \circ [x^2] \circ [x^2 + h^2] \circ \left[x - \frac{d}{2}\right](u), \tag{3.98}$$

$$g_2(u) = [\ln x] \circ [x^2] \circ \left[\frac{1}{x}\right] \circ [x^2 + h^2] \circ \left[x + \frac{d}{2}\right](u) \tag{3.99}$$

Also, the image of each function in the chain composing both g_1 and g_1 is contained in the domain of the following function in the chain that takes the output of the former as its input. Then $g(u)$ is also n-differentiable in $\mathbb{R}$, and from (3.103) it follows that:

$$\left.\frac{\partial^n g}{\partial u^n}\right|_{-u} = -(-1)^n \left.\frac{\partial^n g}{\partial u^n}\right|_u \tag{3.100}$$

and thus:

$$\left.\frac{\partial^{2n-1} g}{\partial u^{2n-1}}\right|_u = -\left.\frac{\partial^{2n-1} g}{\partial u^{2n-1}}\right|_u, \quad n \geq 1 \tag{3.101}$$

$$\left.\frac{\partial^{2n} g}{\partial u^{2n}}\right|_{u=0} = -\left.\frac{\partial^{2n} g}{\partial u^{2n}}\right|_{u=0} \Rightarrow \left.\frac{\partial^{2n} g}{\partial u^{2n}}\right|_{u=0} = 0, \quad n \geq 1 \tag{3.102}$$

By developing $\partial g / \partial u$ and $\partial^3 g / \partial u^3$ it can be found that:

$$\left.\frac{\partial g}{\partial u}\right|_{u=0} = -\frac{4d}{d^2 + 4h^2}, \tag{3.103}$$

Dynamic Inductive Wireless Power Transfer for Lightweight Electric Vehicles
Luiz Alberto Lisboa da Silva Cardoso – University of Minho

184

$$\left.\frac{\partial^3 g}{\partial u^3}\right|_{u=0} = -\frac{32d(d^2 - 12h^2)}{(d^2 + 4h^2)^3}$$ (3.104)

Considering equations (3.108) to (3.104), the Taylor expansion of g to the fourth order, at the vicinity of the center of coil s, which is at $u = 0$, with h and d fixed, it is possible to approximate $g(u, h, d)$ by:

$$g(u, h, d) \cong -\frac{4d}{d^2 + 4h^2} u - \frac{16d(d^2 - 12h^2)}{3(d^2 + 4h^2)^3} u^3$$ (3.105)

So, given that second and the fourth derivatives of g are already zero at $u = 0$, the dependence of the induced voltage g on the lateral displacement u, in the vicinity of the center of coil s, will be maximally linearized when the third derivative of g, given by (3.104), is also zero at $u = 0$. This happens when:

$$d^2 - 12h^2 = 0$$ (3.106)

$$\Rightarrow \frac{h}{d} = \frac{1}{2\sqrt{3}} = \gamma_h$$ (3.107)

In Figure 114, the normalized induced voltage $g(u, h, d)$ is plotted as a function of the normalized displacement $2u/d$, for different ratios h/d, emphasizing the case where best linearity response is found, when $h/d = \gamma_h$.
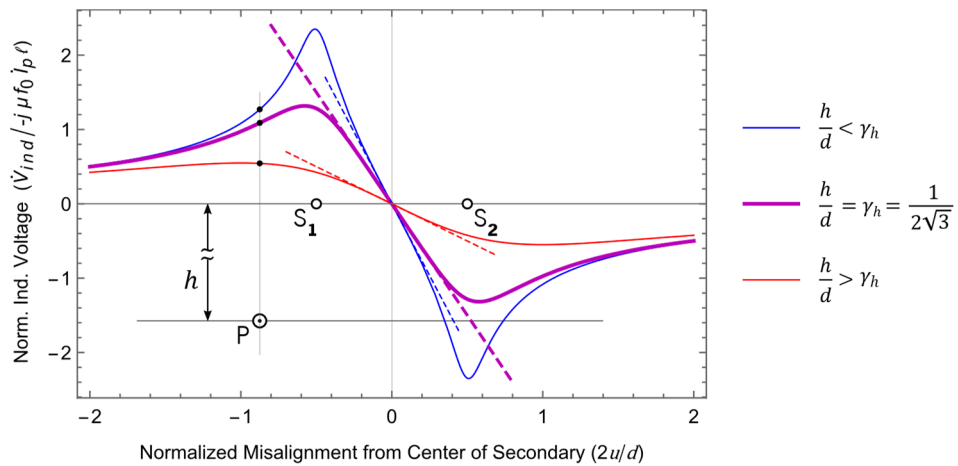
Figure 114: Profile of voltage induced on coil s by a single wire p at distance h.

It can be also observed in Figure 114 that the curves corresponding to the normalized induced voltage, and thus to the induced voltage itself, exhibit maximum and minimum at distances to the center of coils that should be equal, except to the signal, what is due to symmetric

Dynamic Inductive Wireless Power Transfer for Lightweight Electric Vehicles
Luiz Alberto Lisboa da Silva Cardoso – University of Minho

185

nature of the configuration. These points of maximum and minimum, which appear to depart from the center of s as the ratio h/d is increased, are the matter of the following Lemma 2.

Lemma 2: Given a rectangular coil s and a parallel wire p, under the same assumptions and parameters described for Lemma 1, the maximum and the minimum induced voltages on s are obtained when the oriented displacement of p relative to center plane of s, which is perpendicular to the plane containing s and parallel to p, are respectively given by:

$$u_{max} = -\frac{1}{2}\sqrt{d^2 + 4h^2} \tag{3.108}$$

$$u_{min} = +\frac{1}{2}\sqrt{d^2 + 4h^2} \tag{3.109}$$

Proof of Lemma 2: For the visualization of the geometry involved in the problem, Figure 112, used in Lemma 1 is equally applicable. Referring to expression (3.93), it can be realized that the maximization or minimization of $\dot{V}_{ind}$ is respectively obtained by maximization or minimization of the function g with respect to the oriented distance u. This is done by requiring:

i) For the maximum:

$$\frac{\partial g}{\partial u} = 0 \quad \wedge \quad \frac{\partial^2 g}{\partial u^2} < 0 \tag{3.110}$$

ii) For the minimum:

$$\frac{\partial g}{\partial u} = 0 \quad \wedge \quad \frac{\partial^2 g}{\partial u^2} > 0 \tag{3.111}$$

Developing the expressions in (3.110) and (3.111):

$$\frac{\partial g}{\partial u}(u,h,d) = -\frac{4d(d^2 + 4h^2 - 4u^2)}{(4h^2 + (d-2u)^2)(4h^2 + (d+2u)^2)} \tag{3.112}$$

$$\frac{\partial^2 g}{\partial u^2}(u,h,d) = \frac{32du(16h^2(d^2 + 4h^2 + 4u^2) - AB)}{A^2 B^2} \tag{3.113}$$

where:

$$A = 4h^2 + (d-2u)^2 > 0 \tag{3.114}$$

Dynamic Inductive Wireless Power Transfer for Lightweight Electric Vehicles
Luiz Alberto Lisboa da Silva Cardoso – University of Minho

186

$$B = 4h^2 + (d + 2u)^2 > 0 \tag{3.115}$$

Requiring $\partial g / \partial u = 0$ implies in solving the equation:

$$d^2 + 4h^2 - 4u^2 = 0, \tag{3.116}$$

which gives the two solutions:

$$q_1 = -\frac{1}{2}\sqrt{d^2 + 4h^2}, \tag{3.117}$$

$$q_2 = +\frac{1}{2}\sqrt{d^2 + 4h^2}, \tag{3.118}$$

Evaluating $\partial^2 g / \partial u^2$ at q_1 and q_2 results in:

$$\frac{\partial^2 g}{\partial u^2}(u_1, h, d) = -\frac{256\, d\, h^2 (d^2 + 4h^2)^{3/2}}{A^2 B^2} < 0 \tag{3.119}$$

$$\Rightarrow u_{max} = q_1 = -\frac{1}{2}\sqrt{d^2 + 4h^2} \tag{3.120}$$

and

$$\frac{\partial^2 g}{\partial u^2}(u_2, h, d) = \frac{256\, d\, h^2 (d^2 + 4h^2)^{3/2}}{A^2 B^2} > 0 \tag{3.121}$$

$$\Rightarrow u_{min} = q_2 = +\frac{1}{2}\sqrt{d^2 + 4h^2} \tag{3.122}$$

Expressions for the displacements of p that maximize and minimize the induced voltage on coil s, given by (3.120) and (3.122), respectively coincide with (3.108) (3.109), q.e.d.

A direct application of either Lemma 1 or Lemma 2 to the design of a DIWPT configuration is not likely, because a primary coil is not usually formed of a single conductor. However, based on these lemmata, it is possible do easily derive the expression of induced voltage on rectangular coil over an oblong primary coil, and some useful relations involving optimal dimensional parameters, which is of interest for designing DIWPT configurations using oblong coils.

Theorem 1: The voltage V_{ind} induced by a stationary, infinitely long coil p, constituted of a single turn of a filamentary wire carrying a sinusoidal current I_p of constant amplitude and

Dynamic Inductive Wireless Power Transfer for Lightweight Electric Vehicles
Luiz Alberto Lisboa da Silva Cardoso – University of Minho

187

frequency $f_0 = 2\pi\omega_0$, on a parallel rectangular coil s, relatively stationary to p and also constituted of a single turn of a filamentary wire, that is located on a plane that is parallel to the plane that contains p, at a distance h to that plane, is given by:

$$\dot{V}_{ind} = -j\,\mu\,f_0\,\dot{I}_p\,\ell\,\xi(x,h,d,D)\,, \tag{3.123}$$

with the real function ξ, given by:

$$\xi(x,h,d,D) = \frac{1}{2}\ln\frac{\left(\left(x+\dfrac{D+d}{2}\right)^2+h^2\right)\left(\left(x-\dfrac{D+d}{2}\right)^2+h^2\right)}{\left(\left(x+\dfrac{D-d}{2}\right)^2+h^2\right)\left(\left(x-\dfrac{D-d}{2}\right)^2+h^2\right)}\,, \tag{3.124}$$

where:

- $\dot{V}_{ind}$ is the phasor representation of the voltage V_{ind};

- μ is the magnetic permeability of the medium where the conductors are immersed;

- $\dot{I}_p$ is the phasor representing current I_p;

- ℓ is the length of the side of the rectangular coil s which is parallel to the wire p;

- D is the width of the infinitely long coil p, i.e., the distance between its two conductors;

- d is the length of the side of the rectangular coil s which is perpendicular to p;

- x is the oriented displacement of the projection of the longitudinal axis of s on the plane of p to the longitudinal axis of p (if p and s are contained in horizontal planes, x is the lateral misalignment between these coils).

- $j \in \mathbb{C},\, j^2 = -1$

Again, the term filamentary wire is used here in the same sense and with the same assumptions as used for lemmata 1 and 2.

Proof of Theorem 1: For the visualization of the geometry involved in the problem, let's start by considering a cross-section of this configuration where coil p is inducing voltage in coil s, as shown in Figure 115, with equivalently defined parameters as in Figure 112, where S_1.

Dynamic Inductive Wireless Power Transfer for Lightweight Electric Vehicles
Luiz Alberto Lisboa da Silva Cardoso – University of Minho

188
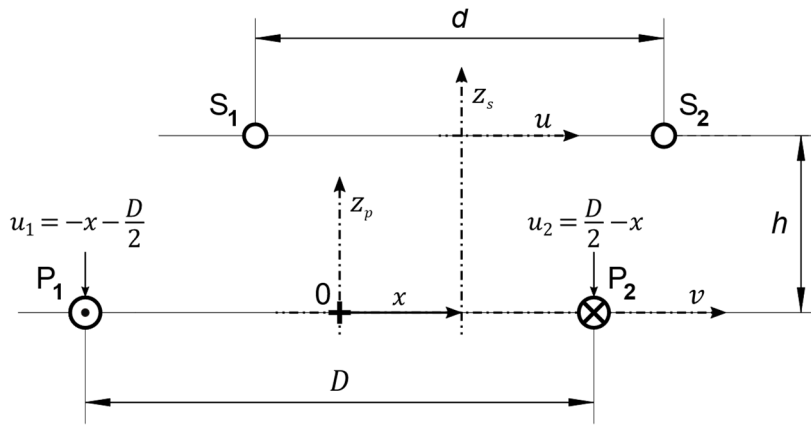
Figure 115: Cross-section of the inductive configuration formed by coils p and s.

Applying the superposition principle to the magnetic fields generated by the currents traversing the two wires of coil p, it can be derived that induced the total induced voltage will be the sum of the two voltages separately induced by currents I_p, flowing out of the paper at P_1, and inwards at P_2, which is equivalent to a current $-I_p$ flowing out of the paper. Then, from Lemma 1, it is possible to use (3.93) twice, adding up the voltages induced on s by the conductor of p at P_1, $\dot{V}_1$, and by the conductor of p at P_2, $\dot{V}_1$:

$$\dot{V}_1 = -j\,\mu\,f_0\,\dot{I}_p\,\ell\,g(u_1, h, d) \tag{3.125}$$

$$\dot{V}_2 = -j\,\mu\,f_0(-\dot{I}_p)\,\ell\,g(u_2, h, d) \tag{3.126}$$

$$\dot{V}_{ind} = \dot{V}_1 + \dot{V}_2 = -j\,\mu\,f_0\,\dot{I}_p\,\ell\,\left(g\left(-x-\frac{D}{2}, h, d\right) - g\left(\frac{D}{2}-x, h, d\right)\right) \tag{3.127}$$

Applying (3.94) to expand the function g, (3.127) becomes:

$$\dot{V}_{ind} = -j\,\mu f_0\dot{I}_p\ell\,\frac{1}{2}\left(\ln\frac{\left(-x-\frac{D}{2}-\frac{d}{2}\right)^2 + h^2}{\left(-x-\frac{D}{2}+\frac{d}{2}\right)^2 + h^2} - \ln\frac{\left(\frac{D}{2}-x-\frac{d}{2}\right)^2 + h^2}{\left(\frac{D}{2}-x+\frac{d}{2}\right)^2 + h^2}\right) \tag{3.128}$$

Reorganizing the terms of (3.128), results in:

$$\dot{V}_{ind} = -j\,\mu f_0\dot{I}_p\ell\,\frac{1}{2}\ln\frac{\left(\left(x+\frac{D+d}{2}\right)^2 + h^2\right)\left(\left(x-\frac{D+d}{2}\right)^2 + h^2\right)}{\left(\left(x+\frac{D-d}{2}\right)^2 + h^2\right)\left(\left(x-\frac{D-d}{2}\right)^2 + h^2\right)}, \tag{3.129}$$

which is can be decomposed in expressions (3.123) and (3.125), q.e.d.

Dynamic Inductive Wireless Power Transfer for Lightweight Electric Vehicles
Luiz Alberto Lisboa da Silva Cardoso – University of Minho

189

The expression for $\dot{V}_{ind}$ (3.123) can be compared to model in Figure 3b, permitting equivalently to express the mutual inductance M between long coils p and s as:

$$M = \frac{\mu}{2\pi} \ell \, \xi(x, h, d, D), \qquad (3.130)$$

Illustrating a possible application of Theorem 1, Figure 116 shows the scalar field of the normalized induced voltage, ξ, computed using (3.124), on the cross-section of an inductive configuration with an infinitely long primary filamentary coil p and a parallel rectangular filamentary coil s, each consisting of a single turn:
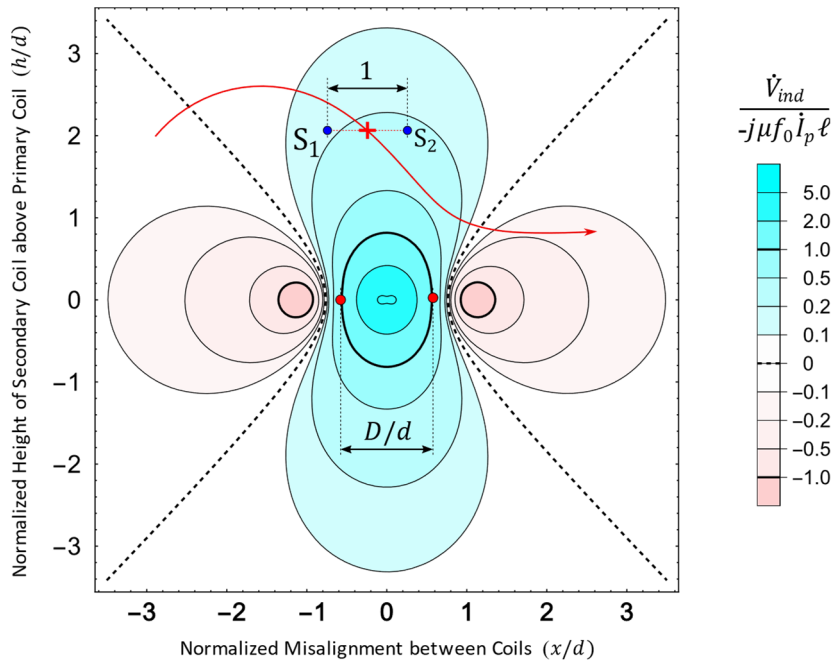
Figure 116: Normalized voltage induced on a single turn secondary coil s by a single turn primary coil p, as a function of the relative position of the center of s to p, under the hypotheses of Theorem 1.

The conductors of the primary coil p, indicated in Figure 116 by two red dots, are placed centered at $h = 0$. The conductors of the secondary coil s are indicated by two dark blue dots, S_1 and S_2, and probe the induced voltage when translated over the cross-section, a typical situation of interest in design of DIWPT configurations. Specifically, for this example, the ratio D/d was set to $2/\sqrt{3}$. The red curve exemplifies a possible path for the displacement of s, with red cross denoting the center of the secondary coil s. The color of the plot shows how the value of the normalized induced voltage, ξ, changes when the center of secondary coil, is displaced on the cross-section plane. The blue regions indicate the positions of the cross-section where $\xi > 0$, i.e., $\dot{V}_{ind}$ is given by $j\alpha\dot{I}_p$, where $\alpha > 0$, and the phase of V_{ind} is $\pi/2$ ahead of the phase of I_p.

Dynamic Inductive Wireless Power Transfer for Lightweight Electric Vehicles
Luiz Alberto Lisboa da Silva Cardoso – University of Minho

190

Similarly, in the pink regions, the phase of V_{ind} is $\pi/2$ delayed from of the phase of I_p. The black dashed curves are the loci of the zero induced voltage, defined by the equation:

$$\xi(x, h, d, D) = 0 \,, \tag{3.131}$$

where d and D are the fixed widths of respectively the secondary and primary coils, and (x, h) is the coordinate pair of a point of the cross-section belonging to the dashed curve where $V_{ind} = 0$.

Developing (3.131) results in an equation on x and h:

$$
\left(\left(x - \frac{D+d}{2} \right)^2 + h^2 \right) \left(\left(x + \frac{D+d}{2} \right)^2 + h^2 \right) = \\
= \left(\left(x + \frac{D-d}{2} \right)^2 + h^2 \right) \left(\left(x - \frac{D-d}{2} \right)^2 + h^2 \right) \tag{3.132}
$$

which simplifies to:

$$d^2 + D^2 + 4h^2 - 4x^2 = 0 \,, \tag{3.133}$$

which is the equation of a rectangular hyperbola on the plane (x, h), with vertices H_1 and H_2 at:

$$\mathrm{H}_1 = \left(-\frac{\sqrt{d^2 + D^2}}{2}, 0 \right) \tag{3.134}$$

$$\mathrm{H}_2 = \left(+\frac{\sqrt{d^2 + D^2}}{2}, 0 \right) \tag{3.135}$$

Remarkably, the fact that the loci of $V_{ind} = 0$ is rectangular hyperbola (eccentricity $\sqrt{2}$) does not depend on the ratio d/D, only its scale factor will depend on the indistinct sum of the squares of the coil widths.

Since in most vehicular DIWPT applications the secondary coil is installed at a fixed distance from the primary coil, another useful application for Theorem 1 is to predict the induced voltage on a rectangular secondary coil as a function of the lateral misalignment on the lane, as exemplified in curves of Figure 117, plotted for different ratios of D/d, from 0.25 (red curve) to 2.5 (blue curve), and $h/d = 1/2\sqrt{3}$.

Dynamic Inductive Wireless Power Transfer for Lightweight Electric Vehicles
Luiz Alberto Lisboa da Silva Cardoso – University of Minho

191
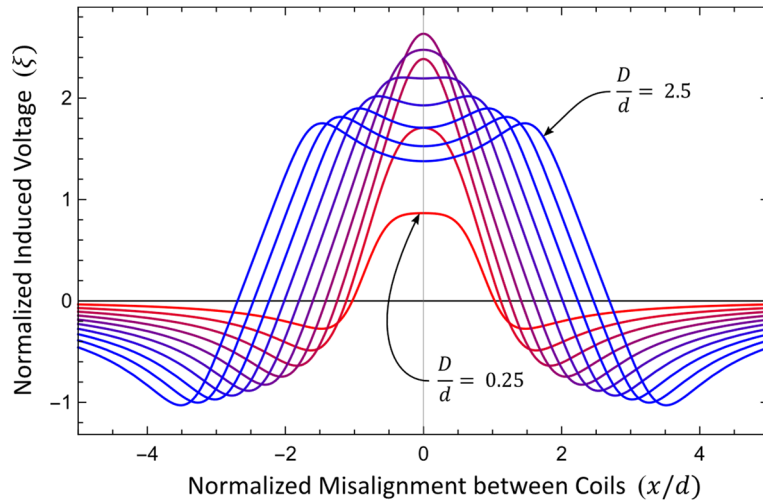
Figure 117: Normalized voltage induced on a single turn secondary coil s that is at a fixed distance from the single turn primary coil p, as a function of the relative position of the center of s to p.

One key consideration to obtain a good numerical approximation for this prediction, using Theorem 1, is to require that the middle cross-section under analysis is far enough from the extremities of the primary coil. However, this is not a problem: While no actual primary coil p has infinite length, in practice, it is verified that the magnetic flux distribution generated by current I_p is fairly regular along all the length of the primary coil, except very close to the extremities of p.

<u>Theorem 2</u>: The maximum value of the normalized voltage $\xi = \dot{V}_{ind}/\left(-j\mu f_0 \dot{I}_p \ell\right)$ induced by a stationary, infinitely long filamentary coil p, of width D, that is constituted of a single turn of wire carrying a sinusoidal current I_p of constant amplitude and frequency $f_0 = 2\pi\omega_0$, on a parallel rectangular coil s, of fixed width d and length ℓ, also constituted of a single turn of filamentary wire, located on a plane that is parallel to the plane that contains p, at a fixed distance h to that plane, is obtained when the coils are symmetrically aligned, with central planes coinciding, and the width D of coil p is equal to w_P:

$$w_P = \sqrt{d^2 + 4h^2} \tag{3.136}$$

and can be calculated by:

$$\xi_{max_{h,d}} = \ln\frac{w_P + d}{w_P - d} \tag{3.137}$$

Additionally, when the coils remain center-aligned and the width D of the primary coil p is varied, the normalized induced voltage observed with $D = \lambda w_P$ is the same as that observed when $D = w_P/\lambda$, for any $\lambda > 0$.

Dynamic Inductive Wireless Power Transfer for Lightweight Electric Vehicles
Luiz Alberto Lisboa da Silva Cardoso – University of Minho

192

Proof of Theorem 2: This proof follows by initially applying Lemma 2 to each of the conductors of p, and separately positioning P_1 and P_2 in order to maximize the induced voltage. The property of the total magnetic flux on s is the sum of the fluxes generated by I_p leaving at P_1, and current $-I_p$ leaving at P_2, due to linear superposition of the respective magnetic fields generated by these two conductors of coil p, and the independence of the fields generated by them. Starting from equations (3.125) to (3.127), it comes:

$$\dot{V}_{ind} = \dot{V}_1 + \dot{V}_2 \tag{3.138}$$

$$\max_{x} \frac{\dot{V}_{ind}(x, h, d, D)}{-j\,\mu\,f_0\,\dot{I}_p\,\ell} = \max_{x} \frac{\dot{V}_1(x, h, d, D)}{-j\,\mu\,f_0\,\dot{I}_p\,\ell} + \max_{x} \frac{\dot{V}_2(x, h, d, D)}{-j\,\mu\,f_0\,(\dot{I}_p)\,\ell} \tag{3.139}$$

By Lemma 2:

$$\max_{x} \frac{\dot{V}_1(x, h, d, D)}{-j\,\mu\,f_0\,\dot{I}_p\,\ell} = \frac{\dot{V}_1(q_1, h, d, D)}{-j\,\mu\,f_0\,\dot{I}_p\,\ell}, \qquad q_1 = -\frac{1}{2}\sqrt{d^2 + 4h^2} \tag{3.140}$$

Due to the anti-symmetry of $\dot{V}_2$, expressed in (3.95), (3.96), to search for the maximum in normalized $\dot{V}_2$ is equivalent to search for the minimum in normalized $\dot{V}_1$, then the second parcel in (3.138) becomes:

$$\max_{x} \frac{\dot{V}_2(x, h, d, D)}{-j\,\mu\,f_0(-\dot{I}_p)\ell} = -\min_{x} \frac{\dot{V}_1(x, h, d, D)}{-j\,\mu\,f_0(\dot{I}_p)\ell} \tag{3.141}$$

which, by using Lemma 2 again, is found a:

$$-\min_{x} \frac{\dot{V}_1(x, h, d, D)}{-j\,\mu\,f_0(\dot{I}_p)\ell} = -\frac{\dot{V}_1(q_2, h, d, D)}{-j\,\mu\,f_0(\dot{I}_p)\ell}, \qquad q_2 = \frac{1}{2}\sqrt{d^2 + 4h^2} \tag{3.142}$$

Hence, the normalized induced voltage on s is maximized when the projections of the conductors of p, P_1 and P_2, are symmetrically placed around the center plane of coil s, $x = 0$, at the following coordinates:

$$P_1: x = q_1 = -\frac{1}{2}\sqrt{d^2 + 4h^2} \tag{3.143}$$

$$P_2: x = q_2 = \frac{1}{2}\sqrt{d^2 + 4h^2} \tag{3.144}$$

and the optimum width $D = w_P$ of coil p will then be given by the difference $q_2 - q_1$:

Dynamic Inductive Wireless Power Transfer for Lightweight Electric Vehicles
Luiz Alberto Lisboa da Silva Cardoso – University of Minho

193

$$w_P = q_2 - q_1 = \sqrt{d^2 + 4h^2} \,, \tag{3.145}$$

which is identical to (3.136), thus consisting in the first item of proof.

For this optimum width w_P, at the central alignment condition, the normalized maximum induced voltage can be further calculated by replacing D in (3.124) by w_P, as given in (3.145),:

$$\xi_{max_{h,d}} = \xi(0, h, d, w_P) = \frac{1}{2} \ln \frac{\left(\left(\frac{\sqrt{d^2 + 4h^2} + d}{2} \right)^2 + h^2 \right)^2}{\left(\left(\frac{\sqrt{d^2 + 4h^2} - d}{2} \right)^2 + h^2 \right)^2} \,, \tag{3.146}$$

which can be simplified to:

$$\xi_{max} = \ln \frac{\sqrt{d^2 + 4h^2} + d}{\sqrt{d^2 + 4h^2} - d} \,, \tag{3.147}$$

due to (3.145), an equivalent expression to (3.137), and this is the second part of the proof.

Finally, it can be calculated that, at the alignment condition, $x = 0$, when $D = \lambda w_P$, $\lambda > 0$, the expression of ξ, given by Theorem 1 (3.124), becomes:

$$\xi(0, h, d, \lambda w_P) = \ln \frac{\left(\frac{\lambda w_P + d}{2} \right)^2 + h^2}{\left(\frac{\lambda w_P - d}{2} \right)^2 + h^2} \,, \tag{3.148}$$

which, by using (3.145), can be developed to:

$$\xi(0, h, d, \lambda w_P) = \ln \frac{w_P(1 + \lambda^2) + 2\lambda d}{w_P(1 + \lambda^2) - 2\lambda d} \tag{3.149}$$

Based on (3.149), ξ, at $x = 0$ and $D = w_P/\lambda$, is equal to:

$$\xi(0, h, d, w_P/\lambda) = \ln \frac{w_P \left(1 + \frac{1}{\lambda^2} \right) + \frac{2d}{\lambda}}{w_P \left(1 + \frac{1}{\lambda^2} \right) - \frac{2d}{\lambda}} = \xi(0, h, d, \lambda w_P) \tag{3.150}$$

Hence, it follows that at center-alignment condition, the normalized induced voltages on coil s are the same (and so are the induced voltages) when the width of the primary coil is either λw_P or w_P/λ, with $\lambda > 0$, q.e.d.

Dynamic Inductive Wireless Power Transfer for Lightweight Electric Vehicles
Luiz Alberto Lisboa da Silva Cardoso – University of Minho

194

Geometric Interpretation for Theorem 2: Despite the tedious algebraic manipulation involved in Theorem 2, it has a simple immediate geometric interpretation: The infinitely long filamentary single turn primary coil carrying a fixed sinusoidal current I_p that will induce the maximum voltage on a parallel rectangular single turn filamentary coil s at distance h from p, is the one in which the projection on a cross-section of this inductive configuration of the support lines of the conductors of p, P_1 and P_2, constitute the diameter $\overline{\mathrm{P}_1\mathrm{P}_2}$ of a circle also containing the projection of the support lines of the conductors of s, S_1 and S_2, as shown in Figure 118.
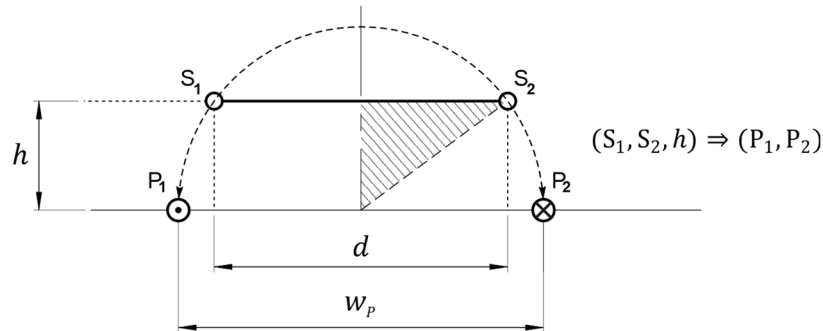
Figure 118: Geometrical interpretation of Theorem 2.

This relative positioning of S_1, S_2, P_1 and P_2 creates a right-angled rectangle where the vertical cathetus is h, the horizontal cathetus is $d/2$, and the hypotenuse, $D/2$, is calculated using Pythagoras' theorem:

$$\left(\frac{D}{2}\right)^2 = \left(\frac{d}{2}\right)^2 + h^2 = \left(\frac{w_P}{2}\right)^2 \tag{3.151}$$

Hence, the geometrical construction in Figure 118 assures $D = \sqrt{d^2 + 4h^2}$, which is the required width w_P of p for maximum induction in s.

Numeric comparison with FEM modeling: As a quick check against any error in its derivation, the optimum positioning, and the maximum induced voltage, given by Theorem 2, were initially verified by numeric simulations, using finite element modeling (FEM). Four inductive configurations, consistent with the geometrical assumptions for this theorem, at different ratios of h/d, ranging in the set $\{1/10, 1/3, 1, 3\}$, were designed and simulated, using the FEMM software tool for FEM simulation [123] [99], with the total number of mesh nodes varying in the range from 50k to 100k. In all configurations, the coils were assumed immersed in air, and μ was approximated by μ_0. The size of the rectangular coil was set to be the same in all configurations, at $d = 282$ mm, $\ell = 645$ mm, modeled with thin copper wire, of diameter 1 mm for all conductors. The frequency of the primary current was set at 51 kHz. For each configuration,

Dynamic Inductive Wireless Power Transfer for Lightweight Electric Vehicles
Luiz Alberto Lisboa da Silva Cardoso – University of Minho

195

several cross-sections were simulated, all at center-alignment condition between the primary and secondary coils, but with increasing size of primary coil widths. The induced voltage was simulated at N_m different widths, from D_{min}^m to D_{max}^m, for all four configurations, $1 \leq m \leq 4$. For generating the N_m simulated voltages in configuration m, the primary coil was then reinstated at N_m different width values, both smaller and larger than w_P. Table 15 summarizes the FEM simulations realized, totalizing $\sum N_m = 217$ virtual stationary induction experiments.

Table 15: Summary of FEM simulations run to test the application of Theorem 2.

m^*	h/d	h (mm)	w_P (mm)	D_{min}^m (mm)	D_{max}^m (mm)	N_m
1	$1/10$	28.2	287.6	40	1000	37
2	$1/3$	94	338.9	80	3400	62
3	1	282	630.6	40	4000	53
4	3	846	1715.3	40	4000	65

*All four configurations run with the same secondary coil size, $d = 282$ mm, $\ell = 645$ mm.

The curves resulting from the FEM simulations, for the four created configurations, are plotted in Figure 119. The colors distinguish each case according to the h/d ratio, from $1/10$, which is shaded in strong orange, to 3, shaded light yellow. The induced voltage is plotted is normalized to both the problem physics, by dividing the resulting simulated induced voltages in all configurations by the quantity $j\mu f_0 I_p \ell$, and the problem geometry, then dividing the results by the predicted individual $\xi_{max_{h,d}}$ of each different h/d ratio, as given by (3.137). This is done to facilitate a visual assessment of the results.
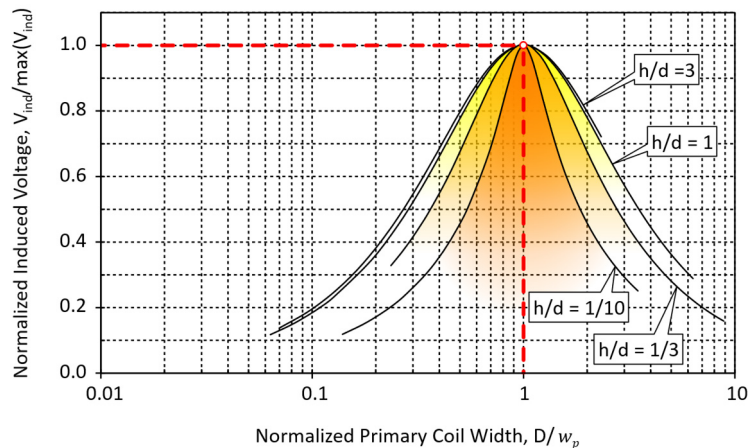
Figure 119: Results of FEM simulations to check Theorem 2.

The coincidence of the maximum normalized induced voltage of 1.0 (linear scale vertical axis) for all curves is an indication of the good predictive quality of the expression for the maximum achievable induced voltage (3.137). On the other hand, the coincidence of these point of maxima

Dynamic Inductive Wireless Power Transfer for Lightweight Electric Vehicles
Luiz Alberto Lisboa da Silva Cardoso – University of Minho

196

at $D/w_P = 1$, for all curves, is compatible with the prediction of the optimum width w_P, as given by (3.136). In logarithm scale, the curves are symmetric around $D/w_P = 1$, due to (3.37).

This coincidence obtained in the FEM simulations does not prove that the developed theorems are correct, the proof is accomplished by mathematical development and is already given. But it is a good practice to have an indication of consistence with other validated numerical approach, such as FEM, which directly computes the solution of magnetic fields in a geometry of conductors that is excited by currents, based on Maxwell equations.

As expected, the FEM simulations require more effort in the preparation of the geometrical description of the problem and the setting of the contour conditions of the configurations. Also, they take much more time to run than using the direct algebraic computation of predicted induced voltages and optimum widths given by analytical analysis, and this is an advantage of using such theorems. In addition, having a geometric interpretation for an optimum configuration is also very helpful to develop some insight on the DIWPT design.

<u>Theorem 3</u>: The maximum value for the normalized voltage $\xi = \dot{V}_{ind}/-j\mu f_0 \dot{I}_p \ell$ induced by a stationary, infinitely long filamentary coil p, of fixed width D, that is constituted of a single turn of wire carrying a sinusoidal current I_p of constant amplitude and frequency $f_0 = 2\pi\omega_0$, on a parallel rectangular coil s, of width d and length ℓ, also constituted of a single turn of filamentary wire, located on a plane that is parallel to the plane that contains p, at a fixed distance h to that plane, is obtained when the coils are symmetrically aligned, with central planes coinciding, and the width d of coil s is equal to w_S:

$$w_S = \sqrt{D^2 + 4h^2} \tag{3.152}$$

and can be calculated by:

$$\xi_{max_{h,D}} = \ln\frac{w_S + D}{w_S - D} \tag{3.153}$$

Additionally, when the coils remain center-aligned and the width d of the primary coil s is varied, the normalized induced voltage observed with $d = \lambda w_S$ is the same as that observed when $d = w_S/\lambda$, for any $\lambda > 0$.

There is a duality relating Theorem 3 and Theorem 2, the expressions (3.152) and (3.153) are exactly those in (3.136) and (3.137), except that D and w_S are used in place of d and w_P.

Dynamic Inductive Wireless Power Transfer for Lightweight Electric Vehicles
Luiz Alberto Lisboa da Silva Cardoso – University of Minho

197

The physical situation in each case is different though: In Theorem 2 the width of the secondary coil is fixed at d, and an optimal diameter of primary coil, D, that maximizes the induced voltage on s, is to be found. While in Theorem 3, the search is reversed, the width D of the primary coil itself is fixed, and an optimal width d for the secondary coil that maximizes the induced on voltage s is to be determined.

Proof of Theorem 3: The reason for the above mentioned duality, which is the proof for Theorem 3, is that, by inspection of the algebraic expression (3.124) of the function ξ, both the induced voltage from p on s, $\dot{V}_{ind}$, as well as the associated normalized induced voltage, ξ, given by Theorem 1, are symmetric on d and D:

$$\xi(x, h, d, D) = \xi(x, h, D, d) , \tag{3.154}$$

and

$$\frac{\partial^n \xi}{\partial d^n} = \frac{\partial^n \xi}{\partial D^n} , \forall n \geq 1 \tag{3.155}$$

Hence, the points of maxima in ξ, with respect to d, when $x = 0$, are expressed in terms of fixed h and D by the same function as the points of maxima in ξ, when $x = 0$, with respect to D, when expressed in terms of fixed h and d, causing the width of maximum induced voltage on s, at $x = 0$, to be also found at an optimum value of d, w_S, given as the function of h and D:

$$w_S = \sqrt{y^2 + 4h^2}\Big|_{y=D} = \sqrt{D^2 + 4h^2} \tag{3.156}$$

In the same manner, the value of the maxima will be given by the same function by which it was calculated in the case of the optimization in D, but evaluated at the pair (h, D), rather than at pair the (h, d):

$$\xi_{max} = \ln\frac{\sqrt{y^2 + 4h^2} + y}{\sqrt{y^2 + 4h^2} - y}\Bigg|_{y=D} = \ln\frac{w_S + D}{w_S - D} \tag{3.157}$$

To prove the last statement of Theorem 3, it can be realized that, for all $\lambda > 0$:

$$\xi(0, h, \lambda w_S, D) = \xi(0, h, D, \lambda w_S) =$$

$$= \xi\left(0, h, y, \lambda\sqrt{y^2 + 4h^2}\right)\Bigg|_{y=D} = \xi\left(0, h, y, \frac{\sqrt{y^2 + 4h^2}}{\lambda}\right)\Bigg|_{y=D} = \tag{3.158}$$

Dynamic Inductive Wireless Power Transfer for Lightweight Electric Vehicles
Luiz Alberto Lisboa da Silva Cardoso – University of Minho

198

$$= \xi\left(0, h, D, \frac{w_S}{\lambda}\right) = \xi\left(0, h, \frac{w_S}{\lambda}, D\right),$$

with the first and last equalities being due to the existing indistinguishability in d and D, as given by (3.154), and the equality in the middle, due to Theorem 2. Hence,

$$\xi(0, h, \lambda w_S, D) = \xi\left(0, h, \frac{w_S}{\lambda}, D\right), \forall \lambda > 0 \tag{3.159}$$

what constitutes the last part of Theorem 3, q.e.d.

Geometric Interpretation for Theorem 3: Similarly to Theorem 2, the dimensions and location of the optimum filamentary secondary coil s for a maximum induced voltage from filamentary primary coil p, at a fixed distance h, also has a simple immediate geometric interpretation: If the projections of the support lines of the conductors of p, in a common cross-section with s, are P_1 and P_2, and the projections of the support lines of the conductors of s parallel to p are S_1 and S_2, then S_1 and S_2 constitute the diameter $\overline{S_1 S_2}$ of a circle also containing P_1 and P_2, as shown in Figure 120.
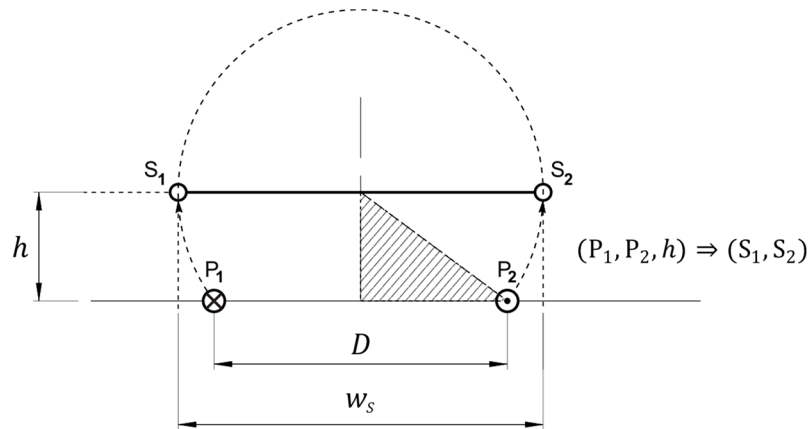
Figure 120: Geometrical interpretation of Theorem 3.

Attention should be paid when comparing and using Theorem 2 and Theorem 3, which geometries can be visualized respectively in Figure 118 and Figure 120: The optimum width for the other coil, in order to attain maximum induced voltage on the secondary, is always larger than that of a first coil which width has been fixed, no matter whether the first coil to have its dimensions fixed beforehand is the secondary or the primary coil, as synthetically represented in Figure 121.

Dynamic Inductive Wireless Power Transfer for Lightweight Electric Vehicles
Luiz Alberto Lisboa da Silva Cardoso – University of Minho

199
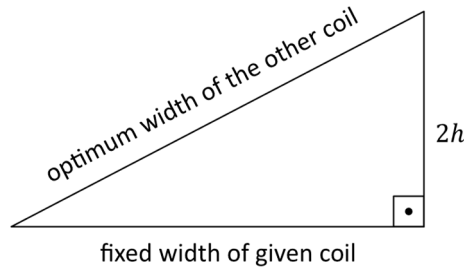
Figure 121: Optimum width of the other coil in an oblong coil configuration, for maximum induced voltage.

<u>Theorem 4</u>: Let p be a stationary, infinitely long filamentary coil p, of width D, that is constituted of a single turn of wire carrying a sinusoidal current I_p of constant amplitude and frequency $f_0 = 2\pi\omega_0$; let s be a parallel to p rectangular coil s of fixed width d and length ℓ, also constituted of a single turn of filamentary wire and located on a plane that is parallel to the plane that contains p, at a fixed distance h to that plane. Then the profile of the normalized voltage $\xi = \dot{V}_{ind} / j\mu f_0 \dot{I}_p \ell$, induced by p on s, as a function of the lateral misalignment of p and s, is maximally flat in the vicinity of the center-alignment condition when the width D of coil p is either equal to w_F or to w_F', as given by the following equations and conditions:

$$w_F = \sqrt{w_P^2 + 4w_P h}\,, \qquad h > 0 \tag{3.160}$$

$$w_F' = \sqrt{w_P^2 - 4w_P h}\,, \quad 0 < \frac{h}{d} < \gamma_h \tag{3.161}$$

where w_P is the width of p for maximum induced voltage on s, as in Theorem 2:

$$w_P = \sqrt{d^2 + 4h^2}\,, \tag{3.162}$$

and γ_h is the optimum h/d ratio for maximum linearity of the induced voltage on s due to a single conductor of p (3.107), as given by

$$\gamma_h = \frac{1}{2\sqrt{3}} \tag{3.163}$$

<u>Proof of Theorem 4</u>: By analogous argumentation to that used in Lemma 1, when considering expressions (3.97), (3.98), (3.99), ξ, as given by (3.124) is also continuous and continuously n-differentiable in $\mathbb{R}$, and, by inspection (3.124), clearly symmetric in the variable u:

$$\xi(u, h, d, D) = \xi(-u, h, d, D) \tag{3.164}$$

Dynamic Inductive Wireless Power Transfer for Lightweight Electric Vehicles
Luiz Alberto Lisboa da Silva Cardoso – University of Minho

200

This implies that:

$$\frac{\partial^n \xi}{\partial u^n} = (-1)^n \frac{\partial^n \xi}{\partial u^n}, \qquad n > 1 \tag{3.165}$$

and thus:

$$\frac{\partial^{2n-1} \xi}{\partial u^{2n-1}}(0, h, d, D) = 0, \qquad n > 1 \tag{3.166}$$

The requirement for a maximally flat response to lateral misalignment between coils p and s can be traduced by a zero in first and second order derivatives of the normalized induced voltage with respect to the lateral displacement, at the point where central alignment condition is met.

The first order derivative $\partial \xi / \partial u$ at $u = 0$ is already guaranteed to be zero by (3.166). By developing $\partial^2 \xi / \partial u^2$, it is found that:

$$\frac{\partial^2 \xi}{\partial u^2}(0, h, d, D) = \frac{32 dD((d-D)^2(d+D)^2 - 8h^2(d^2 + D^2 + 6h^2))}{((d-D)^2 + 4h^2)^2((d+D)^2 + 4h^2)^2} \tag{3.167}$$

Considering equations (3.108) to (3.104), the Taylor expansion of ξ to the third order, at the vicinity of $u = 0$, the center of alignment between coils s and p, with h and d fixed, it is possible to approximate $\xi(x, h, d, D)$ by:

$$(x, h, d, D) \cong \xi(0, h, d, D) + \frac{x^2}{2} \frac{\partial^2 \xi}{\partial u^2}(0, h, d, D) \tag{3.168}$$

So, given that the first and the third derivatives of ξ with respect to u are already zero at $u = 0$, the variation of the induced voltage ξ in response to the lateral displacement x, in the vicinity of the center of alignment of coils s and p, will be minimized when the second derivative of ξ at $u = 0$, given by (3.167), is also zero, condition under which ξ will be approximated by the constant $\xi(0, h, d, D)$. This happens when:

$$(d-D)^2(d+D)^2 - 8h^2(d^2 + D^2 + 6h^2) = 0 \tag{3.169}$$

As $D > 0$ is the free variable geometrical parameter considered in Theorem 4, the only two possibly real positive roots of (3.169) in D are given by w_F and w_F':

$$w_F = \sqrt{d^2 + 4h^2 + 4\sqrt{d^2 h^2 + 4h^4}}, \quad h > 0, d > 0 \tag{3.170}$$

Dynamic Inductive Wireless Power Transfer for Lightweight Electric Vehicles
Luiz Alberto Lisboa da Silva Cardoso – University of Minho

201

$$w_F' = \sqrt{d^2 + 4h^2 - 4\sqrt{d^2h^2 + 4h^4}}, \quad 0 < h < d\frac{1}{2\sqrt{3}} \tag{3.171}$$

By recognizing that $d^2 + 4h^2 = w_P^2$, from Theorem 2 (3.136), and that $\gamma_h = 1/2\sqrt{3}$, from the development of Lemma 1 (3.107), expressions (3.170) and (3.171) can be rewritten respectively as (3.160) and (3.161), q.e.d.

The two possible solutions found, w_F and w_F', have different properties concerning the magnitude of voltage that can be induced in each derived configuration. Also, w_F is visibly a larger width than w_P, and it is always available as a design option, while w_F', when it is defined, is smaller, and associated with lower induced voltages. While both of these values of D will yield a flat response at center alignment condition, the normalized induced voltage on s, under central alignment condition, will be significant less at $D = w_F'$, than at $D = w_F$, except when the ratio h/d is very low (less than 10%), case in which the magnitude of the ratio of the induced voltages will be closer to unity (higher than 90%), as shown in Figure 122. However, a too low value of h/d is usually not practical to implement in a real DIWPT application for electric mobility, due to mechanical restrictions on the minimum required air-gap.
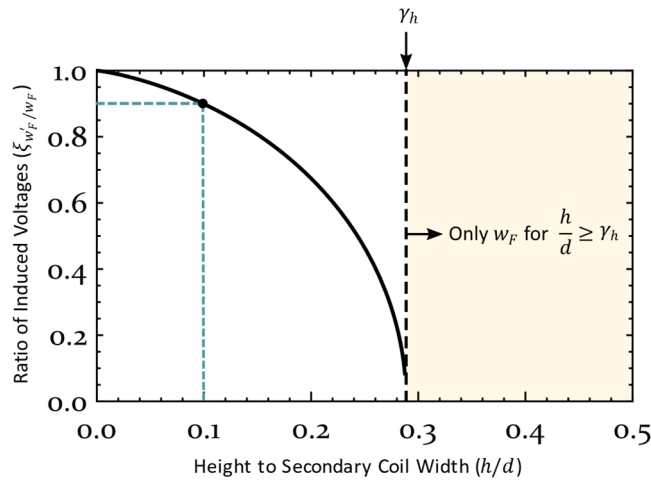
Figure 122: Condition for the existence of a second smaller width for maximum flatness in the induced voltage.

In summary, although two optimum values were found for a maximum flatness in the induced voltage response, which is a desirable characteristic is some applications, one of them, w_F', will only exist if $h/d < 28.8\%$. Even then, the induced voltage will be much less than that provided by at $D = w_F$, unless $h/d < 10\%$, which is likely to be difficult to implement, if the inductive configuration is used for transferring power to terrestrial vehicles. So, the option for the primary coil width of w_F' is apparently not as useful for a DIWPT design aiming electric mobility, as the larger alternative, w_F, and in principle, the existence of w_F' maybe disregarded.

Dynamic Inductive Wireless Power Transfer for Lightweight Electric Vehicles
Luiz Alberto Lisboa da Silva Cardoso – University of Minho

202

Geometric Interpretation for Theorem 4: A geometrical interpretation is given for the main optimum value w_F. Despite not being as straightforward as the geometric construction provided for Theorem 2 and Theorem 3, it provides a tool that enhances the visualization, and a more intuitive design of DIWPT configurations using oblong coils, when maximally flat induced voltage in a secondary coil of given width is sought.

Figure 123 represents a cross-section of the inductive configuration formed by coils p, which width is a free design parameter, and s, of fixed width d, given by points S_1 and S_2, at distance h from the support plane of p. For a maximally flat induced voltage, the positioning of the conductors of the primary, w_F, far apart from each other, is found by first constructing points P_1 and P_2, such that $\overline{P_1 P_2}$ is a diameter of a circle also containing S_1 and S_2, centered at C_1, the intersection of the mediatrix of $\overline{S_1 S_2}$ with the support line at distance h from $\overline{S_1 S_2}$ (P_1 and P_2 are the loci for the conductors of p for a maximum induced voltage on s, as seen in Theorem 2). Then point H_2 is constructed, by making $\overline{P_2 H_2} = h$. The intersection of a circle with center at C_2 and radius $\overline{C_2 H_2}$ with the perpendicular to the support line of the conductors of p, drawn from P_2, is point Z_2. Another circle centered at C_1 and drawn with radius $\overline{C_1 Z_2}$ will intercept the support line for coil p projections at points F_1 and F_2, which are the positioning solution for the conductors of p for a maximally flat induced voltage on s. Incidentally, F_1 and F_2 would be the locus of the conductors of p for maximum voltage on s, if s, with a distinct width, had its conductors placed at Z_1 and Z_2, Z_1 being the point symmetric to Z_2 with respect to the center plane of s that is perpendicular to the support line of p.
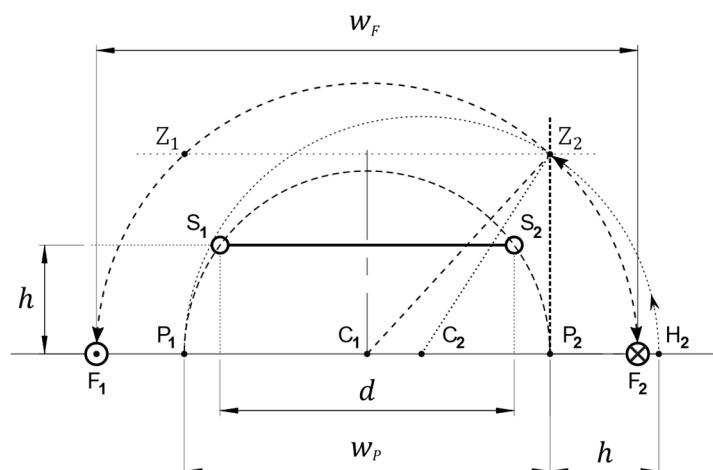
Figure 123: Geometrical interpretation of theorem 4.

Dynamic Inductive Wireless Power Transfer for Lightweight Electric Vehicles
Luiz Alberto Lisboa da Silva Cardoso – University of Minho

203

From this geometric construction, it can be shown that the length of $\overline{F_1 F_2}$ is exactly given by the expression derived for w_F (3.170). For quick visual estimations of the position of F_1 and F_2, it can also be verified that:

$$d + 2h \; < \; w_F \; < \; w_P + 2h \tag{3.172}$$

Theorem 5: Let p be a stationary, infinitely long filamentary coil p, of fixed width D, that is constituted of a single turn of wire carrying a sinusoidal current I_p of constant amplitude and frequency $f_0 \; = \; 2\pi\omega_0$; let s be a parallel to p rectangular coil s of width d and fixed length ℓ, also constituted of a single turn of filamentary wire and located on a plane that is parallel to the plane that contains p, at a fixed distance h to that plane. Then the profile of the normalized voltage $\xi = \dot{V}_{ind} / j\mu f_0 I_p \ell$, induced by p on s, as a function of the lateral misalignment of p and s, is maximally flat in the vicinity of the center-alignment condition when the width d of coil s is either equal to w_F or to w_F', as given by the following equations and conditions:

$$w_F = \sqrt{w_S^2 + 4w_S h}\,, \qquad h > 0 \tag{3.173}$$

$$w_F' = \sqrt{w_S^2 - 4w_S h}\,, \quad 0 < \frac{h}{d} < \gamma_h \tag{3.174}$$

where w_S is the width of p for maximum induced voltage on s, as in Theorem 3:

$$w_S = \sqrt{D^2 + 4h^2}, \tag{3.175}$$

and γ_h is the optimum h/D ratio for maximum linearity of the induced voltage on s due to a single conductor of p, as given by

$$\gamma_h = \frac{1}{2\sqrt{3}} \tag{3.176}$$

Notably, Theorem 5 can be seen as Theorem 4 with d and D reversed. That is, in Theorem 4 the secondary width is fixed at d, and an optimum is sought for the width D of the primary coil, while in Theorem 5 the primary coil has a fixed width D, and the problem to be solved is the determination of an optimum secondary width d that will maximize the flatness of the response of the induced voltage, as a function of the lateral misalignment of the primary and secondary coils.

Dynamic Inductive Wireless Power Transfer for Lightweight Electric Vehicles
Luiz Alberto Lisboa da Silva Cardoso – University of Minho

204

Again, likewise to the case of Theorem 2 and Theorem 3, there is a duality between Theorem 4 and Theorem 5, and the proof of Theorem 5 is based on the same relations and expressions derived for Theorem 4.

Proof of Theorems 5: Since the inductive configuration and its parameters are equivalent and named exactly as in Theorem 4, the expression for the normalized induced voltage for the present situation is the same as (3.167), and so are valid expressions (3.168) and (3.169). In order to find the optimum d is then given by the real positive roots of (3.169), having this time d as the free variable, not D as in the proof of Theorem 4. Since (3.169) is symmetric with respect to d and D, then the optimum values for d, w_J and w_J', are given by:

$$w_J = \sqrt{D^2 + 4h^2 + 4\sqrt{D^2h^2 + 4h^4}}, \quad h > 0, D > 0 \tag{3.177}$$

$$w_J' = \sqrt{D^2 + 4h^2 - 4\sqrt{D^2h^2 + 4h^4}}, \quad 0 < h < D\frac{1}{2\sqrt{3}} \tag{3.178}$$

It can be recognized, from Theorem 3 (3.152), that $D^2 + 4h^2 = w_S^2$, and that from the development of Lemma 1 (3.107), that $\gamma_h = 1/2\sqrt{3}$. So, expressions (3.177) and (3.178) can be rewritten respectively as (3.174) and (3.175), q.e.d.

By analogy to Theorem 4, the geometric evaluation of optimum widths w_J and w_J' for a secondary coil s at fixed distance h to a given primary coil with width D will be entirely similar to that shown in Figure 125, but with the drawing up-side down and the location of points P_1 and P_2 respectively reversed with S_1 and S_2.

A general visualization tool for optimum widths of a second coil for maximum induced voltage (red line segment) and for a maximally flat induced voltage (green line segment) is seen in Figure 124, where the width of the first given coil is represented by the black horizontal line segment and the fixed distance between the two coils. Because of the correspondence of Theorem 3 and Theorem 5, respectively with Theorem 2 and Theorem 4, it is indifferent whether the first coil considered is the primary or the secondary coil, the optimum second coil will be always larger than the first coil.

Dynamic Inductive Wireless Power Transfer for Lightweight Electric Vehicles
Luiz Alberto Lisboa da Silva Cardoso – University of Minho

205
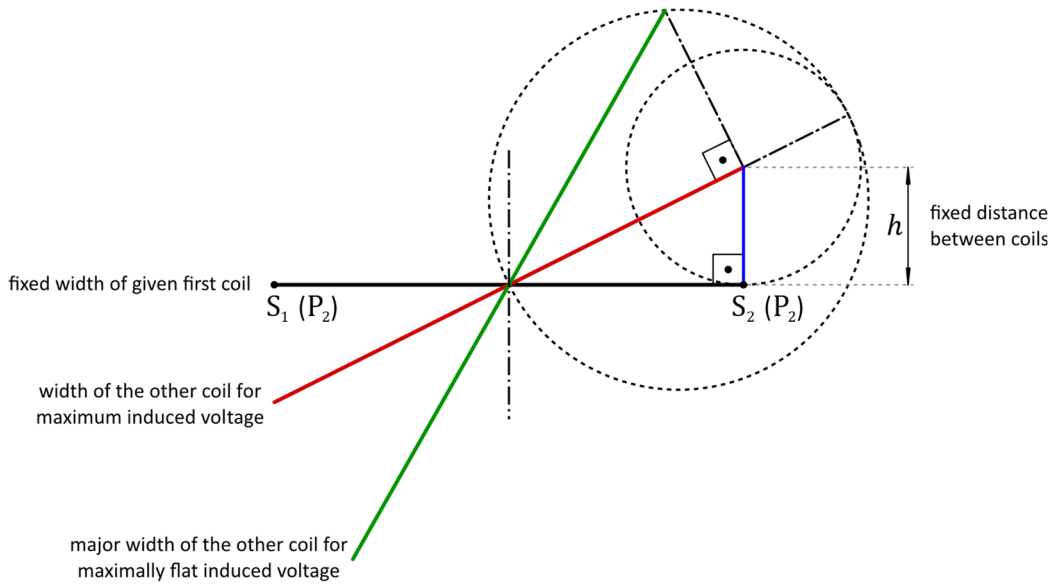
Figure 124: Geometric visualization for the calculation of optimum width coils.

Application of Theorems 1 to 5: Considering the possibility of approximation of real coils by filamentary windings, for both primary and secondary coils, and provided that the quasi-stationary hypothesis can be applied, as showed in 3.1, theorems 1 to 5 can help the design of DIWPT configurations where the primary coil is an oblong coil and the secondary coil is a rectangular parallel coil, at a fixed distance h to the primary coil. This happens because the magnetic field in a central cross-section of this DIWPT configuration is approximately the same as if the primary coil had infinite length, if this considered cross-section is sufficiently away from the extremities of the primary coil.

When the secondary is compensated, the induced voltage ultimately determines the available power in the secondary, and that is the reason for the concern for maximizing it, as in Theorem 2 and 4. For a SS or PS-compensated configuration, for instance, this is promptly recognized by reexamining Figure 6b, from section 2.5, and realizing that, in the circumstances of theorems 1 to 5, $E_2 = \dot{V}_{ind}$, and, for a fully compensated secondary, the power P_L on a resistive load directly connected to the secondary will be given by:

$$P_L = \frac{\dot{V}_{ind} R_L}{R_L + R_2} \dot{I}_L^* = \frac{R_L}{(R_L + R_2)^2} \dot{V}_{ind} \dot{V}_{ind}^* = \frac{R_L (\mu f_0 \ell)^2}{(R_L + R_2)^2} \dot{I}_p \dot{I}_p^* \xi^2(x, h, d, D) \qquad (3.179)$$

So, the power delivered to the load will be proportional to squared normalized induced voltage. Alternatively, depending on the circuit design of the secondary, the design target might be to have the induced voltage with a flat as possible characteristic, in response to misalignment variations of the primary and secondary coils, and that is the usefulness of Theorem 3 and

Dynamic Inductive Wireless Power Transfer for Lightweight Electric Vehicles
Luiz Alberto Lisboa da Silva Cardoso – University of Minho

206

Theorem 5. Theorem 1, on the other hand, provides an analytic method for calculating the induced voltage or the power delivered on R_L, as a function of the circuit parameters and the geometry of the coils, allowing the DIWPT design to be refined.

However, in order to fully benefit from the predictions provided by these theorems, the hypothesis of a constant amplitude and phase of the current in the primary coil must hold, for a good approximation to be obtained. This will happen if the primary circuit can keep a constant current on the primary coil, accommodating the back-induced voltage from any current secondary current, or when this back-induced voltage is sufficiently small, compared to the voltage established on the primary coil, so that the variations on primary current can be neglected. In DIWPT configurations whereas the magnetic coupling coefficient is low, and the secondary has more turns than the primary coil, this is definitely the case, which is also the situation found in the application developed in Chapter 5.

As a summary of the main results achieved in this section, the plots of the normalized induced voltage, calculated on basis of the analytical expressions derived, for designs with different optimal properties, are shown in Figure 125. The configuration corresponds to a given secondary coil with fixed width d, at a fixed distance h from a primary coil in which the width D is a parameter of free election, by design. The fixed location of the secondary coil is indicated by points S_1 and S_2, and, differently from the curves, specially plotted with the vertical axis scale equal to the normalized horizontal scale, for improved perception of the proportions of the geometry adopted in this example, where h/d was set to $1/4$.
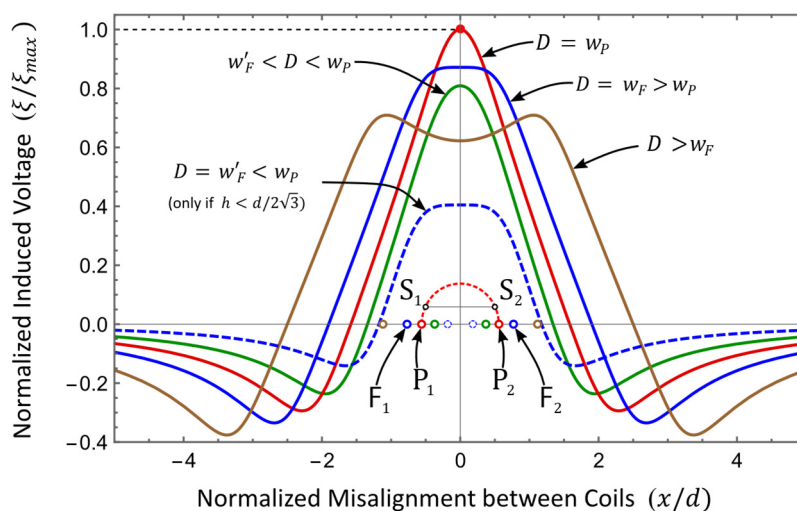
Figure 125: Curves of normalized voltage induced on a single turn rectangular secondary coil by a single turn oblong primary coil, for different primary coil widths, under the conditions of Theorem 1.

Dynamic Inductive Wireless Power Transfer for Lightweight Electric Vehicles
Luiz Alberto Lisboa da Silva Cardoso – University of Minho

207

In the chart of Figure 125, the normalized induced voltage ξ is normalized again by ξ_{max} before plotted, so that maximum assumed value on the vertical axis is one, facilitating the visual comparison of the induced voltage profile of the various configurations. The colors of the curves are in correspondence with the color of the small circles that represent the location of the conductors of the primary coil that generates each curve. The red curve corresponds to the maximum induced voltage condition, obtained for $D = w_P$, as given by Theorem 2. The two blue curves are the maximally flat induced voltage profiles, obtained for $D = w_F$ (continuous blue) and for $D = w_F'$ (dashed blue), given by Theorem 4. The green curve is the resulting of setting the width of the primary coil to a value that is less than w_P, but still higher than w_F', and the brown curve is an example of a profile generated when the width of the primary coil is larger then w_F.

The criterion for a DIWPT design will be strongly dependent on the application. However, in general, the transfer of maximum power with the same primary current is one of the main goals, for the power levers that are required themselves and for the efficiency levels that can be obtained drawing more power from the same primary current, since the primary losses will be strongly related to the square of rms value of the primary current.

An alternative convenient design goal is to keep the induced voltage as constant as possible, while the electric vehicle (secondary coil) harvesting power from the lane (primary coil) drifts laterally around the center of the lane, constantly generating a misalignment input x to the function ξ. This property is obtained when D is close to w_F, and useful when a DC-DC converter is used to match the load impedance, and the ratio between the maximum and minimum input to the converter should not be very high. The in-depth analysis of the application, supported by the tools presented in this section will lead to the best design choices. In general, unless there is some additionally restriction on the width D of the primary coil, there will be no good argument for picking $D < w_P$ or D much greater than w_F.

Concerning electric mobility, although Theorems 3 and 5 do provide solutions for optimum geometries of the secondary pick-up coils to be installed on vehicles, the most usual application is to design the primary coil with an optimal width, given a secondary coil of fixed dimensions. This is because whilst the coils should be as large as possible for a good transfer of power, the maximum dimensions of the secondary coil are a priori constrained by the size of the vehicle and mechanical restrictions imposed by the installation of the coil on the vehicle. In Figure 126 is shown example of inductive coupling of a DIWPT design using Theorem 4 to optimally position a single turn oblong primary coil to work with a single turn parallel rectangular secondary coil.

Dynamic Inductive Wireless Power Transfer for Lightweight Electric Vehicles
Luiz Alberto Lisboa da Silva Cardoso – University of Minho

208
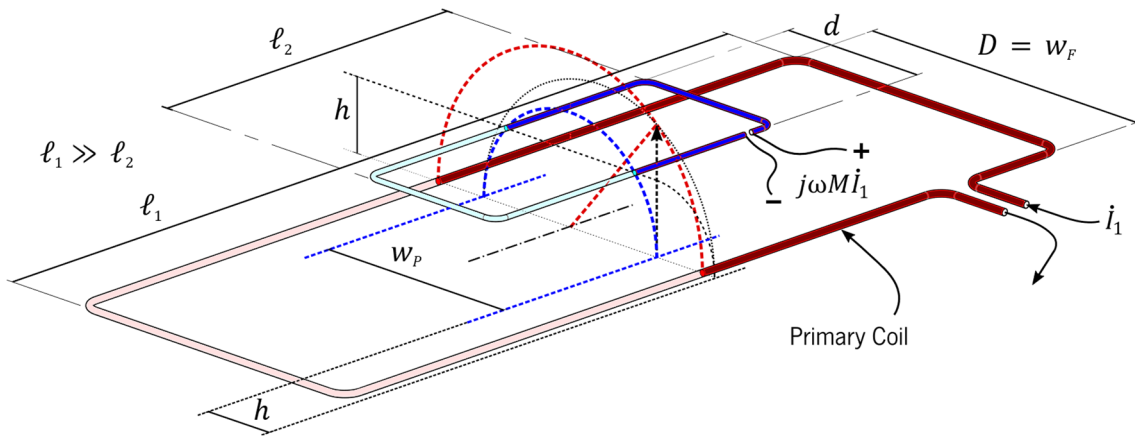
Figure 126: Geometric construction of a DIWPT configuration of oblong primary coils using Theorem 4.

Once fixed the dimensions required for the coils, their equivalent circuit parameters, such as inductances and mutual inductance, can be derived and serve as the basis for circuit design of the primary and the secondary power electronics, which are briefly reviewed in Chapter 2.

3.6.4 Magnetic Flux Shaping

When two or more magnetically coupled coils have alternated current passing on them, the total AC magnetic field generated will induce an electric voltage in each of them. Depending on the relative phase of the currents on the coils and their induced voltages, each coil will receive or transmit electric power to the other in that magnetic coupling, similarly as showed in 2.3 for the case of two coils. The configuration can be analyzed by considering that the total magnetic flux traversing each coil results from sum of the partial magnetic fluxes due to the magnetic fields generated by the current in each coil, if linearity of the medium can be assumed. In a good coupling design, it is desired that the magnetic flux generated in the transmitter (primary) coils is directed, as much as possible, to the receiver (secondary) coils. This is so for the three main reasons:

(i)   The power transferred is increased, for the same currents;

(ii)   The maximum power transfer efficiency can then be also increased;

(iii)   The magnetic flux (and magnetic field intensity) is reduced in other regions, in the vicinity of the coils, where losses could be induced, or the presence of sensitive equipment or live matter (human beings, for instance) is expected, resulting in damage to the equipment or hazards to life.

While all three above concerns are relevant in DIWPT for vehicular applications, failing in compliance with either (i) or (iii) can completely disqualify an EV design.

Dynamic Inductive Wireless Power Transfer for Lightweight Electric Vehicles
Luiz Alberto Lisboa da Silva Cardoso – University of Minho

209

To direct and confine the magnetic field, the most common magnetic-field shaping techniques employed in design of IWPT configuration are: The use of soft-magnetic materials, the use of conductive surfaces, and the use of auxiliary coils, which can either carry active current or be compensated and passively resonant [124].

3.6.4.1 Magnetic shaping with soft-magnetic materials

Soft-magnetic materials, such as ferrites, by having a larger magnetic permeability than the free space, increase the magnetic field intensity in their interior, and tend to concentrate the lines of magnetic induction [125] generated by the magnetic sources represented by the coils in the magnetic coupling. So, by adequately placing some magnetic material, called the magnetic core, in between the transmitter and receiver coils, the lines of magnetic induction are apparently 'attracted' to the interior of the core, and the magnetic flux passing through these coils, the induced voltages, as well as the power transfer can be increased. At the same time, the region of space behind the core (relatively to the current location) becomes more depleted of lines of magnetic induction, and exhibit a weaker magnetic field intensity. This effect is illustrated in by the results of simulations shown in Figure 127, where two coaxial 1 - turn equal coils with 200 mm of diameter, made of 10 mm diameter copper rods, are positioned at a distance $h = 200$ mm from each other, and simultaneously fed with 17.8 A rms, at 50 kHz, with a relative phase of $\pi/2$ (input current to the secondary is delayed 90° with respect to that fed to the primary coil), which will maximize the power transfer. The ferrite core inserted is a 10 mm-thick hollow cylinder with external diameter of 148 mm and length of 186 mm, made of a soft-magnetic material with relative magnetic permeability $\mu = 1000$, and all materials are considered in free space. To simplify the graphical representation, only the induction lines (blue curves) due to the primary coil are plot in both Figure 127a and Figure 127b, where the lines of magnetic induction on the central cross-section plane of the coils are shown. But since the coils and their currents are equal, except in phase, the induction lines due to the secondary (upper) coil would be symmetric to those due to the primary (lower) coil.

Dynamic Inductive Wireless Power Transfer for Lightweight Electric Vehicles
Luiz Alberto Lisboa da Silva Cardoso – University of Minho

210

(a) without ferrite core:
1 W transferred at 56% efficiency

(b) with hollow cylindrical ferrite core:
5.8 W transferred at 88% efficiency
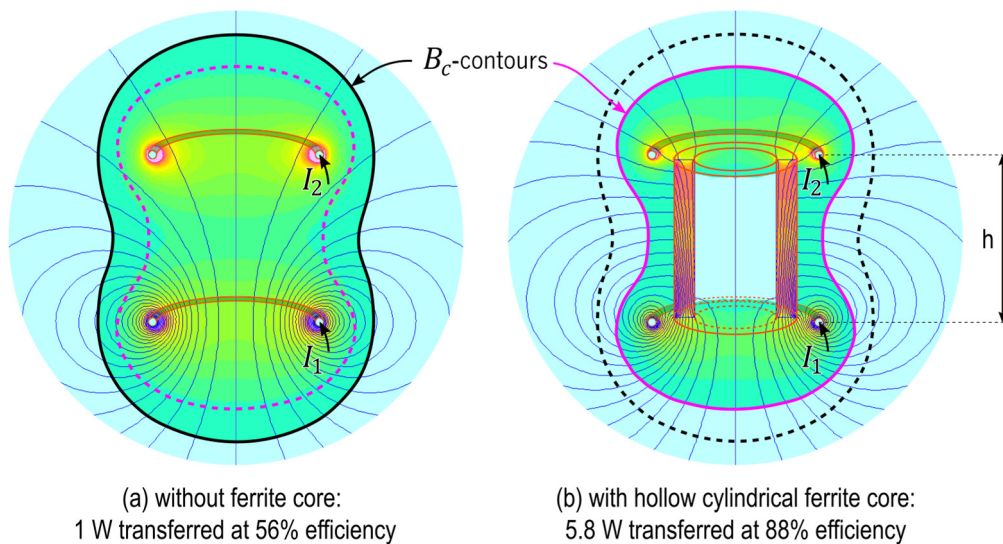
Figure 127: IWPT enhancement and magnetic shaping by the insertion of a core material between two coils.

The result of the simulation indicates that, by inserting the magnetic core coaxially to the coils, in the center of the configuration, the power transferred is increase almost 6 times, from 1 W to 5.8 W, while the efficiency is raised to 88%, from an initial value of 56%. The ferrite was assumed lossless, whereas, in practice, some energy would be dissipated in the ferrite, causing the real efficiency to be somewhat lower than the predicted 88%.

Remarkably, to keep the current intensities constant at $I_1 = I_2 = 17.8$ A rms when the magnetic core is introduced in the coupling, it is necessary to increase the input voltage to the coils from approximately 2.2 V rms to 2.75 V rms (+27%).

It can be also noticed that, at the same time the magnetic flux in between the coils is increased, when concentrated by the ferrite core, the region of the space with a magnetic field intensity higher than $B_c = 21.7$ μT rms, given by the black continuous contour line in Figure 127a, will shrink to the purple continuous contour line in Figure 127b. The magnetic field will also be practically reduced to zero inside the cylindrical core. In general, the maximum acceptable magnetic field intensity in a given region of the space is a design parameter that depends on the sensitivity of further equipment to be placed in that region, or, in case of human live tissue, this is regulated by currently ICNIRP recommendations [72].

Another important point, when considering the use of magnetic cores, is to guarantee that the magnetic field in the core does cause the saturation of the material, condition from which the hysteresis losses on the core will grow significantly. This will both impair the IWPT and potentially cause the fracture of the core, and destroy it. After the core is destroyed, the impedance seen by

Dynamic Inductive Wireless Power Transfer for Lightweight Electric Vehicles
Luiz Alberto Lisboa da Silva Cardoso – University of Minho

211

the external current excitation sources will be reduced, and depending on the circuit protection schemes used, the resulting current elevation can destroy either these power sources or the coils.

In a DIWPT design, the relative position of the secondary and primary coils, which can be more than one, is not fixed. The consideration of the worst and best case for the induced voltages is necessary to design the power electronic that assures the required minimum power transfer. Conversely the ability of the circuitry to handle fluctuations in the induced voltage and coil impedances can determine a range of possible relative positions of the coils where success power transfer can occur at the minimum required power level. Similar happens when trying to establish a contour of a (safe) region where the magnetic field intensity is limited to some design value. The magnetic core materials, if used, are usually fixed to either the primary or secondary coil assemblies.

In most land-based vehicular applications, both primary and secondary coils are often parallel to the ground, with the primary coil lying underneath ground level. It is then a sensible mechanical requirement to have a void layer in between ground and the vehicle, where no coils or support materials reside. In this case, the core, if used, is normally installed behind the coils, in the same relative position as shown in Figure 109. When using ferrite plates in this manner, the power transfer can be estimated by applying the magnetic current mirror model [126].

The Magnetic Current-Mirror Model: In order to estimate the power inductively transferred when magnetic core plates are placed around current carrying conductors, the core plates can be replaced by virtual conductors at the specular position of the actual conductors, with respect to the core surface that is facing these latter conductors, as if they were their images on the mirror. The core plates should not lie in between conductors that exchange power, and the mirrored conductors should carry the same current as their specular images. The application of this modeling can be visualized in the simulation results plot in Figure 128, where the cross-sections of the equivalent magnetic configurations are shown.

(a) Current-carrying conductor backed by a ferrite plate.   (b) Current-carrying conductor and its specular image.
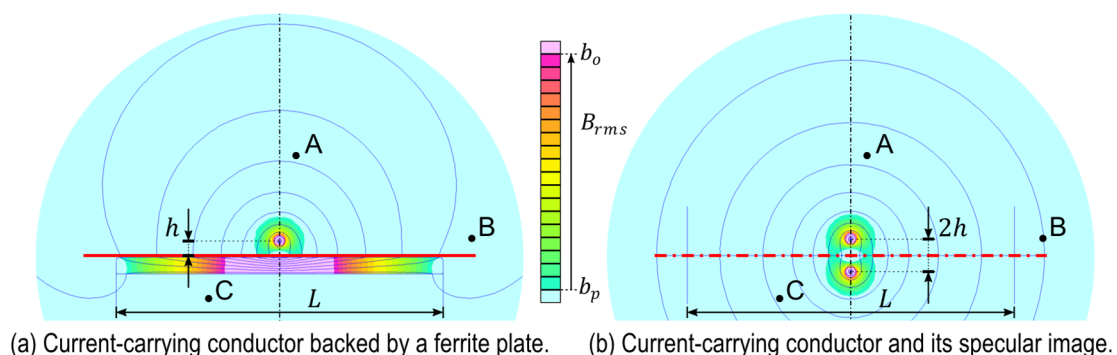
Figure 128: Magnetic current mirror modeling of a core plate for a single current-carrying conductor.

Dynamic Inductive Wireless Power Transfer for Lightweight Electric Vehicles
Luiz Alberto Lisboa da Silva Cardoso – University of Minho

212

It can be shown [127] that, in the region of space immediately above the magnetic core plate (e.g., where point A is located), the magnetic field generated by the current flowing on the conductor backed by the core, in Figure 128a, is approximately equivalent to the magnetic field generated by the pair of conductors in Figure 128b. This equivalence is observed only on the portions of the space that lie enough away from borders of the core (e.g., point B), and that are not located behind the core, i.e., are not on opposite side of the core plate with respect to the conductor (e.g., point C). So, if other voltage sensing conductors were placed in front of the core, the voltage induced on it by this equivalent magnetic field would be approximately equal to that that would be measured in the original configuration using the magnetic core.

The values of the parameters used in the simulation were $L = 1$ m, $h = 50$ mm, with a lossless core material exhibiting a relative permeability of $\mu_r = 1000$, and a long copper conductor (planar axial model) with 2 mm diameter carrying 7.07 A rms of current at 50 kHz. The color scale adopted has a lower clipping at $b_p = 27\,\mu$T rms and a higher clipping at $b_o = 100\,\mu$T rms. These parameters used in the simulations are incidental, however, for the magnetic current mirror model approximation to yield good results, it is necessary that:

- The energy losses in the core plate are negligible with respect to the power being transferred and resistive losses in the conductor, at the frequency used;

- the core plate is thick enough not to saturate,

- the core plate is width L is sufficiently larger than the distance h between the core and its distance to both the transmitting conductor;

- its magnetic permeability μ_r is much larger than that of the region above the core, where lies the current-carrying conductor.

This approximation, mathematically justified in [127], is illustrated by the plots of the magnetic field intensity in both situations, as shown in Figure 129a and Figure 129b.

Dynamic Inductive Wireless Power Transfer for Lightweight Electric Vehicles
Luiz Alberto Lisboa da Silva Cardoso – University of Minho

213

(a) Distance from the center of the magnetic core

(b) Height above core plate
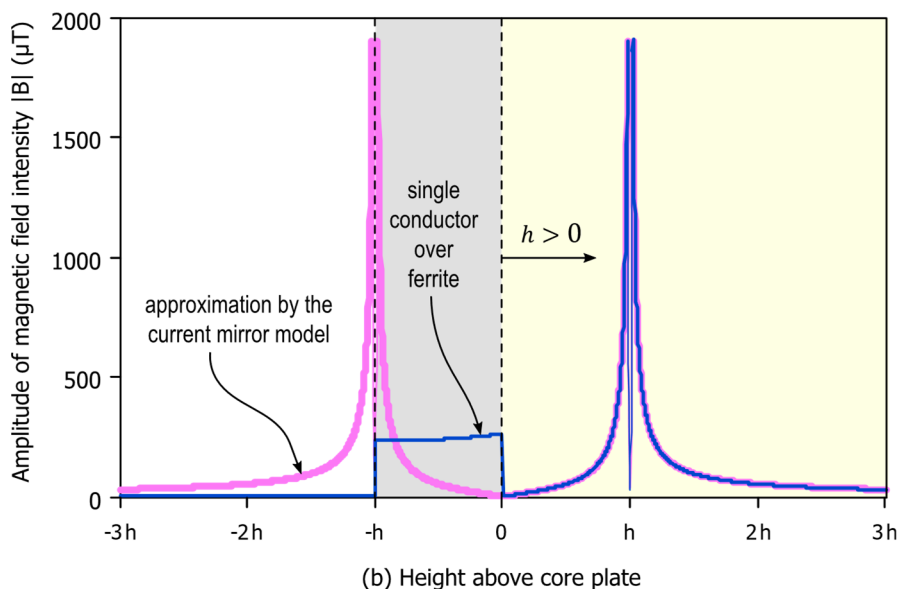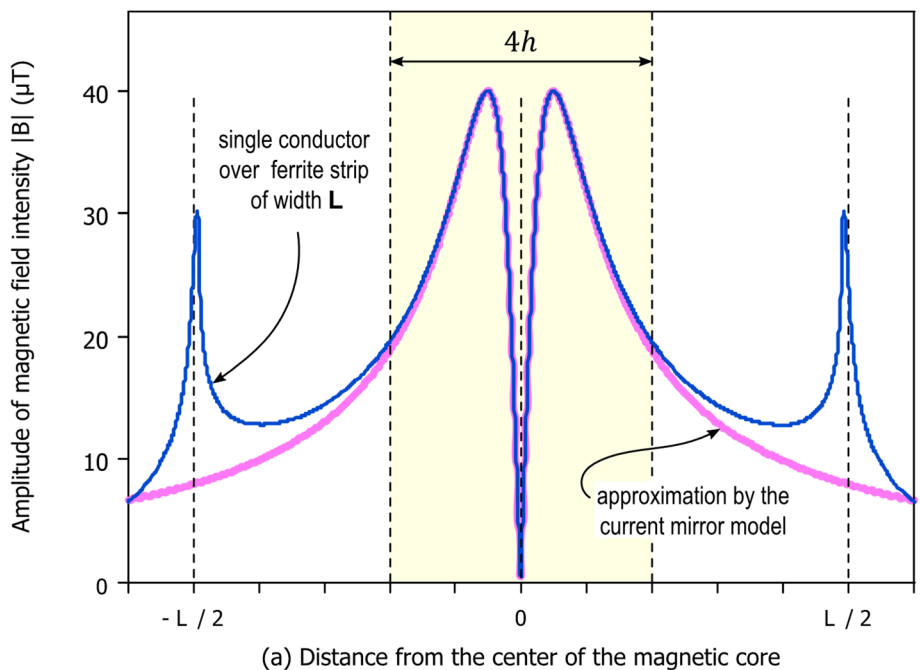
Figure 129: Approximation, under the equivalent current-mirror model of the magnetic field (a) on the surface of the core plate and (b) on the perpendicular plane to the surface of the core plate, centered on the conductor.

Along the plane that is perpendicular to the core plate and centered on the conductor, the magnetic field intensity computed with the current-mirror model coincides, for $h > 0$, with that observed when the core plate is used, as can be seen in the yellow shaded region of Figure 129b. It can be also noticed that above the core plate and within a $4h$-width around the position of the current-carrying conductor there is an excellent concordance between the magnetic field of the actual configuration (blue curves), using the core plate, and the equivalent configuration (pink curves), where the core is replaced by the "reflected" current.

Dynamic Inductive Wireless Power Transfer for Lightweight Electric Vehicles
Luiz Alberto Lisboa da Silva Cardoso – University of Minho

214

The discrepancies observed in the magnetic field close to the extremities of the core plate, visible in Figure 129a, should not disturb the magnetic flux on other conductors and coils, if they are inserted in the configuration as voltage sensing devices, as long as their windings are contained in the central region above and close enough to the core plate (yellow shaded).

The magnetic current-mirror model was also shown to exhibit results of improved precision if multiple "reflections" of the current-carrying conductors are considered [127]. In the case of conductors confined in between planes of core material, a perfect analogy with light reflections in optical mirror is promptly established. An example of the application of this improved model is given in Figure 130, where two parallel ferrite core plates confine two current-carrying conductors.
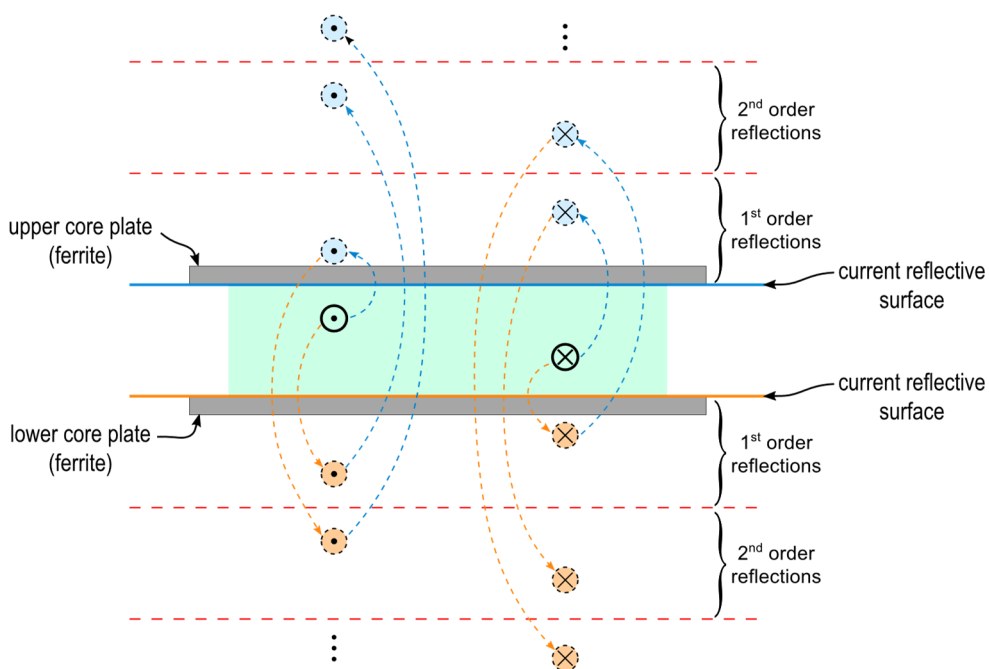
Figure 130: Application example of the improved magnetic current mirror model [127].

Successively improved approximations are obtained when high order current reflections are added to the model. By this equivalence, the magnetic field computed in the gap between the two core plates should be the same as if the core plates were not present, being replaced by reflected currents, each with the same phase of the corresponding actual currents, on the inner surfaces of the cores. As exemplified in the simulation shown in Figure 129, this approximation hold and can be used on the evaluation of induced voltages and transferred power to other conductors, except if these other conductors are too close from the borders of the core plates, i.e., outside the central, green shaded region of Figure 130.

Because this reinforcement of the magnetic field obtained by the core plates, as if there were more current-carrying conductor present, in general, this configuration is highly

Dynamic Inductive Wireless Power Transfer for Lightweight Electric Vehicles
Luiz Alberto Lisboa da Silva Cardoso – University of Minho

215

recommended to achieve higher power transfer levels. In addition, since the "reflected" conductors do not actually exist, they do not dissipate power, higher efficiency levels can also be obtained, provided that the losses in the magnetic cores are negligible, with respect to the resistive losses in the conductors.

A possible exception to this recommendation arises when cost is critical. Nonconductive soft-magnetic core materials with high magnetic permeability and low losses at higher frequencies are very expensive, relatively to the price of the wiring used in a given configuration. Per mass, the cost of a good ferrite for operation up to 100 kHz can be almost twice as costly as litz wire copper windings, per unit of mass. This ratio rises approximately to nine, when prices of ferrite and when standard non-litz wires are used in a IWPT configuration, as shown in Table 16

Table 16: Relative cost of materials frequently used in IWPT configurations.

Material	Cost per kg (Euros, CIF EU)	Relative cost per kg
Copper	5.54*	1.00
Copper in litz cable	27.35**	4.94
Ferrite plate	47.52***	8.58

*Average copper price, London Metal Exchange, May 2019.
**Based on litz wire supplied by Elektrisola Dr. Gerd Schildbach GmbH & Co. KG, to University of Minho, in 2019.
***Based on EPCOS TDK N95 ferrite supplied to University of Minho by Arrow Iberia Electronica S.L.U., in 2019.

The mass of ferrite that is necessary to be used in an IWPT configuration is often larger than the mass of the copper wiring itself, for a significant increase in power transfer and efficiency to be observed. If the relative costs of materials in Table 16 are considered, the relative overall cost of materials for IWPT systems using different configurations are shown in the last column of Table 21, assuming that coil windings are made of copper conductors.

Table 17: Relative cost of materials frequently used in IWPT configurations.

Magnetic Core	Coils Windings	Mass proportion, ferrite to copper	Total relative cost of materials
Not used	Non-litz copper	0	1.0
	Litz copper	0	4.9
Ferrite Plates	Non-litz copper	1	9.6
	Litz copper	1	13.5
	Non-litz copper	2	18.2
	Litz copper	2	22.1

Dynamic Inductive Wireless Power Transfer for Lightweight Electric Vehicles
Luiz Alberto Lisboa da Silva Cardoso – University of Minho

216

Chapter 1 Because of the dominant cost of ferrites, to keep the cost effectiveness of the i-lanes in DIWPT applications for less costly lightweight electric vehicles, such as e-bikes, it is highly desirable to avoid any use of magnetic core materials, especially on the lane side. This is exactly the design case of study in Chapter 5.

3.6.4.2 Magnetic shaping with conductive bodies

The eddy currents induced in conductive bodies, such as metal plates, produce a magnetic field component that tends to cancel the magnetic field inside these bodies caused by external excitation. The eddy currents also reduce magnitude of the magnetic resulting magnetic field in their immediate vicinity, especially, behind the conductive body, as if it worked as a shield, interrupting the magnetic field lines.

A metal plate can be thought of as multiple superposed coils paths, all of these coils short-circuited, which is the limit condition of a serial compensated coil (section 2.5) when the serial capacitance tends to infinite. So, considering the analysis in the graph of Figure 7, if a metal plate would be modeled by just one equivalent coil, the induced current $\dot{I}_2$ on it would an amplitude proportional to the exciting current $\dot{I}_1$, as derived from (2.14):

$$\dot{I}_2 = \lim_{\substack{C_2 \to \infty \\ R_L = 0}} \boldsymbol{v}\, \dot{I}_1 = \lim_{C_2 \to \infty} \boldsymbol{v}\, \dot{I}_1 \; \frac{-j\,\omega\,M}{R_2 + j\left(\omega\,L_2 - \dfrac{1}{\omega\,C_2}\right)}\, \dot{I}_1 = \frac{j\,\omega\,M}{R_2 + j\,\omega\,L_2} - \dot{I}_1, \tag{3.180}$$

where R_2 and L_2 are parameters of this equivalent coil, and M the mutual inductance between the coil with the exciting current and the metal plate.

In plates of good conductivity and sufficient thickness, at higher angular frequencies ω, R_2 is expected to be negligible with respect to the product ωL_2 so the total equivalent induced current $\dot{I}_2$ can be approximated by (3.181) and exhibit an opposite phase to $\dot{I}_1$.

$$\dot{I}_2 = \frac{M}{L_2}\left(-\dot{I}_1\right) \tag{3.181}$$

$\dot{I}_2$ can be interpreted as the total equivalent current induced in the modeled metal plate, and M, the mutual inductance between the exciting coil and the plate. This simple model, however, does not explicitly consider the thickness of the plate and the current density pattern within the plate itself, nor an immediate formulation for M or the equivalent L_2 is given.

What is apparent from this simple model is that, while core materials shape the magnetic field by reinforcing it in the region in between the core and nearby current carrying conductors,

Dynamic Inductive Wireless Power Transfer for Lightweight Electric Vehicles
Luiz Alberto Lisboa da Silva Cardoso – University of Minho

217

conductive bodies contrapose to the magnetic field, and can attenuate or block the AC magnetic field generated by external exciting currents. Because of that, conductive materials are often also used for magnetic shielding of AC currents.

The skin effect, as described in 2.10.1, implies that a metallic plate must have a large enough thickness, g, to attenuate the magnetic field down to a given level. Most of the current density in a metal plate will lie within a few skin depths, δ, away from the surface facing the conductor carrying the excitation current. If g is not much greater than δ, two effects will be observed: First, the metallic plate will not completely block the magnetic field: Second, the resistance to the eddy currents will be increased, and so may increase the power dissipated within the metal plate. At extreme conditions, a plate shield of insufficient thickness may become a risk for the IWPT system; it can either increase the power drawn for the inverter above safety limits and damage it, or it can overheat, causing a generalized failure of the system, for instance it can ignite materials in its vicinity.

In Figure 131, a simple shielding example is shown, where the magnetic field generated by a current carrying copper wire is shielded by an aluminum sheet/plate. The wire is very long (2D-symmetric problem), has a 6 mm-diameter and it is carrying 65.4 A at 51 kHz. The magnetic field is plot in Figure 132, using the same color scale, in two different shield constructions: (a) using 16 μm thick aluminum foil; and (b) using 1-mm thick aluminum sheet. At 51 kHz, the skin depth in aluminum is $\delta_{Al} = 363 \ \mu$m, so that the thickness in (a) and (b) correspond respectively to 0.044 δ_{Al} (poor shielding) and 2.75 δ_{Al} (reasonably good shielding).
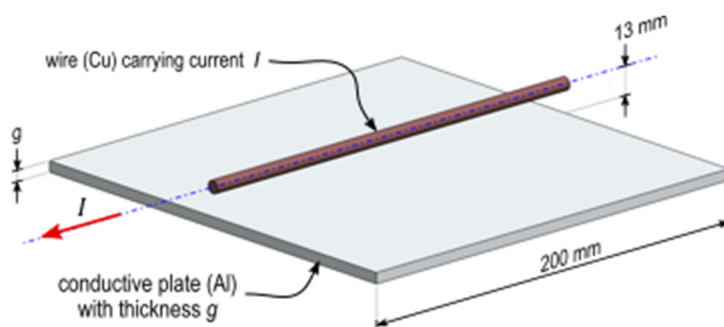
Figure 131: Example of magnetic shielding of an electric current with a conductive plate.

The color scale used in the simulation plots of Figure 132 is not incidental. The intensity is color-plot only on areas of the cross-section where the magnetic field is larger than -91.37 dBT rms (blue extreme), corresponding to the maximum recommended exposure level to the general public, and all regions of the space where the field is larger than -80 dBT rms is plot in red, sign a potential exposure to a magnetic level above the maximum occupational level [72].

Dynamic Inductive Wireless Power Transfer for Lightweight Electric Vehicles
Luiz Alberto Lisboa da Silva Cardoso – University of Minho

218
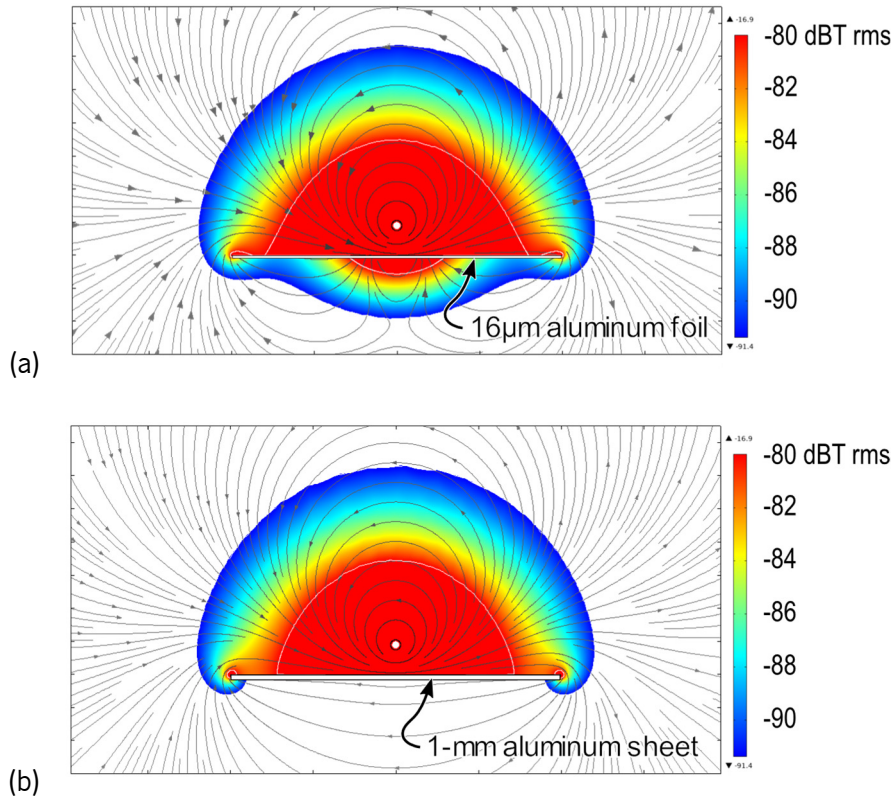
Figure 132: Finite element simulations of the shielding of a copper conductor carrying 65.4 A rms at 51 kHz with (a) 16 μm-thick aluminum foil; and (b) 1 mm-thick aluminum sheet. Color scale shows magnetic field in dBT rms.

The comparison of the two plots, obtained using COMSOL Multiphysics software, clearly indicates that, concerning the ICRNP recommendations, the 1-mm aluminum plate efficiently blocks the magnetic field, at the given current level and distance, but the aluminum foil does not.

It not easily seen in the plots, but carefully observation will also indicate that the constant intensity contours of magnetic field above the shield are slightly contracted inward to the wire, showing that the magnetic field has been also somewhat attenuated in the case of Figure 132b.

The FEM simulation using COMSOL Multiphysics also allows the computation of the total heat generated in the shield plates. As shown in Table 18, the heat generated is much higher in the 16 μm - thick aluminum foil than with the thicker 1-mm aluminum shield, showing that much more heat will be generated in the thinner foil than in the thicker aluminum sheet.

Table 18: Comparison of the heat generated in the two shielding plates of different thickness.

Shield Thickness, g	Frequency	Skin Depth δ_{Al}	g/δ_{Al}	Average Power Dissipated by Shield Plate (W/m^2)
1 mm	51 kHz	363 μm	2.75	16.2
16 μm	51 kHz	363 μm	0.044	313.1

Dynamic Inductive Wireless Power Transfer for Lightweight Electric Vehicles
Luiz Alberto Lisboa da Silva Cardoso – University of Minho

219

The spatial distribution of the heat lost in the shield plate is not uniform over the shield, it concentrates where the magnetic field is stronger, that is, on the vertical projection of the wire on the shield. In this spot, the power density is much higher than the average along the whole shield plate, given in Table 18. Whereas metals, aluminum in particular, are good thermic conductors, when the thickness is too small, there may be not enough time for the heat flow along the plate and be transferred to the environment, and high temperatures may develop on the shield plate, in the zone directly underneath the wire.

In DIWPT design, shielding must be used on the vehicle's side, to protect its occupants. Since the steel normally used in the chassis of cars is ferromagnetic, a protective conductive with low magnetic permeability plate (such as aluminum) is often recommended. It is inserted in between the secondary pick-up coil and the lower part of the chassis of the vehicle. This aluminum sheet should be thick enough, not only to provide the necessary protection for the passengers, but also, not to dissipate too much heat itself, which can be a dangerous condition. In standard passenger cars using IWPT charging, the shield plate must be integrated in the coil design, and comes assembled from factory, both because it is always required and because it is part of the power transfer design itself, to avoid excessive attenuation of the magnetic flux through the secondary coil, which could follow in case of a poor field-installation of the coil in the vehicle.

3.6.4.3 Magnetic Shaping with Active Auxiliary Currents

This technique consists in introducing current carrying conductors in a design, usually at the same current and phase (or opposite phase), to cancel or reduce the magnitude of the magnetic field in a region of the space of special interest, concentrating it in other regions. It is basically to promote the addition of the magnetic field generated by auxiliary windings to that generated by the main current carrying conductors, with the deliberate intention of reshaping the spatial distribution of the magnetic field.

This technique has been used to reduce the magnetitic field in regions nearby IWPT devices were living matter or other sensitive entities might be located during normal operation of the devices, including in automotive DWIPT prototypes and systems [128]. In [124] this method is discussed and compared with . The benefits provided by magnetic shaping currents are counterbalanced by the additional power losses in the windings of the auxiliary coils.

On the i-lane of the proposed HIPLEV system, measures are taken to keep the geometry and main currents under control, and avoid the need for any auxiliary currents for achieving compliance

Dynamic Inductive Wireless Power Transfer for Lightweight Electric Vehicles
Luiz Alberto Lisboa da Silva Cardoso – University of Minho

220

to the maximum recommended exposure levels, concerning pedestrians. The full magnetic and electric field exposure compliance of the HIPLEV vehicle itself and the protection of the rider is left out of the scope of this work. However, due to efficiency reasons, the use of auxiliary currents is not recommended to be used on board of the vehicle as well. Because of that, this topic is not further explored in this work.

3.6.4.4 Magnetic Shaping with Passive Resonant Circuits

Similarly to 3.6.4.3, the magnetic shaping may also be achieved when, instead of using active auxiliary current, parasite currents are induced in aisled resonant auxiliary coils, with the deliberate purpose of altering the magnetic field on a region of the space. More specifically, on the magnetic field being harvested by another coil, which is integrated with either a power supply or a load. This technique, useful to control exposure levels, tends to increase costs and decrease efficiency. It was not required in the design of the HIPLEV, and it is neither explored in this work.

3.6.5 Primary Coil Activation

If the primary coils of a DIWPT system are active all the time, two problems will occur: Firstly, the efficiency of the system as whole will decrease and the total power consumption will increase, unless the traffic is so high that it can be assured the presence of at least one secondary coil on the harvesting space of every primary coil. This is not expected to happen in most applications. Secondly, by being enabled all the time, the magnetic field generated by a primary coil can potentially produce unwanted effects on any entity not prepared for harvesting the magnetic energy, when these entities transit over the primary coil. It may be the case of a non-electric vehicle or human beings traversing a crossing point, or simply walking on the lane due to any mishap.

The primary coils are then supposed to be energized only when a vehicle equipped and ready to harvest power is positioned over their harvesting zone. This synchronous activation is not a unique requirement to DIWPT, stationary IWPT also needs it, to assure that the primary coil is only energized at the right moments, for similar reasons. This synchronization can be achieved by different techniques, among them:

(i)   Photodetection of the vehicle, used, for instance, in the ONR prototype [110];

(ii)   Explicit message exchanging, used, for instance, in the OLEV bus [129] and vehicular stationary charging based on SAE J2954 [92].

Dynamic Inductive Wireless Power Transfer for Lightweight Electric Vehicles
Luiz Alberto Lisboa da Silva Cardoso – University of Minho

221

The most advanced systems use message exchanging for controlling coils activation, which is an effective solution, but of high complexity, due to short periods of power switching on and off and the consequent communications latency and real-time constraints.

In order to avoid the implementation of newer complex message passaging schemes between the vehicle and the lane, a standardized message exchanging system is proposed, based the reuse of RFID protocols in Section 5.18. This provides the DIWPT a hybrid solution where the security and repeatability of digital systems are used in conjunction with near field communications, which allow the vehicle to be detected and uniquely identified when present in the harvesting zone.

3.6.6 Onboard Energy Management System

The onboard energy management system is the circuitry installed in the vehicle with the functionality of storing the excess harvested energy by the secondary coil and storing it in an energy storage component, which can be a battery a bank of supercapacitors, or an association of them. Because of the battery that normally is maintained by this system, it is also frequently called battery management system (BMS).

It its simplest forms, it can be constituted only by a diode in series with the DC output of secondary regulated by a DC-DC converter, which can be normally programmed to a nominal output voltage and to a maximum current level. This configuration works well when the battery used, for instance, is of lead-acid type, which can be charged at constant voltage with current limitation. The battery is then simply connected in parallel to the power input of the powertrain control. It is just necessary to design the nominal regulated output voltage from the secondary conveniently. For instance, for each group of six series-connected lead-acid battery elements, the full load voltage is around $13.2\,\text{V}$. So, if a $36\,\text{V}$ power train is used, a $36\,\text{V}$ lead acid battery should also be used, and the regulated DC output V_{DC} of the secondary coil should be set to $V_L = 3 \times 13.2\,\text{V} + V_D$, where V_D is the forward voltage drop of the diode used. With this simple circuit, when the induced voltage drops below a limit value that forces the DC-DC output not to be sustained at V_L, the powertrain with be sustained by the battery, which will start to drop its voltage. When the power harvesting is reestablished and V_{DC} is brought back to its nominal value, the DC-DC converter will take over the task of energizing the powertrain, and the excess power available not used by the powertrain will recharge the battery. In Figure 133 a diagram illustrating this basic BMS scheme is presented.

Dynamic Inductive Wireless Power Transfer for Lightweight Electric Vehicles
Luiz Alberto Lisboa da Silva Cardoso – University of Minho

222
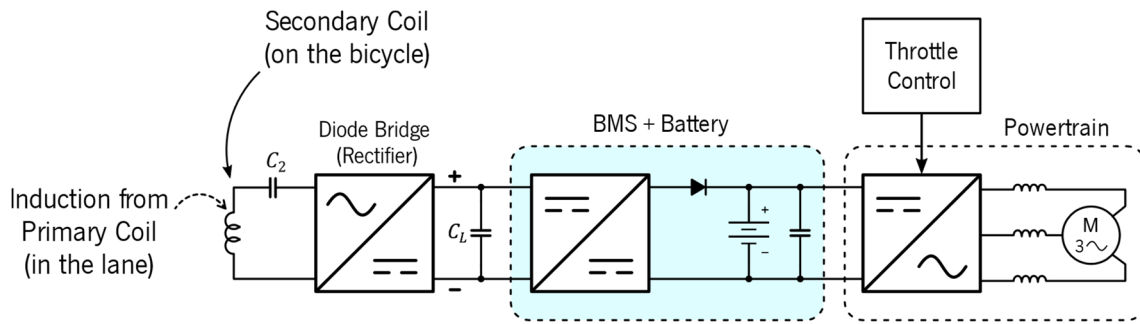
Figure 133: Connection diagram for obtaining basic BMS functionality, while using lead-acid type batteries.

One of the disadvantages of this simple BMS scheme is that energy that could be harvested at lower voltages is not used, which may be acceptable in some low-cost configurations. Other more advanced BMS can use lithium batteries, batteries with different nominal voltages than the powertrain, or even supercapacitors, which are best utilized if deep discharge to low voltages is accomplished. In this case, the BMS must guarantee priority of full nominal power to the powertrain, and only charge the battery with the excess power. In a good DIWPT design, a single pass over an energized primary coil should be enough to store energy to sustain the power train at full nominal power during the next inter-primary coil gap.

The development of the BMS circuit block, though important for a high performance DIWPT system, is not the focus of this research.

3.7   Conclusion

The mathematical analysis in the beginning of Chapter 3, in Section 3.1, showed that in the typical geometric configurations and speeds adopted by land transport system, the design of DIWPT can be understood and treated as a multi-location stationary IWPT. This means that, except possibly from the particular dynamic response of the circuits involved in the implementation, to design IWPT to a moving vehicle is equivalent to design a stationary IWPT that can work well in all positions of space where the vehicle is supposed to harvest energy.

Although this seem a great simplification, in practice it is a hard problem too, because coils are supposed to operate in near field, with magnetic field intensities and induced voltages decreasing rapidly with the third power of the distance between coils. This creates the need for using multiple primary coils, covering different segments of the vehicles' path, and their activation should be synchronized with the presence of vehicles.

Sections 3.2 to 3.4 presented a review of some of the most relevant dynamic inductive wireless power transfer technology milestones, from the early conceptual propositions of the late

Dynamic Inductive Wireless Power Transfer for Lightweight Electric Vehicles
Luiz Alberto Lisboa da Silva Cardoso – University of Minho

223

19th century to the more recent and more efficient first pre-commercial inductive lane prototypes. It can be noticed that DIWPT is anything but a new concept, which was invented (and patented) about only 10 years after the first public commercial tram line was set into operation. But the idea was not developed at that time. Even today, the existing designs are relatively new, and, at the time of this writing, have not yet become widely commercial, due to the complexity and cost of the technology involved.

In Section 3.6 a few more concepts were introduced in preparation for the DIWPT design of the HIPLEV, which is developed in Chapter 5.

In most of these DIWPT developments, it was clearly identified that all efforts were done with the purpose of providing wireless road electrification for the existing electric vehicles type that were popular at the time each DIWPT concept or project was developed. Some of the intrinsic DIWPT characteristics, however, were perceived as being capable of shaping future EV design and urban architecture, due to its particular engineering demands.

Dynamic Inductive Wireless Power Transfer for Lightweight Electric Vehicles
Luiz Alberto Lisboa da Silva Cardoso – University of Minho

224

Chapter 4

Human-Inductively Powered Electric Vehicles

In Chapter 2 and Chapter 3, the main theoretical aspects of IWPT and DIWPT, and some relevant implementation cases for electrical mobility applications are reviewed. From the literature, it becomes evident that the target of the majority of all research and development efforts in DIWPT, so far, has been the standard heavy-weight road traffic. That notion is reinforced by the fact that prototypes, and other demonstration systems, in which the level of transferred power is significantly lower than what it would be necessary to power a car, are commonly referred to as "scale-down" DIWPT models.

In this chapter, the human powered vehicles (HPV) are briefly prospected. More specifically, bikes, velomobiles and their electrified versions are considered. Since all HPV fit in the lightweight category, the hybrid human-electric powered vehicles are also lightweight electric vehicles (LEV). The qualities of the hybrid electric HPV are then discussed and identified as excellent candidates to be combined with the dynamic inductive technology, resulting in the proposal of a new transport mode variant we name human-inductively-powered lightweight electric vehicle (HIPLEV).

Finally, electric or electrifiable HPV types commercially available are compared, to determine which of them would be more interesting to adapt to DIWPT in a first approach, and also, to fix their electrical parameters as the base requirements for the DIWPT design, in Chapters 5.

4.1   Bicycles and Velomobiles

Until the industrial era, land transportation was entirely restricted to walking, rickshaws, and other human-powered carts, as well as horse riding, carriages, and other animal-powered vehicles. The muscular force was the engine. Ancient cities, even the largest ones, survived, grew, and developed in reasonably sustainable manners for centuries, relying only on these transportation modes for fulfilling their needs for terrestrial displacement of people and goods. Because of this limitation, the majority of the most economically developed ancient cities usually had a body of water through which navigation was possible, so that commercial transport at larger scale was facilitated.

Dynamic Inductive Wireless Power Transfer for Lightweight Electric Vehicles
Luiz Alberto Lisboa da Silva Cardoso – University of Minho

225

After the introduction of the steam locomotive, in 1804 [130], and specially, since the middle of the 19th century, railroads started to be increasingly adopted, rapidly replacing horse-powered vehicles in long-distance terrestrial transportation tasks [131]. However, due to the engineering difficulties and high costs of laying the rail tracks over occupied urban spaces, steam locomotives and their railways were somewhat limited in providing intra-urban transport. Consequently, the railroads still left plenty of room for the traditional "legged" transport within the cities and their neighborhoods. Figure 134 shows a photo of a street in London, the most populous and wealthiest city by the end of the 19th century [132], taken in typical working day of that time.

Figure 134: View of Oxford Street, London, at the end of the 19th century (posted by P. Stone [133]).

The situation changed significantly only when motorized cars, of both electric propulsion and thermal engine types, came into scene in the last decade of the 19th century, almost at the same time the bicycles started to become very popular, in the 1880s, after the invention of the safety bike (with chains and rear wheel traction).

The earlier predecessor of the safety bike is an early 19th century design, by the German Karl von Drais, a rudimentary form of bike called the "Laufmaschine", later known as the "draisienne". In 1817, von Drais was publicly recognized to have cruised the distance between Mannheim and Schwetzingen, approximately 15 km, in one hour, riding his newly invented "horseless" vehicle [134]. In 1818, the draisienne was patented and demonstrated in Paris, gaining some popularity. In 1891 a French journalist argued the existence of another previous similar two-wheel design, the "celerifere", supposedly created by Mede de Sivrac, circa 1790, but, apparently, no documental evidence of this, other than his own argument, was provided [135].

These early novelty vehicles were considered fun curiosities, but not very useful as a transport, because they missed pedals and other many other features. After the introduction of pedal models, such as the Penny Farthing, in the 1870s, shown in Figure 135a, the popularity of the bike as a transport started do increase all over the world. These models had a big front wheel,

Dynamic Inductive Wireless Power Transfer for Lightweight Electric Vehicles
Luiz Alberto Lisboa da Silva Cardoso – University of Minho

226

to which axis the crank with pedals was attached, and a smaller rear wheel. The elevated position of the cyclist would constitute a risk for many potential cyclists, thus limiting their application as a transport. The invention of first safety bike, with rear wheel traction and using a chain mechanism to transmit pedaling energy to that wheel, as shown in Figure 135b, is generally attributed to Henry J. Lawson [136], who patented a vehicle of this type on 30th September, 1879, in England an seven years later in the United States [137].
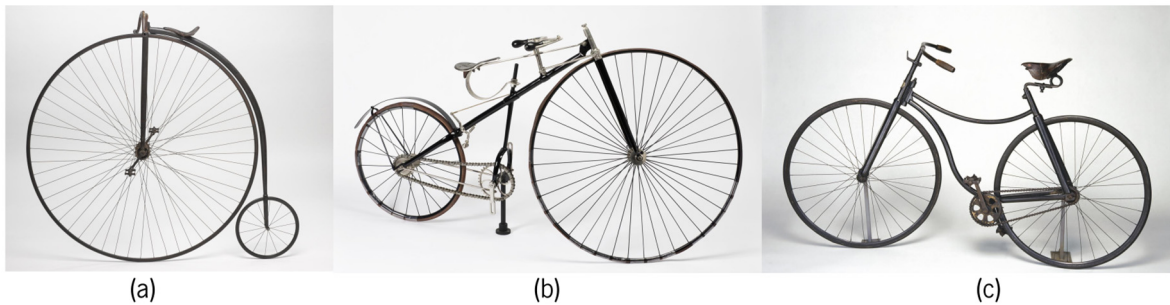
Figure 135: Relevant early bike designs in late 19th century: (a) Penny Farthing, from 1870s to 1880s; (b) Henry Lawnson's "Bicyclette", 1879; and (c) Starley's safety bike

Just a few years after later, in 1885, a new design of safety bicycle was introduced by John K. Starley, as shown in Figure 135c, a bike that basically consists in the modern bike, in its today's most widely known form, and it became very popular [138]. More technical detail about early bike design and an extensive list of these models can be found in [139].

One of the reasons for the large acceptance of both the safety bicycles and motorized vehicles for personal transportation was that they could replace the horses and carriages with advantages, while still using the same roads and streets built for these latter.

Another crucial factor was their affordability, which was immediately achieved by the bikes, and much later, by cars. The availability of bikes grew very fast, with the bikes being manufactured almost completely handmade, by a large number of small companies that started dedicating to their production. For the cars, this would take longer: Although both electric and thermal engine vehicles did exist at the turn of the century, they were not affordable to a major part of the population. Because of all these reasons, the bicycles then experimented an increasing popularization in the late years of the 19th century and apparently coexisted with cars as the transport alternative along the beginning of the 20th century.

Since their introduction, motorized cars followed a steady expansion pace until it could be mass produced and almost completely dominated the urban transports. The safety bike, on the other hand, immediately conquered many adepts due to its affordability and, before the

Dynamic Inductive Wireless Power Transfer for Lightweight Electric Vehicles
Luiz Alberto Lisboa da Silva Cardoso – University of Minho

227

proliferation of the heavier and faster motorized cars, it became very popular for commuting and other urban transportation tasks. Differently from a horse, the bike requires very low maintenance, and it can be parked and stored almost anywhere. It does not have to stop to feed, drink or rest, only the rider has.

Due to its popularity as a transport, the society became interested in establishing the bicycle performance limits and many cycling races and record keeping were promoted. One of the most famous of these was (and still is) the "hour record", i.e., the maximum distance that a cyclist could travel in one hour, or, equivalently, the maximum average speed that can be continuously sustained for one hour. Figure 136 shows a plot of hour records, for two slightly different types purely human-powered cycle: Starting from 1893, on the blue curve, the record achieved with standard upright bike, which are officially registered and kept by the International Cycling Association (Union Cycliste Internationale, UCI) [140]. Other types of bicycles that were later introduced, such as the recumbent and velomobiles types, are plot in in red.
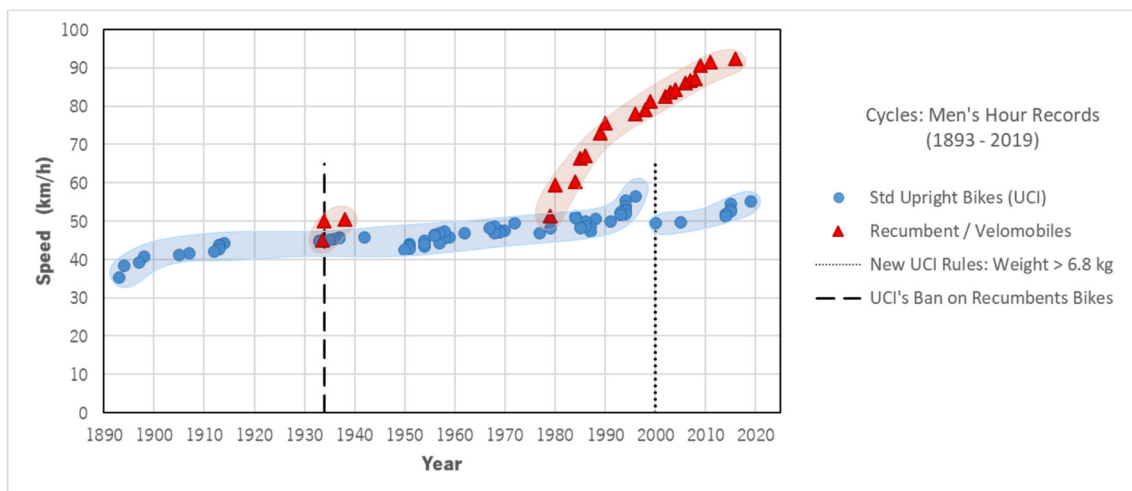
Figure 136: World men's hour records in standard upright bikes, recumbent bikes and velomobiles.

In the graph, four important milestones are especially important to understand the evolution of the bike: The first, in 1893, it is when the bike became worldwide popular, and an official record was initially set by Henri Desgrange, at 35.3 km/h. After continuous advances, in 1914, this record was broken by Oscar Egg, at 44.2 km/h, and remained unbeaten for almost 20 years [140].

In 1933 comes a second milestone for the bikes, the year in which the hour record was broken by a recumbent bike, a design type that was being used for the first time in a UCI competition, and achieved 45.1 km/h in the hour. The pilot, Francis Faure, shown in Figure 137a riding the bike during the competition, was not deemed as a first-class cyclist, but even then, he was able to break the record.

Dynamic Inductive Wireless Power Transfer for Lightweight Electric Vehicles
Luiz Alberto Lisboa da Silva Cardoso – University of Minho

228
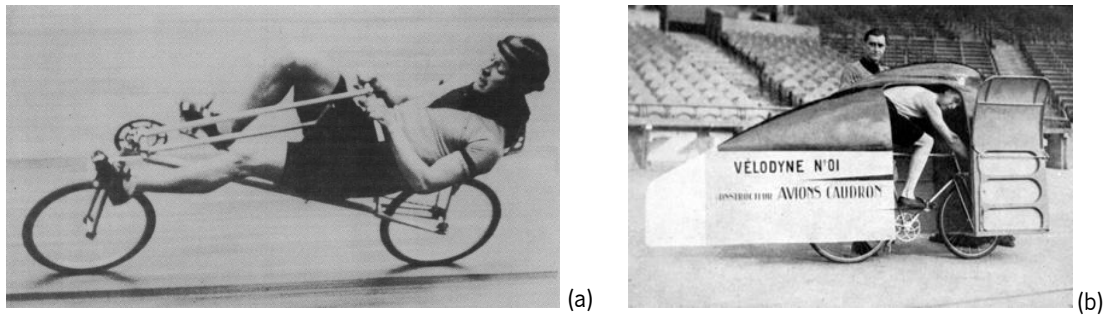
Figure 137: Fastest cycles of 1933: (a) Mochet's Velocar and (b) Berthet's Vélodyne.

Faure mostly relied on the low profile of his recumbent bike, the "Vélocar", designed by Charles Mochet. It was argued that this recumbent characteristic of the Vélocar offered a more natural position for the rider. The Vélocar was more aerodynamic as well, being more energy efficient than the upright bikes, what resulted in more speed with less pedaling power [141].

Later in the same year of 1933, Marcel Berthet's Vélodyne broke the hour record again, to approximately 50 km/h, using another non-conventional bike that, although built under the upright position paradigm, had a streamlined design, as shown in Figure 137b. At that time Berthet was 47, probably being physically outperformed by younger cyclists, what is another good indication that his more aerodynamic bike was also more efficient than previous designs.

Faure's and Berthet's achievements apparently caused a major concern among the newly established manufacturers of cars and bikes. Because of that, neither record was officially recognized, and UCI's official record was set in 44.8 km/h, the best mark achieved by a pilot using an upright bike. To prevent similar happenings, in 1934 these types of cycles were banned from all UCI's competitions, by the introduction of new qualifying rules for the bikes that excluded all similar recumbent or streamlined bikes. In 1938, disregarding these rules, Faure extra-officially broke the record again, using another model of Vélocar that combined both of these concepts: recumbence and streamlining, as shown in Figure 138a, extracted from [142].
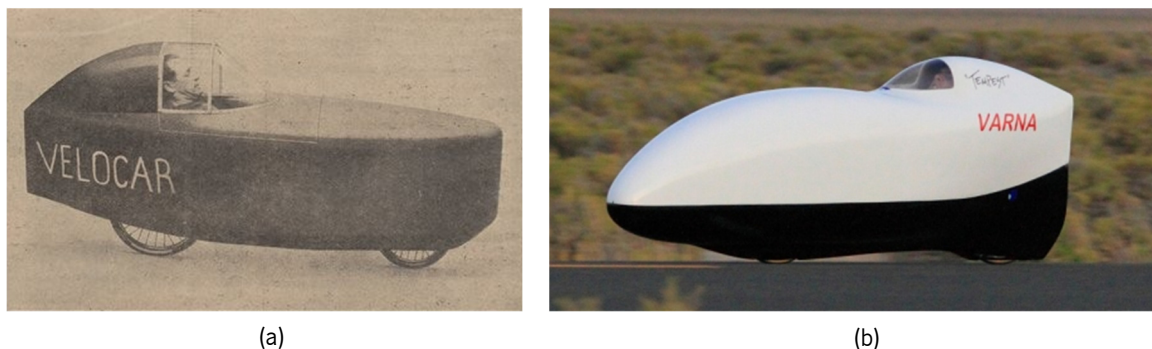
Figure 138: Velomobiles: (a) F. Faure in his 1938 Vélocar and (b) G. Georgi Georgiev's 2009 Varna Tempest.

Dynamic Inductive Wireless Power Transfer for Lightweight Electric Vehicles
Luiz Alberto Lisboa da Silva Cardoso – University of Minho

229

These few designs correspond to the first group of red markers plot in Figure 136, not being considered for official UCI competitions. At this point, the designers forgot about the recumbent bike design and the performance of bikes continued its relatively slow-paced evolution for the next four decades.

In the late 1970s, despite the ban of non-traditional bikes from official competitions, the interest and research on recumbent aerodynamic bikes was resumed, leading to a new developmental line that can be represented by the second group of red plots in Figure 136, those from year 1979 onwards. It can be considered the third most relevant milestone in the history of records. Among other relevant organizations keeping the records of these non-traditional cycles, is the World Human Powered Vehicle Association (WHPVA), founded in 1976 as the International Human Powered Vehicle Association (IHPCA).

The performance of standard upright bikes also has improved since then, mostly due to the use of novel and lighter materials, such as carbon fiber, that allowed their total weight to be decreased – to a point that, in 2000, the rule of a minimum bike's weight of 6.8 kg was introduced [143] [144]. The recumbent aerodynamic bikes became known as velomobiles, and also continued to be improved, benefiting from the same technological advances. Eventually, in 2009, one of them surpassed the limit average sustained speed of 90 km/h in one hour, the Varna Tempest, designed by Georgi Georgiev, shown in shown in Figure 138b. The most recent hour-records for velomobiles, captured by Francesco Russo, in 2011 and 2016, using similarly shaped vehicles, were respectively set at 91.6 km/h and 92.4 km/h [145].

The numeric explanation for this tremendous efficiency advantage of the velomobiles over the standard upright, non-streamlined bike is synthetically understood from the example given in [146]: 80% of the power generated by a cyclist traveling on leveled ground, at 29 km/h, is used to overcome the air resistance, of which 70% is due to the resistance of the cyclist's body to the air, and only 30% due to the resistance of the bicycle to the air. So, the velomobiles are design is the natural response to improve the bike's efficiency, their general design directive consisting in enclosing the body of the cyclist and if possible, the whole bike, in a low profile, streamlined fairing.

Comparing the velomobiles in Figure 138a and Figure 138b, it can be realized that these design general guidelines for better speed (and efficiency) did not change in essence, only better mechanical and aerodynamic design tools and materials became available, resulting in the different vehicles. On the other hand, due to the very low and restrained riding position, these fast

Dynamic Inductive Wireless Power Transfer for Lightweight Electric Vehicles
Luiz Alberto Lisboa da Silva Cardoso – University of Minho

230

velomobiles may be considered by many as not being comfortable to ride as those with a more upright position, being mostly adequate for athletes to ride.

The top high speed that can be achieved and sustained during one hour by streamlined velomobiles (~90 km/h) is comparable to the speed of a heavier standard electric car in a highway, when driven by a range-conscious driver. But efficiency, rather than speed, is the most relevant feature of this "new" (almost 90-year old) bike technology. On dedicated roads, the velomobile design can be a good transport option for non-athletic riders as well, because they require lower pedal power than it would be necessary to ride a standard bike, when riding on the horizontal plane at the same given speed. And this difference becomes more important as the rider moves faster.

4.2   Energy Efficiency of Bicycles

Although the bike does not directly require fuel to function, it requires human power, ultimately coming from ingested food, which also contains calories, and the production of food also has an associated carbon footprint. So, in addition to the health benefits of exercising, when riding a bike as a transport, its efficiency should also be evaluated. It has been proved that bicycles are one of the most energy efficient known transports, as shown in the comparison of Figure 139, adapted from the original Figure 4.16 of David G. Wilson [147].
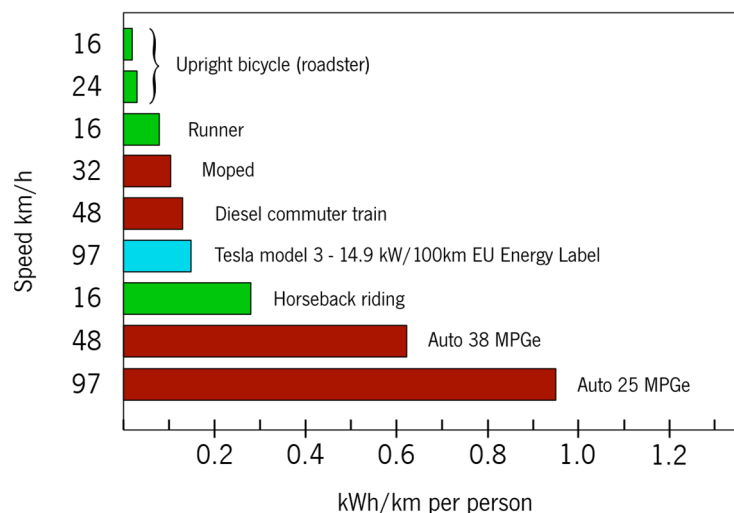
Figure 139: Efficiency of the bicycle compared to other transports, adapted from [147].

In the figure, the intrinsically sustainable transports are plot in green and fossil fuel based are shown in red. One of the most popular and representative electric vehicles in the market today, the Tesla model 3, is plot in blue, indicating that its ultimately degree of sustainability depends on the sustainability of the process of electric generation used to recharge it. The bicycle when ridden

Dynamic Inductive Wireless Power Transfer for Lightweight Electric Vehicles
Luiz Alberto Lisboa da Silva Cardoso – University of Minho

231

at 16 km/h requires an average of only 18 W/km and at 24 km/h, only 28 W/km, in standard riding conditions [147]. The velomobiles variants, not represented in the plot of Figure 139, exhibit even less energy demand, in terms of kWh/km/person than the standard bike.

It is understood that these different transport modes cannot be compared only based on their efficiency. They have different payload capacities, different velocity profiles and can serve in different applications. But in the daily life of modern cities, there is a large number of transport use cases where a small and slower vehicle, such as the bicycle, could entirely replace heavier standard cars. Especially, if the urban architecture is optimized for the use bicycles and other cycles, with the provision of dedicated lanes and parking spaces.

4.3   Human Pedal Power

In addition to the aerodynamics and other constructive factors, the key element defining the behavior of the bicycle is the rider. The age, health and athletic status of the rider, the wind and other climatic conditions, the slope of the lane, which will affect the required pedaling torque and power, will all impact the performance of the rider. For instance, the average power level output per kilogram of body mass for men and women are statistically higher for the men the youth, being, but tend to become approximately equal at older ages [148]. For every rider, there is a maximum effort level that can be sustained for a given time duration. These parameters limit the application of the bicycle as a transport, and may profile or even restrict its adoption by some individuals.

One of the main references available about the subject is obtained from prof. David Gordon Wilson, who extensively studied the design of bicycles [147]. In Figure 140, colored curves are drawn over the original prof. Wilson's graph [149], highlighting the typical human performance limits in terms of mechanical power (left vertical axis) and maximum sustained duration of that effort (horizontal axis, in logarithm scale). The blue curve is that of healthy (non-athletic, but non-sedentary) individuals, the green curve corresponds to first class athletes, and red curve to world records and other exceptional achievements registered in history, most of data referring to pedaling. Although pedaling powers in excess of 1 kW can be observed, this power level is only possible to sustain for very short periods of time, up to about 1 min, and almost exclusively by exceptional athletes.

Dynamic Inductive Wireless Power Transfer for Lightweight Electric Vehicles
Luiz Alberto Lisboa da Silva Cardoso – University of Minho

232
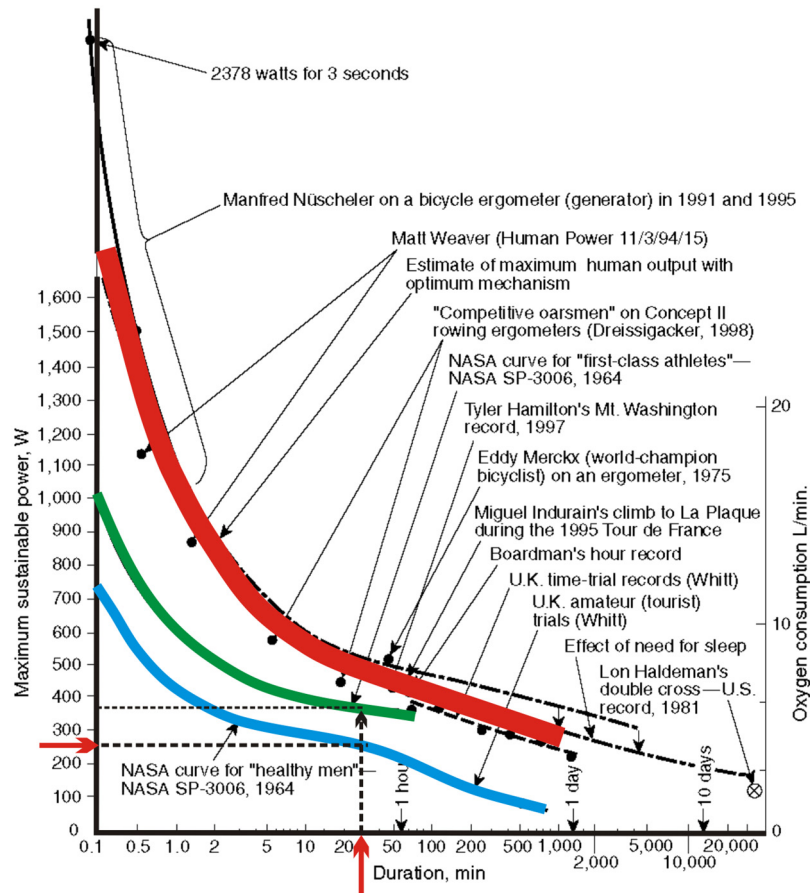
Figure 140: Human pedaling power limits, annotated on the original graph of D.G. Wilson [149].

The normal performance is found when the operation point indicated by red arrows, in the graph of Figure 140 is considered. It indicates that healthy non-sedentary men will sustain a maximum of 250 W of mechanical power for 30 min, a power level that can be elevated to approximately 350 W, with training.

But in practice, most riders do not feel comfortable riding at their maximum possible output power envelope, a typical comfortable pedaling effort for 30 min rather corresponding to the maximum effort that can be sustained for two or three hours, that is, approximately 100 W. For some riders, the easy pace is set even lower, at only 75 W, which is about the power that a non-trained healthy person could sustain for about 8 hours in a day.

Let us consider the statistics of commuting times of employed persons in the European Union (EU-28) in the period of 2013-2020, summarized in Table 19 [150]. It can be noticed that about 64.8% of workers have a commute time of 30 min or less. So, it can be assumed that most people would not appreciate a commuting time over 30 min, a duration only habitually exceeded by 35.2% of the workers.

Table 19: Statistics of commuting time of European employed persons.

Commuting Time, t (min)	Percentage of Valid Responses*
$t < 10$	18.2%
$10 \leq t < 15$	14.5%
$15 \leq t < 20$	13.6%
$20 \leq t < 30$	18.5%
$30 \leq t < 45$	20.2%
$45 < t < 60$	6.2%
$t \geq 60$	8.8%

*Source: EUROSTAT, online data code LFSO_19PLWK28, last update on 04/02/2022 22:00.

The distance that a bicycle rider can travel, in the 30 min duration considered, depends on the speed that can be maintained with the 100 W to 250 W average power supplied by the rider. This speed varies with a large number of factors, most of them directly affected by the lane design and other city planning aspects. As discussed in Section 4.2, the type of cycle used can also greatly influence the travel profile. If using a standard upright roadster bike in still air and on the level, this power range translates into the speed range of 20 km/h to 28 km/h. Conservatively using the lower 75 W reference, this commuting speed would drop to 16 km/h [149].

These speeds estimates are lower than the maximum legal speed of cars in European urban roads, 50 km/h, but, in practice, they can be close to the average car speed actually developed in some congested European cities. In addition, in many large cities, the total commuting time must frequently include the time to find a place to park the car and walk back to the ultimate place of destination, an issue that usually does not affect the cyclist.

In Europe, it is known that 30% of motorized trips are shorter than 2 km, and 50% of motorized trips are shorter than 5 km [151]. So, considering the worst-case speed of 16 km/h (using the 75 W pedaling power a healthy person can comfortably deliver), the resulting commuting times associated to these reference distances, if a bike is used, are respectively 7.5 min and 18.75 min. These durations are well less than the minimum commuting time experimented by 35.2% of the European workers [150], and only respectively 5 min and 13 min more than what, in the best case, it would take a car driver to commute over these same distances, at the maximum legal speed in European urban roads (50 km/h). Therefore, the use of bicycles for commuting is seemingly viable, both in terms of the required physical aptitude (under the hypothesis of healthy persons) and the expected commuting times for this distance range. Their mass adoption is apparently restrained only by cultural inertia and, to a possibly major extent, to the lack of urban architectural facilities for the use of bicycles (lanes with relevant routes, parking places, etc.)

Dynamic Inductive Wireless Power Transfer for Lightweight Electric Vehicles
Luiz Alberto Lisboa da Silva Cardoso – University of Minho

234

4.4   The Electrification of Bicycles

The idea of electric personal mobility as a future prevalent transport is almost as old as the first electric cars and first bikes, as suggested by J. H. Bridge in 1886 [152]. Electric mobility, by means of standard size road vehicles, had been considered a promising technology for imminent adoption in the late 19th century, but that perspective completely failed, after about a decade of great enthusiasm, in the early 1900's. Electric cars are now again deemed as a solution for the future of personal transportation in the cities.

Bicycles, on the other hand, have been continuously used as a popular transport vehicle, and coexisted in the cities with other transport options, since their introduction. This is one of the few vehicles that are also used for pure leisure and for exercising by a large number of people. But, above all, they have long been used for utilitarian urban displacements. As part of the electric mobility development, the electrification of the bike is an interesting old story in itself [153] [154], which will not be presented herein [155] [156]. The focus in this Section, rather than discussing the history of e-bikes and personal mobility, is the identification of market opportunities and tendencies that can confirm the promising short-term future of e-bikes as a transport mode.

Based on the information presented in Section 4.3, it can be estimated that when a bike is adapted with an electric powertrain, 100 W of power is already a practical electrical assistance level for commuting. This would make riders in a wide range of physical conditions exhibit, with no pedaling, approximately the same performance of an average healthy, non-athletic rider, when riding in a comfortable pace, on a leveled terrain with no headwind. If the electric power of the powertrain is brought to 250 W, and sustained at this level for at least 30 min, the bike would perform as being ridden by a healthy rider at his maximum pace. The electric power can level riders, promoting to this category potential users that, due to physical performance limitations, could not use the bike as a transport.

Conversely, if mechanical assistance of the electric powertrain is used in addition to normal pedaling, a cyclist will exhibit an improved performance profile, being able to use the bicycle in an extended number of transport applications. Looking at Figure 140 again, it can be realized that a healthy non-athletic rider would be able to achieve the same performance level of a world recordist class rider in 30 min displacements, if he could add the expected 250 W of his own maximum pedaling power to a 250 W assistance power level provided by the electric motor. These numbers justify why an electrically assisted pedal cycle has its maximum electric power assistance level regulated at 250 W, while still being legally considered a bicycle, in the European Union [5].

Dynamic Inductive Wireless Power Transfer for Lightweight Electric Vehicles
Luiz Alberto Lisboa da Silva Cardoso – University of Minho

235

The electric bicycle, almost as economically accessible as the standard, non-electric bicycle, has a significantly improved performance over its original, purely human-powered version. This permits its use in an extended number of transport use cases, previously not addressable by a purely human-powered vehicle (HPV). This fact, conjugated with the higher cost of both thermal and electric vehicles, may help explain the reason for the great expansion of the e-bike market.

This is confirmed by the analysis of the graph in Figure 141, which shows that bikes (green bars) still sell more in Europe today than passenger cars (brown curve), with an almost constant yearly demand of 20 million units, over the last 12 years. These numbers were not much affected by economic crisis or other contingences, while cars experienced a decrease in its sales from 2007 to 2013, slowly recovered from 2014 on.
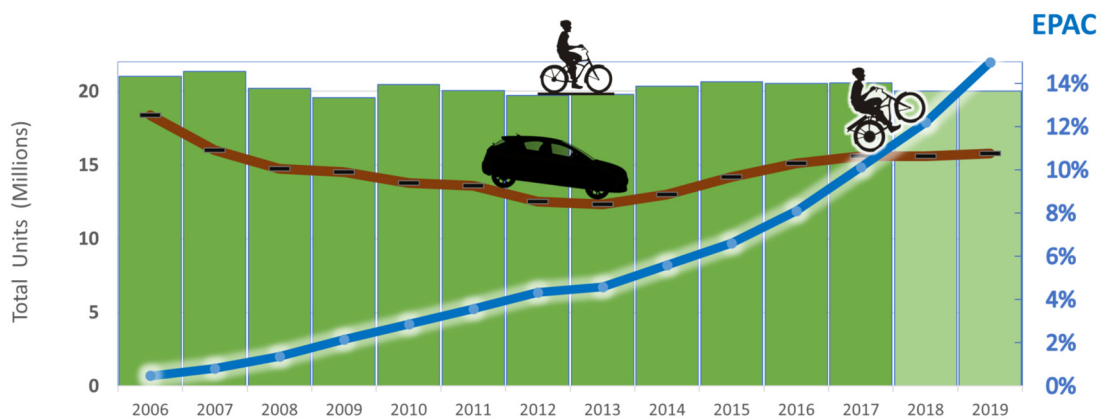
Figure 141: Comparative European market evolution of cars, bicycles in general and EPAC-type bicycles.

The information used for the plots the brown curve on the chart of Figure 141, concerning passenger cars, was sourced by ACEA [157]. The data concerning bicycles and e-bikes until 2017 were sourced by CONEBI [158], while data referring to 2018 and 2019 are estimates, based on other sources [159] [160]. It is apparent that even about 130 years after their introduction in the market, the interest of the population in bicycles is still pronouncedly high, with at least 25% more bikes being sold every year of the last decade, in Europe, than new passenger cars registered.

Another phenomenon that can also be highlighted in the graph of Figure 141 is the electrification of bikes. The participation of Electrically Power Assisted Cycles (EPAC) in the market has been increasing yearly (blue line in Figure 141). The initial estimation of 15% of the total bike sales for e-bikes in 2019 has actually been updated to 17%, later in 2020 [161]. These facts seem to be consistent with an increasing number of people in Europe trying to intensively use bicycles for personal transportation, rather than for recreational activities, as new investment is made in urban infrastructure.

Dynamic Inductive Wireless Power Transfer for Lightweight Electric Vehicles
Luiz Alberto Lisboa da Silva Cardoso – University of Minho

236

The bike is the par excellence terrestrial human powered vehicle (HPV), in the same manner the electric assisted bike is the par excellence lightweight electric vehicle (LEV). This double association makes the e-bike a very special product in the market. From recent historical data, as shown by the blue curve in Figure 141, it can be inferred that the availability of EPAC bicycles will grow until a major part of the bike production is electrically assisted. This is likely to happen much earlier, for instance, than the large-scale adhesion to full size electric vehicles (EV). Firstly, because the latter are still significantly more expensive than their thermal engine counterparts of similar performance. Secondly, because of the major investment that is required to provide all necessary recharging infrastructure for the new standard size EV.

The range limitation of early electrics (and its consequent "range anxiety"), due to the characteristics of old technology lead-acid batteries, together with the complexity of upscaling the recharging infra-structure, made the EV lose the market battle to the thermal engine vehicles a century ago. Absolute acceptance only was granted for those electric vehicles in which the battery was not as crucial, such as trams and trains, which could run almost continuously receiving energy from tracks or aerial cables. Only these types of EV were a great market success that rapidly expanded, remaining continuously in use until our days as a preferable mass transport mode.

The battery technology available today, while marginally good for allowing standard EV to replace thermal engine cars, is sufficient for e-bikes. Independently of the energy storage technology used, the electric bicycle, on the other hand, shall never experiment the same range anxiety observed in heavier standard EV, due to the intrinsic use of human power to propel the vehicle. This reinforces the prevision that the uprise of the e-bike today, contrarily to the first wave of the electric cars in the early 20th Century, is not a temporary tendency. The electric bicycles are prone to dominate at least the utilitarian bike market, in a decade or less.

If velomobiles would be used in place of standard up-right bikes for the 30 min reference commuting time (Section 4.3), at the pedaling power rating of 250 W, the expectable average speed could jump to more than 50 km/h [162], leading to a 25 km trip range in 30 min of commuting time. Naturally, the same speed and distance would result if the velomobile is used in electric model only (no pedaling), at the same power level of 250 W. In the worst case of a 75 W pedaling power, in the same conditions (in still air and on the level), a typical velomobile HPV would still reach about 32 km/h [162], covering 16 km in a 30 min trip. If human power and electric power are conjugated, each adding 250 W to a total 500 W of moving power, speeds in

Dynamic Inductive Wireless Power Transfer for Lightweight Electric Vehicles
Luiz Alberto Lisboa da Silva Cardoso – University of Minho

237

excess of 65 km/h could be expected, what would allow a 32 km commuting distance to be accomplished in 30 min.

As mentioned, these numbers apply to no-wind conditions in horizontal lanes, and they would be worsened in steep or irregular terrain – and the heavier velomobiles are even more sensitive to a good lane design (i.e., flat and smooth, with low grades). For example, for an upright bike to keep a constant speed of 19.3 km/h, when climbing a steep lane, a 75 kg rider would require approximately an extra 57.5 W of power for every additional 1% in the slope grade [163].

Even then, and while not yet popular today, the velomobiles' potential performance also makes them an option to be eventually considered for the electrification, as a sustainable complimentary choice to standard bicycles, in some transport applications and in favorable urban contexts.

4.5 E-Bikes and other Lightweight Electric Vehicles

The term lightweight can have different interpretations. In the context of this work, one of the requirements for a vehicle to be lightweight is to exhibit a low mass, relatively to its payload. The vehicles in consideration are those with a mass that is less, desirably much less, than its maximum payload, i.e., the vehicle rider and, eventually, other passengers and load. Except for the standard bicycle, vehicles in this category are not yet very common to be found in the streets, as standard transportation means, often being indiscriminately associated to recreational activities. The main reason being that the large majority of today's cities and roads were shaped by the thermic engine vehicle, which powertrain, together with the appropriated chassis to handle that engine and other mechanic parts, usually has a much higher mass than the that of its driver and passengers.

Defining the lightweightness coefficient, $л > 0$, as the quotient of the vehicle mass, including fuel and batteries, as required, to the payload mass, including driver and passengers, it can be noticed that the smaller $л$ is, the potentially more efficient is the vehicle for each transport application considered. Typical values for different vehicles and transport configurations are exemplified in Table 20.

Dynamic Inductive Wireless Power Transfer for Lightweight Electric Vehicles
Luiz Alberto Lisboa da Silva Cardoso – University of Minho

238

Table 20: Typical value of the Lightweightness coefficient, л, for different transport modes.

Configuration	Vehicle Mass (kg, fuel and batteries incl.)	Passengers (incl. driver)	Total Payload (kg)	л
Skateboard	4	1	80	0.05
Road bike (racing)	8	1	80	0.10
Urban e-bike	30	1	80	0.38
470 Class Sailboat	122	2	160	0.76
Electric Wheel Chair	75	1	80	0.94
Honda CBF-125 Light Motorcycle	128	1	90	1.42
Volkswagen Beetle (five passengers)	840	5	400	2.10
BMW i3 (five passengers + 50kg luggage)	1,195	5	450	2.66
Bombardier FLEXITY Swift (Porto's tram, full occupancy)	62,500	248	19,840	3.15
Nissan Leaf (five passengers + 50 kg luggage)	1,493	5	400	3.73
Tesla Model S (five passengers + 150 kg luggage)	2,100	5	550	3.82
Air Bus A-380 (519 passengers + luggage)	491,000	544	83,000	5.92
Volkswagen Beetle (driver alone)	840	1	80	10.50
BMW i3 (driver only)	1,195	1	80	14.94
Nissan Leaf (driver only)	1,493	1	80	18.66
Tesla Model S (driver only)	2,100	1	80	26.25
Rolls-Royce Phantom VII	2,550	1	80	31.88
Queen Mary 2 Cruise Vessel	94,720,000	4328	623,232	151.98

Unless otherwise noticed, the term lightweight vehicle will herein refer to those vehicles exhibiting $л \leq 1$ when loaded at their maximum payload. So, for a vehicle carrying two 75 kg persons, the maximum weight for a lightweight vehicle would be 150 kg. If a 150 kg vehicle is transporting just one 75 kg person, the vehicle should be considered lightweight in this configuration. Looking up Table 20 again, it can be noticed that only two EV vehicles from the entire given list qualify as a LEV, the urban e-bike, and the electric wheelchair. Not by mere coincidence, these are electrified versions of vehicles that, originally, were purely man-powered. Specially for land vehicles, this is so because a vehicle cannot be very heavy, if it is expected to be man-powered. Incidentally, the vehicles exhibiting higher л values tend to be associated with more comfortable and luxury transportation, either electric or not. Apparently, under the energy efficiency criterion, the greater luxury of all would be unnecessarily riding a larger capacity vehicle at minimum occupancy.

The sole use of the л coefficient can be misleading when comparing vehicles executing different transportation tasks. However, given a specific task, as described by the triad of basic parameters, {distance, time-of-travel, payload}, it should provide a good indication of intrinsic energetic efficiency. However, concerning the market, the decision to build a heavier or lighter car is guided not only by differences in the main parameters characterizing the transport task and the expected life-cycle cost of the vehicles. Factors such as safety (and safety perception), comfort and social status also influence consumer's decisions, and consequently, the manufacturers'

Dynamic Inductive Wireless Power Transfer for Lightweight Electric Vehicles
Luiz Alberto Lisboa da Silva Cardoso – University of Minho

239

choices for building a heavier vehicle, even in applications where a lighter vehicle could perfectly accomplish the transportation task.

Interestingly, one major technical factor affecting the л coefficient in commercial EV models is the battery weight, which can commonly account for one 20-25% of the total vehicle's weight. Unfortunately, decreasing the battery size and weight normally decreases the EV autonomy, what, at the energy density levels achieved by current battery technology, would render the EV even less competitive with thermic engine cars, in terms of autonomy.

The safety requirements may directly increase the weight of an EV, but this increase is likely less significant when fulfilling safety requirements at the lower operating speeds, at which lightweight EV usually provide their service. The remaining important factors then affecting the tolerance to higher л coefficients in an EV are convenience, comfort, and social status, which are cultural perceptions of customers.

While this work does not aim to address these important and often dominant subjective issues, it does come in the support of reducing the battery capacity and weight of EV, by the adoption of inductive wireless power transfer technology. In this manner, lower л and larger intrinsic efficiency can be achieved without sacrificing the EV autonomy.

A key point favoring the widespread use of the bike is that it is not necessary to register the bike before its use, nor it is necessary to have a driver's license to use it, in most countries. In the case of the US, in most counties, due to the ability of the states and accordingly to the states laws, the counties too, to legislate about this [164]. The absence of the need for registration approaches the condition of an HPV to the man, rather than to the vehicle, and that is likely a factor in the popularization of the bikes. It happens that the legal status of an electrified HPV is affected by the maximum electric power that can be supplied to its powertrain, and how this power is supplied.

In the European Union, if a bike is a pedal assisted electric cycle (EPAC), that is, if the assistance of the powertrain is activated by pedaling, limited to 250 W and cuts off if speed rises above 25 km/h, the bike is legally equivalent to a non-electric bike. It is as if it was not considered a motor vehicle. It can then be used in the same lanes shared with pedestrians, for instance. In the EU, this category of electric bike is entirely different from those regulated as power cycles (category L1e-A), mopeds (categories L1eB and L2e) and light quadricycles (category L6e), as show in Table 21.

Dynamic Inductive Wireless Power Transfer for Lightweight Electric Vehicles
Luiz Alberto Lisboa da Silva Cardoso – University of Minho

240

Table 21: Categorization of lightweight electric vehicles, according to EU and USA norms.

Jurisdiction	Norm / Recommendation	Vehicle Categorization	Name	Wheels	Maximum Speed of Electrical Assistance	Maximum Power
European Union	European Committee for Standardization - EN 15194	EPAC	Electrically power assisted cycles (EPAC)	≥ 2	25 km/h	250 W
	EU Regulation No. 168/2013	L1e-A	Powered cycles	2 to 4	25 km/h	1 kW
		L1e-B	Moped	2	45 km/h	4 kW
		L2e	Moped	3	45 km/h	4 kW
		L6e	Light quadricycle	4	45 km/h	4 kW
USA	U.S.Code, Title 15 - Commerce and Trade, Chapter 47, §2085.	Low speed electric bicycle		2 to 3	20 mph* (32 km/h)	750 W

While clearly motivated by the natural limits of human pedaling power, the EPAC definition in the EN 15194 would better support the widespread adoption of the e-bike in cities where the terrain is often graded.

Ideally, the maximum recommended upward inclination in a bike lane design is 10% (5.71 degrees of arc) [165], even then, when short height differentials are considered. But incidentally, this maximum inclination is very likely to be achieved in some streets of European cities. For a 75 kg rider to climb a lane with 10% inclination and head winds of 10 km/h, approximately 1030 W of power would be required by the power train to keep a 25 km/h speed, if no pedaling is used. This is significantly more than the maximum of 500 W that a rider could sustain for 30 min, if using 250 W of electric assistance to the power train.

Because of that, we share the opinion that a higher than the current 250 W power limit should be legally considered in the future, as long as the speed of assistance is kept limited to 25 km/h, in dedicated lanes. Outside the urban perimeter and in dedicated lanes, even higher speeds, up to 45 km/h should also be evaluted. However, while regulation is not yet reviewed, in order to keep compliance with the PEDELEC class, and benefit from the legal bike equivalence, the maximum electric power supplied to the power train should limited to 250 W.

4.6   Human-inductively Powered Lightweight Electric Vehicles

If the rider of a human-powered LEV is a first-class athlete, pedaling can add more than 1 kW of peak power to the power train for about half a minute or more. However, as seen in Section 4.3, the expected pedaling power by an average healthy man that can be sustained for a 20-minute interval lies in the conservative 250 W – 300 W range [147]. This number comes to a maximum of 250 W for a 30 min period. This statistical fact is likely the basis for the legal power limitation imposed on electrically assisted bicycles, the most popular human powered LEV.

Dynamic Inductive Wireless Power Transfer for Lightweight Electric Vehicles
Luiz Alberto Lisboa da Silva Cardoso – University of Minho

241

Electric bikes, when cruising on steep grades or at higher speeds and distances, are commonly used in full electrical assistance mode. In this condition, the powertrain tends to quickly exhaust the battery of the LEV. Assuming a typical battery capacity between 250 Wh and 400 Wh, the electrical range (autonomy) for this most popular LEV, which electric power is limited to 250 W [5], is between one to one and a half hours, running at full power.

Although this is adequate for most commuting trips in an urban context, the typical electric cycle requires charging after every daily trip, what is not convenient. Especially considering that charging points are usually not available in the parking and storage places, what many times implies in the removal of the battery for recharging.

On the other hand, the battery is one of the most expensive components of a lightweight electric vehicle. In the case of electric bicycles, its cost may typically lie in the range of 50% to 100% of the cost of an equivalent non-electric vehicle. Often, the battery will also cost more than the electric motor and the motor driver circuit together.

If a LEV operates in DIWPT mode, adapted with a pickup coil and the required power circuitry to harvest energy from the magnetic field generated by the inductive lane (i-lane), it will be possible to completely dismiss the use of standard batteries while cruising over these i-lanes. In addition, as a human-powered vehicle, the hybrid LEV can also dismiss the battery when away from the i-lanes, by pedaling, if the vehicle is ridden at lower speeds. The combination of an electric lightweight HPV with the DIWPT thus produces a unique new modal variant, the Human-Inductively-Powered Lightweight Electric Vehicle (HIPLEV).

A HIPLEV is a highly sustainable, flexible, and smart transport because:

(i)   It is a human-powered EV, it may be used with no conventional battery, just a low capacity, short term onboard energy storage is needed. The battery may be optionally added to the vehicle's configuration, to provide more flexibility of employment, but it is not required in all applications.

(ii)   Users with low athletic profile or reduced mobility may permanently install a battery in the HIPLEV. This can also be done for special applications, when the HIPLEV is constantly used, or for cargo services. The battery would automatically charge when the HIPLEV is run over some i-lane, but it could be also alternatively charged on a stationary inductive charger.

(iii)   Even the users that do not need a battery on a daily basis can eventually rent a battery and provisionally install it in the HIPLEV, for satisfying requirements of special trips or use cases.

Dynamic Inductive Wireless Power Transfer for Lightweight Electric Vehicles
Luiz Alberto Lisboa da Silva Cardoso – University of Minho

242

(iv)   It will use inductively electrified lanes (i-lanes) to move fast with indefinite autonomy, provided there exists an i-lane that leads to the intended destination.

(v)   Pedaling hubs can be integrated in the city to connect multiple i-lanes and make it possible for the HIPLEV to relay seamlessly from one i-lane to another, until it comes close enough to its destination. Then, the final segment of the journey is accomplished on battery power or by pedaling only.

(vi)   Similar will happen at departure: If the destination is close enough, the HIPLEV can get there relying on battery energy or solely by pedaling. If not, the HIPLEV should be able to take the closest i-lane leading to the intended destination.

(vii) Intelligence and smart communication with the i-lane management system can be integrated in the HIPLEV, in order to help the vehicle to calculate the best route to destination, and to permit the i-lane system to run more balanced.

(viii) When not running over an i-lane, the HIPLEV can still use standard bike lanes or pathways that can be shared with pedestrians or cars, provided the maximum car speed is regulated on these shared pathways to the same speed limit of the HIPLEV, when this latter is used in non-electric mode.

(ix)   A key point to assure safety is that the maximum speed limit to enforced in shared lanes and i-lanes is the maximum cruise speed of the slowest vehicle. The DIWPT activation scheme can help enforce the maximum speed of electric assistance, by limiting wireless power transfer to the maximum regulated speed.

(x)   Another point to increase safety is to require that all HIPLEV running at higher speeds on dedicated i-lanes have a similar total vehicle weight.

(xi)   The presence of the magnetic field created by the primary coils in the i-lanes will facilitate the future implementation of self-driving capacity on a HIPLEV, when it is run over an i-lane.

(xii) The unfaired upright EPAC type bicycles are the entry level vehicle class to be adapted for DIWPT and become a HIPLEV. Electric velomobiles that can ride on purely electric mode are the next step, if dedicated lanes can be used.

For safe urban operation of the HIPLEV, a maximum speed limit in the range of 25 km/h (as for L1e-A and EPAC) to 32 km/h (as in the US Low speed e-bike) is recommended. This is less than the speed of the fastest human beings running on short tracks, but well over the average speed a person can sustain in medium distance tracks [166].

Dynamic Inductive Wireless Power Transfer for Lightweight Electric Vehicles
Luiz Alberto Lisboa da Silva Cardoso – University of Minho

243

The HIPLEVs have a reduced footprint in terms of material resources used, compared with heavier EVs. So, they should be much less costly to produce and to own, and that will favor a more sustainable economy. This will also promote a reduction of the pollution, not only where the HIPLEV is used, but also that due to the manufacturing process of the vehicle. The HIPLEV can improve the level of humanization of urban spaces and the health standards, being able to fill the gap between the purely human power based soft modes and the convenience of heavier personal transportation. Figure 142 illustrates the use of a HIPLEV for commuting.
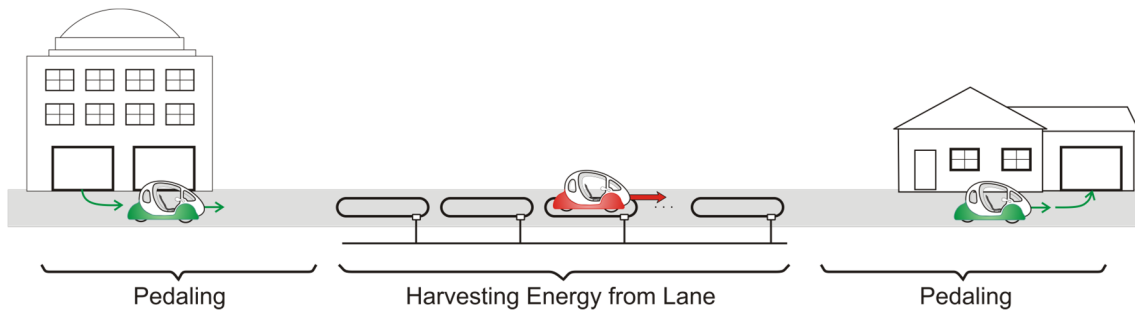
Figure 142: Using a HIPLEV in commuting transport.

The favorable market acceptance of the e-bike (Section 4.4) may be interpreted as an indication of opportunity for the introduction of DIWPT electrification for LEV. This is technically and economically more feasible than the DIWPT electrification for heavier traffic, due to the large difference in power levels involved, in a proportion estimated in the 200:1 to 20:1 range, depending on the vehicles considered in each class.

Velomobiles have been consistently calling attention of conscious advanced riders, mostly in the Netherlands and Germany, with a few models commercially available, launched in the last 10 to 15 years. But it is still a very restrict market, and only a few hundred units of each model have been sold worldwide [167]. Some examples of these models are shown in Figure 143:

Figure 143: Examples of velomobiles of recent design: (a) InterCityBike's model DF, (b) Drymer's model Sinner Mango and (c) Quest.

In most of the velomobiles so far commercialized, an electric powertrain is not included in the basic factory configuration. The buyers of these vehicles are habitual cyclists that solely aim at the efficient use of human power and higher riding speeds.

Dynamic Inductive Wireless Power Transfer for Lightweight Electric Vehicles
Luiz Alberto Lisboa da Silva Cardoso – University of Minho

244

Despite of being reputed as comfortable by their riders, the very low profile of the velomobiles, their sporty and bold design, together with a still high acquisition cost and low availability in the market, may possibly refrain many potential users from adopting them as a commuting transport.

Other human powered LEV recumbent models of higher profile and more upright riding position, not being as efficient as the fully streamed velomobiles, have also been designed in the last years. Usually heavier than the velomobiles, but still exhibiting a lightweightness coefficient $л \leq 1$, these models have received increasing attention from the public in recent years. Representative models of these new LEV cycles are shown in Figure 144.

Figure 144: Examples of human-powered lightweight electric vehicles of recent design:
(a) Sørensen's Podbike, (b) Schaeffler's Bio-Hybrid and (c) Organic Transit ELF.

4.7   Selection of a Cycle Type for HIPLEV Prototyping

Different criteria arise when selecting an electrically assisted cycle type for HIPLEV modification. Two different paradigms are promptly identified for choosing the cycle:

- Best electrically assisted cycle for immediate prototyping and validation of the concepts involved in the proposal of the HIPLEV.

- Best electrically assisted cycle for HIPLEV introduction in urban, one with the largest possible current availability and growing market share.

- Best overall electrically cycle vehicle leading to a fully featured HIPLEV system, one that could more effectively replace standard road EV as a transport mode in specific urban and commuting use case, in the long range.

It is our understanding that this choice is neither irreversible nor exclusive. But it was deemed as a good strategy to start with a design that can be less costly to prototype and test, by using a popular cycle platform. In this manner, the prototype and the results would be more likely to attract immediate consideration, enough to be independently reproduced and evaluated, eventually motivating an implementation in pilot scale.

Dynamic Inductive Wireless Power Transfer for Lightweight Electric Vehicles
Luiz Alberto Lisboa da Silva Cardoso – University of Minho

245

So, the definition of the candidate e-cycle for HIPLEV adaption comes from the analysis of its main characteristics concerning:

Performance. A streamlined profile high mechanical efficiency such as in velomobiles, associated with a low vehicle mass is highly desirable, so that a high electric efficiency can be also achieved. Vehicles with intrinsic higher stability, such as three and four-wheeled cycles are in great advantage under this criterium.

Popularity and availability. The cycle that is used for modification in a HIPLEV should be popular, available, and not costly, so that, once accomplished the successful demonstration of the concept, it could be more easily and faster accepted by the cycling community. Those models that are the most available commercially tend to be least expensive, and that naturally makes the prototype implementation less challenging, in term of required resources and budget. In this category, the two-wheeled e-cycles are dominant over tricycles and quadricycles, or any velomobile. Particularly, as observed in 4.6, the 250 W EPAC type electric bicycle is the most prominent representatives of this class.

Easy of adaption. Virtually all cycle models offer enough room to receive the necessary power electronics associated with the vehicle adaptation, including a small battery. However, the installation of a secondary coil to harvest energy can be a not straightforward task. Three or four-wheeled cycles would offer an intrinsic stability that would simplify both the mechanical clearance from ground and the power harvesting itself. However, conditioned to the design option for a two-wheeled cycle, as mentioned in anterior paragraph, the choice now falls over the different types of two-wheeled electrical pedal-assisted pedal cycles (EPAC).

Potential for EMF compliance. Due to the requirement of specialized equipment, not available at the time of prototype development, this aspect is left outside the main design and verification effort, concerning the rider protection. Only special measures are adopted to assure pedestrian protection by design. In spite of that, the choice of the candidate cycle for the prototype should facilitate the future adoption of shielding measures to protect the rider. In particular, the possibility of installing the secondary coil as far as possible from the rider body is deemed as one of the most important characteristics of the cycle to facilitate the design.

Concerning EMF compliance, all model types should fit, with expectably less design effort in the adaption of closed-cabin vehicles. If only performance and ease of adaptation would be considered, the velomobiles and other three and four-wheeled LEV would be a priority selection for the prototype.

Dynamic Inductive Wireless Power Transfer for Lightweight Electric Vehicles
Luiz Alberto Lisboa da Silva Cardoso – University of Minho

246

However, according to the analysis done so far, our search is strongly limited to popular two-wheeled EPAC, the dominant class of lightweight electric HPV in the market.

The EPAC are still available in different geometries. Discarding the possibility of appending a trailing or side-car vehicle to the bike, to embark a secondary coil, a solution that would, to some extent, restrict the versatility and the maneuverability of the cycle, two main categories are identified for the two-wheeled: personal transportation bikes and cargo bikes.

Cargo bike types with larger frames, such as the longtails and the long Johns, shown in Figure 145, exhibit the interesting possibility of having more room to install a secondary coil. The long Johns type, however, although being a long existing model, is still rare worldwide, more expensive, and require more space to maneuver and to be parked or stored.

(a)   (b)
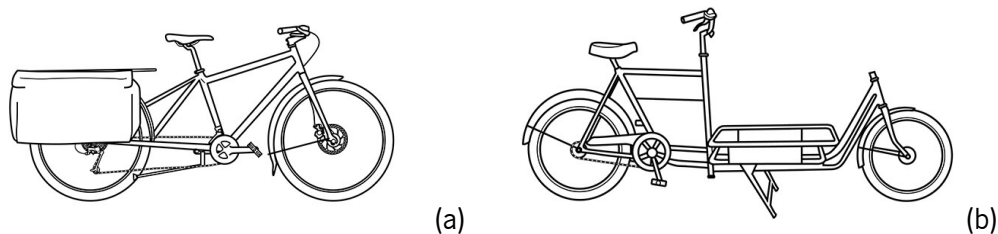
Figure 145: Two of the most popular two-wheeled cargo bikes with larger frames: (a) the longtail and (b) the long Johns. Source: Hilary Angus, Momentum Mag., Dec. 15, 2015.

The selection then becomes restricted to either the longtail cargo bike and other remaining commercial upright and recumbent bike types, where there is no special provision of space for the installation of a secondary coil. In consequence, the options that come into consideration for the location of a secondary coil, close to and parallel to the ground, and with dimensions as large as it can be practical, are:

(i)   Ahead of the front wheel;

(ii) Around the front wheel;

(iii) In between the front and rear wheel;

(iv) Around the rear wheel;

(v) Behind the real wheel;

(vi) Around both wheels and the whole bike;

(vii) Laterally, on one side of the bike.

Dynamic Inductive Wireless Power Transfer for Lightweight Electric Vehicles
Luiz Alberto Lisboa da Silva Cardoso – University of Minho

247

Among these, options (i), (ii), (vi) and (vii) would potentially interfere with the bike's maneuverability, also completely disfiguring the bike's profile and versatility. Options (iii), (iv) and (v) are apparently mechanically feasible. However, in option (iii) the secondary coil would be installed very close to the rider's body, making it more difficult to shield the rider from EMF exposure. Option (v), although viable, would possibly imply in the installation of a cargo trailer, which, on the other hand, would also restrict the vehicle's maneuverability. The design decision then favors the prospection of solutions where the secondary coil is wound around the rear wheel.

The installation of a secondary coil around the rear wheel of most popular and commercially available common variants of two-wheeled cycles, excluding the previously discarded long Johns type, are then represented in Figure 146.
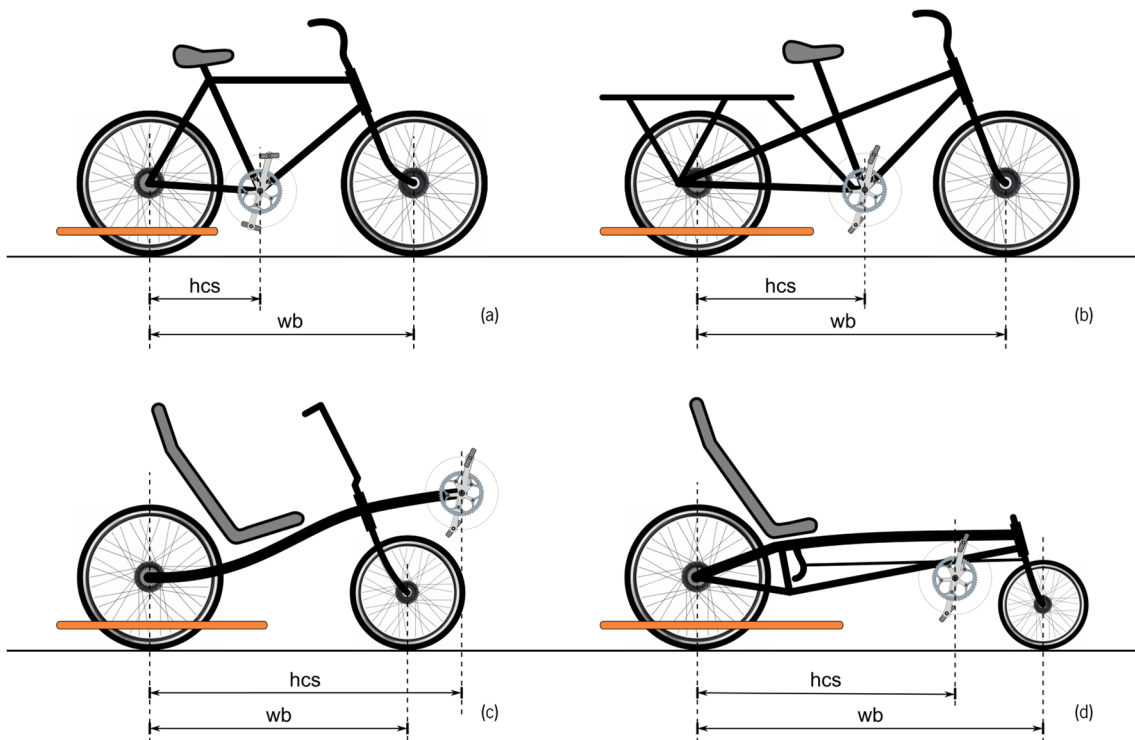
Figure 146: Possible installation position of a pick-up coil in most popular bike frames: (a) Standard; (b) longtail cargo bike; (c) short wheelbase recumbent; and (d) long wheelbase recumbent.

A large wheelbase, wb, such as found in (b), (c) and (d) favors the installation of a larger coil, whereas a large horizontal component of the chainstay, hcs, permits the feet of the rider to be further away from the primary and secondary coils, improving intrinsic EMF protection to the lower limbs. However, in the recumbent models, (c) and (d), the trunk and the head of the rider are lower and closer to the position of the secondary coil, what potentially increases EMF exposure to these more sensitive parts of the body. Because of that, the longtail cargo EPAC bike, the option in Figure 146b, is then considered to be the best candidate for a HIPLEV prototype, while option Figure 146a becomes the second best candidate.

Dynamic Inductive Wireless Power Transfer for Lightweight Electric Vehicles
Luiz Alberto Lisboa da Silva Cardoso – University of Minho

248

The longtails cargo e-bikes seem to be recently gaining much popularity, especially in America. However, these models are still relatively more expensive, and both less popular and less readily available in Europe. So, the final decision was to initially use the cycle with the second best frame type, the standard upright bike, as shown in Figure 146a, which, on the other hand, is the most popular type around the world. By proving the validity of the HIPLEV concept to this latter type of cycle, positive attention feedback is expected, facilitating subsequent interest in the development of other new HIPLEV prototypes based on the more adequate cargo longtails bikes. Later on, with careful EMF design and a expectably higher prototyping cost, the recumbent models of Figure 146c and Figure 146d are also expected to be retrofit with power-harvesting hardware.

4.7.1 The Model of Choice

Not having an electric bike readily available in the laboratory, and in order to learn more about the electrification transformation and cut costs, instead of procuring a finished e-bike for the HIPLEV modification, our option was made for the electrification of a standard aluminum frame bike. This path had the additional advantage of setting the e-bike's electric configuration exactly as required (see section 5.2).

The parts of the bicycle that are very near the ground are expected to be directly exposed to alternating magnetic fields. The bike frame, which is usually metallic, steel or aluminum, does not come very close to the ground surface because of the wheel assemblies, when working with buried primary coils. Aluminum is not ferromagnetic and due to being a highly conductive metal, it would just attenuate the residual field eventually reaching higher positions on the vehicle. Hence, despite its size, the bike is frame is not expected to interfere significantly with the DIWPT. Also, aluminum is a better choice than steel for being lighter, inexpensive and very popular among bike manufacturers.

Since the easy of inductive power transfer is related to the size of the coils and their relative proximity, to start with maximum margin for accommodating a larger secondary coil on the bike, a model with the largest commercially popular wheel size was selected, the so called "twenty-niner" or just "29er". These are popular mountain-bike types in Europe, in which the wheel rims have a bead seat diameter of 622 mm and, after mounted with ERTRO 54-622 tires [168], come to an overall diameter of approximately 29 inches, thus justifying the name.

In order to avoid conductive losses on the single turn coil formed by the bicycle wheels, the ideal material for the wheels would not be conductive. Most bike wheels readily available are

Dynamic Inductive Wireless Power Transfer for Lightweight Electric Vehicles
Luiz Alberto Lisboa da Silva Cardoso – University of Minho

249

metallic, and thus, very conductive. However, carbon fiber reinforced polymer, which is progressively being more used for the obtained reduction in weight, is also a less conductive alternative material. This material is an anisotropic conductor, typically ranging from 100 to 1000 times less conductive than metals [169], depending on the orientation of the fibers inside the composite. However, careful consideration of the circuit parameters must be observed because intermediate resistance values of wheel loop may approach the optimal coupled load, and power dissipation may become even higher than when using highly conductive materials.

All these facts, together with the higher price of these alternative carbon-fiber components, influenced the model procured for a first prototype to be a Berg Trailrock 25, shown in Figure 147, which has both aluminum frame and aluminum wheels.

Figure 147: Bike model procured for adaption as a HIPLEV, a 29er with aluminum frame and wheels.

Tests with the prototype latter confirmed that this choice does not impair a satisfactory IWPT from the lane to the bike, the justification being that the induced current in the wheel is largest when the wheel is very closely over the primary coil windings, a condition in which the lateral displacement is already much greater than the maximum required operational displacement from the center lane alignment condition.

4.8   Conclusions

While yielding more flexible transportation services and convenience, cars greatly contributed to the degradation of the former and healthier lifestyle in cities, at least concerning the strong reduction in the habits of walking and cycling, observed along the 20th century.

The bicycle, on the other hand, is a healthy transport mode, which also has exhibited continuous popularity since it the safety bike has been introduced in the end of the 19th century. This large acceptance of the bicycle as transport, associated with the spontaneous "electrification" of the bike market in the last years, can provide an opportunity to improve transports and rescue

Dynamic Inductive Wireless Power Transfer for Lightweight Electric Vehicles
Luiz Alberto Lisboa da Silva Cardoso – University of Minho

250

the quality of life in the cities, not only by reducing the pollution levels, but also by improving the physical and health condition of the population.

The electrification of bicycles is a well-defined tendency. In the same way that bikes have been popular since their invention, it is very probable that electric bikes will also be available and very popular in the long range, and make a great contribution as a transport mode alternative.

We propose the Human-Inductively-Powered Lightweight Electric Vehicle (HIPLEV), an association of EPAC class vehicles, and other similar lightweight human-powered similar EV, with the ongoing development of the dynamic inductive wireless power transfer (DIWPT) technology. The HIPLEV is deemed to have the potential to take the popularity of bikes and other human-powered velomobiles to unprecedent levels, perhaps higher than those of the horse and horse carriages, back in the 19th century. It can be speculated that the electrically assisted bike has the potential to become the mechanical horse of the future.

This sustainable mobility approach, if adopted along with safeguard policies and new urban architecture guidelines, will likely reduce the demand, in urban areas, for heavier, higher power motorized cars, either electric or with fuel-based engines, thus contributing to the humanization and safety of the traffic in the cities.

A velomobile is a human-powered vehicle (HPV) that would not only presents better efficiency and speed profiles, due to its aerodynamic advantage, but offers protection from the weather and eventual collisions. In this manner, electric versions of velomobiles are possibly the best technical option for DIWPT adaptation. But due to market reasons, it should only later on be considered for HIPLEV adaptation. For now, the upright e-bike and its variants are the best option to be considered for the introduction of HIPLEV systems, and in a second phase, other LEV with more a more conventional upright riding position.

On the other hand, the standard, unfaired upright e-bike, the par excellence representative of the lightweight electric vehicles, is also one most representative HPV. It should then be used as the first vehicle to be adapted as a HIPLEV. Its lower cost, relatively to other HPV options, not only facilitate the implementation of the prototype, but also potentialize its latter adoption.

However, the actual success in the popularization of the HIPLEV, or at least the creation of a window of interest over this proposal, is closely related with the simultaneous introduction and the wide availability of public inductive-lane infrastructure.

Dynamic Inductive Wireless Power Transfer for Lightweight Electric Vehicles
Luiz Alberto Lisboa da Silva Cardoso – University of Minho

251

Chapter 5

Inductive Lane for Lightweight Electric Vehicles

In Chapters 2 and Chapter 3, a review on inductive wireless power transfer for both stationary and dynamic applications was provided. Particularly, in Chapter 2, models and issues involved in IWPT implementation were discussed, including aspects of power electronics. Chapter 3, on the other hand, in addition to a review on DIWPT systems, was concentrated on oblong coil I-lane design, which is used in the implementation reported in this chapter.

In Chapter 4, a brief review of human powered vehicles was followed by the proposition of a human-inductively-powered lightweight electric vehicle (HIPLEV), as a new soft transport mode variation for urban use and neighborhood commuting. Also, an approach for the development and adoption of the HIPLEV transport was presented. Upon consideration of basic technical and market constraints, the upright EPAC bike was chosen as the first hybrid electric-human-powered candidate vehicle to be retrofitted for dynamically harvesting energy from i-lanes, thus demonstrating the viability of the implementation of the HIPLEV concept.

In the present chapter, this design is then detailed, using the theory and models presented in Chapters 2 and 3, and requirements derived from the proposal of the HIPLEV, in Chapter 4. The results obtained from the laboratory prototypes are also presented, with the verification of some key electrical aspects involved in the concept under stationary conditions. While not yet targeting a final product design, in this exploratory development, different technologies are proved to work together well, confirming the technical viability of the power transfer to the HIPLEV.

5.1 Design Guidelines

The application context determines some high level guidelines for the development of an inductive lane for e-bikes. These are not only translated into basic requirements, but also orient every following decision in the prototype design, whereas the degree of freedom for a possible solution is high. These guidelines inevitably add some heuristics to the design, but they are essential to simplify the problem and, ultimately, validate the concept of the proposed HIPLEV system:

Dynamic Inductive Wireless Power Transfer for Lightweight Electric Vehicles
Luiz Alberto Lisboa da Silva Cardoso – University of Minho

252

- <u>Low complexity</u>. Although cost assessment is not performed, to cope with a future low manufacturing and installation cost, it is necessary to simplify the system, as much as possible. The expected result is that the implementation is facilitated, and lifecycle costs of the HIPLEV can be compatible with the lower cost of the base vehicles involved, and so is the cost of implantation of dedicated i-lanes.

- <u>Essential requirements only</u>. In order to validate the development a product, many requirements should be considered and treated. However, this research does not target the development of a product, but rather, a conceptual validation for the HIPLEV, letting detailed engineering effort for a future design of an ultimate system. In these terms, to ease the task and initially demonstrate the viability of the HIPLEV proposal, only the essential requirements are considered to build a first prototype. The only essential requirement intentionally not yet handled in this design is the EMF-safety of the rider. Although of prime importance, the evaluation of compliance to ICNIRP recommendations on a lightweight electric vehicle is a meticulous process, that requires calibrated specialized equipment, which was not available at the time of the design. However, the guidelines adopted ensure that the maximum human exposure levels are at least met from the pedestrian point-of-view. Also, some considerations and suggestions are left for future design effort on the rider protection from the EMF generated by both the primary coils, in the lane, and the onboard secondary coil and electronics.

- <u>Open source / open access design tools</u>. Targeting the popularization of the HIPLEV, and to allow multiple designers to reproduce and create variants of the presented prototype, further contributing to the creation of new HIPLEV systems, opens source software design tools are preferably used, except when the associated design effort would conflict with the thesis development. The open source software tools have generally less resources available to the user, and sometimes lack a professional user interface, but they are also simpler to learn. The excellence of some of them have been widely validated by previous academic research and became popular, such as the finite element modeling tool FEMM [99] [123], the inductance modeling tool FASTHENRY [170] [171] and the circuit simulation tool SPICE ("Simulation Program with Integrated Circuit Emphasis") [63]. While effort was made to use open source software tools, Wolfram Mathematica and COMSOL Multiphysics were also used for their convenience.

Dynamic Inductive Wireless Power Transfer for Lightweight Electric Vehicles
Luiz Alberto Lisboa da Silva Cardoso – University of Minho

253

5.2 General Electrical Requirements

The European standard EN 15194:2017 [5] defines EPAC bicycles as "electrically power assisted bicycles of a type which have a maximum continuous rated power of 0.25 kW, of which the output is progressively reduced and finally cut off as the EPAC reaches a speed of 25 km/h, or sooner, if the cyclist stops pedaling." So, the i-lane and the onboard power harvesting electronics should be able, in the maximum limit condition, to supply an average of 250 W for the powertrain maximum to an EPAC-based HIPLEV.

Expectably, some portions of the i-lane will not have a primary coil providing energy for the vehicle. So, in order to keep this average 250 W transferred to the HIPLEV, the instantaneous power transfer when the vehicle is harvesting energy from a primary coil, should be, also on average, superior to this power level, and the excess energy stored onboard should be enough to sustain electric consumption during the inter-coil transits. This aspect of the design is covered in section 5.13, in a high level of abstraction. Possible solutions for the actual implementation are the use of a small capacity battery (small, compared to what would be necessary if there were no i - lane to harvest energy from) or a bank of supercapacitors, or a combination of them [172], and a battery management system (BMS) to control the charge and discharge micro-cycles along the path of the vehicle. BMS are reasonably well developed subject, and should not be a difficult engineering task to accomplish, with many options existing [173][174].

When present in the vehicular system architecture, a battery may serve not only to store short term energy for the inter-coil transits, but also as a means of providing the vehicle with an extended electrified range away from the i-lanes. But, in the case of a HIPLEV, this can be optional, for human power (pedaling) is a possible alternative.

5.2.1.1 Induction Frequency and Cross-Section of Coil Windings

Another important parameter to be fixed from start is the induction frequency used. In principle, it should be as high as possible, as long as the electronics can handle it and the associated wavelength on the coils do not make them radiate electromagnetic power, as seen in 2.2. In addition, because a higher directive is to keep the system as simple and less costly as possible, this design shall avoid the use of true litz wire. This poses some restriction on the maximum frequency of operation.

The most available multiconductor cables found in the market for residential and industrial use were verified to have cross-sectional areas of 1, 1.5, 2.5 or 4 mm^2. Due to the skin effect,

Dynamic Inductive Wireless Power Transfer for Lightweight Electric Vehicles
Luiz Alberto Lisboa da Silva Cardoso – University of Minho

254

among these options, the natural choices for use in higher frequencies are the multiconductor cables with individual wires of 1 mm² and 1.5 mm². According to the curves in Figure 71, for these latter cross-sections, frequencies up to 10 kHz would not generate important extra loss with respect to DC use. Based on the same chart, $f_{ind} \cong$ 50 kHz can be considered a good ad hoc frequency band for avoiding very large additional losses (> 50%), it is a frequency where the AC resistivities of the of 1 mm² and 1.5 mm² cables are respectively increased by 22.8% and 42.3% from their DC value. The resulting effect is that, for a given rms current flowing in a cable, if the frequency is increased the power dissipation is also increased. Conversely, if the same maximum power dissipation per unit of length is to be observed in a higher frequency, less current should be imposed on the conductor. Based on this reasoning, for their safe use, the maximum amperages for copper cables of 1 mm² and 1.5 mm² of cross-section have to be derated at 50 kHz, according to Table 22:

Table 22: Derated maximum current range for copper cables with cross-sectional areas of 1 mm² and 1.5 mm².

Area of cross-section (mm²)	DC		Max power dissipation (mW/m)	AC at f_{ind} = 50 kHz	
	Maximum current (A)*	Resistivity (mΩ/m)		Resistivity (Ω/m)	Maximum current (A)
1.0	4 to 6	17.1	274	21.0	3.6 to 5.4
1.5	6 to 9	11.4	410	16.3	5 to 7.5

*Depends on manufacturing details and the cable insulation, 4 to 6 A/mm² being a widely accepted safe range.

Exemplifying the use of Table 22, if the maximum current of 10 A rms is to be imposed to some coil of the system, in the worst case, at least two to three 1.0 mm² copper wires should be used for winding this coil or, alternatively, two 1.5 mm² wires should be used. For the assurance of equative distribution of the current over the wires, they should yet be isolated and twisted together. Incidentally, to ease the comparison with former prototypes implemented, the nominal induction frequency selected for the HIPLEV is $f_0 = $ 51.7 kHz, which is close enough to 50 kHz.

5.2.1.2 Main DC Voltage of the Power Train

The IEC 60950-1 establishes that steady state voltages up to 42.4 V peak, or 60 V DC, are not generally regarded as hazardous, under dry conditions, for an area of contact equivalent to a human hand [175], even though, as expected, it also determines that bare parts that have to be touched or handled should be at earth potential or properly insulated. The American Occupational Safety and Health Administration (OSHA), however, establishes that in the construction of installations, live parts of electric equipment operating at 50 volts or more shall be guarded against accidental contact by cabinets or other forms of enclosures [[176]].

Dynamic Inductive Wireless Power Transfer for Lightweight Electric Vehicles
Luiz Alberto Lisboa da Silva Cardoso – University of Minho

255

Concerning EVs, it is common to find batteries and main power train DC voltages exceeding hundreds of Volts. In a standard road EV, due to the power levels involved, the currents would be too high otherwise. But this is not a problem because there is usually enough room to accommodate the necessary protection measures against electric shock, which on the other hand, may not be as easily implemented in a lightweight electric vehicle, such as an e-bike.

Because of that, regarding the power train supply voltages, the EN 15194 Standard [5] limits the battery, and thus, the powertrain DC voltage of EPAC type e-bikes, to 48 V. This maximum voltage is adopted in compliance with standards and recommendations for equipment where there is the possibility of the user coming in direct contact with bare live parts of the power train. For historical reasons, e-bikes are available with powertrains voltages in multiples of with 12 V: either 24 V, 36 V or 48 V DC.

For proof of concept, any of these voltages would be adequate. However, since 36 V is likely the most popular voltage for 250 W EAPC-compliant bicycles currently found in the market, and this type of hardware is less expensive and easier to procure, that was the choice for the prototype. Anticipating some voltage drop on the cables connecting power to the motor, the nominal DC output voltage from the power harvesting unit is then fixed at V_L = 36.5 V, with a minimum accepted input voltage to the power train set at $V_{L,min}$ = 36.0 V.

Despite the low voltage of the powertrain, it is necessary to be aware that higher voltages can develop on the coils, due to the resonance phenomenon in a IWPT configuration, and special care to isolate the onboard secondary coil and compensation circuitry must be observed.

Electrically assisted 29ers (29-inch wheels), for use in mountain trails, such as the model elected for electrification and used in the prototype (section 4.7.1), can be found with different motorizations up to 1 kW or more. However, as seen in Chapter 4, for legal street use as an EPAC bike, the maximum power of electrical assistance is 250 W. This implied in the installation of a 250 W electric motor, which, for ease of assembly, was a hub-motor type, installed in the front wheel. Having previously selected 36.5 V for the main system nominal DC voltage, a compatible three- phase COTS motor controller capable of handling at least 250 W was also procured. Although the average power supplied to the power train is 250 W, to increase the electric safety margin, a motor capable of continuously handling up to 300 W of power and a 350 W controller were preferred. The actual power delivered to the motor would then be limited by the vehicle's power management system. The hub motor and controller kit G-S027, from Suzhou SND Zhenlong Motor Co. Ltd were procured and successfully installed on the bike.

Dynamic Inductive Wireless Power Transfer for Lightweight Electric Vehicles
Luiz Alberto Lisboa da Silva Cardoso – University of Minho

256

5.2.1.3 Inductive Power Transfer Level

Since the inductive lane is composed of many sequential primary coil modules interleaved with by a separation gap, the power level for energy harvesting during the primary coil transits must be more than 250 W. This will allow some extra energy to be harvested and stored for use on the energy-blind lane segments. The choice of this power harvesting level, p, is related with the choice of the inter-primary coil spacing and the efficiency of the energy storage system used, as discussed in 5.13. If p is too low (too close to 250 W), the primary coil will have to be arranged to each other, making the installation of the i-lane not practical. If, on the other closely hand, p is increased much more than 250 W, larger primary coils spacing becomes possible, but the bill of materials, and the total cost of the system is expected to increase, which an undesired characteristic for both the prototypes and an actual system built upon their results. Also, as p is increased, more current-turns are expected to flow in the coil windings, making it more difficult to control EMF exposure levels of the rider, in a vehicle that is intrinsically an open platform, where the shielding might add too much weight to the assembly.

Considering that most peak transient power demand of the power train brushless motor can easily rise to up to 50% of its maximum nominal value, it would be convenient that, during primary coil pass, these peaks could also be supplied by incoming harvested power. For a 250 W motor, this peak is then estimated at 375 W, a value that was rounded up to $P_E = 400$ W in our design, a power transfer level that should be sustained at all lateral displacements within the minimum required electrified width w_d (as specified in Table 25). Since the maximum average power supplied to the motor is 250 W, an average excess of 150 W of the harvested power would then be available to charge the battery or a supercapacitor bank. In 5.13.2 the maximum inter-primary coil spacing distance is determined considering this choice of P_E.

5.2.1.4 Electrical Efficiency

Since the AC to DC voltage is normally an intermediate stage in the primary circuit of an IWPT system, and the load presented at the secondary output is also of DC type, to simplify the measurements, the efficiency in IWPT systems is often benchmarked by this DC-to-DC efficiency. As reviewed in Chapter 2, current technology makes it possible to build stationary WPT systems that can exhibit above 90% of DC-to-DC efficiency, high values being easier to implement when the power levels involved exceed the 10 kW limit. In commercial stationary IWP systems, 80% or, under best coil alignment conditions, 85%, would be a more realistic requirement [92], with some automotive rechargers now being reported at an efficiency level of 90%

Dynamic Inductive Wireless Power Transfer for Lightweight Electric Vehicles
Luiz Alberto Lisboa da Silva Cardoso – University of Minho

257

When it comes to automotive DIWPT, where the power levels are in the 10 kW to 100 kW range, the maximum efficiency of 80% or less is generally a reference value for prototypes. Earlier versions of the OLEV system, for instance, were reported as achieving a maximum of 72% in efficiency [177], this number being later improved up to 83% in the following OLEV designs [120], under the most favorable alignment conditions, which cannot be sustained at all times. Still, these numbers were achieved with strong use of soft ferromagnetic materials (ferrites), for concentrating and shaping the magnetic field and increase the magnetic coupling between primary and secondary coils. Also, to reduce winding losses, litz wire in abundantly used to implement the coils. However, the litz wire cabling and ferrites can be responsible for a major increase in the cost of the components of the system.

Most publications do not detail the average efficiency achieved by prototype systems, which is expectably lower than the best-case efficiency achieved in optimum alignment and load conditions. What is apparent, however, is that lightweight electric vehicles (LEV) are not the current focus of investigators. LEV are mostly used in downscaled models in prototypes, for the economic convenience for the tests.

Because the required power levels exhibited by LEVs and their masses are much lower than that of the standard road EVs, the overall energy savings obtained, when a less electrically efficient LEV is used as a functional replacement for this latter, can be more favorable for the LEV. In this manner, let us consider the use case where two single-rider HIPLEVs using $P_H = 250$ W of power each, with an electric efficiency η_H, measured from grid to the powertrain, can be a functional replacement for a two-person occupancy vehicle, with $P_{EV} = 20$ kW of power, with a similarly defined efficiency η_{EV}, the comparison being made over a commuting route of a total distance d. Let us also consider that the average cruise speed of the of road vehicle is $v_{EV} = 100$ km/h, while that of the HIPLEV running at 250 W is, in an average worst case scenario, $v_H = 15$ km/h.

The energy expenditure of the HIPLEV, E_H, and that of the standard EV, E_{EV}, can then be estimated by:

$$E_H = \sigma \frac{P_H \, d}{v_H \, \eta_H} \tag{5.1}$$

and

$$E_{EV} = \frac{P_{EV} \, d}{v_{EV} \, \eta_{EV}} \tag{5.2}$$

Dynamic Inductive Wireless Power Transfer for Lightweight Electric Vehicles
Luiz Alberto Lisboa da Silva Cardoso – University of Minho

258

where σ is the occupancy of the standard vehicle, and η_H and η_{EV} are respectively the efficiencies of electric to mechanical energy conversion of the HIPLEV and the road EV.

The ratio E_H/E_{EV} is then given by:

$$\frac{E_H}{E_{EV}} = \sigma \left(\frac{\eta_{EV}}{\eta_H}\right)\left(\frac{P_H}{P_{EV}}\right)\left(\frac{v_{EV}}{v_H}\right)$$

(5.3)

So, the HIPLEV will present an overall better energy efficient as a transport when:

$$\frac{E_H}{E_{EV}} < 1,$$

(5.4)

that is, when:

$$\eta_H > \sigma \, \eta_{EV} \left(\frac{P_H}{P_{EV}}\right)\left(\frac{v_{EV}}{v_H}\right)$$

(5.5)

In the above given numerical example, for the HIPLEV to have smaller energy footprint, it is enough that:

$$\eta_H > 2 \, \eta_{EV} \left(\frac{250 \text{ W}}{20 \text{ kW}}\right)\left(\frac{100 \text{ } km/h}{15 \text{ } km/h}\right) \cong 16.7\% \, \eta_{EV}$$

(5.6)

Another similar method of comparatively judging the efficiency of a HIPLEV is to consider the necessary energy for an EV to travel one kilometer. According to the U.S. Environmental Protection Agency (EPA), as of 2020, the most efficient standard road vehicle in production is the Tesla Model 3 Standard Range Plus, exhibiting an energy expenditure of 149 Wh/km in combined city and highway use. For an e-bike running with no pedal assistance, and average rider and lane conditions (head wind, slope) 15 Wh/km can be derived to be a typical equivalent figure in realistic scenarios [147][178]. Based on these figures, in order to outperform a standard road EV with an occupancy of two people, in terms of less energy expenditure, it would be enough for an e-bike based HIPLEV to exhibit an efficiency η_H such that:

$$\eta_H > 2 \, \eta_{EV} \left(\frac{15 \text{ Wh/km}}{149 \text{ Wh/km}}\right) \cong 20\% \, \eta_{EV}$$

(5.7)

Considering the worst estimate between (5.6) and (5.7), and since η_{EV} is limited to 1, it can be derived that any HIPLEV presenting an electric efficiency better than $\eta_{H,min} = 20\%$ is

Dynamic Inductive Wireless Power Transfer for Lightweight Electric Vehicles
Luiz Alberto Lisboa da Silva Cardoso – University of Minho

259

guaranteed to be a more economical choice over any standard road EV, in terms of energy conservation, for a two-occupancy of the road EV.

Based on this analysis, a HIPLEV with an efficiency $\eta_H = 40\%$ would have an overall energy efficiency of at least twice than any current standard road vehicle: This number can then be considered a very satisfactory specification for a HIPLEV, resulting in a significantly reduction in the energy footprint. The final target figure to be adopted for the efficiency in the DC-to-DC conversion of the DIWPT in the HIPLEV system, η_{DC}, should be derived from the product:

$$\eta_H = \eta_{GR}\, \eta_{DC}\, \eta_M \,, \tag{5.8}$$

where η_{GR} is the electrical efficiency in the AC-to-DC conversion of the grid rectifier that supplies energy to the primary inverter, and η_M is the efficiency of conversion of electric to mechanical energy by the powertrain of the HIPLEV, consisting in a BLDC motor either directly connected to e-bike's wheel (direct drive) or through gears (geared drive), and its controller.

Since typical values of efficiency for the grid rectifier and the powertrain are respectively 95% and 80%, the minimum required and the desirable electrical DC-to-DC efficiency of the DIWPT link of the HIPLEV can be respectively set by as:

$$\eta_{DC,min} = \frac{\eta_H}{\eta_{GR}\, \eta_M} = \frac{20\%}{95\%\,80\%} \cong 26.3\% \tag{5.9}$$

$$\eta_{DC} = \frac{\eta_H}{\eta_{GR}\, \eta_M} = \frac{40\%}{95\%\,80\%} \cong 52.6\% \tag{5.10}$$

The above analysis is simplified, for the actual power levels P_{EV} and P_H are strongly dependent of the speed of the vehicles, v_{EV} and v_H, which may be not constant in a given urban scenario, even if the departure and arrival points coincide. Also, the efficiency figures have been conservatively and unfavorably calculated, considering that the HIPLEV is in electric assistance all the time, which may not be the case, since it can move solely on human power in parts of the trip. The main idea in the comparison, however, is that, with a much greater size, mass and speed than a HIPLEV, a standard road vehicle tends to generate more friction with the air, the road and in all its mechanical components, resulting in higher energy losses. Also, it would be required more energy for a heavier vehicle to accelerate and decelerate multiple times along the trip, even if regenerative breaking is used, for the efficiency in regenerative breaking is never 100%. Under

Dynamic Inductive Wireless Power Transfer for Lightweight Electric Vehicles
Luiz Alberto Lisboa da Silva Cardoso – University of Minho

260

similar mechanical constraints, it is then expected that lower mass vehicles moving at lower speeds will require less energy to transport equivalent payloads.

The number in (5.9) is much less than DC-DC efficiencies ordinarily achieved in DIWPT prototypes making use of extensive use of litz wire windings and core materials in the coils. There is a fair a priori expectation that $\eta_{DC} = 52.6\%$ can be achieved even without the use of these resources, what would make the HIPLEV even more attractive economically.

5.2.1.5 Maximum Voltage on Primary Coil

The primary coils should be galvanically isolated, to avoid the risk of electrocution. The voltage applied by the inverter on its terminals should be as small as possible to further minimize EMF exposure in the vicinity of the coil. Even before estimating and verifying the compliance of the electric field generated by the primary coil, an ad hoc heuristic design requirement is introduced: to limit the maximum voltage across its terminals to be less the grid voltage. Around the word, the nominal grid voltage lies from 100 V rms (in Japan) to 230 V rms (in Europe), with a few countries also using 240 V. Since the HIPLEV is conceived under a perspective of global acceptance, so, in order to facilitate future homologation of a HIPLEV i-lane in every country, the absolute maximum primary coil voltage should match that of the power grid. In the case of the EU, this is 230 V rms. A lower voltage, however, closer to 100 V, is desirable as a target design parameter.

5.2.1.6 Summary of Basic Electric Requirements Established for the HIPLEV

After the considerations in this section, the basic electric requirements established for the development of a HIPLEV system based on a EPAC type bicycle are summarized in Table 23:

Table 23: Summary of basic electric requirements established for the first HIPLEV protype.

Parameter	Symbol	Value	Unit
Powertrain power	P_H	250*	W
Maximum regulated power transfer over w_d	P_E	400	W
Nominal DC output voltage to powertrain	V_L	36.5	V
Minimum input voltage to powertrain	$V_{L,min}$	36.0	V
Maximum Primary coil voltage	$V_{L1,max}$	230	V rms
Induction frequency	f_{ind}	~50	kHz
Minimum Overall Electric Efficiency	$\eta_{H,min}$	20%	-
Target DC-DC efficiency of the IWPT**	η_{DC}	≥ 53%	-

*Maximum legal power assistance level for an EN 15194 compliant EPAC.
**Desirable, to be at least twice more efficient than any current standard road vehicle with up to two occupants.

Dynamic Inductive Wireless Power Transfer for Lightweight Electric Vehicles
Luiz Alberto Lisboa da Silva Cardoso – University of Minho

261

5.3 Dimensional Requirements for the i-Lane

In Chapter 4, considering technical and marketing reasons, the best prospective candidate for a first prototype DIWPT electrification was determined to be the popular and readily available standard upright e-bike. In this case, since the cyclist goes exposed, and it is more feasible to embed EMF protection in the lower parts of the frame of the bike, the design decision was to seek an installation for a pick-up coil close and parallel to the ground, with buried primary coils. In addition, by adopting this solution the impact on the urban architecture can be minimized and the hardware on the lane becomes more difficult to tamper with, leading to a more robust system installation. In general, lateral or aerial coupling are more acceptable only in restricted industrial areas. For land transports, the energy transfer from ground is more suitable and has been a preferable choice for prototyping DIWPT for heavier vehicles as well.

5.3.1 Lane Width and Lane Electrified Width

In order to design a DIWPT lane and proceed with the adaptation of an e-bike for harvesting power from existing bike lanes, it is first necessary to consider the dimensions of this vehicle and its dynamic behavior on these original lanes. Bicycles are inherently unstable and while on normal riding, they require the cyclist to continuously exhibit a lateral oscillatory movement with an average amplitude that varies with speed, wind, grade of the lane, and also with the cyclist proficiency and physical condition. This lateral movement and the stationary width of the bike-cyclist assembly define the dynamic kinetic envelope for the bicycle, which should be enclosed in the lane operating width. The statistical characterization of the width w_d of the dynamic kinetic envelope of a bike and a final the decision on the minimum electrification width for the DIWPT system is a hard task that can be replaced by the exam of the current recommendations for cycle infrastructure design. While not previously concerned with DIWPT, many urban administration institutions have gathered the expertise on the required dimensions for lane bikes in documents [4] [179] [180] [181] [182] [183] [184] [185], where the maximum bike width generally observed and the minimum required lane width are listed. From that, w_d can be indirectly derived. In Figure 148 are illustrated the essential parameters implied in the definition of the width of a one-way single track bike lane (no side-by-side riding admitted):

- w_B: the maximum width of a bike that is considered for using the lane.

- w_L: the minimum recommended paved lane width, where the bike tires can eventually touch the lane, but, more restrictively, also where the vertical projection of the cyclist envelope is expected to be enclosed.

Dynamic Inductive Wireless Power Transfer for Lightweight Electric Vehicles
Luiz Alberto Lisboa da Silva Cardoso – University of Minho

262

- w_T: the total minimum recommended bike lane width, which is greater than w_L by an extra amount of lateral spacing in order to provide a safer and more comfort riding. The lateral zones enclosed in the total lane width, w_T, but beyond the paved width, w_L, are not expected to be crossed by any by the bicycle or any body part of the cyclist, but they are there to provide room for exceptional maneuvering of the vehicle.

- w_d: the minimum required width to accommodate the oscillatory movement of the bike, in order to allow the cyclist to dynamically keep the equilibrium.
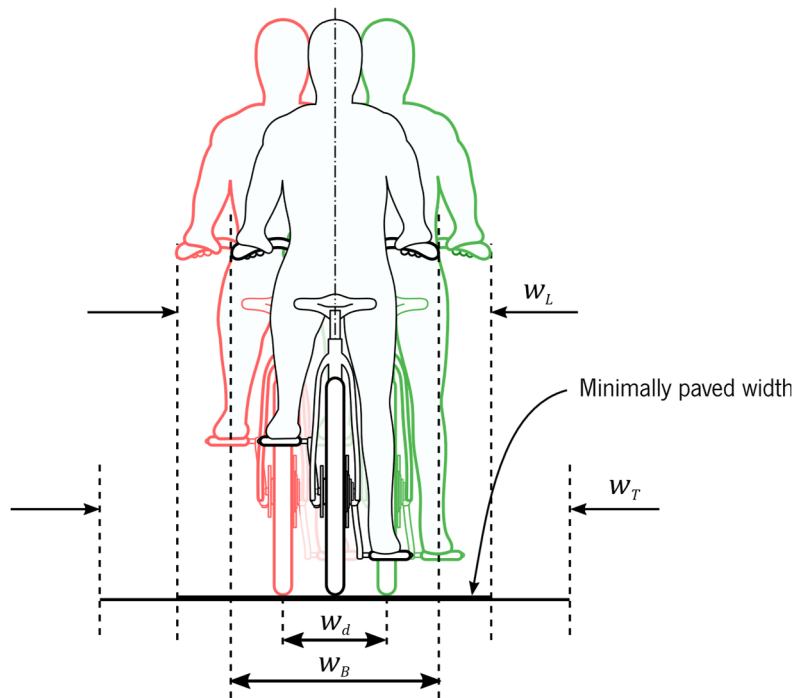
Figure 148: Lane and bike essential width parameters.

The recommended minimum bike lane width, found in bike lane design technical notes of the UK Department for Transport is 100 cm, implied by a maximum bike width of 80 cm and a minimum lateral oscillatory movement of 20 cm, which provides enough balance margin for cyclist to keep a straight line when in motion over 11.3 km/h [4]. The American Association of State Highway and Transportation Officials consider the maximum width of the bike and cyclist assembly to be 75 cm, while the recommending minimum lane width is set at 1.2 m, resulting in a guaranteed lateral dynamic in-lane alignment width of 45 cm [179], but smaller safety distances are recognized as possible if speed differentials between bicyclists and other road users are relatively small. In Brazil, the Ministry of Cities recommends 100 cm for the minimum cyclable width of 100 cm, enclosed in a dedicated lane width of 150 cm, considering a bike width of up to 60 cm [180]. In the Netherlands [181], a recommendation document for construction of bridges for bikes and pedestrians assumes 75 cm for the maximum width of a bike, and establishes

Dynamic Inductive Wireless Power Transfer for Lightweight Electric Vehicles
Luiz Alberto Lisboa da Silva Cardoso – University of Minho

263

100 cm and 140 cm respectively for the minimum operational width for the bike and the total lane width. In Spain, the government of Catalonia also established 60 cm as maximum width of the vehicle, with a minimum width of maneuver of 100 cm, resulting in a dynamic width margin of 40 cm, although a total lane width of 150 cm is recommended for comfort [182]. In Portugal, Institute for Mobility and Transport endorses the UK Department for Transport also referring that, at 10 km/h, a minimum of 20 cm extra width to the bike dimensions is enough margin for the cyclists to maintain dynamic equilibrium, but that this distance may be as high as 0.8 m at lower speeds or high speed descends [183]. The European Commission sponsored a cycling infrastructure guide referring that at normal cycling speeds, in normal conditions, the zigzagging movement of a bicycle is about 20 cm, but it may be wider, if cyclists are forced to travel at speeds less than 12 km/h [184], or on uphill stretches, due to the larger effort of the cyclist. According to a Implementation Fact Sheet sponsored by the European Commission, the minimum total lane width recommended by the is 0.9 m, but 1.5 m "increases the safety margin and makes driving comfortable and less stressful" [185].

It is more common to find, in design recommendation documents, the specified values of w_B and w_L, rather than the recommended value for w_d, because w_B and w_L are the parameters that directly impact on construction works. However, when omitted from an explicit reference, w_d can be calculated as.

$$w_d = w_L - w_B \tag{5.11}$$

A summary of the figures found in the literature is shown in Table 24.

Table 24: Assumptions and lane width parameters in different recommendation documents.

Country	w_B max	w_L min	w_T min	w_d min	Obs.
UK	80	100	150	20	[4] This w_d at speeds greater than 11.3 km/h.
USA	75	120		45	[179] w_d may be smaller
Brazil	60	100	150	40	[180]
Netherlands	-	-	-	25	[181]
Spain	60	100	-	40	[182]
Portugal	-	-	-	20	[183]
EU	75	90	150	20	[184] This w_d at speeds greater than 12 km/h; up to 80 cm when pulling away from stationary position or cycling uphill.

The conclusion is that the minimum required width for the bike lateral oscillatory movements that assure enough margin for the cyclist to establish dynamic equilibrium is $w_d = 20$ cm, if a

Dynamic Inductive Wireless Power Transfer for Lightweight Electric Vehicles
Luiz Alberto Lisboa da Silva Cardoso – University of Minho

264

minimum speed of 12 km/h is sustained, although more width is recognized as necessary, at lower speeds. In some references the implicit value of w_d can be as high as 45 cm. The electrified width of the lane, D_e, should than equal or greater than w_d.

For a HIPLEV system based on standard upright e-bikes, the best choice optimizing zig-zagging performance would then be $D_e \geq 45$ cm. However, by selecting a higher value of D_e, larger coils are also likely to be necessary. So, in order to optimize the viability of a first HIPLEV prototype, the preferential option for D_e is the to be just larger than the absolutely minimum necessary w_d in the EU, that is, $D_e \geq w_d = 20$ cm. After a successful concept demonstration, a second prototype could posteriorly seek to attain higher values of D_e, which would allow full lane compliance in other countries.

For the total lane width, w_T, the value of 1.5 m is practically a unanimous recommendation. Hence the specified total lane width for the HIPLEV prototype also becomes $w_T = 150$ cm. Concerning the lane operating (paved) width, the recommendation for an absolute minimum from 0.9 m (EU) to 1.2 (US) was observed in the literature, with a dominant incidence of the minimum value of 1.0 m. Contrarily to the case of the specification of w_d, for these parameters, the implementation of a first prototype is facilitated when the choices are larger number, since this will give more margin to avoid EMF exposition of eventual nearby pedestrians. However, larger values for the paved path make the lane less viable to build in old European cities. Hence, to be conservative in this very important aspect, which might lead or not to the future acceptance of the system, a first target value for the HIPLEV prototype is set at $w_L = 100$ cm, which is the most popular recommended value worldwide (except in the US), and currently satisfy individual requirements of EU countries and the UK.

Similarly, concerning the safety of pedestrians, in the vicinity of a powered i-lane it is mandatory that the maximum, $D_{EMF,MAX}$, of the width D_{EMF} of potentially risky EMF exposure, should also be limited by the minimum total lane width, w_T:

$$D_{EMF} \leq D_{EMF,MAX} = w_T \tag{5.12}$$

The EMF exposure control of the rider is also an absolutely essential feature, to be achieved by shielding the vehicle lower parts and, especially, by shielding the secondary coil and onboard power electronics, which will expectedly intensify both the magnetic and electric fields in their vicinity. The shield design is a standard procedure, not requiring any different knowledge than that

Dynamic Inductive Wireless Power Transfer for Lightweight Electric Vehicles
Luiz Alberto Lisboa da Silva Cardoso – University of Minho

265

used for the power transfer design itself. However, due to its own complexity and the necessity of very specialized test equipment for a complete and conclusive experimental evaluation, this task was intentionally left outside the initial focus of the initial HIPLEV prototype, which aims are limited to demonstrate the technical viability of power transfer and power handling in the DIWPT.

The essential target design values adopted for a first i-lane prototype established in this section, with which are deemed to lead to a full validation of the basic HIPLEV concept, are summarized in Table 25:

Table 25: Summary of width-related target parameters for the first HIPLEV protype.

Parameter	Symbol	Value	Unit
Minimum electrified width (WPT $\geq P_E$)	D_e	20*	cm
Minimum lane paved width	w_L	100**	cm
Minimum total lane width	w_T	150	cm
Maximum width of risky EMF exposure	$D_{EMF,MAX}$	150***	cm

*For minimum vehicle speeds of 12 km/h. Higher values up to 45 cm should be considered for a product.
**After a successful prototype demonstration, 120 cm could be next considered for a product.
***Applicable for pedestrians. The rider's protection depends on shielding on the vehicle.

The zone in between the paved path (w_L) and the total guarded width (w_T) is where lane power electronics hardware, such as junction boxes, and power distribution lines, could eventually be accommodated, below ground level. This would minimize possible conflicts with external installations, in case of eventual roadworks, or, in case of the maintenance of the i-lane itself, minimize repair costs.

5.4   Secondary Coil Dimensional Requirements

The maximum total HIPLEV width is a parameter of great importance, since it delimits the maximum width of the hardware for power harvesting (secondary coil included) that can be installed on the bike. Because the coil width is an initial design commitment that is difficult to later diminish, the maximum bike width adopted should than be less than the minimum of all observed recommended maxima. As summarized in Table 24, in all recommendation documents retrieved, the maximum width of the bike-cyclist ensemble varies from 60 cm (in Brazil and Spain) to 80 cm (in UK). The conservative choice for the maximum width of the DIWPT hardware to be installed on the first prototype of the HIPLEV is then $w_B = 60$ cm.

To avoid any possible mechanical interferences with other bikes and riders, as well objects outside the lane limits, the maximum width of the secondary coil, d_{max}, should not be greater

Dynamic Inductive Wireless Power Transfer for Lightweight Electric Vehicles
Luiz Alberto Lisboa da Silva Cardoso – University of Minho

266

than the maximum allowable width for the HIPLEV, which is this maximum allowable width of a bike travelling on the lane, w_B.

$$d_{max} \leq w_B \tag{5.13}$$

Since the secondary coil is expected to be installed somewhere close to the lane, and to pedals' height above ground, in addition to this essential requirement, it is also highly desirable that, d_{max} should also be limited to the width of the crank and pedals assembly, as shown in Figure 149. This diminishes the need for adjustments in the rider's awareness of the dimensions of the modified bike, and helps avoiding eventual obstacles on the lane, thus facilitating the acceptance of the HIPLEV as a means of transport.

d_{Pd}: pedal total length
d_{Sp}: pedal spindle length

W_q: "Q-factor"
W_{SW}: pedal stance width
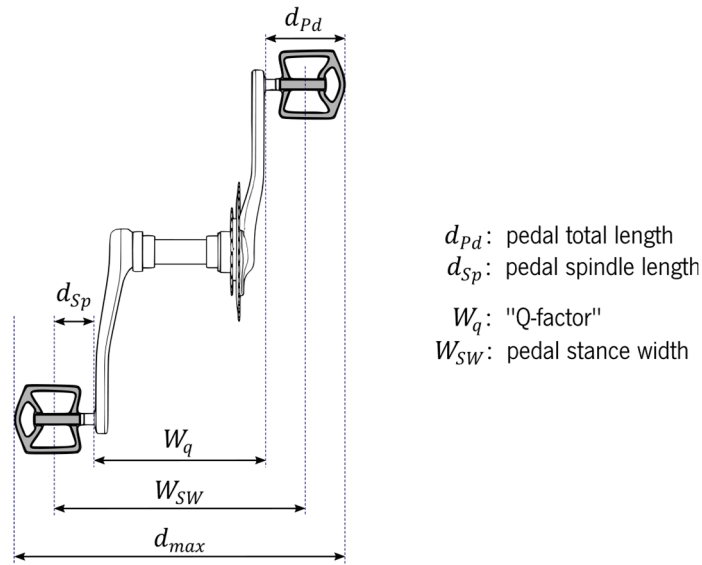
Figure 149: Crank and pedal horizontal dimensions.

Typical pedal total lengths (d_{Pd}) are around 105 mm, while the pedal stance widths (W_{SW}) of at least 171 mm can be expected in larger bikes. This means that the secondary coil is entitled to expand up to this probable maximum total width of the crank and pedal assembly:

$$d_{max} \leq \{w_q + 2d_{Pd}\}_{max} \cong 171 + 2 \times 105 = 381 \text{ mm} \tag{5.14}$$

Since this length is smaller than w_B, it dominates the requirements for the maximum width of the secondary coil.

The typical ground clearance of the bike's pedals is around 100 mm. To match this dimension and preserve the bike's original interference contour in the direction of movement, the

Dynamic Inductive Wireless Power Transfer for Lightweight Electric Vehicles
Luiz Alberto Lisboa da Silva Cardoso – University of Minho

267

ground clearance of the secondary coil, with the bike in the upright position, c, is also set at 100 mm:

$$c = 100 \text{ mm}$$

(5.15)

A two-wheeled vehicle is expected to incline laterally when making turns, or even along the natural oscillatory motion that is necessary for the rider to execute, in order to keep balance (especially in low speeds). Then a dynamic minimum clearance from ground c_d has also to be verified at the maximum expected lean angle φ_{max}, as illustrated in Figure 150.

When the bike leans, it pivots not on the point of contact of the tire with ground, but rather, approximately on the center of its approximately circular cross-section. The ERTRO 54-622 tires used (see section 4.7.1) have a nominal width of 54 mm. The pivoting point was experimentally estimated to be at a height $r_T = 23$ mm, the effective radius of tire roll over ground surface. This value is close to half of the width of the tire, $54/2 = 27$ mm, but 4 mm less, possibly due to both the shape of the tire cross-section not being perfectly circular, and to the compression against the ground surface the ground surface the tire is submitted.
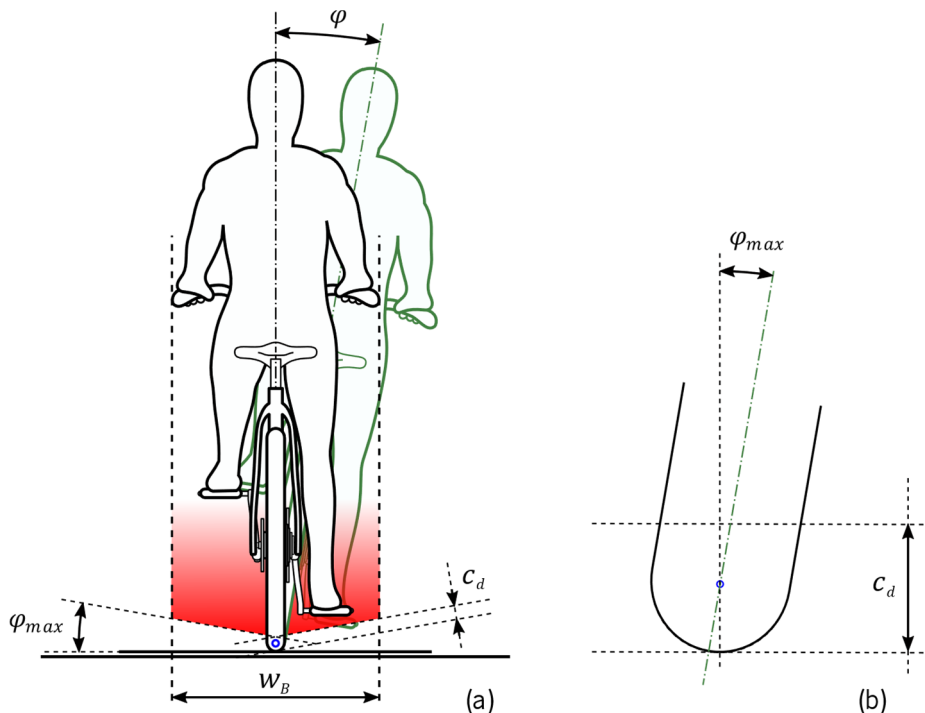
Figure 150: Mechanically viable zone for pick-up coil installation on the e-bike for ground level WPT.

In the worst case, the minimum ground clearance c_d with bike at limit lean angle condition can be assumed zero, and the coil structure will touch the ground. At this limit condition, the relation between the ground clearance, c, of the secondary coil, with the bike in the perfectly

Dynamic Inductive Wireless Power Transfer for Lightweight Electric Vehicles
Luiz Alberto Lisboa da Silva Cardoso – University of Minho

268

upright position on a horizontal surface, the tire pivoting radius, r_T, the maximum expected lean angle, φ_{max}, and the maximum coil diameter, w_e, can be derived from Figure 151.
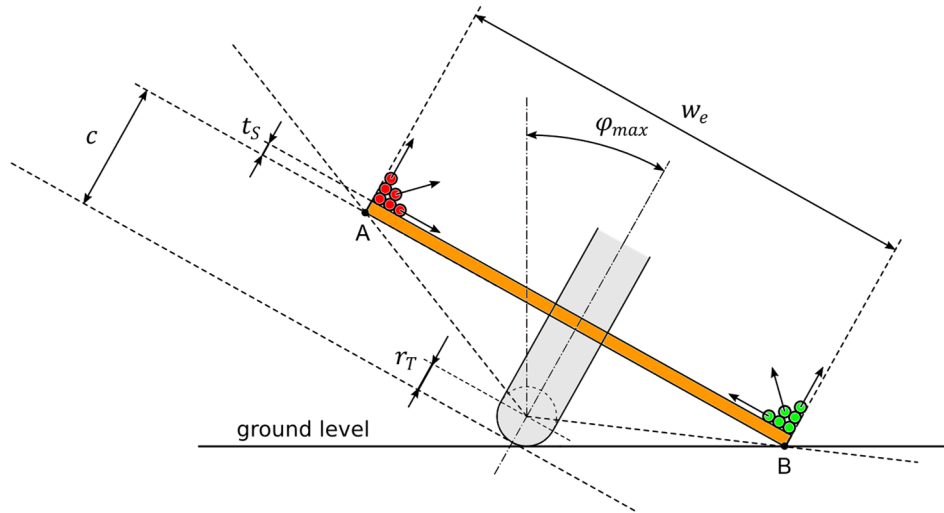
Figure 151: Geometric relation among the maximum possible width d_{max} of secondary coil, its clearance from ground c, and the maximum lean angle φ_{max} of the bike. Drawn to scale.

The analysis of this geometry, assuming a filamentary secondary coil, results in (5.16):

$$c \geq \frac{w_e}{2} \tan \varphi_{max} + r_T \left(1 - \frac{1}{\cos \varphi_{max}} \right) \qquad (5.16)$$

The maximum lean angle depends on different factors. On a steady turn, φ_{max} is basically given by the required angle φ_L to cause the center of mass of the ensemble (vehicle and rider) to be projected onto the ground point of contact, at the speed and curvature radius of the bike on its trajectory:

$$\varphi_L = \tan^{-1} \left(\frac{a_c}{g} \right), \qquad (5.17)$$

$$a_c = \frac{v^2}{R_c}, \qquad (5.18)$$

where a_c is the centripetal acceleration of the vehicle, g is the gravity of the Earth, v and R_c are respectively its instantaneous speed and radius of curvature on its trajectory. It has been also reported that, for a bike of similar frame structure and 26 inches wheel, at higher speeds, the observed lean angle can actually vary approximately in the range $\varphi_L \pm 3$ degrees of arc, due to the possible the existence of angle of the body of the rider with respect to the bike central plane, with smaller deviations expected from experienced riders [186].

Dynamic Inductive Wireless Power Transfer for Lightweight Electric Vehicles
Luiz Alberto Lisboa da Silva Cardoso – University of Minho

269

The maximum lean angle observed, conservatively considering a minimum curvature radius of 10 m for a top speed of 25 km/h (6.944 m/s), is than estimated by:

$$\varphi_{max} = \tan^{-1}\left(\frac{(6.944 \text{ m})^2}{10 \text{ m } \times \text{ } 9.81 \text{ m/s}^2}\right) + 3° = 29.17° \tag{5.19}$$

At lower speeds, the rider still has to oscillate the lean angle, in order to keep its balance. It was experimentally found that this angle, given by (5.100), is verified to be a conservative estimate of the maximum lean angle at lower speeds as well [187], when the radii of curvature are also smaller. This value is consistent and, as expected, for considering a wider sample of riders, a more conservative value than that found in our own experiments (Chapter 6).

So, after adopting $\varphi_{max} = 29.17°$, (5.16) simplifies to:

$$w_e \leq 3.583 \times (c + 3.34 \text{ mm}) \tag{5.20}$$

Since the ground clearance adopted is $c = 100$ mm, to match the pedals clearance from ground, then w_e should also satisfy:

$$w_e \leq 370.26 \text{ mm} \tag{5.21}$$

From (5.14) and (5.21):

$$w_e \leq min\{370.26, 381\} \text{ mm} = 370.26 \text{ mm} \tag{5.22}$$

Thus, considering that the primary coil width is not yet fixed, and in order to improve the induced voltage on a filamentary secondary coil and the power transfer, w_e is fixed at the maximum possible value given by (5.22) round to the millimeter:

$$w_e = 370 \text{ mm} \tag{5.23}$$

Using (5.16) to recalculate the maximum accepted lean angle for this newly fixed exact value of d, results $\varphi_{max} \cong 29.2°$.

If the secondary wiring could be considered filamentary, then it would be possible to make $d_{max} = w_e$. In general, however, the secondary cannot be considered filamentary, then:

Dynamic Inductive Wireless Power Transfer for Lightweight Electric Vehicles
Luiz Alberto Lisboa da Silva Cardoso – University of Minho

270

$$d_{max} = w_e - \frac{b_2}{2}, \tag{5.24}$$

where b_2 is the external diameter of the secondary coil wiring cable.

Concerning the positioning of the turns in the winding of the secondary coil, they should be distributed such that the magnetic flux of the primary coil traversing the area of the secondary coil is maximum: The turns should lie as low and, symmetrically around wheel, as wide-spread as possible. Hence, they should be located as concentrated as possible around points A and B of Figure 151, but within the limits of lateral distance from the center plane of wheel given by d_{max}, and on the upper side of the supporting board. Noticeably, the clearance $c =$ 100 mm is not the distance from the secondary coil winding to ground, but the height above ground of the support structure for the secondary coil (orange cross-section), with the bike in upright position, as shown in Figure 152.
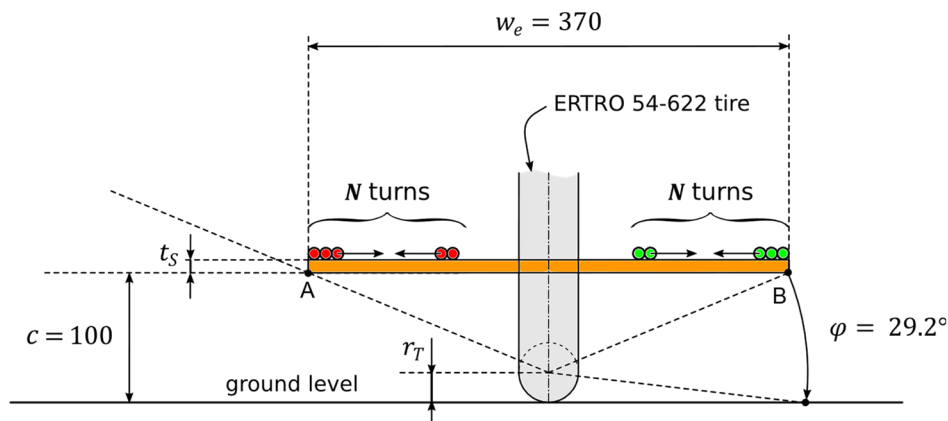
Figure 152: Geometric directives for the secondary coil and its positioning around the rear wheel. Drawn to scale, except windings, which are not yet determined at this point of the design.

Depending on the size of the air-gap between the primary and the secondary coil, the best distribution of the secondary turns can prioritize a horizontal or a vertical piling of the turns, or a combination of them. However, for the benefit of the mechanical simplicity of the first prototype, even though potentially sacrificing some performance in the power transfer, the option for a flat secondary coil with N horizontal turns per 1 single turn along the vertical dimension was adopted, with N yet to be determined, as shown in Figure 152.

In the prototype implementation, the support structure for the secondary coil, in orange color, was then built with a $t_S = $ 10 mm thick plywood sheet, a material that is resistant enough to support the weight of the windings of the coil, yet easy to handcraft.

Dynamic Inductive Wireless Power Transfer for Lightweight Electric Vehicles
Luiz Alberto Lisboa da Silva Cardoso – University of Minho

271

The secondary coil should be enough large to surround the rear wheel, but not mechanically interfering with it. It is also desirable that it can be as long as possible, for receiving more magnetic flux from the primary coil. No clear maximum limit was identified for its length, but this coil, upfront limited by the pedals, should not be too long as well, not to add a long "tail" to the bike, which could impair its mobility and difficult the maneuver in narrow paths. For a practical installation on the bike frame, the coil support plate should also not exceed 75 cm in length. Trials made winding turns around the 29- inch rear wheel experimentally revealed that the coil should have limits on their inner and external dimensions of their flat section. To simultaneously avoid mechanical interference with the tire and not to have the coil extended too much behind the wheel, the average turn length of the secondary coil, ℓ_2, should lie in between 60 cm and 70 cm:

$$600 \text{ mm} \leq \ell_2 \leq 700 \text{ mm} \tag{5.25}$$

The satisfactory solution found for compromising the mechanical clearance of the coil from the wheel and a good incorporation of the coil into the bike's profile is shown in Figure 153:
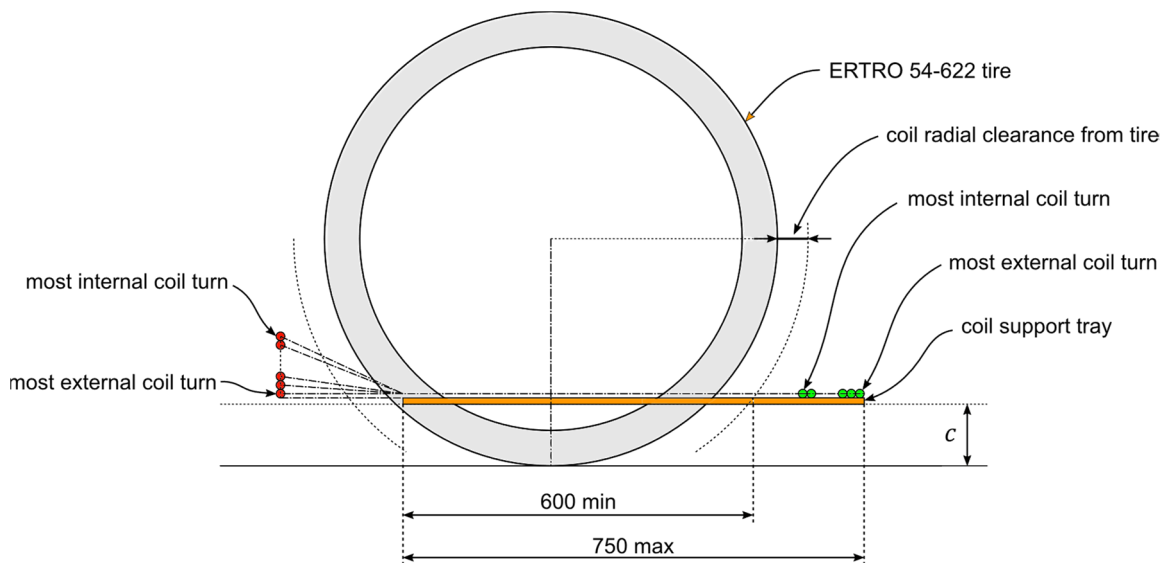
Figure 153: Secondary coil size adjustment for a 29-inch wheel.

5.5   Secondary Coil Maximum Current and Wiring

In 5.4 some dimensional requirements for the secondary coil were obtained:

- Its external width, $w_e = 370$ mm.

- The viable interval for the average length of its turns, $600 \text{ mm} \leq \ell_2 \leq 750 \text{ mm}$.

Dynamic Inductive Wireless Power Transfer for Lightweight Electric Vehicles
Luiz Alberto Lisboa da Silva Cardoso – University of Minho

272

- The general parametric layout of the coil cross-section, according to Figure 152.

From 5.2, the maximum expected power current I_{DC-out} on the DC load DC is:

$$\max(I_{DC-out}) = \frac{P_E}{V_{L,min}} = \frac{400\ \text{W}}{36.5\ \text{V}} = 10.96\ \text{A}\ , \tag{5.26}$$

Then, considering a COTS DC-DC converter with a typical $\Delta V_{DC-DC} \cong 2\ \text{V}$ minimum required voltage drop from input to output and a worst case efficiency of $\eta_{DC-DC} = 88\%$, the maximum input current to DC-DC converter is estimated by (2.103):

$$\max(I_{DC-in}) = \frac{36.5\ \text{V}}{88\%\ 38.5\ \text{V}}\ 10.96\ \text{A} \cong 11.8\ \text{A}\ , \tag{5.27}$$
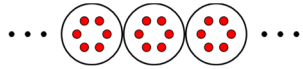
for which, the maximum secondary coil current can be estimated by (2.104):

$$I_{2,max} = \max(I_2) \cong \frac{\pi}{2\sqrt{2}}11.8\ \text{A} \cong 13.1\ \text{A rms} \tag{5.28}$$

Following section 5.2.1.1 and Table 22, a general requirement for winding is to (try to) use low-cost $1\ \text{mm}^2$ and $1.5\ \text{mm}^2$ cabling, so the secondary coil would conservatively require $4 \times 1\ \text{mm}^2$ or $3 \times 1.5\ \text{mm}^2$ cables. For improved performance, a multiconductor cable type 6G1 was selected (Top Cable FLEXTEL 110 ES05VV-F 6G1), consisting of 6 individually isolated $1\ \text{mm}^2$ flexible cables, with a total cross-sectional area $A_S = 6\ \text{mm}^2$, 65% larger total cross-section than strictly required, with an external diameter $b_2 = 8\ \text{mm}$.

As an immediate consequence of the definition of the cross-section of the secondary coil it is possible to use the FEM numeric simulation to determine its characteristic resistance per unit of length, when used either in a stand-alone configuration or in the middle of linear array of equally spaced cables. The results of the simulation are show in Table 26, and can be used in the estimation of the of the required induced voltage on the secondary coil at its limit lateral displacement, where it is still possible to harvest the maximum power P_E (5.57), Section 5.8.

Table 26: Results from FEM numeric simulation of two possible configurations for the 1-turn primary coil.

6G1.0mm^2 at $f_0 = 51.7\ \text{kHz}$	Stand-alone use	Average, in a linear array of a multiturn coil*
AC Resistance (Ω/m)	$\rho_{2,a} = 5.20 \times 10^{-3}$	$\rho_{2,b} = 7.49 \times 10^{-3}$

*Assuming a pattern pitch with the same length of the diameter of the cable.

Dynamic Inductive Wireless Power Transfer for Lightweight Electric Vehicles
Luiz Alberto Lisboa da Silva Cardoso – University of Minho

273

5.6   Primary Coil Depth below Ground Level

In order to lower the required primary current levels, the distance between the primary and secondary coil planes, h, should be as low as possible. Since the ground clearance of the secondary coil support tray, c_{min}, is already determined, h will be fully defined by the depth of the primary coil below ground level. While trying to keep h as small as possible, the primary coil winding should be covered with a mechanically resistant layer of some low permeability, highly insulating material, since the vehicle cannot directly run directly over the primary coil windings.

The primary coil depth below ground level is a purely mechanical requirement. Considering the workbench conditions, at this point of the design, it is arbitrarily established that the lane support should be constituted of 16 mm thick Medium Density Fiberboard (MDF) sheets, and that the primary coil cable diameter will be limited to 20 mm. These MDF sheets can then be supported by 34 mm × 21 mm wooden laths, which will leave the required vertical clearance to lay the primary windings standard dimensions. In addition, by using these dimensions, materials can be easily procured in the local lumber retail stores. The laboratory prototype of the HIPLEV i-lane is then formed by covering the primary coils with wooden modules, which base cross-section is shown in Figure 154.
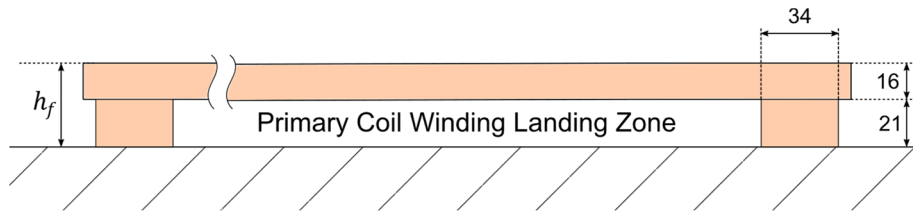
Figure 154: Cross-section of the prototype inductive of lane, detail of pick-up coil winding.

The resulting depth h_f of the primary coil support plane is then $16 + 21 = 37$ mm. Omitted in Figure 154, but also implemented in the prototype, extra wooden laths of the same 34 mm × 21 mm cross-section, were inserted in the unused portions of the primary coil winding landing zone, to allow the lane covers to better support the weight of the vehicle and the rider without any noticeable deformation.

In a real outdoors implementation of an i-lane, concrete and asphalt can directly cover the primary coil windings, as it done in the OLEV prototype [188]. Or the windings can be embedded in pre-cast modules, which are then laid underneath the pavement. In the first known pilot DIWPT design for standard EVs with a total electrified length over 1 km, recently deployed by Electreon (section 3.4.8), this depth, for instance, is claimed to be 8 cm [114], and the coils are embedded

Dynamic Inductive Wireless Power Transfer for Lightweight Electric Vehicles
Luiz Alberto Lisboa da Silva Cardoso – University of Minho

274

in sealed rubber modules. This latter is a preferred manner to deploy the primary coils because it makes easier to implement the quality control on the geometry of the coils, in industrial production scale, which is an important factor for the system functionality and performance. Also, there is an evidence that only the material in close proximity to the copper turns is relevant to model the coil impedance and losses [189]. So, by embedding the primary coil in rubber or other low loss material, it would be also easier to reduce the losses eventually caused by the pavement.

5.6.1 Primary Coil Winding and Vertical Inter-Coil Distance

Let us assume that the center axis of the primary and secondary coil cables will be at respectively a height h_p above the floor of the primary coil landing zone, and a height h_s above the secondary coil support tray. Then, by considering the cross-section layout details and parameters already defined in Figure 152 and Figure 154, the vertical inter-coil distance, h, can then be expressed as:

$$h = h_f - h_p + c_{min} + t_s + h_s \, , \qquad (5.29)$$

Replacing in (5.29) the already attributed values of h_f, c_{min}, and t_s:

$$h = 147 \text{ mm} - \left(h_p - h_s \right) \qquad (5.30)$$

The heights of the centers of the primary and secondary cables above their support surfaces, h_p and h_s, should be approximately equal to the radii of these cables. Since the primary coil current is expected to be higher than the secondary coil current, the primary coil cable diameter should be also larger than that of the secondary coil, then $h_p - h_s > 0$. Then

$$h \le h_{max} = 147 \text{ mm} \qquad (5.31)$$

In 5.5 the external diameter of the windings of secondary coil, $b_2 = 2h_s$ was set at 8 mm. Not a priori knowing the required primary current, in order to fix h, an initial assumption about the constitution of the primary coil winding is made: It will be constituted by as many 10G1.5mm cables in parallel as necessary, to carry the necessary primary current yet to be determined. In one 10G1.5mm2 cable there are 10 conductors each with 1.5 mm of cross-sectional area. In this cable there are two conductors that remain in the center of the cable, while the eight others are twisted around the central conductors along all the longitude of the cable.

Dynamic Inductive Wireless Power Transfer for Lightweight Electric Vehicles
Luiz Alberto Lisboa da Silva Cardoso – University of Minho

275

At the frequency f_0 used, the skin depth in copper is approximately 0.3 mm, whereas the external diameter $h_p = 11$ mm of the 10G1.5mm2 cable adopted is much higher. So, due to the cross-section layout the cable, the two central conductors, if short circuited at the terminals of the cable, are not expected to carry significant current. Looking up in and Table 22, the eight remaining conductor in the cable can safely carry 5 A rms to 7.5 A rms each, a total of 40 A rms to 60 A rms per 10G1.5mm2 cable. This hypothesis can be interactively reviewed if the actual current capacity of the cable is significantly smaller than 40 A rms. If, it is not, by using the necessary number of 10G1.5mm2 cables electrically in parallel, in carefully twisted paths, the required primary coil current will be eventually satisfied. For instance, if 70 A rms are required, two of these cables in parallel should be used. But yet, both will lie side by side on the surface of the primary coil winding landing zone (Figure 154), keeping unchanged the vertical distance to secondary coil. Under this hypothesis, the radius h_p becomes defined, and h can be fixed in the design:

$$h = 147 \text{ mm} - \frac{(11 \text{ mm} - 8 \text{ mm})}{2} = 145.5 \text{ mm} \tag{5.32}$$

5.6.2 Maximum Primary Coil Width

The first and most immediate restriction on the maximum primary coil width is a consequence of the fact that the primary coil should be entirely confined underneath the pavement. So, its maximum width, D_{max}, should be limited by the minimum lane paved width, w_L:

$$D_{max} \leq w_L \tag{5.33}$$

Having fixed the number of turns in the primary coil to be one, the depth underneath the ground surface it is installed, and the maximum secondary coil width, it is possible to further refine a limit size for the primary coil width, by introducing the directive of maximization of the induced voltage on the secondary coil by the primary coil. According to Theorem 2 in section 3.6.3, for each isolated secondary coil turn, there is width $D = w_P$ that maximizes the induced voltage that turn. Since all secondary turns are connected in series, the total induce voltage on the secondary coil can be estimated by the sum of the individually induced voltage in each of its turns, as given by (3.123) and (3.124). The maximum primary coil diameter is then dominated by optimum primary coil diameter for the most external secondary coil turn, which width w_e was already defined at 370 mm in section 5.4. So, applying Theorem 2 and (3.136), and using the values of

Dynamic Inductive Wireless Power Transfer for Lightweight Electric Vehicles
Luiz Alberto Lisboa da Silva Cardoso – University of Minho

276

$d_{max} = w_e$, as given by (5.23), and h_{max} as in (5.31), the maximum width for the primary coil can be calculated by:

$$D \leq D_{max} = \sqrt{d_{max}^2 + 4h_{max}^2} \cong 472.6 \text{ mm} \tag{5.34}$$

5.7 Voltage Induced on the Secondary Coil

The minimum induced voltage required on the secondary coil is established at the limit relative position of the secondary coil that still permits the required power P_E to be regulated on the load. For a serial compensation of the secondary coil this is voltage is given by (2.63), where DC voltage is the input DC voltage to the DC-DC converter used in the secondary circuit, which is modeled as being ΔV_{DC-DC} higher than the voltage V_L output to the load (constant voltage drop). Using a commercial DC-DC converter model ZXY-6010S (Zhengzhou Minghe Electronic Technology Co., Ltd) with a voltage drop $\Delta V_{DC-DC} \cong 2$ V, multiple Schottky rectifier diodes in parallel, with a maximum direct current voltage drop $V_D \cong 0.7$ V, and setting the load voltage to 36.5 V, (2.63) then provides the numeric value for the minimum required $E_{2,rms}$:

$$\min(E_{2,rms}) \cong \frac{2\sqrt{2}}{\pi}(36.5 \text{ V} + 2 \text{ V} + 2 \times 0.7 \text{ V}) + I_{2,rms} R_2 \cong$$
$$\cong 35.9 + I_{2,rms} R_2 \tag{5.35}$$

5.7.1 Secondary Coil Model for Calculating the Induced Voltage

The minimum required induced voltage established in (5.35) should now be used as a restriction to select the remaining parameters of the primary and secondary coils. Under the simplifying hypothesis of filamentary coils, if the secondary coil would be constituted of a single turn, the family of induction voltage profile curves for a rectangular secondary coil over an oblong primary coil follows the pattern could be computed by Theorem 1, (3.123) and (3.124) is shown in Figure 117. In this first HIPLEV prototype, to make it easier meeting power transfer requirements, the selected design paradigm is to maximize the peak power available at the center of the lane. If the number of turn in the secondary would be equal to one, a relationship among the widths of the primary of the primary coil, D, the width of the secondary coil, d, and the vertical distance in between then, h, given by Theorem 2, (3.136) and (3.137), could be used for determining the optimum primary width corresponding to the simple geometric construction in Figure 118.

Dynamic Inductive Wireless Power Transfer for Lightweight Electric Vehicles
Luiz Alberto Lisboa da Silva Cardoso – University of Minho

277

However, with just one turn, a desirably low primary coil voltage and a low expected magnetic coupling coefficient, multiple secondary coil turns are necessary. The secondary coil is then modeled as N concentric multiple turns connected in series, so that the total induced voltage can be estimated as the sum of the individual induced voltages in each of the turns. If the average turn width is d, the average turn length is ℓ_2, and the pitch distance between neighbor turns is p_d, each k-th turn can be approximated by a single-turn rectangular coil with length $\ell_{2,k}$ and width d_k as respectively given respectively by (5.36) and (5.37).

$$\ell_{2,k} = \ell_2 + (N - 2k + 1)p_d \tag{5.36}$$

$$d_k = d + (N - 2k + 1)p_d \tag{5.37}$$

The simplified model of the secondary coil is shown in Figure 155, where the most external turn is associated with $k = 1$, and the most internal with $k = N$.
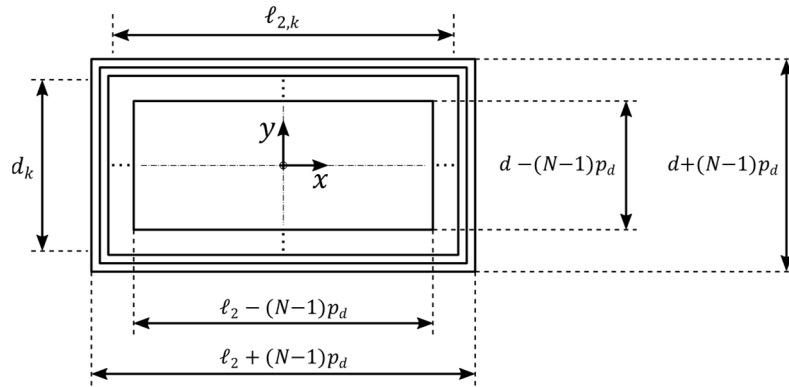
Figure 155: Simplified model of secondary coil for 3-dimensional simulation, where N is the number of turns.

The model of the secondary coil can also be seen. in more detail, at its cross-section (perpendicular plane to axis x), where the wiring of each coil turn is contained in a cable with diameter b_2, as shown in Figure 156, already determined in section 5.5 as $b_2 = 8\text{mm}$, for this specific design case.
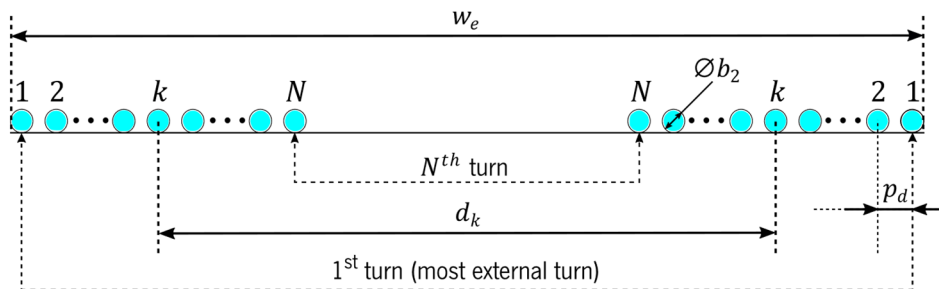
Figure 156: Cross-section of the secondary coil.

Dynamic Inductive Wireless Power Transfer for Lightweight Electric Vehicles
Luiz Alberto Lisboa da Silva Cardoso – University of Minho

278

Figure 156 an alternative formulation for d_k, based on the already fixed width w_e (section 5.4), is given by:

$$d_k = w_e - 2(k - 1)p_d - b_2 \tag{5.38}$$

To avoid increased losses due to the proximity effect, the conductors of the coil's windings should ideally not be very close. However, since the secondary coil is flat and the actual conductors in the cable of any turn already have some minimum separation from other conductor in the neighbor turns, p_d does not need to be much large, as long as $p_d \geq b_2$. On the other hand, to increase the area of each interior turn and capture more magnetic flux, thus increasing the induced voltage, p_d should be as low as possible. Then, at this point of the design, p_d is made equal to diameter b_2 of the cable:

$$p_d = b_2 \tag{5.39}$$

In this particular case, where the sections of cable wiring of neighbor turns are touching each other, (5.38) then simplifies to:

$$d_k = w_e - (2k - 1)p_d \tag{5.40}$$

Once fixed w_e, p_d and b_2, the use of the particular mechanical configuration in Figure 152 poses an immediate restriction on the maximum number N of turns that can be accommodated in a single row in the secondary:

$$N \leq N_{max} = \left\lceil \frac{(w_e - w_g)}{2p_d} \right\rceil \tag{5.41}$$

where is the required minimum void width in the center of the coil support, through which the wheel and tire assembly can freely rotate. By experimental verification, $w_g = 95$ mm is a safe election. With the values w_e, w_g and p_d now fixed, (5.41) can be evaluated to:

$$N \leq N_{max} = \left\lceil \frac{(w_e - w_g)}{2p_d} \right\rceil = 17 \tag{5.42}$$

The total voltage induced by the primary coil on the secondary coil is the sum of the induced voltages by the primary coil in each of secondary coil turns, because they are series-connected. Since the number of primary coil turns is set at one, according to the considerations in (3.123),

Dynamic Inductive Wireless Power Transfer for Lightweight Electric Vehicles
Luiz Alberto Lisboa da Silva Cardoso – University of Minho

279

Theorem 1 then implies that, for each secondary turn k, with $1 \leq k \leq N$, the total induced voltage will be given by:

$$\dot{V}_{ind} = j\mu f_0 \dot{I}_p \sum_{k=1}^{N} \ell_{2,k}\, \xi(x, h, d_k, D)\ ,$$

(5.43)

where $\dot{I}_p$ is the primary coil current and $\ell_{2,k}$ are defined in (5.36).

According to Theorem 2 (3.136), for each k, there will be an optimum diameter $\widehat{D}_k$:

$$\widehat{D}_k = \sqrt{d_k^2 + 4h^2}$$

(5.44)

From (5.44), the optimum positioning of primary conductors that maximizes the induced voltage on turn k_1 is different from that for turn k_2. The primary coil has just one turn, and there cannot be a single value D that simultaneously maximizes the induced voltage in all turns. Because of this, Theorem 2 cannot be directly applied to find a global optimum width $\widehat{D}$ for the primary coil. However, since the width of each secondary turn is not expected to differ much from the average turn width, in 5.7.2 an heuristic is introduced to simplify the design and approximate the primary coil width $\widehat{D}$ that, under center-alignment conditions, induce maximum voltage amplitude on the secondary coil.

5.7.2 Quasi-Optimum Heuristic Determination of Primary Coil Width

Under the assumption that the oblong primary coil is much longer than the secondary coil, the expression of the induced voltage for a single-turn rectangular coil contained in a plane that is parallel to the single-turn primary coil, can be approximated by (3.123) and (3.124), when their longitudinal axes are also parallel. Under the hypothesis of filamentary windings, the total secondary coil voltage under center-alignment with the primary coil, is then estimated by the sum of the voltages induced on the secondary turns of the coil model, which is given by:

$$\dot{V}_{ind}(x, N, D) = j\,\mu\,f_0\,\dot{I}_p \sum_{k=1}^{N} \ell_{2,k}\, \xi(0, h, d_k, D)\ ,$$

(5.45)

where $\ell_{2,k}$ is secondary coil turn length along the primary coil longitudinal axis, as given by (5.36), and the normalized induced voltage function ξ and the other parameters are given as defined for (3.124).

Dynamic Inductive Wireless Power Transfer for Lightweight Electric Vehicles
Luiz Alberto Lisboa da Silva Cardoso – University of Minho

280

Since for each individual turn there will be a maximum induced voltage when $D = \widehat{D}_k$ (5.44), a possible good estimator $\overline{D}$, for $\widehat{D}$, is the average value of all $\widehat{D}_k$:

$$\overline{D} = \frac{1}{N}\sum_{k=1}^{N}\widehat{D}_k = \frac{1}{N}\sum_{k=1}^{N}\sqrt{d_k^2 + 4h^2} \qquad (5.46)$$

A second possible heuristic to estimate $\widehat{D}$ is to consider that all N turns of the secondary coil, being closely together, have approximately the same width $\bar{d}$, corresponding to the average of all turn widths d_k:

$$\bar{d} = \frac{1}{N}\sum_{k=1}^{N}d_k, \qquad (5.47)$$

which is equivalent to:

$$\bar{d} = \frac{d_1 + d_N}{2} \qquad (5.48)$$

Then using (5.44), produce the estimate $\widetilde{D}$:

$$\widetilde{D} = \sqrt{\bar{d}^2 + 4h^2} \qquad (5.49)$$

The approximation of $\widehat{D}_k$ by $\widetilde{D}$ can therefore be interpreted as if all the secondary coil turns were concentrated at the position of the central turn of that coil, while the use of the estimator $\overline{D}$ assumes that all $\widehat{D}_k$ would approximately coincide at $D = \widehat{D}$.

Both estimators $\overline{D}$ and $\widetilde{D}$ are simple to calculate algebraically, but $\widetilde{D}$ is even simpler, and has an easy geometric interpretation, adapted from that of Theorem 2 itself (in Figure 118): $\widetilde{D}$ is the diameter of the circle circumference drawn with center at the intersection of the vertical symmetry plane with the support line for the primary coil windings, passing through the central turn of the secondary coil, as shown in Figure 157.

Dynamic Inductive Wireless Power Transfer for Lightweight Electric Vehicles
Luiz Alberto Lisboa da Silva Cardoso – University of Minho

281
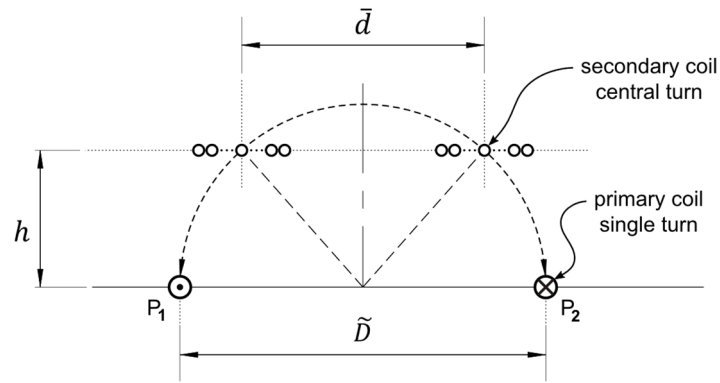
Figure 157: Geometric interpretation of the quasi-optimum primary coil width $\widetilde{D}$.

Under the considerations of Theorem 2, for $k = 1$, both expressions (5.46) and (5.49) give the exact optimum value for $\widehat{D}$. Intuitively, the heuristic estimators $\overline{D}$ or $\widetilde{D}$, would still provide configuration where the maximum induced voltage is close enough to its maximum possible value realizable value by choosing D. This should especially hold if the secondary turns are concentrated in a relatively narrow range, compared to its average width $\overline{d}$, not falling to much apart from each other. Or, equivalently, if the number of secondary turns N is not very high and the turn pitch is low, such that $N(p_d - 1)$ is enough smaller than $\overline{d}$.

The parametric design of the cross-section of the inductive magnetic link, formed by the oblong primary and the rectangular secondary coil, considering all dispositions taken into account so far in the design, is illustrated in Figure 158, for the case in which $\widetilde{D}$ (5.49). The secondary coil (pick-up) tray, previously assumed in Figure 151 and Figure 152 is now shown with an empty central section with a minimum required width estimated at 95 mm, where the rear wheel is to be inserted and spin freely.
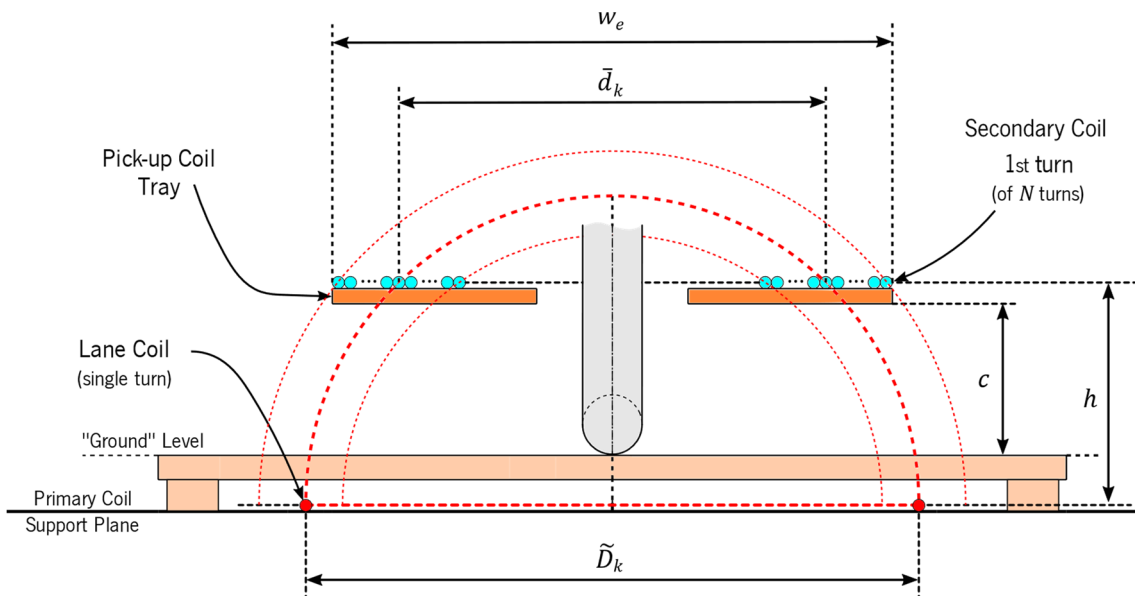
Figure 158: Laboratory configuration for the parametric design of the inductive link cross-section.

Dynamic Inductive Wireless Power Transfer for Lightweight Electric Vehicles
Luiz Alberto Lisboa da Silva Cardoso – University of Minho

282

Values for c, w_e and h are given respectively by (5.15), (5.23) and (5.32). Other applicable dimensions to Figure 158 are quoted in Figure 154.

5.7.3 Error Due to the Approximation of the Optimum Primary Coil Width

Errors in the estimation of $\widehat{D}$ could potentially increase as k is increased too. The accuracy of the heuristic methods for establishing the primary coil width in 5.7.2 can be exemplified in the design case of the HIPLEV lane, where $h = 145.5$ mm (5.32), $w_e = 370$ mm (5.23), and $p_d = b_2 = 8$ mm (5.39) have already been determined. Initially, the estimators for the optimum primary coil width $\widehat{D}$ are numerically compared, by plotting, in Figure 159, the values of $\overline{D}$ and $\widetilde{D}$, as functions of the number of turns N.
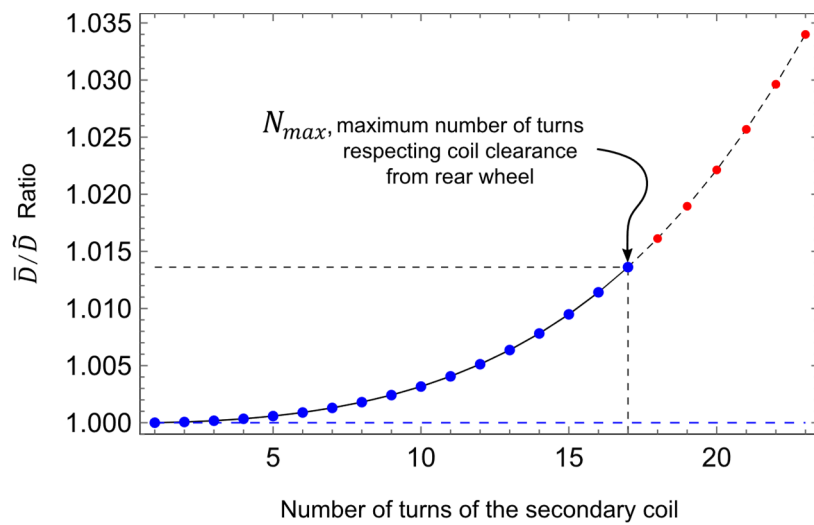
Figure 159: Comparison of the heuristic estimators $\overline{D}$ and $\widetilde{D}$ for the optimum primary coil width.

Examining the results in Figure 159, it is noticeable that $\overline{D}$ and $\widetilde{D}$ differ from each other by less than 1.4%, along all valid range for N (5.42). This difference is further limited to less than 1%, if $N \leq 15$. So, in any practical means, $\overline{D}$ and $\widetilde{D}$ provide equivalent estimates for $\widehat{D}$. As $\widetilde{D}$ is easier to compute and it is associated with a simple geometric interpretation (Figure 157), its absolute accuracy in the prediction of the induced voltage is next evaluated against that provided by the finite element modeling of the same configuration.

The voltage $V_{ind}(x, \widehat{D})$ can be estimated as $\widetilde{V}_{ind}$, by replacing D by $\widetilde{D}$ in (5.45), or with an additional simplification, it can still be estimated by considering that all $\ell_{2,k}$ can approximated by ℓ_2. This second approximation results in the simpler expression:

$$\widetilde{V}_{ind}(x, N) = \mu\, f_0\, I_p\, N\, \ell_2\, \xi\big(x, h, \bar{d}, \widetilde{D}\big), \tag{5.50}$$

Dynamic Inductive Wireless Power Transfer for Lightweight Electric Vehicles
Luiz Alberto Lisboa da Silva Cardoso – University of Minho

283

where $\bar{d}$ (5.47) and $\widetilde{D}$ (5.49) are also functions of N.

Similarly to the analysis done on the plot of Figure 159, it is possible to evaluate the errors introduced by considering this new approximation, by comparing the induced voltage estimated close to $x = 0$, more precisely, x within the interval $[-w_d/2, w_d/2]$, where the power harvest it expected to occur at the nominal level $P_E = 400$ W. Using the same values currently fixed for h (5.32), w_e (5.23), p_d and b_2 (5.39), the variation of the ratio $V_{ind}(0, \widetilde{D})/\tilde{V}_{ind}(0, N)$ can be observed in the plot of Figure 160.
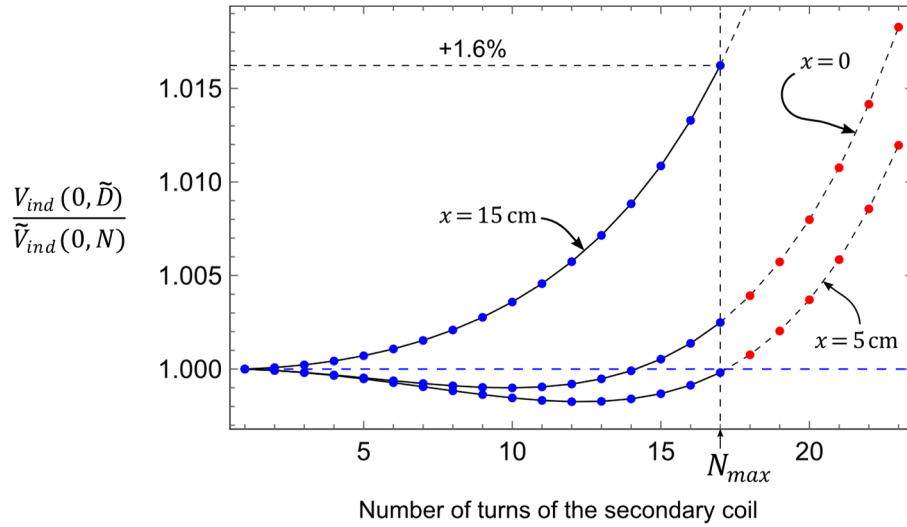
Figure 160: Relative error in the estimation of the induced voltage, using and not using different coil turn lengths.

The maximum relative error found between $V_{ind}(x, \widetilde{D})$ and $\tilde{V}_{ind}(x, N)$ is 1.6 %, which is considered acceptable, so $\tilde{V}_{ind}(x, N)$ (5.50) can replace the estimator $V_{ind}(x, \widetilde{D})$. But the real question concerning the acceptability of taking the quasi-optimum width $\widetilde{D}$ for the primary coil is whether the deviation of $V_{ind}(x, \widetilde{D})$ from $V_{ind}(x, \widehat{D})$ is relevant or not. To answer that, in the scope of this design, FEM simulations were executed, to evaluate $V_{ind}(0, D)$, as D is increased, for N varying from 1 to 20. In this manner, the actual point $\widehat{D}$ of maximum in V_{ind}, at the center position $x = 0$, can be numerically determined and compared with $\widetilde{D}$.

A family of curves for different number N of turns in the secondary coil is plot in Figure 161, using the results from numeric simulations using finite element modeling. The normalized average induced voltage per turn is plot against the primary coil width, normalized to quasi-optimum width $\widetilde{D}$ (which is also depends on N):

Dynamic Inductive Wireless Power Transfer for Lightweight Electric Vehicles
Luiz Alberto Lisboa da Silva Cardoso – University of Minho

284
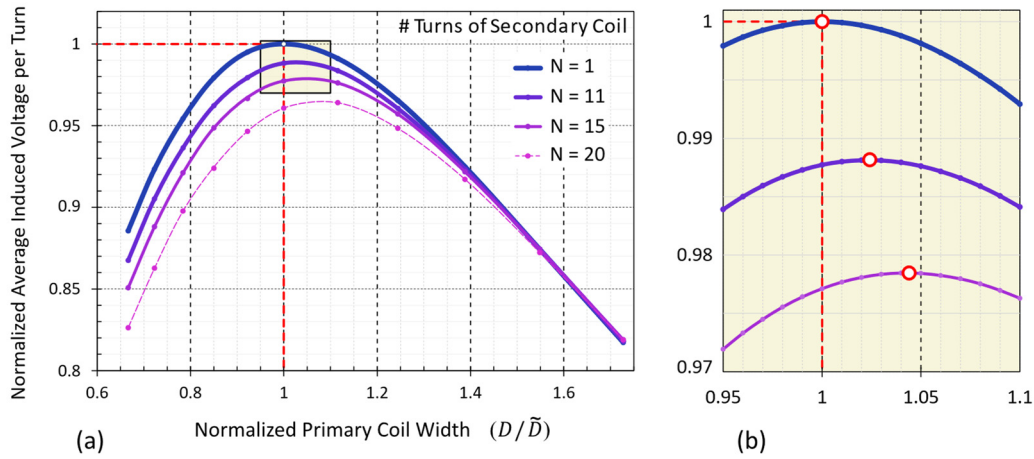
Figure 161: Results from FEM simulation of the induced voltage, $V_{ind}(0, D)$, with secondary and primary coils center-aligned, for different number N of secondary coil turns.

The plots (a) and (b) in Figure 161 are the same, at different zoom scales, with the yellow shaded area in Figure 161a corresponding to Figure 161b. Figure 161a was generated using the software tool FEMM [99], while Figure 161b, as a second verification, was generated with COMSOL Multiphysics, both showing excellent numeric agreement.

It can be noticed that as N increases, the turns spread over a larger region around the central turn position, and the average induced voltage per turn in center alignment conditions also decreases. Also, the primary coil width D that maximizes the induced voltage is progressively increased above the single-turn optimum value $\widehat{D} = w_p$, plot as one in the normalized scale. For $N \leq 15$, however, the optimum primary coil width will be less than 4.5% larger than that estimated by (5.49), and the average induced (and total) voltage will be only about 2.2% lower than the value predicted by (5.50). If $N \leq 11$, these errors drop respectively to 2.5% and 1.3%. These errors are deemed as acceptable discrepancies for the HIPLEV design application, face to the great simplification it introduced in the design process.

5.8   Secondary Coil Voltage, Turns and Primary Coil Current

The approximate expression for the induced voltage on the secondary coil (5.50) and the electrical and mechanical requirements previously derived in Section 5.2, can be used in the joint determination of the open-secondary primary coil current, I_p, the number of turns of the secondary coil, N, and the average length ℓ_2 of these turns along the longitudinal axis of the coil.

Dynamic Inductive Wireless Power Transfer for Lightweight Electric Vehicles
Luiz Alberto Lisboa da Silva Cardoso – University of Minho

285

The primary coil current is driven by the Mazzilli-Baxandall, where the driving voltage is constant. The primary coil current, $\dot{I}_1$, is the open-secondary primary coil current, $\dot{I}_p$, plus the current, $\dot{I}_b$, backed induced in the primary coil by the current $\dot{I}_2$ established in the secondary coil.

$$\dot{I}_1 = \dot{I}_p + \dot{I}_b \tag{5.51}$$

Under perfect compensation of both circuits, which, in the primary, is guaranteed by the establishment the oscillation frequency by auto-resonance, and, in the secondary, is obtained by the adjustment of the series compensation capacitor, and small enough coil resistances (compared to their impedances at f_0), the phase of the back-induced current is approximately $\pi/2$ ahead of the primary current $\dot{I}_1$. This means that $\dot{I}_p + \dot{I}_b$ is approximately orthogonal to $\dot{I}_b$, as shown in the vector plot in Figure 162.
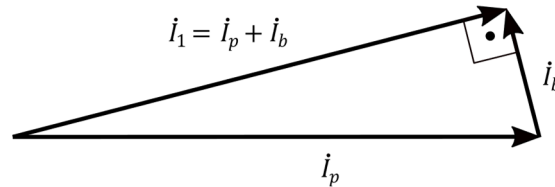
Figure 162: The effect of the back induced current on the primary coil.

In the Mazzilli-Baxandall inverter configuration, the back induced current $\dot{I}_b$ is given by:

$$\dot{I}_b = -\frac{j\,\omega\,M\,I_2}{j\,\omega\,L_1} = \frac{M}{L_1}\left(\frac{j\,\omega\,M\,I_1}{R_{2,AC}}\right), \tag{5.52}$$

and the magnitude ratio of $\dot{I}_b$ to $\dot{I}_1$ can be calculated as:

$$\frac{\dot{I}_b}{\dot{I}_1} = j\,k^2\,\frac{\omega\,L_2}{R_{2,AC}}, \tag{5.53}$$

where, in (5.52) and (5.53), k is the magnetic coupling factor between primary and secondary coils, L_1 and L_2 the respectively the inductances of the primary and secondary coils, $\omega = 2\pi f_0$ and $R_{2,AC}$ is the total equivalent AC load of the secondary.

For a not too heavily loaded secondary and a small enough k, which is the usual case for IWPT over oblong primary coils (3.78), $I_{b,rms}$ is significantly smaller than $I_{p,rms}$, so that $I_1 \cong I_p$, in terms of magnitude. That is, the back-induced voltage in the primary coil due to the secondary coil current can be neglected, and the primary current can be taken as approximately constant, for the effect of determining the induced voltage. Therefore, the minimum required value for the

product $I_p \times \ell_2 \times N$ can be determined by relating the estimated open secondary induced voltage in (5.50) to the required minimum induced voltage, at the critical limit where nominal power to the load (power train) can still be regulated by the DC-DC converter:

$$\mu \, f_0 \, I_{p,rms} \, N \, \ell_2 \, \xi\left(x, h, \bar{d}, \widetilde{D}\right) \geq \min\left(E_{2,rms}\right) , \tag{5.54}$$

for $-D_e/2 \leq x \leq D_e/2$, where $\bar{d}$ and $\widetilde{D}$ are calculated by respectively (5.47) and (5.49).

Since the design paradigm being used is to use the geometry where ξ is maximized at the center of the lane, the symmetric bell-shaped curve will imply that (5.54) is satisfied for all x such that $|x| < D_e/2$, if it is satisfied by $x = D_e/2$.

$$I_p \, N \, \ell_2 \geq \frac{\min\left(E_{2,rms}\right)}{\mu \, f_0 \, \xi\left(D_e/2 \, , h, \bar{d}, \widetilde{D}\right)} , \tag{5.55}$$

Replacing $\min\left(E_{2,rms}\right)$ by the value in (5.35) and the other numeric values already established for the right side of inequation (5.55), and considering $\mu = \mu_0$ as a good approximation to the magnetic permeability of the air, a minimum required value is determined for the product $I_p N \ell_2$:

$$I_p \, N \, \ell_2 \geq \frac{37.1 \, \text{V} + I_{2,max} R_2}{\mu \, f_0 \, N \, \xi\left(D_e/2 \, , h, \bar{d}, \widetilde{D}\right)} , \tag{5.56}$$

where $I_{2,max} = 13.1 \, \text{A rms}$ is the already estimated (5.28) maximum required secondary coil current at $x = D_e/2$, and R_2 is the total series resistance of the secondary tank circuit, which, neglecting the equivalent serial resistance of the secondary capacitor, can be approximated as:

$$R_2 \cong 2N\left(\ell_2 + \bar{d}\right) Z_2 , \tag{5.57}$$

where $\bar{d}$ is also a function of N, given by (5.47) and $Z_2 = 7.49 \, \text{m}\Omega/\text{m}$ is estimated by FEM numeric simulation, based on the cross-section determined for the secondary coil and the frequency of operation (Table 26).

Additionally, other restrictions apply to I_p, ℓ_2 and N:

(i) The number of secondary coil turns is limited to a maximum possible value $N_{max} = 17$, due to the required mechanical clearance between the coil and the rear wheel (5.42).

Dynamic Inductive Wireless Power Transfer for Lightweight Electric Vehicles
Luiz Alberto Lisboa da Silva Cardoso – University of Minho

287

(ii)   Due to the required mechanical clearance from the pedals and crank, the minimum and maximum length of the secondary coil is limited, and the average length of its turns, ℓ_2, should lie in the interval from 600 mm to 700 mm.

To keep the area outside de paved width of the lane intrinsically safe for pedestrians, without the need for shielding structures on the lane side, the magnetic field on the extreme laterals of the lane pavement should have a magnetic field intensity limited to the ICNIRP maximum public exposure recommended level for the frequency band used. So, at distance $w_L/2$ to either side of the center of the lane, the magnetic field should exceed 27 μT rms [72], which is equivalent to -91.4 dBT rms. The magnetic field increases with the current and it is also dependent on the distance to the primary coil windings, which parametrically vary with N. For each N, a maximum primary current level can be calculated. This has been done using FEM numeric simulation (COMSOL Multiphysics), and the results are shown in Table 27.

Table 27: Maximum primary current to limit magnetic field intensity at the lateral extremities of the lane.

N	Average Secondary Coil Width $\bar{d}$ (mm)*	Primary Coil Width $\widetilde{D}$ (mm)**	Maximum Peak Current (A)***	Maximum RMS Current (A rms)***
1	362	464.5	81.6	57.7
3	346	452.1	85.0	60.1
5	330	440.0	88.5	62.6
7	314	428.1	92.1	65.1
9	298	416.5	95.8	67.7
11	282	405.2	99.6	70.4
13	266	394.3	103.3	73.0
15	250	383.7	107.2	75.8
17	234	373.4	111.1	78.56

*Calculated using (5.47). **Calculated using (5.49).
***Using ICNIRP recommended maximum exposure level to general public individuals.

The curves of minimum required primary current for different possible ℓ_2, from 600 mm to 700 mm, are then plot in Figure 163, showing the current as a function of the number of secondary turns N.

Dynamic Inductive Wireless Power Transfer for Lightweight Electric Vehicles
Luiz Alberto Lisboa da Silva Cardoso – University of Minho

288
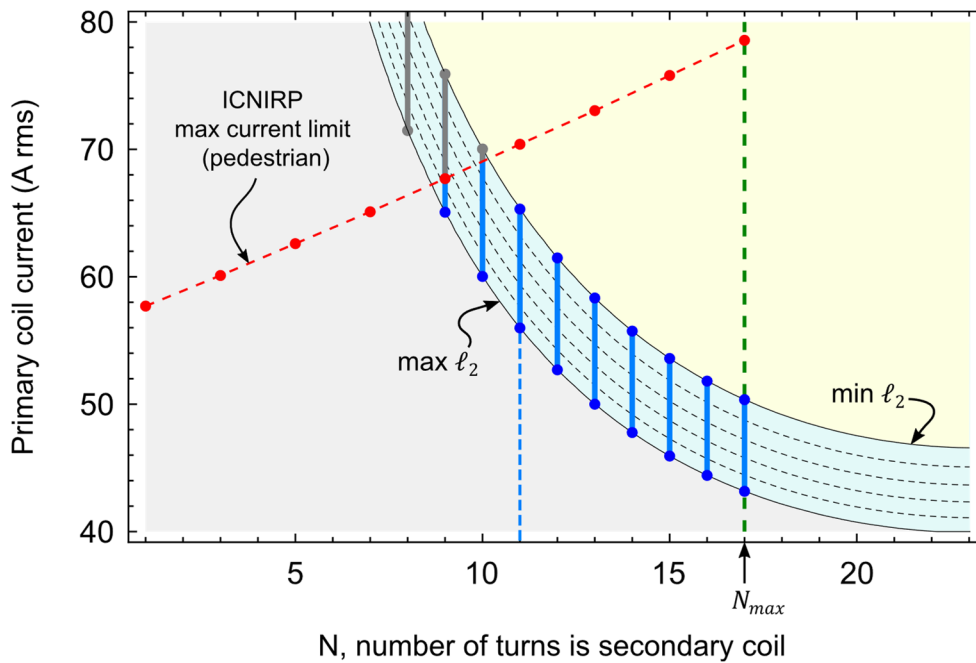
Figure 163: Viable joint variation of I_p, ℓ_2 and N..

In the yellowish shaded area, the primary current exceeds the above required minimum value for obtaining the corresponding minimum induced voltage $E_{2,rms}$, which would imply in undesirable extra resistive losses on the primary coil windings. In this region is where other curves corresponding to $\ell_2 < 600$ mm would lie, if that would be mechanically viable. Similarly, the grayish shaded area corresponds to $\ell_2 > 700$ mm, which is deemed as not practical, in this mechanical design. This relation poses a first limitation on the possible combination of values to the bluish-shaded area between the most extreme curves of constant ℓ_2. The viable solution region for I_p, ℓ_2 and N is further reduced by considering that $N \leq N_{max} = 17$ to mechanical restrictions, marked by the green dashed vertical line on the plot.

Finally, the maximum primary coil current that would still permit compliance with ICNIRP recommendation concerning maximum magnetic field exposure levels is considered, by requiring that the viable solution region should also lie below the red dashed line also plot of Figure 163. Remarkable, the current limit is not constant with N because in this design, to keep maximum power transfer level, the primary coil width and the positioning of the primary coil windings, also vary with N.

Since is not practical to have a coil with a non-integer number of turns, the viable solution set is constituted by the nine vertical blue line segments plot in Figure 163. Their thicker portion, delimited by the "min ℓ_2" and "max ℓ_2" curves, are where some minimum value ℓ_2 strictly above min ℓ_2.should mandatorily be implemented, while in their thinner portion, any value in the possible

Dynamic Inductive Wireless Power Transfer for Lightweight Electric Vehicles
Luiz Alberto Lisboa da Silva Cardoso – University of Minho

289

range for ℓ_2 will satisfy. The possible number of turns is than constricted in the interval from 9 to 17, with the required primary coil currents in correspondingly increasing range values. The lower limit of each of these current intervals, corresponds to the coil designed with the largest possible ℓ_2, the higher limit, to the smaller possible ℓ_2. If the current is above the min ℓ_2", the electrified width will be larger than strictly necessary, with the disadvantage of dissipating more heat on the primary coil. The selection of the I_p current level compromises efficiency and assurance of the specified functional requirements.

After direct physical considerations and mathematical development, the design has come to a point where there is still some degree of freedom in the selection of the remaining parameters for the HIPLEV prototype. Some additional engineering considerations are now introduced:

(i) N should be as small as possible, to privilege the construction of a simpler, lighter and less costly secondary coil. But, the first two options, $N = 9$ and $N = 10$ are choices that a priori restrict the full range of sizes for ℓ_2 (due to the magnetic field intensity limitation), which could later reduce the flexibility, in case of a future minor adjustment in the design. So, the selection for the number of secondary coil turns is:

$$N = 11 \tag{5.58}$$

(ii)   By selecting $N = 11$, the minimum required primary current will be in the range from 56.0 A rms to 65.0 A rms (5.56), depending on the average length ℓ_2 of the secondary coil turns, constrained in between approximately 600 mm and 700 mm.

The exact average value of ℓ_2 is a design parameter difficult to establish a priori in the prototype implementation, because the shape of the secondary coil, in practice, cannot be perfectly rectangular, to accommodate the windings away from the pedals and the crank. So, it is advantageous to commit ℓ_2 to be as close as possible to its minimum possible value, 600 mm, and to guarantee a sufficient current level for any possible value of ℓ_2, work with minimally above 65.0 A rms, in order to minimize resistive losses in the primary coil. Considering the maximum current in Table 27 for $N = 11$, a final safe range for the primary current I_p results:

$$65.0 \text{ A rms} \leq I_p \leq 70.4 \text{ A rms}, \tag{5.59}$$

The target value $I_p = 92.5/\sqrt{2}$ A rms $\cong 65.4$ A rms, within the possible range but just slightly above the minimum possible value, is then selected.

Dynamic Inductive Wireless Power Transfer for Lightweight Electric Vehicles
Luiz Alberto Lisboa da Silva Cardoso – University of Minho

290

5.9   Detailed Primary Coil Design

In this design, the primary coil is of the oblong type, being modeled as rectangular coil $\ell_1 \times D$, which has more length (ℓ_1) than width (D). According to section 5.2.1.5, the voltage V_{L1} established on the terminals of the primary coil when submitted to a current I_1 should be limited to $V_{L1,max} = 230$ V rms.

In order to work with the minimum possible voltage exciting its terminals, in a given geometry $\ell_1 \times D$ and frequency of operation f_0, the inductance of the coil should also be as low as possible. Since the inductance increases with the number of turns for a coil of any given length and width, the number of turns in the primary coil should ideally be the minimum, that is, one. A single turn coil, a priori possibly wound with multiple paths constituted by several cables in parallel, is then adopted for the HIPLEV i-lane.

5.9.1 Primary Coil Cross-Section

The simplified model of the primary coil is shown in Figure 164, where the p_D is the horizontal width occupied by the multiple cables connected in parallel of each turn winding.
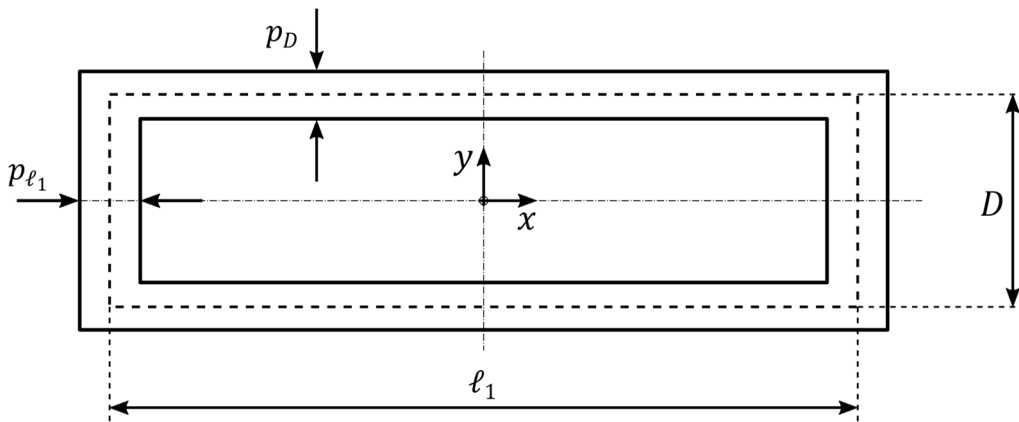
Figure 164: Simplified model of single turn, multiple-path, primary coil.

After the number of secondary turns N is determined (5.58), the width $\widetilde{D}$ can also be found, by first computing $\bar{d}$:

$$\bar{d} = w_e - N p_d = 282 \text{ mm} \tag{5.60}$$

and then substituting $\bar{d}$ and h (5.32) in (5.49):

$$\widetilde{D} = \sqrt{\bar{d}^2 + 4h^2} \cong 405 \text{ mm} \tag{5.61}$$

Dynamic Inductive Wireless Power Transfer for Lightweight Electric Vehicles
Luiz Alberto Lisboa da Silva Cardoso – University of Minho

291

From (5.59), it is known that the worst case current expected in the primary current is 70.4 A rms. The assumptions in 5.6.1 of using 10G1.5mm2 cable with eight useful 1.5 mm^2, useful for anticipated arbitration of the cable diameter, can now be validated. At 50 kHz, according to considerations in 5.6.1 and Table 22, the number of 1.5 mm^2 conductors necessary to safely carry the worst case primary current is 70.4 A / 5 A $\cong$ 14. So at least two 10G1.5mm2 in parallel are required for the implementation of the single turn primary coil, for a total current capacity of $2 \times 8 \times 5$ A rms $= 80$ A rms, at 50 kHz. To further increase the safety margin and to promote a reduction in the primary coil losses, a third 6G1mm2 cable (of the same type used in the secondary coil) was laid in between the two 10G1.5mm2 cables. The total cross-sectional conductive area of each side of the primary coil windings then becomes $A_p = 16 \times 1.5^2 + 6 \times 1.0^2 = 30$ mm^2. As a first approximation, the new maximum primary coil current capacity $I_{p,max}$ would then increase to:

$$I_{p,max} = 80 \text{ A rms} + 1 \times 6 \times 3.6 \text{ A rms} = 101.6 \text{ A rms} \tag{5.62}$$

Both the 6G1mm2 and the 10G1.5mm2 cables used in the design have their conductors twisted along the cable. This, in addition to rendering better mechanical properties to the cable, makes the choice of the current path approximately indistinct, when all conductors are submitted to the same voltage. So, by connecting all the conductors together at the terminals of their cable, the cable itself behaves as a litz wire, and the current in the cable can be assumed evenly distributed among its conductors, as illustrated in Figure 165 for the case of the 10G1.5mm2 cable, where the two central conductors are not used. In the figure, the cross-section is drawn approximately to scale, but the twist pitch was shortened, for improved visualization of the helical paths.
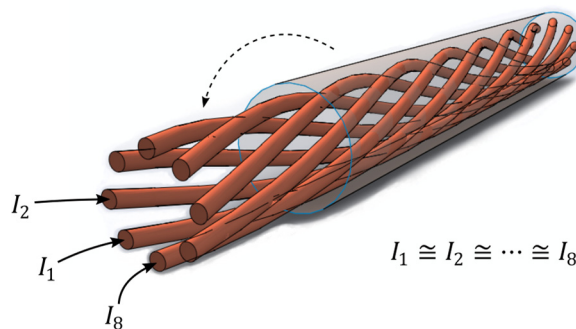
Figure 165: Layout of the eight external conductors twisted in the 10G1.5mm2 cable.

The only violation of this similarity to a standard litz wire is that, at the frequency used, the skin depth on copper is such that the cable AC resistance is already noticeably higher than its DC

Dynamic Inductive Wireless Power Transfer for Lightweight Electric Vehicles
Luiz Alberto Lisboa da Silva Cardoso – University of Minho

292

resistance, as calculated in 2.10.1. Nevertheless, this design paradigm can provide a good compromise between performance and resources used. This decision made the prototype viable, not only due to a lower cost of materials, but principally, because true litz wire for the required 70.4 A rms capacity was not available in the lab at the time of the implementation. This may likely apply to many use cases worldwide. The 6G1mm2 type cable, used in both the primary and the secondary coils, also has a similar constitution as that shown in Figure 165.

In the prototype, to hold the cables firmly in place and keep the geometry of the primary coil stable, the 10G1.5mm2 cables were laid inside rigid PVC tubes with 12 mm of internal diameter and 16 mm of external diameter. The tubes were then immobilized on the workbench, with wooden restrainers. Not to significantly decrease the induced voltage on the secondary coil, the cables in the same winding are laid close together, with the third 6G1mm2 cable confined in between the 10G1.5mm2 cables, as shown in Figure 166:
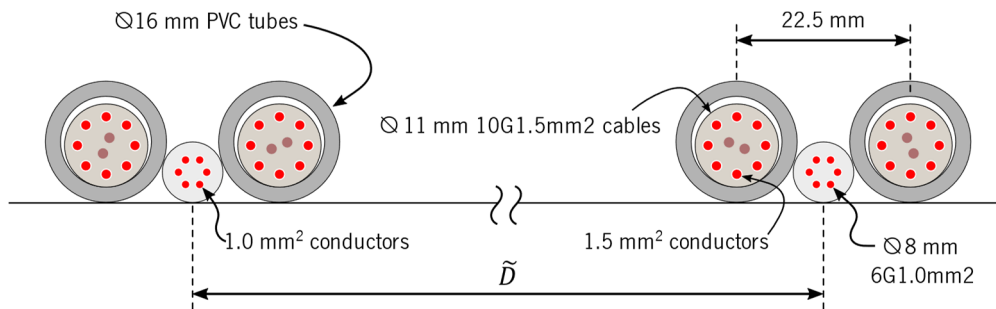
Figure 166: Cross-section detail of the primary coil winding positioning.

Despite the type of cables used, which cause the current to be equally distributed among the conductors of each particular cable, the actual current distribution among the primary coil windings is yet dependent on the exact relative positioning of its cables. Two variant connections for the windings were then considered: The first, with parallel cables wound in concentric paths, and the second, shown in Figure 167, with cables twisted in one end of the primary coil.
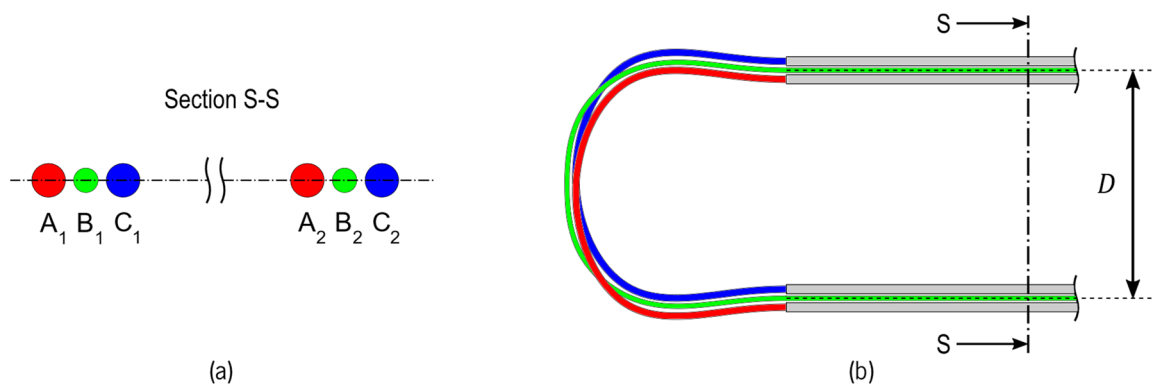
Figure 167: Design option of twisted cables, keep currents symmetrically distributed on the primary coil windings: (a) cross-section view and (b) top view.

Dynamic Inductive Wireless Power Transfer for Lightweight Electric Vehicles
Luiz Alberto Lisboa da Silva Cardoso – University of Minho

293

Based on the hypothesis of homogeneous distribution of currents among the conductors of each same cable (Figure 165), FEM simulations for the proposed configurations were carried on, using COMSOL Multiphysics. In both cases, the same total current of 65.4 A rms, close to but higher them the minimum required (5.59), was imposed to the coil.

In the simulation model, the winding segments A_1, B_1 and C_1 (on the left) and A_2, B_2 and C_3 (on the right) were associated to individual coils entities circuit connected in series-parallel, with a current source connected to terminal of the primary coil, as shown in Figure 168.

Conventions for the FEM simulation:

Voltage reference on coil windings:
P(+) terminal is behind cross-section;
N(-) terminal is in front of cross-section

Voltage on coil terminals:
$V_{AC} = V_1 - V_0 = V_{A1} - V_{A2}$

Currents on coil windings:
$Re(\dot{I}) > 0$
$Im(\dot{I}) > 0$

for phasor currents flowing out of the cross-section plane
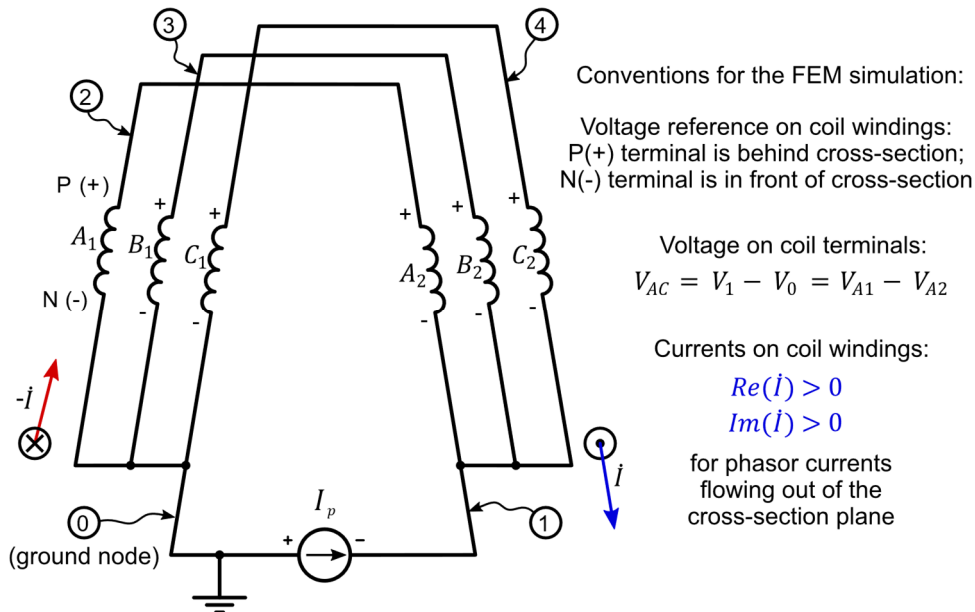
Figure 168: Polarity conventions for currents and voltages, used in modeling the cross-section of the primary coil.

The current distribution and voltage developed across the primary coil obtained from simulation are shown in Table 28.

Table 28: Results from FEM numeric simulation of two possible configurations for the 1-turn primary coil.

Current distribution and voltage developed	Concentric Paths (non-twisted) $A_1\ B_1\ C_1$ ---- $C_2\ B_2\ A_2$		Laterally Shifted Paths (twisted) $A_1\ B_1\ C_1$ ---- $A_2\ B_2\ C_2$	
Current I_A on cable "A" (A rms)	$27.3 + 1.1j$	(41.7%)	$28.4 + 1.2j$	(43.4%)
Current I_B on cable "B" (A rms)	$8.6 - 2.4j$	(13.1%)	$8.6 - 2.4j$	(13.1%)
Current I_C on cable "C" (A rms)	$29.5 + 1.4j$	(45.2%)	$28.4 + 1.2j$	(43.4%)
Voltage across coil* (V rms/m)	$0.867 + 31.8j$		$0.866 + 31.5j$	
Coil inductance* (μH/m)	1.498		1.4983	
Power dissipated (W/m)	56.7		56.6	

*Assuming an infinitely long primary coil.

Dynamic Inductive Wireless Power Transfer for Lightweight Electric Vehicles
Luiz Alberto Lisboa da Silva Cardoso – University of Minho

294

As expected, due to the proximity effect, the simulation results show the existence of a current unbalance between the internal and external cables, in the case of the first proposed configuration. On the other hand, in the second case, with one of the external cables twisted, the current became evenly distributed between these loops.

The current unbalancing between the main cables "A" and "C", experimentally verified in the case of concentric paths, increases when their separation is also increased, relatively to the primary coil diameter. To overcome this inconvenience, which can change the intended magnetic field distribution on the lane profile, and potentially stress the cables differently, the selected design option for winding the primary coil was that in Figure 167. Imposing less maximum electric stress on individual cables, this design option additionally favors a minor decrease (1%) on the reactive voltage of primary coil, while keeping approximately the same power loss on windings. The driving voltage per unit of length of the primary coil is then given by:

$$V_{1,rms} = 31.5 \ V \ rms \ / \ \text{m} \qquad (5.63)$$

This voltage drop includes the forward and backward paths of the current, of a hypothetical infinitely long primary coil. Similarly, the resulting inductance is distributed along the longitude of the primary coil according to:

$$\Lambda_1 = 1.4983 \ \mu \text{H} \ / \ \text{m} \qquad (5.64)$$

Due to the fact that the third central primary coil cable has a smaller diameter and rests on the same horizontal surface of the other two cables, the concept of an unique vertical distance between primary and secondary coil windings h, established in 5.6.1, has to be revised. Because the distance from the secondary coil to cables "A" and "C" is slightly different of that to cables "B", a new average value for h should be evaluated. An ad hoc estimation for the new position of the electrical center plane of the primary coil windings above the supporting surface, based on the simulated vertical distribution of the currents in the conductors of the cables, is given by y_a:

$$y_a = \frac{I_A \left(\frac{b_1}{2} + t_{PVC}\right) + I_B \left(\frac{b_2}{2}\right) + I_C \left(\frac{b_1}{2} + t_{PVC}\right)}{I_A + I_B + I_C}, \qquad (5.65)$$

where b_1 and b_2 are the diameters of the $10G1.5\text{mm}^2$ and the $6G1.0\text{mm}^2$ cables, and $t_{PVC} = 2$ mm is the thickness of the PVC tube used. This estimation is based on the values of

Dynamic Inductive Wireless Power Transfer for Lightweight Electric Vehicles
Luiz Alberto Lisboa da Silva Cardoso – University of Minho

295

I_A, I_B, and I_C, obtained by simulation, reported in Table 28. Whereas the previous value implicitly considered for y_a in the model (using only $10G1.5mm^2$ cables and no PVC tubes) was:

$$y_a = h_p = \frac{b_1}{2}$$

(5.66)

The vertical inter-coils distance, previously given by (5.29) then becomes:

$$h = h_f - y_a + c_{min} + t_s + h_s$$

(5.67)

Calculating (5.67) under the different considerations of y_a, a small difference of 1.5 mm is found, with the re-estimated value for h being 144 mm, instead of 145.5 mm (5.32). This 1% difference is deemed as irrelevant, being smaller than the intrinsic modeling errors of 2.5% and 1.3% estimated 5.7.3, for respectively the optimum width $\widehat{D}$ of the primary coil and the resulting induced voltage V_{ind}. Because of that, to simplify the design and avoid a second iteration in (5.49) and (5.56), which would require new FEM simulations and produce just a minor modification of the values in Table 27 and the graph in Figure 163, the model is left unchanged, and the approximations given by (5.29) and (5.66) are kept.

In this manner, the cross-section of the primary coil becomes totally defined, as shown in the detail of Figure 169, with the primary coil width $\widetilde{D}$ being calculated by (5.47) and (5.49).
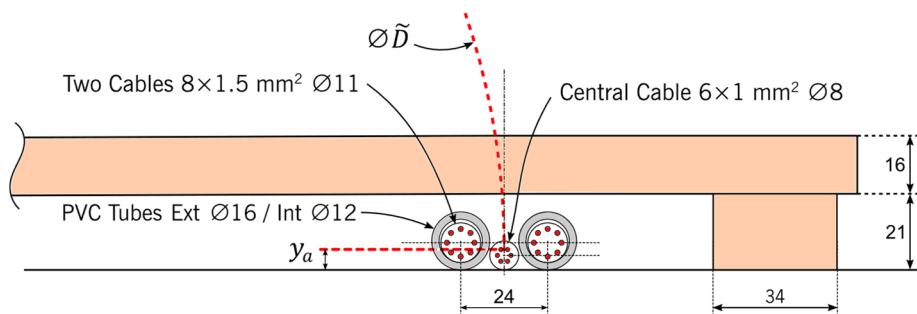
Figure 169: Cross-section of the prototype inductive of lane, detail of primary coil winding, dimensions in mm.

5.9.2 Required Primary Coil Length and Driving Voltage

The cross-section designed in 5.9.1 can safely sustain the required current level of 65.4 A rms. When this current is imposed to an infinitely long coil having this cross-section the resulting voltage drop and inductance per unit of length on the primary coil with the secondary coil open has been respectively determined by (5.63) and (5.64), assuming an infinitely long coil.

Dynamic Inductive Wireless Power Transfer for Lightweight Electric Vehicles
Luiz Alberto Lisboa da Silva Cardoso – University of Minho

296

As seen in Section 2.4.1, the inductance of rectangular coils made of circular cross-section wire can also be characterized by a affine function of the length (2.10), thus having approximately constant incremental inductances, if both the length and the width are much larger than the diameter of wire, and the length is larger than the width. As an initial simplification, let us then assume that the primary coil is perfectly rectangular, with the required calculated width $\widetilde{D}$ (5.49), and derive the radius r of the wire of an equivalent rectangular coil of same size, but built with a single circular wire, by numerically solving:

$$\Lambda_1 = \frac{\mathfrak{n}(\widetilde{D}, \ell_0 + \Delta\ell, r, \mu_0) - \mathfrak{n}(\widetilde{D}, \ell_0 + \Delta\ell, r, \mu_0)}{\Delta\ell}, \tag{5.68}$$

for some ℓ_0 much larger than $\widetilde{D}$ (5.59), where $\mathfrak{n}$ is the inductance of a rectangular coil (2.9), μ_0 is the permeability of free space, Λ_1 is the characteristic inductance of the designed cross-section and $\Delta\ell > 0$. Since $\mathfrak{n}$ is approximated as an affine function in ℓ, the actual values of ℓ_0 and $\Delta\ell$ are irrelevant, as long as ℓ_0 is much larger than $2\widetilde{D}$. Let us then make $\ell_0 = 100$ m, and $\Delta\ell = 1$ m. The solution $r = \hat{r}$ is then numerically found:

$$\hat{r} = 12.2821 \text{ mm} \tag{5.69}$$

and the inductance of the rectangular coil, as a function of ℓ, becomes:

$$L_1(\ell) = \mathfrak{n}(\widetilde{D}, \ell, \hat{r}, \mu_0), \tag{5.70}$$

with all arguments expressed in the International Systems of Units.

Table 29: Inductances and voltages for different choices of rectangular primary coil lengths.

ℓ (m)	L_1 (µH)*	V_{L1} (V rms)*
1.0	1.88	39.9
2.0	3.38	71.9
3.0	4.88	103.8
4.0	6.38	135.6
5.0	7.88	167.5
6.0	9.38	199.3
6.9	10.7	228.0

*At the nominal design current $I_p = 65.4$ A rms.

The required excitation voltage is directly calculated as $2\pi f_0 I_p L_1(\ell)$. If the primary is driven by a resonant inverter of fixed frequency, it is possible to select any length ℓ_1 of the primary coil,

Dynamic Inductive Wireless Power Transfer for Lightweight Electric Vehicles
Luiz Alberto Lisboa da Silva Cardoso – University of Minho

297

by adjusting the excitation voltage, as long as it does not exceed the maximum acceptable voltage $V_{L1,max} = 230 \text{ V rms}$ defined for the design, (Table 23), as illustrated in Table 29:

A non-auto resonant inverter driver can be designed to automatically adjust its output voltage to match the primary coil inductance and keep the primary current constant, without previous awareness of its length, if the length is limited to the maximum possible value of approximately 6.9 m. In this manner, driver modules with identical settings could be deployed with coils of different lengths, in the admissible range.

On the other hand, when an auto resonant circuit such as the Mazzilli-Baxandall inverter is used, the natural oscillation frequency is also dependent on the inductance L_1, according to (2.101). This will require that all primary coils in an inductive lane have the same nominal length, and the operation frequency will have increased sensitivity to circuit parameters and, consequently, to the geometry of the coils, which must be carefully build, as much as possible, to the same size.

In the particular case of the HIPLEV design using modified e-bikes, in addition to the size limitation due to the maximum acceptable driving voltage, the length of the primary coil has another constraint to its maximum value: Under the hypothesis of riders preserving the distance of at least one e-bike length to the closest rider ahead in the i - lane, the requirement for ℓ_1 to be smaller than the twice the length of one bike. This will guarantee the impossibility of having two e-bikes simultaneously harvesting energy from the same primary coil, independently of how short the inter-primary coil gap is.

The typical length of bicycles lies in the range 1.7 m to 1.8 m. So, the length of the primary coil for the HIPLEV i-lane is further required to satisfy:

$$\ell_1 \leq 3.4 \text{ m} \tag{5.71}$$

But, to minimize the number of inverters required per kilometer of i-lane, ℓ_1 should also be as large as possible. This brings the design selection for the nominal value of ℓ_1 in the safe range of approximately 90% to 100% of its maximum value:

$$3.1 \text{ m} \leq \ell_1 \leq 3.4 \text{ m}, \tag{5.72}$$

Dynamic Inductive Wireless Power Transfer for Lightweight Electric Vehicles
Luiz Alberto Lisboa da Silva Cardoso – University of Minho

298

5.9.3 Driving the Primary Coil with the Mazzilli-Baxandall Inverter

Despite the sensitivity of this type of circuit to variations on circuit parameters, in the first HIPLEV prototype, for the sake of simplicity and economy, a Mazzilli-Baxandall inverter is used to drive the primary coil. The natural oscillation frequency should then be made equal to the selected desired operation frequency f_0. This establishes a direct relation among the required value of the capacitance C_1 and the choke inductances $L_{M,1} = L_{M,2}$ (Figure 46), and the desired length ℓ_1 for the primary coil, given by (5.73) and (5.74):

$$2\pi f_0 \sqrt{L_{eq}C_1} = 1, \tag{5.73}$$

$$L_{eq} = \sqrt{\frac{\mathfrak{n}(\widetilde{D}, \ell_1, \hat{r}, \mu_0)\, L_{M,1}}{\mathfrak{n}(\widetilde{D}, \ell_1, \hat{r}, \mu_0) + L_{M,1}}}, \tag{5.74}$$

where $\mathfrak{n}$ is the inductance of the rectangular coil of single, circular cross-section wire, $\widetilde{D}$ is the width of the primary coil, and $\hat{r}$ specific radius of the wire of the equivalent single wire rectangular coil that has the same characteristic inductance per unit of length as the primary coil.

The choice of ℓ_1 (5.72) implies in:

$$5.04\,\mu H \le L_1 = \mathfrak{n}(\widetilde{D}, \ell_1, \hat{r}, \mu_0) \le 5.48\,\mu H \tag{5.75}$$

Considering the choke $L_{M,1}$ in the range of 50 µH to 250 µH, L_{eq} could lie in the range of 4.58 µH to 5.36 µH, thus requiring a value for C_1 in the range of 1.768 µF to 2.069 µF, for a natural oscillation frequency f_0 = 51.7 kHz.

To save CAD design and board manufacturing time, a COTS driver was procured. A commercially available Mazzilli-Baxandall driver module, for recommended used in induction heating, was found with a factory installed capacitor bank C_1, rated for the 50 kHz band, sufficiently high current capacity, and a promising nominal capacitance value of $6 \times 0.33\,\mu F = 1.98\,\mu F$. The module was tested with its original chokes and the actual value of C_1 was estimated at 1.92 µF.

After replacing the original chokes on the module with two newly built chokes $L_{M,1} = L_{M,2} = 150\,\mu H$, the required value of L_1 becomes:

Dynamic Inductive Wireless Power Transfer for Lightweight Electric Vehicles
Luiz Alberto Lisboa da Silva Cardoso – University of Minho

299

$$L_1 = \frac{1}{C_1 \, (2\pi f_0)^2 - L_{M,1}} \cong 5.104 \, \mu H \,, \tag{5.76}$$

for which the length ℓ_1 of the rectangular primary coil with the designed cross-section is computed by numeric solving (5.70), resulting in:

$$\ell_1 \cong 3.144 \, m \,, \tag{5.77}$$

by construction, in the desired length range (5.72).

For the selected value of L_1 (5.76), the required voltage V_{L1} on the terminals of the primary coil is then:

$$V_{L1} = 108.4 \, V \text{ rms,} \tag{5.78}$$

for which the DC voltage V_{DC} of the DC power supply feeding the Mazzilli-Baxandall driver can be estimated (2.99) at:

$$V_{DC} = V_{L1,rms} \frac{\sqrt{2}}{\pi} \cong 48.8 \, V \tag{5.79}$$

5.9.4 Length Adjustment of Oblong Primary Coils with Round Extremities

Due to the mechanical characteristics of the cables forming the windings of the primary coil, it is difficult to build this coil with an exactly rectangular shape, the ends of the coil have to be curved. This slightly affects the inductance. To compensate this effect, the length of the coil is corrected, by the length $\breve{\ell}_1$ estimated for a coil with curved end to have approximately the same inductance as a rectangular coil with length ℓ_1 and the same width $\widetilde{D}$, as shown in Figure 170.
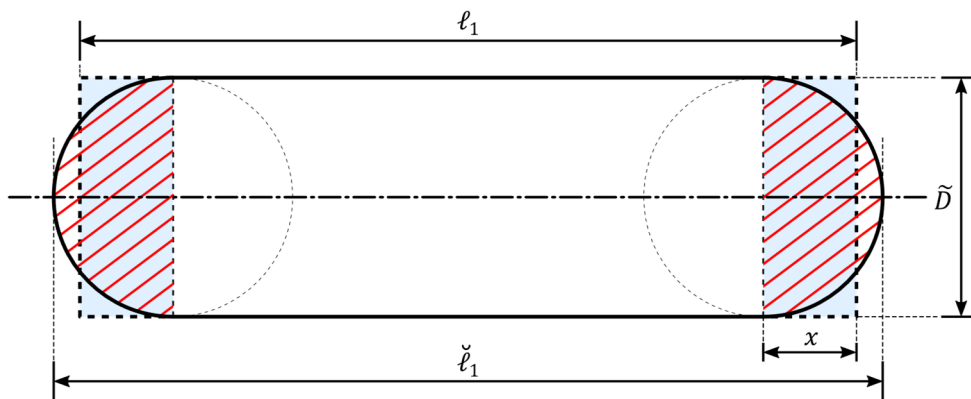
Figure 170: Approximation of the inductance of rectangular coil by affine function of its length.

Dynamic Inductive Wireless Power Transfer for Lightweight Electric Vehicles
Luiz Alberto Lisboa da Silva Cardoso – University of Minho

300

Intuitively, as in the case of the rectangular coil, the inductance of the coil with round extremities will also behave as an affine function of its length, for large enough lengths, and exhibit the same characteristic inductance Λ_1 (5.68), because they are built with the same width and cross-section. Only the constant term of the affine induction functions might be different, due to the different "inductances of the extremities". For coils of the same lengths, i.e., $\ell_1 = \breve{\ell}_1$, the inductance of the rectangular coil should be higher. For the same inductance, $\breve{\ell}_1$ should by higher than ℓ_1, by the amount $2(\widetilde{D} - x)$.

The distance x is then estimated by considering that the coils should have approximately the same inductance at their extremities, if they have the same area. Under this heuristically proposed method, numerically supported by x is such that:

$$2x\widetilde{D} \cong \pi\left(\frac{\widetilde{D}}{2}\right)^2 \tag{5.80}$$

The length of the primary coil with rounded extremities with an equivalent inductance to that of the rectangular primary coil built with the same cross-section is then approximated by:

$$\breve{\ell}_1 = \ell_1 + \widetilde{D}\left(1 - \frac{\pi}{4}\right) \tag{5.81}$$

In the case of the HIPLEV laboratory prototype, this length is then numerically found by replacing $\widetilde{D}$ and ℓ_1 (5.77) in (5.81):

$$\breve{\ell}_1 = 3.144 \text{ m} + 0.405 \text{ m} \times \left(1 - \frac{\pi}{4}\right) \cong 3.23 \text{ m} \tag{5.82}$$

5.10 Mechanical Detail of the Secondary Coil

Once determining the geometry and cable constitution of the secondary (pick-up) coil, along Sections 5.4, 5.5 and 5.8, it is necessary to develop a support to its windings that can be perfectly adapted to the frame of the e-bike, in such a way that the coil rests around the rear wheel at the required clearance distance to ground. According to the parameters defined for the cross-section of the magnetic link, each of the sides of this support, or coil tray, could have a cross-section as shown in Figure 171.

Dynamic Inductive Wireless Power Transfer for Lightweight Electric Vehicles
Luiz Alberto Lisboa da Silva Cardoso – University of Minho

301
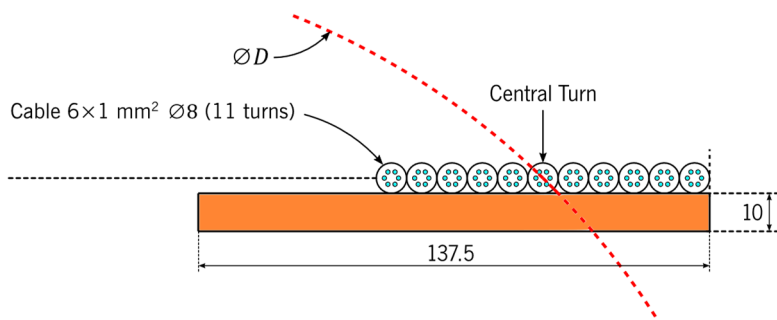
Figure 171: Cross-section of the prototype inductive of lane, detail of pick-up coil winding.

While many different designs could be suggested for implementing a secondary coil support, the tools available for making the prototype were basic, and the craftsmanship limited. So, after some trials using cardboard, a simple design of an U-shaped tray, in 10 mm-thick plywood was hand-cut, in the dimensions shown in Figure 172.
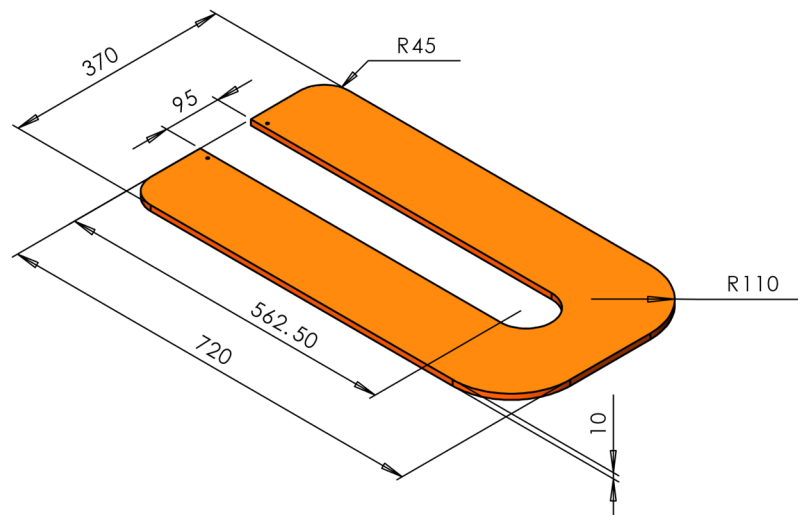
Figure 172: Dimensions of the designed support tray for the pick-coil windings.

The total length of the secondary coil tray was deemed as adequate to support the 11-turn coil with an average turn length slightly superior to 60 cm (Section 5.8). However, before proceeding with the final coil winding and installation on the bicycle, a simpler prototype, including both the primary coil and the sketch of the secondary coil, was built, and tested to confirm the electrical characteristics of the DIWPT link, as shown in Figure 173.

Dynamic Inductive Wireless Power Transfer for Lightweight Electric Vehicles
Luiz Alberto Lisboa da Silva Cardoso – University of Minho

302
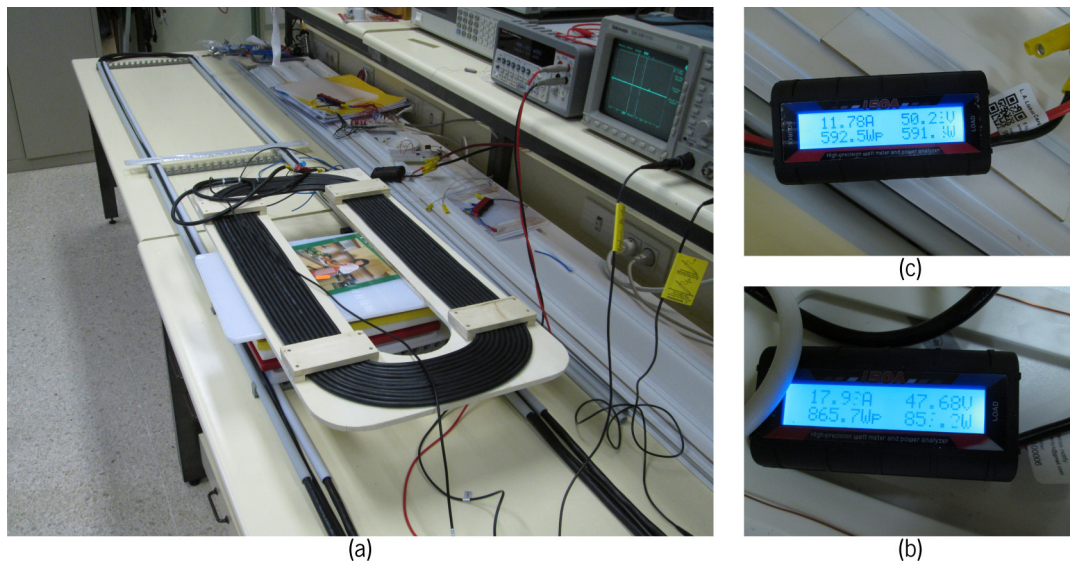
Figure 173: (a) DIWPT inductive configuration on workbench, with main dimensions defined, before final modification of the secondary coil for installation on the bicycle, showing (b) input and (c) output power readings.

In the configuration show in Figure 173, two electronic loads model 6060B were attached in parallel directly to the output of the rectifier stage, for total programmable load capacity of 600 W. No DC - DC converter was yet installed on the secondary circuit. IWPT was obtained, providing 592.5 W of output power, while on the primary side, a 48 V power supply provided 865.7W to the Mazzilli driver. As expected, the power output was significantly higher than $P_E = 400$ W, because with the coils at approximately center alignment conditions, there was not a DC-DC converter limiting the load voltage to $V_L = 36.5$ V, causing the load voltage to climb to more than 50 V. In this quick check of the configuration, not yet with the new chokes $L_{M,1}$ and $L_{M,2}$ installed in the inverter, 68.4% of DC to DC efficiency was obtained.

Due to the lack of strong control on the relative positioning of the secondary coil to the primary coil, the numbers of this test assumedly provided a mere positive indication of absence of major issues with the design. After this successful partial assembly of the configuration, the installation of the secondary coil was then proceeded.

The analysis in section 4.7 identified that the best configuration for the secondary coil is to be wound around the rear wheel. However, at the optimum clearance distance found, $c = 100$ mm, there is still a potential mechanical interference handled, with the crank and pedals, and ultimately, with the feet of the rider. It is then necessary to use a special arrangement in the winding: The solution found is that the secondary coil should be flat, except close to the crank-set and pedals, where all the winding should be concentrated very close to the tire and the

Dynamic Inductive Wireless Power Transfer for Lightweight Electric Vehicles
Luiz Alberto Lisboa da Silva Cardoso – University of Minho

303

center plane of the rear wheel, contouring the wheel in between the crank axis and the tire, and staying clear from the pedals, as shown in Figure 174.
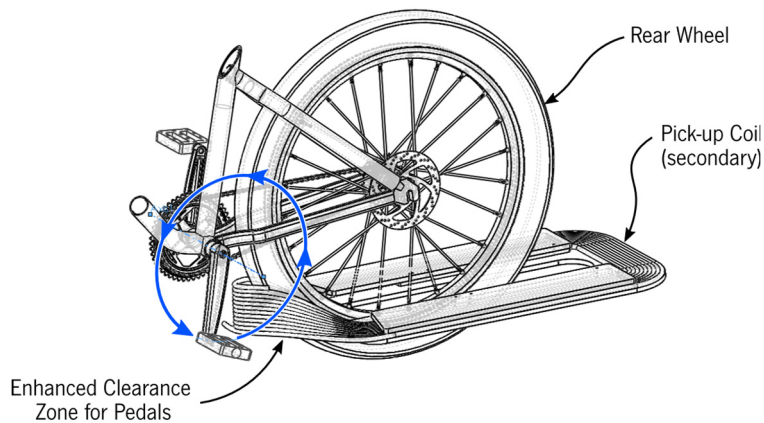
Figure 174: Design concept of a pick-up coil for rear wheel installation.

This shape of the coil makes the calculation of its precise self-inductance and mutual inductance to the primary more complex. But, in a good approximation, the secondary coil can still be modeled as a multi-turn rectangular coil, which average effective length could be obtained either simulated with finite element modeling software or estimated with the use of the theorems developed in section 3.6.3. This deviation of the perfectly rectangular models becomes apparent when if the top view drawing of the secondary coil, after installed on the bike, as shown in Figure 175, is examined:
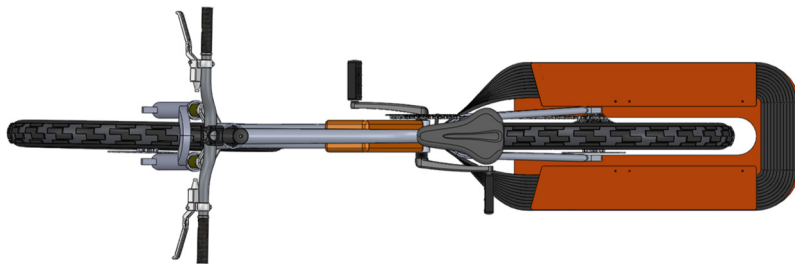
Figure 175: Predicted top-view of secondary coil assembled around of the rear wheel of the e-bike.

The last steps of the design of the secondary coil, which are the establishment of the detailed path for the coil turns and its anchorage to the bike frame were accomplished by direct adjustments on the prototype, in which the average turn length is estimated at $\ell_2 = 63$ cm, within the target range from 60 cm to 70 cm, as determined in Section 5.8.

Different steps for the installation of the secondary coil to bicycle are shown in Figure 176.

Dynamic Inductive Wireless Power Transfer for Lightweight Electric Vehicles
Luiz Alberto Lisboa da Silva Cardoso – University of Minho

304
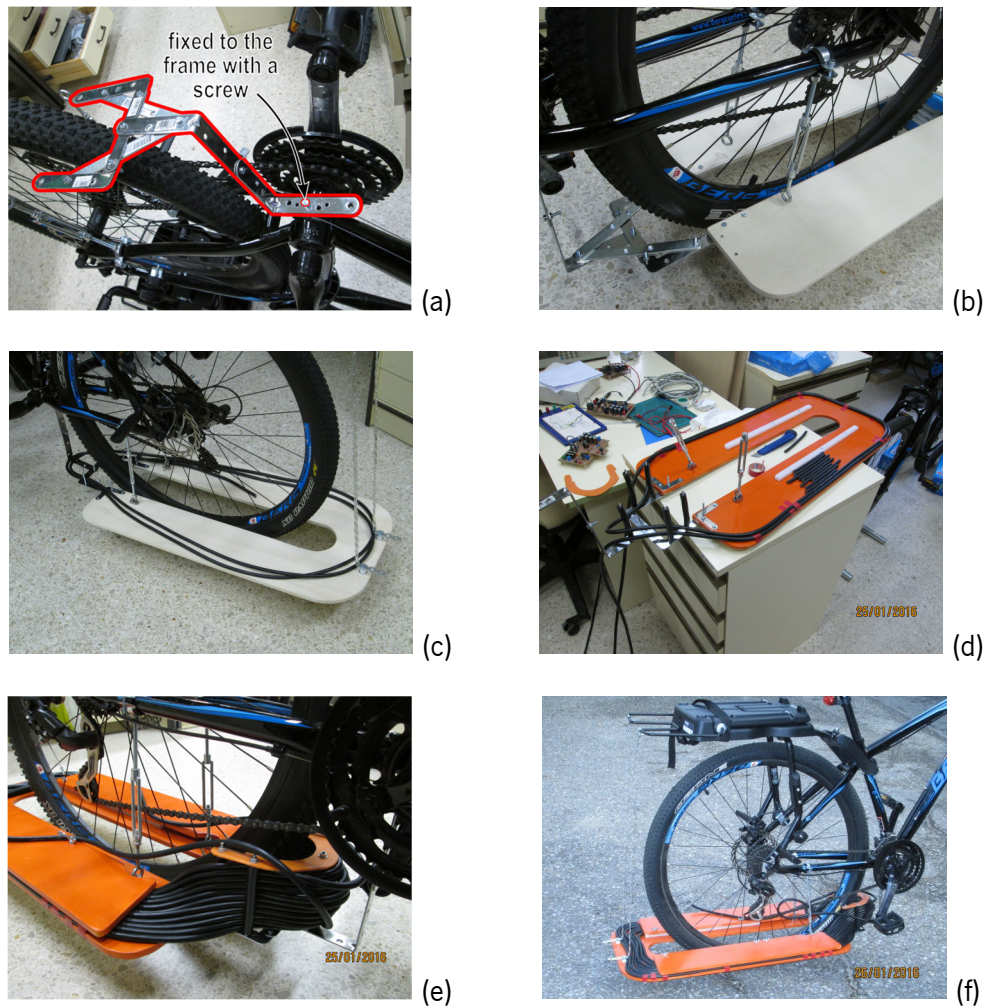
Figure 176: Steps for the adaption of a pick-up coil to the bike.

The bike stand was removed, and the secondary coil trail was fixed to the bike frame at the point the stand was previously screwed. This is accomplished by means of a stainless steel fork structure that is also screwed to the coil tray bike frame, as shown in the photo in Figure 176a, where the fork structure is contoured in red. The coil tray is directly attached to the bike frame, on both sides, by modified stretchers with screws, as shown in Figure 176b, and also on the rear most point, to distribute the weight of the coil.

On the fork structure, a plastic support structure is devised to hold the coil turns tight together when contouring the tire, and direct estimates of the total deformed coil length are made, as shown in Figure 176c. Due to mechanical stress, the coil turns tend to become circular when wound over the coil tray, so fixing wooden structures are developed to hold them in place, maintain most of the coil turns longitudinal path in a rectangular shape, as shown in Figure 176d.

After the secondary is completely wound, with the bike in the upright position, the stretchers are adjusted to allow the ground clearance of design, of $c = 100 \text{ mm}$, as shown in Figure 176e, where a better view of the tridimensional arrangement of the windings is also better visible.

Dynamic Inductive Wireless Power Transfer for Lightweight Electric Vehicles
Luiz Alberto Lisboa da Silva Cardoso – University of Minho

305

Finally, before, proceeding with the installation of the electronics, the bicycle is tested dynamically by riding, confirming that the pedals and the feet have enough mechanical clearance from the coil, and that the coil is not interfering with the normal maneuvering of the bicycle. The photo in Figure 176f was taken during these tests for free movement, which were successful.

5.11 Mechanical Detail of the Primary Coil Assembly

In order to guarantee geometric stability for the primary coil of the laboratory prototype, it was necessary to devise a restraining system for the windings that could also support the vehicle, emulating the lane pavement on the workbench. The main cables of the primary coils were mounted passing through PVC tubes, which served as guides to these cables, as described in 5.9.1. On each side of the primary coil winding, the two PVC tubes restraining the main $10G1.5mm^2$ cables and the thinner $6G1mm^2$ were immobilized with wooden slotted guides at approximately every 60 cm of the lane. The primary coil and these guides were then covered by 60 cm × 60 cm MDF modules as shown by the CAD design in Figure 177. To cover all the primary coil and provide a leveled surface for the positioning of the adapted e-bike, a total of six MDF covers were used, composing a 3.6 m-long pathway.

(a)

(b)
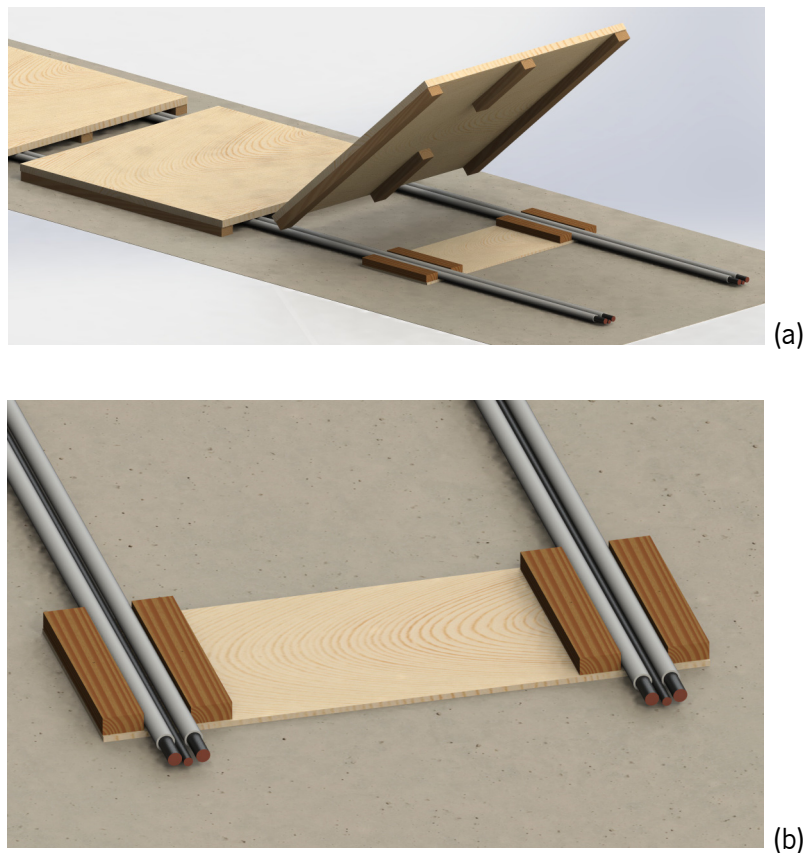
Figure 177: Drawings showing constructive detail of the primary coil modular restraining system designed for the inductive lane prototype: (a) MDF modules covering the coil guides. (b) Detail of the wooden restrainers.

Dynamic Inductive Wireless Power Transfer for Lightweight Electric Vehicles
Luiz Alberto Lisboa da Silva Cardoso – University of Minho

306

The PVC tubes used restraining system are $2.40\ m$ long, what left leaves about $42.5\ cm$ of unrestrained length at each extremity of the primary coil, also protected with a $60\ cm \times 60\ cm$ MDF cover. Figure 178a and Figure 178b show photographs taken of actually implemented primary coil and its restraining system.

(a)

(b)
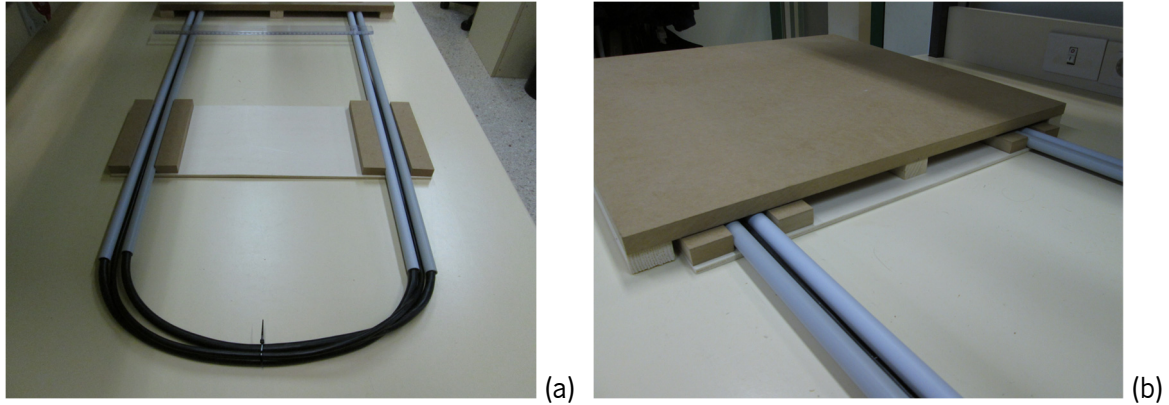
Figure 178: Photos of the modular restraining system implemented for primary coil: (a) Detail of cable twisting at the return extremity of the coil; and (b) extremity covered with a MDF module.

5.12 Estimated Electric Efficiency of the HIPLEV

Referring to Figure 42, in the case of only one primary coil and one secondary coil, the overall DC to DC electric efficiency η_H of the HIPLEV module can be expressed as:

$$\eta_{DC} \;=\; \eta_P\,\eta_{Link}\,\eta_S\,, \tag{5.83}$$

where η_P and η_S are respectively the efficiencies of the electronic circuits attached to the primary and secondary coils, and η_{Link} is the efficiency of the magnetic link, the electric transformer by the primary coils and the compensation network attached to them. η_P is promptly identified as the efficiency of the Mazzilli-Baxandall inverter. η_S can be identified as the efficiency of the DC-converter regulating the load voltage. Using Figure 46 as a representation of the whole IWPT circuit, it is possible to compute an estimate for η_H at the nominal output power $P_E \;=\; 400\ W$, assuming that the compensation and filter capacitors are lossless:

$$\eta_{DC} \cong \; \eta_P\,\frac{P_E/\eta_S}{P_1 + P_2 + P_R + P_E/\eta_S}\,\eta_S = \eta_P\eta_S\frac{P_E}{(P_1 + P_2 + P_R)\eta_S + P_E}\,, \tag{5.84}$$

where P_1 and P_2 are respectively the power losses in the primary and secondary coils, and P_R is the power loss on the rectifier, which is equal to $2V_D I_L$ for a diode full-bridge.

Dynamic Inductive Wireless Power Transfer for Lightweight Electric Vehicles
Luiz Alberto Lisboa da Silva Cardoso – University of Minho

307

Since during IWPT the currents on primary and secondary coil are expectably $\pi/2$ delayed from each other, it is possible to estimate the power dissipation on their windings based exclusively on the current passing through their own windings, what can be accomplished by FEM numeric simulation in both cases.

The power loss P_1 depends on the current I_1 which is approximately constant, and can be calculated by considering the power losses per unit of length on the primary coil, 56.6 W/m, a value already reported in Table 28 multiplied by the length ℓ_1 of the rectangular coil equivalent to the primary coil (5.77):

$$P_1 \cong 56.6\frac{W}{m} \times 3.144 \text{ m} \cong 178 \ W \tag{5.85}$$

By design, the power P_E will be met at the load all the way from central alignment condition to the maximum lateral displacement $|x| = w_d/2$, to either left (negative x) or right (positive x). At this limit condition, the secondary current will reach its maximum value, given by similar expressions to (5.26), (5.27) and (5.28). Noticeably, the dimensions of the cross-section of both the primary and the secondary windings have some margin to accommodate higher currents and higher powertrain voltages, above the 36.5 V.

An estimate for the efficiency η_H is obtained when the nominal voltage of $V_{DC-out} = 36.5$ V is used in (5.26) and (5.27), what leads to:

$$I_{DC-out} = \frac{P_E}{V_L} = \frac{400 \text{ W}}{36.5 \text{ V}} = 10.96 \text{ A} \tag{5.86}$$

Using the nominal DC-DC converter efficiency provided by the manufacturer, $\eta_{DC-DC} = 94\%$, with a typical voltage drop $\Delta V_{DC-DC} \cong 2$ V from input to output, the expected current on the secondary coil at the limit condition $|x| = w_d/2$, is estimated by (2.105):

$$\max(I_{2,rms}) \cong \frac{\pi}{2\sqrt{2}} \frac{36.5 \text{ V}}{94\% \ (36.5 \text{ V} + 2 \text{ V})} 10.96 \text{ A} \cong 12.3 \text{ A rms} \tag{5.87}$$

Similarly to what was done for the primary coil cross-section, it is also possible to simulate the resistive power loss on the secondary coil using FEM numeric simulation, under the simplifying consideration that the resistive power loss is uniformly distributed along its total cable length, of approximately $2N(\bar{d}+\ell_2)$.

Dynamic Inductive Wireless Power Transfer for Lightweight Electric Vehicles
Luiz Alberto Lisboa da Silva Cardoso – University of Minho

308

The FEM simulation was developed based on the geometry determined for secondary coil (Section 5.5), constituted by N turns of single 6G1mm2 cable, as represented in the cross-section of the left side of the coil windings, shown in Figure 189.
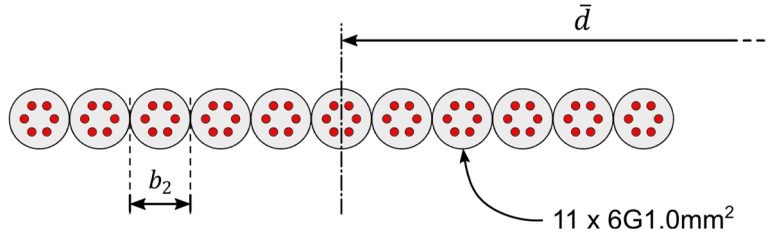
Figure 179: Photos of the modular restraining system implemented for primary coil: (a) Detail of cable twisting at the return extremity of the coil; and (b) extremity covered with a MDF module.

By imposing a current of $12.3\ A$ rms on the coil windings, an average power dissipation of approximately 1.13 W per meter of cable resulted.

The estimated power dissipation of the secondary coil at the critical displacement $x = w_d/2$, which the most critical point with the DIWPT region, is then given by:

$$\hat{P}_2 = 1.13 \text{ W} \times 2N(\bar{d}+\ell_2) = 1.13 \text{ W} \times 2 \times 11(0.282 \text{ m} + 0.63 \text{ m}) \cong 22.7 \text{ W} \qquad (5.88)$$

For obtaining the average power $\hat{P}_R$ at this same critical condition, the forward voltage drop on the Schottky diodes used in the rectifier can be estimated at 0.7 V, since six matched diodes were used in parallel, in place of each one, for a total of 24 diodes in the rectifier bridge. Assuming that the forward voltage drop is observed at all current levels, this results in an average power limited to:

$$\hat{P}_R \cong 2 \times 0.7 \text{ V} \times \max(I_{2,rms})\sqrt{2}\ \frac{2}{\pi} \cong 15.5 \text{ W} \qquad (5.89)$$

Since the efficiency at the critical displacement $x = w_d/2$ is the worst along all interval from $x = -w_d/2$ to $x = w_d/2$, it can be expected that the DC-DC efficiency of HIPLEV, in its entire DIWPT operation range at full nominal power will be at least:

$$\eta_{DC} \geq \hat{\eta}_{DC} = \eta_P \eta_S \frac{P_E}{(P_1 + \hat{P}_2 + \hat{P}_R)\eta_S + P_E}, \qquad (5.90)$$

which, assuming as exact the value $\eta_S = 94\%$ informed by the manufacturer of the DC-DC converter used, and a adopting an average value of $\eta_P = 95\%$ for the Mazzilli-Baxandall inverter, numerically becomes:

Dynamic Inductive Wireless Power Transfer for Lightweight Electric Vehicles
Luiz Alberto Lisboa da Silva Cardoso – University of Minho

309

$$\eta_{DC} \geq \hat{\eta}_{DC} \cong 0.95 \times 0.94 \frac{400}{(178 + 22.7 + 15.5) \times 0.94 + 400} \cong 59.2\% \qquad (5.91)$$

This design value for the DC-DC efficiency not only meets the minimum required for the HIPLEV (5.9), which is expectedly trivial to meet, but also exceeds the desirable target IWPT DC-DC efficiency (5.10) by approximately 6.6%.

Comparing the computed values of P_1, $\hat{P}_2$ and $\hat{P}_R$, with the expected power levels dissipated on the Mazzilli-Baxandall inverter and on the DC-DC converter, it can be seen that the efficiency η_{DC} is entirely dominated by losses on the primary coil windings, as show in Table 30.

Table 30: Power breakdown of the i-lane/HIPLEV system.

Subsystem	Symbol	Power (W)
DC-DC inverter power source (power supplied to i-lane)	P_{Inv}	674
Auto-resonant inverter (95% efficiency)	P_{Inv}	34
Primary coil*	$\hat{P}_1$	**178**
Secondary coil*	$\hat{P}_2$	22.7
Rectifier	$\hat{P}_R$	15.5
DC-DC converter (94% efficiency)	P_{DC-DC}	25
Power train / BMS (power delivered to vehicle)	P_E	400

*At the nominal design current $I_p = 65.4$ A rms and frequency, $f_0 = 51.7$ kHz.

The predicted efficiency of magnetic link itself is given by:

$$\eta_{Link} = \frac{P_E + P_{DC-DC} + \hat{P}_R}{P_E + P_{DC-DC} + \hat{P}_R + \hat{P}_2 + \hat{P}_1} \cong 68.7\% \qquad (5.92)$$

Increasing the efficiency of the electronic circuitry, for instance, by considering an evolution of the rectifier bridge to a synchronous rectifier, can provide only minor improvements on the overall η_{DC} efficiency. On the other hand, the largest power loss is observed on the primary coil. Even if, hypothetically, all circuits were 100% efficient and the power losses on the secondary coil were also brought to zero, still, the overall η_{DC} efficiency at the critical limit of the DIWPT operation region would be, at best, $400/(400 + 178) = 69.2\%$. In other words, the efficiency of the magnetic link itself, which in the critical maximum displacement condition is estimated at 68.7%, is dominated by the losses on the primary coil, and does not leave much margin for improvement in the overall DC-DC efficiency.

Dynamic Inductive Wireless Power Transfer for Lightweight Electric Vehicles
Luiz Alberto Lisboa da Silva Cardoso – University of Minho

310

To reduce the losses on the primary coil windings and increase the efficiency, the following strategies can be followed, each of them not necessary exclusively:

- Increase the frequency of operation and simultaneously use true litz cables for the windings, with the adequation of all components and circuits to the new frequency band.

- Increase the cross-sectional area of the primary coil, carefully, to assure that the new geometry used permits all conductors to be equally used.

- Work with shorter primary coils, at the expense of having to deploy (and maintain) proportionally more inverters per unit of length of the i-lane.

- Increase the magnetic coupling between primary and secondary coils, as well as their self-inductance, and reduce the primary coil current. This can be achieved by magnetic field shaping, by using ferrites or other soft magnetic materials.

It can be seen that either of these alternatives would imply in the use of either more materials or higher quality materials and, consequently, in the elevation of the system cost as well, which, under the philosophy of the HIPLEV, is not desirable. On the other hand, the predicted minimum DC-DC efficiency of approximately 59 % (5.91), is satisfactory, for it would still represent a major economy over the heavier standard electric vehicles (Section 5.2.1.4).

As the use of litz wire becomes more popular, their relative cost to that of the pure metal conductor (copper, or even aluminum) may drop, approaching that of standard cables (Table 16). Then it might be possible to work at higher frequencies, obtaining higher electric efficiencies, without diminishing the economic accessibility of the HIPLEV proposal.

5.13 Inter-Primary Coil Spacing

In addition to the IWPT design over a single primary coil, for a complete i-lane system constitution is necessary that several primary modules are laid sequentially along the vehicle path. For simplicity of analysis, let us assume that all primary coils are equal with diameter D and length ℓ_1, and evenly distributed at a pattern-distance ℓ_P, that is, with an inter-primary coil spacing distance $\ell_G = \ell_P - \ell_1$ (distance in between adjacent primary coils), as drawn in Figure 180.

Dynamic Inductive Wireless Power Transfer for Lightweight Electric Vehicles
Luiz Alberto Lisboa da Silva Cardoso – University of Minho

311
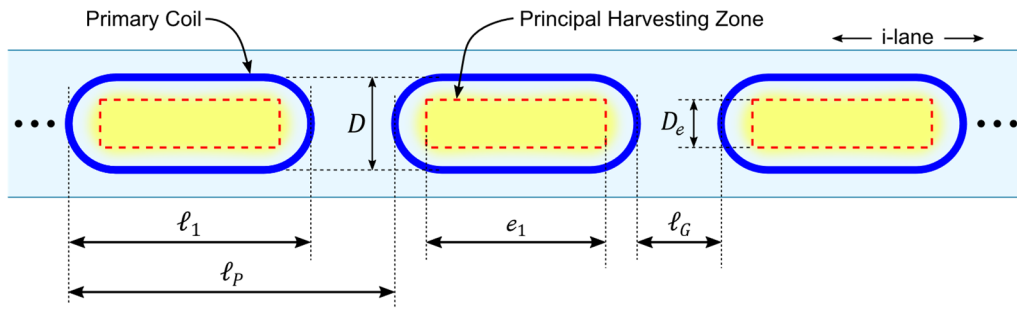
Figure 180: Inductive lane formed by a sequency of equally spaced identical primary coils.

For a given assured harvesting power level p, the locus of the vertical projection of the center of the secondary coil installed on the vehicle in general will not coincide with the area delimited by primary coil winding perimeter itself (blue contour). Rather, depending on the power level to be established, the primary and secondary design current levels, and the airgap (height) between coils, this zone, referred to as the p-harvesting zone, will usually be a smaller area inside this perimeter (the yellowish zones in Figure 180).

5.13.1 Power Harvesting Zone

After the system dimensions and other parameters are determined, additional validation of two design aspects is proceeded: (i) the two-dimensional size of power harvesting region over one primary coil and (ii) the validation of the maximum exposure level of the pedestrian in the neighborhood of the i-lane to the magnetic and electric fields. Although it is highly expectable that some type of shield is required to be installed in the lower parts of the bicycle to project the body of the rider, this part of the design, is not the focus of this prospective research.

In the same manner, while it is possible to fully test the system for power transfer in stationary condition, the test for electromagnetic safety compliance would constitute an effort out of the limits defined for this thesis, and require testing equipment that was not available in the laboratory. Simulations regarding the pedestrian safety are necessary and a first step towards the qualification of the prototype as a usable transport.

The full three dimensional finite element modeling simulation of the designed inductive configuration is computationally intense. However, for the estimation of the induced voltage on the secondary coil, what is the ultimate interest for predicting the spatial power transfer characteristics of a magnetic link, it is enough to compute the vertical magnetic field $\dot{B}_z$, since the secondary coil is assumed to be horizontal all the way along the vehicular displacement.

Dynamic Inductive Wireless Power Transfer for Lightweight Electric Vehicles
Luiz Alberto Lisboa da Silva Cardoso – University of Minho

312

In order to speed up the simulation, $\dot{B}_z$ can instead be algebraically calculated by (3.84), if some simplifying additional assumptions in the geometry of the model are adopted:

- Both primary and secondary coils are considered to be formed of rectangular concentric filamentary elements, which main dimensions are kept parallel, as the vehicle is displaced either laterally or along the lane.

- The currents on each of the primary winding are considered constant, and the total current divided over the conductor according to the current distribution previously computed using FEM numeric simulation of a single cross-section of the lane.

- The secondary coil is modeled as N-turn ($N = 11$) coil formed by N concentric, serial connected, rectangular coils.

It can be further assumed that the losses on the aluminum frame of the bicycle are negligible, because the frame is high enough above the primary coil, and does not contain large closed-loop circuits. The only incidental short-circuited loops on the bike frame with non-null horizontal projection are those formed by (i) the chain-stays, the bottom bracket, and the rear wheel axis; and, less relevant, (ii) the chain-stays, the seat-stay and the seat tube. These are much smaller than the secondary coil and the, in terms of projected horizontal area, much narrower than the primary coil, and because the wheels' radius is 368 mm (29 inch wheels) the chain-stays are about three times higher above the primary coil than the secondary coil windings. This is the justification for the diminutive parasite electric losses experimentally observed in the, as long as the bicycle remains approximately center-aligned in the lane and in normal upright position.

On the other hand, the aluminum wheels are much closer to primary coil, because the tires touch the lane, and the losses on the wheels cannot be a priori neglected. Ideally, as discussed, non-conductive wheels should have been used in the design. However, because aluminum rims are the most popular alternative to steel, the aluminum wheels were prospectively kept in the design.

The impact of using aluminum wheels, however, is minimized, because the short-circuited loops that the wheel rims represent are, by construction, always center-aligned and perpendicular to the secondary coil. So, any current induced in the rear wheel is not expected to directly disturb the induced voltage on the secondary coil, and vice versa, i.e., they are in magnetic orthogonality. When the bike is turning, the front wheel is not perpendicular to the secondary coil, but, being too far away from the secondary coil, any current flowing on it will not produce noticeable effects on the secondary coil.

Dynamic Inductive Wireless Power Transfer for Lightweight Electric Vehicles
Luiz Alberto Lisboa da Silva Cardoso – University of Minho

313

In summary, concerning the power transfer, the expected effect of the aluminum rear and front wheels are the extra resistive losses, due to the currents induced by the primary coil. If the primary current is kept constant, these power losses do not directly affect the induced voltage on the secondary, only reduce the efficiency in the power transmission. However, on a Mazzilli-Baxandall inverter, as the load is increased due to the parasite loss, the primary coil current is expected to slightly decrease, until the inverter is critically loaded, as shown in Section 2.9.4.5, Figure 57. This will should cause the induced voltage to decay from the predicted value when the bike is misaligned in the lane.

Nevertheless, by symmetry, the voltages and currents induced on the wheel loops are null, when the bike is exactly on the longitudinal center-lane plane. Only minor losses due to eddy currents are expected, because when the wheel is at the center of the lane it is about 20 cm away from either primary coil winding. Based on this reasoning, the final effect resulting from the use of aluminum wheels is that, initially starting from center alignment condition, the induced voltage on the secondary shall progressively decrease from that predicted without modeling the wheel, as the bicycle is moved laterally. But when a Mazzilli-Baxandall inverter is used to drive the primary coil, this interaction is even more complex though. The coupling of the inductance represented by the wheels will also produce a decrease in the equivalent inductance of the resonant coil in the primary circuit, causing an elevation of the inverter oscillating frequency. Since the induced voltage is also proportional to the inverter frequency, this could have a partial contribution to the elevation of the induced voltage on the secondary coil that could partially compensate the decrease in the induced voltage caused by the decrease of the primary col current.

So, based on this qualitative analysis only, it is unclear how much the induced voltage on the secondary could be affected, as the bicycle is moved laterally away from the center of the lane. But measurements on the prototype experimentally verified that the power loss on the wheels does not significantly affect the primary current, to a point the induced voltage on the secondary becomes noticeably impaired, as long as the bike misalignment in lane is kept limited to 50% of the primary coil width. $D_e/2$ away from the center line of the primary coil. Additionally, even with the wheels standing over the primary coil windings, the system is still functional, although extra losses become apparent.

Since the neighborhood within radius $D_e/2$ is the one that really matters for predicting nominal power harvesting and, in this particular design, $D_e < \widetilde{D}/2$, the aluminum wheels, as well as the bicycle's aluminum frame, do not need to be considered in a basic prediction model

Dynamic Inductive Wireless Power Transfer for Lightweight Electric Vehicles
Luiz Alberto Lisboa da Silva Cardoso – University of Minho

314

for the P_E-energized zone. At least in the specific case of a standard frame, all-aluminum 29-inch wheel bicycle standing in an approximately upright position.

By simulating the magnetic field generated by each of the primary coil cables, and its individual interactions with the secondary coil windings, it is possible to map the 3D-surface of the induced voltage scalar field, which is bidimensional, since the bike keeps its height above ground constant. This scalar field can then determine the predicted zones for different power levels, with minor errors in the central fringe of the lane limited in width to half of that of the primary coil.

To evaluate the induced voltage, the magnetic field generated by the primary coils winds is first analytically computed by applying the Biot-Savart Law for each line segment modeling the filamentary coil windings, as shown in Figure 181. However, only the vertical component (z) of the partial magnetic field contributions are relevant and added up to result in the total vertical magnetic field component.
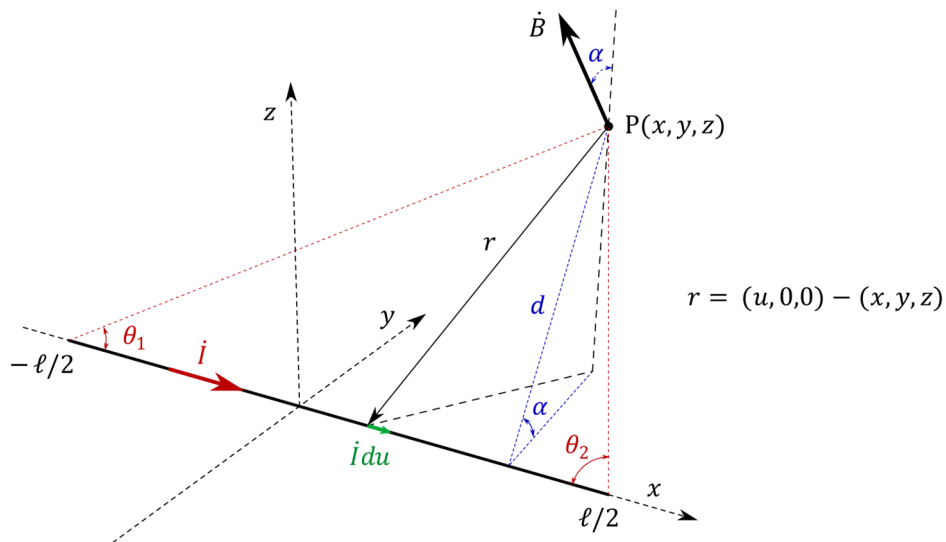
Figure 181: Contribution a filamentary current to the magnetic field in a given point P of the space.

The partial contribution $\dot{B}$ of the filamentary current $\dot{I}$ is then given by:

$$\dot{B} = \mu \int_{-\ell/2}^{+\ell/2} \frac{r \times \dot{I}\, du}{4\pi r^3} = \frac{\mu \dot{I}}{4\pi} \int_{-\ell/2}^{+\ell/2} \frac{(u - x, -y, -z) \times (1,\, 0,\, 0)}{r^3}\, du \,, \tag{5.93}$$

which can be further simplified to:

$$\dot{B} = \frac{\mu \dot{I}}{4\pi} \int_{-\ell/2}^{+\ell/2} \frac{(0, -z, -y)}{((x-u)^2 + y^2 + z^2)^{3/2}}\, du \tag{5.94}$$

$\dot{B}_z$, the vertical component of $\dot{B}$ is then analytically calculated:

Dynamic Inductive Wireless Power Transfer for Lightweight Electric Vehicles
Luiz Alberto Lisboa da Silva Cardoso – University of Minho

315

$$\dot{B}_z = \frac{\mu\,\dot{I}}{4\pi}\,\frac{y}{d^2}\left(\frac{\ell/2 - x}{\sqrt{(\ell/2 - x)^2 + d^2}} + \frac{\ell/2 + x}{\sqrt{(\ell/2 + x)^2 + d^2}}\right), \tag{5.95}$$

where $d^2 = y^2 + z^2$. Incidentally, (5.125) can be rewritten in a geometrically more intuitive expression:

$$\dot{B}_z = \frac{\mu\,\dot{I}}{4\pi d}\,\cos\alpha\,(\cos\theta_1 + \cos\theta_2)\,, \tag{5.96}$$

Looking into (5.96), it is immediately recognizable that:

$$\dot{B}_z = \dot{B}_\varphi(d)\cos\alpha\left(\frac{\cos\theta_1 + \cos\theta_2}{2}\right), \tag{5.97}$$

where $\dot{B}_\varphi(d) = \mu\dot{I}/2\pi d$ is the tangential component of the magnetic field in cylindrical coordinates of an infinitely long filamentary wire with a current $\dot{I}$, which depends only on the distance d to the wire. The term $\cos\theta_1 + \cos\theta_2$ indicates that even if the distance of a sensing point P to the support line of the wire is kept, the magnetic field will quickly vanish when the projection of P lies outside the wire, as its longitudinal distance from the midpoint of the wire is increased. This explains why the induced voltage drops fast, as the secondary coil projection lies outside the primary coil, especially on the longitudinal direction.

Expressions similar to (5.125) are found when the filamentary current segment is arbitrarily positioned in space, with respect to the refence system $(1_x,\ 1_y,\ 1_z)$. The total vertical magnetic field component in any point $(x,\ y,\ z)$ in space is then expressed as the sum of all partial vertical components $\dot{B}_{z,k}$ due to each individual filamentary wire k modeling the primary coil.

$$\dot{B}_z = \sum_k \dot{B}_{z,k}\,, \tag{5.98}$$

The induced voltage is computed by firstly numerically integrating the magnetic flux in each component coil of in the simplified model of the secondary coil. The induced voltage is then calculated by the derivative with respect to time of the total flux. Under the stationary approximation, the only factors to depend on the time variable are the currents $\dot{I}_k$ in each filamentary wire k, all assumedly in phase at frequency, for which the derivate is $-j2\pi f_0\dot{I}_k$.

The simulation gives estimates not only to the effective lane widths for guaranteed 400 W (D_e) and 250 W (D_e') power availability, but also for the associated longitudinal size to these zones,

Dynamic Inductive Wireless Power Transfer for Lightweight Electric Vehicles
Luiz Alberto Lisboa da Silva Cardoso – University of Minho

316

which are normally shorter than the actual physical length of the primary coil. The simulation was accomplished using numeric integration over the analytical expressions of the magnetic field and the simplified circuit model of section 2.9.4.1, using Wolfram Mathematica software. As a simplification, to speed up the simulations, both coils were considered to be formed by perfectly rectangular filamentary bodies, with concentric rectangles representing the different current paths for the single turn of the primary coil and the 11 turns of the secondary coil. Due to the symmetric position of cable A to cable C with respect to cable B, and their close proximity relatively to the distance between primary and secondary coils, as an additional simplification, the current in cable B was assumed to flow entirely on cables A and C, which according to Table 28, already carry 86.8% of the primary coil current. The resulting data is summarized in Table 31, and plot in detail in Figure 182 and Figure 183.

Table 31: Summary of 3D magnetic field simulations run to estimate the induced voltage on secondary coil.

Parameter	Symbol	Value determined by simulation	Unit
Length of 400 W corridor	e_1	270.9	cm
Width of 400 W corridor	D_e	19.8	cm
Length of 250 W corridor	e_1'	273.4	cm
Width of 250 W corridor	D_e'	27.4	cm
Zero induced voltage contour length	e_0	376.4	cm
Zero induced voltage contour width	D_0	58.1	cm
Peak induced voltage in lateral alignment	V_{max}^p	50.9	V (rms)
Induced voltage, fully centered	V_{max}	47.7	V (rms)

*Configuration run with secondary coil size, $\bar{d} = 282$ mm, $\bar{\ell}_2 = 62$ cm, $N = 11$.

Figure 182 shows a plot of the induced voltage on the secondary coil as a function of the relative position (x, y) of its center, with respect to the center of the primary coil. The induced voltage obtained with the secondary coil positioned over the center of primary coil, V_{max}, was 47.7 V rms, while the peak induced voltage V_{max}^p was 50.9 V rms (6.7% higher), obtained closer to the extremities of the primary coil, at the positions (-123.3 cm, 0) and (123.3 cm, 0). The pink shaded part of the surface indicates a region of negative voltages, which are much smaller in magnitude than the positive voltages obtained near the central alignment condition. The red perimeter marks the central spot where the induced voltage is above 37.8 V, yielding enough margin to be converted and regulated to the 36.5 V that are required to generate 400 W on the load. Similarly, the upper black dashed contour indicates the minimum voltage level required for

Dynamic Inductive Wireless Power Transfer for Lightweight Electric Vehicles
Luiz Alberto Lisboa da Silva Cardoso – University of Minho

317

250 W on the load The locus of the zero induced voltage is the lower black dashed contour, which is circumscribed in a rectangle of dimensions e_0 and D_0.
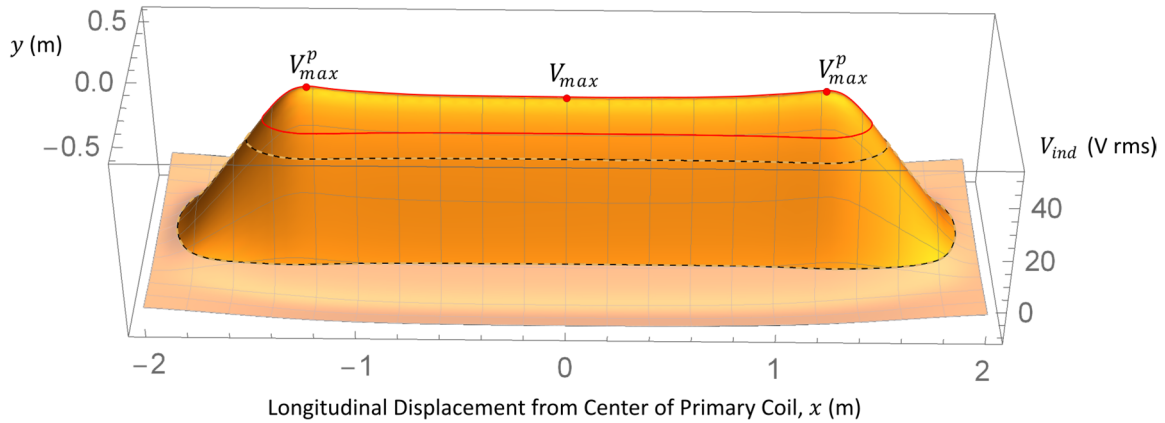
Figure 182: 3D representation of the induced voltage on the secondary coil placed at $h = 145.5$ mm.

Figure 183 is a simplified, top view representation of the same data plotted in Figure 182. The primary coil position and main dimensions, ℓ_1 and D, are indicated by the black dashed rectangle. The central white zone is where 400 W of power is available. It has a width D_e at the middle section of the primary coil, where it is narrower. Similarly, the yellow zone is where at least 250 W, but less than 400 W of power, is available. This zone is externally delimited by a dashed black curve, with a width D_e' at the middle section.
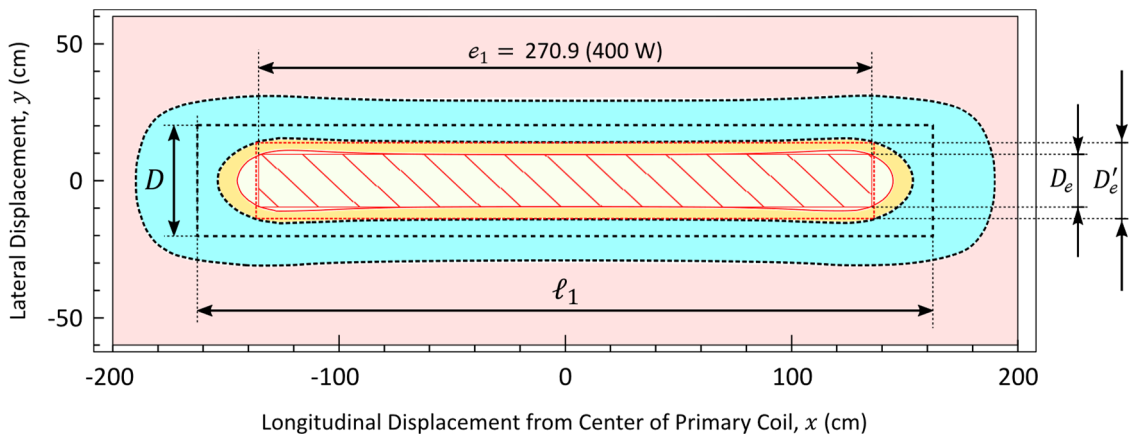
Figure 183: Top view of lane module, showing energy harvesting zones (x and y not drawn to the same scale).

Most importance for our analysis, the central rectangle cross-hatched in red is the corridor of maximum width over the primary coil where 400 W of power transfer is guaranteed. Its length, e_1 (270.9 cm), and width, D_e (19.8 cm), as expected, less than the respective dimensions of the primary coil, ℓ_1 (325 cm) and D (405 mm). As a consistency check, it can be observed that the value of D_e resulted from simulation is in good agreement with that previously used as an input design parameter for the configuration, $D_e = 20$ cm, used in Section 5.8 (5.55).

Dynamic Inductive Wireless Power Transfer for Lightweight Electric Vehicles
Luiz Alberto Lisboa da Silva Cardoso – University of Minho

318

In the yellow region less than 400 W, but more than 250 W is still available for harvesting. However, this availability would only be used if a more complex secondary circuit than that implemented in the prototype is adopted. In the simplified circuit of the prototype, the power harvesting can is ignored when the regulated voltage provided by the DC-DC converter falls below 36.5V, that is, outside the 400 W. The blue painted region is where less than 250 W would be available, but, likewise, this energy is also not used in this design.

5.13.2 Sustaining Vehicular Power during Inter-Coil Transit

For rectangular oblong primary coils and similar secondary coils, the p-harvesting zone will often consist in a symmetrical oblong shape that has its extremities dilated, being narrower in the middle zone of along its longitude. In order to establish a relation among p, the nominal maximum power required by the vehicle, P_H, and the relative spacing of the primary coils, let us first identify the p-principal harvesting zone of an energized primary coil with respect to an also given loaded secondary coil as being the rectangular zone with maximum width D_e and, secondarily, with maximum length e_1, that lies entirely within the limits of the p-harvest zone. So, if the vehicle moves along the lane at constant speed, keeping a maximum lateral misalignment width of D_e, and it able to harvest energy even outside the p-harvesting zone, then the expectable average harvested power P_X should be:

$$P_X \geq \frac{e_1}{\ell_P} p \qquad (5.99)$$

While moving on the i-lane, at the moments the vehicle is harvesting more power than P_H, the excess energy can be stored, to be used when moving outside a P_H-harvest zone. Otherwise, to achieve full nominal power P_H, energy must be retrieved from the storage device to complement power being harvested. This is a situation that can momentarily happen either when the vehicle drifts laterally outside the P_H-harvest zone or during the proximity of an inter-primary coil transit. If absolutely no power is currently being harvested, P_H will have to be entirely retrieved from the storage device.

In order to keep a positive energy balance on the storage device (usually, a standard electrochemical battery, a supercapacitor, or an association of them) in such a way that no stationary charging has to be periodically executed, it is sufficient that the average harvested power P_X be greater the maximum nominal power that can be demanded by the vehicle:

$$P_X \geq P_H \qquad (5.100)$$

Dynamic Inductive Wireless Power Transfer for Lightweight Electric Vehicles
Luiz Alberto Lisboa da Silva Cardoso – University of Minho

319

Considering (5.99), it is then sufficient to require that p satisfies:

$$p \geq P_H \frac{\ell_P}{e_1} \qquad (5.101)$$

Or, if p is fixed, that ℓ_P satisfies:

$$\ell_P \leq e_1 \frac{p}{P_H} \qquad (5.102)$$

For the particular design case in section 5.1, $P_H = 250 \, \text{W}$, $p = P_E = 400 \, \text{W}$ and $e_1 = 270.9 \, \text{cm}$, so a maximum pattern distance $\ell_{P,max}$ must be observed :

$$\ell_{P,max} = 270.9 \, \text{cm} \times \frac{400 \, \text{W}}{250 \, \text{W}} \cong 433 \, cm \qquad (5.103)$$

Inequation (5.99), however, is too optimistic, because it implicitly considers an ideal storage system, one from which 100% of the energy stored can be retrieved with no losses. In practice, the circuits used to store and retrieve energy from a storage device, and the storage device itself have electrical efficiencies that are not the unity. Of particular interest in DIWPT is the short-term efficiency of such energy storage system, η_{batt}, the one that is verified during the transit times over the energy-blind zones in between two adjacent p-harvesting zones.

Considering a general η_{batt}, that is not 100%, the general expression for (5.99), becomes:

$$\frac{e_1}{v_K}(p - P_H)\eta_{batt} \geq P_H \frac{(\ell_P - e_1)}{v_K}, \qquad (5.104)$$

where v_K is the assumed constant speed of the vehicle. Then, instead of (5.102), the new constraint on ℓ_P becomes:

$$\ell_P \leq e_1 \left(1 + \eta_P \left(\frac{p}{P_H} - 1\right)\right) \qquad (5.105)$$

or, conversely, for given (ℓ_P, e_1, P_H, p):

$$\eta_{batt} \geq \left(\frac{\ell_P}{e_1} - 1\right) \Big/ \left(\frac{p}{P_H} - 1\right) \qquad (5.106)$$

Again, for the design case in section 5.1, where $P_H = 250 \, \text{W}$, $p = P_E = 400 \, \text{W}$ and $e_1 = 270.9 \, \text{cm}$, based on equation (5.105), Table 32 can be easily derived, illustrating how does

Dynamic Inductive Wireless Power Transfer for Lightweight Electric Vehicles
Luiz Alberto Lisboa da Silva Cardoso – University of Minho

320

the maximum primary coil pattern distance varies with the decrease in the short term storage efficiency η_{batt} (which should include the circuit to charge the battery):

Table 32: Numeric example of the interdependence of storage efficiency and primary coil pattern spacing.

Short Term Storage Efficiency (η_{batt})	Maximum Pattern Distance ($\ell_{P,max}$, cm)
100%	433.4
90%	417.2
80%	400.9
70%	384.7
60%	368.4
50%	352.2
34%	$325 \cong \ell_1 *$

*The condition $\ell_P < \ell_1$, by design, is not allowed.

Using current store technology, with $\eta_{batt} \geq 80\%$, it is then additionally necessary to require that $\ell_P \leq \ell_{P,max} = 4$ m, to guarantee that the vehicle will have full nominal power available while traversing the inter-primary coil spacing (where there is no energy to harvest).

5.13.3 Cross-Talk between Adjacent Primary Coils

A primary coil will eventually act as secondary coil, to other adjacent primary coils, which is an a priori undesirable side-effect of the proximity of the primary coils in the i-lane. So, another constraint should be introduced to limit the maximum cross talk voltage, which is the induced voltage on a primary coil by another adjacent energized primary coil.

While (5.105) imposes a maximum value for ℓ_P, as η_{batt} is decreased, a minimum value for ℓ_P could possibly arise, because the magnitude of the cross talk voltage in a primary coil, due to an active neighbor primary coil, is increased in magnitude as ℓ_P decreases. In principle, the cross talk voltage is not exact at the same frequency as that of the coils being affected, but it might interfere with the coil driving voltage, what is not desirable, if the magnitude of this interference is excessive. The avoid crosstalk, the positioning of the primary coils could be such that neighbor coils were in magnetic orthogonality, but since they are not solidary, or embedded in the same module, the positioning would require precision that is not practical to achieve at the deployment and installation of the system.

The crosstalk voltage is then simulated, assuming the designed primary voltage excitation, V_{L1}, and length ℓ_1. The curve in Figure 184 shows how the simulated crosstalk between neighbor primary coils increases in magnitude, for the particular system designed (section 5.1), as the

Dynamic Inductive Wireless Power Transfer for Lightweight Electric Vehicles
Luiz Alberto Lisboa da Silva Cardoso – University of Minho

321

pattern distance between them, ℓ_P, is decreased from the maximum possible value of 433 cm (5.103). The percentual numbers annotate along the curve are drawn from Table 32.
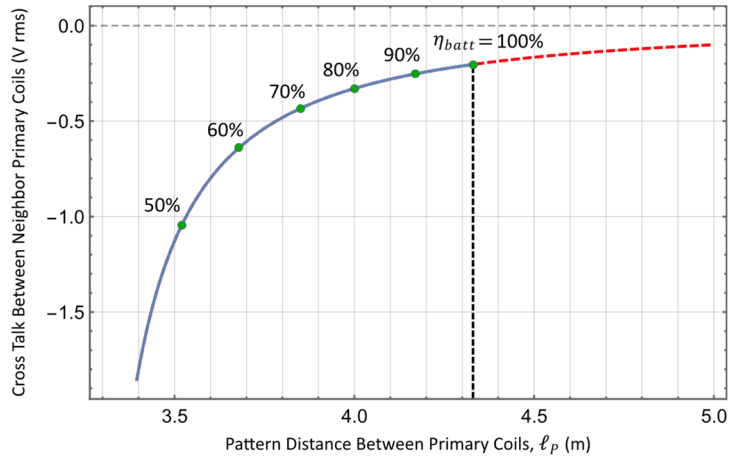
Figure 184: Cross talk between neighbor primary coils and minimum required short-term storage efficiency.

The crosstalk voltages are less than 1.0% of the normal excitation voltage of the primary coil (5.78), for the required primary current when $\ell_P \geq \ell_{P,min} = 3.6\,\text{m}$, which are deemed not to significantly perturb the operation of the coil driver circuit, either if that other coil is deactivated or energized for WPT.

At the superior limit condition, where the required efficiency η_{batt} is 100%, the pattern distance ℓ_P has achieved its maximum possible value $\ell_{P_{max}}$, beyond which (red dashed thread of the curve), if it is increased further, the e-bike is prone to arrive at next primary coil field with less short term energy stored than it had in the preceding coil pass. As a consequence, the short term energy storage would expectably decrease until it is fully depleted. This implies that either the HIPLEV would have to enter pedal-only mode, or rely on the vehicle's main battery, if it has one installed.

In summary, the need to keep a positive balance on the short term energy storage on board of the vehicle limits the maximum distance between the neighbor primary coils, while the potential crosstalk between neighbor coils limits the minimum distance between them. Combining the resulting requirements for the minimum and maximum value of the ℓ_P:

$$3.6\,\text{m} \leq \ell_P \leq 4\,\text{m} , \tag{5.107}$$

or, equivalently, considering the length ℓ_1 of the primary coil, the distance ℓ_G between two consecutive primary coils should be limited to:

Dynamic Inductive Wireless Power Transfer for Lightweight Electric Vehicles
Luiz Alberto Lisboa da Silva Cardoso – University of Minho

322

$$35\,\text{cm} \leq \ell_G \leq 75\,\text{cm}\,, \qquad\qquad (5.108)$$

5.14 Verification of EMF Exposure Levels of the Pedestrian

The recommendations for controlling maximum human exposure to electric and magnetic fields presented in section 2.11 are valid for the HIPLEV design. This control must focus people in different two role positions of the system, the riders and the pedestrians. The pedestrians can be assumed to be relatively far apart from the vehicles when they are cruising on i-lanes, so, for them, the major concern is the EMF generated by the primary coils in the lanes. Concerning the protection of riders, two classes of riders can be distinguished: riders of HIPLEV and riders of other electric and non-electric bicycles sharing the lane. Contrarily to pedestrians, the proximity of riders to both the lane and the vehicles are presumed.

Both categories, riders and pedestrians, are considered in the stricter protection level, described as "general public", in the ICNIRP recommendations [72]. This means that the maximum tolerable levels of magnetic and electric fields in the region of space that users are expected to be when the system is energized must be limited to respectively 27 μT rms and 83 V rms/m, at the bandwidth of the operation frequency, $f_0 = 51.7$ kHz, as reported in Section 2.11, Table 9. Although essential for the homologation of the system as a transport, estimated of EMF values must be verified, but the required equipment for precise measurements of the magnetic and electric fields targeting human exposition were not available at the time of the prototype design and construction. In addition, it is anticipated that the amount of extra work and industrial effort necessary to develop, test and validate the EMF shielding of the vehicle would extrapolate the resources available for the thesis development. Because of that, the shielding design and the detailed EMF exposure control is left out of the scope of this work, only an initial assessment of pedestrians' safety is presented, showing that, even without shielding of the secondary coil, the pedestrian is safe when the HIPLEV harvests up to the nominal maximum power anywhere within the center portion of the lane where maximum power transfer is available.

5.14.1 EMF Exposure of Pedestrians

Inductive lanes are specifically designed for cycles and are not expected to be shared with pedestrians, except at crossings, where for mechanical reasons and the risk of collision. Even at the crossings, it should be enforced that pedestrians cannot occupy the lane at the same time cycles are present, either non-electric or electric of any kind. On the other hand, while standing or

moving over an i-lane by themselves, the pedestrians have no means of activating the primary coils, so voltage is not applied to power windings, and both the main electric and magnetic fields are not generated by these coils. The magnetic and electric fields generated by the RFID readers embedded in the lane (Section 5.18) may be active at the pedestrian crossings as well, but the voltage and current level of these devices are too low, and the associated fields do not pose any harm to the pedestrians.

While standing outside but close to an inductive lane, the pedestrian has its EMF safety assured by the exclusion from the zones contoured by maximum electric and magnetic of field intensity levels. Two representative cases are considered: (i) The pedestrian is standing as close as possible to the i-lane, in a cross-section where no HIPLEV is present; (ii) the pedestrian is standing as close as possible to the i-lane, right in front of the secondary coil of a HIPLEV in transit, harvesting maximum power from the lane. The maximum electric and magnetic fields to which the pedestrian is exposed under these two circumstances are then evaluated by FEM numeric simulation.

5.14.1.1 Magnetic Field Exposure Level Compliance

The two cases identified in 5.14.1 are then separately considered. The numeric simulation of the magnetic field of an energized primary coil is run using FEMM [99], according to the geometric (Section 5.9.1) and current specifications (Section 5.8) of the primary coil embedded in the i-lane. The results of the magnetic field intensity are shown in Figure 185, with the contours of the ICNIRP reference levels [72] annotated.

It can be noticed that the pedestrian, by being outside the lane is at least 750 mm away from the center of the lane, is entirely outside the region where the magnetic field intensity is higher than the limit value of 27 µT rms, which is limited to a diameter of $978 \, \text{mm}$ around the center of the lane. Even if the pedestrian invades the 25 cm-wide external guard bands of the w_T-wide lane, there will be no contact with the dangerous field level, provided the pedestrian do not step on the w_L-wide central paved band of the i-lane, or extends any part of the body over the space directly above the paved portion of the lane.

Dynamic Inductive Wireless Power Transfer for Lightweight Electric Vehicles
Luiz Alberto Lisboa da Silva Cardoso – University of Minho

324
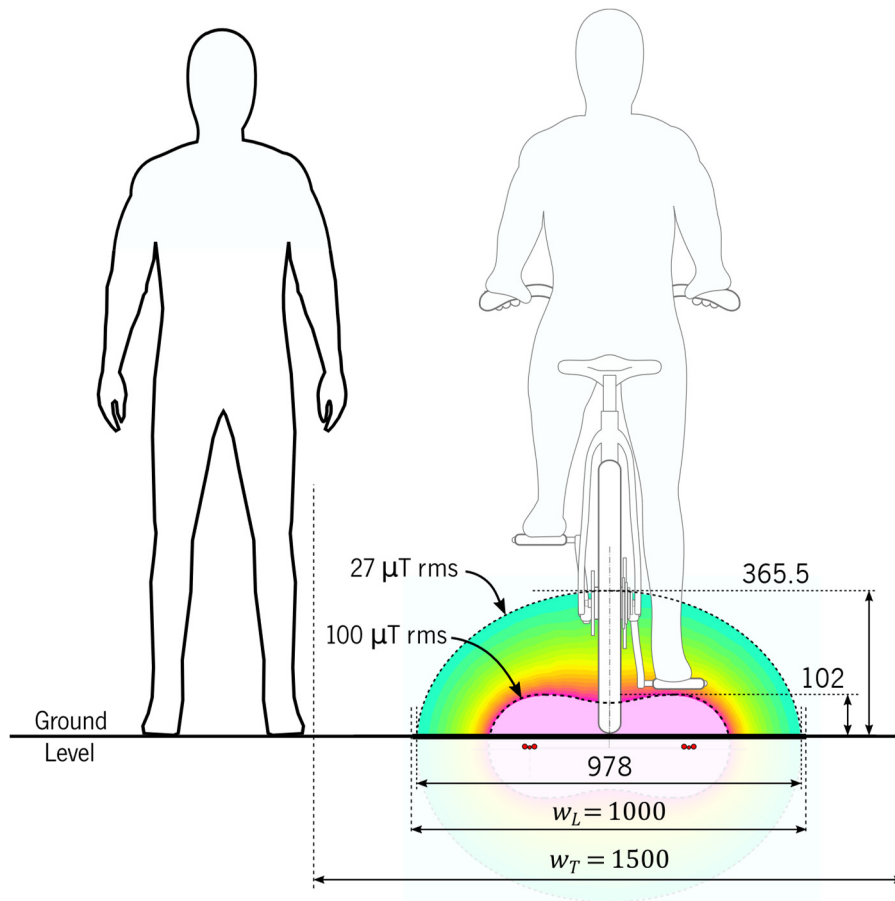
Figure 185: Pedestrian exposure to magnetic field, with primary coil energized, no HIPLEV harvesting.

The most critical case comes when, in addition to the i-lane being energized, there is also a HIPLEV on the i-lane transiting side by side with the pedestrian, while the maximum power is being harvested. At this limit condition, both the nominal primary coil current $I_p = 65.4$ A rms (Section 5.8) and the maximum secondary coil current $I_{2,max} = 13$ A rms (5.28) need to be taken into consideration. This time the FEM simulation was run with COMSOL Multiphysics, with the HIPLEV harvesting full power P_E and displaced $D_E/2$ towards the pedestrian. The resulting magnetic field intensity is also concentrated towards the pedestrian as well, as shown in Figure 186, where, again, the contours of the ICNIRP reference levels are annotated.

Dynamic Inductive Wireless Power Transfer for Lightweight Electric Vehicles
Luiz Alberto Lisboa da Silva Cardoso – University of Minho

325
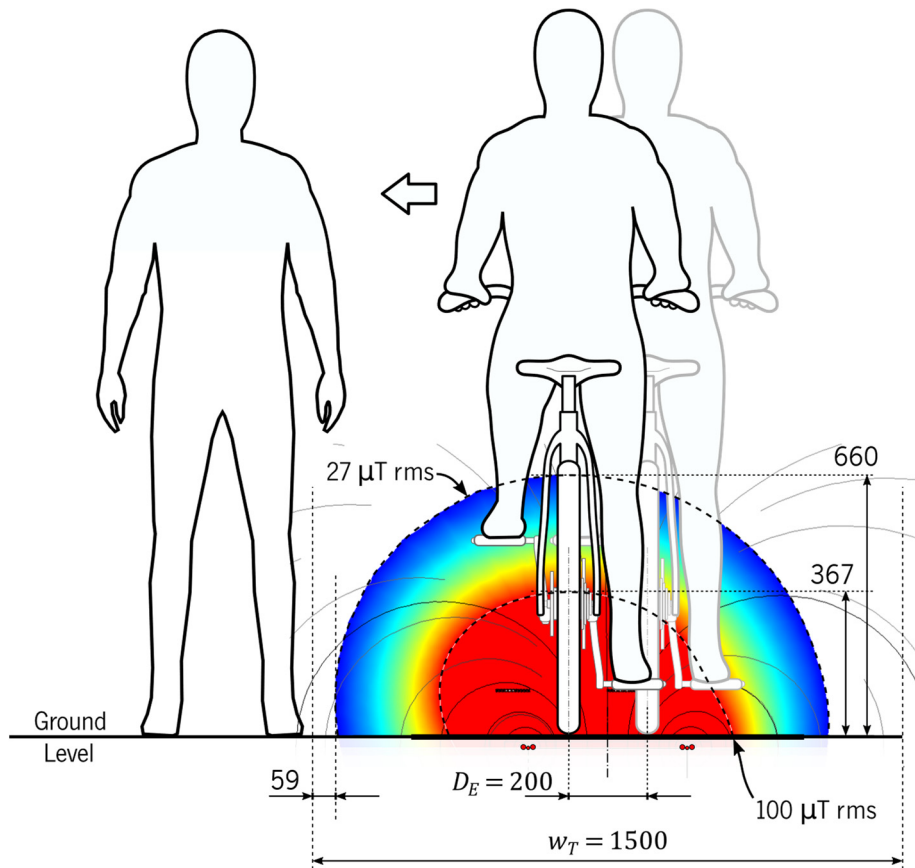
Figure 186: Pedestrian exposure to magnetic field side by side with a HIPLEV harvesting maximum power.

It can be notice that the high total current flowing in the windings of the secondary coil reinforces the magnetic field, expanding the safe exposure contours, up, towards the body of the rider and laterally, more towards the direction of displacement of the rider from the center of the lane. But still, the 27 µT rms contour lies 59 mm away from the limits of the i-lane, and thus, at least 59 mm away from the body of a pedestrian outside the lane. At 13 A rms, the maximum displacement of the HIPLEV from center lane (towards the pedestrian) that would still guarantee the 27 µT rms contour to be entirely confined to the total lane width w_T is also determined by FEM simulations as 164 mm. For displacements larger than 164 mm, the secondary current has to be less than $I_{2,max}$, in order to keep the 27 µT rms contour confined to the lane limits, and consequently away from the pedestrian.

Figure 187 shows the results from several runs of FEM simulation using COMSOL Multiphysics, similarly to that run to generate Figure 186, one for different lateral displacement. In the figure, the blue curve gives the maximum current allowed in the secondary coil, in order to prevent the 27 µT rms magnetic field contour from trespassing the lane width.

Dynamic Inductive Wireless Power Transfer for Lightweight Electric Vehicles
Luiz Alberto Lisboa da Silva Cardoso – University of Minho

326
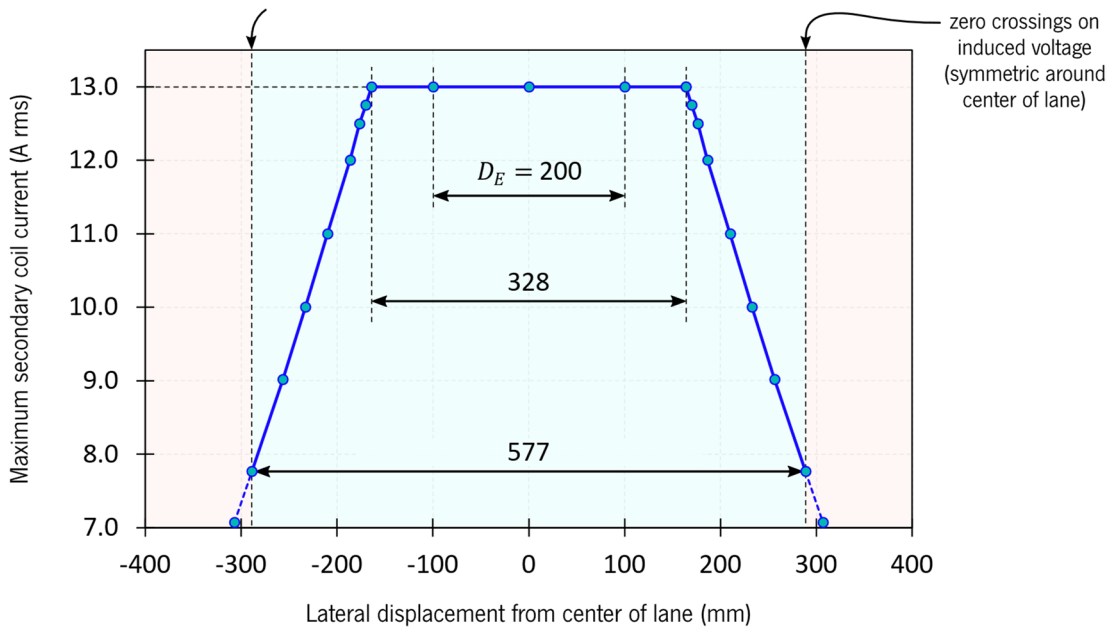
Figure 187: Profile of the maximum secondary coil current, after the required pedestrian EMF safety compliance is considered, obtained by FEM numeric simulation of the magnetic field of a cross-section containing the primary coil, the secondary coil and the pedestrian, standing as close as possible to the i-lane.

The conclusion is that the width within which $I_{2,max}$ can be drawn from the secondary coil exceeds D_e, therefore, full power harvesting at the design zone does not generate any hazard risk for a pedestrian standing outside the lane. Because of that, concerning the pedestrian protection, a more advanced harvesting circuit could extract power at the nominal maximum secondary current as long as the vehicle keeps inside a 328 mm-wide central portion of the lane. However, if a HIPLEV circuit tries to harvest power beyond that limit, the maximum current has to be derated by approximately $-0.43\ \mathrm{A\ rms/cm}$. Remarkably, this is unlikely to become a major issue because, at larger lateral displacements, it becomes more difficult to obtain large currents from the secondary anyway, because the induced voltage is also progressively reduced as the position of the secondary coil approaches the lines of zero-crossing.

The exact behavior of the secondary current depends on the particular energy harvesting and BMS strategy used. In the simple circuit implemented for the HIPLEV prototype, the above additional limitation to I_2 is not a problem, because if the vehicle leaves the region of maximum power availability, the DC-DC converter becomes unable to regulate the nominal voltage, and power is supplied to the powertrain by onboard energy storage, forcing the secondary current to a diminutive standby level.

Dynamic Inductive Wireless Power Transfer for Lightweight Electric Vehicles
Luiz Alberto Lisboa da Silva Cardoso – University of Minho

327

5.14.1.2 Electric Field Exposure Level Compliance

Similarly to the case of the magnetic field, the exposure level to the electric field could only be fully evaluated if all circuits sustaining the i-lane were also defined, including the layout of the power grid lines in the neighborhood of the lane. On the other hand, looking into Figure 185 and Figure 186, it is apparent that the magnetic shielding for the secondary coil on board of the HIPLEV is essential to be developed, but this development in not included in the scope of this work. Since the magnetic shield can also be designed to promote electric shielding, if grounding of metallic components and careful design, it would be of not of much usefulness to try to evaluate the electric field generated by the HIPLEV before the shield is developed. So, as an initial assessment, the ICNIRP compliance concerning the pedestrian exposure to the electric field is only evaluated on the field generated by the primary coil.

The amplitude of the excitation voltage fed by the inverter at one of the extremities of the primary coil can be considered practically constant. So, to evaluate the worst case electric field on a pedestrian outside, but close to the i-lane, it is then necessary to consider the closest cross-section to the energized extremities of that coil. As a simplification, the primary coil is assumed to be constituted by two parallel windings at distance $\widetilde{D}$ according to the design in Figure 166, to which the excitation voltage V_{L1} (5.78) is applied.

The results from FEM simulations (using the FEMM software) of the electric field in the vicinity of the primary coil, represented only above ground level, are shown in Figure 188. All linear dimensions are in millimeters, and indicated voltages are rms. In the plots, the colors correspond to the rms values of the intensity of the electric field E in a cross-section of the lane close to the extremity of a primary coil, where the driving voltage V_{L1} of 106 V rms (measured on the prototype), is applied to its terminals and where the electric field is stronger, the worst case to consider. The central pink colored region, containing the cross-sections of the cables of the primary coil (red circles), refers to values of $|E| > 170$ V rms, that is, above the maximum recommended acceptable value for occupational exposure according to ICNIRP [72] at the frequency used. The external light blue colored region is associate with values of $|E| < 83$ V rms, which is the safe exposure limit for the general public [72]. Other colors ranging from magenta (higher values of $|E|$) to cyan (lower values of $|E|$) are use in the transition region, associated with intermediate values of $|E|$, that is, 83 V rms $< |E| < 170$ V rms.

Dynamic Inductive Wireless Power Transfer for Lightweight Electric Vehicles
Luiz Alberto Lisboa da Silva Cardoso – University of Minho

328
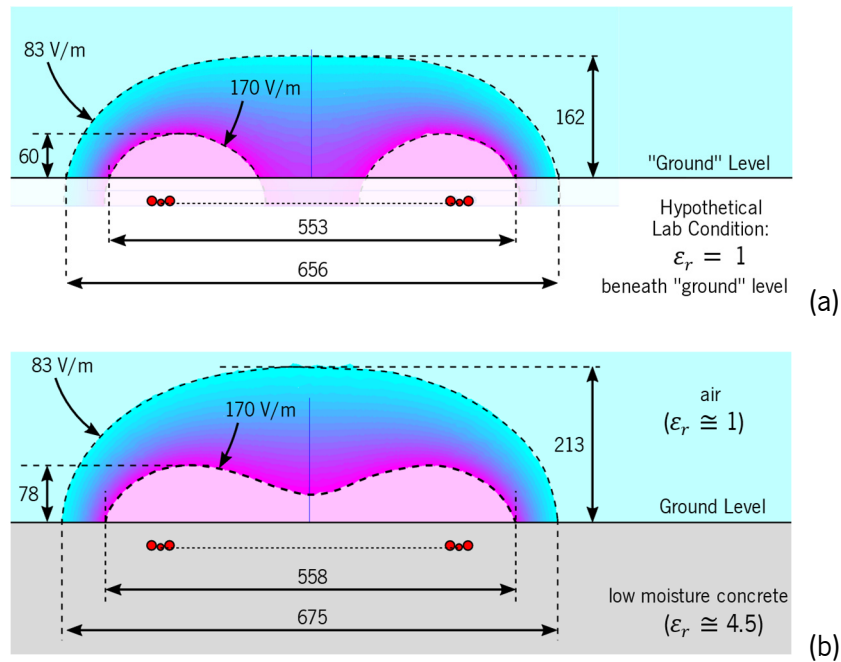
Figure 188: FEM simulation of the electric field intensity on a lane cross-section close to the feeding extremity of the primary coil, where the e-bike is not present, in two cases: (a) Prototype at ideal workbench conditions and (b) a possible outdoor implementation with concrete bed and concrete lid covering the primary coil.

Since the minimum distance of the pedestrian to the center of the lane is $w_T/2 = 750$ mm, these simulations indicate that the pedestrian is sufficiently away from the cross-section under analysis, if standing outside the lane. Two cases are considered. In the first case, shown in Figure 188a, the simulation considers the hypothetical situation where the PVC-insulated cables are idealistically suspended in air, $\varepsilon_r = 1$, or equivalently, only support materials with this relative dielectric permittivity are used. In the second case, shown in Figure 188b, the windings are considered to be buried in concrete of low moisture content (0.2%), with a relative dielectric permittivity $\varepsilon_r = 4.5$ [190]. As expected, the worst case (stronger electric fields) occurs in the case where concrete covers the primary coil, because its permittivity is higher, a situation where the recommended maximum electric field is only observed anywhere outside a diameter of 675 m from the center of the lane. This result is even compatible with the lane paved width adopted of 1.0 m. So, it can be inferred that a pedestrian standing arbitrarily close to the lane, but outside it, would not be affected by the electric field of an energized primary coil of the designed system.

5.14.2 EMF Exposure of Non-HIPLEV Riders

Riders of non-electric and standard electric bikes are deemed as pedestrians crossing the lane, because standard bikes are not capable of activating the primary coils, which will remain not energized when they are riding over them. This holds as long as the minimum longitudinal

Dynamic Inductive Wireless Power Transfer for Lightweight Electric Vehicles
Luiz Alberto Lisboa da Silva Cardoso – University of Minho

329

separation of one primary coil length $\breve{\ell}_1 \cong 3.25$ m (5.82) between a normal bike and a HIPLEV is observed, which is a reasonable requirement, a normally observed safety distance for vehicles riding at 25 km/h.

Despite the compliance to this minimum guard distance depends on rider's conscious mindset, it should be enforced as a rule. Periodic patterns painted on the lane equidistant to each other by $\breve{\ell}_1$ (or more) can help the riders to keep this minimum distance, in the same way some highways have markings to help the drivers keep safety distance for emergency breaking.

Special cases arise if a rider incidentally stops on the lane. This can be due to an accident or a mechanical failure of the vehicle, for instance. If this happens, the rider should pull the bike to the sides of the lane, at least 50 cm away from the center of the lane. The HIPLEV's rider incoming to the scene should avoid harvesting energy while passing closer than $\breve{\ell}_1$ to the stopped rider. Since the lane is relatively narrow for another rider coming to the scene to pass in good center alignment with the lane while a second rider is standing with his bike in the same lane, the primary coil activation is unlikely to happen anyway.

5.15 Summary of HIPLEV Dimensional and Power Specifications

In the previous sections of this chapter, using a step-by-step method of calculating the parameters and deciding the system geometry, the detailed DIWPT configuration and the corresponding adaptation of an e-bike as a HIPLEV was derived. The i-lane is modular, with each module consisting of an oblong rectangular primary coil, with rounded extremities, which are mechanically easier to implement.

For a first validation prototype, the IWPT design effort privileged the maximization of power transfer in the center of the lane, satisfying the minimum electrification requirements for the demonstration of the HIPLEV feasibility, while keeping the electronics as simple as possible. The resulting main mechanical and electric parameters of the system is presented in Table 33:

Dynamic Inductive Wireless Power Transfer for Lightweight Electric Vehicles
Luiz Alberto Lisboa da Silva Cardoso – University of Minho

330

Table 33: HIPLEV parameters for the.

Parameter	Symbol	Nominal Value	Reference
Minimum total lane width	w_T	1.50 m	5.3.1
Minimum lane paved width	w_L	1.00 m	5.3.1
Minimum cruise speed for stable full power transfer	v_{min}	12 km/h	[184]
Maximum speed of electrical assistance	v_{max}	25 km/h	[5]
Depth of primary coil support surface below ground	h_f	37 mm	5.6
Number of turns of primary coil	-	1	
Primary coil width	$\widetilde{D}$	405 mm	5.7.2
Primary coil length	$\breve{\ell}_1$	3.23 m r	5.9.4
Primary coil winding total cross-sectional area	A_p	30 mm^2	5.9.1
Primary coil nominal driving voltage at f_0	V_{L1}	108.4 V rms	5.9.3
Primary coil nominal current with open secondary coil	I_p	65.4 A rms	5.8
Secondary coil to ground clearance	c	100 mm	5.4
Vertical inter-coil distance	h	145 mm	5.6.1
Number of turns of secondary coil	N	11	5.8
Secondary coil external width	w_e	370 mm	5.4
Average width of secondary coil turns	$\bar{d}$	282 mm	5.7.2
Average length of secondary coil turns	ℓ_2	63 cm	5.10
Secondary coil winding total cross-sectional area	A_s	6 mm^2	5.5
Induction frequency	f_0	51.7 kHz	5.2.1.1
Maximum electric assistance to power train	P_H	250 W	[5]
Nominal DC regulated output voltage to power train	V_L	36.5 V	5.2.1.2
Maximum regulated power transfer	P_E	400 W	5.2.1.3
Minimum lane width where maximum power is available	D_e	20 cm	5.3.1
Minimum electric efficiency within maximum power range	$\hat{\eta}_{DC}$	59%	5.12
Minimum primary coil pattern-distance	$\ell_{P,min}$	3.6 m	5.13.3
Maximum primary coil pattern-distance	$\ell_{P,max}$	4.0 m	5.13.2

The dimensions of the i-lane were adjusted to match existing regulation and practices used for building electric pedal-Assisted cycles [5] and bike lanes, the same methodology could have been used for other vehicles and power levels. It is however the unique low level of required power range of such electric vehicle that allow the design to be satisfied without the use of more elaborated materials and components, while keeping the exposure to magnetic and electric fields limited to maximum recommended values, on the pedestrian reference.

A key point in the HIPLEV design is the determination of the cross-section of the magnetic link, composed by the primary and secondary coils. This was facilitated by the use of the theorems developed in Chapter 3, as approximation tools for finding a quasi-optimum solution to the positioning of the primary coil windings, once fixed the secondary coil dimensions. A cross-

Dynamic Inductive Wireless Power Transfer for Lightweight Electric Vehicles
Luiz Alberto Lisboa da Silva Cardoso – University of Minho

331

sectional view of the magnetic link for the HIPLEV prototype, annotated with the symbols of the most relevant dimensions, is shown in Figure 189. In this figure, the red dashed semicircle corresponds to the construction given by the Theorem 2 developed in Section 3.6.3, extended by one of the heuristic approximations introduced in Section 5.7.2, as given by (5.47) and (5.49).
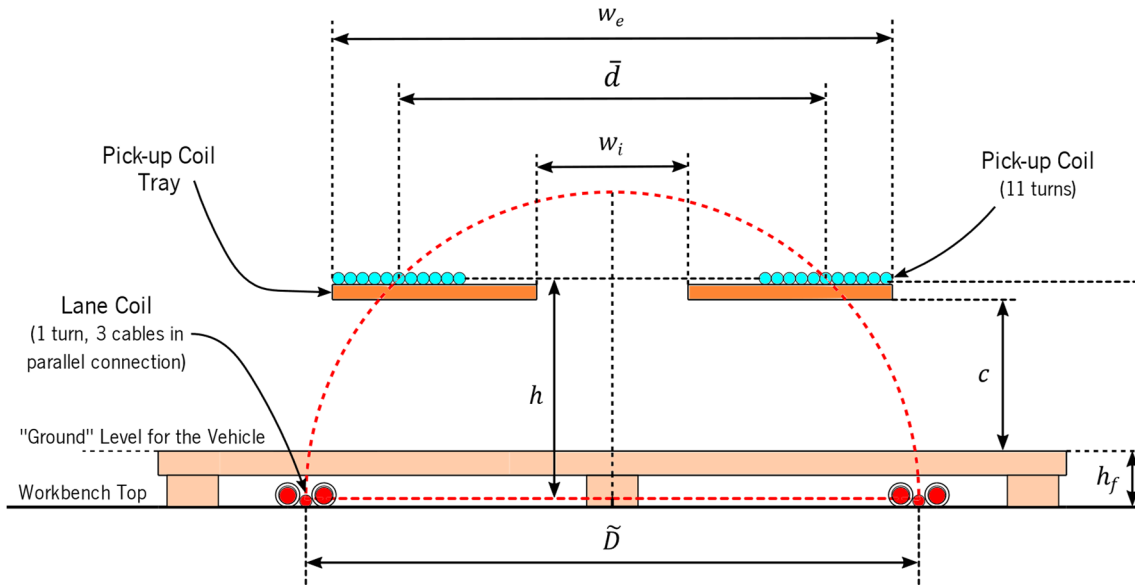
Figure 189: Cross-section magnetic link of the laboratory prototype of the HIPLEV, shown with secondary coil aligned at the center of the lane.

This simple and easily repeatable geometric construction should provide the basis for the design solution of similar applications where the dimensions of the vehicle, the maximum viable secondary coil size, the vehicle to ground clearance and the required depth below of the primary coil ground vary.

Concerning the circuitry exciting the primary coil, no special requirement on the topology is made. In the HIPLEV prototype, an auto-resonant Mazzilli-Baxandall type inverter was used for being one of the most economical choices, for being implemented with only two power transistors and using the primary coil itself in conjunction with a single capacitor bank as its resonating tank. This simple circuit automatically regulates its output voltage, keeping it approximately constant, independently of the load, what is good. However, it introduces an interdependency between the primary coil inductance (and length) and the operation frequency, which is not good, requiring all primary coils in an i-lane to have a tighter dimensional tolerance, to be driven by identical inverters in the case of real application.

For the benefit of decreasing the sensitivity of the system to the length of primary coils, thus facilitating the eventual mass production of the system, a standard H-bridge inverter 2.9.1 using

four power transistors, fixed frequency, and automatic amplitude stabilization by means of duty cycle control, could be used in future versions of the system.

5.16 Results from the Implemented Laboratory Prototype

After the secondary coil was installed on the electrified bicycle (Section 5.10) and the i-lane had been independently assembled (Section 5.11), the prototype advances for a two-step integration test. Initially, the prototype is tested without DC-DC regulation on the secondary, which allows the estimation of the magnetic link efficiency at unconstrained maximum power transfer. Then the DC-DC converter is installed, and the final performance parameters are evaluated.

5.16.1 Tests before the Integration of the DC-DC Converter

The terminals of the primary coil are connected to the Mazzilli-Baxandall inverter and the system initially powered-on with $V_{DC} = 48$ V, supplied by an Agilent 6574A programmable power source. In a first test, before installing the powertrain (hub motor and motor driver) and the DC-DC converter, the secondary was loaded up to approximately 550 W, with the aid of a pair of DC electronic loads type 6060B (Agilent and HP) connected in parallel direct to the output of the rectifier stage. The inverter starts oscillating ant the resulting excitation voltage V_{L1} produced on the terminals of the primary coil is measured at 106 V rms. A photo of the workbench configuration for this first test is shown in Figure 190.

Figure 190: First test of the partially adapted e-bike on the energized primary coil.

The electric measurements taken directly from the readings of the power source and electronic loads are normally sufficiently precise, when the equipment is calibrated, however, this

Dynamic Inductive Wireless Power Transfer for Lightweight Electric Vehicles
Luiz Alberto Lisboa da Silva Cardoso – University of Minho

333

was not assured. In order to have a consistence check on the measures and also, to avoid including in the measurements the voltage drops on the long power connection cables, other two wattmeters model I-50A were also installed in the configuration, make readings closer to the DC input of the i-lane and the DC output of the HIPLEV, as shown in the diagram of Figure 191. To simplify the figure, the multimeter used for reading the frequency, a current probe LEM model PR 30 (for reading the secondary current) and an oscilloscope Tektronix TDS320, also used, are not drawn.
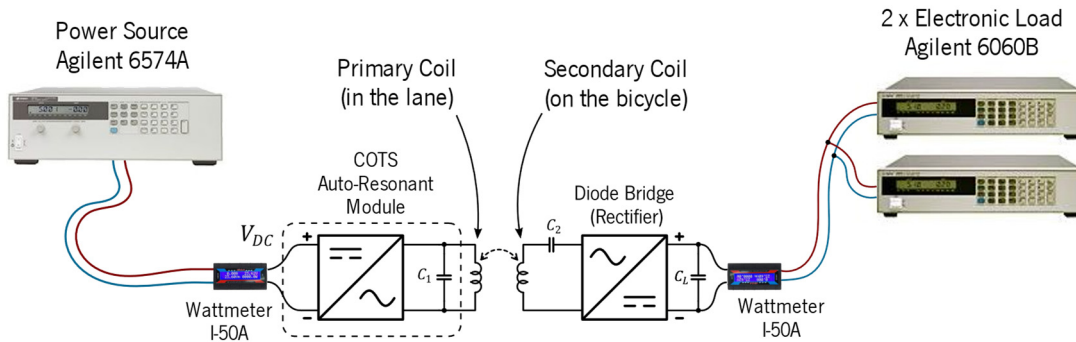
Figure 191: Configuration of the instruments used to measure the DC-to-DC power transfer to the HIPLEV, before the installation of the DC-DC converter in the secondary.

The inverter oscillation frequency was initially established at 51.9480 kHz, as measured with a Keithley 2100 Multimeter, sampling the magnetic field with a small auxiliary open-circuit coil placed over the primary coil, as shown in Figure 192b. Along the tests, the oscillation frequency was observed to slowly drift in the range of $f_{0,min} = 51.4$ kHz to $f_{0,max} = 52.1$ kHz, depending on load and temperature conditions, values which are congruent to the design value of 51.7 kHz plus a deviation of $\pm 0.5\%$.

(a)   (b)
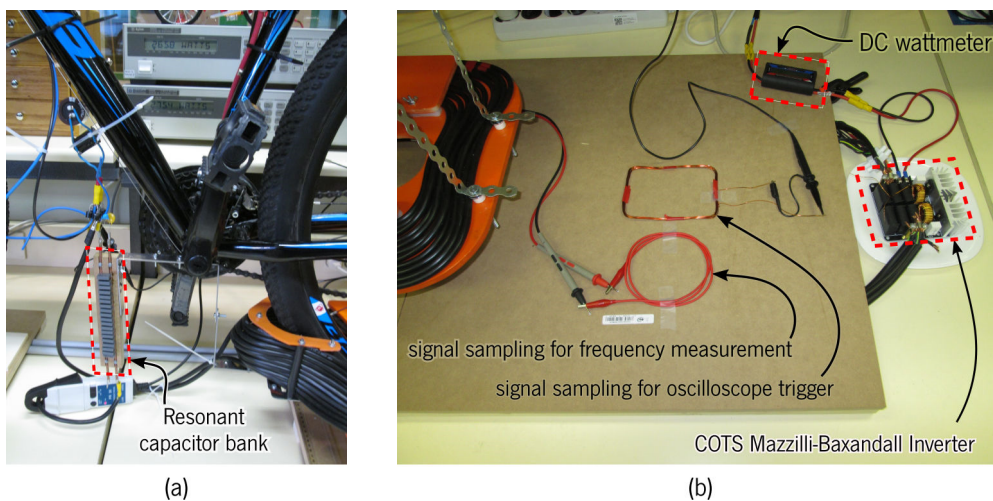
Figure 192: First tests with the secondary coil installed on the bike: (a) Position of the resonant capacitor bank and (b) connection of the COTS inverter module to the primary coil and signal sampling of primary coil voltage.

Dynamic Inductive Wireless Power Transfer for Lightweight Electric Vehicles
Luiz Alberto Lisboa da Silva Cardoso – University of Minho

334

The series resonance capacitor bank was installed on the bike in a relatively fragile assembly, as shown Figure 192a, privileging the ease of access for measurements. But since the prototype was not intended for dynamic tests, this was not a problem. It was possible to establish a good resonance in the secondary, despite the $\pm 0.5\%$ variation of the induction frequency.

The power transfer was sustained for long periods, and the instruments indicated approximately constant readings along all the time, so it was not necessary to synchronize these readings with an external clock, and the measured vales were just annotated for analysis. The measurements taken with the HIPLEV center aligned over the primary coil, crucial to an initial assessment of the power transfer capability and efficiency of the design, are shown in Figure 193 and Figure 194, and transcribed in Table 34.
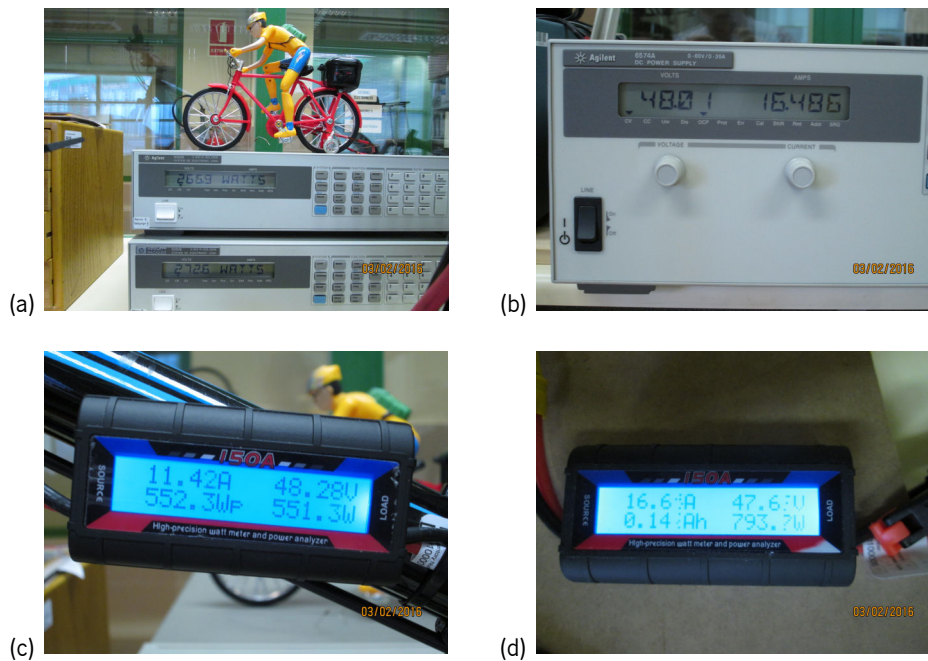
Figure 193: Photos of instruments reading DC power levels in test configuration: (a) electronic loads, (b) power source for the inverter, and wattmeters reading (c) output from secondary and (d) input to inverter.

Figure 194: Photos of the other auxiliary instruments reading: (a) secondary coil current and secondary link voltage, which is the input to the diode bridge and (b) induction frequency.

Dynamic Inductive Wireless Power Transfer for Lightweight Electric Vehicles
Luiz Alberto Lisboa da Silva Cardoso – University of Minho

335

Table 34: Summary of 3D magnetic field simulations run to estimate the induced voltage on secondary coil.

Instrument	Voltage (V)	Current (A)	Resistance (Ω)	Power (W)
Power source, Agilent 6574A	48.01	16.486	—	791.5
Wattmeter I-50A #1, at inverter input	47.68	16.63	—	793.2
Wattmeter I-50A #2, at rectifier output	48.28	11.42	4.228	551.3
Electronic load I, Agilent 6060B	47.63	5.606	8.496	267.0
Electronic load II, HP 6060B	48.27	5.682	8.496	274.3
LEM PR 30 probe (via TDS 320)**	1.76	17.6	—	—
TDS 320, square wave input (level)***	52.8	—	—	—

*The numbers in color violet were obtained by computation, based on other readings of the same equipment.
**Peak value, the current probe sensitivity is 100 mV/A.
***Average value estimated on the oscilloscope screen (peak value was 52.8 V).

By looking at Table 34, it can be realized that, although the measurements from the different instruments do not match perfectly, there is a good general agreement. The electronic loads, stacked on topo of each other and connected together in parallel by a short wire, after being programmed in resistive mode with the same resistance ($8.496\ \Omega$), they should provide equal power readings, but their readings differ by 2.7 %. The I-50A used are newer equipment, but the manufacturer does not specify precision, only resolution. But in previous tests, their precision was indicated as being better than 0.5%. Particularly, they showed a good agreement with the HP 6060B, diverging from the readings of the electronic load I Agilent 6060 B, which was deemed as exhibiting more error. So, considering the load power, instead of using the direct readings provided by the electronic loads, $267\ \mathrm{W} + 274.3\ \mathrm{W} = 541.2\ \mathrm{W}$, the decision was to discard the measurement provided by electronic load I and replace it by the same value read by electronic load II, making an average with the value read by Wattmeter I-50A #2, $551.3\ \mathrm{W}$, which in incidentally is closer to the double of the value measured by the HP 6060B, $2 \times 274.3\ \mathrm{W} = 548\ \mathrm{W}$, further supporting the hypothesis that the measurement provided by electronic load II is better than that provided by electronic load I. The estimated power delivered to the load is then $(551.3\ \mathrm{W} + 548\ \mathrm{W})/2$, at a voltage $V_L = 48.28\ \mathrm{V}$ and current $I_L = (11.42 + 2 \times 5.682) \cong 11.4\ \mathrm{A}$.

The power loss in the primary coil, $P_{1,0}$, can be indirectly evaluated based on the knowledge of the sum $P_{Inv,0} + P_{1,0} + P_{2,0} + P_{R,0}$:

Dynamic Inductive Wireless Power Transfer for Lightweight Electric Vehicles
Luiz Alberto Lisboa da Silva Cardoso – University of Minho

336

$$P_{Inv,0} + P_{1,0} + P_{2,0} + P_{R,0} = \frac{791.5 + 793.2}{2} - \frac{551.3 \text{ W} + 548 \text{ W}}{2} \cong 243 \text{ W}, \qquad (5.109)$$

where $P_{Inv,0}$, $P_{1,0}$, $P_{2,0}$ and $P_{R,0}$ are similarly defined as in Table 30, but sub-indexed by zero, to indicate the particular condition center alignment condition in this test prior to the DC-DC integration. By noticing that $P_{Inv,0} = (1 - \eta_P)(791.5 + 793.2)/2 = 39.6 \text{ W}$, it can be inferred that:

$$P_{1,0} + P_{2,0} + P_{R,0} \cong 203.4 \text{ W} \qquad (5.110)$$

But $P_{2,0}$ and $P_{R,0}$ can be estimated on basis of the secondary current:

$$P_{2,0} = 2N(\bar{d} + \ell_2)\rho_{2,b}\left(I_L \frac{\pi}{2\sqrt{2}}\right)^2 = 24.1 \text{ W} \qquad (5.111)$$

$$P_{R,0} \cong 2V_D\, I_L \cong 16.0 \text{ W} \qquad (5.112)$$

From (5.110), (5.111) and (5.112) it results that:

$$P_{1,0} \cong 163.3 \text{ W} \qquad (5.113)$$

Concerning the measurement of the input power to the inverter, both the I-50A wattmeter and the power source Agilent 6574A are in good agreement (0.2%). The decision was to consider the average of these two values. The estimate for the experimental DC-DC efficiency before the installation of the DC-DC converter is than given by (5.83):

$$\eta_P\, \eta_{Link} = \frac{(551.3 \text{ W} + 548 \text{ W})/2 + 2 \times 0.7 \times 11.4}{(791.5 + 793.2)/2} \cong 71.4\% \qquad (5.114)$$

Most relevant for the performance of the core part of the prototype design, the estimated efficiency of the magnetic link, based on (5.114), is evaluated at:

$$\hat{\eta}_{Link} = \frac{\eta_P\, \eta_{Link}}{\hat{\eta}_P} = \frac{71.4\%}{\hat{\eta}_P} \cong \frac{71.4\%}{95\%} \cong 75\%, \qquad (5.115)$$

which is 6% above the predicted minimum of 68.8%, established along the design procedure (Section 5.12) by using FEM numeric simulations and circuit considerations.

The experimentally obtained overall DC-DC efficiency, with inverter energized at $V_{DC} = 47.68\, V$ and in center alignment conditions of the unregulated output configuration, i.e., before the inclusion of the DC-DC converter between the rectifier and the load, is then determined:

Dynamic Inductive Wireless Power Transfer for Lightweight Electric Vehicles
Luiz Alberto Lisboa da Silva Cardoso – University of Minho

337

$$\eta_{DC,u}^0 = \frac{(551.3\text{ W} + 548\text{ W})/2}{(791.5 + 793.2)/2} \cong 69.4\% \tag{5.116}$$

5.16.2 Power Transfer on the Fully Integrated Prototype

The COTS DC-DC converter model used is the Zhengzhou Minghe Electronic Technology model ZXY - 6010S buck converter [191], with an input voltage range of 13 V to 62 V, with a maximum of 600 W power output. It works as programmable constant output voltage converter, provided that the DC input voltage exceeds the desired output by at least $\Delta V = 2\text{V}$. For lower input voltages, the output voltage follows input voltage, but with a constant voltage drop of ΔV from the input. The converter turns to constant current mode if the load tries to sink more than an also pre-programmed current value, up to 11 A. In the HIPLEV the ZXY-6010S was programmed for a 36.5 V output, with a limit output current of 11 A, because the maximum expect current is $400\text{ W}/36.5\text{ V} = 10.96\text{ A}$.

The DC-DC converter was individually tested before integration in the HIPLEV. Its efficiency η_S for representative operating conditions is reported in Figure 195, where the converter was programmed to a 36 V output voltage and 10 A maximum output current.
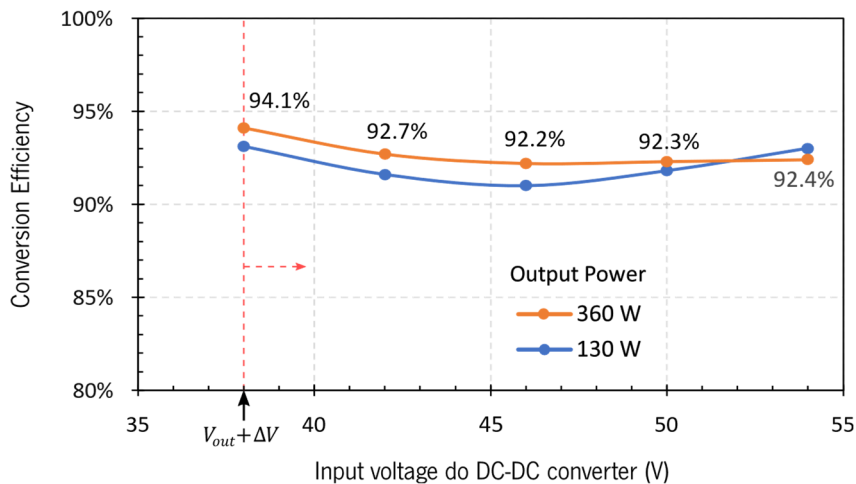
Figure 195: Experimental characterization of the DC-DC converter used in the secondary circuit.

At 360 W of output power, which is 90% of the nominal maximum HIPLEV power (400 W), η_{DC-DC} ranges from 92.2% to 94.1%, provided that the input voltage is the minimum necessary for regulation, i.e., ΔV higher than the programmed output voltage.

Using the measured values of η_S and $\eta_P \, \eta_{Link}$ in (5.83), results in a quick rough estimate for the best and worst case overall DC-DC efficiency of the HIPLEV/i-lane system prototype, at full-power (550 W) and center-alignment conditions:

Dynamic Inductive Wireless Power Transfer for Lightweight Electric Vehicles
Luiz Alberto Lisboa da Silva Cardoso – University of Minho

338

$$\eta_{DC,u}^0 \times 92.2\% \leq \hat{\eta}_{DC}^0 \leq \eta_{DC,u}^0 \times 94.1\%$$

$$64.2\% \leq \hat{\eta}_{DC}^0 \leq 65.2\% \qquad\qquad (5.117)$$

This estimated range for η_{DC}^0 (5.117), already based on measurements of the individual modules, is higher than the previously conservative estimation $\hat{\eta}_{DC}$ (5.91). This is due to the fact that $\hat{\eta}_{DC}^0$ is obtained in center alignment conditions, while $\hat{\eta}_{DC}$ is the worst-case estimate for the critical limit displacement of $D_E/2$, with the DC-DC converter acting as an impedance matching circuit.

On the other hand, this preliminary estimated range for $\hat{\eta}_{DC}^0$ is further affected in the final prototype by two different effects of opposite influences:

(i) the power source voltage in the final prototype is brought from the 48 V of the preliminary experiment to closer to its design value, $V_{DC} = 48.8$ V (5.79), what increases the power dissipation in the primary coil and tends to decrease efficiency, and

(ii) by restricting the maximum output power to $P_E = 400\ W$, the current on secondary coil decreases from its previous value, thus reducing the power dissipation of the secondary coil and rectifier.

Since the nominal power dissipation on the primary coil is much higher than that on the secondary coil, the first effect will likely dominate the variation of the efficiency, and the resulting range for $\hat{\eta}_{DC}^0$ should be lower than that indicated by (5.117).

In the final configuration of the prototype, with the DC-DC inverter installed on the secondary, to simplify the set-up, V_{DC} is then fixed at 49 V. The induced voltage in the secondary coil is measured directly on the open circuit secondary coil, resulting in 48.89 V rms, which is just incidentally close to V_{DC}, by mere design options for the primary coil and powertrain voltages. At this nominal V_{DC}, the voltage on the primary coil became approximately 108.3 V rms, for which a nominal (open secondary) primary current of 65.3 A rms was indirectly estimated using f_0 and L_1 (5.76), since no current probe for this current level was available, at the time of the experiment.

A similar testing configuration to that used before the integration of the DC-DC converter in Figure 191 is again used, but now with the electronic loads connected instead to the output of the DC-DC converter. An annotated photo of the prototype is shown in Figure 196, with all featured circuits installed on the adapted e-bike.

Dynamic Inductive Wireless Power Transfer for Lightweight Electric Vehicles
Luiz Alberto Lisboa da Silva Cardoso – University of Minho

339
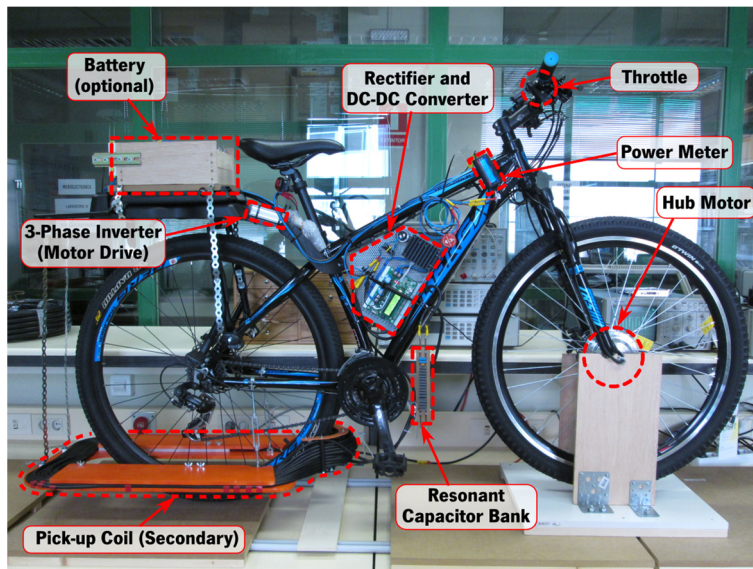
Figure 196: Adapted e-bike and DIWPT lane on workbench, ready for final power tests.

An annotated rear view of the configuration is also shown in Figure 197, where it is clearly seen the establishment of the center-alignment condition.
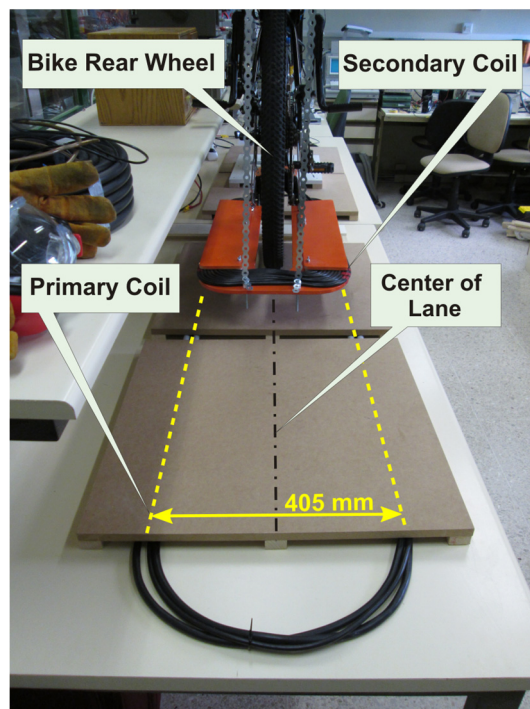
Figure 197: Workbench test with bike aligned on the center of lane (zero misalignment), rear view.

The output power level is restrained to $P_E = 400\,\text{W}$, so the unrestrained power levels previously observed without the DC-DC converter, in excess of $550\,\text{W}$, will never occur during normal operation of the system. This is done by programming the DC-DC converter to clip the rectified induced voltage to $V_L = 36.5\,\text{V}$, and limit the output current to $11\,\text{A}$, thus forcing the power output to be limited to $401.5\,\text{W}$, independently of the connected load.

Dynamic Inductive Wireless Power Transfer for Lightweight Electric Vehicles
Luiz Alberto Lisboa da Silva Cardoso – University of Minho

340

The input power to the primary coil inverter and the output power at the output of the DC-DC converter is than measured at several lateral misalignment values, from which both the experimental efficiencies and width D_e can be evaluated. This experimental data is shown in the first three columns of Table 35, where the fourth column contains the computed efficiency value.

Table 35: Experimental power data in HIPLEV prototype.

Displacement (mm)		Input Power (W)	Output Power (W)	Efficiency (%)
Raw*	Centered**			
47	-205.5	199.7	37.66	18.9
55	-197.5	217.9	52.65	24.2
75	-177.5	278.9	102.1	36.6
93	-159.5	343.4	155.9	45.4
105	-147.5	395.7	198.9	50.3
118	-134.5	456.6	248.6	54.4
132	-120.5	523.5	302.9	57.9
146	-106.5	587.9	355.2	60.4
161	-91.5	646	400.3	62.0
172.5	-80	646.8	400.4	61.9
202.5	-50	635.5	400.7	63.1
252.5	0	627.6	400.9	63.9
302.5	50	635.7	400.4	63.0
332.5	80	644.9	400	62.0
345	92.5	645.2	399.8	62.0
363	110.5	580.6	351.3	60.5
377	124.5	514.3	298.4	58.0
390	137.5	455.9	250.5	54.9
403	150.5	397.3	202.7	51.0
418	165.5	336.5	153.1	45.5
436	183.5	274.1	101.7	37.1
459	206.5	212.4	50.54	23.8
467	214.5	194	35.3	18.2

*The raw measurement is the average of two readings on millimetric rulers, one installed at the rear extreme of the secondary coil and the other a the aft of the secondary coil.
**Displacement relative to the center alignment position, for which the raw readings are 252.5 mm.
***Numbers in color violet are computed from direct measurements.

The number of points obtained in Table 35 was not too high due to the difficult of precisely realigning the e-bike at each new displacement. However, by the use of curve fitting, it was possible to extract the 400 W clipping point with resolution better than 1 mm. However, although the rulers used had uniform quality and provided good linearity and consistent measures to other available rulers available in the lab, their precision was not assured by manufacturer and they were not calibrated, thus real precision is unknow. The power levels are measured to 0.3% precision.

The power data obtained is then plotted in Figure 198 for analysis.
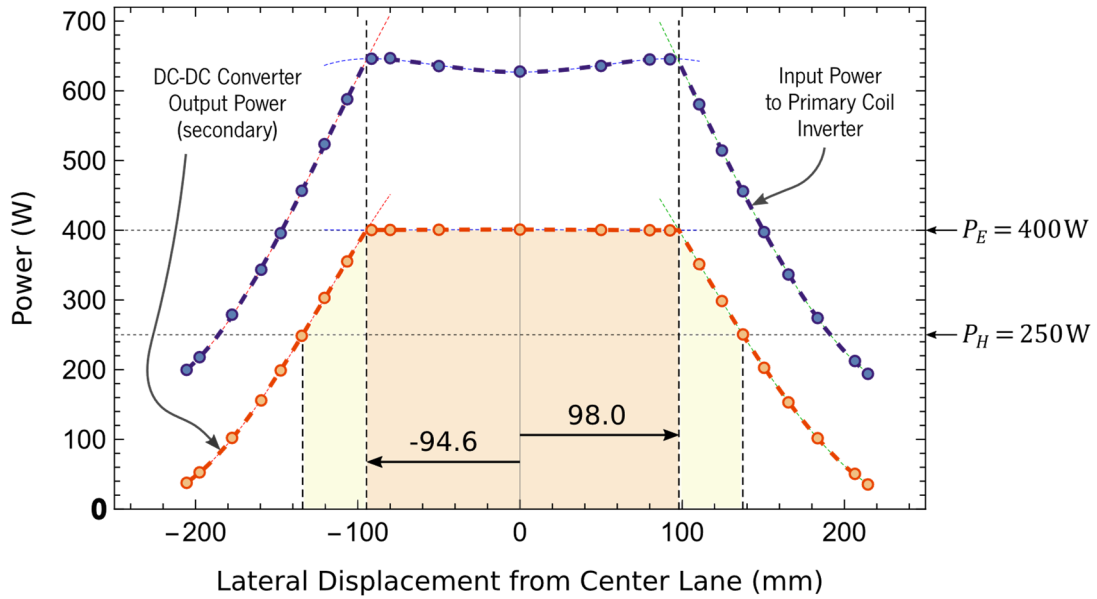
Figure 198: Experimental i-lane input and output power, as a function the lateral misalignment.

Curve fitting models of the side skirts and central output power values, and the interception points of these curves (thin red, blue and green dashed) is numerically solved for the critical lateral displacements $D_{e,left}$ and $D_{e,right}$. The solutions found (using Wolfram Mathematica) are:

$$D_{e,left} = -94.6 \text{ mm} \tag{5.118}$$

$$D_{e,right} = -98.0 \text{ mm} \tag{5.119}$$

The resulting experimental value for D_e is then given by:

$$D_e = D_{e,right} - D_{e,left} = 192.6 \text{ mm} \cong 193 \text{ mm} , \tag{5.120}$$

which is 3.5% smaller than the design value.

This error is compatible with the total error effect resulting from different simplifications used in the design. Firstly, in the approximations used in the design method, an error of up to 2.5% in the simplified heuristic estimation of $\widehat{D}$ (Section 5.7.3) is expected. To this error, an additional 1.25% error from other sources can be easily attributed, for instance, to errors in the measurements of the displacements and power levels. Then the $\varepsilon = -3.5\%$ error in D_e is completely justifiable. In addition, a simple correction initially devised for this error could consist in the reiteration of the design procedure, using $D_e = D_{e,2} = 200 \text{ mm} \times (1 - \varepsilon)$.

Dynamic Inductive Wireless Power Transfer for Lightweight Electric Vehicles
Luiz Alberto Lisboa da Silva Cardoso – University of Minho

342

The voltage supplied to the constant resistive load, mimicking the association of the powertrain and a battery management system (BMS), remained constant along all electrified width D_e, as shown by the red curve in the graph of Figure 199.
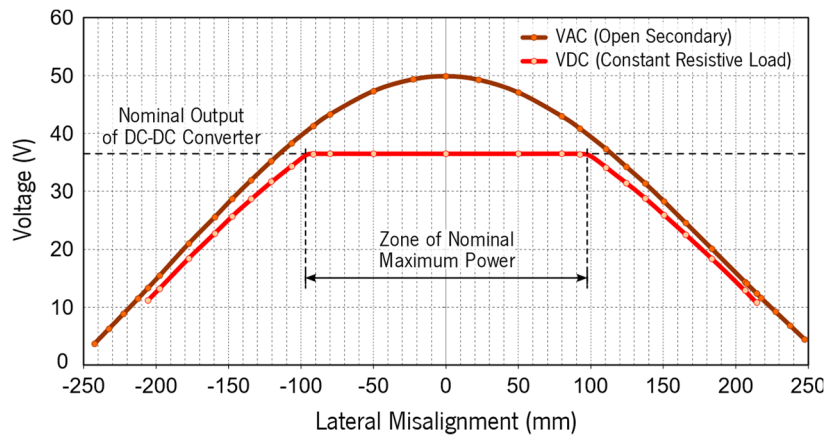
Figure 199: Experimental characterization of the open secondary voltage and the output of the DC-DC converter.

The relation between the regulated output voltage from the DC-DC converter in the secondary and the rms induced voltage, which can be measured with the secondary coil in open-circuit, was analyzed in Section 2.5.5. For buck converters as that used in the prototype., the DC output voltage should then be sustained at V_L, for $E_{2,rms} \geq E_{2,min} \cong 37.8$ V (2.75).

Concerning the efficiency, the numbers obtained were very much in the range expected, from a lower value at the maximum critical displacements, as given by (5.91), to its best value, in center alignment conditions, as approximated by (5.117). Using the experimental data of Table 35, the efficiency curve, as a function of the lateral displacement, is then plot in Figure 200.
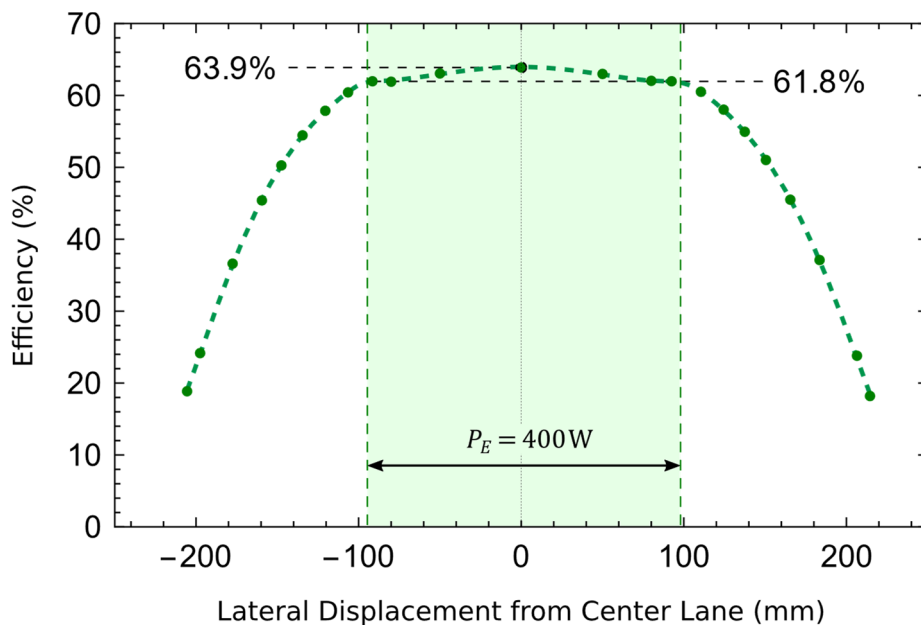
Figure 200: Experimental efficiency curve, all as a function the lateral misalignment.

Dynamic Inductive Wireless Power Transfer for Lightweight Electric Vehicles
Luiz Alberto Lisboa da Silva Cardoso – University of Minho

343

It can be concluded that the efficiency figures found for the HIPLEV, ranging from approximately 64% in center alignment conditions to approximately 62% in critical lateral displacements were entirely compatible with the design estimates. These values are also in excellent agreement with the partial efficiency estimated for individual modules of the HIPLEV.

As a conclusion, the design power and efficiency levels were successfully achieved, with the 7 mm (−3,5%) error observed in the center strip of maximum transfer power considered not to interfere with the HIPLEV proof of concept. Both because the error is not relevant itself and because it can be easily corrected by iterating the design.

5.16.3 Analysis of Errors and Correction of the Experimental Setup

Although the error $\varepsilon = -3.5\%$ obtained in the width of the i-lane's P_E-electrified width, D_e, is within its maximum expected range, it originated a few concerns, since in previous free-play experimentations with the theorems and procedures developed, errors less than 2.5% were usually found. That small elevation in the error, compared to that observed in other prototypes, was also accompanied by the reduction of the predicted best efficiency also by about 1%. This raised the suspicion of some ongoing unforeseen losses, or the presence of some unintentional magnetic shaping effect, affecting the magnetic link.

The mere repetition of the measurements did not show any improvement in the error, on the contrary the measures exhibited consistency from trial to trial. Not many repetitions were carried out, due to the difficult to take measurements in many points, which required manual realigning the bicycle on top of the workbench, at newer displacements. The repositioning of the bike also tends to move the cover lids of the primary coil slightly. Despite the fact that the primary coil windings are immobilized by a restrained system, a new fine alignment check of the primary coil underneath the lids is necessary, before proceeding with each new measure.

Although the high aluminum bike frame and aluminum wheel rims were considered not to interfere significantly with the power transfer, for the sake of the investigation of the error source, a new set of measurements was carried out, with only the secondary coil on the lane, connected to the secondary circuitry as is the HIPLEV diagram. The secondary coil was removed from the bike and positioned on the lane, as shown in Figure 201a, for ease in obtaining more detailed and precise measures. Any eventual discrepancies found in the measurements taken in this new configuration could indicate an unexpected higher influence of the bike frame. The reason could be that the bike frame could either be limiting the precision of the positioning, or, due to unforeseen

Dynamic Inductive Wireless Power Transfer for Lightweight Electric Vehicles
Luiz Alberto Lisboa da Silva Cardoso – University of Minho

344

losses, it could be affecting the power transfer itself. The displacement values were again similarly averaged from measures taken on the two opposite extremities of the secondary coil, as illustrated in Figure 201b.

(a) (b)
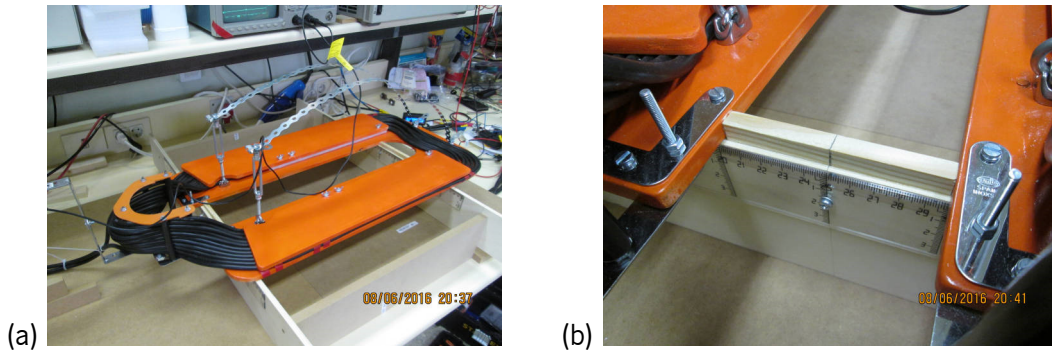
Figure 201: Measuring induced voltage with the secondary coil only positioned over the primary coil.

To eliminate other source of errors, before measuring the transferred power, this time a consistency check of the induced voltage with open circuit secondary was first conducted, with a larger number of displacement points inspected, from about -250 mm to 250 mm. The values were compared not to the predicted values provided by the approximation given by (3.123) (3.124), of Theorem 1, but to full FEM model of the coils, with their multiwire conductors. If the bike frame could cause any disturbance on the power transfer, at least in this test this disturbance would not appear, and a good agreement with the FEM numeric simulations should be obtained.

However, the new results did show a small divergence between the measured induced voltage, and the induced voltage that was expected in the model, even with the bike removed from the secondary coil. While the errors observed in displacements close to zero were negligible, but they became increasingly higher, as the coil position was moved away from center lane in both directions, specially above $D_e/2$. The distribution of the error was also noticed to be slightly asymmetric (left and right) around the center of the lane, being higher inward the workbench (negative displacements), as show in the graph of Figure 202. This was a clear indication that some factor not related to bike frame was affecting the setup. Also, since this measurement was done with the secondary unloaded (secondary coil with open circuit), the error could not be attributed as well to the approximations done by neglecting the back induced current.

Dynamic Inductive Wireless Power Transfer for Lightweight Electric Vehicles
Luiz Alberto Lisboa da Silva Cardoso – University of Minho

345
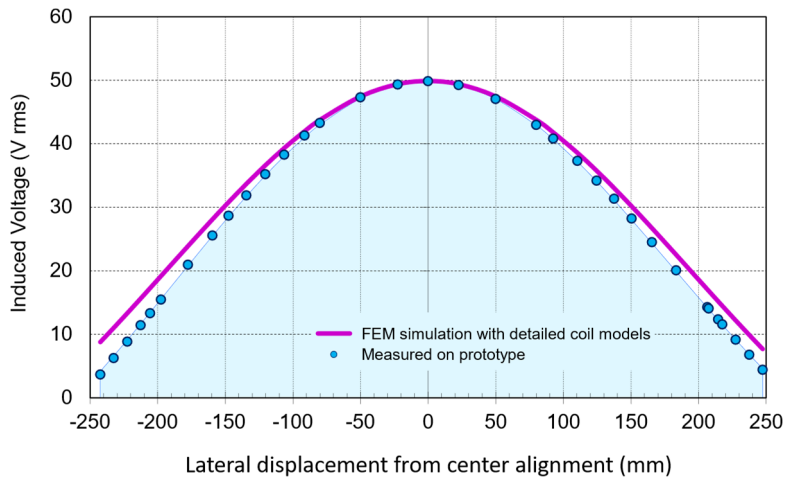
Figure 202: Anomaly found in the induced voltage.

The anomaly found in the induced voltage was small close to the center of the lane, and up to approximately 100 mm away for the center, the region of upmost importance for the HIPLEV application, and it did not interfere with the proof of concept for the design. However, at higher displacements and lower induced voltages, the error could amount to more than 50%, what is not acceptable. For instance, at -252.5 mm, the induced voltage predicted by the FEM model is $\sim\!6.6\text{ V}$, whereas the voltage measured was $\sim\!1.8\text{ V}$. At 247.5 mm, the predicted voltage is $\sim\!7.7\text{ V}$ and $\sim\!4.5\text{ V}$ was measured. This unexpected error, observed despite the bike not being attached to the secondary coil, could easily contribute to the small reduction observed in the electrification width D_E, from 200 mm to 193 mm, as reported in 5.16.2.

At this point of the investigation, the major concern of the design became the coil activation schema, and the prototype was translated to a new, more spacious test site for the HIPLEV, in another laboratory room. As a last improvement in the power circuitry, a new rectifier bridge with multiple matched Schottky diodes in parallel and higher breakdown voltage (100 V) was installed on the secondary, next to the DC-DC converter, as shown in Figure 203.
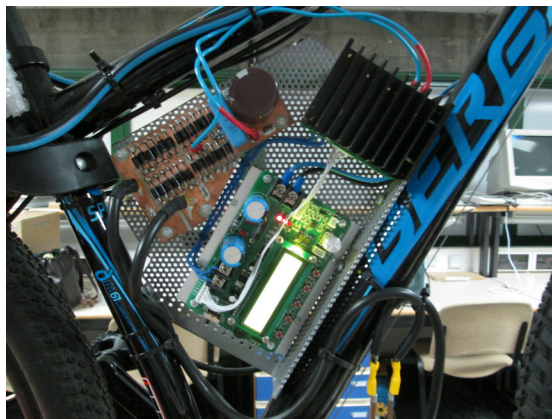
Figure 203: Detail of the installation of improved rectifier and DC-DC converter on the bike's frame.

Dynamic Inductive Wireless Power Transfer for Lightweight Electric Vehicles
Luiz Alberto Lisboa da Silva Cardoso – University of Minho

346

This new set up, using all wooden workbenches, is shown in Figure 204.

Figure 204: HIPLEV prototype on new all-wooden test workbench, shown with primary coil totally covered.

Before proceeding with other scheduled design activities, related to the development of the activation of the primary coils based on RFID detection (Section 5.18), it was deemed as a good practice, to test the HIPLEV prototype again, for power transfer and efficiency.

In this new test site, another faster but less precise method for measuring the lateral displacement of the bicycle was used: The position of the bike was simply estimated by measuring the distance of the center of the bike rear tire to the center of the lane, with a metric tape. Preliminary tests indicated an estimated precision tolerance of $\pm\,0.3$ cm. It was then verified that a new nominal value for the P_E - electrified width of 19.7 cm was achieved, this time with no asymmetric pattern shown on the induced voltage, even at higher lateral displacement values.

The efficiency in central alignment conditions was also observed to increase to 65.5%, approximately 1.5% higher than was obtained in the previous setup (Figure 196 and Figure 197).

In addition to validating once more the power transfer design, these new observations provided an indication of the existence of a vicious factor affecting the measurements in the first set up. In order to completely clarify the facts, it was then necessary to go back and reexamine the first setup.

Dynamic Inductive Wireless Power Transfer for Lightweight Electric Vehicles
Luiz Alberto Lisboa da Silva Cardoso – University of Minho

347

Reviewing the several photos taken at the first test site, it was realized that the wooden workbenches used to support the primary coil (and the bicycle over it) had a metal frame structure, as shown in Figure 205. Although this had had no apparent effect in earlier, smaller stationary and dynamic prototypes previously tested on the same workbench, it could have affected the HIPLEV, due to its larger dimensions. The reason could be related to either the larger size of the prototype, or the higher current levels involved.
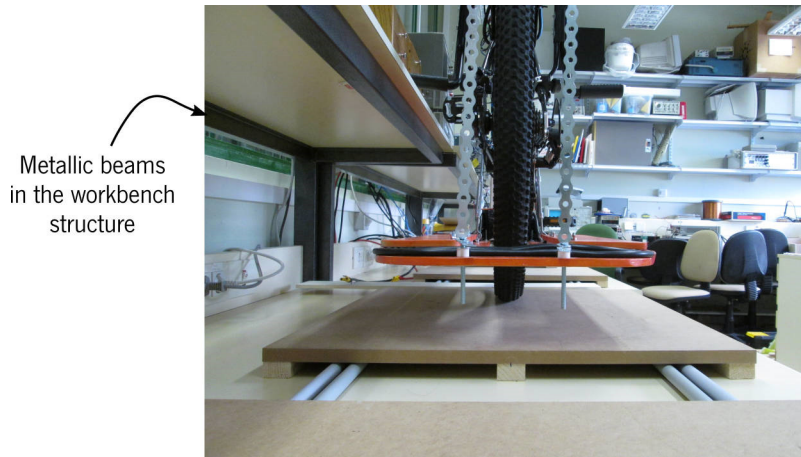
Figure 205: Another rear view of e-bike on DIWPT lane, showing detail of workbench steel beams.

The carbon steel beams embedded in the workbench were initially assumed to be far enough from the primary and secondary coils, and were neglected. In the first study prototypes, the coils were small and could be well centered on the workbench top. However, as the sizes of the prototype coils become larger, relatively to distance between these coils and the steel beams, they might have become less negligible. It was also noticed that the steel beams are soldered together, incidentally forming concealed coils, which can be induced by the same magnetic field generated by the main pair of coils in the prototype, exhibiting parasitic currents and parasitic losses. These are difficult to measure directly, because it might be necessary to damage the furniture do it, but they can be evaluated based on FEM modeling.

To mechanically support the HIPLEV prototype, three 1.50 m long workbenches were aligned side by side. The workbench used was measured and modeled in 3D and then the model was simplified, as shown in Figure 206.

Dynamic Inductive Wireless Power Transfer for Lightweight Electric Vehicles
Luiz Alberto Lisboa da Silva Cardoso – University of Minho

348
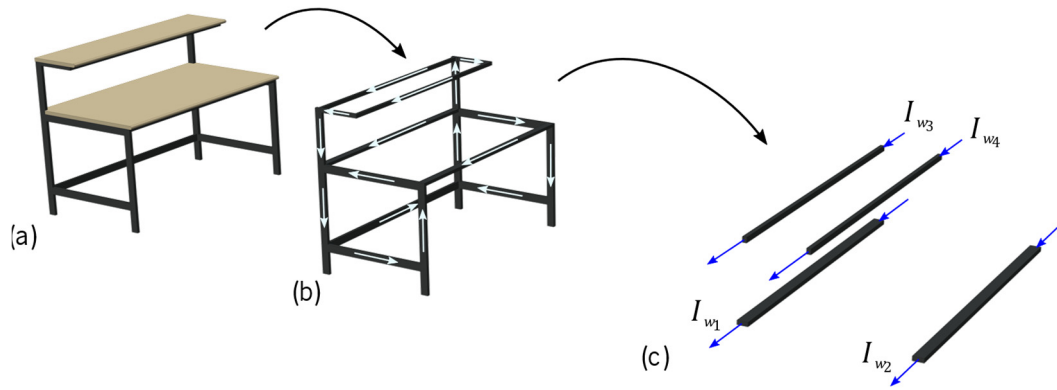
Figure 206: Identification of the most relevant structural elements of the workbench interfering with the magnetic field generated by the primary coil: (a) From the original workbench, (b) only the metallic structural elements are considered, and (c) from these, only the closer loops to the primary coil are modeled.

Considering that the three vertical loops on the sides of the workbench are orthogonal and further away from the primary coil than the upper loops, they were initially suppressed from the electric model of workbench. Based on this simplification, the sum of the currents I_{w_k}, $1 \leq k \leq 4$, traversing the steel beams that are closest to the prototype coils (Figure 206c) should be approximately equal to zero, as if the steel beams were simply short circuited together at their extremities:

$$I_{w_1} + I_{w_2} + I_{w_3} + I_{w_4} \cong 0, \tag{5.121}$$

This new experimental configuration can be simulated using the 2D geometry of the cross-section, with (5.121) as a constraint in the FEM model. A circuit model with series lumped inductances for each steel beam was integrated with the FEM model, each of these inductances being equivalent to the partial contribution of each beam to the loop inductance. The values of these lumped inductances were experimentally adjusted at $L_{U_k} = 400$ µH for beams numbers $k = 1$, 3 and 4, and at $L_{U_2} = 615$ µH for beam number 2, the bean on the front of the workbench, the one that is most detached from the group of steel beams. In summary, the simulation integrated the primary and secondary coils with the finite element model and circuit elements of the steel beams, as represented in Figure 207.

Dynamic Inductive Wireless Power Transfer for Lightweight Electric Vehicles
Luiz Alberto Lisboa da Silva Cardoso – University of Minho

349
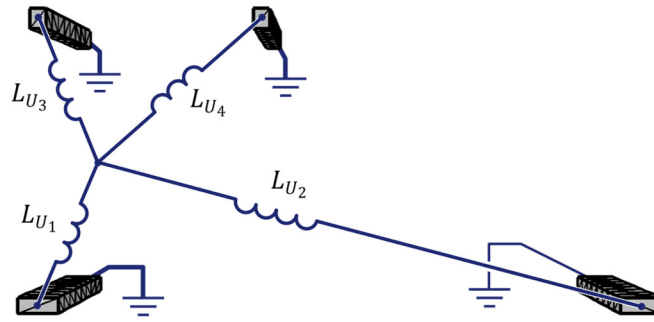
Figure 207: Hybrid circuit-FEM with lumped serial inductances, as a simplified model for the workbench.

The steel beams are hollow rectangular carbon steel bars, with a wall thickness of about 1.5 mm, and two different cross-section dimensions are used in the construction of the workbench. The resistivity of carbon steel is about eight times higher than that of copper, while its magnetic permeability is approximately 100 times higher. The electromagnetic skin depth (2.107) in carbon steel is then $\sqrt{8/100} \cong 28\%$ that of copper, at the same frequency. At the frequency used, $f_0 = 51.7$ kHz, the skin depth of the steel beams is approximately 80 μm, almost 20 times smaller than the average thickness of their walls. Because of that, as a further simplification of the geometry, the hollow steel beams can be modeled as solid carbon steel parts, for the effect of computing AC resistance, currents, their influence on the magnetic field generated by the primary coil, and consequently, the induced voltages on the secondary coil.

After creating the profiles of the steel beams in the cross-section, at the correct relative position to the primary coil, and including the equivalent inductances in the circuit definitions of the model, a hybrid circuit-FEM simulation is run using COMSOL Multiphysics. This resulted in estimations for the currents flowing in the steel beams, and reveal that the workbench metal structure is capable of producing a magnetic field component, in response to the current being imposed on the primary coil, as shown in Table 37. It can be noticed that, although the currents found on the primary coil cables are very similar to that found when not considering the workbench, there is an unexpected slight asymmetry in the currents of cable A and C. Specially, there are now currents on the steel beam, previously unconsidered.

Dynamic Inductive Wireless Power Transfer for Lightweight Electric Vehicles
Luiz Alberto Lisboa da Silva Cardoso – University of Minho

350

Table 36: Currents and losses in primary coil and structural elements of the workbench.

Conductors	Symbol	Current (A rms)**		Losses (W/m)
Cable "A"*	I_A	28.2+1.18j	(43.2%)	26.6
Cable "B"*	I_B	$8.57 - 2.42j$	(13.1%)	2.64
Cable "C"*	I_C	28.6+1.24j	(43.7%)	27.3
Steel Beam #1	I_{w_1}	$-8.72 - 0.046j$	(13.3%)	0.291
Steel Beam #2	I_{w_2}	$13.6 + 0.070j$	(20.8%)	0.806
Steel Beam #3	I_{w_3}	$-2.94 - 0.016j$	(4.50%)	0.041
Steel Beam #4	I_{w_4}	$-1.49 - 0.008j$	(2.28%)	0.034

*Current established by imposing a total real current of 65.4 A rms on the parallel association of A, B and C.
**For single conductors, currents are positive when going outwards of the cross-section; for cables of the primary coil, current is positive when leaving the cross-section on the left.

The losses reported in Table 37 are entirely due to resistive losses. The losses due to the magnetic field in the carbon steel core were also estimated, but turned out to be negligible, in face of the ohmic losses and the relatively low field intensity to which the steel beams were exposed. The workbench beam loops are approximately 1.50 m x 0.80 m (supporting the workbench top), 1.50 m x 0.35 m (supporting the shelf) and 1.50 m x 0.40 m (back frame). Then the total power loss in one workbench can be estimated as:

$$P_{wb} \cong 0.291 \frac{W}{m} \times 1.50 \text{ m} + 0.806 \frac{W}{m} \times (1.50 \text{ m} + 2 \times 0.80 \text{ m}) + \tag{5.122}$$

$$+ 0.041 \frac{W}{m} \times 1.50 \text{ m} + 0.034 \frac{W}{m} \times (1.50 \text{ m} + 2 \times 0.35 \text{ m}) +$$

$$+ 0.806 \frac{W}{m} \times \left(\frac{I_{w_3} + I_{w_4}}{I_{w_2}}\right)^2 \times (2 \times 0.40 \text{ m}) \cong 3.14 \text{ W}$$

As one primary coil is about 3.25/1.50 times longer than one workbench, requiring the support of three of them, the total estimated power loss in the workbenches, P_{LOSS}, is estimated at approximately:

$$P_{LOSS} \cong 3.14 \text{ W} \times 3.25/1.50 = 6.8 \text{ W} \tag{5.123}$$

This is a little more than 1% of the required power input to the primary inverter to transfer the nominal power $P_E = 400$ W to the vehicle. So, expectedly the use of that particular setup to test the HIPLEV can additionally reduce the efficiency at full load by approximately 0.7% as well.

Dynamic Inductive Wireless Power Transfer for Lightweight Electric Vehicles
Luiz Alberto Lisboa da Silva Cardoso – University of Minho

351

Although the power transfer and the efficiency are not significantly impaired due to the use of a less than ideal metallic-frame workbench, the parasite currents in the steel beams also affect the magnetic field sensed by secondary coil. This non-intentional effect is equivalent to shaping the magnetic field (Section 3.6.4.3) generated by primary coil. The results as shown by the plots of the magnetic field intensity on the cross-section of the magnetic link resulting from FEM simulations, in Figure 208.
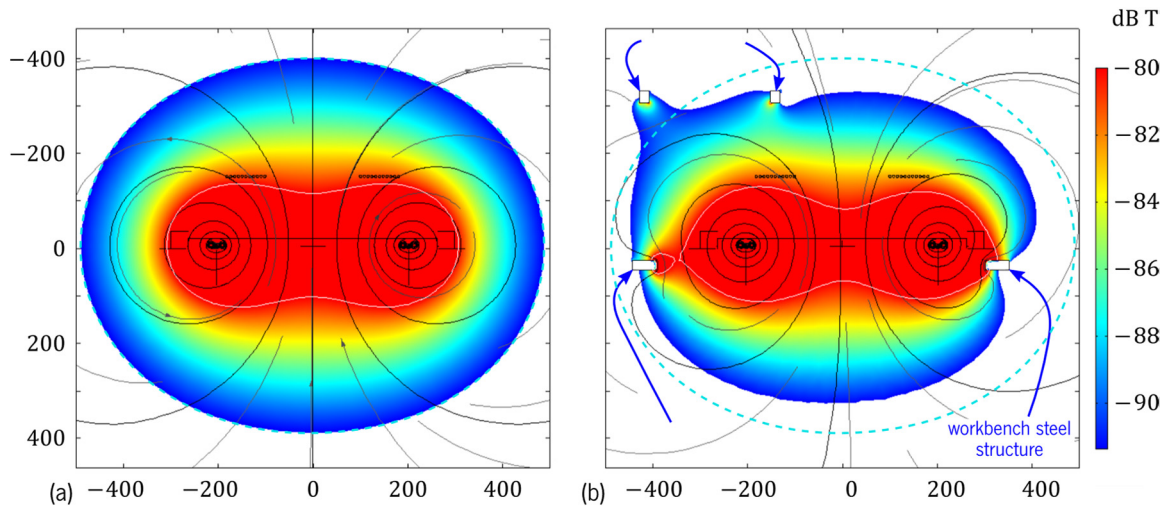
Figure 208: The effect of the workbench in the model of the magnetic field: (a) Workbench is not considered, and (b) workbench steel structure is included in the model. Cross-section dimensions are in mm.

The steel beams, though relatively far from the primary coil, function as a semi-open metallic cage around that coil, which contain loops that tends to confine the magnetic field somewhat, as shown in Figure 208b.

The concordance of the experimentally obtained induced voltage data with that predicted with two models, the first of them, not considering, and the second, considering the effect of the workbench metallic structure, can be compared in Figure 209. It can be noticed that by considering the workbench steel frame in the model, excellent agreement is now obtained between the experimental induced voltage and the values predicted by the full model, including with the justification of a slightly asymmetric distribution on the edges of the lane.

Dynamic Inductive Wireless Power Transfer for Lightweight Electric Vehicles
Luiz Alberto Lisboa da Silva Cardoso – University of Minho

352
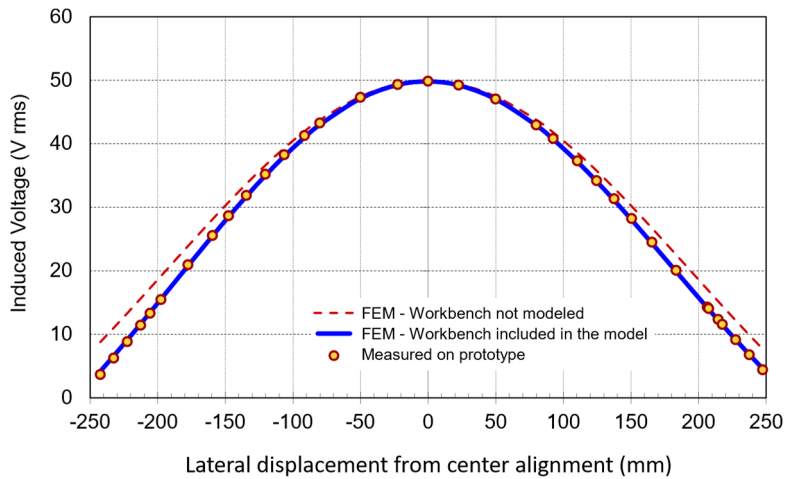
Figure 209: Comparison of prediction models for the induced voltage on secondary coil with data measured on the prototype: with and without the metal structure of the workbench considered.

For easier visualization of predicted voltages under the two models, the same information presented in Figure 209 is plotted in terms of relative errors, in the graph of Figure 210. The blue curve (b) representing the errors of the adjusted model using the workbench geometry and material information has an essentially flat error, less then $\pm 0.5\%$, along all the displacement interval from -200 mm to 200 mm. The red curve (a), on the other hand, representing the prediction errors using the excessively simplified model (which unconsidered the workbench) exhibits negative errors with magnitude in excess of 2.5%, for displacements of ± 100 mm and over.
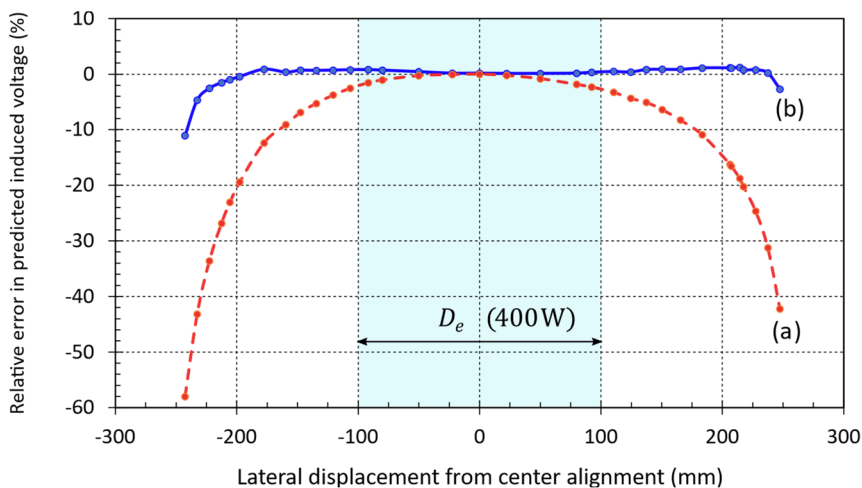
Figure 210: Prediction error of induced voltage on secondary coil: (a) Workbench steel structure neglected (b) workbench steel structure included in the model.

This explains the acceptable but, at the same time, unexpected error of 3.5% initially found in the measurement of D_e, in the prototype, and why this error disappeared when the prototype was moved to a new test site.

Dynamic Inductive Wireless Power Transfer for Lightweight Electric Vehicles
Luiz Alberto Lisboa da Silva Cardoso – University of Minho

353

5.16.4 Conclusions Derived from the Power Transfer Tests

It is requirement for the HIPLEV that the DC-DC efficiency, $\eta_{DC,min}$, is higher than 26.3% (5.9), a number high enough to guarantee overall superior energetic efficiency for the HIPLEV over heavier standard electric vehicles. This value was a priori considered totally feasible, using current technology, based on DIWPT prototypes described in the literature which claim 70% to 80% under the most favorable conditions. One of the challenges in the realization of the HIPLEV prototype was to avoid the use of the best currently available technology, including advanced materials and costly circuitry. Even then, the target DC-DC efficiency, η_{DC}, was then fixed at 52.6% (5.10).

During the design phase, it was identified that the critical point for measuring the DC-DC efficiency are the extremes of the wirelessly electrified path, i.e., the external limits of the zone of assured nominal power transfer. At these points, larger currents than in any other position of the HIPLEV are expected on the secondary coil, and the nominal maximum power transfer to the vehicle is exercised under the least favorable conditions.

Using FEM simulation of the power losses and predicted efficiencies of the commercial circuit modules used to excite the primary coil and to regulate the voltage to the load, the DC-DC efficiency of the design was estimated to be greater or equal to $\hat{\eta}_{DC} = 59.3\%$ (5.91), with the vehicle harvesting full power $P_E = 400$ W. At misalignment values lesser than $D_e/2$, i.e., with the vehicle better aligned in the lane, efficiencies slightly better than $\hat{\eta}_{DC}$, but certainly less than 69.2% were expected.

The prototype vehicle was tested under stationary conditions, in the upright position, immobilized over the inductive lane module by means of a wooden front wheel support. The measurements of input power to the Mazzilli-Baxandall inverter and the output of the DC-DC converter at the secondary connected to a digital electronic load were then logged. An electronic load array was programmed into the constant resistance mode, to emulate the powertrain, which was actually installed and fully functional, but was not used in the tests.

Though using simple materials (no true litz wire and no ferrites) the design presented is deemed satisfactory due to its peak efficiency of 64%, and a sustained efficiency of 62% over the entire operational range of vehicle misalignment. These values surpass the requirements established for the system and lie well within the predicted range of efficiency, at design time, of 59% to 69%.

Dynamic Inductive Wireless Power Transfer for Lightweight Electric Vehicles
Luiz Alberto Lisboa da Silva Cardoso – University of Minho

354

5.17 HIPLEV and Inductive Lane Integration

Whilst the first HIPLEV prototype consists of a single primary coil, built solely to test the power transfer capability of the system, in a real i-lane application, several are primary coils must be deployed on the lane, to provide an electrified path for the HIPLEV. Each of the coils has to be compensated by a compensation network, which, in the case of the protype, is made of a single bank of capacitors that resides in the Mazzilli-Baxandall inverter board. However, another arrangement for the circuitry, using resonant inverters, is also proposed, pairing each two consecutive primary coils' circuitry in one box, in order to reduce the number of manhole boxes along the lane, thus simplifying the installation and maintenance routines.

In this context, the minimum lane module, instead of consisting of a single primary coil, could be composed of two neighbor primary coils, one single common DC power supply, two resonant inverters and two passive compensation networks. A general view of a possible implementation of the electronics in one of these modules, which details are not in the focus of this work, is shown in Figure 211.
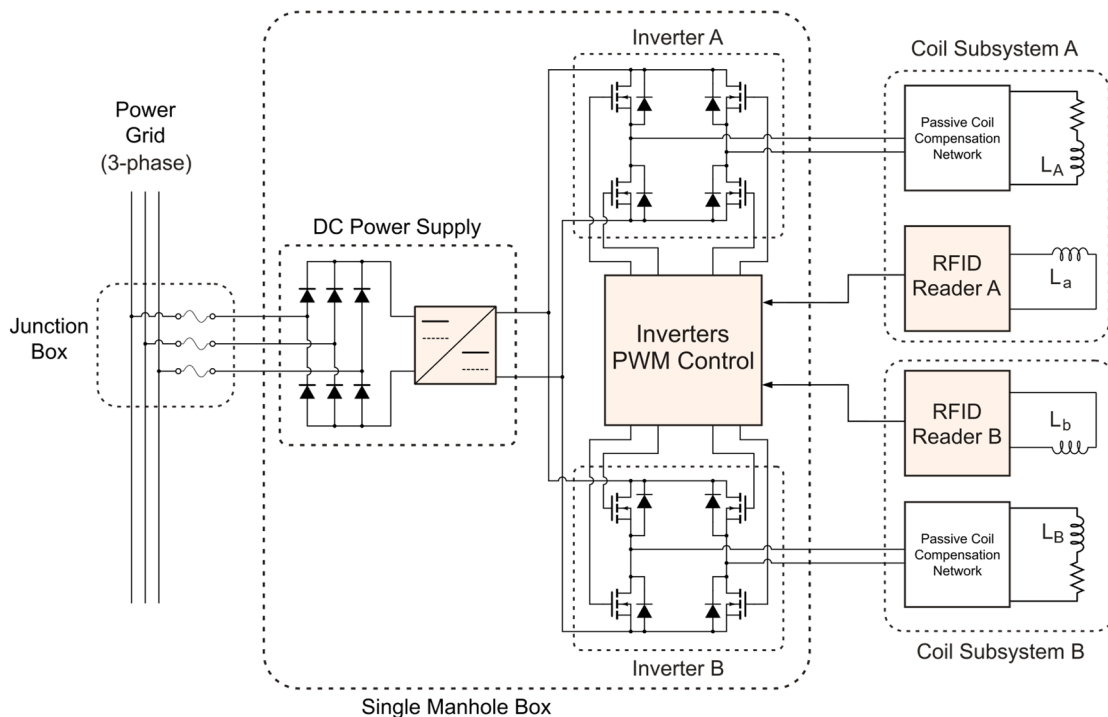
Figure 211: Block diagram of the electronics for controlling an i-lane module with two primary coils.

Derivations of the power grid are taken in junction boxes, which may contain fuses or other type of protection against abnormally low impedances of the module. The grid power is rectified and then optionally filtered and converted to the multiple DC power levels used by the inverters and the control circuit, which include RFID readers (Section 5.18) or, in future implementations, other sensor devices than can detect vehicles demanding power.

Dynamic Inductive Wireless Power Transfer for Lightweight Electric Vehicles
Luiz Alberto Lisboa da Silva Cardoso – University of Minho

355

Each primary coil, A and B, has a separate sensor and activation line to request the respective inverter to turn on. The rectifier, the DC power source, the inverters and their control should reside int the same board, in the same single manhole box. The activation sensors and their low level controllers should lie together with their respective primary coil. Particularly in the case of RFID detection, the RFID reader should be directly attached by short cables to the RFID reading coil, which is partially superposed with the associated primary coil, collocated in magnetic orthogonality with this power coil.

The passive compensation networks for the primary coils could either be located on the inverter board, inside the manhole box, or they could be split, with some components in the inverter and others close together with the coils. This second option, if carefully designed, would keep the higher currents restrained to the primary coil assembly, while still avoiding electrical noise being radiated from the switching voltages on the outputs of the inverter half-bridges.

The concept of integrating the control of two primary coils can be extended for three or more coils in the same lane, or in parallel lanes, for two-way systems. This would be particularly interesting if the compensation networks are split. In this case, the cables connecting the inverter cluster in the manhole box and coils would carry less current than the primary coil windings, and not much extra cost for these cables would result.

The complete system for a one way lane should resemble the one depicted in Figure 212.
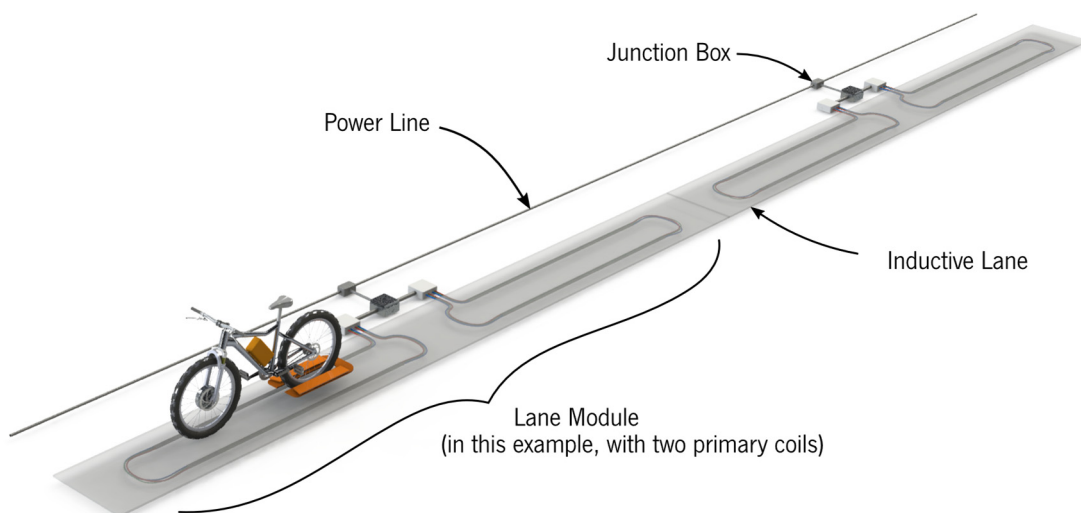
Figure 212: DIWPT-adapted e-bike, shown on inductive lane constitute by several primary coils.

The power grid line is shown running parallel to i-lane, but it is expected to be segmented, since the number of i-lane modules drawing power from the same power transformer is limited.

Dynamic Inductive Wireless Power Transfer for Lightweight Electric Vehicles
Luiz Alberto Lisboa da Silva Cardoso – University of Minho

356

5.18 Power Activation of Primary Coils

Dynamic inductive systems basically consist in embedding primary coils underneath the vehicle's path and energizing them in sequence, with AC currents, at the right timing, every time a vehicle with an on-board secondary coil is presented over each primary coil. Figure 213 shows a simplified system architecture representation of such a system. As the vehicle moves forward along its path, its pick-up (secondary) coil will sequentially cross the magnetic field generated by the stationary primary coils placed underneath vehicle's path floor surface. For safety and efficiency reasons, only the primary coils in position of significant mutual induction with secondary coils should be activated at a given time. The effectiveness of the system depends not only on good magnetic coupling and power electronic design, but also on the appropriated time-spatial coil activation pattern.
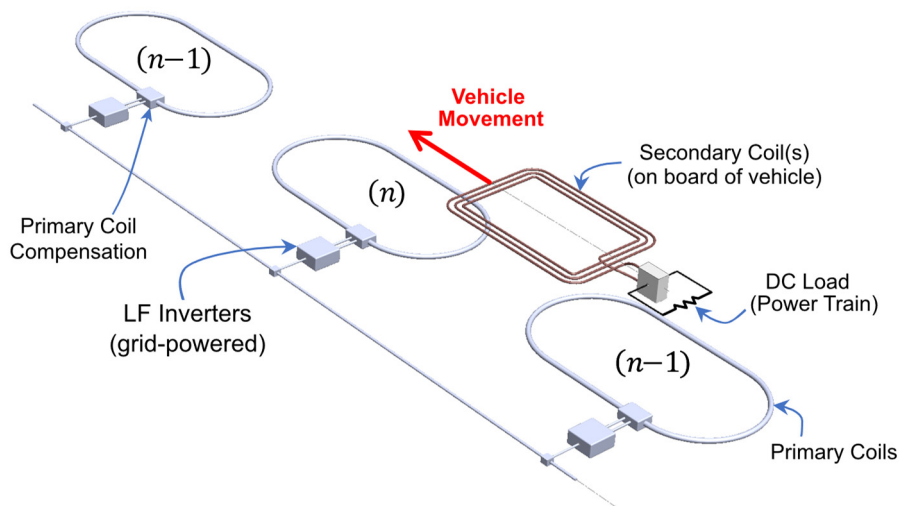
Figure 213: Schematic representation of a typical dynamic inductive wireless power transfer configuration.

Considering the vehicle cooperative behavior, the detections schemas maybe either passive as in [110] or active, draining some vehicle on-board power, as in [192].

RFID (Radio Frequency Identification) systems have been used before for wirelessly powering and reading low power sensors integrated to tags [193]. This work, however, prospects the utilization of standard near-field RFID, with both reader and tag antennas modified, as a strategy to detect primary to secondary coil alignments and activate other specialized wireless power transfer circuitry. A design was conceived targeting lightweight electric vehicles, such as pedal electric cycles (PEDELEC), also referred as electrically power-assisted cycles (EPAC) [5], where vehicles` nominal power is limited to 250 W, with possible peaks of 400W, and the maximum vehicles' speeds range from 25 to 35 km/h, depending on local legislation [3]. The principles and the analysis method can be, however, extended to higher speed electric vehicles and i-lanes.

5.18.1 RFID-Triggered Power Activation for Smart DIWPT to HIPLEV

Early lab experiments with DIWPT used photocell interruption to sense vehicle's secondary coil to lane's primary coil alignment, and sequentially power them on [110]. One passive sensing strategy has been recently proposed by Kamineni et al., at the University of Auckland [194], which is based on the magnetic coupling enhancement between two sequential primary coils when a third pick-up coil, the vehicle's on-board secondary coil, is travelling in between them. This strategy was demonstrated to work with double "D" primary coils [195] but could expectably be adapted to any other primary coil configuration, provided that these coils are closely enough spaced along the vehicle's path. The sole use of this technique, however, should not permit the initial positive vehicle identification after its detection at the first primary coil in a row.

RFID, on the other hand, have long been used on board of vehicles for both road tolling and access control. The inductive wireless power transfer concept is implicit in all passive near-field RFID. However, IWPT is used in this RFID application just to power a tag device, which can receive, store, process, retrieve and transmit information back to RFID reader, by modulating the load at the secondary that is reflected on the primary circuit through the RFID magnetic coupling.

To handle the proper activation of the primary coils for the HIPLEV i-lane, a RFID-triggered power activation system was devised, implemented, and tested as the key sensing mechanism for controlling wireless power transfer from an inductive lane to a moving lightweight electric vehicle. The RFID would then provide the means for both the detection and the identification of the vehicle.

In order to fit lightweight electric mobility application requirements, the RFID magnetic antennas were redesigned to larger than standard sizes, both at reader and tag sides, increasing the detection volume without increasing the required reading power, and permitting the reuse of commercial RFID circuits and embedded protocol software. To trigger the wireless power transfer, an RFID reader coil is placed magnetically orthogonal to each primary power coil to be controlled, at the extremity where electric vehicles are expected to come from, in a one-way traffic. After triggering the WPT, the RFID operation becomes irrelevant, and the power is turned off automatically when the vehicle leaves the primary coil field and the power demand is extinguished, or when time-out is reached. An inductive lane constituted of a sequence of such RFID-controlled primary coils can detect the presence of authorized electric vehicles and smartly energize the lane, manipulating the unique identifier codes and other information stored in the on-board tag to handle dissimilar power level demands more efficiently, and to implement tolling. The performance of the system is predicted based on the reconstructed 3D digital model of the RFID main detection lobe.

5.18.2 RFID Subsystem Requirements for WPT Activation

In order for an RFID subsystem, constituted by an RFID reader installed on the lane side, in association with an specific primary coil or a primary coil set, and an RFID tag, placed on the vehicles, be able to successfully control the activation of the primary coils, some requirements must be observed:

(R.1) Guaranteed speed of detection and identification. For a tag to be detected and read, it must remain continuously within the region of the space where detection can occur, the so called the detection volume. The guaranteed speed of detection can then be estimated by the ratio between the shortest travel distance of the tag, while crossing the detection volume, and the maximum time required to successfully process a tag, detecting and identifying it. For the e-bike study case considered, the value was established at 25 km/h.

(R.2) Detection distance. Both the RFID reader and primary power coils are stationary, while the tag and the secondary coil are installed on board of the vehicle, at fixed relative position, it is convenient that the maximum detection distance be slightly larger than the IPT inter-coil distance, which was designed at 13.5 cm for the e-bike lane.

(R.3) Lateral displacement tolerance. The RFID reader should be capable of correctly detecting and identifying the tag, even if laterally misplaced up to a certain width embracing the center detection line. The RFID detection center line does not necessarily coincide with the center of the lane. But it is expected to be parallel to both, which usually shall coincide. The lateral displacement tolerance of the RFID should be equal to or slightly greater than the lateral displacement tolerance of the secondary coil with respect to the primary coil, arbitrated at 39 cm, as justified in Table III.

(R.4) Decoupling from magnetic power circuit. The RFID subsystem is assumed to perform its task of detecting tags and issuing a triggering signal to activate the power inverter before the primary coil is energized. So, functional sensitivity to the magnetic field used to transfer power is not critical. However, both the reader and the tag must at least withstand the voltages possibly inducted in their coils during the energization periods.

5.18.3 Characterization and Selection of an Adequate RFID Technology

The correct recognition of codes retrieved from RFID tags as the key to activate devices and systems is the typical application for this technology. Today's existing standards use the frequency band of LF (125 kHz or 134.2 kHz), HF (13.56 MHz), UHF (860 MHz – 960 MHz) or SHF

Dynamic Inductive Wireless Power Transfer for Lightweight Electric Vehicles
Luiz Alberto Lisboa da Silva Cardoso – University of Minho

359

(2.45 GHz). When selecting a RFID technology for DIWPT, the following considerations should be observed:

UHF and higher frequency RFID systems operate in far-field mode (radiative), with high data bit rates and fast response, favoring the processing of faster vehicles. They are already used in applications involving detection of moving vehicles. However, their detection distances are usually much greater than the typical airgap in IPT configurations, what may lead to a too large anticipation in turning the corresponding primary coil on, if used as a sole method of detection. These higher frequency RFIDs are also more sensitive to propagation conditions and potential interferences from other tags in nearby vehicles. That makes it difficult to predict the correct time to turn each power coil in the lane on, based on the detection signal coming from the RFID reader unit.

HF and lower frequency RFID systems, operating in near-field (inductive) mode may have reading distances of up to 1 m (see Table I). These distances are compatible with inter-coil distances in current vehicular IPT applications. The field strength from the primary power coil, however, tends to affect the operation of the RFID: In a first level, by interfering in the modulation process that permits communication between the RFID reader and the tag. Further, if the IPT field is too strong, induced voltages, in tag or reader coils, can damage the RFID circuits, in spite of the frequency separation of power and RFID signals. Among these systems, higher frequency band correlates with higher bit rates and lower response times, what favors the lane power response time and higher vehicle speeds.

This initial screening process pointed out 13.56 MHz as the most a priori promising RFID band. Two commonly found non-proprietary standards at 13.56 MHz were compared, the ISO/IEC-14443 (with variants A and B) and the ISO/IEC-15693. Their main performance parameters are summarized in Table 37. While ISO/IEC-15693 provides reading distances that better complies with requirements R.2 and R.3, the ISO/IEC-14443 standards have faster bit rates. Also, the larger reading distances of the ISO/IEC 15693 is associated with a higher sensitivity and higher dynamic range tolerance in the magnetic field strength, which is not a desirable property for a better precision in positioning when detecting a RFID tag. Last, but not least, ISO/IEC-14443 have higher availability and lower cost than other nearfield technologies. So, decision was towards initial experimentation with the ISO/IEC-14443A

Dynamic Inductive Wireless Power Transfer for Lightweight Electric Vehicles
Luiz Alberto Lisboa da Silva Cardoso – University of Minho

360

Table 37: Some relevant characteristics of near field RFID standards at 13.56 MHz.

Performance Parameter	ISO/IEC 14443A/B	ISO/IEC 15693
Magnitude of Maximum Reading Distance (m)	0.1 ("Proximity")	1 ("Vicinity")
Maximum Data Rates (kbit/s)	A: 105.9 B: 847.5	26.4
Required Field Strength (A/m)	1.5 to 7.5	0.15 to 5
Anti-collision Protocol	Yes	Yes

The RFID 14443 standards [196] [197] [198] refers to the RFID reader as the proximity coupling device (PCD) and the RFID tag as the proximity integrated circuit card (PICC).

The RFID reader and tag used to test the feasibility of the RFID-triggered WPT activation, the NXP MIFARE Classic, is a relatively old technology, marketed by the NXP Semiconductors, under the name MIFARE Classic [199], and it is commonly used in public transportation, car parks and electronic toll collection cards applications worldwide. This RFID technology was first introduced in 1994, by Philips (now NXP Semiconductors), and incorporates a proprietary 48-bit key cryptographic algorithm that, in 2008, has already been demonstrated to be unsecure [200]. However, the MIFARE is a well-documented ISO/IEC-14443A-compatible RFID type that works in nearfield operation at a frequency (13.56 MHz) that is easily separable from the WPT frequencies (from 10 kHz to 100 k) normally used in vehicular applications and, equally important, it is currently one of the least expensive and readily available passive near-field technologies. Because of these reasons, it was selected in our research as the basis for prototyping and testing the WPT by RFID activation concept. Upon successful demonstration of this technique, it is expected that other more advanced RFID standards, using the same frequency band can also be employed, just by reusing the proposed principles.

The dimensions for MIFARE PICC antenna are standardized [196], limited to a fixed contour inside an ISO/IEC-7810:2003 card, which is 85.60 mm x 53.98 mm, while the PCD antenna dimensions are not size constrained. Smaller MIFARE tags using an antenna of approximately 21 mm in diameter are also popular, however their usual reading range is equally limited to a few centimeters. The dimensions of the printed circuit board (PCB) antenna used in the characterization were 38 mm x 42 mm, typical in commercial card readers.

Experimental plots of detections contours, taken on plans that are parallel to the reader coil, at different heights, are shown Figure 214a. Due to the small dimensions of the reader PCB and

Dynamic Inductive Wireless Power Transfer for Lightweight Electric Vehicles
Luiz Alberto Lisboa da Silva Cardoso – University of Minho

361

the presence of a connector and other electronic components on its surface, some mechanical restriction to measure points close to the reading coil ($z = 0$) was observed, and these were extrapolated by presumed symmetry and continuity, generating the curves drawn in blue. The black and red plots on the contours were individually measured by displacing the card on the plane. The red contour indicates a central exclusion bone-shaped region, about 2 mm high, where, due to larger size of the tag over the reader coil, no tag detection is observed.
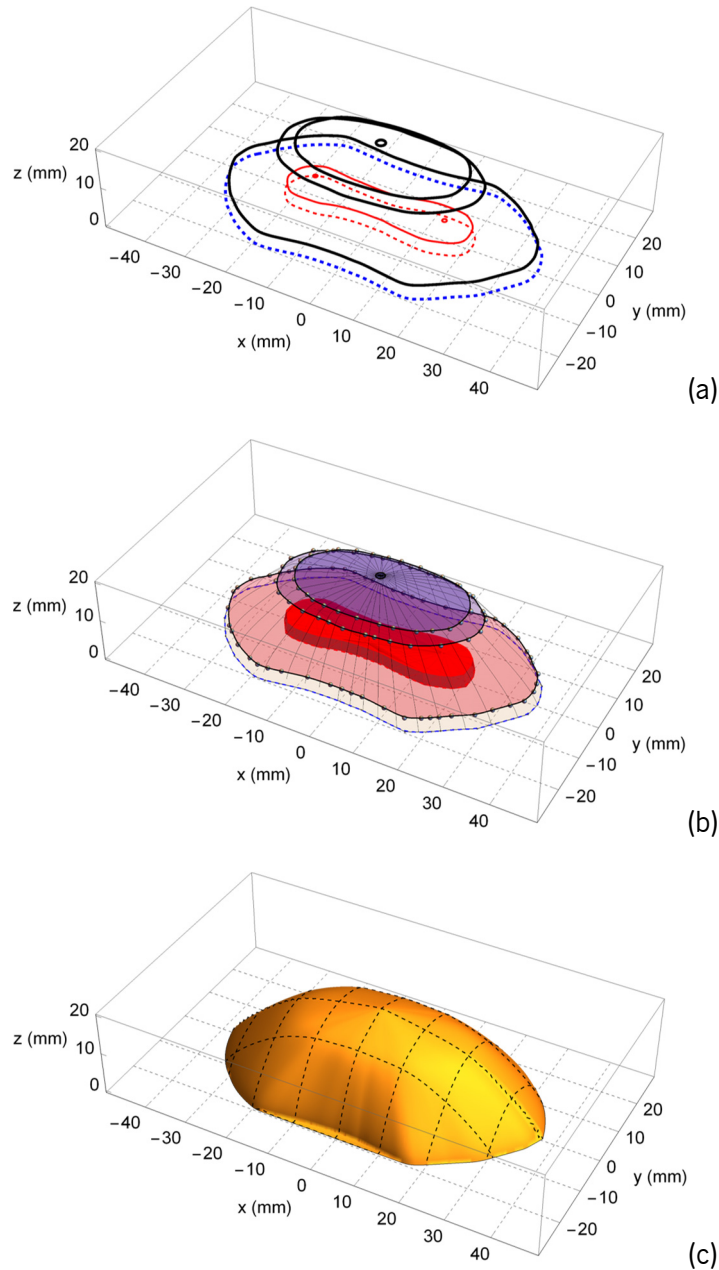
Figure 214: Reconstruction sequence of the major detection lobe of an ISO/IEC-14443A reader-tag antenna pair: (a) contour curves from direct measurements at different heights above RFID coil plane; (b) coarse interpolation with meridians; and (c) fine interpolation of detection lobe surface.

The plots were digitalized and used to create a 3D model of the detection volume for the reader/tag pair, as show in Figure 214b and Figure 214c. The maximum detection height

Dynamic Inductive Wireless Power Transfer for Lightweight Electric Vehicles
Luiz Alberto Lisboa da Silva Cardoso – University of Minho

362

(operation range) was found to be 20 mm, with the base of the detection volume inscribed in a rectangle of roughly 75 mm x 40 mm.

5.18.4 Extending the Operation Range of RFID 14443A

Commercial ISO/IEC 14443A-based RFID systems were designed to exhibit an operation range up to of 10 cm from the RFID reader, depending on the reader coil dimensions and attached circuitry. However, the actual operation distance of most commercially available systems usually lies in the 2 to 5 cm range. One method of extending the reading range of ISO/IEC-14443A, further than that, while keeping near field operation, is to amplify reading currents and reading antenna dimensions [201], keeping the total coil length of the coils small enough not to radiate significant power levels. If this is done in conjunction with the use a battery powered tag that actively emulates load modulation, ranges of a few meters are possible [202].

However, in DIWPT applications the RFID readers are expected to be permanently scanning for vehicles, to activate power at vehicle/tag presentation: Therefore, increasing the reading current level would result in an inconvenient higher lane stand-by power, reducing overall electrical efficiency. Also, the need to replicate these upgraded reading circuits along the lane would make the system more expensive. Battery operated tags on the other hand, while very effective in extending the detection range, would require an auxiliary battery on board of vehicle, to guarantee the energy harvest can be started. The option adopted in this work was, however, to first test the limits of the achievable range extension just by enlarging the reader and tag antenna coils, using no signal amplification, and keeping the tag purely passive.

5.18.4.1 Scaling the Dimensions of Coils and Preserving Inductances

Coils of different sizes can have the same inductance, if their number of turns, geometry and core material are properly adjusted. Similarly, two different pairs of coils at different distances from each other may be designed to exhibit the same mutual inductance as the original pair. In air cored coils made of concentrated, filamentary windings, the inductance increases and is approximately proportional to the square of the number of turns. But the inductance also increases with the cross-section area enclosed by the windings and decreases with the cross-section of the conductor used in the windings, with many formulations existing to support these experimental facts [31].

One possible way to design a new pair of coils C_1 and C_2 which magnetic coupling has the same inductive circuit parameters as that exhibited by a given pair of coils c_1 and c_2, is to firstly

Dynamic Inductive Wireless Power Transfer for Lightweight Electric Vehicles
Luiz Alberto Lisboa da Silva Cardoso – University of Minho

363

design two new coils that have the same inductances L_1 and L_2 of respectively c_1 and c_2. The proportion used to transform the main linear dimensions of the windings of c_1 to C_1 should be approximately the same as that use to transform the dimensions of c_2 to C_2. If the series equivalent loss resistances are relevant for the circuit, the cross-section of the windings of the new coils should also be changed to match that of the original coils, at the required operation frequency.

Once the two new "proportional" coils are built, it can be experimentally found a new relative positioning (expressed by the distance) between them that will result in the same original magnetic coupling coefficient (and mutual inductance), as long as the mutual inductance of these new coils at zero distance is greater or equal to mutual inductance of the original pair of coils. In fact, the mutual inductance increases from zero, when coils are placed at an infinite distance of each other, to this maximum inductance value, when the distance is shortened. Additionally, if all coils can be assumed as having filamentary windings, and the new coils C_1 and C_2 are homothetic to respectively c_1 and c_2, the relative distance where the same mutual inductance is found should also be in the same homothetic ration to the distance between the original coils.

This general case of non-filamentary coils can be visualized in the example of Figure 215.
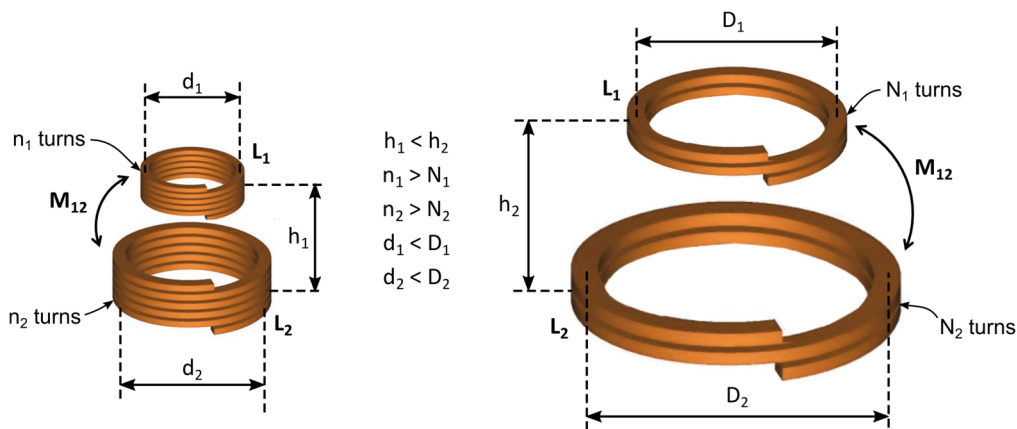
Figure 215: Qualitative example of coil pairs of different sizes still resulting in the same inductive circuit model.

5.18.4.2 Enlarging the PCD Antenna

The strategy for enlarging the reader antenna without changing its circuit parameters was to simultaneously reduce the number of coil-turns and increase the $a \times b$ rectangular coil dimensions.

The original MIFARE reader coil, consisted a of four-turn rectangular spiral coil laid on printed-circuit board, with external dimensions of 38 mm x 42 mm. An enlarged antenna was then obtained with the same inductance of the original antenna, in the range of 1 μH to 1.5 μH,

Dynamic Inductive Wireless Power Transfer for Lightweight Electric Vehicles
Luiz Alberto Lisboa da Silva Cardoso – University of Minho

364

by a single turn coil with double 0.5 mm^2 flexible wire, with dimensions of approximately 50 cm x 29 cm, as shown in Figure 216.
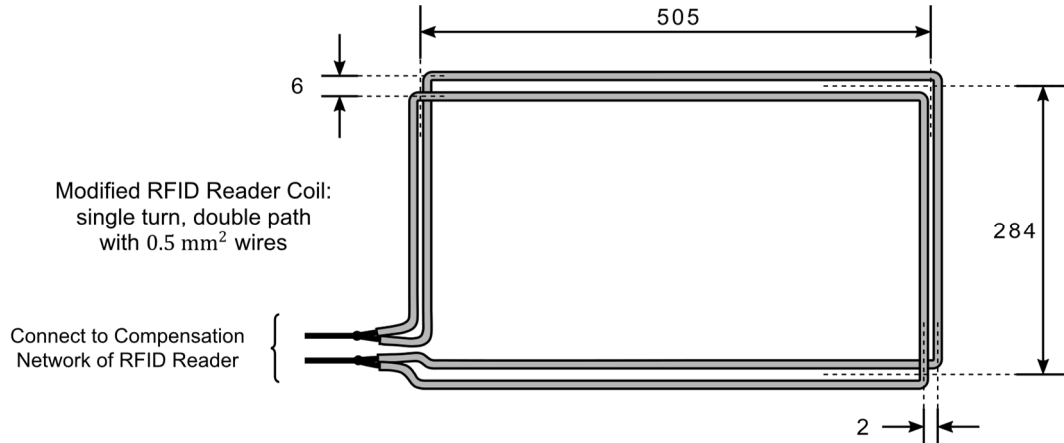
Figure 216: New enlarged rectangular antenna built for the RFID reader (dimensions in mm).

Even larger reader antennas could have been obtained with the same inductance as that of the original reader coil, by using thicker wire and multiple paths. However, for near-field operation at the frequency of 13.56 MHz, the antenna perimeter, $2a + 2b$, in order to reduce radiation losses, should be kept below the near-field mode limit dimension given by:

$$2a + 2b \;\; \ll \;\; \frac{\lambda}{2\pi} \;\; = \;\; \frac{22.1 \text{ m}}{2\pi} \;\; \cong \;\; 3.5 \text{ m} \tag{5.124}$$

A practical and more conservative limit value, often adopted as a recommendation, is $\lambda/10$ instead, numerically equivalent to 2.21 m at 13.56 MHz. In this way, the newly designed reader coil, with $a = 50 \text{ cm}$ and $b = 29 \text{ cm}$, has a perimeter of 1.58 m, within a 30% margin away from the maximum recommended length of $\lambda/10$. Once near-field operation is presumed, negligible radiation losses are observed, and the reader and the tag behave as electric circuits that are coupled by an air-core transformer.

5.18.4.3 Modification of the PCD Circuit

The new larger reader coil has been made to exhibit approximately the same electric circuit parameters as the original antenna. By appropriately adjusting an external capacitive compensation network [203], this antenna can be driven by the same circuit used in the original Proximity Coupling Device (PCD). The PCD is then combined with a microcontroller to enable intelligent activation of the power inverter that energizes the primary coil. The resulting circuit, based on the MFRC522 MIFARE frontend processor [204] is shown in Figure 217.

Dynamic Inductive Wireless Power Transfer for Lightweight Electric Vehicles
Luiz Alberto Lisboa da Silva Cardoso – University of Minho

365
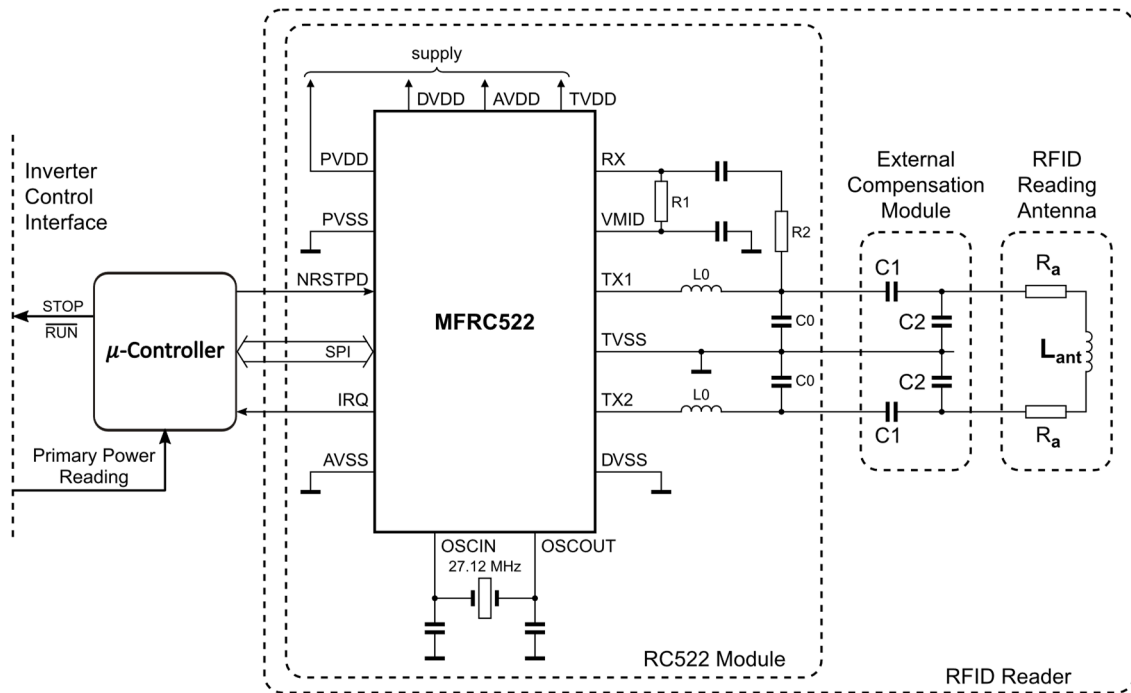
Figure 217: Circuit used for activation of primary coil inverter by an RFID reader.

The MFRC522 integrated circuit is commercially available in a PCB module (the RC522) that also integrates a small antenna. For fast prototyping, the RC522 was used; however, this module was modified by disabling the onboard antenna and connecting the driver circuit to the newly designed larger antenna, through an external compensation module. The values computed for C1 and C2 were respectively 47 pF and 122 pF (C2a = 100 pF in parallel with C2b = 22 pF). The Q-factor of the antenna used the remained close enough to that recommended for the original smaller antenna, so no impedance matching resistors R_a were necessary to be added. The implementation of the modified RFID reader circuit is shown in Figure 218 (compare with schematic diagram in Figure 217):
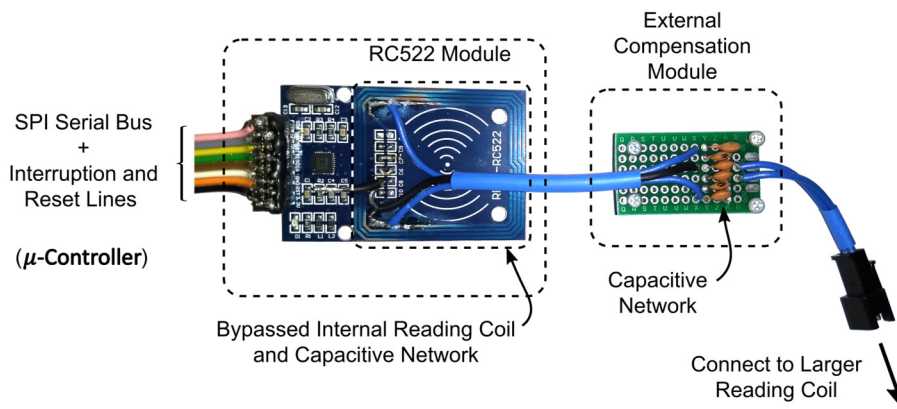
Figure 218: Implementation of the modified RFID reader circuit.

Dynamic Inductive Wireless Power Transfer for Lightweight Electric Vehicles
Luiz Alberto Lisboa da Silva Cardoso – University of Minho

366

At power-on condition, the MFRC522 on board of the RC522 is programmed to use its Serial peripheral interface (SPI) bus in the slave mode [205] to communicate with the microcontroller, which is used to control the on/off state of the inverter that feeds the primary coil associated with that specific RFID reading coil.

5.18.4.4 Enlarging the PICC Antenna

A larger designed PCD antenna will generate a weaker field strength over a larger area. To compensate for that, the PICC (tag) coil was also modified, with an increase in the area of its cross-section and a reduction in the number of turns, using a thicker conductor, to keep the self-inductance approximately constant. A balanced design was made to match the same inductance of the original tag coil, approximately $6\ \mu H$. The newly built tag coil is also connected to the tag chip through a compensating capacitive network, adjusted as a 15 pF series capacitance.
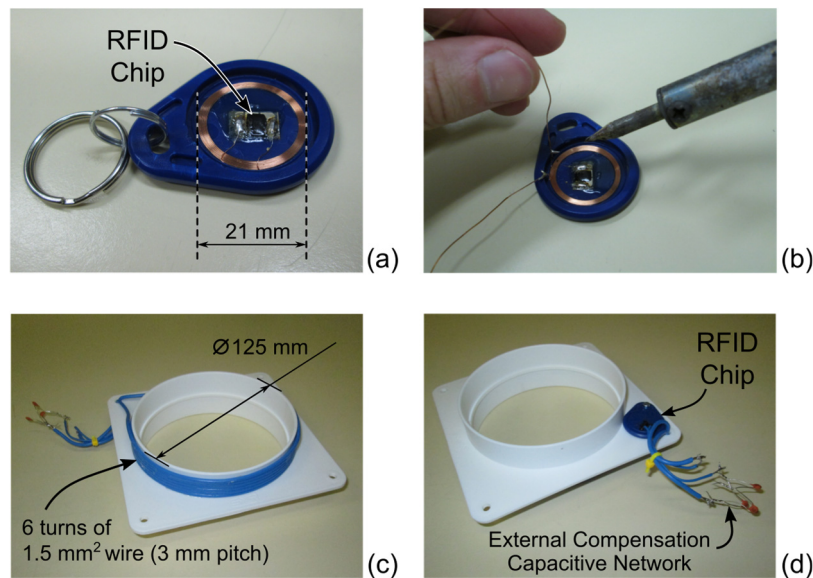
Figure 219: Construction of an enlarged MIFARE-compatible RFID tag: (a) Original RFID tag; (b) Separation of original tag coil and tag chip; (c) larger tag with equivalent coil built, bottom view; and (d) top view.

5.18.4.5 Characterization of the New PCD/PICC Pair

Tests were configured and proceeded as shown in Figure 220, where the RFID reader coil position, is indicated by a red dashed contour line. Initially plastic sheets, and later precisely cut wooden plates, were stacked to produce several controlled separation distances between the RFID reader and tag coils. The new reader/tag pair is then immediately verified to exhibit an extended range of operation. Using a reference wood frame and a variable number of stacked insert medium density fiberboard (MDF) sheets 10 mm thick, the relative position in space of the center of the tag coil with respect to the reading coil could be measured with an accuracy estimated at ± 1 mm

Dynamic Inductive Wireless Power Transfer for Lightweight Electric Vehicles
Luiz Alberto Lisboa da Silva Cardoso – University of Minho

367

in all axes. The resolution was 1 mm in horizontal measurements and, due to the quantization introduced by the MDF inserts, 10 mm in vertical (height) measurements.
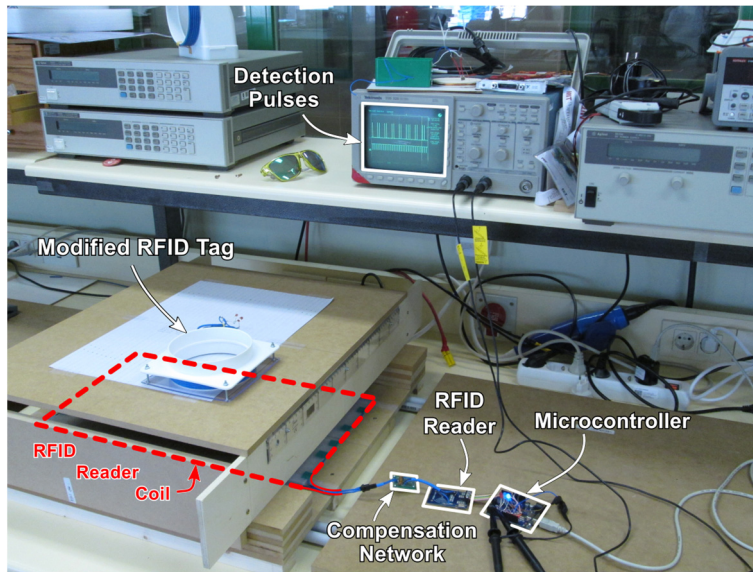
Figure 220: Experimental configuration for evaluating de main detection lobe of the new RFID coil pair.

The same procedure previously used to characterize the main detection lobe of the MIFARE standard card, by measuring and registering on graph paper the limit contours of 100% detection, was then used to characterize the new enlarged reader/tag coil pair, generating the curves plotted in Figure 221a, and the 3D model in Figure 221b.
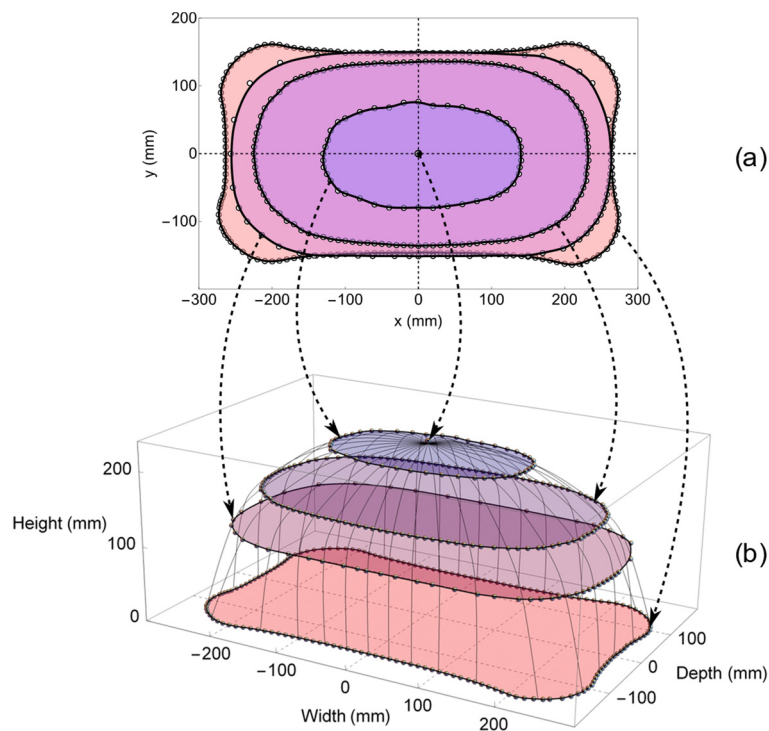
Figure 221: Reconstruction by interpolation of the main detection lobe for the modified ISO 14443A reader-tag antenna pair (b), from limit detection contour measurements at different heights (a).

Dynamic Inductive Wireless Power Transfer for Lightweight Electric Vehicles
Luiz Alberto Lisboa da Silva Cardoso – University of Minho

368

The new total detection volume is visibly larger than that of the original MIFARE card, shown in Figure 214b. In the present case, however, no detection-blind zone was observed inside the main lobe, what is very convenient for the detection of vehicles (and their onboard RFID tags) crossing the detection volume of the PCD antenna.

The new envelope dimensions of the reading volume are shown in Table 38. The result is an increase in the detection range from 20 mm (as extracted from the model in Figure 214) to 236 mm, that is, a linear gain in range of approximately 12 times, if compared with the detection range of the original MIFARE card-reader pair.

Table 38: Detection contours for re-designed RFID antennas

Principal Dimensions of Detection Contours for 100% RFID Detection Rate			
Height (mm)	Transversal Width (mm)	Longitudinal Depth (mm)	Cross-Section Area (cm^2)
0.0	527	295	1606
111	521	301	1423
160	457	272	1068
221	270	155	345
236	0	0	0

Beyond obtaining better range detection and lateral tolerance alignment parameters with the new reader/tag pair, the total detection volume was increased. Thus, the transit time of the tag when crossing the detection space of the main detection lobe of the PCD antenna was also increased, at a given tag/vehicle speed. Or conversely, for a fixed given identification rate to be performed by the PCD, more tag/vehicle speed can be handled.

5.18.5 Maximum Speed of Guaranteed Tag Detection

Based on the digital model of the major lobe of the reading volume, reconstituted from measurements by numerical interpolation, programmed in Wolfram Mathematica software tool, it is possible to anticipate important system behavior characteristics, such as misalignment tolerances and maximum vehicle speed for assured detection and correct radio-frequency identification. With the aid of the model, is also possible to select the best possible height to install the tag on the vehicle.

The maximum speed of guaranteed tag detection will depend not only on the geometry of the RFID coils, which will determine the zone in space in which the tag can be detected, but also on the duration of time this tag remains continuously inside this detection zone, while the vehicle

Dynamic Inductive Wireless Power Transfer for Lightweight Electric Vehicles
Luiz Alberto Lisboa da Silva Cardoso – University of Minho

369

moves over the lane. This will also depend on the protocols and the performance of the software and hardware implementing it, while executing the tasks detecting the tag, reading its contents, and deciding whether the vehicle associated to these contents is entitled to harvest energy from the lane.

5.18.5.1 Lateral Alignment Tolerance

The power transfer capacities of the target DIWPT system, an experimental inductive lane for e-bikes [3], are given at different misalignment conditions, in Table 39.

Table 39: Power Transfer Capacities and Corresponding Vehicle Alignment Tolerances.

EV Power Demand Level	Power (W)	EV to Lane Maximum Misalignment Width, w (cm)
Peak	400	20
Nominal	250	27
-3 dB	200	29
Low	100	39

Arbitrarily considering 100 W as the minimum level of useful assistance power ("Low" level, in Table 39), RFID correct operation must be verified at corresponding alignment tolerance, that is, vehicle detection must be assured for any $w \leq 39\text{ cm}$. For a given height, h, this width, w, can be directly checked by inspecting the cross-section of the major detection lobe at the height h, as illustrated in Figure 222 . If a rectangle of width w is inscribed in the cross-section perimeter, its other side, d, will be the minimally assured depth of crossing, for all lateral displacements $\pm x$ such that $|2x| \leq w$.
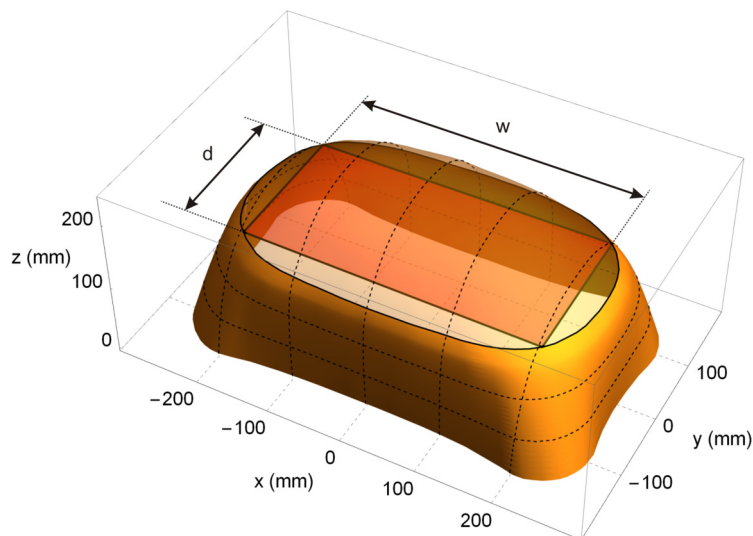
Figure 222: Numerically computed horizontal cross-section of the main RFID detection lobe for the modified reader-tag antenna pair.

Dynamic Inductive Wireless Power Transfer for Lightweight Electric Vehicles
Luiz Alberto Lisboa da Silva Cardoso – University of Minho

370

By examining the contour plot cross-sectioned from the main detection lobe, in Figure 222, which will shrink as the height of cut is increased, it is possible to infer that, using a rectangular reader coil, except possibly at very low tag heights, which are not practical, the maximum tolerance alignment will decrease with height, until the cross-section collapses to a point at $h = 236$ mm, the maximum possible tag height, above which there will be no tag detection.

5.18.5.2 Maximum Vehicle Crossing Speed for Detection

The amplitude modulation (ASK) used in ISO/IEC-14443A is not affected by vehicle's speed, provided the tag coil is kept within the reader detection volume and parallel to reader coil, often a reasonable assumption in vehicular applications. In this manner, to assure detection is sufficient for the tag to remain inside the detection volume enough time for the exchange of the defined messages in the RFID protocol, then to process the tag UID data and decide whether the power activation triggering signal should be issued. In laboratory experiments, this time, Δt_p, was consistently measured to be limited to 32 milliseconds, working with an ATmega328P processor (Arduino UNO R3), an RFID PCD module based on the NXP MFRC522 reader/writer IC [204] and reused software from Arduino RFID Library for MFRC522, with minor modifications, for measuring the duration of the identification cycles.

For a vehicle/tag assembly to be detected, its transit time along the main lobe cross-section, at height h and lateral misalignment x, should be greater or equal to Δt_p. Then its average speed crossing the detection volume at any displacement within the width w, should be given by (5.125) and (5.126):

$$v(x) \leq v_{max}(x) = \frac{d(x)}{\Delta t_p} \leq \frac{d_{min}}{\Delta t_p} \tag{5.125}$$

$$v_{max} = \frac{d_{min}\,(h,\ w)}{\Delta t_p} \tag{5.126}$$

This maximum speed can be numerically computed from the reconstructed digital model of the main detection lobe, for given values of h and w. At the limit case whereas $w = 0$, i.e., perfect vehicle alignment, the relationship between tag the height and the maximum vehicle speed is given by the black dashed curve in Figure 223. The other curves in Figure 223 show how the maximum speed decays, as the required alignment tolerances, w, are increased. The curves are homothetic to intersections of the detection lobe in Figure 222 with vertical parallel planes at $x = w/2$.

Dynamic Inductive Wireless Power Transfer for Lightweight Electric Vehicles
Luiz Alberto Lisboa da Silva Cardoso – University of Minho

371
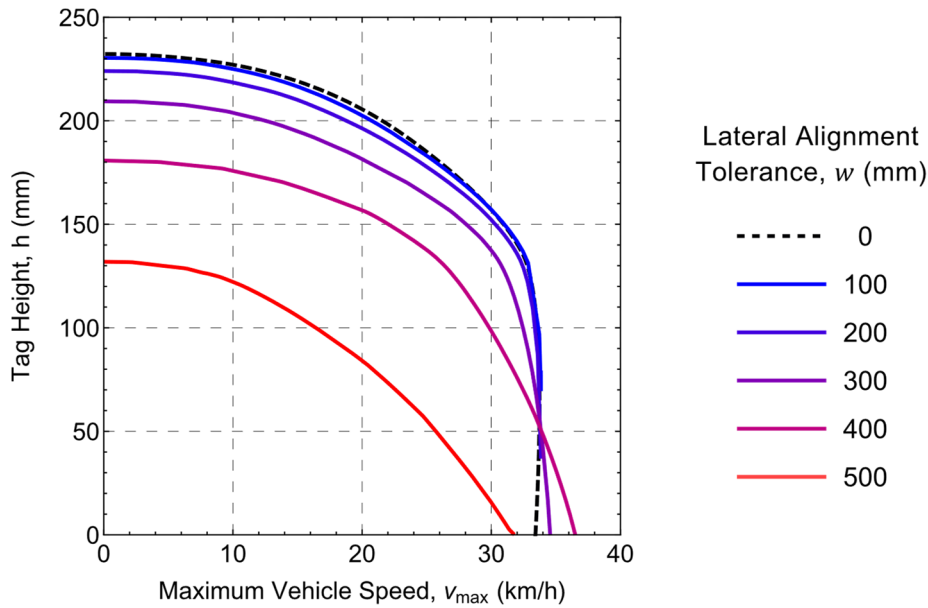
Figure 223: Predicted maximum electric vehicle speed for guaranteed detection, as a function of the height of the tag above the RFID reader antenna and the desired lateral alignment tolerance.

In practice, tag heights less than the power coils "air-gap" (which is greater than the vehicle-to-ground clearance distance) are not mechanically allowed, and the curves in Figure 223 should only be considered as a valid design option above that quota, in the present case of the HIPLEV prototype system developed,135 mm.

The use of MIFARE ISO/IEC-14443A RFID with modified antennas was then verified to be compatible with the requirements of lateral tolerance widths of 40 cm and vehicle speeds up to 25 km/h, being adequate to be used in conjunction with the prototype e-bike inductive lane tested. Measurements with an instrumented moving vehicle are yet due to be realized, as an ultimate design check for maximum achievable speed.

While this analysis methodology holds in other applications, the impossibility of significantly further increasing the coil size, without leaving the desired near-field operation, would likely prevent its application at speeds higher than 45 km/h — a number that results if the reader coil is rotated $\pi/2$ with respect to direction of movement. This would be obtained, however, at the expense of a tighter alignment tolerance, in the order of 25 cm.

5.18.6 RFID System Integration

Each of the RFID reading coils must be installed close to the corresponding primary power coil which activation it will trigger, and the tag coil on board of the vehicle, close to the secondary power coil (R.4, in section 5.18.2). The proximity of power coils to the RFID coils can impair their normal operation and even potentially damage the RFID controller circuits. The collocation of the

Dynamic Inductive Wireless Power Transfer for Lightweight Electric Vehicles
Luiz Alberto Lisboa da Silva Cardoso – University of Minho

372

coils, while allowing the detection of vehicle approach, has also to preserve the integrity of the RFID circuits upon energization of the power coils. The proposed solution for obtaining safe operation was to install the RFID and power coils at magnetically orthogonal relative positions, both on the primary (lane) side and on the secondary (vehicle) side. In this special relative position of the coils, the total magnetic flux from one coil to another is zero, due to positive and negative fluxes cancelling each other, as illustrated in Figure 224. So, their mutual inductance, as well as the induced voltage in one coil by the other coil, will be equally zero. Since they have to be parallel, and almost in the same plane, due to mechanical constraints of the lane construction, the coils must be placed at eccentric positions.
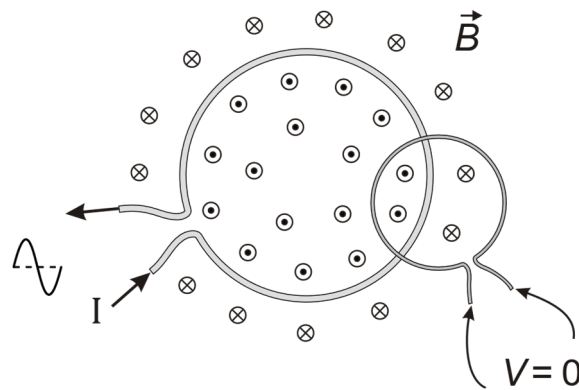
Figure 224: Example of coils in magnetically orthogonal relative position.

5.18.6.1 RFID Reader Installation on Lane

The modified single turn 50 cm x 29 cm rectangular RFID reader coil (Section 5.18.4.2), is then to be installed at one of the extremities of the primary coil. To assign its best position, initially the locus of the center of the RFID reader coil for magnetic orthogonality, between this coil and the primary coil, is experimentally determined, using the configuration shown in Figure 225.
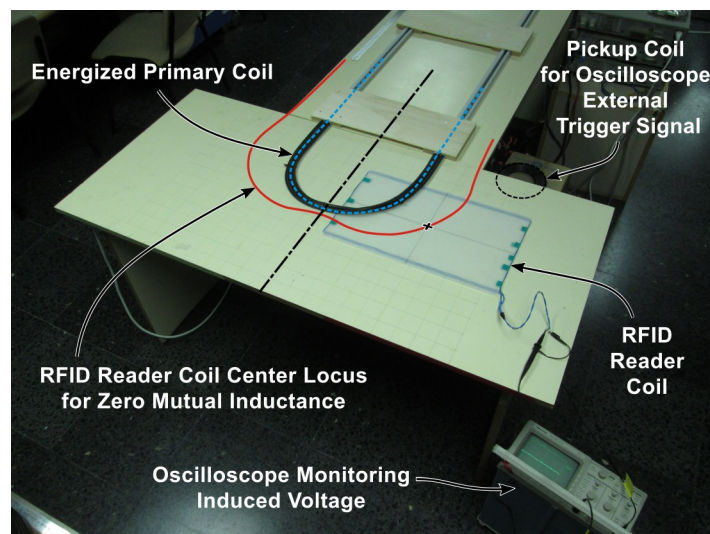
Figure 225: Experimental determination of the locus of the center of the RFID reader coil.

Dynamic Inductive Wireless Power Transfer for Lightweight Electric Vehicles
Luiz Alberto Lisboa da Silva Cardoso – University of Minho

373

In the experiment, the voltage induced on the RFID coil is constantly monitored, as this coil is manually displaced on the support table, keeping its rectangular winding parallel to the longitudinal axis of the primary (power) coil (black dash-dotted line). This procedure seeks to determine the positions of the center of the RFID reader coil where the induced voltage measured on the oscilloscope is zero. When such a point is found, its coordinates are annotated. After interpolation, these points generate the red curve drawn over the photo in Figure 225. If the RFID reader coil is centered over this curve, the RFID reader coil and the primary power coil will be decoupled, except by a minor parasitic capacitive coupling, which was experimentally verified to be irrelevant to the RFID operation.

The choice of the exact position to place the center of the reader coil along this red curve is a function of the misalignment of the RFID tag with respect to the longitudinal axis of the secondary coil attached to the vehicle. It can be obtained by intersecting the red curve with line r_2, parallel but eccentric to the primary coil longitudinal axis by the same distance y_{tag} which is the lateral offset of the RFID tag in the secondary integration, as derived in the in next section.
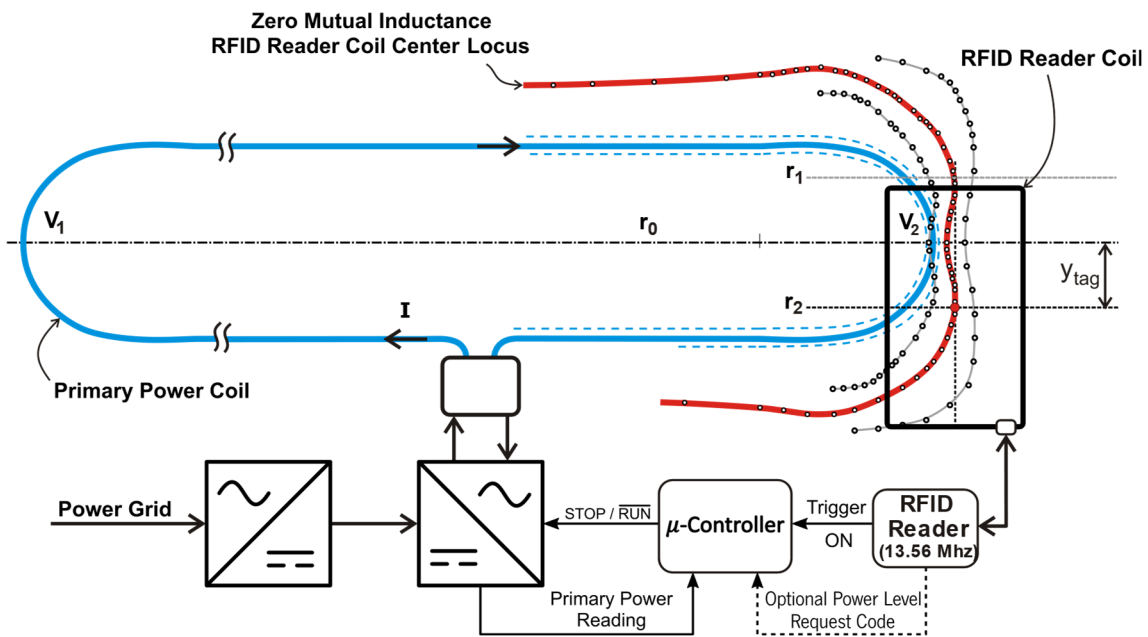
Figure 226: Integration on the lane, with the RFID reader coil positioned at the extremity of the primary coil the vehicle is expected to come from.

When the RFID tag coil crosses the attack detection contour (on the right side, if the vehicle comes from right traveling leftwards), the vehicle is detected and, if identified as able to harvest energy from the lane, the inverter is activated. After activation, the intensity levels of the currents in primary and secondary coils, although not being enough to damage the RFID circuits, they can interfere with the normal RFID operation. However, this is not a problem, because the RFID status becomes irrelevant after primary power is activated.

Dynamic Inductive Wireless Power Transfer for Lightweight Electric Vehicles
Luiz Alberto Lisboa da Silva Cardoso – University of Minho

374

In the identification process, the RFID reader reads a unique identifier (UID) code, transponded by the tag, which can be 4 or 7 bytes long, depending on the RFID chip model. For the MIFARE S50 chip tested in the prototype the UID is 4 bytes long. For DESFire chip models, it is 7 bytes long, what would enable the system to distinguish more than 720 million of different vehicles, with less than 10^{-8} of chances of successfully counterfeiting a tag by randomly picking an UID code.

In the current prototype used for testing and demonstrating the concept, the UID is merely checked to be in a predefined list of enabled users, by a supervisor program running on the lane microcontroller. If the code is validated, the controller issues an activation signal that triggers the power inverter on. In real applications, other more complex algorithms and on-line database checking can be engineered, provided a fast enough response is guaranteed.

In addition to the UID, other values could be stored in the registers of the tag chip, and manipulated, for instance, at toll-collection points. The user energy "credit" could then be stored in the registers, and decremented for tolling, in a similar manner the ISO/IEC-14443A MIFARE cards are used in current ticketing applications.

5.18.6.2 RFID Tag and Secondary Power Coil Integration

The vehicle used to test the HIPLEV concept is an electric bike, with the secondary power coil wound around the rear wheel, what results in an intrinsic difficulty to position the tag simultaneously aligned with the longitudinal center axis and close to the secondary power coil. This centered position is anyway inconvenient, due to the higher possibility of interference by magnetic coupling between the RFID tag and secondary coils. Since the secondary coil is multiturn and has much larger dimensions than the developed tag coil, the magnetic orthogonality position occurs when the RFID tag coil is installed over the secondary windings, approximately centered to the middle turn. Similarly, to what has been done in the collocation of the coils on the lane side, the exact offset from the longitudinal axis of the secondary coil is also determined experimentally.

The redesigned RFID tag with a newly built antenna, consisting of 6 cylindrical-helix turns of 1.5 mm² cross-section copper wire, 128 mm of diameter and 18 mm height, is then placed on a lateral side of the secondary coil, as schematically shown in Figure 227. The passive tag circuitry then stays electrically decoupled from the secondary power circuitry.

Dynamic Inductive Wireless Power Transfer for Lightweight Electric Vehicles
Luiz Alberto Lisboa da Silva Cardoso – University of Minho

375
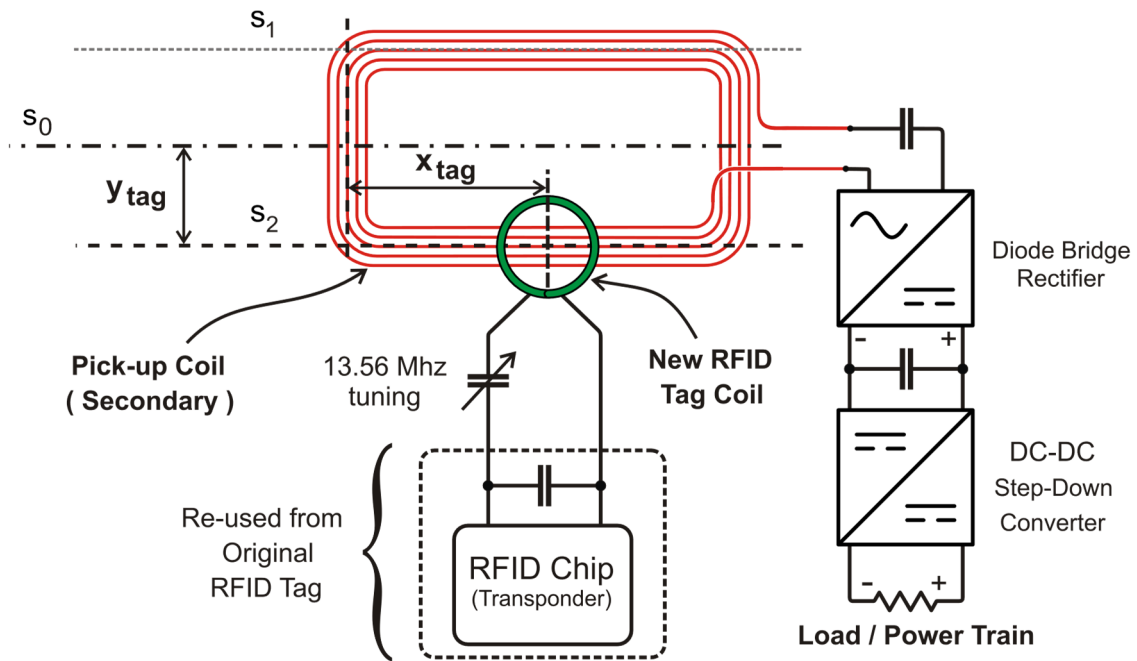
Figure 227: RFID tag integration on board of electric vehicle.

When the bike moves, the RFID tag (green) and the secondary (red) coil are kept mechanically solidary, with their longitudinal axes separated by distance y_{tag}. In this manner, when the longitudinal axis of the secondary power coil and the longitudinal axis of the primary coil are perfectly aligned, so are the axes s_2.(in Figure 227) and r_2 (in Figure 226).

The exact location of the center of the RFID tag coil with respect to the secondary coil is the established by further determining the position x_{tag} along s_2. This can be done by adopting an operation setting in between two different optimum strategies:

(i) **Guaranteed vehicle presence**, aiming to assure that vehicle will be in a position ready to harvest when the primary power is activated. A condition that is achieved by requiring that the center of the RFID tag coil should be crossing the attack contour of the main detection lobe of RFID reader antenna exactly when the center of the secondary coil is entering the intended harvesting zone of the primary power coil, as calculated by numeric simulation in Section 5.13.1. So, the vehicle would be already in the power harvesting zone when the tag is detected. At the vehicle speed of 25 km/h and maximum tag detection time of 32 ms, this would imply missing, in the worst case, the first 22 cm of lane. For lane modules about 3 m long, for instance, this is equivalent to waste about 7% of the lane energizing length.

(ii) **Anticipated power activation**, aiming to assure that the primary power is already enabled when the vehicle enters the harvest zone. A condition that is achieved by

Dynamic Inductive Wireless Power Transfer for Lightweight Electric Vehicles
Luiz Alberto Lisboa da Silva Cardoso – University of Minho

376

requiring that, when the secondary center enters the harvest zone, the RFID tag coil center is on the verge of leaving the detection volume of the RFID reading antenna. This leads to the use of the full harvest length over the lane.

Using anticipated power activation is better under the perspective of increasing the maximum possible primary coil spacing, without having a negative energy balance on the short term storage or battery, installed on board of the vehicle. On the other hand, by using this strategy, there is a chance of keeping the primary power on up to a maximum of 32 ms before the vehicle is in a good position to start harvesting.

This effect can slightly diminish the overall electric efficiency of the system. But not in the same proportion as in the case of guaranteed vehicle presence. Because, in addition to the limited fraction of 7% of maximum extra time energizing the primary coil, when the vehicle is not harvesting energy, the standby power supplied to the primary coil circuitry is much less than that when IWPT to the vehicle is occurring. For instance, if the standby power is as implied by the power estimates in Table 30, the new overall DC-DC efficiency of the system, instead of η_{DC}, at the worst case becomes:

$$\eta'_{DC} = \frac{400 \text{ W} \times \Delta t_{transit}}{\frac{400 \text{ W}}{\eta_{DC}} \times \Delta t_{transit} + (178 \text{ W} + 34 \text{ W}) \times 7\% \times \Delta t_{transit}}, \tag{5.127}$$

where $\Delta t_{transit}$ is the to traverse the harvest zone of the primary coil, assuming a constant speed of the vehicle. This simplifies to:

$$\eta'_{DC} = \eta_{DC} \frac{1}{1 + \eta_{DC} \times 53\% \times 7\%} \geq \eta_{DC}(1 - \eta_{DC} \times 3.71\%) \tag{5.128}$$

In the specific case where the predicted worst case efficiency is 59.3%, the new predicted worst case efficiency considering the use of anticipated primary coil activation becomes $\eta'_{DC} = 58.0\%$. This new efficiency value is not significantly less than in the case where the guaranteed vehicle presence strategy is used, and still above the minimum target efficiency (5.10).

5.18.6.3 Verification of Other Collocation Issues

Using the design procedures formerly described, adequate collocation of primary power coil and the RFID reader coil, as well as that of the secondary coil and the RFID tag coil, have been separately established. However, these collocations, respectively on the lane side and on board of the vehicle, do not cover all possible interference issues.

Dynamic Inductive Wireless Power Transfer for Lightweight Electric Vehicles
Luiz Alberto Lisboa da Silva Cardoso – University of Minho

377

Although the power coupling coil pair operates at a frequency band (LF) that is well apart from the operating frequency of the RFID (HF), the current-turns levels in both the primary and secondary coils may be very high, in the order of 100 A rms. Observing Figure 228, it can be seen that possible non-desirable interactions between coils pairs are {(1A, 1B), (2A, 2B), (1A, 2B), (2A, 1B)}.
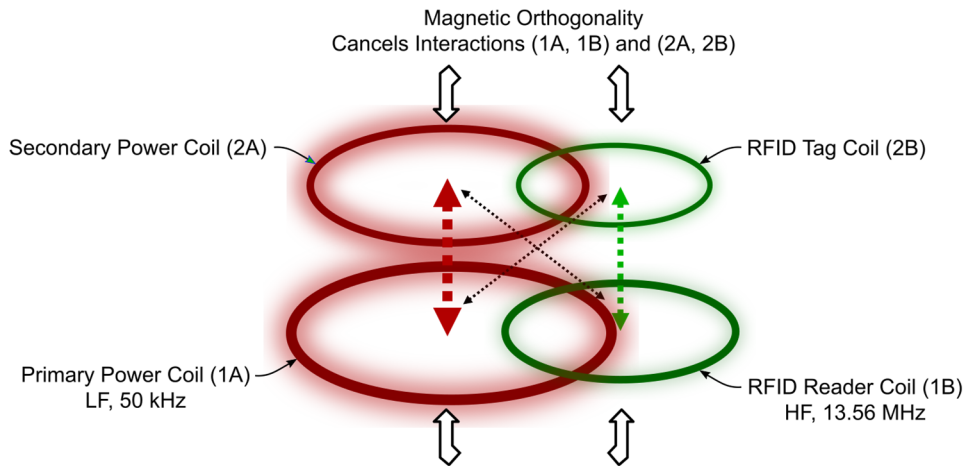
Figure 228: Possible interferences between coil pairs in the lane and on board of vehicle.

While interactions {(1A, 1B), (2A, 2B)} have been cancelled in the design by placing the coils in magnetic orthogonality, there is a priori still possibility that the primary power coil interferes in the tag coil, and that the secondary power coil interferes with the coil reader, even with the large difference operation frequencies. This interference can occur at two levels of severity: (i) it can impair the normal functionality of the RFID tag detection and the communication between the PCD and the PICC; or (ii) it can damage either the PICC or the PCD circuits.

The compensation circuits that connect the reading antenna to the PCD and that other connecting the tag antenna to the tag chip, together with their own antennas, behave as high Q-factor band-pass filter, attenuating the LF signal incoming from the power coils. Because of that, the total induced voltage on the RFID coils by the power coils, at the distance they are installed from each other, were verified to be less than the maximum safe levels, according to the RFID chips manufacturers.

On the other hand, the interference level was verified to be enough to cause erroneous RFID operation. However, this was not considered a major problem, because the RFID detection only needs to occur at the approach of the vehicle, when the primary and secondary power coils are not yet energized.

5.18.6.4 Dynamic of the WPT Activation Triggered by RFID Detection

The designed dynamic interaction of the vehicle electronics with each i-lane module is explained based on Figure 229, where three relative positions of the secondary coil assembly, on board of the vehicle, with respect to the primary coil, at three sequential times are shown:

(1) When the vehicle, moving leftward, approaches the primary coil module and the RFID tag (green circle) enters the main detection lobe (green dashed contour) of the RFID reader coil (black coil), being detected by the PCD.

(2) When the vehicle, continuing its movement, advances to a position where the RFID tag leaves the main detection lobe of the RFID.

(3) During the energy harvesting time, transiting over the primary coil (blue coil).
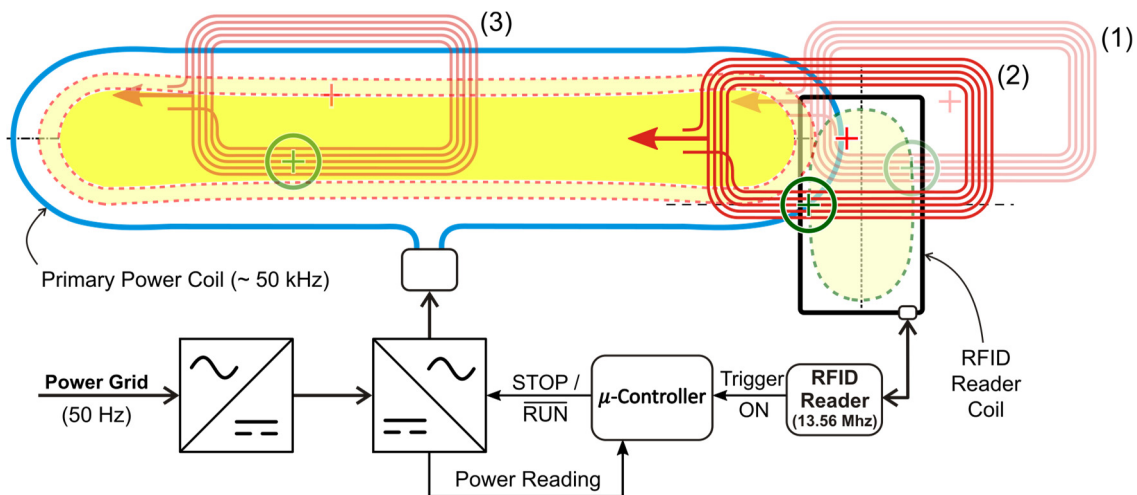
Figure 229: Interaction of the vehicle at different relative positions on route over one i-lane module: (1) RFID tag entering detection main lobe of RFID reader antenna; (2) RFID tag leaving detection main lobe of RFID reader antenna, and (3) secondary coil harvesting power from primary power coil. Not drawn to scale.

The vehicle speed, which is the speed of the secondary coil assembly, illustrated in Figure 229 by its principal components, the secondary power coil (red rectangular spiral coil) and the attached RFID tag coil (green circle), is represented by a red arrow. The red and green crosses respectively represent the centers of the secondary and tag coils.

The two concentric horizontally oblong yellowish zones inside the primary coil, which are contoured by a red dashed line, are the zones over which positioning the center of the secondary coil (red cross) maximum power harvesting of 250 W (lighter yellow) and 400 W (darker yellow) are possible. These zones are calculated by numeric simulation, and coincide with the corresponding central yellowish zones of Figure 183, in Section 5.13.1.

Dynamic Inductive Wireless Power Transfer for Lightweight Electric Vehicles
Luiz Alberto Lisboa da Silva Cardoso – University of Minho

379

The yellowish zone inside the RFID reader coil (black coil), contoured by a green dashed line, is the horizontal cross-section of the main RFID detection lobe (Figure 222), taken at the height at which the tag is installed on the bike (close but in magnetic orthogonality with the secondary coil winding), as measured from the RFID reader coil.

The program running on the lane module microcontroller enforces the following dynamic behavior for the interaction between the vehicle and the lane module:

- At rest, when there is no vehicle coming to, transiting over or recently run over the lane model, the power inverter is turned-off, and the RFID reader is kept in scanning mode, waiting for tags to enter the detection zone of the RFID reader antenna.

- When the vehicle arrives at position (1), it becomes possible for the detection of the RFID tag to occur. But it may still take some time until it is effectively detected.

- Detection will occur sometime during the transit of the vehicle from position (1) to position (2). So, at position (2) the primary coil is guaranteed to be already energized.

  Clearly, the primary coil will be energized sometime between positions (1) e (2)

- The vehicle rides along the coil harvesting power from the primary coil, as long the center of the secondary coil is properly positioned in the lane, that is, within a maximum misalignment from the center. In position (3), the vehicle is on the verge of crossing the 400 W power transfer level. At this position, if the vehicle is drifting right, the maximum transferred power will start to decrease, still being greater than 250 W while its position is within the limits of the light yellowish zone.

The RFID detection triggers the power transfer, but its reading is disregarded after that. The primary coil activation is sustained while the power supplied to the inverter is larger than a minimum value that can be programed. To accommodate possible dramatic reductions in energy demand of the powertrain of the vehicle during its transit over the primary coil, what could terminate the energy supply, a minimum "ON" time $t_{ON,min}$ is guaranteed by an internal timer managed by the controller. This time can be adjusted to be the minimum required time for a vehicle at the maximum speed of electric assistance (25 km/h) to travel over the total length of the primary coil, which is 3.25 m:

$$t_{ON,min} = \frac{3.25 \text{ m}}{25000 \text{ m} / 3600 \text{ s}} \cong 0.47 \text{ s} \tag{5.129}$$

Dynamic Inductive Wireless Power Transfer for Lightweight Electric Vehicles
Luiz Alberto Lisboa da Silva Cardoso – University of Minho

380

For safety reasons, and to avoided unintended stationary IWPT operation modes, the primary coil should not be continuously energized for a more than an absolute maximum transit time $t_{OFF,max}$, after which it should be turned off. Assuming that the minimum reasonable speed, for a bike travelling on the lane, to receive energy is 125% of the average speed of person walking, which is 4 km/h, $t_{OFF,max}$ can be calculated by:

$$t_{OFF,max} = \frac{3.25 \text{ m}}{1.25 \times 4000 \text{ m} / 3600 \text{ s}} \cong 2.34 \text{ s} \tag{5.130}$$

In steep terrain, the speed of a 250 W EPAC bike can be seriously impaired, so in this condition $t_{OFF,max}$ should be enlarged accordingly. If an inertial sensor would be included in the microcontroller board, this timeout constant could be automatically adjusted to the grading of the lane where the primary coil module is installed. The geometry of the controller housing and the lane module should then be carefully designed to facilitate installation of the reference axis of the inertial sensor to be parallel to the lane.

5.18.7 Future Improvements in the Power Activation Design

Although one-way traffic is required in the configuration tested, the present results could be extended for non-simultaneous two-way traffic as well, by using one RFID reader at each extremity of the controlled primary coils. To minimize the complexity and cost added in a larger lane system, this method can be used as a strategy for identifying the vehicle and activating the lane power start, by controlling the first coil only in a row of coils, since other simpler methods to control the coils following the first can be found, if the coils are close enough. The design for a two-way traffic on the same lane however is doubted as a good urbanistic solution.

The RFID have some known security issues that are being researched, and improvements are constantly made to this technology. The risk of tag cloning and eavesdropping attacks may however require detailed analysis before the use of this technology in high-end wireless power transfer and associated tolling applications. For low-end, low-cost applications of IWPT, such as e-bikes and similar lightweight electric vehicles, the use of RFID technology for activation and tolling is expected to offer an acceptable trade-off between security and functionality.

In this first implementation, the RFID software was not optimized for timing. The RFID standard considers the possible existence of multiple simultaneous tags in the detection volume and the firmware implements algorithms to handle the potential collision of messages from the different tags. In the vehicular application described, however, it is unlikely that two or more

Dynamic Inductive Wireless Power Transfer for Lightweight Electric Vehicles
Luiz Alberto Lisboa da Silva Cardoso – University of Minho

381

vehicles can coincide over the extremity of the same primary coil. If the coil is not wide enough for more than one vehicle at a time, as it is in the developed prototype, this is actually a physical impossibility. So, in this case, there may be margin for reduction of the tag identification time, by simplifying the anti-collision protocol. That would allow a higher maximum vehicle speed to be handled by the RFID detection and identification system, and thus, a higher maximum DIWPT speed itself.

Other RFID standards in HF band, such as the ISO/IEC-14443B variant, which can achieve higher bitrates, could also be tested, possibly yielding faster cycle response and higher maximum vehicle speeds as well. The creation of a specialized RFID standard, working at a carrier frequency 1/4 to 1/5 of the current 13.56 MHz standard, is perceived as opportune, as it would allow reader coils with perimeter up to $\lambda/10 = 8.8$ m, capable of handling vehicle detection in larger volumes and at higher speeds, but still operating in the desired near-field mode. The 3.155-3.400 MHz band has already been recommended for RFID, access control and automatic road tolling applications [206], and should better fit the DIWPT application.

The limitation on the available instrumentation to dynamically evaluate the DIWPT prototype developed originated another related but independent contribution, which is reported in Chapter 6: the development of a special electro-optical instrument to dynamically and synchronously monitor the lateral misalignment of the bike on the lane, its angular attitude, the electric power supplied by the lane, and the power transferred to the power train.

5.19 Summary of Achievements

An EPAC (PEDELEC) e-bike was adapted for harvesting electric power from an inductive lane module, which was also especially designed to match the requirements of this type of vehicle. Despite no major effort having been made to optimize the design as a product, to limit the effort and allocation of resources in the prototype implementation, the viability of the HIPLEV concept, as proposed in Chapter 4, has been proved.

The vehicle used in the prototype, the standard upright e-bike, is one of the most popular representatives of the electrically assisted HPV. Other classes of HPV, such as quadricycles or longtail cargo bikes, would more easily be adapted to function as a HIPLEV.

The initial evaluation of the prototype was made by means of stationary tests only, with the bike being immobilized and manually displaced over the lane, in order to plot the curves of transferred power and its efficiency, as a function of the misalignment of the vehicle with respect

Dynamic Inductive Wireless Power Transfer for Lightweight Electric Vehicles
Luiz Alberto Lisboa da Silva Cardoso – University of Minho

382

to center of the lane. The measurements of electric-spatial performance parameters are in excellent agreement with that expected by design and by the numeric simulations realized. Peak power levels of 400 W were verified to be sustained indefinitely, at misalignment widths up to 20 cm, which, as reviewed in section 5.3, is the minimally required envelope margin for a cyclist to keep the balance, when cruising at speeds over 12 km/h. Since the power assistance for electrically assisted power cycles is currently limited to 250 W [5], the harvested power that is not consumed in the powertrain, at least 150 W, can be stored onboard of the vehicle, and used to sustain the maximum nominal power on the powertrain during the transit between neighbor primary coils, where there is no power to be harvested. Other design variants using the same method could achieve larger electrified widths or power transfer levels.

The peak efficiency DC-DC level initially obtained was 64%. However, after the prototype was reinstalled and tested on 100% wooden workbench, this efficiency raised over 65%. It was then identified that a carbon steel support structure, intrinsic to the workbench initially used, was functioning as unintended secondary coils and a parasitic load. Not only the efficiency improved after this incidental conductive material was removed from the configuration, but also the magnetic field shaping effect disappeared, which was producing a slight constriction of the magnetic line fields, and the electrified length was restored to approximately 20 cm, as expected in the design, from an initial value only slightly over 19 cm. All the linear measurements were made using non-calibrated millimetric rulers, but due to the difficult to keep the alignment and perfect verticality of the bike on the lane, they should be considered precise to ±0.3 cm, at best.

While the efficiency figure obtained is less than typical best cases reported for DIWPT using similar oblong coil prototypes, in the range of 70% to 85%, in our prototype, top efficiency was not the target. Instead, simple electric materials and low-cost electronics was used. Especially, the power coils were built without using true litz wire, which would exhibit less losses, or any soft magnetic materials in their core, which could better shape the magnetic field and increase the magnetic coupling coefficient. This directive for simplicity did not aim the cost reduction by itself. Rather, the motivation was to validate the HIPLEV concept, demonstrating, at the same time, that the design method, using simple geometric calculation tools, can be replicated almost anywhere in the world using largely available material resources.

In this manner, no special effort was made in circuit development, and the reuse of existing circuit modules in a system design approach was the adopted option, whenever possible. Rather,

Dynamic Inductive Wireless Power Transfer for Lightweight Electric Vehicles
Luiz Alberto Lisboa da Silva Cardoso – University of Minho

383

the technical contributions that uniquely made it possible to achieve the design goals are related to magnetic field design, namely:

(i)   The cross-section design procedure, establishing an optimal primary coil width for maximum power transfer level between the lane and the secondary (pick-up) coil, on board of the vehicle, for the case of oblong primary coils.

(ii)   The DIWPT design procedure itself, that starts with the identification of the vehicle dimensions, dynamic characteristics, and powertrain, and sequentially determines the parameters for the secondary and primary coils, as well as the required excitation for the primary coil and the architecture of the harvesting circuitry in the secondary, with minimum heuristic considerations.

(iii)   The electromechanical design of the secondary coil, with its windings specially adapted around the rear wheel of the e-bike, taking into consideration its unique maneuvering and dynamic characteristics, thus producing the first known inductively powered electric bike.

(iv)   The power activation scheme for the primary coils, based on the colocation of a ISO/IEC 14443A RFID reader on the lane, and the corresponding RFID tag on the vehicle. In both cases, the RFID coils were placed in magnetic orthogonality with the power coils, minimizing crosstalk that could potentially destroy the sensors. For that, the reader and tag antennae were modified to allow tag detection at larger distances, while still operating in near-field mode.

The reuse of standard near-field operation ISO/IEC-14443A RFID circuitry and software provides a simple and effective means of triggering dynamic inductive wireless power transfer to electric vehicles. This scheme not only can detect approaching electric vehicles, but also extract vehicles' authorization, tolling and power demand level codes, enabling more efficient electrification of an inductive lane [9]. If lane segments are adequately limited in length, no two vehicles can be simultaneously over the same segment, and the entire lane could efficiently handle vehicles with dissimilar power requirements, by automatically adjusting the power level at each primary coil.

In a future project, if the vehicle power train control is integrated with the tag, the same vehicle could present different power demand codes to be transponded to the lane through the RFID interface, at different times, optimizing the requested power level to that instantaneously

Dynamic Inductive Wireless Power Transfer for Lightweight Electric Vehicles
Luiz Alberto Lisboa da Silva Cardoso – University of Minho

384

required for electric assistance in the HIPLEV. Analogously, by replying with the correct RFID codes, vehicles with dissimilar power level demands could share the same i-lane.

Trial experiments were conducted using the NXP MIFARE 1k, a commercial family of RFID products, which is ISO/IEC-14443A compatible and operates at 13.56 MHz. Actual measurements of the major lobe for a newly designed reader-tag antenna pair indicate a maximum vehicle speed, for guaranteed detection and successful DIWPT operation, in the range of 25 km/h to 30 km/h, at a lateral alignment tolerance of 40 cm. While this speed is not high enough to address traffic in highways, it fits satisfactorily slower moving lightweight electric vehicle applications, such as electrically power assisted cycles and industrial applications using similarly speed-rated electric vehicles.

At a large-scale production, it is estimated that other improved power electronics configuration options could be alternatively used to drive the primary and secondary coils while still exhibiting low complexity. For instance, the microcontroller and RFID reader circuit can be integrated in the same board of the inverter. However, this power electronics related engineering effort was considered out of the scope of this work.

On the workbench, with no cyclist on the bike, and the bike standing on the inductive lane, while harvesting its power by means of a dummy load replacing the powertrain, it was possible to incline and turn the bike with respect the lane by angles up to approximately 10 to 15 degrees of arc, without disrupting the maximum required power transfer, provided the lane alignment was within design limits. A more detailed characterization of the lane, concerning the angular attitude and the power demand fluctuation of the HIPLEV was not realized though, due to the unavailability of instrumental resources to dynamically test the DIWPT system created.

Not being possible to quantitatively implement these other tests, after the workbench tests were concluded, the lane was also assembled on the floor, and the bike was successfully used over its i-lane during a public exposition at the School of Industrial Engineering of the University of Vigo in June 2017, being capable of accelerating by means of electric assistance only, with the use of a manual throttle control, while the battery was removed. Because only a single inductive module was built, which is electrically 3.25 m long, after a first boost provided by the electric powertrain, the bike would naturally leave the inductive module and, from this point on, rely on pedal-only mode.

Dynamic Inductive Wireless Power Transfer for Lightweight Electric Vehicles
Luiz Alberto Lisboa da Silva Cardoso – University of Minho

385

Chapter 6

Electro-Optical Tool for Evaluation of DIWPT

Inductive lanes share a common characteristic that limits the nominal level power transferred and the efficiency achieved by a DIWPT design, which is, the reduction of performance when the vehicle is laterally displaced with respect to the center of the lane. In the case of two-wheeled vehicles, such as electric scooters and bicycles, lateral inclination can also be pronounced enough as to interfere with power coupling.

Experimental evaluation of DIWPT is usually implemented based on the stationary model, by immobilizing the vehicle at different offset distances from the center of the lane and measuring the power transfer parameters. Under the point of view of the induction process itself, this approach is reasonable approximation under the usually valid assumptions that the induction frequency is high enough compared with maximum predicable speed of the vehicle and the gradient of the primary magnetic flux on the secondary coil. However, this method does not account for the statistical pattern of the misalignment and the angular attitude of the vehicle itself, that may be especially relevant in two-wheeled vehicles. Also, the stationary approach does not fully and precisely access the effect of the power electronics response delay when the primary coil drivers are switched on and off as the vehicle is detected when moving over the primary coil embedded in the inductive lane.

In order to experimentally evaluate the characteristics of vehicular dynamic power transfer schemes, it is then necessary to synchronously log the vehicle's electric data, the lateral displacement, and the angular attitude. In this chapter, the design and implementation of an electro-optical measuring system with these capabilities, based on Light Detection and Ranging (LIDAR) technology and inertial sensors, is reported. A testing range with specific reference geometry, consisting of a corridor of parallel walls, is used to simplify the continuous and accurate estimation of lateral displacement. The design was validated by statistical characterization of the measurement errors, using simulated trajectories. A prototype was built and mounted on a non-electric bicycle, with the first tests confirming its positioning measurement qualities. The findings

Dynamic Inductive Wireless Power Transfer for Lightweight Electric Vehicles
Luiz Alberto Lisboa da Silva Cardoso – University of Minho

386

and results reported in this Chapter were firstly and recently published by the author in [7], from where the text and figures in this Chapter are greatly derived.

Although the development of this tool aimed to be an advanced testing resource for HIPLEVs, its principle of operation and characteristic are expected to fit many other DIWPT applications, where primary coils lay underneath ground surface, only being necessary to adjust LIDARs and other sensors, as well as their control circuits and processing parameters, accordingly to the maximum speed and power demand levels of the EVs involved.

6.1   Inductive Lane Technology Considerations

In a DIWPT system, when the vehicle moves forward along its path, its pick-up (secondary) coil will cross the magnetic field generated by stationary primary coils placed underneath the floor, along the vehicle's path. The system effectiveness will depend on the appropriated time-spatial coil activation pattern, which is ensured by the power electronic design, but also and fundamentally by good magnetic coupling between the lane and the vehicle, which is ultimately influenced by distance and misalignment between primary and secondary coils.

The EV running over and harvesting energy from the power lane can be either manually or automatically driven, in case a more precise on-lane positioning ca be achieved, and the misalignment errors minimized. But even with the use of precise autonomous navigation, some tolerance in the vehicle-to-lane lateral misalignment must be handled by the system [207], this parameter being perhaps the most critical one to be handled in the case of human-driven EVs, such as the HIPLEVs, introduced in Chapter and which development and successful prototyping was reported in Chapter 5. The measurement of power availability on board of a vehicle as a function of lateral displacement over the i-lane is then crucial to enhance the evaluation of any DIWPT system, particularly, of the intrinsically unstable e-bike based HIPLEVs.

6.2   Measurement of Vehicular Positioning

The evaluation of DIWPT requires tracking the position and attitude of an EV relative to the lane, while power is also being monitored. Desirable dynamic accuracies are in the order of one to two centimeters for positioning, and of a few degrees of arc for the estimation of attitude, this latter being achieved by inexpensive inertial measurement units (IMU). All position variables are expected to be sampled tens of times per second, to adequately represent EV trajectories.

Dynamic Inductive Wireless Power Transfer for Lightweight Electric Vehicles
Luiz Alberto Lisboa da Silva Cardoso – University of Minho

387

In the FABRIC project [208], a recent representative effort in the quest for practical DIWPT, a 100 m long i-lane was tested for vehicle lateral misalignment using a RTK Real-Time Kinematic (RTK) global navigation satellite system (GNSS). In this phase-sensing based variant of Differential GPS (DGPS), positioning accuracies in the order of one centimeter can be achieved [209]. However, current best commercial RTK-GNSS receivers have a maximum positioning update rate in the order of 20 Hz [210][211], which is just marginally acceptable for DIWPT analysis. These systems are also costly and relatively complex, requiring the transmission of a correction signal from a base station to the mobile station whose positioning is being measured.

Optical positioning measurements, using calibrated cameras and visual fiducial markers [212] and, often, infrared dot-markers, can deliver better accuracies at the required speed rates, in indoors tracking applications [213]. However, their simplicity is diminished when positioning objects over longer paths, due to the need of increasing the number of coordinated cameras to cover extended areas.

Here, a special reference geometry was imposed to the test site, allowing the use of LIDARs fixed on an instrument, which is attached to the EV, to directly measure its position. The calculation of the vehicle-to-lane lateral misalignment was significantly simplified by a robust computation neither involving computer vision processing techniques nor requiring inertial data, which are still required for determining vehicle's attitude and forward progress on lane.

6.2.1 Requirements

The current system implementation is to be used in the evaluation of DIWPT to lightweight electric vehicles, such as electrically assisted bicycles [214]. For this application, the nominal kinematic parameter limits are given in Table 40.

Table 40: Limit parameters assumed for the EV (electrically assisted bike).

Parameter	Maximum Absolute Value
Speed	36 km/h (10 m/s)
Lateral Acceleration	3g (3 x 9.81 m/s^2)
Relative (to lane) Yaw Angle	30°
Roll Angle	15°

The range of measurements and the respective desirable order of error magnitude will vary with application and the objectives of the analysis, as well as the specific characteristics of the power train of the vehicle in test. For instance, typical nominal powertrain voltages for electrically

Dynamic Inductive Wireless Power Transfer for Lightweight Electric Vehicles
Luiz Alberto Lisboa da Silva Cardoso – University of Minho

388

assisted bikes are multiple of 12 V, often 24 V or 36 V. Without much information found on general DIWPT evaluation tools currently available, as well as on DIWPT systems specifically implemented for e-bikes [3], values from own experience guided the adoption of the representative values shown in Table 41:

Table 41: Target range and precision for vehicle onboard measurements.

Parameter	Range	Std Dev of Error
Lateral Displacement	-0.5 m to 0.5 m	< 2.5 cm
DC Harvested Voltage	0 to 100 V	2% of full scale
Power Train Voltage	0 to 40 V	2% of full scale
Powertrain demand	0 to 500W	3% of full scale
Relative Yaw	-30° to 30°	5°
Pitch	-10° to 10°	2°
Roll	-15° to 15°	2°

6.3 Overview of the System Design

The system is implemented as a remote sensing unit to be mounted onto an electric vehicle. Figure 230 shows its high-level block diagram representation.
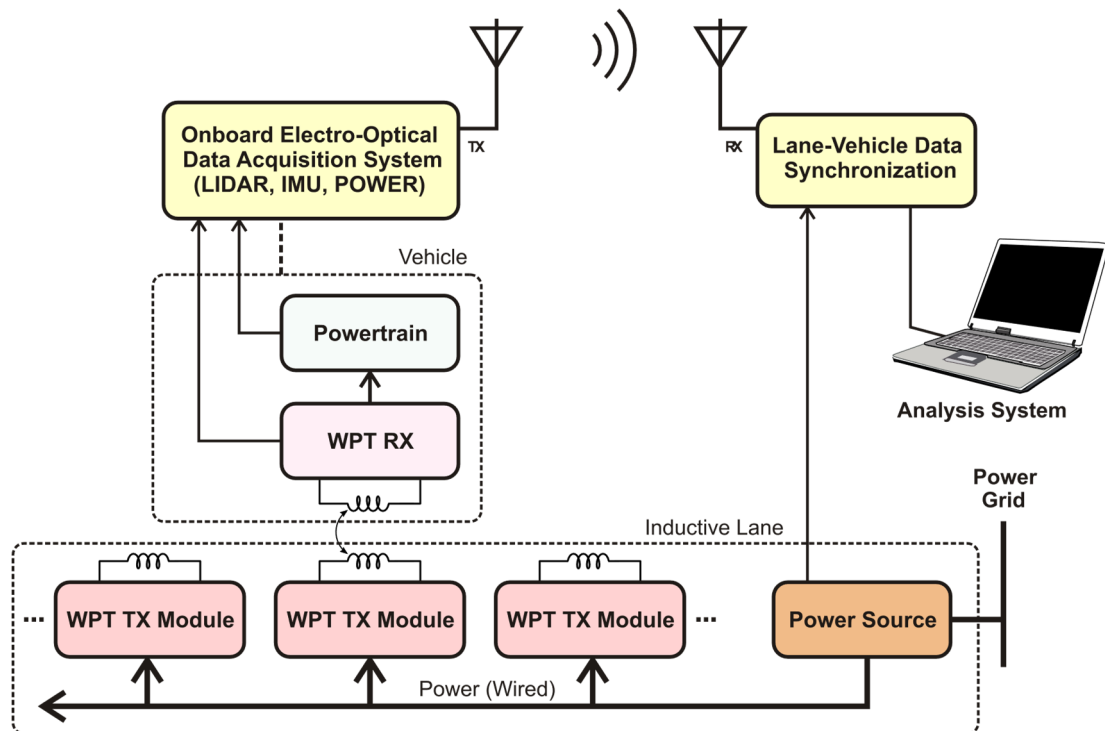
Figure 230: System global architecture, showing vehicle and lane subsystems. All data collected are synchronized and logged for off-line analysis.

Dynamic Inductive Wireless Power Transfer for Lightweight Electric Vehicles
Luiz Alberto Lisboa da Silva Cardoso – University of Minho

389

Positional and electric data from the vehicle's WPT receiver (WPT RX) and powertrain are collected and wirelessly transmitted via a UHF channel, in real time, to a receiver unit that is connected to a computer (running the Analysis System) through a USB communication port. Electric data coming from the i-lane WPT transmitters (WPT TX) can optionally be monitored and synchronized to the vehicular data.

In order not to affect the power consumption of the vehicle itself, the onboard electro-optical data acquisition system is designed with its own battery, which is also installed on the vehicle.

6.4 Reference Geometry and Position Estimation

The system works on the principle that the vehicle's position can be established by knowing the position of a fixed reference geometry. Three individual LIDAR sensors are simultaneously used to measure the lateral distance to the walls of a reference corridor, where the primary inductive modules of the i-lane to be tested lie underneath the floor. Figure 231 illustrates the top view of such configuration, where a single inductive module is under test. Inductive lane modules are aligned and centralized in between the parallel walls (1) of a reference corridor. The measurement unit is installed on the electric vehicle running over the inductive lane, indicated in Figure 231 by a blue dashed curve (3). For lanes of short length, a rear flat vertical surface (2) can be optionally used for referencing the rear LIDAR, if measurements of vehicle speed and longitudinal progress on lane are also required in the analysis.
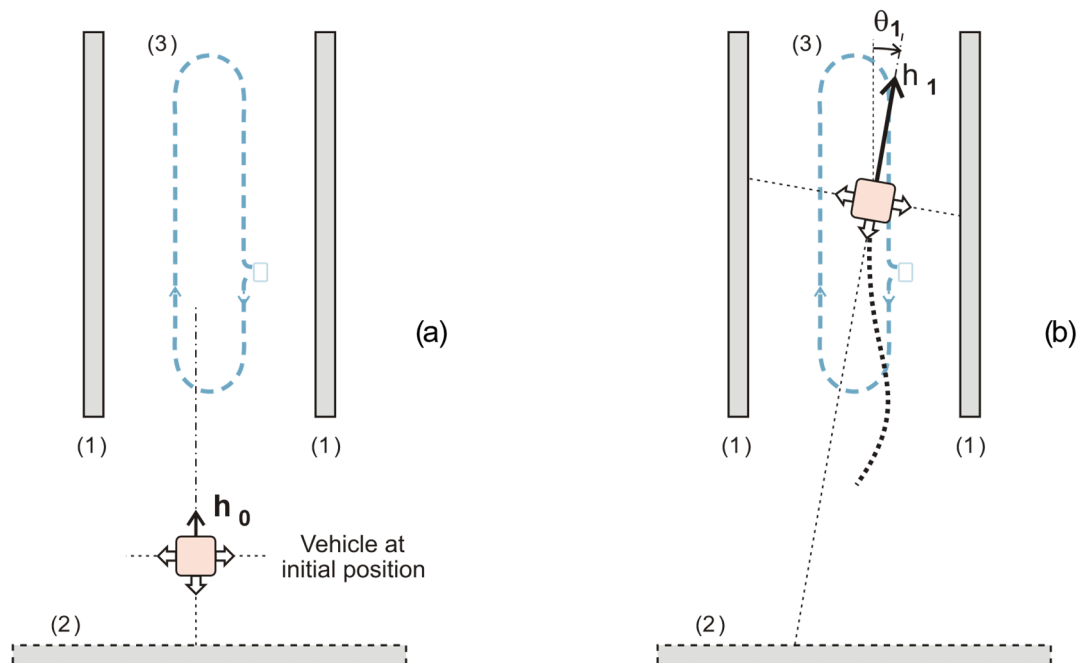
Figure 231: Top view of test range: vehicle at initial position (a) and running in corridor (b).

Dynamic Inductive Wireless Power Transfer for Lightweight Electric Vehicles
Luiz Alberto Lisboa da Silva Cardoso – University of Minho

390

6.4.1 LIDAR-IMU Head Design

The heart of the measuring system is the LIDAR-IMU mounting head, drawn in Figure 232, is a precision machined prismatic rectangular aluminum block of squared base, fixed to the vehicle's structure, mechanically solidary to the pick-up coil used to receive power from the i-lane, where all LIDARs and the IMU are mounted to.
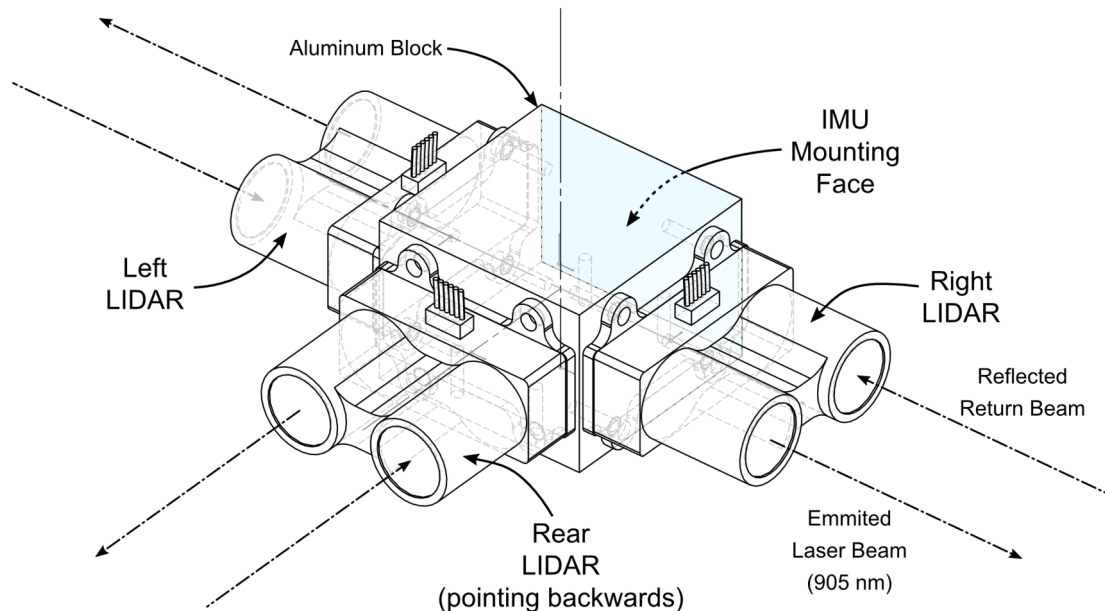
Figure 232: Perspective view of the LIDAR head mounting. An inertial sensor, not shown in the figure, is fixed to the face of the block which is opposite to the face the rear LIDAR is mounted on, with its inertial refence axes orthogonal to the faces of the block.

The left and right LIDAR are aligned-mounted on opposite parallel faces of the block, with beams pointing opposite directions. A third rear LIDAR is mounted on a face of the block that is orthogonal to the faces of the left and right LIDAR, with its beam pointing backwards, in such a way that all the LIDAR beams are in the same plan, adjusted to be as horizontal as possible, when the assembly is fixed to the vehicle's frame, while the vehicle is resting in a neutral position.

The IMU unit, Bosch BNO-055 [215], is installed in small board (Adafruit BNO-055) which is fixed to the fourth vertical face of this precisely machined aluminum block that has parallel opposite faces and orthogonal adjacent faces, as show in Figure 233. This is done in such a way that, when the light beams from the three LIDARs mounted on the other vertical faces are all horizontal, the IMU will indicate zero pitch and roll angles.

Dynamic Inductive Wireless Power Transfer for Lightweight Electric Vehicles
Luiz Alberto Lisboa da Silva Cardoso – University of Minho

391
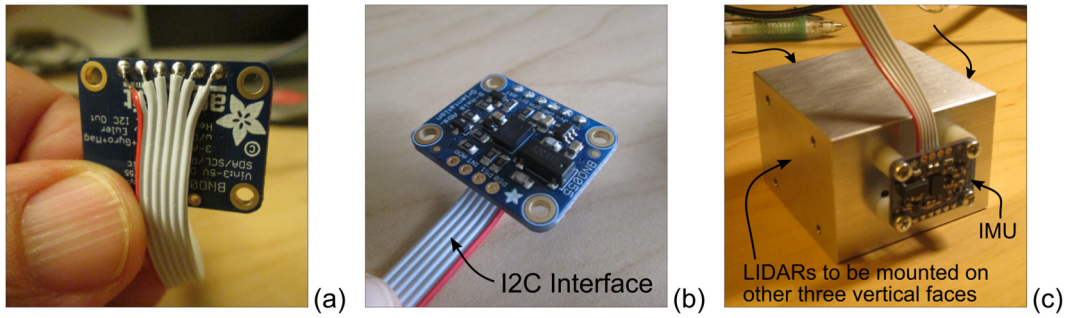
Figure 233: Detail of IMU assembly on the LIDAR head: (a) Cable soldering on the back face; (b) component side shown; and (c) fixed to the LIDAR head block, where the LIDAR are fixed too.

The use of this IMU unit greatly simplifies the task of measuring spatial orientation of the LIDAR header (and thus, of the vehicle). The BNO-055 has an embedded data processor (a 32-bit microcontroller Cortex M0+) running an algorithm that fuses all raw data from a 3-axis 14-bit accelerometer, a 3-axis 16-bit gyroscope and a 3-axis magnetometer, and produces an absolute attitude estimation at a 100 Hz rate, accurate to 2 to 3 degrees of arc.

6.4.2 Attitude Estimation

The IMU embedded in the instrument continuously computes estimates for the absolute spatial orientation of the vehicle, given by the Euler angles heading, pitch and roll (h_k, ρ_k, γ_k). By construction, yaw (horizontal orientation) and heading (direction of movement) will always coincide, unless the vehicle is skidding on the lane, so these terms are indistinctly used in this work. The last two of these angles represent inclination with respect to the horizontal and vertical. The absolute yaw h_k estimated by the IMU at any given measurement cycle k, however, has to be transformed in the relative orientation angle θ_k, by subtracting the yaw reading obtained at the initially aligned start position (h_0, on Figure 231a) from the current yaw reading (for instance, h_1, as shown on Figure 231b):

$$\theta_k = h_k - h_0 \tag{6.1}$$

6.4.3 Progress on Lane

The progress on lane is the distance y from the vehicle (LIDAR-IMU head) to the back-wall, taken along the lane. It is measured by computing the projection of the back-LIDAR beam length $d_B(k)$ onto the lane longitudinal axis:

$$y = d_B(k) \, \cos \theta_k \, \cos \gamma_k \tag{6.2}$$

Dynamic Inductive Wireless Power Transfer for Lightweight Electric Vehicles
Luiz Alberto Lisboa da Silva Cardoso – University of Minho

392

If the reference point on the vehicle is not the center of the LIDAR-IMU head, the corresponding coordinate transform should be additionally applied.

6.4.4 Lateral Displacement

While the Euler angles are necessary to estimate the distance progressed on the lane, to correct the readings of back LIDAR beams to the back wall, (2) in Figure 231, the lateral displacement can be directly and precisely computed as function of the lateral LIDAR measurements only: Due to deliberate construction of the LIDAR head (section 6.4.1) and control circuit, beams of the left and right LIDAR at any cycle k are both simultaneous and colinear, so the lateral displacement x_k of the EV, with respect to center line of the lane, can be determined by the relative proportion of the left and right LIDAR readings, according to (6.3):

$$x_k = \frac{w_C}{2} \frac{\left(d_L(k) - d_R(k)\right)}{(d_L(k) + d_R(k) + w_L)},$$

(6.3)

where $d_L(k)$ and $d_R(k)$, also shown in Figure 234, in red and green, are respectively the calibrated readings of the left and right LIDAR (as in Figure 247); $w_c > 0$ is the constant width of the corridor and $w_L > 0$ is the distance between opposite external faces of the housing of the measurement unit, from where LIDAR distances to the target (wall) are calibrated.
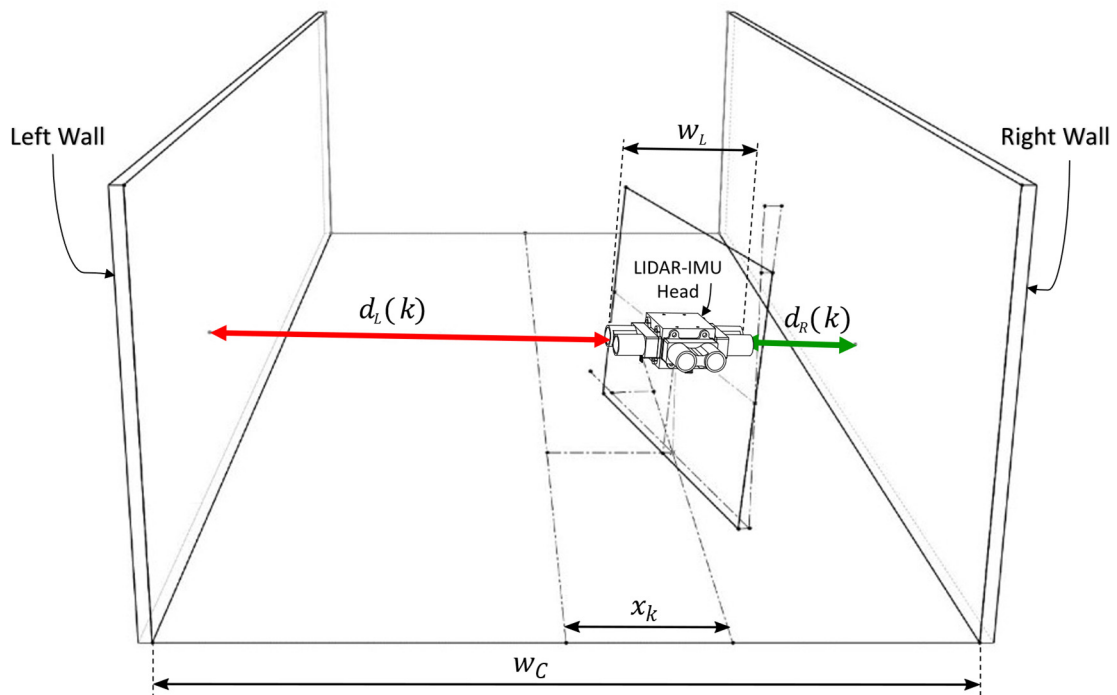
Figure 234: Misalignment determination based on simultaneous left and right LIDAR measurements.

Dynamic Inductive Wireless Power Transfer for Lightweight Electric Vehicles
Luiz Alberto Lisboa da Silva Cardoso – University of Minho

393

The walls should be high enough, considering their distance w_C, the height above ground of the installation of the LIDAR head on the vehicle, H_L, and the maximum expected heading angle, h_k, and vertical roll inclination angle, γ_k. Otherwise, one of the LIDAR beams may miss the wall, and the estimation of x_k will be undefined. As a first approximation, the height for the reference walls, H_W, should be bounded by:

$$H_W \geq w_C \tan \gamma_{max} + H_L \cos \gamma_{max},$$
(6.4)

6.5   Modeling of Errors

Using (6.3) to compute the raw lateral displacement, x_k, which can be modeled as a sample of the associated aleatory variable X_k, has one more benefit other than not depending on the inertial sensor data processed at the IMU: the standard deviation for X_k can be smaller than those of individual measurements coming from any of the LIDARs, left or right.

Let us assume that both lateral LIDARs have the same behavior and the errors in their measurements are statistically independent and, after calibration, with normal distribution of zero mean. Because the lidar sensors are all of the same type, it is reasonable to assume that the standard deviation of this normal distribution is equal to a constant σ_L, which is a characteristic of the LIDAR model. So, $d_L(k)$ and $d_R(k)$ are samples of aleatory variables $D_L(k)$ and $D_R(k)$, such that:

$$D_i(k) = T_i(k) + E_i, \quad E_i \sim N(0, \sigma_L{}^2), \ \text{i} \in \{L, R\},$$
(6.5)

where $T_L(k)$ and $T_R(k)$ are the true, but unknown, beam lengths from each LIDAR to its respective target wall, and E_L and E_R are aleatory errors that can be modeled by independent identical normal distributions with zero mean and standard deviation σ_L. Under these simplifying assumptions, a vehicle running parallel to the corridor will have a normalized standard deviation σ/σ_L varying according to its relative lateral displacement, σ_L/w_C, as shown in the plot of Figure 235 (obtained by numerical simulation).

Dynamic Inductive Wireless Power Transfer for Lightweight Electric Vehicles
Luiz Alberto Lisboa da Silva Cardoso – University of Minho

394
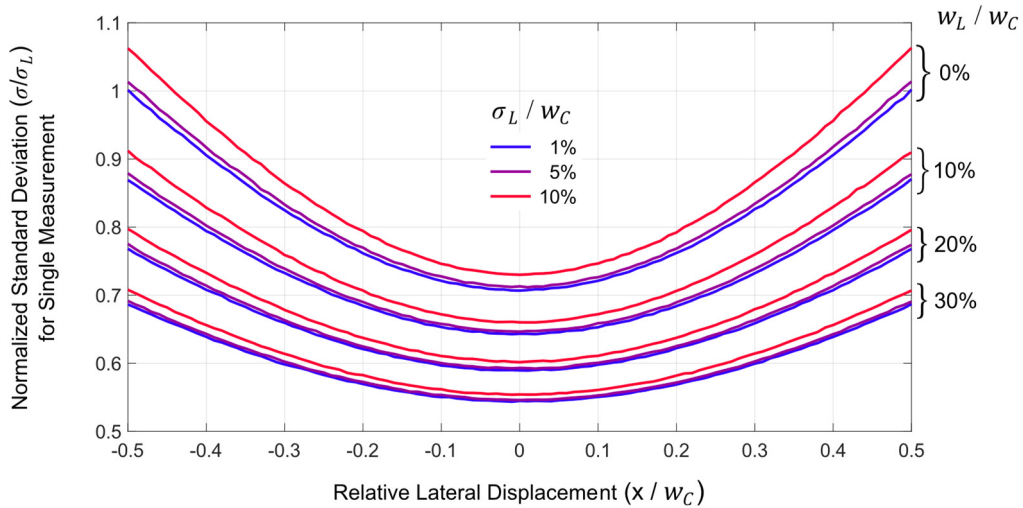
Figure 235: Normalized standard deviation of lateral displacement estimation, as a function of the true relative lateral displacement in the corridor (-0.5 means vehicle at left wall and +0.5, at right wall). The curves are shown for different constructive w_L/w_c ratios and relative standard deviations σ_L/w_c of the LIDAR measuring errors.

At the limit condition $w_L/w_c = 0$, for small σ_L/w_c ratios (5% or less), the standard deviation of X_k can still be up to approximately 30% smaller than σ_L, when the vehicle is close to the center of the lane, thus improving the quality of the lateral displacement measurement with respect to a single LIDAR measurement, as expected under the assumption of statistical independence of the errors on the two measurements $d_L(k)$ and $d_R(k)$. For the LIDAR components used in the design, the standard deviation errors E_i of are proportional to the distances to be read, $T_i(k)$, ranging around 1% for distances 1 m and above. So, by using calibrated LIDARs, the standard deviation of a single measurement of the lateral displacement can be reduced up to approximately 0.7 %, when the vehicle lies in the central region of the corridor. That corresponds to a ±7 mm error for 2 m wide corridor, when travelling parallel to the reference walls. By filtering or smoothing a series of consecutive measurements along a trajectory, the random error can be further minimized, depending on vehicle kinematics.

In the analysis of DIWPT applications, rather than logging the position of the mounting head itself, often the center of the pick-up coil installed on the EV will be the point of reference for measuring misalignment. Since the pick-up coil is also mechanically solidary to the frame of the vehicle, a simple transform can compute the movement of the coil center (or any other point fixed on the vehicle), based on the estimated position of the center of the LIDAR-IMU block.

6.5.1 Reduction of Error Variance

Assuming a smooth and flat lane with no obstacles, and no intrinsic vehicle vibration due to the power train or other factors, the perturbation on the vehicle movement can be entirely

Dynamic Inductive Wireless Power Transfer for Lightweight Electric Vehicles
Luiz Alberto Lisboa da Silva Cardoso – University of Minho

395

attributed to the human control when riding (or steering), which is ultimately related with human skeletal muscles movements. Since the fastest human hand or finger movements that can be produced lie in the range between 6 to 12 Hz [216], the sampling rate for measuring the vehicle position, f_{pos}, can be conservatively set at 60 Hz. A low-pass filter matching this expected bandwidth, with cutting frequency of 12 Hz, is used to condition the sequence of calibrated readings of each LIDAR, reducing the standard deviation of distance estimations.

A Finite Impulse Response (FIR) smoothing window, associated with a low-pass filter with a cutting frequency of 12 Hz and maximally flat response over the pass band, was designed and integrated in the analysis software. Filter coefficients and frequency magnitude response characteristics are shown in Figure 236.
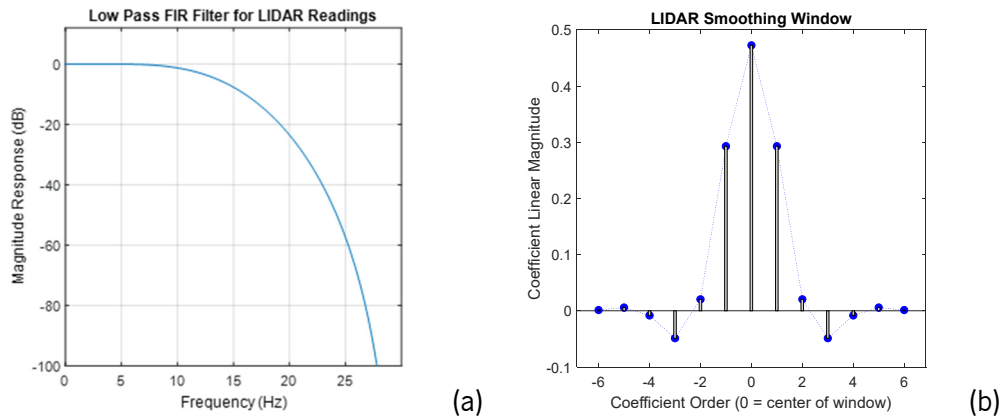
Figure 236: Characteristics of the smoothing window for the LIDAR readings, implemented as a low-pass FIR filter of order 12, for the design LIDAR sampling frequency of 60 Hz: (a) Frequency response. (b) Filter coefficients.

Let us assume that the vehicle moves in a zigzag pattern, with a sinusoidal trajectory along the center lane, with amplitude A and constant speed v. Then it can be showed that, at the points of maximum lateral displacement A, the modulus of the lateral acceleration a_x will be maximum, with a_x being calculated as:

$$a_x = -A\left(\frac{2\pi}{\sigma}\right)^2 v^2 \,, \tag{6.6}$$

where σ is the periodic distance along the path required for vehicle to repeat the oscillatory movement.

Exemplifying, at the constant speed $v = 36$ km/h (10 m/s), if the amplitude of the movement $A = 20$ cm and the oscillatory pattern distance is as short as $\sigma = 5.2$ m, the resulting maximum instantaneous lateral acceleration $|a_x|$ is 29.2 m/s^2, which is about 3g, i.e., three times the acceleration of the gravity on Earth's surface.

Dynamic Inductive Wireless Power Transfer for Lightweight Electric Vehicles
Luiz Alberto Lisboa da Silva Cardoso – University of Minho

396

Considering the error modeling as in Section 6.5, for all LIDARs in the system, the statistical behavior of the error in lateral displacement (6.3) estimation for this trajectory can then be computed by Monte Carlo simulations. The results obtained for this exemplary case, of a vehicle at the limit design maximum speed of 10 m/s, zigzagging with an amplitude of 20 cm in a sinusoidal pattern every 5.2 m, which is a very extreme maneuver for a bike (which would doubtfully be achieved by a rider, in real traffic conditions), are shown in Figure 237, assuming the measurements are performed within the walls of corridor with a width $w_c = 178$ cm.
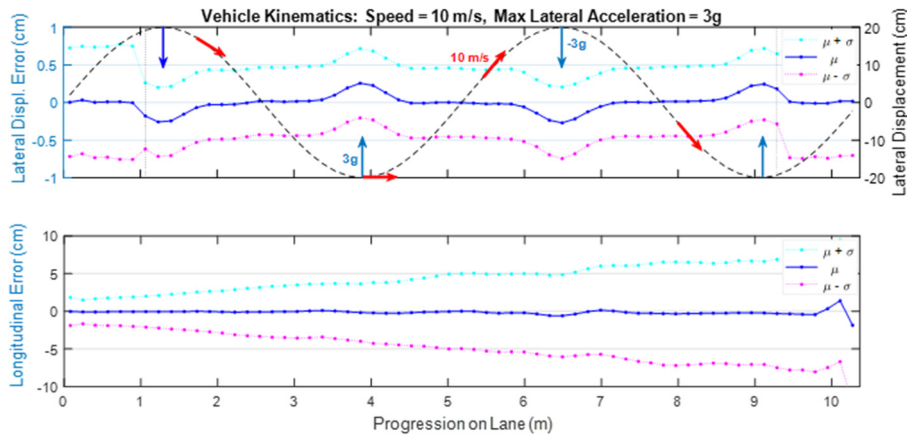
Figure 237: Simulated statistics of positioning error, showing expected mean and standard deviation error for a vehicle on sinusoidal trajectory at limit design kinematics. (a) Error behavior in vehicle's lateral displacement measurement, as the vehicle progresses forward on the lane; (b) tendency for errors in longitudinal position.

The error pattern in lateral displacement is regular along the vehicle's trajectory, with mean µ very close to zero most of the time, except at maximum excursions, when the measurement will lag behind the movement, resulting in a biased error up to approximately 3 mm. The standard deviation of the error remains practically constant, about 5 mm along all the lane, except for the first and last $N/2$ measurements on the lane, due to the smoothing window filter order N, where it raises to values of the standard deviation of a single measurement. These values will vary proportionally to the standard deviation characteristic of the LIDAR readings, which will depend on the actual LIDAR model and the geometry (w_c) of the reference corridor being used.

6.5.2 Longitudinal Error

In Figure 237b, the longitudinal error can be noted to be unbiased along all the vehicle's path. The standard deviation, however, starts with a minimum value σ_L in the order of 2 cm, and increases approximately in proportion to the progression on the lane, due to the dependency of the forward displacement estimation on a single back LIDAR reading, which has a standard deviation that is also proportional to the distance to the back wall, in the case of our experiment, located 2 m behind the corridor entrance, the point of zero progression on lane.

Dynamic Inductive Wireless Power Transfer for Lightweight Electric Vehicles
Luiz Alberto Lisboa da Silva Cardoso – University of Minho

397

This behavior limits the application of the proposed configuration to lane modules up to about 6 m long, in the case secondary measurements related to forward movement of a vehicle are to be performed. For lateral displacement measurements, there is no such limitation, if the reference corridor is long enough to enclose the lane module to be evaluated.

6.6   Detailed System Architecture

As depicted in Figure 230, the system has two main components, the first, which is attached to the electric vehicle under test, consisting of an electro-optical monitor (EOM), and the second, the lane data logger (LDL), which is electrically connect to the inductive lane. These two components have independent measuring capabilities and can work in stand-alone operation. However, they are normally wirelessly connected, by means of a real-time dedicated UHF link, what allows the time-referenced electrical and positioning data coming from the vehicle (EOM) to be automatically synchronized at the lane side by the LDL.

6.6.1 Onboard Wireless Electro-Optical Monitor (EOM)

This unit, which is mechanically solidary to the vehicle frame, is detailed in the block diagram of Figure 238. It has three LIDARs, one pointing right, one pointing left and one pointing backwards. All these LIDAR (Garmin Lite v3) and the IMU (Bosch BNO-055) are connected by a 400 kbit/s I2C bus to a master 32-bit STM32F103C8T6 microcontroller [217] [218], the "Position Processor", which runs a supervisor program that every 16.67 ms gets the distance measurements from the LIDAR sensors, the Euler angles from the IMU, and the vehicle electric data coming through a dedicated 230.4 kbaud/s asynchronous serial bus from another STM32F103C8T6 microcontroller functioning as a multimeter and wattmeter, the "Electric Data Processor". To accommodate different timing requirements, data from different sensors are buffered in one cycle and transmitted in the next cycle.

In order to simplify real timing programming, a serial channel transponded in the UHF band was chosen to connect the vehicle with the lane analysis system. The modules used in this implementation were the readily available and easy to program HC-12 wireless serial port communication, which working frequency programable to any of the 100 channels of 400 kHz bandwidth existing in the 433.4 MHz to 473.0 MHz band. The transmitting power of module is also programable, up to a maximum 100mW (20 dBm), and the receiving sensitivity is -117dBm at baud rate of 5,000bps in the air, conditions under which, according to the manufacturer, successful communication is achieved at a distance of up 1,000m in open space, in low noise

Dynamic Inductive Wireless Power Transfer for Lightweight Electric Vehicles
Luiz Alberto Lisboa da Silva Cardoso – University of Minho

398

conditions [219]. By actually experimenting with these modules in a laboratory environment, it was verified that the bit error rate was estimated to be less than 10^{-5}, at 38400 baud, 14 dbm and distances in excess of 20 m, which is more than enough for the intended test conditions in the HIPLEV application, when testing lane modules from 1 m to 10 m long. To further increase data integrity, a 16-bit checksum was introduced at the end of each 24-byte long data frame.
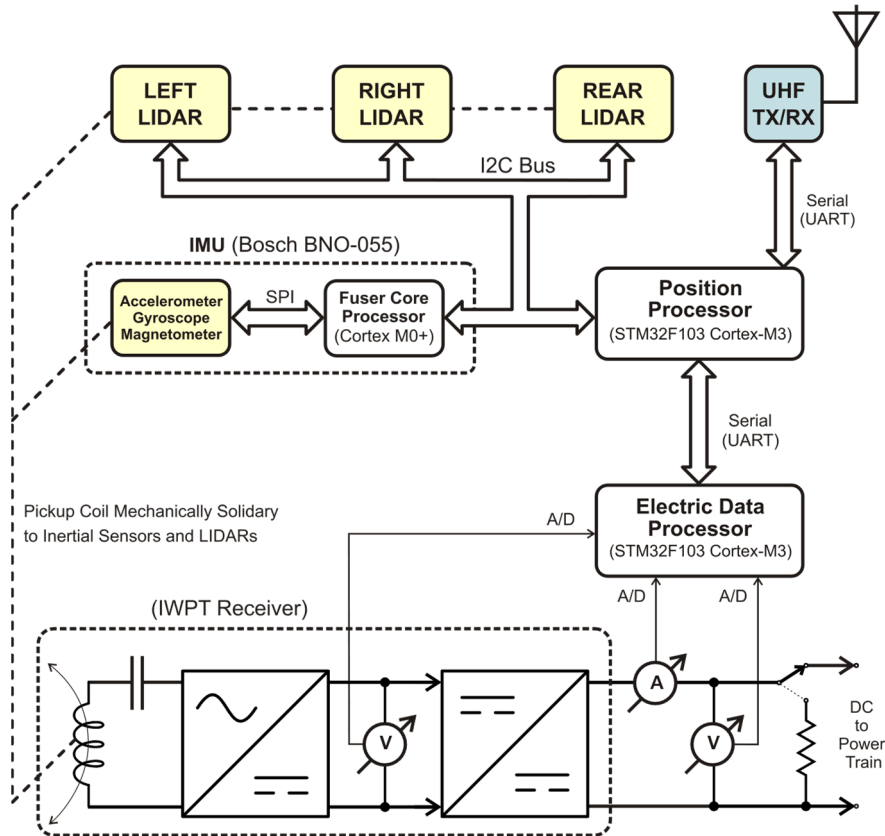
Figure 238: Electro-optical data acquisition system architecture on board of the electric vehicle.

The adoption of a sampling period T_{pos} = 16.67 ms for the positional data, corresponds to a sampling frequency, f_{pos}, of 60 Hz, which implies (Nyquist Theorem) in a maximum tolerable bandwidth for the vehicle movement $BW_{pos} = f_{pos}/2 = 30$ Hz. Based on the predicted bandwidth limitation of 6 Hz to 12 Hz, as seen in section 6.5.1, all LIDAR calibrated measures can be further subjected to a low pass filter to reduce the variance of measurement errors.

The Electric Data Processor, on the other hand, performs analog-to-digital conversion on the signals coming from two voltmeter channels, which share a common ground reference, and a third channel sending data from a galvanically isolated Hall-effect amperemeter. When monitoring the electric vehicle, the amperemeter channel is intended to be associated with one of the voltage channels in a series-parallel connection. Power is then computed by discrete integration of the product of these readings.

Dynamic Inductive Wireless Power Transfer for Lightweight Electric Vehicles
Luiz Alberto Lisboa da Silva Cardoso – University of Minho

399

The sample rate of the electric signals, f_{power}, was set to 6 kHz, a hundred times greater than f_{pos}. A new power estimate, integrated over the most recent 16.67 ms interval, is produced every T_{power} = 166.7 µs = 16.67 ms/100, and becomes available to be asynchronously read upon request of the Position Processor. The rms values for all other electric signals are similarly computed. In this manner, although the electric data is read just once every 16.67 ms, there will be no loss of information on the total power and average effective values of voltages and current, except where induced by noise or arithmetic rounding errors, if the maximum electric data bandwidth is limited to $BW_{power} = f_{power}/2 = 3$ kHz.

The power transferred in a DIWPT configuration is expected to depend mostly on: (i) the relative position of the WPT receiver (in the vehicle) and the WPT transmitter (in the lane), which is also assumed to be bandwidth limited to BW_{pos}; (ii) the fluctuations on the power demand of the powertrain; and (iii) the switching state (ON/OFF) and time response of the power electronics driving the IWPT transmitter and receiver. To facilitate evaluating the profile of the maximum WPT as a function of lateral displacement, the IWPT transmitter should be kept always activated, and the load coupled to the IWPT receiver, on board of the vehicle, should be made constant. The system developed is then furnished with a dummy DC load to momentarily replace the power train during maximum transferred power profile tests.

Positional and electric data are packed together into 26-byte frames, including a time tag and a check-sum word, and periodically transmitted over UHF at 38400 baud/s. The UHF radio-modem used can be programmed to output power levels up to 20 dBm (100 mW), using any of 100 channels in the 433.4 MHz to 473.0 MHz band. This is enough power to achieve virtually errorless transmission up to 30 m range in free space, a distance by design much larger than the length of the inductive modules and lane segments the equipment was built to monitor.

6.6.2 Lane Data Logger (LDL)

This unit receives and logs the vehicle data to a "Data Log Computer", as shown in the block diagram of Figure 239. It can also optionally monitor and log electric data coming from the i-lane. A "Lane Activity Log Processor" acquires electrical data from the lane and merges it into data frames coming from the electro-optical measuring system installed on board of the vehicle. Because of the delays involved in measuring and transmitting over the UHF link the positional and electrical data coming from the EV, the "Lane Activity Log Processor" has to introduce compensatory delays in the lane data stream, to time-align both data sources.

Dynamic Inductive Wireless Power Transfer for Lightweight Electric Vehicles
Luiz Alberto Lisboa da Silva Cardoso – University of Minho

400
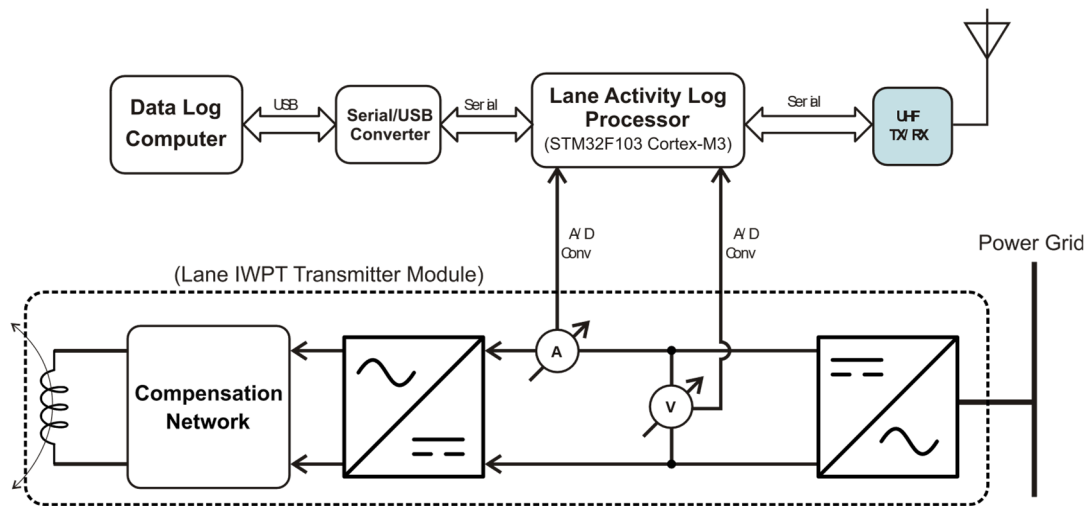
Figure 239: System architecture on the lane side: Real time data coming from vehicle is received and associated with simultaneous electric data sampled from the lane WPT transmitter module.

6.7 Supplementary System Sensors

In addition to the LIDAR-IMU based power and positioning monitoring system, other two independent subsystems were integrated into the developed equipment as general tools for future use, in support of the evaluation of DIWPT of EVs: an Auxiliary Scanning LIDAR (ASL) and a Secondary Data Logger (SDL). These units were directly connected to an onboard computer running Windows 10, which was also wirelessly linked to the analysis system running on the lane-based computer.

Differently from the main data collection, which is time tagged, transmitted from vehicle to the lane analysis system via a dedicated UHF link, and synchronized with lane data, the data collected from supplementary sensors need further processing, if synchronization is to be achieved. In the initial version of the EOM, the only of the supplementary sensors currently in use is the ASL. By producing a clear visual profile of the walls around the vehicle, the ASL imaging facilitates the selection of most significative experiment runs.

6.7.1 Auxiliary Scanning LIDAR (ASL)

A short range (8 m) scanning LIDAR that rotates continuously at 5 Hz to 15 Hz (300 rpm to 900 rpm), providing 360° horizontal scan, with up to 4000 distance readings per second (model A2M8, manufactured by Shanghai Slamtec Co., Ltd.) It will allow future investigation of simultaneous localization and mapping (SLAM) techniques [220] as an alternative for positioning determination. Its current function is solely to provide panoramic LIDAR scene visualization, for checking consistence of the positioning data logged in the test runs.

Dynamic Inductive Wireless Power Transfer for Lightweight Electric Vehicles
Luiz Alberto Lisboa da Silva Cardoso – University of Minho

401

6.7.2 Secondary Data Logger (SDL)

The SDL is an independent, four-channel, differential analog-to-digital converter, of up to 40 kSamples/s per channel, data-logging system, for monitoring any electrical signal on board of the vehicle was also installed in the system rack. The gain of each channel can be independently programmed to allow measuring signals up to ±100 V in amplitude. Data can be logged locally on disk, for posterior analysis, or relayed over a Wi-Fi link, for remote real-time system monitoring. It can, for instance, be used as a redundant power logging system, to validate the consistence of the main data collected by the EOM. Depending on the intended use and signals to be monitored, the SDL may require further specialized interface sensors to be installed on the EV.

6.8 System Implementation

In this section a brief overlook of the implementation of our Electro-Optical Measurement System for evaluation of DIWPT configurations, which is constituted by the Electro-Optical Monitor (EOM) and the Supplementary Sensors.

The EOM has four connections with the external world:

- The power cord, which brings +5 VDC to the system through an IP68 watertight USB connector. The line is supplied by a dedicated 10.000 mA USB power bank.

- The current input cable, with two conductors that are short circuited through the Hall sensor in the PMM, so that the instantaneous current on the powertrain can be read and used to compute, by discreet integration, the net supplied power to the vehicle.

- The current and power to be measured can be that supplied to the powertrain or, optionally, to a battery, depending on the purpose of each test or study.

- The voltage signal input cable, with three twisted pairs: (i) one for reading the high side voltage, V_H, which is used to monitor induced voltage, after its rectification stage in the secondary; (ii) one for reading the low side voltage, V_L, which should be connected in parallel with the DC input to the motor controller; and (iii) the

- Two local OLED displays, that continuously report the electrical data being measured by the PMP and the positional and attitude data being measured by the LIMUM.

- The UHF antenna, from where the vehicle data stream is broadcast to the receiver at the lane side, where data frames are assembled and the information is passed to the DIWPT software analysis system, running on a computer.

Dynamic Inductive Wireless Power Transfer for Lightweight Electric Vehicles
Luiz Alberto Lisboa da Silva Cardoso – University of Minho

402

In the EOM, the LIDAR-IMU head is assembled in the same enclosure with the main other modules: the Power Measurement Module (PMM) and the LIDAR and IMU controller module (LIMUM), where a UHF transceiver module (HC-12, from Seeed Technology Co., Ltd.) is also installed. Figure 240 is a simplified representation of the EOM assembly.
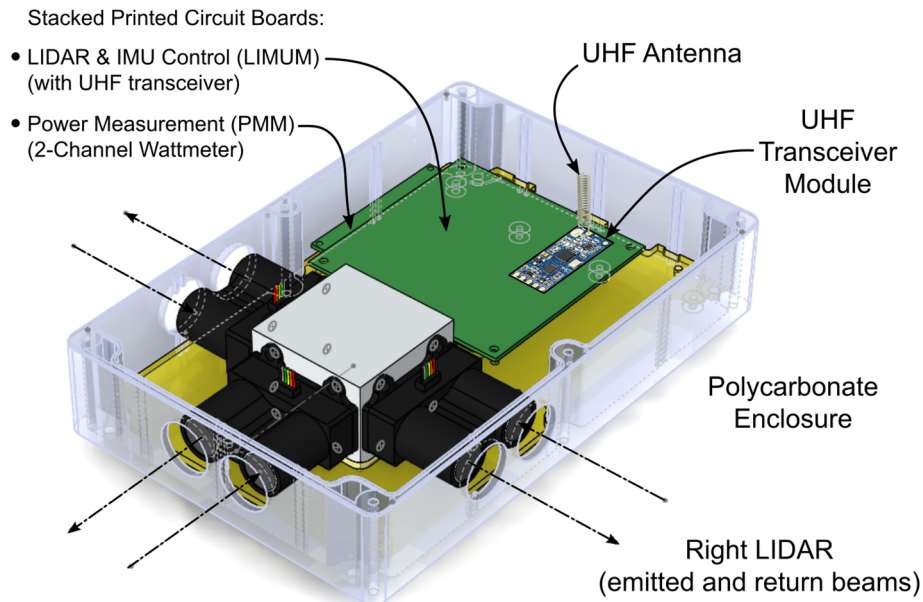
Figure 240: Electro-Optical Monitor (EOM) simplified layout.

All wired connections are communicated with the exterior of the EOM enclosure via IP68 watertight connectors. The polycarbonate enclosure itself has a transparent polycarbonate lid that, when closed, serve as a protective dome for the UHF antenna and the OLED displays, and makes the whole assembly also IP68 watertight, except, as expected, concerning the lateral and rear openings for the LIDAR beams. The IP68 capability could be retained by sealing the beam windows with 2 mm clear transparent acrylic sheets, which were actually cut to size and tested no to significantly interfere with the measurements, after calibration (only a slight reduction in the maximum detection range of 40 m was noticed). However, for this first prototype the watertight capability was not essential, because all tests pursued were indoors.

6.8.1 Power Measurement Module

The implementation of power measurement subsystem was conceived and cost-optimized to evaluate electrically assisted DIWPT bicycles [214] [3]. It has two independent voltmeters and one amperemeter. One of the two voltmeter channels is associated with the amperemeter channel to provide power readings of the input to the power train or the substitute dummy load. The other voltmeter channel can be used, for instance, to measure the voltage at the DC output of the WPT receiver and pattern the voltage and power availability at any given position. All channels and the

Dynamic Inductive Wireless Power Transfer for Lightweight Electric Vehicles
Luiz Alberto Lisboa da Silva Cardoso – University of Minho

403

power product are sampled at 6 kHz and integrated over the most recent period of 16.67 ms, to provide readings of rms values over the positioning measurement cycles. The Hall sensor used in the design (ACS-712-30A, from Allegro MicroSystems, LLC) converts current to voltage with a factor of 66 mV/A, at a worst-case output accuracy of 1.5% at 25 C, due to non-linearity. The zero current level corresponds to a 2.5 V output of the Hall sensor. The voltmeter channels have a maximum 0.5% error due to restive networks (voltage divisor). All conditioned signals are presented before the A/D (analog to digital) converter inputs of the STM32F103C8T6 microcontroller, from ST Microelectronics, with a reading range from 0 to 3.3 V at 12-bit, with a maximum total conversion error of ±7.5 LSB (least significant bit) and a typical maximum error of ±4.3 LSB at 25°C, as shown in Table 42.

Table 42. Electric data typical maximum errors at 25°C for uncalibrated single measurements.

Channel	Reading	Range	Multiplier	Uncalibrated Error
V_H	High side voltage	0 to 134.2 V	1/41.6667	0.5%+4.3/4096 = 1.6%
V_L	Low side voltage	0 to 45.1 V	1/13.6667	0.5%+4.3/4096 = 1.6%
I	Current	-12.1 to 30 A	66 mV/A	1.5%+4.3/2703 = 3.1%
P_H	High side power	-1.6 to 4 kW	(indirect)	1.6% + 3.1% = 4.7%
P_L	Low side power	-545 to 1353 W	(indirect)	1.6% + 3.1% = 4.7%

The instantaneous maximum power error (of a single measurement), given by the product of I x V_k, can be computed by adding the relative errors of I and V_k, that is, 1.6 % + 3.1 % = 4.7 %. System calibration, however, can greatly compensate errors due to non-linearity, leaving practically only the typical random A/D conversion errors of respectively 1.1 % and 1.6 % for voltages and current. This gives a precision of 2.7 % for instantaneous power readings, a figure that is further reduced when the Electric Data Processor integrates the N = 6 kHz / 60 Hz = 100 power samples and computes the average power along every 16.7 ms cycle.
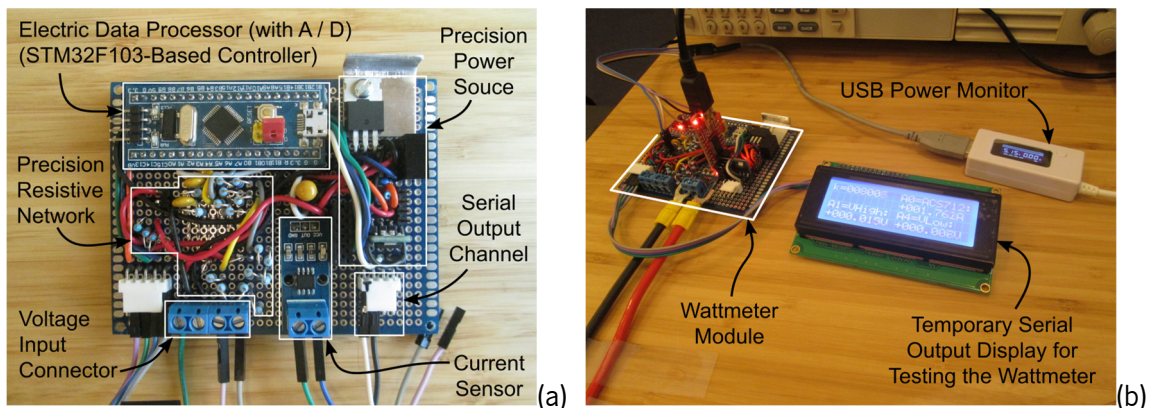
Figure 241: EOM-Wattmeter: (a) Identification of main block components; (b) during initial isolated module tests.

Dynamic Inductive Wireless Power Transfer for Lightweight Electric Vehicles
Luiz Alberto Lisboa da Silva Cardoso – University of Minho

404

6.8.2 Attitude, Positioning and Electric Data Synchronization

Each single LIDAR measurement computed and logged at $f_s = 60$ samples per second, is obtained from the integration of individual pulse readings at a faster rate (> 10 kHz), until a good correlation peak is detected in the return signal, backscattered by the reference walls. The maximum number of scan pulses used in this scan process can be programmed, and was experimentally optimized at 16, for a good balance between fast, stable, and accurate readings. The correlation analysis of each of these pulse trains is accomplished in the average time $t_{corr} = 2$ ms.

Euler angles are also logged at 60 samples per second, but their readings come from an inner data fusion estimation process running on the IMU, at a rate $f_{IMU} = 100$ Hz. Since f_s and f_{IMU} are asynchronous, the IMU data can be up to $1/f_{IMU} = 10$ ms "old" with respect to the reading time. Similarly, the supervisor program running on the Position Processor executes several tasks along each 16.67 ms cycle, in such a manner that different sensors are not read at the same time. UHF transmission is not an instantaneous process as well: beyond the almost negligible propagation delay, the data is cached into a dedicated modulation processor and transmitted at 38.4 kbaud/s. The supervisor program running on the Position Processor executes tasks briefly described in Table 43 in a pipeline, according to the scheduling shown in Figure 242.

Table 43. Main tasks executed by the LIDAR and IMU controller unit (LIMUM).

Activity Description		
A1 - Write data frame to the buffered UHF channel.	**A4** -Start new set of LIDAR measurements.	**A7** - Write data frame to buffered serial debugging channel.
A2 - Buffered UHF transmission of data frame.	**A5** - Read Euler angles from IMU.	**A8** - Echo data to optional debugging terminal.
A3 - Read LIDARs' internal data buffers.	**A6** - Compute checksum.	**A9** - Controller Idle.

Dynamic Inductive Wireless Power Transfer for Lightweight Electric Vehicles
Luiz Alberto Lisboa da Silva Cardoso – University of Minho

405
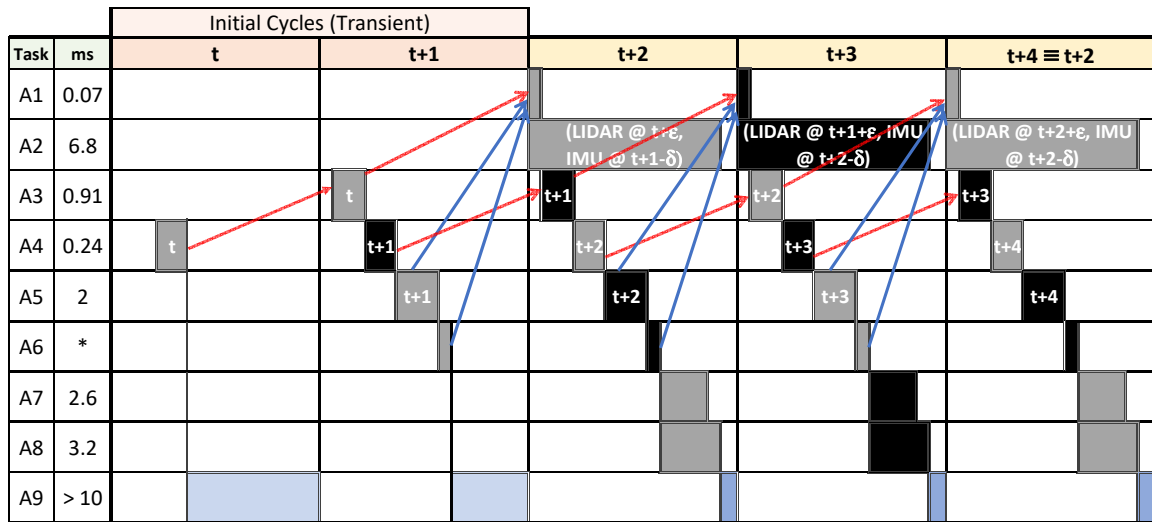
Figure 242: Task schedule for synchronous LIDAR and IMU data acquisition and transmission. Time bars are not drawn to scale. Tasks numbered A1 to A9 are described in Table 43

LIDAR data sampled in cycle t (task A4) is read in cycle $t+1$ (task A3) and transmitted in cycle $t+2$, in the same frame with IMU data collected (task A5) at cycle $t+1$. Therefore, the mean delay $\overline{t_d}$ between LIDAR to IMU readings that are packed in the same data frame will be:

$$\overline{t_d} = \frac{1}{f_s} + \left(t_{A1} + t_{A3} + t_{A4} + \frac{t_{A5}}{2} - \frac{1}{2f_{IMU}} \right) - (t_{A1} + t_{A3} + t_{A4} + t_{corr}) \qquad (6.7)$$

$$\overline{t_d} = \frac{1}{f_s} - \frac{1}{2f_{IMU}} + \frac{t_{A5}}{2} + \frac{t_{corr}}{2} \cong 13.7 \text{ ms} \qquad (6.8)$$

with the actual delay t_d ranging in the interval:

$$7.7 \text{ ms} \cong \overline{t_d} < t_d < \overline{t_d} + \frac{1}{2f_{IMU}} + \frac{t_{corr}}{2} \cong 19.7 \text{ ms} \qquad (6.9)$$

All the positioning data, together with the vehicle electrical data, suffer an additional transmission latency: Due to the intrinsic characteristics of the UHF radio modem used, the transmission of the first bit of the data frame is only started about $t_{Lat} = 14$ ms after it is transferred to the associated UART buffer (task A2). The last bit of the measurement data frame coming from the vehicle is then received at Lane Activity Log Processor t_V after the beginning of the transmission:

$$t_V = t_{Lat} + \frac{(26 \text{ bytes/frame}) \times (10 \text{baud/byte})}{38400 \text{ baud}} \cong 20.8 \text{ ms} \qquad (6.10)$$

The precise analysis of the logged data takes these delays into consideration, to time-align the lagging lateral displacement measurements, based only on LIDAR readings, with respect to

Dynamic Inductive Wireless Power Transfer for Lightweight Electric Vehicles
Luiz Alberto Lisboa da Silva Cardoso – University of Minho

406

the attitude measurements, the electric measurements of the powertrain, and the electric measurements coming from the i-lane. Figure 243 shows the timing of the main events in the system, from LIDAR reading start until data from measurements on board of the vehicle is available on the stationary receiver, ready to be associated to the i-lane power metering subsystem. A new aligned data set of measurements is available every 16.67 ms (60 Hz rate).
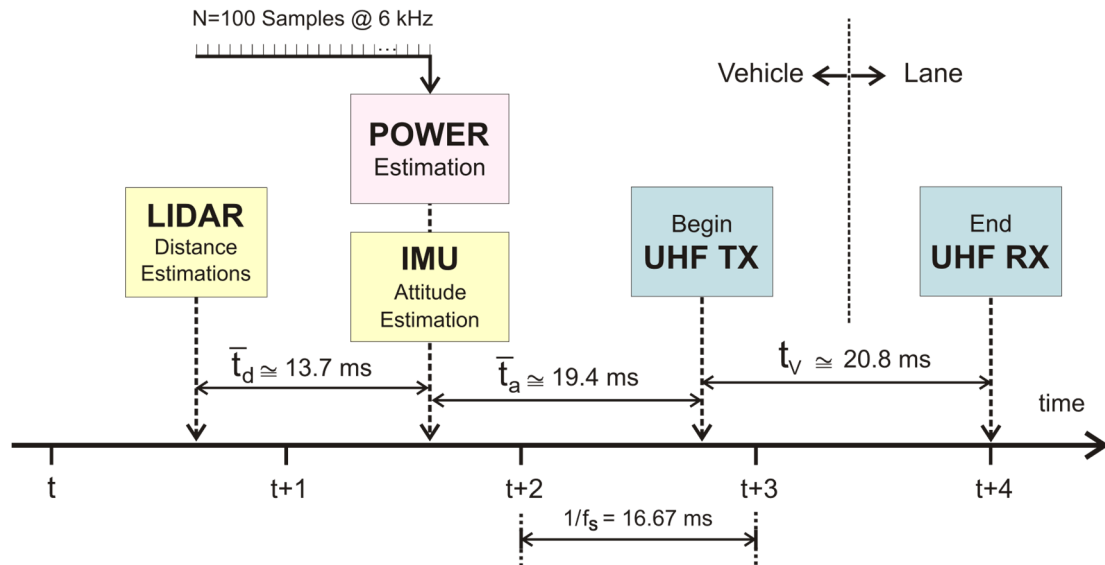
Figure 243: Timeline of main events in the system, from measurements on board of EV to UHF transmission and synchronization with lane data.

6.9 Prototype Integration

The electronics of the system were organized into two printed circuit board units, one for the LIDAR-IMU control and the other for power measurement, both using STM32F103 32-bit microcontrollers (Cortex-M3 core architecture), with a clock speed of 72 MHz. To permit local monitoring of the Electro-Optical Monitor (EOM), two organic LED (OLED) displays were added to this unit, one to monitor the Power Measurement Module (PMP) and the other, the LIDAR and IMU readings from their controller module (LIMUM).

During normal operation, commanded by an external "LOG" switch being closed by the rider, the data frames are continuously transmitted through the UHF channel and remotely logged, and both local OLED displays will show the status message "RECORDING MODE ACTIVATED". When this external switch is open, the data frame transmission is suspended, and the all the measurements are continuously refreshed on the OLED displays. On the PMP display, P (power), V_L (low voltage), V_H (high voltage), and I (current) measurements are displayed, while on the

Dynamic Inductive Wireless Power Transfer for Lightweight Electric Vehicles
Luiz Alberto Lisboa da Silva Cardoso – University of Minho

407

LIMUM display, the readings of h (heading), r (roll) and p (pitch) are, every 4 s, alternately displayed with the LIDAR distance readings, B (backwards), R (right) and L (left).

Figure 244 shows all the modules of the EOM, except the external LOG activation switch, interconnected and powered-up. Since the LOG switch, which is externally attached to the bike's handlebar, is not connected, the LOG terminals are left open and the system is induced to operate in local mode, reason for the displays are showing measurements.
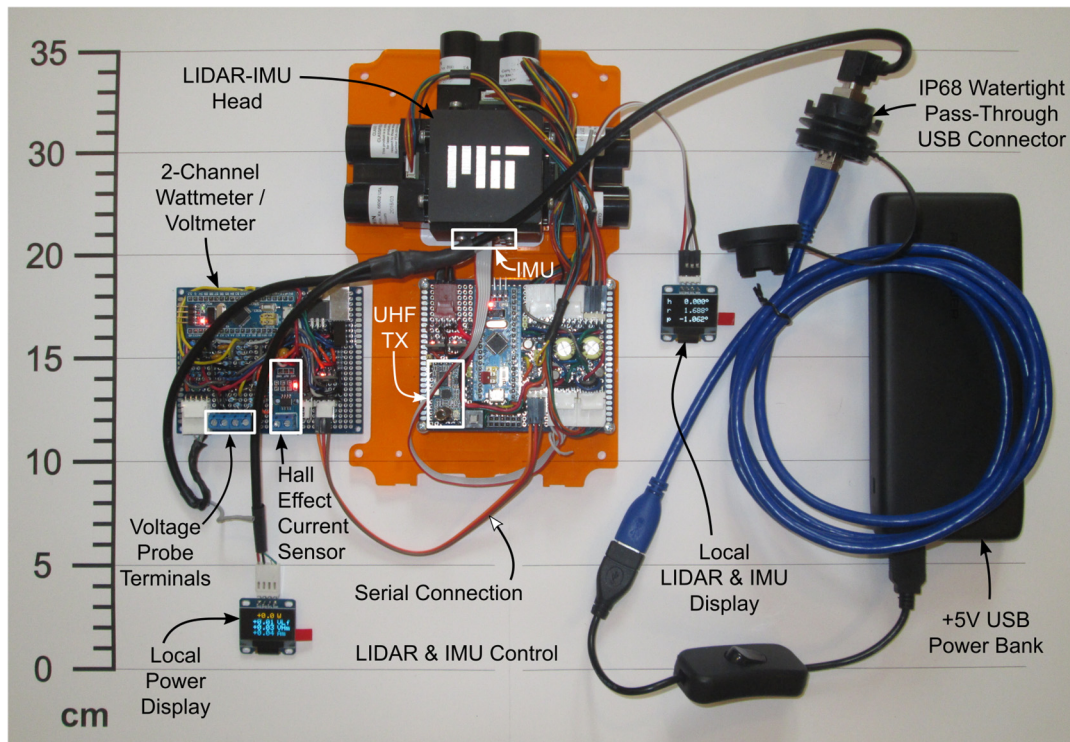
Figure 244: Modules of the electro-optical monitor electrically connected during functional tests, just before being mechanically assembled (except the power bank) into an IP68 enclosure, and integrated in the bike rack.

The LIDAR-IMU control and the power measurement units are assembled stacked on top of each other, housed in an IP68 (according to IEC standard 60529) polycarbonate enclosure with clear lid, resulting in a total w_L = 14 cm (LIDAR box width). The only external electrical wired connections are those for power, voltage and current sensor inputs, and the LOG switch. These lines are bundled into three IP68 compatible pass-through connectors transfixing the enclosure. Inside the enclosure and visible through the clear lid were installed OLED displays, for local reading of measurements made by each of the two modules. The watertightness of the assembly was, however, severely impaired by the holes drilled to let the LIDAR beams and their respective back scattering rays pass through the laterals of the box. For dust protection, 2 mm cast transparent acrylic windows were introduced to cover the LIDAR beam holes. These acrylic windows are also transparent (> 85% transmission) at the 905 nm wavelength (infrared) emission of the LIDAR type used. Their effect in attenuating and delaying the LIDAR signals can be compensated by calibration

Dynamic Inductive Wireless Power Transfer for Lightweight Electric Vehicles
Luiz Alberto Lisboa da Silva Cardoso – University of Minho

408

procedures, with the maximum detection range being slightly degraded, but experimentally verified to be still well over 10 m, enough for the application. For testing vehicles outdoors, in arbitrary weather, it would be necessary to redesign the LIDAR protection windows, so that the adequate watertightness grade is met.

Figure 245 shows the UHF wireless Electro-Optical Measurement unit (EOM), (A), integrated in a bike rack with the other onboard subsystems: (B) Scanning LIDAR; (C) Resistive loads and heatsink, mounted on both sides of vehicle, to emulate power train; and (D) Redundant voltage data logger model DI-1120, from DATAQ Instruments Inc., and management system, running on a Microsoft Windows 10 Pro PC Stick, manufactured by Azulle Tech.
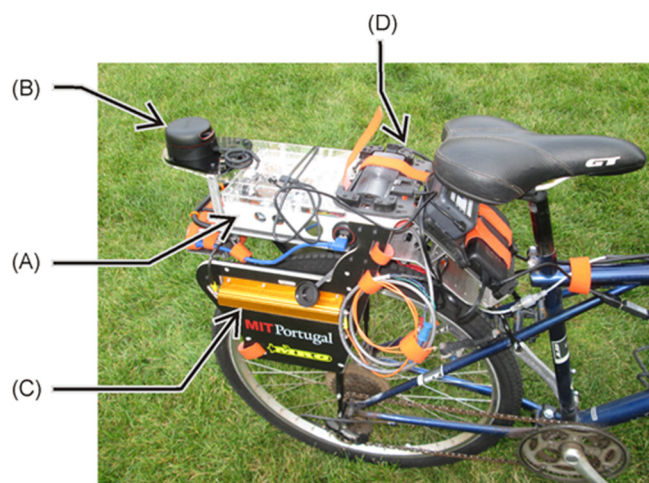
Figure 245: Bike with measurement rack with EOM and auxiliary subsystems installed.

The power demand of the electric powertrain will depend on the acceleration and mechanical drag forces imposed on the vehicle, greatly varying along the vehicle progression on its path. A useful test condition is then to force the power consumption to the nominal maximum power demand of the powertrain. This can be achieved by momentarily replacing the powertrain circuit by a resistive dummy load of appropriated value. Such resistive load was also integrated in the prototype, as seen in Figure 245 (C), to facilitate the evaluation tests.

6.10 Experiments and Results

The general purpose DIWPT evaluation tool developed is based on two types of positional sensors, the LIDARs and the IMU. In principle, both need calibration. In the case of the IMU, this can be easily achieved with some special service routines provided by the inertial processor used in the LIDAR head implementation, which are run in the beginning of operation. This automatically calibrates the zero pitch and zero roll attitude of the vehicle to coincide with those measured with the bike in initial upright positioning. In addition to that, all heading measurements are also

Dynamic Inductive Wireless Power Transfer for Lightweight Electric Vehicles
Luiz Alberto Lisboa da Silva Cardoso – University of Minho

409

referenced to the initial heading, that read when the system is turned on. For establishing a zero reading in the direction of the corridor, the vehicle is aligned with the center line of the corridor and the reference walls before it is turned on. From this point on, all angular heading measurements are relative to the walls.

The optical components, however, require manual calibration for distance reading, to allow curve fitting parameters to be extracted, after a reference plane (zero distance) is established.

6.10.1 LIDAR Calibration

According to the manufacturer (GARMIN) of the LIDARs model Lite v3 used, non-linearity in the LIDAR readings is expected when measuring distances of 1 m and shorter. The lateral LIDARs (left and right) were calibrated using 9 reference distances from 24.1 cm to 145 cm, using metallic bars of known lengths, as shown in Figure 246a.

(a)

(c)

(b)
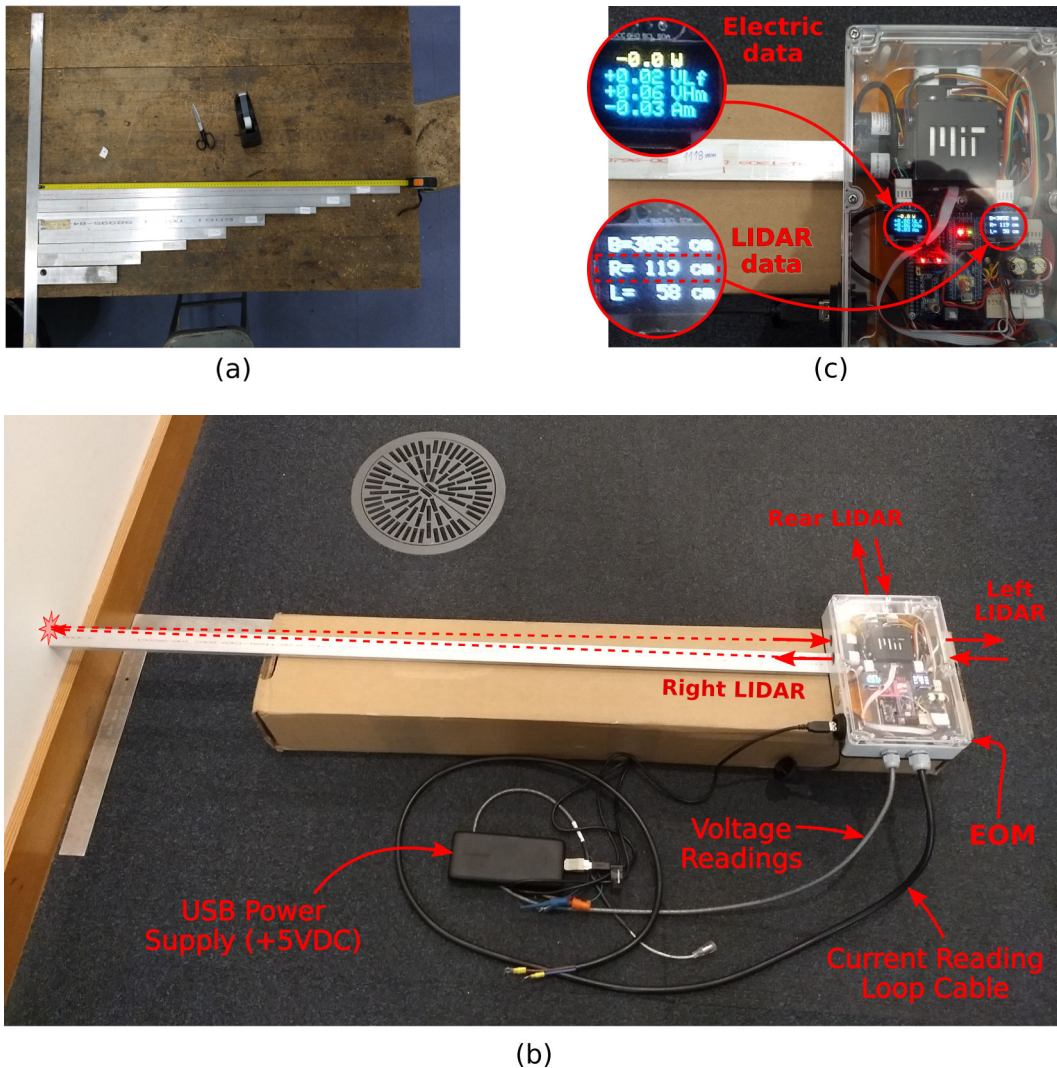
Figure 246: Left and Right LIDAR calibration using metallic bars of known size.

Dynamic Inductive Wireless Power Transfer for Lightweight Electric Vehicles
Luiz Alberto Lisboa da Silva Cardoso – University of Minho

410

The lengths of these reference metallic bars cover the entire range of expected measurements, according to the width of the corridor used in the experiment. The LIDAR measurements were made with each metallic bar perpendicularly touching the wall and the corresponding lateral side of the EOM unit, for both left and right sides, as shown in Figure 246b and, in a closed-up view, in Figure 246c. A similar procedure was also conducted with the rear LIDAR, where instead of metal bars of known sizes, an digital laser tape measuring unit was used, as a reference, due to the distances involved being larger. A total of 5 reference distances, from 112 cm to 766 cm were used.

According to the manufacturer, the LIDAR sensors used exhibit an almost fixed proportional maximum error behavior for distances larger than 1 m, and up to the maximum laser detection range, which is 40 m. The manufacturer also warns that, when detecting distances closer than 1 m, these LIDAR should normally present pronounced non-linearity. This was actually observed in the calibrating curves individually fitted for the three LIDARs used, as highlighted in yellowish shaded areas of the chart in Figure 247. In fact, the non-linearity is noticed up to approximately 100 cm to 115 cm, depending on the specific specimen considered.
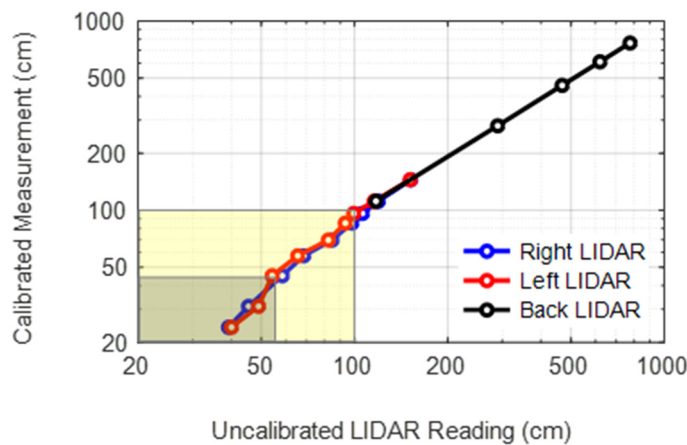
Figure 247: LIDAR calibration curves experimentally obtained.

An observed increase in the standard deviation of readings at distances less than 0.45 m, however, strongly restricts practical operation of these LIDARs at too short range, the measures corresponding to the gray-shaded area Figure 247.

For the usually slim lightweight electric vehicles at lower speeds, such the HIPLEV bikes, narrow corridors can be used, and the calibration of the LIDARs is very important, because the reading distances can often be less than 1 m. In order to improve precision of the measures and the estimated lateral displacement of the vehicle, calibration procedures of all three main LIDARs have always to be individually executed, before running the actual experiments.

6.10.2 Test Site Configuration

The ideal dimensions of the reference corridor depend on: (i) the range of the lateral displacements to be measured; (ii) the maximum expected tilt angles of the vehicle, with respect to the corridor longitudinal axis; (iii) the maximum speed of vehicle; and (iv) the characteristics of the LIDAR used in the design.

According to the manufacturer (GARMIN) of the LIDARs used (model LIDAR-Lite v3), the maximum range of detection, d_{max}, is 40 m, with an error of ±1% in the mean value read, and another ±1% error due to dispersion, for distances above 1 m, with non-linear behavior when reading distances less than 1 m. From experimentation, it was verified that the standard deviation of the distance measurements is reduced (down in the 7 mm to 9 mm range) at the distances of approximately 0.6 m to 1.2 m, increasing rapidly as the distance falls below 0.5 m, and proportionally to distance itself, at distances above 1.2 m.

Non-linearity in the readings can be compensated by calibration procedures, if operation distances are kept above $d_{min} = 0.5$ m. The reference corridor width w_c should be such that the minimum distance from the LIDAR head to the wall, at the condition of maximum displacement from the center of lane, should be not less than the above marked minimum recommended operation distance d_{min} for the LIDAR. Thus, a good choice w_{min} for the minimum value of the corridor width, without experimenting LIDAR increased dispersion errors, would be expressed by:

$$w_{min} = d_{min} + d_L + w_L + d_{min} = 2d_{min} + d_L + w_L , \qquad (6.11)$$

where d_L is the maximum anticipated lateral displacement width for the vehicle and w_L is an equipment parameter, as defined for (6.3). Particularly, for a bike, it is also necessary that $d_L > w_d$, where w_d is the minimum required width to accommodate the oscillatory movement of the bike, in order to allow the cyclist to dynamically keep the equilibrium, as defined in section 5.3 and illustrated in Figure 148.

The maximum detection range d_{max} also restricts the maximum corridor width, w_{max}. Considering the vehicle can assume relative heading (α) and pitch (β) angles limited in absolute values respectively to α_{max} and β_{max}, then:

$$w_{max} \leq d_{max} \cos(\alpha_{max}) \cos(\beta_{max}) \qquad (6.12)$$

Dynamic Inductive Wireless Power Transfer for Lightweight Electric Vehicles
Luiz Alberto Lisboa da Silva Cardoso – University of Minho

412

There is, however, one more condition on the maximum value of w_c, that can be derived by requiring the LIDAR beam not to touch the floor, what would invalidate the simple expression in (6.3) for calculating the lateral displacement. The limit condition is when the vehicle is maximally tilt (roll angle) inside the corridor:

$$\frac{w_{max}}{cos(\alpha_{max})} \leq \frac{h_{LIDAR}}{sin(\beta_{max})}, \tag{6.13}$$

where h_{LIDAR} is the height of the center of the LIDAR mounting head above the floor plane. So, reuniting conditions given in (6.12) and (6.13), the maximum corridor width, w_{max}, is given by:

$$w_{max} = cos(\alpha_{max}) \; min \left\{ d_{max} cos(\beta_{max}), \frac{h_{LIDAR}}{sin(\beta_{max})} \right\} \tag{6.14}$$

For a bicycle, a typical d_L of interest will be around 1 m, so the desirable minimum corridor width to be used with measurement unit, as given by (6.11), should be 2.15 m. During the experiments with the bicycle, it was verified that heading (relative to lane longitudinal axis) and roll angles, under normal ridging conditions, were respectively limited to 30 degrees and 15 degrees. Using (6.14) and considering a mounting height of 1 m and the characteristic d_{max} of the LIDAR used in the design, results that the maximum corridor width should be approximately 3.35 m.

In the first test runs herein reported, a corridor 1.778 m wide (Figure 248) was used, due to its prompt availability (near to our lab). This value lies outside the calculated ideal corridor width range though. The consequence, based on (6.11), is that, for this width, lateral displacements estimations d_L such that:

$$d_L > 1.778 - 2 \times 0.5 - 0.15 = 0.628 \text{ m}, \tag{6.15}$$

are expected to have increased dispersion errors. In practice, however, there was no problem with that, because, for such a narrow corridor, lateral misalignment widths greater than 0.63 m are not likely to be observed in the experimental runs, due to the natural tendency of the cyclist to ride away from the walls, to avoid collision.

In the verification of operation envelops of a HIPLEV, for instance, the lateral displacement width of interest goes at most to about 60 cm. Particularly for the evaluation of the first HIPLEV prototype designed and tested in Chapter 5, 30 cm would be enough, because its sufficiently higher than the specified $D_e = 20$ cm (Table 25).

Dynamic Inductive Wireless Power Transfer for Lightweight Electric Vehicles
Luiz Alberto Lisboa da Silva Cardoso – University of Minho

413

The experimental setup for acquiring data for testing the EOM positioning capabilities was created by placing a large back reference wall perpendicular to the test corridor, as shown in Figure 248. The perpendicularity of this back wall was checked by the verification of equal distances, on the left and on the right, to a given cross-section of the corridor.
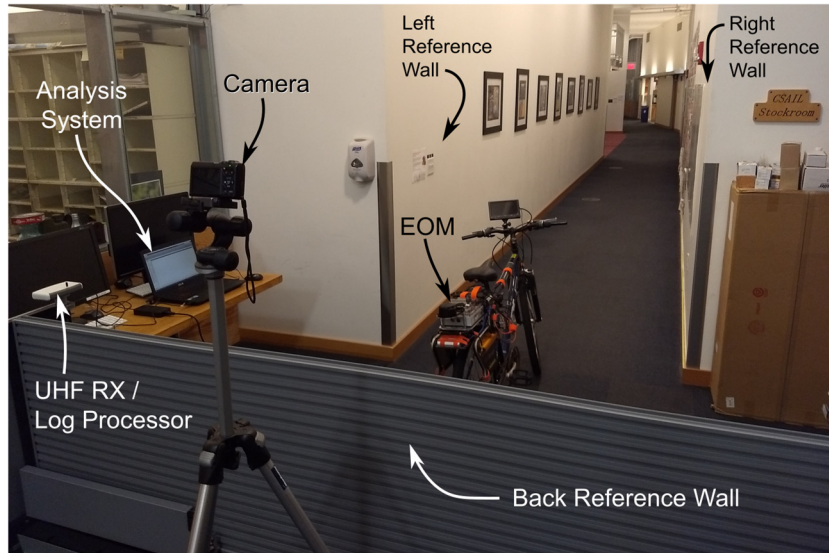
Figure 248: Experimental setup temporarily established during nighttime, in one of the corridors of MIT Computer Science and Artificial Intelligence Laboratory.

A lateral view of the bicycle with the EOM installed, positioned at the start-run point, at the beginning of the corridor is show in Figure 249. No primary coils were installed in the test site, and the bicycle was not equipped with the inductive energy harvesting system, because these tests aimed position measurement verification only. At this stage of the EOM development, electric tests were separately conducted, on the workbench only.
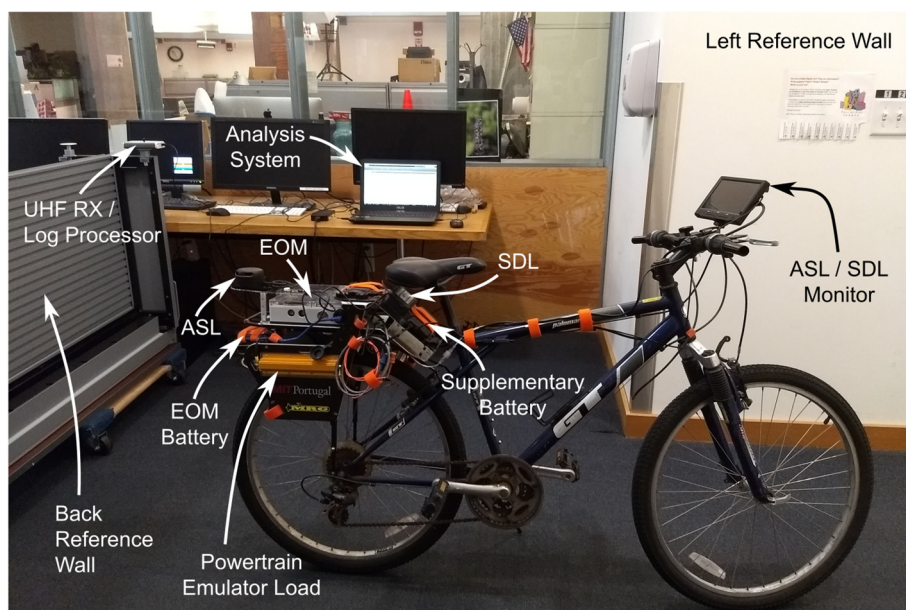
Figure 249: Lateral view of the bike with the Electro-Optical Monitor (EOM) installed and ready for tests.

Dynamic Inductive Wireless Power Transfer for Lightweight Electric Vehicles
Luiz Alberto Lisboa da Silva Cardoso – University of Minho

414

The expected EOM precision in measurements of lateral displacements is better than 1 cm. In order to perform an experimental characterization of this error, a reference system of higher precision would be required, for computing measurement deviations from the trustable reference. However, such a high precision reference system for dynamically measuring positioning was not available. In this first assessment of the EOS functionality and measurement capabilities, the evaluation was performed by comparing the measurements with those extracted by processing the video recorded during the experiment. Still, the video configuration used yields an expectedly lower precision than that of the EOM itself. Because of that, in this first experiment, only a gross quantitative evaluation was possible.

Further assessment of the EOM measuring capabilities would require more complex equipment, for instance, high resolution image processing using infrared markers [213] or real-time kinematic global navigation satellite systems (GNSS RTK) [210] [211]. Even then, to match the 60 Hz measuring rate of the EOM, some extra design effort on the reference system is expected.

6.10.3 Trajectory Reconstitution Using the EOM

The use of a camera positioned behind and close to the back reference wall, overlooking the corridor and its left and right reference walls, as shown in the setup of Figure 248, permitted the reconstruction of the bike position with techniques of computer vision, as illustrated in Figure 250. The average accuracy of estimates of the lateral displacement of the bike is calculated at approximately 1.5 cm, when the bike is in a central position of the corridor. A reference point on the bike frame is video-tracked, and the resulting estimated trajectory is then compared with that estimated by the EOM, making use of as special video tracking software [221]
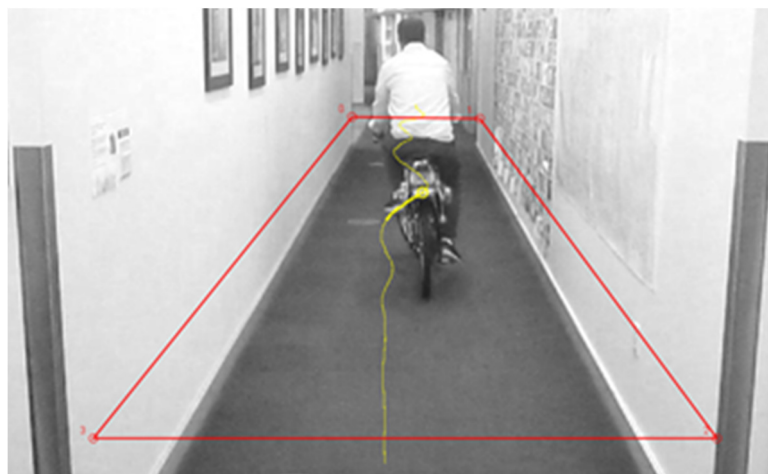
Figure 250: Tracking the bicycle on the video, as a reference for consistency check of the computed position estimations of the EOM.

Dynamic Inductive Wireless Power Transfer for Lightweight Electric Vehicles
Luiz Alberto Lisboa da Silva Cardoso – University of Minho

415

The raw LIDAR and IMU data are wirelessly transferred to an analysis program developed in MATLAB (from MathWorks), running on a fixed station. The time sequences corresponding to these data are then plotted, and any segment of interest in the run is located and cropped manually. In a real DIWPT evaluation, the duration of this segment should correspond to the transit time of a vehicle over at least one primary coil. The positional data collected correspond to the estimated distances of the EOM to the reference walls, rear and lateral (left and right), which are plot in the upper panel (a) of the analysis program screen, as shown in Figure 251. The rear LIDAR data, plot in black, shows a smooth ramp, demonstrating that, in this run, the bicycle departs from the back wall with an approximately constant speed. The red and blue curves in the same panel show the LIDAR estimated distances to the left and right walls of the corridor, which vary relatively more slowly, because the magnitude of the lateral velocity is smaller than that of the forward velocity.
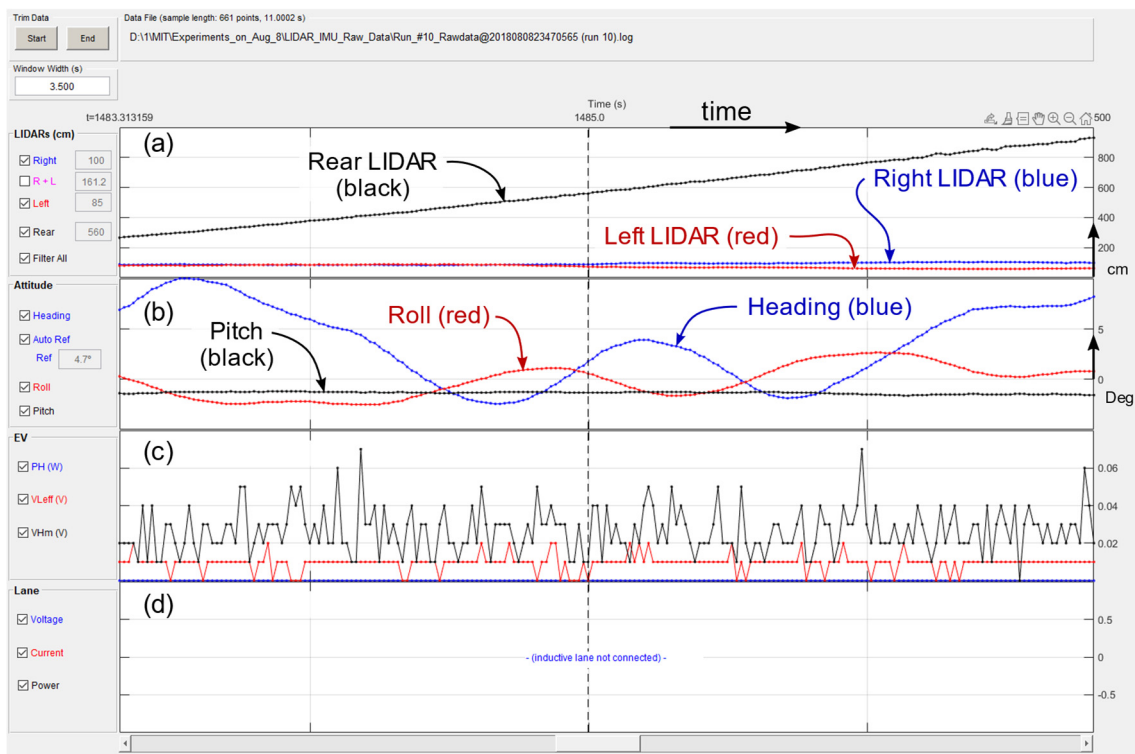
Figure 251: Raw positional and electrical data capture onboard of the vehicle: (a) LIDAR data panel; (b) IMU data panel; (c) vehicle electric data panel (reading zero values); and (d) i-lane electric data panel (not connected).

The Euler angles captured from the IMU installed in the EOM are the Euler angles of the bike itself, since the EOM is firmly attached to the frame of the bike. These angles are shown in panel (b) of Figure 251. As expected, since both wheels are kept in contact with the ground surface all the time, the corridor floor is almost perfectly horizontal (one of the few regularities people can count on in the Stata Center [222]) and turns are range-limited, the pitch angle remains almost constant and close to zero. So, in this particular configuration, the pitch does not apport relevant information by itself.

Dynamic Inductive Wireless Power Transfer for Lightweight Electric Vehicles
Luiz Alberto Lisboa da Silva Cardoso – University of Minho

416

In fact, by careful installation of the EOM on the bike frame, the pitch angle could be brought very close to zero. But this is not necessary, because this angle is considered in the transformations that calculate the position of the secondary coil in the lane reference system.

The other two angles plotted in Figure 251b are the roll and the heading. The roll is the lateral inclination angle of the vehicle (presently, the bike), zero at the vertical, positive if the bike is inclined to the right. The heading angle in the plot is actually the relative heading angle, using the zero reference the heading angle at the start of the run, when the bike is intentionally set parallel to the corridor. Both the heading and the roll angles have an expectedly average value approximately equal to zero, along the central segment of a run.

The trajectory of the vehicle, or, more specifically, of any object rigidly attached to the vehicle frame (and thus, to the EOM), is the determined by the analysis program by using the algorithms derived in Section 6.4 and the low pass FIR filter introduced in Section 6.5.

The electric data synchronously collected on board of the vehicle, a measurement of current and two measurements of voltage, are presented in panel (c) of Figure 251. In this particular run, since the bicycle has not an electric powertrain and neither nor energy harvesting devices, the current and voltages sensors were floating, and the reading are all zeroed, except from electric noise. Because the power signal is computed by the integration of the product of the current reading by the reading of one of the voltages, this noise is essentially canceled, at the power value read is zero.

Similarly, because there are no primary coils in the lane in this particular test run, and no electric data is being captured from the lane side, the analysis system, instead of displaying the lane electric data, the message "-(inductive lane not connected)-" simply displayed in its panel (d), and not curves are plot, as shown in Figure 251. The analysis system, however, is prepared for future dynamic tests of the HIPLEV, when a test range is built, and all signals become available.

In a DIWPT study, the usual interest would be to track and find the trajectory of the center of the secondary coil, or, at least, its coordinates in the x axis, which is transversal to the lane, and represents the relative lateral displacement of the secondary coil, assuming the primary coil is aligned with the lane. However, as explained, the bike neither is adapted with a secondary coil nor with the harvesting circuits, in the tests accomplished so far. So, just to exercise the analysis program, it was assumed that the center of the secondary coil is located at a fixed distance $H_C = 62$ cm straight below the center of the EOM head.

Dynamic Inductive Wireless Power Transfer for Lightweight Electric Vehicles
Luiz Alberto Lisboa da Silva Cardoso – University of Minho

417

The chart in Figure 252 shows the reconstructed trajectory using the IMU and raw calibrated LIDAR data in Figure 251, as generated by the interactive analysis program. The total time interval in all panels are exactly the same, with the black dashed lines in all of them, vertical in panels (a) (b) and (c), of Figure 251, and horizontal in the panel in Figure 252, also representing the same moment in the run. However, while the horizontal axis in panels (a), (b) and (c) represent time, the vertical axis in the chart of Figure 252 represents the distance travelled forward. Speed cannot be directly read in this latter chart, but other algorithms could have been used to plot the speed and its longitudinal and transversal components, if that would be necessary.
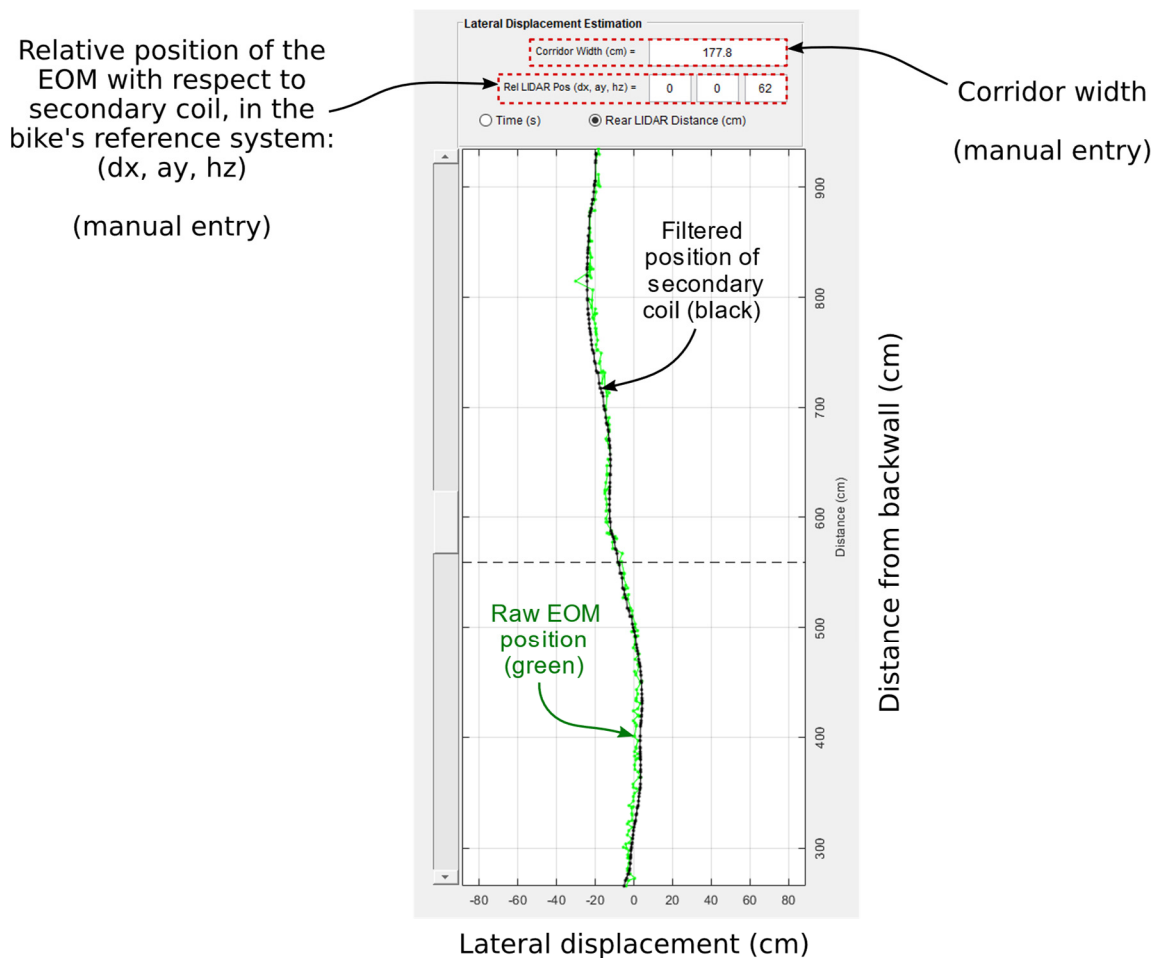
Figure 252: Reconstitution of the trajectory of the center of a pick-up coil fixed on vehicle frame, based on the range readings from the LIDARs the Euler angle readings from the IMU.

Yet in Figure 252, in the top of the panel, the corridor width is manually entered in the system. Just below it, the relative position of the center of the secondary coil (or other point of interest on the vehicle – such as the position of the RFID tag) with respect to the center of the EOM head, $(0,0,H_C)$, is also manually entered. The green dots are computed by applying the expressions developed in Section 6.4 to the IMU and raw LIDAR data. The black curve is the

Dynamic Inductive Wireless Power Transfer for Lightweight Electric Vehicles
Luiz Alberto Lisboa da Silva Cardoso – University of Minho

418

estimated trajectory using the same IMU provided (which is already filtered internally to the IMU) but, instead, the LIDAR data filtered by the FIR filter introduced in Section 6.5.1.

6.11 Conclusion

The immediate unavailability of a reference instrument capable of dynamically measuring vehicle trajectories more accurately, in the same way the presently developed instrument does, made it difficult to experimentally estimate the errors in the measurement of lateral displacement, currently only estimated by simulation, at approximately 0.7% of the corridor width. The optical accuracy and the resolution of the camera used further limited the accuracy of trajectory estimation by video tracking, so far not permitting a reliable numeric evaluation of the error in trajectories measured with developed electro-optical instrument. The computed trajectories were still compared to those obtained by video tracking Open Source Physics software [221], as exemplified in Figure 250, with consistent qualitative results.

The bike, equipped with the Electro-Optical Monitor (EOM), dummy replacement loads for the powertrain, the auxiliary scanning LIDAR (ASL), the secondary data logger (SDL), and an onboard computer with wireless TCP/IP over Wi-Fi, was still ridden outdoors, in the same configuration shown in Figure 253, to check mechanical robustness during normal street maneuvers. Functional conformity was checked afterwards. The results were entirely satisfactory.

Figure 253: Electro-optical DIWPT evaluation system mounted on a regular bike.

Dynamic Inductive Wireless Power Transfer for Lightweight Electric Vehicles
Luiz Alberto Lisboa da Silva Cardoso – University of Minho

419

So, while not providing the actual precision limits of the EOM, a simple verification procedure, based on video processing, allowed us to have first a consistency check of the measurements, which indicated the adequacy of the system to be used in the evaluation of DIWPT configurations where a 60 Hz data capture rate and lateral displacement errors up to 0.7% of the corridor width are acceptable. Using the same proposed technique, improvements in this error are expected, if more accurate LIDARs and faster processing circuits are used.

Dynamic Inductive Wireless Power Transfer for Lightweight Electric Vehicles
Luiz Alberto Lisboa da Silva Cardoso – University of Minho

420

Chapter 7

Conclusion

In this final chapter, a summary of the contributions of this work is provided along with some reflections on their impact and limitations. Finally, suggestions for follow-up work are given.

7.1   Reflections on the Contributions of this Research

The contributions of this research can be grouped into three different categories. In the first category are those related to the IWPT technology that are useful and most directly related with DIWPT implementation. In the second category are the proposal, the development, and the proof of concept by the implementation of a new transport mode, conceived by the conjunction of Human Powered Vehicles (HPV) and the DIWPT technology, the Human-Inductively Powered Lightweight Electric Vehicle (HIPLEV). In the last category are contributions that can be considered minor, collateral findings in the IWPT domain.

In the first category, the following achievements can be listed, which are not known to have been addressed in previous works or publications:

(i)   The development of a closed algebraic expression for the voltage induced by an infinitely long coil, constituted of a single turn of a filamentary wire carrying a sinusoidal current of constant amplitude and frequency on a parallel rectangular coil, also constituted of a single turn of a filamentary wire (Theorem 1, Section 3.6.3). As an approximation, this expression can be applied to most of the central section of oblong coils, thus facilitating the calculation of induced voltages in such configurations.

(ii)   The development of closed algebraic expressions for the optimum values of primary and secondary coils widths that maximize the induced voltage in center alignment conditions, when a sinusoidal current of constant amplitude and frequency is imposed on the primary coil (Theorems 2 and 3, Section 3.6.3).

(iii)   A simple and unified graphic interpretation for Theorem 2 and Theorem 3, which facilitates the design of inductive lanes based on oblong coils, when maximum power transfer is of most concern (Figure 118, Figure 120 and Figure 121).

Dynamic Inductive Wireless Power Transfer for Lightweight Electric Vehicles
Luiz Alberto Lisboa da Silva Cardoso – University of Minho

421

(iv)   The development of closed algebraic expressions for the optimum widths of oblong primary coils and rectangular secondary coils that produce a maximally flat induced voltage, as a function of the relative lateral alignment of the coils, when a sinusoidal current of constant amplitude and frequency is imposed on the primary coil (Theorem 4 and Theorem 5, Section 3.6.3). Similarly as in (iii), the theorems are directly appliable in the case of low magnetic coupling static and dynamic inductive wireless power transfer configurations.

(v)   A unified graphic interpretation for Theorems 4 and 5, which facilitates the design of inductive lanes based on oblong coils, when a maximally flat induced voltage is convenient, simplifying the circuit requirements, for instance, as in the case of a secondary load regulated by a DC-DC converter (Figure 123 and Figure 124).

(vi)   General DIWPT design guidelines and a DIWPT design procedure (Chapter 5), for the situation when the geometry and the power requirements of the vehicle are fixed, and both an inductive lane composed of primary coils and the secondary coils satisfying these power requirements are to be fully determined. Differently, in previously known works and DIWPT application projects based on oblong coils, the geometry and excitation of the primary coils are initially presumed or ad hoc introduced, without detailed justification, and then the power transfer and efficiency levels are estimated and experimentally validated.

All contributions in this first category are relevant to the design of HIPLEV systems using oblong primary coils, and were not previously published, being unveiled with the publication of this thesis. Heuristic approximations based on Theorem 1 and Theorem 2 were used in support of the design of the first HIPLEV prototype, detailed in Chapter 5. These approximations were shown to be enough precise, by means of FEM simulations. They were also verified to be in very good agreement with experimental observations, even considering that, in practice, the primary current and frequency were not perfectly constant.

In this HIPLEV design, the paradigm of maximum power transfer availability in the center of the lane was used, because, in the preliminary DIWPT experiments, the WPT at the distances involved in automotive applications was perceived as difficult to implement. Especially, in configurations in which the magnetic coupling coefficient between primary and secondary coils is small. So, to increase the chances of achieving the required power transfer of 400 W to the prototype while using simple materials, the maximum power criterium was adopted.

Once the required power transfer was obtained at an efficiency level also higher than the minimum required, the analysis of the experimental results indicates that there is enough margin

Dynamic Inductive Wireless Power Transfer for Lightweight Electric Vehicles
Luiz Alberto Lisboa da Silva Cardoso – University of Minho

422

in the induced voltage envelope to use, instead, the paradigm of a maximally flat induced voltage. This suggests the opportunity for the construction of a new system, where, although the maximum power level availability at the center of the lane is lower than in the currently built prototype, the electrified width of the lane is larger, permitting a more relaxed riding. Also, the DIWPT design using the maximally flat induced voltage paradigm, to be supported by Theorem 4 and Theorem 5, shall permit the use of DC-DC converters in the secondary with a smaller dynamic range for the input DC voltage. This shall allow the use of simpler (and less costly) DC-DC converters. It is speculated that, in some applications, even the use of a DC-DC converter could be dismissed, if the powertrain and the battery manage system is enough tolerant to poor load regulation.

The second category of contributions is related with the proposal and validation of a new variant of transportation mode, the Human-Inductively-Powered Lightweight Electric Vehicles (HIPLEV), and consists in the main innovative engineering component of the thesis work. These contributions include:

(vii) The proposal of the HIPLEV concept itself, which is the integration of dynamic inductive wireless power transfer to hybrid, human-electrically powered lightweight vehicles, a wide range of lightweight electric or electrifiable vehicles that are propelled by human power, including e-bikes, e-velomobiles and other three and four-wheeled e-cycles. In this manner, the HIPLEV can be thought of as a wheeled exoskeleton, specialized in transport tasks, which is electrically powered by the lane it rides on.

(viii) The analysis and prediction of some operational characteristics for this new transportation mode, which reveals its adequacy to commuting applications in urban spaces.

(ix) The anticipation of some new urban architectural guidelines that should be recommended for the adoption of the HIPLEV in smart cities.

(x) The unprecedented design, prototyping and testing of an energy harvesting subsystem for an electrically assisted two-wheeled bicycle, which includes the mechanical and the electrical justification for the installation of a secondary coil around its rear wheel.

(xi) The design of an inductive lane profile for operating DIWPT adapted e-bikes. When the HIPLEV and its inductive lane are paired up, the net transferred design power of 400 W at a top efficiency of 64% was achieved, a number that was later improved over 65%. These efficiency figures were obtained without the use of litz wires or any software magnetic materials for shaping the field, and are expected to be further improved if these more expensive components would be used in the design. Concerning the transferred power,

400 W was chosen to cover the maximum powertrain demand of 250 W, which is the maximum power allowed in PEDELEC bikes in most European countries. The excess power of 150 W can be stored and used to propel the vehicle during inter-primary coil transits. The elevation of the power can be easily accomplished by new similar designs, if needed, what is expected to happen if a new LEV class is considered for the HIPLEV or if a revision of the European normative for the PEDELEC with such provision comes into effect.

(xii)   The design, prototyping and testing of an RFID detection system that can be used to activate the energization of individual primary coils of a DIWPT system. Although many design options for power control of IWPT modules have been observed in the literature, the method proposed has the advantage of being simple and inexpensive, for it is based on the reuse of the ISO/IEC-14443A, one of the most popular and inexpensive near field RFID technologies. The coil activation solution adopted could be used as well in other non-WPT applications that could benefit from the near field RFID-based activation in enlarged detection volumes.

(xiii)   The design and implementation of an electro-optical system to evaluate the dynamic behavior of a DIWPT vehicle running over an inductive lane, which can simultaneously measure power and efficiency fluctuations, vehicle lateral misalignment on the lane, and other information, such as the travelled distance and vehicle's attitude, as expressed by its heading, roll, and pitch angles. Although the design was made having the LEV in focus, particularly the HIPLEV, its principle is general enough to provide the base for the construction of similar instruments that can evaluate DIWPT to any EV.

Concerning the above contributions directly related to the proposal of the HIPLEV, those numbered (vii), (viii) and (ix) were published in [8]. Some aspects of contributions (x), (xi) and (xii) generated publication [3] and [6], but other are only being unveiled with the publication of this thesis. Contribution in (xiii) was published in [7].

In the third category of achievements, these minor contributions to the study of IWPT can be listed:

(xiv)   A geometric interpretation of the relationship among the split-frequencies f_{even} and f_{odd}, the resonant frequency f_0 and the magnetic coupling k, which can serve as fast graphical calculation tool for predicting the split frequencies.

(xv)   A technical review validating the first known design of DIWPT, that of Hutin and Leblanc, from 1891, based on available historical information contained in or presumed from the original patent document, and some complementary assumptions. The DWIPT system

Dynamic Inductive Wireless Power Transfer for Lightweight Electric Vehicles
Luiz Alberto Lisboa da Silva Cardoso – University of Minho

424

architecture, including its geometry and circuits were simulated, assuming the use of materials and technology not available at the time to Hutin and Leblanc. The results of the simulations prove that, although rudimentary, Hutin's and Leblanc's design would work. Using a single wire transmitter at a 14 cm airgap, the DIWPT design would expectedly deliver the nominal required power for the traction of the first commercially operated Siemens' and Halske's tram, which was first operated in 1881, in Berlin, if at least three pick-up sections were installed on the tram. It was also demonstrated that this design, however, would not be EMF-safe for the occupants of the tram, mostly made of wood. But this was probably not a matter of any concern at the end of the 19th century. Although frequently cited in the literature, this patented design is not known to have been prototyped, nor had it been analyzed before in detail.

(xvi) Inductive wireless power transfer systems, either stationary or dynamic, rely on the use of compensation circuits on both primary and secondary. Any passive reactive network can in principle be used, but the simpler ones, the serial-serial (SS) compensation, the parallel-serial (PS) compensation, the serial-parallel (SP) compensation and the parallel-parallel (PP) have sufficient flexibility of employment, for most applications. Many authors, such as Terman in 1943 and, Wang, Covic and Stielau, in 2004, have mathematically analyzed these configurations with respect to power transmission and efficiency, providing general graphical interpretation of power transfer and general formulation for designing. Whang and Mi, in 2016, have confirmed and extended this analysis. But in none of the observed studies provide a joint graphical visualization, fusing the information of output power and efficiency, as those represented in Figure 16 and Figure 22, which is believed to facilitate the intuitive prediction of characteristics of SS, PS, SP and PP-compensated magnetic links. An equivalent derived two-dimensional graphic visualization scheme is also newly suggested, as a complementary IWPT design tool, as illustrated in Figure 17 and Figure 23. The charts can be computationally and interactively drawn, making it easier to design an IWPT configuration, and to establish its operation point.

(xvii) An elementary analysis of the voltage in wireless power transfer when there is relative motion of primary and secondary coils, confirming that DIWPT can be approximated by the quasi-stationary approach in most applications involving terrestrial vehicles, when high enough induction frequencies are used, such as those (in the HF band) currently seen in modern DIWPT application. This consideration is intuitive and widely accepted, but, although finding

Dynamic Inductive Wireless Power Transfer for Lightweight Electric Vehicles
Luiz Alberto Lisboa da Silva Cardoso – University of Minho

425

similar modeling in the theory of electric machines, it is not known to have previously been explicitly and formally analyzed in the automotive DIWPT context.

(xviii) A method for indirectly measuring the transferred power over the airgap of a magnetic coupling is provided. The method is based on the Fourier decomposition of the transferred power, the direct measurement of primary and secondary currents and an estimate of the mutual inductance, and follows directly from the linear modeling of the magnetic coupling. Although very straightforwardly derived, it was not previously seen in the literature. It can help evaluate partial efficiency figures of primary and secondary circuits of the magnetic coupling, which ultimately can give a better indication of how the efficiency of an existing IWPT circuit can be improved. This contribution, inspired by, but collateral to the thesis work, was documented in [11].

Contributions (xiv) to (xvii) are considered incidental. They were so far not addressed in the previously listed publications, being first reported in this thesis.

The e-bikes, par excellence representatives of the hybrid electric human powered lightweight vehicles, have been in the market for the last years, and are believed to provide a functionally adequate, sustainable, and economically favorable substitution for both higher power electrics and thermal engine-based mobility, in some transportation tasks. With the presently accomplished research, it is demonstrated that when these vehicles are used in conjunction with Dynamic Inductive Wireless Power Transfer (DIWPT), a newly proposed soft transport variant, with even more interesting characteristics, the HIPLEV – Human-Inductively-Powered Lightweight Electric Vehicle is created.

In addition to the cultural inertia, the higher manufacturing costs of the heavier personal transports may pose economic pressure towards the pure translation of current thermal engine vehicles into compatible electric vehicles of similar functionality and performance. After all, today's automobile industry generates high levels of employment and profit, which would be greatly reduced if a significant fraction of the personal transport market would be occupied by lighter, less expensive vehicles. Because of that, the optimum window opportunity for the adoption of the HIPLEV technology is still uncertain. It is conditioned to the conscientiousness of the users towards sustainability, to the expected future increase in carbon emissions, policies, taxations, and the prices of fossil fuels themselves.

Many cities are now creating new bike lanes that help promote the resurgence of bikes as a primary personal urban transport. These lanes may become the base for a future network of i-

Dynamic Inductive Wireless Power Transfer for Lightweight Electric Vehicles
Luiz Alberto Lisboa da Silva Cardoso – University of Minho

426

lanes for HIPLEVs. But the adoption of some new architectural urban design guidelines and electrification paradigms that specifically support the installation of i-lanes for HIPLEVs are necessary, such as the pedaling hubs. Recent DIWPT efforts targeting the heavier EV, for example, the implantation of the first large-scale inductive lane for standard road electric vehicles, as discussed in section 3.4, and particularly, the more recent pilot projects by Electreon (Section 3.4.8), may help the population to assimilate the idea, and consider the application of DIWPT to lighter vehicles as well.

Systems using the inductive technology and the HIPLEV concept can be developed and deployed without mobilization of major material and design resources, without requiring special supplies or logistic facilities only accessible to highly developed economies. Compared to other types of transportation infrastructure, the HIPLEV is a technology that can be expected to be more easily installed in countries undergoing economic difficulties or recovering from catastrophes, using local design and engineering workforce.

The HIPLEV concept has been demonstrated as technically viable by analysis, design, prototyping and successful experimentation, and it is believed to have the potential to replace a significant part of all short to medium-distance personal transportation modes, becoming a non-exclusive answer to the quest for sustainability. However, the successfully introduction of the HIPLEV as a transport mode is conditioned to the redesign of the urban space, with the necessary investment made in the electrification of lanes that are currently dedicated to either lightweight or standard traffic. Above all, conscientiousness for sustainability is essential, as not all technological innovations are necessarily beneficial for mankind in the long term, if adopted in large scale.

Bikes, e-bikes and HIPLEVs are not expected to completely replace other existing heavier transports, either electric or non-electric. But is predictable that in not many years all utilitarian bikes will be e-bikes. If the proper urban infrastructure is made available, all these e-bikes can be transformed into HIPLEVs, which can offer a much higher utilitarian potential than standard e-bikes (and other e-cycles).

It should be noticed that HIPLEVs and bikes, or e-bikes, are not competitive, they are complimentary. In the same way HIPLEVs are not expected to replace all the standard EV in all transport tasks. Much as horses and horse-carriages co-existed as the main land transport resources until the beginning of the 19th century, HIPLEVs and full sized electric cars have potential to become the popular personal transports of the future.

Dynamic Inductive Wireless Power Transfer for Lightweight Electric Vehicles
Luiz Alberto Lisboa da Silva Cardoso – University of Minho

427

Since technical resources have been developed, whether or not the widespread adoption of the HIPLEV will become a reality now seems to depend on cultural changes towards sustainability and economic issues.

7.2 Suggestions for Future Work

Successful adaptation of an Electrically Power Assisted Cycle (EPAC bicycle) to use the Dynamic Inductive Wireless Power Transfer (DIWPT) technology has been achieved. However, in the first HIPLEV prototype, the rider protection against the exposure to EMF levels higher than that currently recommended by the International Commission on Non-Ionizing Radiation Protection (ICNIRP) [72] was intentionally left out of the scope of this work. In particular, the proximity of the secondary coil to the rider's ankles and feet should be a matter of concern. For the HIPLEV to be adopted as a means of transport, further design effort in this direction is still necessary, to assure fully safety compliance. The EMF safety of the pedestrian was already considered in the current prototype design though.

So, while the HIPLEV concept has been proved as viable, the design and validation of the EMF protection for the rider was out of the scope of this work, and it is left for future works. The design for EMF safety could be enormously facilitated if other HPV frame types are adopted as the basis for the HIPLEV, such as recumbent bikes and recumbent electrically assisted velomobiles. Even exhibiting better performance, these cycle types were not selected for the first laboratory prototype, because they are still less popular and more expensive than the standard upright bicycles. But they should be considered in a later implementation approach.

In the same way, after the successful tests of the HIPLEV prototype, it was realized that the use of the maximally flat induced voltage, also supported by the mathematical analysis developed, could be alternatively adopted, and it should result in a new version of the HIPLEV with an improved performance-cost relation. This design exercise is also left for future implementations.

One of the few heuristics introduced in the design is the option for a flat rectangular spiral secondary coil. This is not the optimal coil design that provides a maximum induced voltage, for coils of the same dimensions. This choice was motivated solely by the ease of construction, as the prototype was hand-made in the machine shop. Other more efficient winding layouts, still using rectangular turns, could have been more advantageously used. The concentration of secondary coil turns on the external limits of the mechanically viable coil installation region could render a more efficient coil, and new improved design variants could possibly be achieved.

Dynamic Inductive Wireless Power Transfer for Lightweight Electric Vehicles
Luiz Alberto Lisboa da Silva Cardoso – University of Minho

428

Other three and four-wheeled faired human-powered lightweight EVs, of recent design, can provide full weather protection and more value to the user, and should be considered as the next class of candidate vehicles for DIWPT adaptation. The technology for implementing wireless power transfer circuits for these HIPLEV based on more efficient vehicles is readily available, at the required power levels, but the market for these vehicles is still incipient. It is conjectured that the demonstration of DIWPT applications involving these vehicles would not only be technically well succeeded, but could also impulse the velomobile market. This development and demonstration, fully supported by the tools presented in this thesis, is also left for future work.

The lightweight electric market is growing, but in order for the users to justify the additional investment in the conversion of e-bikes and other lightweight vehicles to HIPLEVs, smart networks of wireless, inductively electrified bike lanes have to be implanted and supported by new regulations. Social and economic impact must also be carefully evaluated, and might indicate complimentary design directives.

The adoption of the HIPLEV requires above all a cultural change, which is always a difficult process. It depends on the rediscovery that "small is beautiful", and that there are many long-term advantages in using a more humanized technology [223]. For that, the continuous discussion and the dissemination of the idea among local administrators, and the public in general, may help to open doors for this new transport variant. It is also possible and very plausible that, when the required massive dedication of natural resources and the large investment necessary to electrify the roads for heavier EVs is fully realized, the interest in DIWPT may turn in favor of the less expensive, less impactful in the power grid, and more sustainable electrification of lanes for lightweight electric vehicles.

Dynamic Inductive Wireless Power Transfer for Lightweight Electric Vehicles
Luiz Alberto Lisboa da Silva Cardoso – University of Minho

429

References

[1]   GHG Protocol Team, "The GHG Protocol Corporate Value Chain (Scope 3) Accounting and Reporting Standard (Supplement to the GHG Protocol Corporate Accounting and Reporting Standard)," 2011.

[2]   Ministry for Foreign Affairs, *Sustainable Futures: Replacing Growth Imperative and Hierarchies with Sustainable Ways*. 2009.

[3]   L. A. L. Cardoso, M. C. Martinez, A. A. N. Melendez, and J. L. Afonso, "Dynamic inductive power transfer lane design for e-bikes," in *2016 IEEE 19th International Conference on Intelligent Transportation Systems (ITSC)*, 2016, pp. 2307–2312.

[4]   Department for Transport UK, "Cycle Infrastructure Design - Local Transport Note 1/20," 27-Jul-2020.

[5]   European Committee for Standardization, "European standard NF EN 15194, Cycles - Electrically power assisted cycles - EPAC bicycles," European Committee for Standardization, 04-Oct-2017.

[6]   L. A. L. Cardoso, J. L. Afonso, M. C. Martinez, and A. A. N. Meléndez, "RFID-Triggered Power Activation for Smart Dynamic Inductive Wireless Power Transfer," in *IECON - The Annual Conference of the IEEE Industrial Electronics Society (IES), October 29 - November 1, 2017*, 2017.

[7]   L. A. Lisboa Cardoso, D. Fourie, J. J. Leonard, A. A. Nogueiras Meléndez, and J. L. Afonso, "Electro-Optical System for Evaluation of Dynamic Inductive Wireless Power Transfer to Electric Vehicles," in *Green Energy and Networking*, 2019, pp. 154–174.

[8]   L. A. L. Cardoso, A. A. N. Meléndez, L. A. S. B. Martins, and J. L. Afonso, "Human-Inductively Powered Lightweight Electric Vehicles: Sustainable Transportation for the Smart City," in *Proc. 4th International Conference on Energy and Environment: bringing together Engineering and Economics*, 2019, pp. 185–190.

[9]   J. A. Afonso, H. G. Duarte, L. A. L. Cardoso, V. Monteiro, and J. L. Afonso, "Wireless Communication and Management System for E-Bike Dynamic Inductive Power Transfer Lanes," *Electronics*, vol. 9, no. 9, p. 1485, 2020.

[10]   V. Monteiro, J. A. Afonso, T. J. C. Sousa, L. L. Cardoso, J. G. Pinto, and J. L. Afonso, "Vehicle Electrification: Technologies, Challenges, and a Global Perspective for Smart Grids," in *Innovation in Energy Systems*, T. S. Ustun, Ed. Rijeka: IntechOpen, 2019.

[11]   L. A. L. Cardoso *et al.*, "Design of an Intrinsically Safe Series-Series Compensation WPT

Dynamic Inductive Wireless Power Transfer for Lightweight Electric Vehicles
Luiz Alberto Lisboa da Silva Cardoso – University of Minho

430

System for Automotive LiDAR," *Electronics*, vol. 9, p. 86, 2020.

[12] J.L. Afonso, L.A.L. Cardoso, D. Pedrosa, T.J.C. Sousa, L. Machado, M. Tanta, V. Monteiro, "A Review on Power Electronics Technologies for Electric Mobility," *Energies*, vol. 13, no. 23, p. 6343, 2020.

[13] British Broadcasting Corporation (BBC), "A History of the World - Michael Faraday's induction ring." [Online]. Available: http://www.bbc.co.uk/ahistoryoftheworld/objects/nSFvkPPCRdWQJ0hzSzrB4A. [Accessed: 05-Feb-2017].

[14] J. T. Boys and G. A. Covic, "The inductive power transfer story at the University of Auckland," *IEEE Circuits Syst. Mag.*, vol. 15, pp. 6–27, 2015.

[15] A. Kurs, A. Karalis, R. Moffatt, J. D. Joannopoulos, P. Fisher, and M. Soljačić, "Wireless Power Transfer via Strongly Coupled Magnetic Resonances," *Science*, vol. 317, no. 5834, pp. 83–87, Jul-2007.

[16] A. Karalis, J. D. Joannopoulos, and M. Soljačić, "Efficient wireless non-radiative mid-range energy transfer," *Ann. Phys. (N. Y).*, vol. 323, no. 1, pp. 34–48, Jan. 2008.

[17] International Commission on Non-Ionizing Radiation Protection (ICNIRP), "Guidelines for Limiting Exposure to Electromagnetic Fields (100 khz to 300 Ghz)," *Health Phys.*, vol. 118, no. 5, pp. 483–524, 2020.

[18] J. W. Coltman, "The transformer [historical overview]," *IEEE Ind. Appl. Mag.*, vol. 8, no. 1, pp. 8–15, Jan. 2002.

[19] F. B. Jewett, "The Faraday centenary," *Bell Syst. Tech. J.*, vol. 10, no. 4, pp. i–vii, Oct. 1931.

[20] Michael Faraday, *Experimental researches in electricity. Vol. 1*, 2nd, 1849 ed. London: Richard and John E. Taylor, 1839.

[21] J. C. Maxwell, *A Treatise on Electricity and Magnetism*, 3rd, 1891, ed. New York: Dover Publications, Inc., 1873.

[22] J. F. Mulligan, "Heinrich Hertz and the Development of Physics," *Phys. Today*, vol. 42, no. 3, pp. 50–57, 1989.

[23] C. S. Helrich, *The Classical Theory of Fields*, 1st ed. Springer, 2012.

[24] F. E. Terman, "Two Resonant Circuits Tuned to the Same Frequency and Coupled Together , Sections 3.5 and 3.6," in *Radio engineer's handbook*, McGraw-Hill Book Company, Inc., 1943, pp. 154–164.

[25] V. R. Gowda, O. Yurduseven, G. Lipworth, T. Zupan, M. S. Reynolds, and D. R. Smith,

Dynamic Inductive Wireless Power Transfer for Lightweight Electric Vehicles
Luiz Alberto Lisboa da Silva Cardoso – University of Minho

431

"Wireless Power Transfer in the Radiative Near Field," *IEEE Antennas Wirel. Propag. Lett.*, vol. 15, pp. 1865–1868, 2016.

[26] M. L. Ng, K. S. Leong, and P. H. Cole, "RFID Tags for Metallic Object Identification," in *RFID HANDBOOK - Applications, Technology, Security, and Privacy*, S. Ahson, Ed. CRC Press, 2008, pp. 255–256.

[27] C. A. Balanis, "Chapter 5, Item 5.2.3, Power Density and Radiation Resistance," in *Antenna Theory Analysis and Design*, 3rd ed., John Wiley & Sons, Inc., 2005, pp. 237–238.

[28] N. Tesla, *Nikola Tesla on His Work With Alternating Currents and Their Application to Wireless Telegraphy, Telephony, and Transmission of Power - An Extended Interview (Tesla Presents Series, Part 1)*. Breckenridge, Colorado: Twenty First Century Books, 1992.

[29] F. W. Grover, *Inductance Calculations - Working Formulas and Tables. Special 1973 Edition Prepared for Instrument Society of America*. New York: Dover Publications, Inc., 1946.

[30] P. L. Kalantarov and L. A. Zeitlin, *Calculation of Inductances (in Russian)*, 3rd ed. Leningrad: Знергоатомиздат, 1986.

[31] F. W. Grover, "Chapter 8 - Circuits Composed of Combinations of Straight Wires, Rectangle of Round Wire," in *Inductance Calculations - Working Formulas and Tables. Special 1973 Edition Prepared for Instrument Society of America*, New York: Dover Publications, Inc., 1946.

[32] P. H. Smith, *Electronic Applications of the Smith Chart - In Waveguide, Circuit and Component Analysis*, 2nd (1995). Raleight, NC: Scitech Publishing, Inc., 1969.

[33] F. Caspers, "RF engineering basic concepts: the Smith chart," *Cern Yellow Rep.*, vol. CERN-2011-, pp. 95–116, 2011.

[34] K. Van Schuylenbergh and R. Puers, *Inductive Powering - Basic Theory and Application to Biomedical Systems*. Springer, 2009.

[35] S. Li and C. C. Mi, "Wireless Power Transfer for Electric Vehicle Applications," *IEEE J. Emerg. Sel. Top. Power Electron.*, vol. 3, no. 1, pp. 4–17, 2015.

[36] C. Liao, J. Li, and S. Li, "Design of LCC impedance matching circuit for wireless power transfer system under rectifier load," *CPSS Trans. Power Electron. Appl.*, vol. 2, no. 3, pp. 237–245, 2017.

[37] M. Iordache, I. Sîrbu, L. Mandache, A. Marinescu, D. Niculae, and L. Iordache, "Comparative study of the frequency splitting and bifurcation phenomena for equivalent circuits of the wireless power transfer system," in *2016 International Conference on*

Dynamic Inductive Wireless Power Transfer for Lightweight Electric Vehicles
Luiz Alberto Lisboa da Silva Cardoso – University of Minho

432

Applied and Theoretical Electricity (ICATE), 2016, pp. 1–7.

[38]   W. Niu, J. Chu, W. Gu, and A. Shen, "Exact Analysis of Frequency Splitting Phenomena of Contactless Power Transfer Systems," *IEEE Trans. Circuits Syst. I Regul. Pap.*, vol. 60, no. 6, pp. 1670–1677, Jun. 2013.

[39]   Y. Lyu *et al.*, "A Method of Using Nonidentical Resonant Coils for Frequency Splitting Elimination in Wireless Power Transfer," *IEEE Trans. Power Electron.*, vol. 30, no. 11, pp. 6097–6107, Nov. 2015.

[40]   X. Y. Zhang, C. Xue, and J. Lin, "Distance-Insensitive Wireless Power Transfer Using Mixed Electric and Magnetic Coupling for Frequency Splitting Suppression," *IEEE Trans. Microw. Theory Tech.*, vol. 65, no. 11, pp. 4307–4316, Nov. 2017.

[41]   W. Zhang and C. C. Mi, "Compensation Topologies of High-Power Wireless Power Transfer Systems," *IEEE Trans. Veh. Technol.*, vol. 65, no. 6, pp. 4768–4778, Jun. 2016.

[42]   J. Li and K. Ji, "Frequency splitting research of series-parallel type magnetic coupling resonant wireless power transfer system," in *2018 13th IEEE Conference on Industrial Electronics and Applications (ICIEA)*, 2018, pp. 2254–2257.

[43]   Chwei-Sen Wang, G. A. Covic, and O. H. Stielau, "Power transfer capability and bifurcation phenomena of loosely coupled inductive power transfer systems," *IEEE Trans. Ind. Electron.*, vol. 51, no. 1, pp. 148–157, Feb. 2004.

[44]   O. C. Onar, M. Chinthavali, S. L. Campbell, L. E. Seiber, C. P. White, and V. P. Galigekere, "Modeling, Simulation, and Experimental Verification of a 20-kW Series-Series Wireless Power Transfer System for a Toyota RAV4 Electric Vehicle," in *2018 IEEE Transportation Electrification Conference and Expo (ITEC)*, 2018, pp. 874–880.

[45]   R. K. Jha, S. Giacomuzzi, G. Buja, M. Bertoluzzo, and M. K. Naik, "Efficiency and power sizing of SS vs. SP topology for wireless battery chargers," in *2016 IEEE International Power Electronics and Motion Control Conference (PEMC)*, 2016, pp. 1014–1019.

[46]   M. Rehman, P. Nallagownden, and Z. Baharudin, "Efficiency investigation of SS and SP compensation topologies for wireless power transfer," *Int. J. Power Electron. Drive Syst.*, vol. 10, no. 4, pp. 2157–2164, 2019.

[47]   V. Shevchenko, O. Husev, R. Strzelecki, B. Pakhaliuk, N. Poliakov, and N. Strzelecka, "Compensation Topologies in IPT Systems: Standards, Requirements, Classification, Analysis, Comparison and Application," *IEEE Access*, vol. 7, pp. 120559–120580, 2019.

[48]   "W. Zhang and C. C. Mi, 'Compensation Topologies of High-Power Wireless Power Transfer Systems,' IEEE Trans. Veh. Technol., vol. 65, no. 6, pp. 4768–4778, Jun. 2016."

[49]   M. Zargham and P. G. Gulak, "Maximum Achievable Efficiency in Near-Field Coupled

Dynamic Inductive Wireless Power Transfer for Lightweight Electric Vehicles
Luiz Alberto Lisboa da Silva Cardoso – University of Minho

433

Power-Transfer Systems," *IEEE Trans. Biomed. Circuits Syst.*, vol. 6, no. 3, pp. 228–245, Jun. 2012.

[50]   D. A. Hapidin, I. Saleh, M. M. Munir, and Khairurrijal, "Design and Development of a Series-configuration Mazzilli Zero Voltage Switching Flyback Converter as a High-voltage Power Supply for Needleless Electrospinning," *Procedia Eng.*, vol. 170, pp. 509–515, 2017.

[51]   M. Engelhardt, *LT Spice XVII(x64)*. Linear Technology Corporation, Analog Devices Inc., 2020.

[52]   A. Scuto, "Half Bridge Resonant LLC Converters and Primary Side MOSFET Selection - Application Note AN4720 (DocID027986 Rev 1)," STMicroelectronics NV, 2015.

[53]   S. Valtchev, B. Borges, K. Brandisky, and J. Ben Klaassens, "Resonant contactless energy transfer with improved efficiency," *IEEE Trans. Power Electron.*, vol. 24, no. 3, pp. 685–699, 2009.

[54]   S. Abdel-Rahman, *Resonant LLC Converter: Operation and Design - Application Note AN 2012-09 V1.0*, no. September. Infineon Technologies North America (IFNA) Corp., 2012.

[55]   Society of Automobile Engineers (SAE), "SAE International Surface Vehicle Recommended Practice, 'Communication between Wireless Charged Vehicles and Wireless EV Chargers,' SAE Standard J2847/6," 05-Aug-2015.

[56]   G. Lee, J. Park, Y. Sim, and D. Cho, "Implementation of WPT communication system based on SAE J2847 standard for electric vehicle," in *2017 IEEE Vehicular Networking Conference (VNC)*, 2017, pp. 251–254.

[57]   P. J. BAXANDALL, "Transistor Sine-Wave LC Oscillators - Some General Considerations and New Developments," in *Transactions of the 1959 International Convention on Transistors and Associated Semiconductor Devices*, 1960, no. 2978 E, pp. 748–758.

[58]   R. L. Bright and G. H. Royer, "Electrical Inverter Circuits," filed 6-Apr-1954, United States Patent nᵒ 2783384, 1957.

[59]   D. Edry and S. Ben-Yaakov, "Capacitive-loaded push-pull parallel-resonant converter," in *Proceedings Eighth Annual Applied Power Electronics Conference and Exposition,* 1993, pp. 51–57.

[60]   J. D. Paolucci, *Novel Current-Fed Boundary-Mode Parallel-Resonant Push-Pull Converter*, no. June. San Luis Obispo: California Polytechnic State University, 2009.

[61]   S. L. McClusky, *High Voltage Resonant self-Tracking Current-Fed Converter*, no. March. San Luis Obispo: California Polytechnic State University, 2010.

[62]   D. J. Thrimawithana and U. K. Madawala, "Analysis of Split-Capacitor Push–Pull Parallel-

Dynamic Inductive Wireless Power Transfer for Lightweight Electric Vehicles
Luiz Alberto Lisboa da Silva Cardoso – University of Minho

434

Resonant Converter in Boost Mode," *IEEE Trans. Power Electron.*, vol. 23, no. 1, pp. 359–368, Jan. 2008.

[63] L. W. Nagel and D. O. Pederson, *SPICE : Simulation Program with Integrated Circuit Emphasis*. Berkeley: Electronics Research Laboratory, College of Engineering, University of California, 1973.

[64] M. Engelhardt, "LTspice XVII (x64) 17.0.21.0," 2020. [Online]. Available: https://www.analog.com/en/design-center/design-tools-and-calculators/ltspice-simulator.html. [Accessed: 10-Jan-2021].

[65] M. N. O. Sadiku, *Numerical Techniques in Electromagnetics with MATLAB*, 3rd ed. CRC Press, 2009.

[66] V. T. Morgan, "The Current Distribution, Resistance and Internal Inductance of Linear Power System Conductors—A Review of Explicit Equations," *IEEE Trans. Power Deliv.*, vol. 28, no. 3, pp. 1252–1262, Jul. 2013.

[67] C. R. Sullivan, "Optimal choice for number of strands in a litz-wire transformer winding," *IEEE Trans. Power Electron.*, vol. 14, no. 2, pp. 283–291, 1999.

[68] X. Tang and C. R. Sullivan, "Optimization of stranded-wire windings and comparison with litz wire on the basis of cost and loss," in *2004 IEEE 35th Annual Power Electronics Specialists Conference*, 2004, no. June, pp. 854–860.

[69] C. R. Sullivan and R. Y. Zhang, "Simplified Design Method for Litz Wire," in *2014 29th Annual IEEE Applied Power Electronics Conference and Exposition (APEC)*, 2014, pp. 2667–2674.

[70] K. de S. Lourenço, "EFEITOS BIOLÓGICOS DOS CAMPOS ELECTROMAGNÉTICOS - Aplicação ao caso dos transportes colectivos com tracção eléctrica," Universidade do Porto, 2009.

[71] International Commission on Non-Ionizing Radiation Protection, "Guidelines for Limiting Exposure to Time-Varying Electric, Magnetic, and Electromagnetic Fields (Up to 300 GHz)," *Health Phys.*, vol. 75, no. 5, p. 535, 1998.

[72] International Commission on Non-Ionizing Radiation Protection, "Guidelines for limiting exposure to time-varying electric and magnetic fields (1 Hz to 100 kHz).," *Health Phys.*, vol. 99, no. 6, pp. 818–36, 2010.

[73] João L. Afonso, J. G. Pinto, and H. Gonçalves, "Active Power Conditioners to Mitigate Power Quality Problems in Industrial Facilities," in *Power Quality Issues*, A. Zobaa, Ed. InTechOpen, 2013.

[74] Siemens Historical Institute, "The Siemens tram from past to present." [Online]. Available:

Dynamic Inductive Wireless Power Transfer for Lightweight Electric Vehicles
Luiz Alberto Lisboa da Silva Cardoso – University of Minho

435

https://www.siemens.com/history/pool/innovationen/mobilitaet/the_siemens_tram_fro m_past_to_present.pdf. [Accessed: 28-Feb-2017].

[75]   W. von Siemens, "Letter of May 12, 1881, to Professor Wiedemann of Leipzig, in Conrad Matschoß, ed., Werner von Siemens. Ein kurzgefaßtes Lebensbild nebst einer Auswahl seiner Briefe [Werner von Siemens: A Summary of His Life Together with Selected Letters]. p. 691. Trans," 1916. [Online]. Available: http://germanhistorydocs.ghi-dc.org/pdf/eng/115_von Siemens_Elec Trolleys_15.pdf. [Accessed: 28-Feb-2017].

[76]   H. Liu *et al.*, "Dynamic Wireless Charging for Inspection Robots Based on Decentralized Energy Pickup Structure," *IEEE Trans. Ind. Informatics*, vol. 14, no. 4, pp. 1786–1797, Apr. 2018.

[77]   S. H. Kang and C. W. Jung, "Textile Resonators With Thin Copper Wire for Wearable MR-WPT System," *IEEE Microw. Wirel. Components Lett.*, vol. 27, no. 1, pp. 91–93, Jan. 2017.

[78]   Smart Road Gotland, "Electric truck ready for dynamic wireless charging on public roads in Sweden," 05-Mar-2020. [Online]. Available: https://www.smartroadgotland.com/ post/electric-truck-ready-for-dynamic-wireless-charging-on-public-roads-in-sweden. [Accessed: 01-May-2010].

[79]   M. Kane, "Sweden To Test Dynamic Wireless Charging On Island Of Gotland," *InsideEVs*, 20-Apr-2020. [Online]. Available: https://insideevs.com/news/345858/sweden-to-test-dynamic-wireless-charging-on-island-of-gotland/. [Accessed: 01-May-2020].

[80]   J. C. Maxwell, "On Physical Lines of Force - Parts I and II, Fourth Series," *Philos. Mag. J. Sci.*, vol. XXI, no. March, pp. 171–175, 281-291-348, 1861.

[81]   J. C. Maxwell, "On Physical Lines of Force - Parts III and IV, Fourth Series," *Philos. Mag. J. Sci.*, no. April and May, pp. 12–24, 85–95, 1861.

[82]   O. Heaviside, *Electromagnetic Theory, Vol. I*. London: "The Electrician" Printing and Publishing Company Ltd., 1894.

[83]   J. C. Rautio, "The Long Road to Maxwell's Equations," *IEEE Spectr.*, vol. 51, no. 12, pp. 36–56, Dec. 2014.

[84]   J. D. Jackson, "Transformation of Electromagnetic Fields," in *Classical Electrodynamics*, 3rd ed., John Wiley & Sons, Inc., 1998, pp. 558–561.

[85]   M. Abraham and R. Becker, "Time Rate of Change of the Flux through a Moving Element of Area," in *The Classical Theory of Electricity and Magnetism, English translation to the 8th German Edition, 1932*, Glasgow: Blackie & Son, Ltd., 1932, pp. 39–40.

[86]   H. Flanders, "Differentiation under the Integral Sign," *Am. Math. Mon.*, vol. 80, no. 6, pp.

Dynamic Inductive Wireless Power Transfer for Lightweight Electric Vehicles
Luiz Alberto Lisboa da Silva Cardoso – University of Minho

436

615–627, 1973.

[87] J. D. Jackson, "Section 5.15, Faraday's Law of Induction," in *Classical Electrodynamics*, 3rd ed., John Wiley {&} Sons, Inc., 1998, pp. 208–211.

[88] S. Cho and J. Kim, "Linear electromagnetic electric generator for harvesting vibration energy at frequencies more than 50 Hz," *Adv. Mech. Eng.*, vol. 9, p. 168781401771900, 2017.

[89] J. T. Cheung, "Frictionless Linear Electrical Generator for Harvesting Motion Energy - Rockwell Scientific Company LCC Report nr. 71222." Thousand Oaks, CA, USA, 2004.

[90] T. L. Chow, "Field of a Small Current Loop: The Magnetic Dipole," in *Introduction to Electromagnetic Theory - A modern perspective*, Jones and Barlett Publishers, Inc., 2006, pp. 146–150.

[91] International Organization for Standardization, *ISO 4130:1978(E) - Road vehicles -- Three-dimensional reference system and fiducial marks -- Definitions*. 1978, pp. 1–2.

[92] Society of Automobile Engineers (SAE), "SAE Technical Information Report J2954 - Wireless Power Transfer for Light-Duty Plug-In/ Electric Vehicles and Alignment Methodology," May-2016.

[93] M. Hutin and M. Leblanc, "Un nouveau système de traction électrique des véhicules (A new electric traction system for vehicles)," filed 5-Nov-1890, French Republic Patent 209323, 18-Feb-1891.

[94] R. A. Davies, "'Wireless' Autos: A Russian Dream," *Maclean's Magazine*, vol. 58, no. 13, p. 19, 34 and 36, 01-Jul-1945.

[95] G. I. Babat, "High Frequency Electric Transport System with Contactless Transmission of Energy," filled 26-Mar-1946, United Kington Patent 657035, 12-Sep-1951.

[96] Systems Control Technology Inc., "Roadway Powered Electric Vehicle Project Track Construction And Testing Program Phase 3D." prepared for California Partners for Advanced Transit and Highways (PATH), University of California, Berkeley, Palo Alto, California, p. California PATH Research Paper UCB-ITS-PRR-94-07, 1994.

[97] C. N. Pyrgidis, *Railway Transportation Systems*. Boca Raton: CRC Press, 2016.

[98] M. Hutin and M. Leblanc, "Transformer System for Electric Railways," filed 16-Nov-1892, US Patent 527,857, 23-Oct-1894.

[99] D. C. Meeker, "Finite Element Method Magnetics - Version 4.2 (12 Jan 2016 Build)." 2016.

[100] J. C. Vaudois, *Le Tramway à la Française: Toute une histoire !* Lulu.com, 2017.

Dynamic Inductive Wireless Power Transfer for Lightweight Electric Vehicles
Luiz Alberto Lisboa da Silva Cardoso – University of Minho

437

[101] G. Mantovani, "Which role for tramways in the next years," in *Proceedings of the AIIT International Congress on Transport Infrastructure and Systems (TIS 2017), Rome, Italy, 10-12 April*, G. Dell'Acqua and F. Wegman, Eds. Leiden: CRC Press/Balkema, 2017, pp. 1123–1130.

[102] M. Lozinsky and B. Kholmsky, "New Applications of Science to Industry and Transport," *USSR Inf. Bull. Publ. by Embassy Union Sov. Social. Republics USA*, vol. VI, no. 56, p. 12, Aug. 1946.

[103] S. S. Valtchev, E. N. Baikova, and L. R. Jorge, "Electromagnetic field as the wireless transporter of energy," *Facta Univ. - Ser. Electron. Energ.*, vol. 25, no. 3, pp. 171–181, 2012.

[104] J. G. Bolger, "Supplying Power to Vehicles," filed 10-Sep-1974, United States Patent 3914562, 21-Oct-1975.

[105] J. G. Bolger and F. A. Kirsten, "Investigation of the Feasibility of a Dual Mode Electric Transportation System," Lawrence Berkeley Laboratory, University of California, Berkeley, CA, USA, May-1977.

[106] G. A. Covic, G. Elliott, O. H. Stielau, R. M. Green, and J. T. Boys, "The design of a contactless energy transfer system for a people mover system," in *PowerCon 2000. 2000 International Conference on Power System Technology. Proceedings (Cat. No.00EX409)*, 2000, vol. 1, pp. 79–84 vol.1.

[107] S. Ahn, N. P. Suh, and D.-H. Cho, "The All-Electric Car You Never Plug In," *IEEE Spectrum, March 26th, 2013*, Mar-2013.

[108] K. Throngnumchai, A. Hanamura, Y. Naruse, and K. Takeda, "Design and evaluation of a wireless power transfer system with road embedded transmitter coils for dynamic charging of electric vehicles," in *2013 World Electric Vehicle Symposium and Exhibition (EVS27)*, 2013, pp. 1–10.

[109] O. C. Onar, J. M. Miller, S. L. Campbell, C. Coomer, C. P. White, and L. E. Seiber, "A novel wireless power transfer for in-motion EV/PHEV charging," *Conf. Proc. - IEEE Appl. Power Electron. Conf. Expo. - APEC*, pp. 3073–3080, 2013.

[110] J. M. Miller *et al.*, "Demonstrating dynamic wireless charging of an electric vehicle: The benefit of electrochemical capacitor smoothing," *IEEE Power Electron. Mag.*, vol. 1, no. March, pp. 12–24, 2014.

[111] P. Guglielmi, "The story of the Italian test site," *FABRIC Final Conference presentations*, Torino, Italy, Jun-2018.

[112] A. Amditis, "Final Report Summary - FABRIC (Feasibility analysis and development of on-road charging solutions for future electric vehicles)," Athens, 2019.

Dynamic Inductive Wireless Power Transfer for Lightweight Electric Vehicles
Luiz Alberto Lisboa da Silva Cardoso – University of Minho

438

[113] M. Emre, V. Cirimele, P. Guglielmi, and H. Bludszuweit, *FABRIC - Feasibility Analysis and Development of On-Road Charging Solutions for Future Electric Vehicles - Analysis of Results and Recommendations - Deliverable D3.7.2*. 2017.

[114] D. Bateman *et al.*, "TRL Academy Report PPR875 - Electric Road Systems : a solution for the future," *TRL PPR875*, 08-Nov-2018.

[115] Electreon, "Tel Aviv Pilot Launch 2021," 2021. [Online]. Available: https://www.electreon.com/media. [Accessed: 21-Jun-2021].

[116] Electreon, "Gotland Sweden Deployment," 2020. [Online]. Available: https://www.electreon.com/media. [Accessed: 21-Jun-2021].

[117] "The Galvanometer," *Ann. Electr. Magn. Chem. Guard. Exp. Sci.*, vol. 1, no. Oct. 1836, p. 4, 1837.

[118] Massachusetts Charitable Mechanic Association, "First Exhibition and Fair of the Massachusetts Charitable Mechanic Association, at Faneuil and Quincy Halls, in the City of Boston." Dutton and Wentworth, Boston, MA, 1837.

[119] S. Ahn *et al.*, "Low frequency electromagnetic field reduction techniques for the On-Line Electric Vehicle (OLEV)," *2010 IEEE Int. Symp. Electromagn. Compat.*, pp. 625–630, 2010.

[120] J. Huh, W. Lee, G.-H. Cho, B. Lee, and C.-T. Rim, "Characterization of Novel Inductive Power Transfer Systems for On-Line Electric Vehicles," *2011 Twenty-Sixth Annu. IEEE Appl. Power Electron. Conf. Expo.*, pp. 1975–1979, 2011.

[121] J. Shin *et al.*, "Contactless power transfer systems for On-Line Electric Vehicle (OLEV)," in *2012 IEEE International Electric Vehicle Conference*, 2012, pp. 1–4.

[122] M. Zahn, "Chapter 6, Electromagnetic Induction," in *Electromagnetic Field Theory: A Problem Solving Approach*, 2nd ed., Malabar, FL: Krieger Publishing Company, 2003, p. 397.

[123] K. Baltzis, "The FEMM Package: A Simple, Fast, and Accurate Open Source Electromagnetic Tool in Science and Engineering," *J. Eng. Sci. Technol. Rev.*, vol. 1, 2008.

[124] Y. H. Sohn, B. H. Choi, E. S. Lee, and C. T. Rim, "Comparisons of magnetic field shaping methods for ubiquitous wireless power transfer," in *2015 IEEE PELS Workshop on Emerging Technologies: Wireless Power (2015 WoW)*, 2015, pp. 1–6.

[125] D. Jiles, *Introduction to Magnetism and Magnetic Materials*, 1st ed. Ames,: Springer Science+Business Media, B.V., 1991.

[126] C. H. Moon, H. W. Park, and S. Y. Lee, "A design method for minimum-inductance planar magnetic-resonance-imaging gradient coils considering the pole-piece effect," *Meas. Sci.*

Dynamic Inductive Wireless Power Transfer for Lightweight Electric Vehicles
Luiz Alberto Lisboa da Silva Cardoso – University of Minho

439

Technol., vol. 10, no. 12, pp. N136–N141, Nov. 1999.

[127]   C. T. Rim and C. Mi, "Chapter 6 - Magnetic Mirror Models," in *Wireless Power Transfer for Electric Vehicles and Mobile Devices*, 1st ed., John Wiley & Sons Ltd. - IEEE Press, 2017, pp. 99–124.

[128]   S. Cruciani, T. Campi, M. Feliziani, and F. Maradei, "Optimum coil configuration of wireless power transfer system in presence of shields," in *2015 IEEE International Symposium on Electromagnetic Compatibility (EMC)*, 2015, pp. 720–725.

[129]   N. P. Suh and D. H. Cho, *The On-line Electric Vehicle: Wireless Electric Ground Transportation Systems*. Springer International Publishing, 2017.

[130]   K. Gibbs, *The Steam Locomotive: An Engineering History*. Amberley Publishing, 2012.

[131]   D. Bogart, L. Shaw-taylor, and X. You, "The development of the railway network in Britain 1825-1911," in *The Online Historical Atlas of Transport, Urbanization and Economic Development in England and Wales c.1680-1911*, L. Shaw-Taylor, D. Bogart, and M. Satchell, Eds. University of Cambridge, 2018.

[132]   M. C. Howard, "Megacities and Global Cities," in *Transnationalism and Society-- An Introduction*, Jefferson, North Carolina, USA: McFarland & Company, Inc., Publishers, 2011, pp. 90–91.

[133]   P. Stone, "The History of London - Horses and carriages in the Victorian era." [Online]. Available: https://www.thehistoryoflondon.co.uk/horses-and-carriages-in-the-victorian-era/. [Accessed: 27-Oct-2020].

[134]   "Extract from the 'Karlsruher Bitterungs-Beobachtungen' of July 31, 1817," in *Kalrsruher Zeitung*, no. 211, Digital collection of the Badische Landesbibliothek Karlsruhe, 1817, p. 1016.

[135]   P. Smethurst, *The Bicycle — Towards a Global History*. Palgrave Macmillan UK, 2015.

[136]   A. Sharp, "Chapter XIV - The Rear Driving Safety," in *Bicycles & Tricycles - An Elementary Treatise on Their Design and Construction*, London: Longmans, Green, and Co., 1896, pp. 153–155.

[137]   H. J. Lawson, "Velocipede," filed 16-Mar-1886, US Patent 345,851, 20-Jul-1886.

[138]   D. V. Herlihy, *Bicycle: the history*. New Haven: Yale University Press, 2004.

[139]   A. Sharp, *Bicycles & Tricycles - An Elementary Treatise on Their Design and Construction*. London: Longmans, Green, and Co., 1896.

[140]   Union Cycliste Internationale (UCI), "Men World Record - One hour," 2020.

[141]   A. Schmitz, "Why Your Bicycle Hasn't Changed for 106 Years," *Hum. Power - Tech. J. Int.*

Dynamic Inductive Wireless Power Transfer for Lightweight Electric Vehicles
Luiz Alberto Lisboa da Silva Cardoso – University of Minho

440

Hum. Powered Veh. Assoc., vol. 11, no. 3, pp. 3–9, 1994.

[142]   P. Desbordes, "Le mariage de La bicyclette et de l'aerodynamique," *Les Ailles*, no. 932, Paris, p. 12, 27-Apr-1939.

[143]   H. Robertshaw, "UCI considering scrapping 6.8kg bike weight limit," *Cycling Weekly*, 14-Dec-2015.

[144]   Union Cycliste Internationale (UCI), "Clarification guide of the UCI Technical Regulation (01.10.20 version)," 2020. [Online]. Available: https://www.uci.org/inside-uci/constitutions-regulations/regulations. [Accessed: 31-Oct-2020].

[145]   World Human Powered Vehicle Association, "Land - Men's 1 Hour Standing Start (Single Rider)," 2020. [Online]. Available: http://www.whpva.org/land.html#300. [Accessed: 01-Nov-2020].

[146]   A. C. Gross, C. R. Kyle, and D. J. Malewicki, "The Aerodynamics of Human-powered Land Vehicles," *Sci. Am.*, vol. 249, no. 6, pp. 142–153, Oct. 1983.

[147]   D. G. Wilson, *BICYCLING SCIENCE Third edition*. Cambridge, MA, USA: The MIT Press, 2004.

[148]   S. J. Brown, H. J. Ryan, and J. A. Brown, "Age-associated changes in VO2 and power output – A cross-sectional study of endurance trained New Zealand cyclists," *J. Sport. Sci. Med.*, vol. 6, no. December, pp. 477–483, 2007.

[149]   D. G. Wilson, "Chapter I, Human Power, Section 2, Human Power Generation, Critical power: curve fitting to power-duration pedaling data, Fig. 2.4," in *Bicycling Science Third edition*, Cambridge, MA, USA: The MIT Press, 2004, p. 44.

[150]   Eurostat, "Persons in employment by commuting time, educational attainment level and degree of urbanisation," *Online data code: LFSO_19PLWK28*, 2019. [Online]. Available: https://ec.europa.eu/eurostat/databrowser/view/LFSO_19PLWK28/default/bar?lang=en&bookmarkId=96ad2e59-267b-404c-97e2-133b7fa05022. [Accessed: 28-Oct-2020].

[151]   M. Miyake and M. Crass, "National Policies to Promote Cycling," in *European Conference of Miniisters of Transport (ECMT)*, 2004, p. 24.

[152]   J. H. Bridge, "Chapter V - Electric Pedestrianism," in *A fortnight in heaven; an unconventional romance.*, New York: Henry Holt and Company, 1886.

[153]   Ogden Bolton Jr., "Electrical Bicycle," filed 19-Sep-1895, US Patent No. 552,271, 31-Dec-1895.

[154]   H. W. Libbey, "Electric Bicycle," filed 14-Dec-1895, US Patent No. 596,273, 28-Dec-1897.

[155]   K. Desmond, *Electric Motorcycles and Bicycles - A History Including Scooters, Tricycles,*

Dynamic Inductive Wireless Power Transfer for Lightweight Electric Vehicles
Luiz Alberto Lisboa da Silva Cardoso – University of Minho

441

Segways and Monocycles. Jefferson, North Carolina, USA: McFarland & Company, Inc., Publishers, 2019.

[156] A. Petrillo, S. Mellino, F. De Felice, and I. Scudo, "Design of a Sustainable Electric Pedal-Assisted Bike: A Life Cycle Assessment Application in Italy," in *New Frontiers on Life Cycle Assessment - Theory and Application*, 2018.

[157] European Automobile Manufacturers' Association (ACEA), "Historical series 1990-2019 new passenger car registrations by country (EU+EFTA)." 2020.

[158] Confederation of the European Bicycle Industry (CONEBI), "European Bicycle Industry & Market Report 2018 edition (2017 statistics)," 2018.

[159] J.-W. van Schaik, "European industry reports 60% surge in e-bike production," 20-Jul-2020. [Online]. Available: https://www.bike-eu.com/market/nieuws/2020/07/european-industry-reports-60-surge-in-e-bike-production-10138302. [Accessed: 23-Oct-2020].

[160] M. Sutton, "3 million e-Bikes sold in Europe in 2019, Belgium hits 51% of sales," *Cycling Industry News*, 09-Jul-2020. [Online]. Available: https://cyclingindustry.news/3-million-e-bikes-sold-in-europe/. [Accessed: 23-Oct-2020].

[161] Confederation of the European Bicycle Industry (CONEBI), "The 2020 CONEBI Bicycle Industry & Market Profile With 2019 Figures Is Now Available," 2020. [Online]. Available: https://www.conebi.eu/the-2020-conebi-bicycle-industry-market-profile-with-2019-figures-is-now-available/. [Accessed: 10-Oct-2022].

[162] D. G. Wilson, "Chapter II, Some Bicycle Physics, Section 4, Power and Speed, Steady-speed power equation, Fig. 4.8," in *Bicycling Science Third edition*, 2004.

[163] W. C. Morchin and H. Oman, "Chapter 2 - Mathematical Model of Bicycle Performance: Power Required," in *Electric Bicycles - A Guide to Design and Use*, IEEE Press Editorial Board, Ed. Hoboken, New Jersey: Wiley-Interscience, 2006, pp. 23–42.

[164] D. Gutierrez, "Visual comparisons of laws affecting bicyclists in the United States," *U.S. Bicycle Laws*. [Online]. Available: https://cyclingsavvy.org/u-s-bicycle-laws-by-state/#tab-id-2.

[165] CROW - Centrum voor Regelgeving en Onderzoek in de Grond- Water- en Wegenbouw en de Verkeerstechniek, "Section 3.5 - Inclines," in *Design Manual for Bicycle Traffic*, Ede, The Netherlands: Dutch Bicycle Council (Fietsberaad), 2016, pp. 53–56.

[166] M. W. Denny, "Limits to running speed in dogs , horses and humans," *J. Exp. Biol.*, vol. 211, pp. 3836–3849, 2008.

[167] Christoph Moder et al., "Velomobile Knowledge Base - Version 3.0," 2022. [Online]. Available: https://cmoder.gitlab.io/velomobil-grundwissen/velomobile_knowledge.html.

Dynamic Inductive Wireless Power Transfer for Lightweight Electric Vehicles
Luiz Alberto Lisboa da Silva Cardoso – University of Minho

442

[Accessed: 17-Oct-2022].

[168] *ISO 5775-1:2014 Bicycle tyres and rims - Part 1: Tyre designations and dimensions*, 6th ed. International Organization for Standardization, 2014.

[169] Q. Zhao *et al.*, "Review on the Electrical Resistance / Conductivity of Carbon Fiber Reinforced Polymer," *Appl. Sci.*, vol. 9, no. 11, p. 2390, 2019.

[170] M. Kamon, M. J. Tsuk, and J. White, "FastHenry: A Multipole-Accelerated 3-D Inductance Extraction Program," in *30th ACM/IEEE Design Automation Conference*, 1993, pp. 678–683.

[171] M. Kamon, M. J. Tsuk, C. Smithhisler, and J. White, "The Best of ICCAD," A. Kuehlmann, Ed. Boston, MA: Springer, 2003, pp. 403–412.

[172] "IEEE TRANSACTIONS ON VEHICULAR TECHNOLOGY, VOL. 59, NO. 6, JULY 2010 Battery, Ultracapacitor, Fuel Cell, and Hybrid Energy Storage Systems for Electric, Hybrid Electric, Fuel Cell, and Plug-In Hybrid Electric Vehicles: State of the Art Alireza Khaligh, Se."

[173] S. M. Lukic, J. Cao, R. C. Bansal, F. Rodriguez, and A. Emadi, "Energy Storage Systems for Automotive Applications," *IEEE Trans. Ind. Electron.*, vol. 55, no. 6, pp. 2258–2267, Jun. 2008.

[174] H. Rahimi-Eichi, U. Ojha, F. Baronti, and M. Chow, "Battery Management System: An Overview of Its Application in the Smart Grid and Electric Vehicles," *IEEE Ind. Electron. Mag.*, vol. 7, no. 2, pp. 4–16, Jun. 2013.

[175] International Electrotechnical Comission, *Information Technology Equipment - Safety - Part 1: General Requirements - Iternational Standard IEC 60950-1:2005*, 2nd ed. Geneeva, Switzerland, 2005.

[176] Occupational Safety & Health Administration (OSHA), "Standard 1926.403 - Safety and Health Regulations for Construction, General Requirements, Subpart K, Electrical," *Fed. Regist.*, vol. 61, no. 30, p. 5507, 1996.

[177] N. Suh, D. H. O. Cho, and C. Rim, "Design of On-Line Electric Vehicle (OLEV)," 2011.

[178] M. Toll, "The truth: How far can an electric bicycle really go on a single charge?," *Electrek*, 12-Jun-2020. [Online]. Available: https://electrek.co/2020/06/12/how-far-can-an-electric-bicycle-really-go-on-a-charge/. [Accessed: 15-Oct-2020].

[179] American Association of State Highway and Transportation Officials (AASHTO), *Guide for Development of Bicycle Facilities*, 4th ed. Washington, 2012.

[180] Ministério das Cidades Brasil, *Caderno de Referência para Elaboração de Plano de Mobilidade por Bicicleta nas Cidades*. Brasília: PROGRAMA BRASILEIRO DE MOBILIDADE

Dynamic Inductive Wireless Power Transfer for Lightweight Electric Vehicles
Luiz Alberto Lisboa da Silva Cardoso – University of Minho

443

POR BICICLETA – BICICLETA BRASIL, 2007.

[181]   C. van den Berg, *Brief Dutch Design Manual for Bicycle and Pedestrian Bridges*. ipv Delft creatieve ingenieurs, 2017.

[182]   L. Medina and S. Hernández, *Manual for the design of cyclepaths in Catalonia*. Barcelona: Generalitat de Catalunya Departament de Política Territorial i Obres Públiques, 2008.

[183]   Instituto da Mobilidade e dos Transportes Terrestres (IMTT), "Rede Ciclável - Princípios de Planeamento e Desenho," in *Colecção de Brochuras Técnicas / Temáticas*, 2011.

[184]   D. Dufour and Ligtermoet & Partners Netherlands, *Promoting Cycling for Everyone as a Daily Transport Mode - PRESTO Cycling Policy Guide Infrastructure*. European Commission, 2010.

[185]   European Commission, "Cycle Lanes - Implementation Fact Sheet." [Online]. Available: https://ec.europa.eu/energy/intelligent/projects/sites/iee-projects/files/projects/documents/presto_fact_sheet_cycle_lanes_en.pdf. [Accessed: 01-Nov-2020].

[186]   S. M. Cain, *An Experimental Investigation of Human/Bicycle Dynamics and Rider Skill in Children and Adults*. University of Michigan, 2013.

[187]   S. M. Cain, "Section 3.4, Results," in *An Experimental Investigation of Human/Bicycle Dynamics and Rider Skill in Children and Adults*, University of Michigan, 2013, pp. 35–37.

[188]   C. T. Rim and C. Mi, *Wireless Power Transfer for Electric Vehicles and Mobile Devices*, 1st ed. John Wiley & Sons Ltd. - IEEE Press, 2017.

[189]   V. Cirimele, R. Torchio, A. Virgillito, F. Freschi, and P. Alotto, "Challenges in the Electromagnetic Modeling of Road Embedded Wireless Power Transfer," *Energies*, vol. 12, no. 14, 2019.

[190]   A. Ogunsola, U. Reggiani, and L. Sandrolini, "Shielding effectiveness of concrete buildings," 2005, pp. 65–68.

[191]   Zhengzhou Minghe Technology Electronic Co. Ltd., *User manual - Programmable power supply ZXY-6010S Rev 2.1*. Zhengzhou, China.

[192]   G. R. Nagendra, L. Chen, G. A. Covic, and J. T. Boys, "Detection of EVs on IPT Highways," *IEEE J. Emerg. Sel. Top. Power Electron.*, vol. 2, no. 3, pp. 584–597, Sep. 2014.

[193]   B. S. Cook *et al.*, "RFID-Based Sensors for Zero-Power Autonomous Wireless Sensor Networks," *IEEE Sens. J.*, vol. 14, no. 8, pp. 2419–2431, Aug. 2014.

[194]   A. Kamineni, G. A. Covic, and J. T. Boys, "Interoperable EV detection for dynamic wireless

Dynamic Inductive Wireless Power Transfer for Lightweight Electric Vehicles
Luiz Alberto Lisboa da Silva Cardoso – University of Minho

444

charging with existing hardware and free resonance," *IEEE PELS Work. Emerg. Technol. Wirel. Power, WoW 2016*, pp. 169–173, 2016.

[195] M. Budhia, J. T. Boys, G. A. Covic, and C. Y. Huang, "Development of a Single-Sided Flux Magnetic Coupler for Electric Vehicle IPT Charging Systems," *IEEE Trans. Ind. Electron.*, vol. 60, no. 1, pp. 318–328, Jan. 2013.

[196] International Organization for Standardization;, *ISO/IEC 14443-1:2008(E), Identification cards - Contactless integrated circuit cards - Proximity cards - Part 1: Physical characteristics*, 2nd ed. 2008.

[197] International Organization for Standardization;, *ISO/IEC 14443-2:2001(E), Identification cards - Contactless integrated circuit(s) cards - Proximity cards - Part 2: Radio frequency power and signal interface*, 1st ed. 2001.

[198] International Organization for Standardization;, *ISO/IEC 14443-3:2001(E), Identification cards - Contactless integrated circuit(s) cards - Proximity cards - Part 3: Initialization and anticollision*, 1st ed. 2001.

[199] NXP Semiconductors, *MF1S50yyX/V1 MIFARE Classic EV1 1K - Mainstream contactless smart card IC for fast and easy solution development*, Rev. 3. 2014.

[200] K. E. Mayes and C. Cid, "The MIFARE Classic story," *Inf. Secur. Tech. Rep.*, vol. 15, no. 1, pp. 8–12, 2010.

[201] I. Kirschenbaum and A. Wool, "How to Build a Low-cost, Extended-range RFID Skimmer," in *Proceedings of the 15th Conference on USENIX Security Symposium - Volume 15*, 2006.

[202] K. Finkenzeller, F. Pfeiffer, and E. Biebl, "Range Extension of an ISO/IEC-14443 type A RFID System with Actively Emulating Load Modulation," in *RFID SysTech 2011 7th European Workshop on Smart Objects: Systems, Technologies and Applications*, 2011, pp. 1–10.

[203] NXP Semiconductors, *AN1445 - Antenna design guide for MFRC52x, PN51x and PN53x, Rev. 1.2 - 11 October 2010*, no. October. 2010.

[204] NXP Semiconductors, *MFRC522 Standard performance MIFARE and NTAG frontend, Rev. 3.9 – 27 April 2016*. 2016.

[205] P. Dhaker, "Introduction to SPI Interface," *Analog Dialogue*, vol. 52, no. 3, pp. 1–5, 2018.

[206] CEPT Electronic Communications Committee, "ERC Recommendation 70-03, Relating to the use of Short Range Devices (SRD)," May, 2017., European Conference of Postal and Telecommunications Administrations.

[207] N. D. Mazharov, S. M. Hristov, D. A. Dichev, and I. S. Zhelezarov, "Some Problems of Dynamic Contactless Charging of Electric Vehicles," *Acta Polytech. Hungarica*, vol. 14, no.

Dynamic Inductive Wireless Power Transfer for Lightweight Electric Vehicles
Luiz Alberto Lisboa da Silva Cardoso – University of Minho

445

4, pp. 7–26, 2017.

[208]   S. Laporte, G. Coquery, M. Revilloud, and V. Deniau, "Experimental performance assessment of a dynamic wireless power transfer system for future EV in real driving conditions," in *3rd Workshop on Electric Vehicle Systems, Data, and Applications (EV-Sys 2018), Proceedings of the 9th ACM International Conference on Future Energy Systems*, 2018, pp. 570–578.

[209]   Y. Feng and J. Wang, "GPS RTK Performance Characteristics and Analysis," *J. Glob. Position. Syst.*, vol. 7, no. 1, pp. 1–8, 2008.

[210]   M. Supej and I. Čuk, "Comparison of Global Navigation Satellite System Devices on Speed Tracking in Road (Tran)SPORT Applications," *Sensors*, vol. 14, pp. 23490–23508, 2014.

[211]   Leica Geosystems AG, "Leica GS18 T Data sheet." Heinrich-Wild-Strasse 9435 Heerbrugg, Switzerland, pp. 1–2, 2017.

[212]   P. Lightbody, T. Krajník, and M. Hanheide, "A Versatile High-performance Visual Fiducial Marker Detection System with Scalable Identity Encoding," in *Proceedings of the Symposium on Applied Computing*, 2017, pp. 276–282.

[213]   A. Mossel, "Robust 3D Position Estimation in Wide and Unconstrained Indoor Environments," *Sensors*, vol. 15, pp. 31482–31524, Dec. 2015.

[214]   Association française de normalisation (AFNOR), *European Standard NF EN 15194*. 2009.

[215]   Bosch Sensortec GmbH, *BNO055 Data sheet - Intelligent 9-Axis Absolute Orientation Sensor - Document nr. BST-BNO055-DS000-12, Rev. 1.2*, no. November. 2014.

[216]   H.-J. Freund, "Time control of hand movements," *Prog. Brain Res.*, vol. 64, pp. 287–294, 1986.

[217]   STMicroelectronics NV, "STM32F103x8 and STM32F103xB Medium-density performance line ARM®-based 32-bit MCU with 64 or 128 KB Flash, USB, CAN, 7 timers, 2 ADCs, 9 com. interfaces - DocID13587 Rev 17," 2015.

[218]   STMicroelectronics NV, "RM0008 Reference manual for STM32F101xx, STM32F102xx, STM32F103xx, STM32F105xx and STM32F107xx advanced ARM®-based 32-bit MCUs - DocID13902 Rev 17," 2017.

[219]   Seeed Studio, "HC-12 Wireless RF UART Communication Module V2.4 - User Manual," 2016. [Online]. Available: https://statics3.seeedstudio.com/assets/file/bazaar/product/HC-12_english_datasheets.pdf%0A. [Accessed: 02-Dec-2016].

[220]   S. Thrun, J. Leonard, B. Siciliano, and O. Khatib, "Simultaneous Localization and Mapping," in *Springer Handbook of Robotics*, B. Siciliano and O. Khatib, Eds. Springer,

Dynamic Inductive Wireless Power Transfer for Lightweight Electric Vehicles
Luiz Alberto Lisboa da Silva Cardoso – University of Minho

446

2008, pp. 871–889.

[221] Douglas Brown, "Tracker - Video Analysis and Modeling Tool." Open Source Physics Project, 2018.

[222] N. Joyce, *Building Stata - The Design and Construction of Frank O. Gehry's Stata Center at MIT*. Cambridge, MA: The MIT Press, 2004.

[223] E. F. Schumacher, *Small is Beautiful - Economics as if People Mattered*. New York: Harper & Row, 1973.

Dynamic Inductive Wireless Power Transfer for Lightweight Electric Vehicles
Luiz Alberto Lisboa da Silva Cardoso – University of Minho

447